Mobile brain imaging to study visuo-spatial perception with ecological paradigms. Applications to healthy aging and visual restoration

Alexandre Delaux

Mobile brain imaging to study visuo-spatial perception with ecological paradigms

Applications to healthy aging and visual restoration

Emploi de l'électroencéphalographie mobile pour l'étude de la perception visuo-spatiale dans des paradigmes écologiques

Applications au vieillissement sain et à la restauration visuelle

Alexandre DELAUX

Sorbonne Université - Faculty of Life Sciences
Doctoral School 130: Informatique, Télécommunications et Électronique (EDITE)
Vision Institute - Aging in Vision & Action team

Jury composition

Barbara F. Händel Research group leader, University Hospital Würzburg	Reviewer
Radoslaw M. Cichy Professor, Freie Universität Berlin	Reviewer
Marlene Behrmann Emeritus Professor, Carnegie Mellon University	Examiner
Virginie van Wassenhove Research Director, CEA/NeuroSpin	President/Examiner

Thesis Supervision

Denis Sheynikhovich Associate Professor, Sorbonne Université	Supervisor
Klaus Gramann Professor, Technical Universität Berlin	Co-Supervisor
Angelo Arleo CNRS Research Director, Sorbonne Université	Team leader

Defended in Paris, on October 25th, 2023.

Doctoral Thesis

Abstract

Based on the observation that the three-dimensional and multisensory nature of the world shapes the functioning of the brain, this doctoral project focused on the study of human cognition through ecological experiments, particularly in the context of visual perception and spatial navigation. Current neuroimaging tools restrict the mobility of participants and thus fail to capture the full complexity of everyday activities. In order to overcome these limitations, this project developed methods to acquire and interpret brain activity under mobile conditions. To this end, recent technological improvements were leveraged to facilitate robust extraction of brain-related signals from electro-encephalography (EEG) recordings during motion. To deepen the interpretation of cortical dynamics by fully exploiting the potential of the improved temporal resolution of EEG, the mobile brain/body imaging approach was adopted, which advocates the co-registration of neural recordings with biometric measures such as body and eye movements.

The primary goal of this thesis was to better understand changes in visuo-spatial cognition during healthy aging. Spatial navigation, a ubiquitous skill in everyday life, relies on the integration of multiple sensory inputs, among which vision plays a central role. A major motivation for research on this topic is that aging is associated with a decline in navigational abilities, which affects the autonomy and well-being of older adults and may lead to isolation and neurodegenerative disorders such as Alzheimer's disease. By adopting an approach that considers more ecological aspects of spatial navigation, the results of this work challenge some established views in the literature on visuo-spatial cognition. They provide novel insights into the dynamic neural mechanisms underlying spatial behavior, and in particular into the scene-selective regions whose activity was modulated by expectations generated by natural environments. By illustrating how a downward gaze bias may interact with an impaired control of attention evident at the cortical level, they shed light on the detrimental effects of visual aging on navigation.

Furthermore, this project addressed the potential of mobile neuroimaging tools in the evaluation of visual restoration therapies for retinal diseases while patients performed visuo-spatial tasks relevant to daily activities. The study of neural markers associated with visual recovery promotes an objective assessment of the effectiveness of therapeutic interventions. In particular, EEG frequency analysis helped unravel an occipital alpha rhythm typical of natural visual processing induced by a novel optogenetic therapy in a late-stage *Retinitis Pigmentosa* patient.

These findings may have substantial socio-economic implications given the aging of the

global population and the associated increase in the prevalence of visual disorders. The outcomes of this research may be translated into urban planning recommendations to help older adults navigate complex, unfamiliar environments. They can also contribute to the development of more effective visual restoration therapies, ultimately making a significant difference in the daily lives of low vision patients.

In conclusion, this doctoral thesis emphasized the importance of ecological experiments for understanding human cognition and perception. By using mobile EEG and innovative paradigms, it contributed to the fields of visuo-spatial cognition, healthy aging, and visual restoration therapies. Its findings may have broader implications for improving the autonomy of older adults and visually impaired patients.

This thesis was carried out within a collaborative ecosystem, benefiting from the resources and expertise of the Paris Vision Institute. Cooperation with other research institutions, both national and international, contributed greatly to enrich its methodological approach and broaden the scope of its applications.

RÉSUMÉ

En constatant l'influence de la nature tridimensionnelle et multisensorielle du monde sur le fonctionnement du cerveau, ce projet s'est axé sur l'étude de la cognition humaine par le biais d'expériences écologiques, en particulier la perception visuelle et la navigation. Les outils de neuro-imagerie actuels entravent la mobilité des participants et ne reflètent donc pas toute la complexité des activités du quotidien. Pour y remédier, ce projet a développé des méthodes d'acquisition et d'interprétation de l'activité cérébrale dans des conditions de mobilité. À cette fin, de récents progrès techniques ont été mobilisés pour garantir l'extraction robuste des signaux cérébraux issus d'enregistrements d'électro-encéphalographie (EEG) pendant le mouvement. Pour enrichir l'interprétation de la dynamique corticale en exploitant pleinement la résolution temporelle accrue de l'EEG, l'approche mobile brain/body imaging *a été adoptée, préconisant le couplage des données EEG avec des mesures biométriques telles que les mouvements du corps et des yeux.*

L'objectif principal de cette thèse était de mieux comprendre les changements dans la cognition visuo-spatiale au cours du vieillissement sain. L'orientation dans l'espace, une aptitude essentielle au quotidien, repose sur l'intégration de multiples signaux sensoriels, parmi lesquels la vision est centrale. Une forte motivation à étudier ce sujet est que le vieillissement est associé à un déclin des capacités d'orientation, ce qui affecte l'autonomie et le bien-être des personnes âgées et peut mener à l'isolement et à des troubles neurodégénératifs. En étant plus proches des conditions écologiques de la navigation, les résultats obtenus remettent en question certains points de vue établis de la littérature. Ils apportent un nouvel éclairage sur la dynamique des mécanismes neuronaux sous-tendant les aptitudes visuo-spatiales, et en particulier dans les régions sélectives aux scènes. En rapportant un contrôle déficient de l'attention, évident au niveau cortical, associé à une tendance systématique à regarder vers le bas, ils illustrent les effets néfastes du vieillissement visuel sur la navigation.

En outre, ce projet s'est intéressé au potentiel de l'EEG mobile pour évaluer des thérapies de restauration visuelle au cours de tâches visuo-spatiales pertinentes pour les activités quotidiennes. Étudier les marqueurs corticaux associés à la récupération visuelle favorise une analyse objective de leur efficacité. En particulier, l'analyse EEG a mis en évidence un rythme alpha occipital, typique du traitement normal de l'information visuelle, induit par une nouvelle thérapie optogénétique chez un patient atteint de rétinite pigmentaire.

Ces résultats peuvent avoir des implications socio-économiques substantielles étant donné le vieillissement de la population mondiale et l'augmentation associée de la prévalence des troubles visuels. Les fruits de cette recherche pourront se traduire en recom-

mandations en matière d'urbanisme pour favoriser l'orientation des personnes âgées dans des environnements complexes. Ils pourront également servir à développer des thérapies de restauration visuelle plus efficaces afin d'accroître leur impact dans la vie quotidienne des patients.

En conclusion, ces travaux soulignent l'importance des expériences écologiques pour comprendre la cognition et la perception humaine. En s'appuyant sur l'EEG mobile et des paradigmes innovants, ils ont contribué aux domaines de la cognition visuo-spatiale, du vieillissement sain et de la restauration visuelle. Ces résultats peuvent avoir des répercussions sur l'amélioration de l'autonomie des personnes âgées et des patients malvoyants.

Cette thèse a été réalisée au sein d'un écosystème collaboratif, bénéficiant des ressources et de l'expertise de l'Institut de la Vision de Paris. La coopération avec d'autres instances de recherche a largement contribué à enrichir son approche méthodologique et à élargir le champ de ses applications.

ACKNOWLEDGEMENTS

First of all, my sincere appreciation to professors Barbara Händel, Radoslaw Cichy, Marlene Berhmann and Virginie van Wassenhowe for agreeing to evaluate this thesis dissertation. I'm also grateful to Benoit Cottereau and Fabrizio de Vico Fallani for taking part each year in the *Comité de Suivi de thèse*, and for their kind guidance of this work.

Obviously, my deepest gratitude goes to my thesis supervisors, Denis Sheynikhovich, Klaus Gramann and Angelo Arleo. Denis, many thanks for the relevance of your remarks and your ability to always pull up the projects and scientific communications with your rigor. Klaus, I am immensely indebted to you for having opened both the way to the methodology at the core of this thesis and the doors to your laboratory in Berlin, where I was kindly welcomed by you and your team to learn the rudiments of the MoBI approach. Thank you for your commitment to open science and international scientific collaboration, which has been very inspiring in my career as a young researcher. Angelo, I don't know if I'm quite capable of realizing how lucky I've been to have such a caring, available and attentive mentor. Thank you for the great trust and freedom you've given me throughout these four years, while always knowing how to challenge my ideas and help them mature. I am aware of the many efforts you have made to build a positive and synergistic working environment so that we can all conduct our research projects as smoothly as possible. I hope that the new chapter you are embarking on will give you full satisfaction in both your professional and personal life.

More broadly, I'm very grateful to all the people who have enabled me to conduct the research presented here. Firstly, the *StreetLab* team (especially Mylène and Johan) who generously shared their equipment and expertise with me as I struggled to develop my experimental paradigms. Many thanks to Francesco and Chloé for their help with the PIONEER project, an indispensable support in all the bumps we encountered when adapting the paradigms to EEG experiments. On the methodological side, I'd particularly like to mention Marius Klug and Lukas Gehrke, who provided me with the solid foundations of the mobile EEG pipeline during my time at the BPN in Berlin. I would also like to extend my warmest thanks to Benoit, who was always available to support me in the implementation of his source reconstruction method.

I'd also like to thank the staff at the Quinze-Vingts hospital, who made it possible to set up and characterize the *SilverSight* cohort. Many thanks to Stephen and Marion for their dedication to MRI acquisitions, without whom I wouldn't have had much data for the source

reconstruction model. But none of this would have been possible without the tremendous work of Jérôme, Sonia, Fabienne and all the other people who played a vital role with the members of the cohort, both through their professional and human qualities. In this light, I would also like to thank all the participants in the experiments, especially the members of the SilverSight cohort, who were always willing and patient, even when the sessions became uncomfortable or the technical bugs piled up. I also have a special thought for the patients in the PIONEER clinical study, whose courage and hope in research have won my admiration. I won't forget our discussions during the long 'gelling periods', which were often the occasion for inspiring life lessons.

Speaking of enriching encounters, I'm also very lucky to have been able to count on motivated and enthusiastic students to support me in my ever more ambitious experiments. In particular Ainhoa, who was essential in perfecting the famous 'shaving technique' to perfect 3D models, and Ilaria, with whom I discovered a passion for artificial grass that was no picnic. Bravo for what you've achieved during these internships, thank you for your dedication, always in a good mood, I hope I've been able to match you in my supervision and I wish you all the best in your professional career!

Nor should I forget those who invited me to share my know-how on their own projects, which greatly contributed to enhancing the value of my approach and enriching its scientific outlets: Stephen and Clément, whom I visited in Nice, and Sandrine and Louise, who made the trip from Switzerland. I'd particularly like to offer my support to Clément and Sandrine for the rest of their PhD journey, and wish them every success in their future endeavours.

However, it would have been very difficult to complete this thesis without the exceptional group of people in the *Aging in Vision & Action* laboratory, who brought fun and conviviality to these long years of hard work. Thank you Adrien for your inquisitive mind, which triggered more than one existential thought in me! Thank you Astrid for your enthusiasm and all those good times in St-Maur! Thank you Jérôme for all your gastronomic advice (I'm still actively following your Mapster)! Thank you Fabienne for enlivening our lunches with all your stories! Thank you Ornella for all those forced (but nonetheless enjoyable) breaks and our always stimulating and interesting discussions! Thank you Sonia for your constant kindness and all your sugary little attentions! Thank you Youri for sharing your passions and culinary talents! Thanks also to all the others who were there for varying lengths of time, but who brightened up this adventure during meal breaks or other game nights... I'll end this tour of the lab with its heart, the *bureau 4*, which helped me get through all the challenges. Jimmy, the youngest of the team but perfectly integrated nonetheless, thanks for your lively spirit and your sense of humor, and good luck with the end of the thesis on your own! Jothini, our animal specialist: the mice, of course, but I will also always remember the rippling rainbow parrot and the 'chollythomonthe'. Keep your guard up until the end, round 4 is almost over! JB, always a pleasure to work with you on the many projects we've undertaken together, I certainly couldn't have done so much without your help. Stay strong for the final stretch, remembering that it is better to let well alone! Last but not least, Marion, so many good memories in mind it's hard to sum up these rich years spent back to back in just a few

sentences... Thank you for your brilliant ideas, I've really appreciated our complementarity in our shared projects, and it's a good thing we didn't give in to the 'sloth' emoticon after all. Have fun in your next job, and go all out: they're not ready for your talent!

Finally, to put this thesis back in its ecological context, I would like to thank my friends and family for their support and encouragement. My special thoughts go to Jacques and Marylène, who have more than once warmly welcomed me into their home, without being upset by my lack of talkativeness during the complicated periods of writing. To my brother, who generously agreed to contribute his brain to science. To my sister, who has always been supportive and who made me proud that she also embarked on a doctoral adventure. And to my parents, who have never doubted me and have always been faithful advisors in my decisions. Thank you for looking after me from the start.

Of course, I've saved the best for last, my love, Florie. You always were on the front line of the emotional tides of the PhD, thank you for your essential and unfailing support. Patient to the end (despite the last extra year), you gave me the necessary balance between hard work and intensive cocooning. I look forward to the next 80 years at your side.

TABLE OF CONTENTS

List of Figures

List of Tables

ABBREVIATIONS

AIC	Akaike Information Criterion
AMICA	Adaptative Mixture Independent Component Analysis
ANOVA	Analysis of Variance
AR	Augmented Reality
BA	Brodmann Area
BEM	Boundary Element Model
BOLD	Blood Oxygen Level Dependent
CI	Confidence Interval
DT	Dwell Time
ECD	Equivalent Current Dipole
EEG	Electro-encephalography
EOG	Electro-oculography
ERP	Event-related Potential
ERSP	Event-related Spectral Perturbation
fMRI	functional Magnetic Resonance Imaging
fNIRS	functional Near-Infrared Spectroscopy
FoV	Field of View
IC	Independent Component
ICA	Independent Component Analysis
MoBI	Mobile Brain/Body Imaging
LSL	Lab Streaming Layer
MD	Mahalanobian Distance
MEG	Magneto-encephalography
MNE	Minimum Norm Estimation
MNI	Montreal Neurological Institute
MPA	Medial Place Area
MRI	Magnetic Resonance Imaging
OCT	Optical Coherence Tomography
OPA	Occipital Place Area
PCA	Principal Component Analysis
PPA	Para-hippocampal Place Area
RB	Rigid Body
ROI	Region of Interest
RMS	Root Mean Square
RP	*Retinitis Pigmentosa*
RSc	Retrosplenial Cortex
RSC	Retrosplenial Complex
SD	Standard Deviation
SEM	Standard Error of the Mean
SNR	Signal-to-Noise Ratio
SPV	Simulated Prosthetic Vision
SSR	Scene-Selective Region
VEP	Visually Evoked Potential
VF	Visual Field
VR	Virtual Reality
WSRT	Wilcoxon Signed Rank Test

OVERVIEW

Rationale of the thesis

The three-dimensional and multisensory nature of the world in which it operates shapes the functioning of the brain. Methodology-wise, this doctoral work stresses the idea that, for a more realistic study of both behavioral and neural correlates, human cognition should be investigated through ecological experiments (*i.e.*, as close as possible to the situations encountered in daily life). However, current state-of-the-art neuroimaging tools hinder participants' mobility and prevent experimental protocols from reproducing the multimodal aspect of everyday activities (J. L. Park et al., 2018). In order to shed new light on the understanding of human perception and cognition, this doctoral work aimed at developing methods that allow for the acquisition and the interpretation of neural activity in mobile conditions. Considering how humans primarily rely on vision to collect information from their environment (Barton, 2004), this thesis strived to demonstrate the validity and appeal of this approach for the study of cortical correlates associated with visual perception of space. With the ultimate intention of making this work relevant to contemporary social and health challenges, this project was designed to provide novel insights on the evolution of visuo-spatial perception throughout adulthood in both healthy and pathological contexts.

On a fundamental level, the main contributions of this work concern the study of visuo-spatial cognition during healthy aging. Spatial navigation is an essential daily ability that requires the integration of multimodal information (Arleo & Rondi-Reig, 2007) while being deeply reliant on vision (Ekstrom, 2015). Thus, it is one of the neuroscientific fields that would benefit the most from a methodological renewal involving the investigation of brain correlates of spatial cognition in more ecological settings. The interest for this topic also stems from the numerous reports that navigational skills decline across the life span (Lester et al., 2017). Impairments in spatial navigation and orientation (*e.g.*, spatial disorientation and wayfinding issues) have a detrimental impact on older adults' autonomy and well-being, including decreased mobility and increased avoidance of unfamiliar environments (Taillade et al., 2016). These self-inhibitory spatial behaviors can lead to isolation and lower visuo-cognitive stimulation, ultimately resulting in an increased risk of progression of age-related neurodegenerative disorders (Gelfo et al., 2018). At the same time, spatial navigation tasks have been shown to provide early-stage behavioral and neural indicators of pathological aging including preclinical markers of Alzheimers disease (Allison et al., 2016; Coughlan et

al., 2018). Hence, investigating spatial navigation in the older adult population could have far-reaching implications for societies and individuals. Although the decline of spatial abilities with age has been extensively studied from the perspective of memory and executive functions degradation, the influence of age-related visual impairments has received relatively little focus to this day (Lester et al., 2017). Interestingly, recent studies provided neuroimaging evidence that altered visual processing could contribute to spatial navigation deficits in aging (Koch et al., 2020; Ramanoël et al., 2020), in line with accumulating literature showing that visual impairments in older adults are a significant risk factor for cognitive decline (Vu et al., 2021). The widespread use of structural and functional magnetic resonance imaging (MRI) has nonetheless hindered the possibility of considering spatial navigation in its entirety because perceptual (other than visual) and motor aspects are omitted. To address this caveat, a critical next step for obtaining a more accurate characterization of human brain aging is to take into account the multimodal nature of spatial navigation by designing studies that encompass multiple perceptual, locomotor, and cognitive factors (Holtzer et al., 2014).

For this purpose, this thesis harnesses recent developments in techniques for recording the brain in moving humans, more specifically mobile electro-encephalography (EEG). It follows the guiding steps of the mobile brain/body imaging (MoBI) approach (Gramann et al., 2011), which involves the co-registration of neural recordings with biometric measures such as body and eye movements to enable neuroscientists to design mobile experiments that unveil new dimensions of brain signal interpretation. Successful implementations of this approach have already provided evidence that accounting for mobility was pivotal to fully understand brain correlates of spatial behavior. These novel paradigms challenge the results of prior studies conducted in static conditions, for example regarding multisensory integration during spatial orientation (Ehinger et al., 2014; Gramann et al., 2021). Such experiments have also begun to unravel the complex interplay between visuo-cognitive processes and locomotion at the cerebral level (Cao & Händel, 2019; Ladouce et al., 2019), which is not accessible to functional magnetic resonance imaging (fMRI) studies where the participant lies in the scanner. Furthermore, a seminal mobile EEG work about healthy aging identified neural markers associated with worsened visual processing during ambulation that were more pronounced in older adults (Protzak et al., 2021). These results bring into focus the importance of understanding how cognitive resources are reallocated between perceptual, motor, and higher-order processing in older adults during natural, active spatial behavior.

On a more translational level, this project aimed at demonstrating how this methodological framework could benefit to the understanding of perception in a pathological visual aging context. Specifically, it explored the potential of mobile neuroimaging tools to provide objective neural markers for the evaluation of visual restoration approaches. The eye and the brain work together in a coordinated manner to process visual information. The eye captures visual stimuli and transmits them to the brain, where specialized regions, such as the visual cortex, process and interpret the information, before making them available to the rest of the cortex. When attempting to restore vision in patients with retinal diseases, understanding the efficient transmission of signals from the restored retina to cortical visual areas is crucial

for the successful development of these therapies (Chaffiol et al., 2022). Indeed, as the adult visual cortex demonstrates high degrees of neuroplasticity (*i.e.*, the reorganization of brain circuits to serve alternative functions), there is no guarantee that it retained the potential to "see" after a prolonged period of abnormal or absent visual experience (Castaldi et al., 2020), all the more so when restored visual input is not strictly identical to the original. At the same time, it suggests that the adult visual brain still possesses the capacity to adapt to interpret the signal coming from a treated retina. This all-the-more advocates for the monitoring of cortical activity along the therapeutic journey, to understand and evaluate the neural mechanisms triggered by the medical intervention. As the ultimate goal of these treatments is to deliver a sufficient visual recovery to help blind patients in their daily lives (Ghezzi, 2023), mobile EEG provides the opportunity to study brain correlates associated with tasks as close as possible to patient' needs. Furthermore, it enables to put the perceptual experience in a holistic context and to study the consequences of artificial vision on the interplay with other domains of cognition. Of particular relevance when designing visual restoration devices that patients will adopt on a daily basis is the cognitive fatigue resulting from its usage (Erickson-Davis & Korzybska, 2021). Suitably, EEG is a widely used physiological index to provide an online and continuous measure of cognitive load (Antonenko et al., 2010). Thus, its integration into protocols evaluating the efficiency of visual recovery is an important asset for advancing the field of vision restoration and improving outcomes for patients with severe visual impairments.

Socio-economic impact

The investigation of visuo-cognitive aging targets a crucial socio-economic issue insofar as it profoundly affects the quality of life while being part of a long-term demographic evolution. Global population changes will make the number of people aged 65 or older to nearly triple between 2010 and 2050 and become about 1.5 billion, *i.e.* 15% of the world population (source: United Nations). In Europe, which harbors most of the worlds oldest countries in terms of population age, around 28% of people will be more than 65 years old in 2050 (source: United Nations). Aged people are subject to a loss of productivity and autonomy due to visual disturbances and visuo-cognitive deficits, with a substantial economic impact of approximately US$ 650 billion annually in indirect costs (source: International Federation on Ageing). The loss of autonomy is directly related to the inability of older adults to move about in large and complex environments (*e.g.*, train stations or shopping centers), and therefore better understanding how they process and use information in these situations could help propose important changes in urban planning. Additionally, by broadening our understanding of age-related navigation deficits, the neuroimaging of spatial navigation in mobile conditions could shed light on the etiology of neurodegenerative diseases in which spatial navigation can deteriorate dramatically, as it is the case in mild cognitive impairment and Alzheimers disease. The earlier diagnosis of these dementias, which may concern up to 115.4 million people in 2050, has societal benefits now clearly established (*e.g.*, delayed institutionalization; Prince et al. 2013).

Restorative vision technologies raise enormous hopes for the patients suffering from visual loss, and research efforts in this field are steadily increasing (Borda & Ghezzi, 2022). In 2020, an estimated 596 million people suffered from distance vision impairment worldwide, of which 43 million are considered legally blind (Burton et al., 2021). For individuals themselves, blindness dramatically affects educational and employment opportunities (Bourne et al., 2021), leading to physical and mental comorbidities (Court et al., 2014). Severe vision impairments often indirectly impact family members, friends and other carers, due to the resulting high degree of disability in people affected. Hence, visual impairment poses a global financial burden for society, with an estimated cost of productivity loss as high as US$ 16.5 billion in the United States of America (WHO team, 2019). Despite significant efforts to develop and commercialize visual prostheses in the past 30 years, companies have faced economic problems related to cost of research and development, regulatory approval, and low acceptance of the device by clinicians and patients (Chevrie, 2020). In complement to direct measures of the visual gain from novel therapies, cortical correlates of visual restoration acquired in more ecological conditions can enrich our understanding of the adaptive and compensatory changes occurring within the brain. Such quantitative and standardized assessments can ultimately guide research towards more efficient solutions directed at improving the capacity of patients to make practical use of their devices in the long-term (Borda & Ghezzi, 2022).

Ecosystem of the project

This doctoral work was carried out within the *Aging in Vision and Action* laboratory headed by Dr. Angelo Arleo, at the Vision Institute in Paris. The Vision Institute is a world-renowned center for integrated research on vision and eye diseases. It brings together clinicians, researchers, and companies in a vast, synergistic ecosystem that was highly beneficial to this thesis.

First, the set-up of the Vision Institute in the heart of the *Quinze-Vingts* National Ophthalmology Hospital was essential to enable the *Aging in Vision and Action* laboratory to form a cohort study population of ~300 participants, named *SilverSight*. This cohort, established and followed-up ever since 2014, is devoted to clinical and functional investigations of visuo-spatial aging with high-dimension cross-sectional and longitudinal data (Lagrené et al., 2019). Notably, each enrolled participant is profiled through a manifold screening, including ophthalmological, visuo-functional, audio-vestibular, sensorimotor, cognitive, and neuropsychological evaluations. Additionally, a series of questionnaires are administered to evaluate the medical record as well as self-reported quality-of-life items with respect to vision and autonomy. This clinical setting also gives access to a neuroimaging center equipped with a MRI scanner providing structural and functional information on the brain of cohort participants that was pivotal to this work.

Second, the Vision Institute hosts the *StreetLab* company, which operates a set of innovative research platforms (*e.g.*, reproducing a portion of a street or an apartment) dedicated to the investigation of human behavior in ecological-like conditions. These platforms enable numerous environmental parameters to be monitored in a standardized and repro-

ducible manner (*e.g.*, light intensity & temperature, 3D surround sound). Full body and gaze kinematics can be simultaneously recorded through an optical motion capture system and a wearable eye tracker, respectively. In addition, virtual reality (VR) headsets are available, considerably enlarging the possibilities for immersing subjects in more controlled and tunable environment while maintaining a high-level of mobility.

Third, as the Vision Institute produces cutting-edge research on blindness and visual disorders, it breeds companies whose ambition is to bring visual restoration therapies to the target patients. These companies benefit from the institute ecosystem to conduct clinical trials to assess the safety of the treatment and test its efficacy in close to daily life conditions. It was thanks to this facilitating situation that a collaboration with the *GenSight* company on their clinical trial named PIONEER was initiated on these questions during this doctoral thesis (see Chapter 10).

In complement to its host laboratory ecosystem, this thesis also inscribed into a network of international collaborations that contributed to enrich its methodological approach and the scope of its applications. First and foremost, the *Biological Psychology and Neuroergonomics* laboratory at the *Technische Universität Berlin*, headed by the Pr. Klaus Gramann who co-supervised this work. This laboratory is the pioneer of the MoBI approach and thanks to an initial and continued knowledge sharing, this collaboration was key to the successful development of the methodological axis of this thesis. Second, owing to a former member of the *Aging in Vision and Action* laboratory, Dr. Stephen Ramanoël, this project also took part in the design and analysis of an EEG experiment on visuo-spatial perception throughout adulthood conducted in the *Laboratoire Motricité Humaine, Expertise, Sport, Santé* at *Université Côte d'Azur*, in Nice, France (see Chapter 11). Finally, owing to the participation of the host laboratory and *StreetLab* to the *European network for integrated training on innovation therapies for vision restoration*, this doctoral work also contributed to the project of Sandrine Hinrichs, PhD student from the Laboratory of Neural Engineering at *École Polytechnique Fédérale de Lausanne*, entitled "Use of virtual reality for a rational design of retinal prostheses" (see Chapter 12).

Ethical considerations

This thesis involved clinical screening and experimental testing of a human study population. All experiments were compliant with European ethical regulations (including Helsinky Declaration and the Charter of Fundamental Rights). Data management procedures were approved by the *Commission Nationale de l'Informatique et des Libertés*, and they were compliant with the European General Data Protection Regulation.

To the exception of the PIONEER clinical trial (see below), all experimental procedures were non-invasive and were ethically approved by the respective local ethics committees: the *Comité de Protection des Personnes Ile de France V* and the *Agence Nationale de Sécurité du Médicament et des Produits de Santé* in Paris, the ethics committee of the Institute of Psychology & Ergonomics, of *Technische Universität Berlin* in Berlin, and the *Comité d'éthique pour la Recherche*, of *Université Côte d'Azur* in Nice. Clinical examinations con-

cerning *SilverSight* cohort enrollment were performed under medical supervision at Clinical Investigation Center of the *Quinze-Vingts* Hospital, and experiments with cohort participants were all conducted at the Vision Institute in authorized laboratories for biomedical research (approved by the *Agence Régionale de Santé Ile de France*). All participants were informed about the purpose of the study and the clinical and experimental protocols, they signed a consent form on a voluntary basis, received compensation per each clinical/experimental session, and they were able to retract any time.

The PIONEER study protocol was approved by the *Agence Nationale de Sécurité du Médicament et des Produits de Santé*, the United States Food and Drug Administration, the Medicines and Healthcare products Regulatory Agency and the following national/local ethics committees and institutional review board: *Comité de Protection des Personnes Île-de-France III*; North East-York Research Ethics Committee; and Human Research Protection Office at the University of Pittsburgh. Study participants provided written informed consent before enrollment, according to the CARE guidelines.

Roadmap of the manuscript

Part I of this manuscript provides the reader with the theoretical framework of this doctoral work. The first four chapters of this part (*i.e.*, Chapters 1 to 4) review the state-of-the-art by crossing the fields of research that underlie this thesis, *i.e.*, visuo-spatial perception (Chapter 1), healthy aging in the context of spatial cognition (Chapter 2), restoration approaches to pathological visual aging (Chapter 3), and neuroimaging in near-ecological conditions (Chapter 4). Chapter 5 concludes this part by listing the main objectives that stemmed from the reviewed body of literature and that have been addressed by this project.

Part II presents the main original contributions of this thesis. The first chapter (*i.e.*, Chapter 6) describes the methodological approach set forth to address all experimental questions (*e.g.*, the conception of MoBI paradigms, the processing of mobile EEG data, the construction of individualized EEG source localization models). The three next chapters (*i.e.*, Chapters 7 to 9) detail the original experimental contributions to the fundamental axis of this thesis, *i.e.* visuo-spatial cognition in mobile conditions throughout adulthood. Chapter 7 first provides a proof-of-concept for the application of the MoBI approach to landmark-based navigation in young adults. Then, Chapter 8 puts the focus on the scene-selective regions (SSRs) and on the study of their activity with EEG source localization. The study presented in this chapter specifically tests the influence of the vertical position of navigational cues on the oculomotor behavior and brain oscillatory dynamics of older adults compared to young adults. Finally, Chapter 9 illustrates the combination of MoBI with source reconstruction to study properties of the occipital place area (OPA) in mobile conditions throughout adulthood, focusing on the perception of navigational affordances, and more precisely on the walkable distance between the observer and a door at the end of a path. The last chapter of this part (*i.e.*, Chapter 10) regroups the experimental investigations associated with the EEG ancillary study of the PIONEER clinical trial, contributing to the translational axis of this project, *i.e.* providing objective neural markers for the evaluation of an optogenetic therapy to late-stage *Retinitis Pigmentosa* (RP). The work presented in this part led to two original contributions in international peer-reviewed journals, one publication is currently in preparation, and three others are planned in the months following the end of the thesis.

Part III presents additional contributions to this thesis, yielded by external collaborations that benefited from the methodological framework developed during this doctoral work. The first chapter (*i.e.*, Chapter 11) extends the study of brain dynamics attributable to SSRs in a navigational context throughout adulthood. The second chapter (*i.e.*, Chapter 12) provides an additional example where mobile EEG was applied to assess the cognitive benefit of an alternative design of visual prosthesis with an objective measure. One original publication in an international peer-reviewed journal relative to the work presented in this part is currently in preparation.

Part IV first proposes a synthetic discussion of all contributions (*i.e.*, Chapters 13 to 15), in the light of the theoretical considerations reviewed in Part I. Chapter 13 puts in perspective the methodological contributions, and it proposes ideas for future improvements. Chapter 14

assembles the various lines of research addressing the fundamental axis to condense its most significant achievements, and it attempts to define the next promising hypotheses to investigate. Chapter 15 summarizes contributions to the translational axis, and it tries to identify the next key steps to pursue the seminal work presented in this thesis. Finally, it concludes on the main outcomes of this doctoral work (*i.e.*, Chapter 16).

Appendix A provides a complete list of contributions, *i.e.*, journal papers, international and national conferences presentations.
Appendix B presents the set of decision-making rules followed during the manual inspection of Brain independent components.
Appendix C presents useful tips for the usage of *RecFusion* software.
Appendix D presents the supplementary material associated with Chapter **7**.
Appendix E presents the supplementary material associated with Chapter **8**.
Appendix F presents the supplementary material associated with Section **10.1**.

Part I

THEORETICAL FRAMEWORK

CHAPTER 1

VISUO-SPATIAL PERCEPTION

The primary goal of this chapter is to define the scope of visuo-spatial perception as it has been addressed throughout this doctoral work. It proposes an overview of the main concepts in this field that are relevant to this thesis in order to familiarize the reader with the scientific questions posed in the experimental paradigms (Section **1.2**). Specifically, it will first focus on how visual field asymmetries interact with the spatial structure of visual information in natural environments. It will then discuss what are the essential properties an object should have in order to achieve navigational relevance. Finally, it introduces the core concepts necessary to understand the importance of agency and mobility in the perception of real-world scenes.

Subsequently, the current state-of-the-art on the neurophysiological basis of human visuo-spatial perception is reviewed (Section **1.3**). Proceeding from the lowest to the highest hierarchical level in the visual system, it first recalls the evidence for how the visual system inherits from the retinotopic organization of the retina, then discusses the properties of the ensemble of cortical regions that have been found to be dedicated to scene processing, and finally introduces the major cerebral nodes involved in navigational abilities.

The notions introduced in this chapter illustrate how visual-spatial perceptual abilities can be influenced by the natural properties of the environment, taking into account both its three-dimensional, interactive character and the regularity of its structural organization. By presenting the known neural bases underlying these abilities, it also provides potential targets for studying them in ecological paradigms combined with neuroimaging. In particular, the literature review identified scene-selective regions (SSRs) as key elements of visuo-spatial information processing at the interface between the early visual system and high-hierarchical cognitive regions. Interestingly, knowledge of their properties is largely limited to static scene presentation and suffers from a lack of temporal resolution, motivating electro-encephalography (EEG) neuroimaging approaches to address this caveat.

1.1 Background

1.1.1 What is spatial cognition?

Spatial cognition may be defined as the manifold processes by which an individual acquires, uses and stores knowledge about the surrounding world ultimately serving orientation and navigation within it, consciously or not. In particular, it involves the ability to perceive and estimate spatial metrics (*e.g.*, distances, angles, *etc.*), to memorize and recognize objects and places which are useful for orientation, and eventually to form internal representations of space and manipulate them mentally (Cona & Scarpazza, 2019; Wei et al., 2020).

Spatial cognition is not bound to visual perception as it actually requires the integration of a myriad of multimodal cues into a representation of surrounding space that allows the agent to know its own position, and to select the proper navigation strategy to achieve its intended goal (Arleo & Rondi-Reig, 2007). As human navigation is primarily dependent on vision (Ekstrom, 2015), this chapter puts the focus on the aspects directly concerning the visual pathway, but the integration with other perceptual and motor processes as well as higher cognitive abilities will be discussed in the context of healthy aging in Section **2.3**.

1.1.2 What kind of spatial information is available from vision ?

A great diversity of spatial information is available from the visual sensory input, which can be classified according to two distinct origins: allothetic and idiothetic.

From an allothetic perspective (*i.e.*, external stimuli coming from the environment), vision is the dominant source of information for spatial cognition. Central to navigation, spatial relationships are extracted from the visual input to form representations of the environment and locate the observer within it. Vision is also the principal contributor to object recognition (*i.e.*, the ability to rapidly recognize objects despite substantial appearance variation; DiCarlo et al. 2012) that is essential to identify elements that may serve later as landmarks (see Section **1.2.2** for more details about this concept). Additionally, real-world scenes contain a wealth of structural and functional information useful for navigation (Greene & Oliva, 2009a). When they introduce a polarization of the environment, geometric features of space can directly serve as cues for orientation, *e.g.* a rectangular room where one can identify a long *vs.* a short axis (Stankiewicz & Kalia, 2007; Tommasi et al., 2012). Eventually, properties of spatial layout, such as an environment's mean depth and openness, critically frame the navigable space defining boundaries thus restricting locomotion. It deeply influences our expectations about where and how we can move in this space (see Section **1.2.3.3**; Oliva and Torralba 2001). For example, one can run in an open field, but not in a small and enclosed cave. From an evolutionary perspective, perceiving how navigable a place is or whether it affords concealment is of high survival value (Kaplan, 1992).

From an idiothetic perspective (*i.e.*, sensory signals related to self-motion), vision provides the navigator with the optic flow, *i.e.* the pattern of relative visual motion perceived when moving in the environment (Fortun et al., 2015). It inherently conveys information

related to body and head motion that contributes to the dynamic update of the position and orientation of the navigator by the brain (a process known as path integration; Mittelstaedt and Mittelstaedt 1980).

Furthermore, spatial information about location can be represented according to two distinct types of reference frames. In an *egocentric* frame of reference, locations are represented relative to self position, whereas in an *allocentric* frame of reference, locations are encoded relatively to an element of the external world, including the body of the observer (Burgess, 2008). This dissociation is further reflected in the solving orientation tasks and remembering the route to a goal, where egocentric strategies refer to the adoption of an automatic response to a cue (*e.g.*, "I must turn right when arriving at the bakery") and allocentric strategies rely on a map-based representation of the environment (Ekstrom et al., 2018).

1.2 Visuo-spatial perception

Throughout this doctoral work, visuo-spatial perception refers to the neuro-physiological processes involved in acquiring, extracting, and interpreting spatial information contained in the visual input captured by the eyes. It encompasses a wide range of processes along the entire visual pathway, from the organization of photosensitive cells onto the retina to the integration of consolidated visuo-spatial concepts into higher-level areas of the brain involved in spatial cognition. In the scope of this thesis, the following aspects of visuo-spatial perception were addressed:

- How does the spatial distribution of visual stimuli onto the retina shape visual processing?
- What characteristics of an object are important to make it relevant for navigation?
- What kind of information useful for mobility is available in real-world scenes?

1.2.1 The visual field: spatial asymmetries

The visual field (VF) is the entire area that can be seen when the eyes are fixed on a central point. A typical monocular VF spans approximately 60° nasally to 107° temporally and from 70° above the horizontal meridian to 80° below. The combined VF size from both eyes spans ±107° across the horizontal axis. The binocular zone, *i.e.* the area which is seen by both eyes at the same time, covers ±60° around the fixation point (Ghezzi, 2023). It can be separated into spatial regions associated with distinct functional roles (see Figure **1.1** for an illustration). This division owes to the inhomogeneous topographic organization of retinal cells and the intrinsically biased distribution of visual information available from different parts of the VF.

1.2.1.1 Central *vs.* Peripheral

A first level of spatial division lies in the eccentricity of the stimulus from the fixation point, distinguishing a central *vs.* a peripheral region. The central VF corresponds to the area of

the VF that is focused on the fovea, *i.e.* the central region of the retina. The density of photoreceptors peaks in the fovea (Curcio et al., 1990), granting this region the highest spatial resolution of the retina. It is thus associated with a high acuity and contrast sensitivity which permits the perception of fine spatial details (Stewart et al., 2020). Outside the fovea, as the resolution decreases with eccentricity, the peripheral VF is tuned for coarse spatial scales, in line with the naturally occurring distributions of depths and disparities in the real-world (Maiello et al., 2020). In that regard, the peripheral VF is mostly involved in processing motion, detecting objects in the environment to guide eye movements or actions, and providing spatial context (Stewart et al., 2020).

1.2.1.2 Left *vs.* Right

A second level of spatial division is linked to the horizontal axis, along which the left and right VFs are separated. This distinction pertains to the wiring of the visual system from the eye to the brain. Indeed, the primary visual areas in the left hemisphere receive input from the right VF while those in the right hemisphere process input from the left VF (Wurtz & Kandel, 2000). This organization may have an impact on visuo-spatial perception as the right hemisphere is often reported to be more involved in spatial processing that the left hemisphere (Weintraub & Marsel Mesulam, 1987).

1.2.1.3 Upper *vs.* Lower

The third and final level of spatial division is linked to the vertical axis, with the upper and lower VFs located respectively above and below the horizontal meridian. A first asymmetry between these regions pertains to the anatomy of the eye and the skull (*i.e.*, the eyebrow arch restricts the upper VF), which typically reduce the extent of the upper VF with respect to the lower VF (see Figure **1.1**). Second, the superior hemiretina of humans exhibits a greater density of ganglion cells than the inferior hemiretina (Curcio et al., 1987), suggesting a bias towards processing information coming from the lower VF. Lastly, it appears

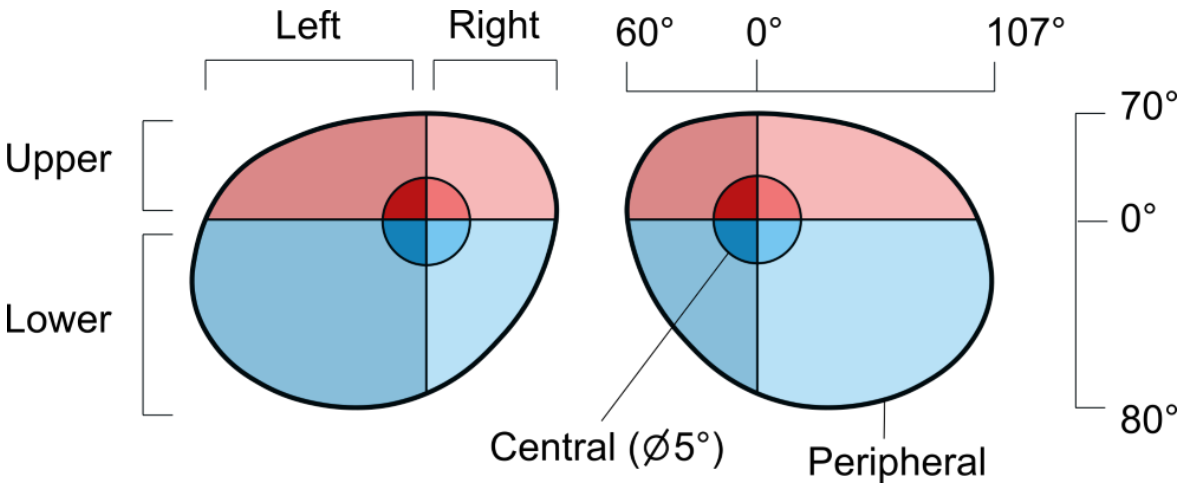

Figure 1.1: Schematic illustration of the main spatial divisions of the visual field from both eyes. Values indicate the typical visual field extent for a young healthy adult (Ghezzi, 2023).

that this separation is reflected in the structural organization of the visual pathway in the brain. Neuroscientists have identified a dorsal stream and a ventral stream with distinct functional specializations (see Section **1.3.1.2**), exhibiting preference for the lower and upper VFs inputs (Kravitz et al., 2013; Silson et al., 2015). These specializations are dictated by the fundamentally different nature of the visual information available in each VF. Indeed, the far (*i.e.*, extrapersonal) visual space, which involves extensive visual search and action planning, falls mainly within the upper VF, while the near (*i.e.*, peripersonal) visual space, which calls for visuo-motor manipulation skills, is exclusively encompassed by the lower VF (Previc, 1990). Thus, upper-lower heterogeneity is pervasive across a wide array of perceptual and cognitive tasks. On the one hand, the lower VF allows for better visual acuity, contrast sensitivity, spatial attention, and motion processing of stimuli (Carrasco et al., 2001; Lakha & Humphreys, 2005; Levine & McAnany, 2005; Regan et al., 1986; Rezec & Dobkins, 2004; Skrandies, 1987). The upper VF, on the other hand, favors abilities such as visual search, change detection, and categorical processing (Niebauer & Christman, 1998; Pflugshaupt et al., 2009; Previc & Naegele, 2001; Rutkowski et al., 2002).

1.2.2 What makes an object a landmark?

A landmark is a discrete element of the environment associated with a position, a behavioral response or a spatial relation with other elements (Presson & Montello, 1988). To be actually used in a navigation context, it is required for a landmark to be persistent (*i.e.*, immutable, stable), salient (*i.e.*, detectable and identifiable), and informative (*i.e.*, uniquely associated with a known position or action; Stankiewicz and Kalia 2007). Landmarks can be of various kinds, the most common forms being either a particular object in the environment (*e.g.*, a monument or a remarkable tree) or an element integrated into a flat surface (*e.g.*, a storefront or graffiti on a wall).

The characteristics which allow certain objects, among the multitude of incoming visual information, to attain navigational relevance is still a matter of debate (Chan et al., 2012). Inherent attributes contributing to the saliency of objects encompass factors such as size, color, and distinctiveness (Auger & Maguire, 2018; Auger et al., 2012; Miller & Carlson, 2011; Stankiewicz & Kalia, 2007). Large, colorful objects than can easily be spotted from a distance, and displaying unique traits with respect to the surrounding environment tend to be favored choices for wayfinding endeavors. While saliency holds a pivotal role, the paramount criterion for employing a particular object as a spatial reference relies on its informativeness, primarily dependent upon non-physical attributes such as location. A wealth of research has unequivocally demonstrated that object positioning within an environment significantly influences spatial behavior. Notably, objects situated at decision points (Janzen, 2006) or in close proximity to the goal destination (Waller & Lippa, 2007) emerge as the most discernible and pragmatic stimuli for navigation. Additionally, the embedding in spatial representations depends on the relative distance of objects from the navigator. While proximal cues may offer heightened reliability, as they engage action-based memories of

learned trajectories, distant cues facilitate the formulation of precise cognitive maps (Foo et al., 2005; Hartley et al., 2003; Hurlebaus et al., 2008; Jabbari et al., 2021).

1.2.3 Scene perception

Apart from the processing of objects useful to orient, the visuo-spatial system also needs to process the surrounding environment as a whole to understand spatial relationships and navigate within it, an ability referred to as "scene perception".

1.2.3.1 What is a scene?

Henderson and Hollingworth (1999) offer the following definition of a scene: *"A scene is a semantically coherent (and often nameable) view of a real-world environment comprising background elements and multiple discrete objects arranged in a spatially licensed manner"*. Under this definition, a scene should not be limited to a specific viewpoint of a real-world environment (*i.e.*, a photograph; G. L. Malcolm et al. 2016). It involves the observer within it and this level of interaction makes a fundamental distinction between object perception and scene perception: whereas objects are spatially compact entities that one *acts upon*, scenes are spatially distributed entities that one *acts within* (Epstein, 2005).

There are several reasons why the brain might care about scenes and why the human visual system may have specialized systems for processing them (see Figure **1.2**; Epstein and Baker 2019; G. L. Malcolm et al. 2016). Scenes are associated to locations in the world, so a goal of scene processing is to recognize if a scene is a known place ("this is *my* kitchen", *i.e.*, identification) or presents the characteristics of a particular kind of place ("this room is a kitchen", *i.e.*, categorization). During navigation, scene processing is directed towards the extraction of the spatial structure of a scene to orient relatively to it or plan a path through it. As objects always appear in scenes, scene processing systems analyze scenes to understand the typical location of an object within it to ultimately guide visual search or to obtain clues as to an object's identity. These considerations demonstrate how scene perception is ecolog-

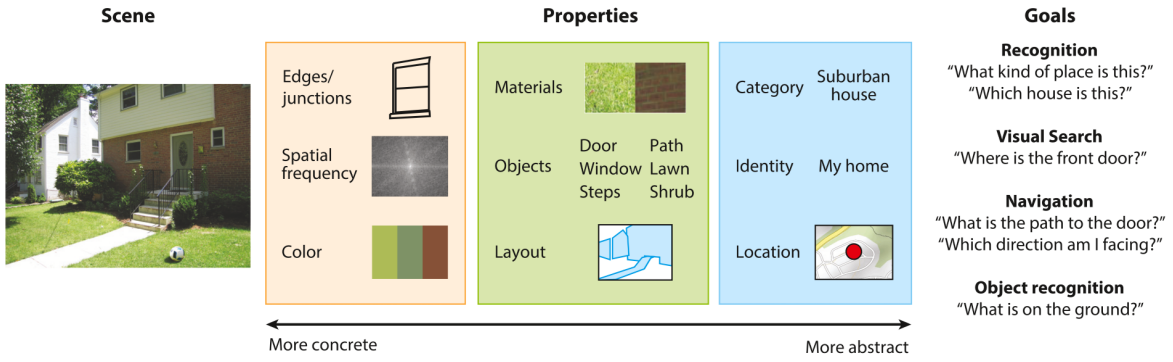

Figure 1.2: Main components of scene perception. Scene perception depends on both multilevel properties of the image and the observer's goals. The visuo-spatial system analyzes many properties of scenes, including low-level features (*e.g.*, edges, color), mid-level elements (*e.g.*, layout, objects), and high-level semantic and spatial properties (*e.g.*, scene category). The results of these analyses can service several behavioral goals. Reused from Epstein and Baker 2019.

ically important for humans, that are remarkably good at it: parsing landscapes, cityscapes, and rooms is just as natural as understanding faces, bodies, animals, and tools (Epstein & Baker, 2019).

Grasping the variety of these reasons is important to pose the theoretical framework to investigate the cognitive mechanisms underlying scene processing (G. L. Malcolm et al., 2016). While the physical attributes of our proximate environment are generally stable, our immediate objectives within it are inherently variable. At any given moment, different visual aspects of an environment will be prioritized based on our current goal. Nonetheless, this dynamic essence of scene understanding is frequently overlooked, as research endeavors tend to center around isolated tasks. Consequently, it is hard to discern the extent to which these empirical findings generalize to scene understanding in the real world (G. L. Malcolm et al., 2016).

1.2.3.2 Scene properties

Real-world scenes are complex visual stimuli (see Figure **1.2**; Epstein and Baker 2019; G. L. Malcolm et al. 2016) encompassing multiple descriptive layers. These layers span from fundamental low-level attributes originating in the retinal image (*e.g.*, edges, spatial frequency, color) to more intricate characteristics forged within higher-order cerebral regions (*e.g.*, object identity, scene category, action affordance). Although each property might individually predict particular behaviors, their inherent co-occurrence across scene categories is frequently overlooked (Torralba & Oliva, 2003). For example, these properties can either be correlated (*e.g.*, beach scenes typically encompass expansive open spaces, distant objects, and low spatial frequencies) or independent (*e.g.*, both urban and forest scenes might be characterized by high spatial frequencies and vertical edges). Consequently, disentangling the distinct contributions of individual properties to scene understanding without considering their potential interactions is a complex task, potentially leading to misguided interpretations.

The spatial structure of natural scenes, *i.e.* the likelihood of finding specific objects and features together, or in different parts of the visual space, is deeply rooted in the surrounding environment (see Greene 2013 for an extensive review). As the diagnostic value of a visual property also depends on prior experience of the observer (Greene et al., 2015) as well as its co-occurence with other features (G. L. Malcolm et al., 2014), the constant exposure to such regularities form expectancies that bias the processing of visual stimuli (Bonner & Epstein, 2021; Kaiser & Cichy, 2018a, 2018b). The consistency of the expected *scene grammar* (Võ & Wolfe, 2013) was observed to enhance the efficiency of interactions with objects, to strengthen memory of the environment, and to speed search within it (Draschkow & Võ, 2017).

These considerations highly interact with the VF biases described above, especially for the dichotomy between the upper and the lower VFs, as the vertical distribution of elements in the VF is the least dependent in the oculomotor behavior. This observation is particularly relevant for navigational cues. Indeed, objects that will serve as landmarks are naturally distributed along the vertical axis, but the ones expected in the lower part of the scene are

proximal to the observer while the ones anticipated in the upper part are usually distal objects (Greene, 2013; Groen et al., 2017; Hafed & Chen, 2016; Saleem, 2020). Conversely, it is interesting to note that the spatial layout of the scene is often extracted from salient geometric features in the lower VF, typically boundaries (Tommasi et al., 2012).

1.2.3.3 Affordances

As highlighted above with the many behavioral goals that can be associated with scene understanding, there is a strong link between vision and action in real-world scenes. This interaction between the observer and its environment was introduced long ago in theoretical frameworks of cognition with the concept of 'affordance' (Gibson, 1986). This term regroups *"the possibilities for use, intervention, and action which the physical world offers a given agent [which] are determined by the 'fit' between the agent's physical structure, capacities, and skills and the action-related properties of the environment itself"* (Clark, 1999). Action affordance is a well-known component of how we consider objects (Bainbridge & Oliva, 2015), and it has even been shown to guide visual search for items in scenes (Castelhano & Witherspoon, 2016). However, apprehending scenes themselves from the perspective of what actions they can afford is relatively new in the literature (G. L. Malcolm et al., 2016). Interestingly, a recent work demonstrated that affordances are better predictors of scene category in the human brain than other visual features (*i.e.*, a bedroom is primarily classified as *'a place that affords sleeping'*; Greene et al. 2016), suggesting that this is a central component of natural scene understanding.

Navigational affordances, *i.e.* possibilities for movement and navigation within a scene, constitute a particular sub-category of the concept of affordance that was of interest to this thesis. Indeed, one of the primary roles of the visuo-spatial system is to identify the navigability options in the vista space, *e.g.* available paths and blocking obstacles (Greene & Oliva, 2009b). Navigational affordances may characterize intrinsic properties of the environment owing to its spatial layout, such as the number of exits in a room (Bonner & Epstein, 2017), but as underlined in the definition given by Clark, they must always be considered from the observer's perspective. For example, an aperture in a wall will only be perceived as an exiting pathway if it is large enough (Djebbara et al., 2019) and if no obstacles prevent from reaching it (Persichetti & Dilks, 2018).

1.3 Neural bases of visuo-spatial perception

A large collection of cortical areas are involved in the processing of aforementioned concepts before they can be accessed and manipulated at a conscious level. First, the early visual system incrementally aggregates the local visual information transmitted from the retina over larger areas of the VF to build more and more complex patterns. Later in the visual pathway, areas specialized in the processing of intermediate-level categories (*e.g.*, objects, scenes) play a significant role in visuo-spatial cognition. Eventually, the percepts are embedded into a complex network of higher hierarchical areas responsible for the construction and the updating of abstract representations of space. The flow of information between these regions

is bidirectional, called *bottom-up* when driven by external stimulation and *top-down* when coming from inner representations.

1.3.1 The early visual system

The course of evolution has granted primates, and humans in particular, a high level of specialization in visual processing. Evolutionary traits like frontally directed, highly convergent orbits, which allow for stereoscopic vision, or the presence of a foveal region in the retina, have considerably influenced the expansion of brain structures dedicated to fine-tuned vision (Barton, 2004; Rolls & Wirth, 2018).

1.3.1.1 Retinotopic organization in the visual system

Modern neuroimaging experiments demonstrate that much of the posterior human brain responds to visual stimulation. Human visual cortex includes the entire occipital lobe and extends significantly into the temporal and parietal lobes, spanning about 20% of cortex (Wandell et al., 2007). The human primary visual cortex (V1) is organized retinotopically, along the so-called visual field map. This map reflects the organization of the retina in the sense that the receptive field of V1 neurons is associated to a specific location in the VF, and that neighbor neurons are responsive to neighbor locations of the VF (Wandell et al., 2005). The advent of functional magnetic resonance imaging (fMRI) has enabled to gain considerable insights on the organization of the visual field maps and has permitted to identify them in subsequent hierarchical areas of the visual stream (V2, V3, V4, MT/V5; Wandell et al. 2007). The most striking property of these maps is the contralateral specialization, as the visual information coming from the left (*resp.* right) hemifield is exclusively processed by the right (*resp.* left) cortical hemisphere. Retinotopic rules exhibit their influence up to higher hierarchical regions dependent on the visual inputs, such as the scene-selective regions (Silson et al. 2015, 2016; see Section **1.3.2**) and the hippocampus (Silson et al., 2021).

1.3.1.2 Two streams in the visual system

The hierarchical organization of the visual system is further subdivided into two specialized streams, or pathways (Mishkin et al., 1983). One stream runs ventrally along occipito-temporal structures until the hippocampal region, and it has been attributed to object processing, *i.e.* identifying *what* the viewer is currently observing. The other stream runs dorsally along the parietal cortex, and it has been linked to spatial processing, *i.e.* identifying *where* the object under view is located. The functional dissociation between these two pathways has sparked much debate and is still not settled today (Goodale & Milner, 1992; Previc, 1990). It is more probable that this separation is associated with multidimensional factors and cannot be so simply resolved, especially when considering that category selective regions are redundant across both streams (Silson et al., 2015).

Of matter to this thesis, it is important to note that these pathways carry a vertical bias with respect to the visual field, since areas along these streams exhibit distinct preferences for the lower (in the dorsal stream) and upper (in the ventral stream) VFs inputs.

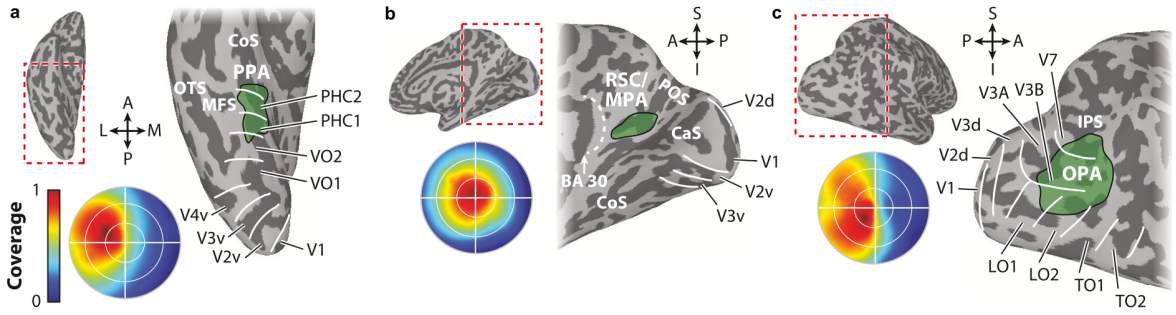

Figure 1.3: Depiction of scene-selective cortical regions. Group average data showing the location of scene-selective cortical regions with respect to anatomy and retinotopically defined areas. Circular insets show the portion of the VF eliciting the strongest response within each scene region based on population receptive field mapping. **a**. PPA is located in and around the collateral sulcus on the medial part of the ventral temporal cortex. It responds most strongly to stimuli in the contralateral upper VF. **b**. MPA is located in the medial parietal cortex in and around the ventral portion of POS. It responds most strongly to stimuli in the contralateral VF with no clear bias to the upper or lower VF. **c**. OPA is located near the transverse occipital sulcus in the occipito-parietal cortex. OPA responds most strongly to stimuli in the contralateral lower VF. Reused from Epstein and Baker (2019).

1.3.2 Scene-selective regions

Scene-selective regions (SSRs) are cortical areas in-between the primary visual areas and the higher-level cognitive areas like the hippocampus and the prefrontal cortex, that preferentially respond to scene stimuli (*e.g.*, landscapes, cityscapes, rooms) over other categories (*i.e.*, objects, faces, bodies) in fMRI (Epstein & Baker, 2019). To date, three of these areas have been identified: the para-hippocampal place area (PPA), the medial place area (MPA), and the occipital place area (OPA). They are not anatomically defined (*i.e.*, they are not associated with a precise location in the cortex) but they require a fMRI protocol contrasting images of scenes with other categories to be identified at the individual level.

Each of these areas has been studied extensively in the past 20 years and has been associated with distinct visual and functional properties (reviewed by Epstein and Baker 2019). The purpose of the following sections is not to present an exhaustive list but rather focus on the properties that were relevant to this thesis, especially the retinotopic preferences and the high-level properties that can directly be related to orientation functions. It is important to note that these areas were mostly studied with paradigms briefly presenting static images of scenes in the scanner, thus little is known about their activity in a dynamic context of navigation (Epstein & Baker, 2019).

1.3.2.1 The para-hippocampal place area

It was the first of the SSRs to be reliably reported (Epstein & Kanwisher, 1998), and it lies in the posterior region of the para-hippocampal cortex, in the ventral visual stream (Figure **1.3a**). The PPA responds preferentially to stimuli in the upper contralateral portion of the VF (Silson et al., 2015). It is also more sensitive to peripheral rather than foveal inputs (Hasson et al., 2003).

Of the three SSRs, the PPA seems to be particularly interested in tasks where categorization and recognition of the incoming stimulus is involved (Dilks et al., 2022). Persichetti and Dilks (2018) were able to decode from the PPA the category of the room presented (*i.e.*, a bedroom *vs.* a kitchen). At a finer level of identification, Marchette et al. (2015) showed that the PPA signal was specific to individual places, independently of the presented viewpoint. After a navigation task, Janzen and van Turennout (2004) demonstrated that the PPA exhibited a specific response to landmarks that were relevant to orient in the previously experienced maze. Therefore, it can be speculated that the role of this region during navigation is to identify the spatial context from previously memorized places or landmarks, enabling reorientation from the current location (Epstein et al., 2017; Julian et al., 2018; Sun et al., 2021).

1.3.2.2 The medial place area

This second scene-preferential locus was identified in the medial-parietal/retrosplenial region along the banks of the parietal-occipital sulcus (Figure **1.3b**), and it was initially labeled retrosplenial complex (RSC) (O'Craven & Kanwisher, 2000). It was recently proposed to be renamed with the more neutral term MPA, in order to avoid confusion with the cytoarchitectonically defined retrosplenial cortex, with which it does not necessarily overlap (Silson et al., 2016). Apart from a contralateral bias, the MPA shows little preference for any vertical hemifield (Epstein & Baker, 2019).

Evidence points to a higher integrative role for the MPA. First, because it has been found especially responsive to familiar places (Epstein et al., 2007) and permanent landmarks (Auger et al., 2015), thus highlighting its implication in memory functions. Second, it has been found to be sensitive to spatial quantities expressed in an allocentric reference frame such as heading and location (Baumann & Mattingley, 2010; Marchette et al., 2014; Shine et al., 2016; Vass & Epstein, 2013), which puts it in the middle between the local perception of scene and inner representations of space (Alexander et al., 2005; Epstein & Baker, 2019). For both these reasons, the MPA has been posited to be essential in map-based navigation (Dilks et al., 2022).

1.3.2.3 The occipital place area

The third SSR was identified in the occipital lobe (Hasson et al., 2003; Nakamura et al., 2000), in the dorsal visual stream (Figure **1.3c**). Initial reports labeled it TOS, based on the proximity with the transverse occipital sulcus but the final label was changed to the more neutral OPA after doubts were raised about the accuracy of the anatomical location (Dilks et al., 2013). The OPA responds preferentially to stimuli in the lower contralateral portion of the VF (Silson et al., 2015).

The specificity of the OPA among the other SSRs seems to lean towards navigation in the immediately surrounding environment, *i.e.* visually guided navigation (Dilks et al., 2022). First, its activity was found to be dependent on properties that are relevant to the egocentric reference frame, such as sense (*i.e.*, left/right direction with respect to the observer, Dilks et al. 2011), perceived depth in the scene (Persichetti & Dilks, 2016), and first-person per-

spective motion (Kamps et al., 2016a). Second, it was involved in the representation of local elements in scenes that could influence its navigability, *i.e.* walls bounding the navigable space and furniture that could be obstacles for locomotion (Kamps et al., 2016b). Using transcranial magnetic stimulation (TMS), Julian et al. (2016) even provided causal evidence for its role in perceiving the boundaries of the environment. Following studies extended these results to the more general perception of navigational affordances, as the signal decoded from the OPA was predictive of the number and the direction of exit paths present in the perceived scene (Bonner & Epstein, 2017; Patai & Spiers, 2017; Persichetti & Dilks, 2018).

1.3.3 The human spatial navigation network

In addition to the SSRs, which undoubtedly contribute to the cognitive functions at stake during navigation, higher hierarchical regions of the brain are thought to orchestrate the main spatial abilities required to successfully orient. Different models of the human navigation network are highly debated and here the findings that yield the most general agreement are summarized (Ekstrom et al., 2018).

1.3.3.1 The posterior parietal cortex

Posterior parietal cortex, at the end of the dorsal visual stream, is thought to be a multimodal brain area integrating visual, vestibular, and kinesthetic information, central to coding the environment from an egocentric reference frame (Ekstrom et al., 2018). It allows movements and visually guided actions to be coordinated with respect to landmarks observed in the scene.

1.3.3.2 The retrosplenial cortex

The retrosplenial cortex (RSc) is located in the posterior cingulate cortex. As already mentioned above, it is anatomically close to the functionally-defined MPA and therefore some properties ascribed to the latter are based on the role attributed to the RSc. In particular, it is widely acknowledged that this region codes for heading direction with respect to an external reference (*e.g.*, a stable landmark), making it a cornerstone of spatial reorientation for its translational role between egocentric and allocentric reference frames (Ekstrom et al., 2018; Julian et al., 2018).

1.3.3.3 The medial temporal lobe

The medial temporal lobe, including the hippocampus and the para-hippocampal cortex hosting, among others, the entorhinal cortex and the PPA was placed at the center of the spatial navigation network by the seminal book by O'Keefe and Nadel (1978). They introduced the hippocampus as the main protagonist in creating and maintaining an allocentric cognitive map of the environment in the brain, based on the discovery in the rodent model of cells uniquely firing at specific locations, called *place cells*. Thanks to intracranial and fMRI recordings, their presence in the human hippocampus was later confirmed (Ekstrom et al.,

2003), along with other spatially responsive cells, the *grid cells* in the entorhinal cortex (Jacobs et al., 2013). Accordingly, fMRI experiments as well as lesion studies have coherently shown an involvement of hippocampal areas when participants performed virtual navigation tasks using an allocentric reference frame (Hartley et al., 2003; Iaria et al., 2003). As part of this structure, the landmark recognition role attributed to the PPA may be fundamental to the updating of the position in the observer into this inner spatial representation (see Section **1.3.2.1**).

Unfortunately, the hippocampus is one of the deepest regions of the brain and its anatomical structure prevents its recording with scalp EEG (Buzsáki et al., 2012). However, intracranial electrodes have demonstrated the presence of low-frequency oscillations (below 12 Hz) during virtual (Ekstrom et al., 2005; Watrous et al., 2011) and real movements (Bohbot et al., 2017) that could be the signature of place cells firing (Ekstrom et al., 2018).

1.3.3.4 The frontal lobe

Eventually, through its numerous projections in and from both visual streams, the medial prefrontal cortex has been posited to integrate the information coming from both streams necessary for orienting based on visual landmarks (Ekstrom et al., 2018). More generally, the prefrontal cortex activity in fMRI studies as been associated with goal-directed navigation, tracking distance to the goal, keeping the route options in mind, and detecting changes in the environment (Javadi et al., 2017; Spiers & Gilbert, 2015). These functions are particularly important to take decisions upon spontaneous route planning, *i.e.* when required to consider a detour when the familiar path is blocked or imagining a shortcut (Ekstrom et al., 2018).

CHAPTER 2

HEALTHY AGING & VISUO-SPATIAL COGNITION

Healthy aging is characterized by heterogeneous modifications that affect perceptual, motor, and cognitive functions (Salthouse, 2019), causing spatial cognition to decline across the lifespan (Lester et al., 2017). This chapter reviews the state-of-the-art knowledge on the impact of healthy aging on visuo-spatial cognition. It starts with investigating the consequences of healthy aging on the perceptual properties of the visual system. Then, it focuses on the neural bases responsible for the generalized age-related decline affecting higher-level cognitive abilities and how it has been shown to influence visuo-spatial cognition. Finally, it discusses the embodiment aspects of aging, recognizing their essential role in the navigational deficits experienced by older adults in their everyday lives.

Overall, this chapter strives to demonstrate the need for a holistic approach to the study of brain aging in the context of visuo-spatial cognition in order to better account for the full spectrum of behavioral and neural changes that occur across the lifespan. It emphasizes the importance of considering the reorganization of the use of the visual environment that accompanies healthy aging in order to better characterize how the processing of visuo-spatial information in the cortical scene system alters spatial navigation abilities in older adults. It is also argued that the interplay between sensory (especially visual), motor, and cognitive processes involved in spatial navigation is particularly exacerbated by aging, thus compelling a shift toward more ecologically valid experimental paradigms that test these abilities simultaneously.

2.1 Healthy aging of visual perception

As accumulating literature shows that visual impairments in older adults are a significant risk factor for cognitive decline (Vu et al., 2021), spatial cognition abilities should be increasingly considered in light of the modifications of the visual system that accompany healthy aging.

2.1.1 Modified perception of spatial quantities in static and dynamic conditions

Older adults experience various changes in visual perception (*e.g.*, visual acuity and contrast sensitivity; Lester et al. 2017) but these modifications do not necessarily translate into degraded skills.

When it comes to the perception of the static position of objects and boundaries relatively to the self, a crucial property for identifying and counting navigational affordances, older adults often demonstrate more accurate estimations than younger adults, although with a slight bias for overestimation (Bian & Andersen, 2013; Sugovic & Witt, 2013). Younger adults, on the contrary, largely underestimated the distance, demonstrating a gradual worsening with distances of increasing lengths, a phenomenon called *foreshortening* (Bian & Andersen, 2013; Sugovic & Witt, 2013). These results are in line with other studies showing intact perception of surface slant in old age (Norman et al., 2009), which is an important cue for distance perception. Similarly, other studies found no impairment when older participants estimated the distance between two external objects (Norman et al., 2015).

In contrast to static spatial relationships, the perception of the optic flow has been reported to decrease in older adults, with higher perceptual thresholds required for detecting coherent movement in the optic flow (Warren et al., 1989), associated with a degraded performance in real-world tasks (Kavcic et al., 2006). In ambulatory conditions, this dynamic perception of the optic flow contributes to the self-monitoring of the walking speed and heading orientation, along with body-based cues. In path integration paradigms, older adults underestimate traveled distances and turns, and they are less accurate when returning to the start of a journey. This has been shown when navigation is based either on optic flow information or external visual cues (Adamo et al., 2012; Harris & Wolbers, 2012). Further arguing for the influence of less precise perception on inner representations, in a recent fMRI study, Koch et al. (2020) were able to demonstrate that worsened directional signals in older adults could be attributed to a broadening of the representation of directional information in the early visual cortex, mediated by the RSC.

2.1.2 Aging introduces biases in the use of the visual environment

Visuo-spatial processing declines in older age and modifies the way in which older adults sample the outside world and encode navigationally relevant visual information (Dowiasch et al., 2015; Kimura et al., 2019; Ramanoël et al., 2020; Zhong & Moffat, 2016). Indeed, slower and more error-prone navigation in older compared to young adults was correlated with

an impairment at rapidly acquiring visual information from the surrounding environment (Kirasic, 1991; Wilkniss et al., 1997). However, the impairment may only be partial, since a recent study found that healthy older adults' orientation capabilities are rescued when geometry, instead of landmark, is available to guide behavior (Bécu et al., 2023; Bécu et al., 2020a).

Interestingly, accumulating evidence is pointing towards a possible influence of verticality on visuospatial function in healthy older adults. First, it was observed that the vertical asymmetry of the VF, *i.e.* the relatively higher extent of the lower VF compared to the upper VF, accentuates with aging (Durteste et al., 2023). Second, vertical anisotropies in visual search appear to undergo significant changes throughout adulthood, shifting progressively to a lower VF dominance (Brennan et al., 2017; J. Feng et al., 2017). Moreover, older adults have been found to gaze preferentially at the ground when reorienting in ecological laboratory settings (Bécu et al., 2020a) and to show impaired spatial memory specifically for upper VF objects (Durteste et al., 2023).

2.1.3 Older adults are impaired at encoding associated stimuli

The ability to follow a route is often based on the knowledge of landmarks that can be encountered along this specific route, and on contextual information associated with these landmarks (*e.g.*, spatial, directional, and temporal; Head and Isom 2010; Wiener et al. 2012). In their systematic literature review, van der Ham and Claessen (2020) did not find significant evidence for impaired perception and recall of landmarks. In contrast, retrieving the relevant information associated with the landmarks is impaired with age, both concerning the spatial (Jansen et al., 2010), directional (Head & Isom, 2010), and temporal (Head & Isom, 2010; Wilkniss et al., 1997) context. This goes hand in hand with the manifestation of an impaired associative memory in aging (Naveh-Benjamin, 2000).

2.2 Neural bases of visuo-spatial cognition throughout adulthood

As demonstrated in the previous chapter, successful navigation requires numerous cognitive processes varying in complexity. While the literature has extensively focused on hippocampal deficits for the key role of this structure in allocentric spatial cognition, well-described degradation of general executive functions may also be pivotal in explaining the overall decline of spatial abilities with healthy aging. Eventually, the neural bases reviewed in this section also encompass SSRs, of principal interest to this thesis, for which there is currently only emergent data indicating that they may also endorse a key role in spatial navigation deficits observed during aging. As noted by Li and King (2019), only a limited number of fMRI studies have investigated the neural bases of spatial cognition in the context of healthy aging, thus the literature insights reviewed here often lack direct relationship between behavioral results and the activity of the described regions.

2.2.1 Hippocampal deficits

The hippocampus is one of the earliest structures to show atrophy with advancing age (Raz et al., 2004) and numerous studies have positively correlated the hippocampal volume with better spatial memory in wayfinding tasks (K. H. Chen et al., 2010; Driscoll et al., 2003; Head & Isom, 2010). More specifically, in accordance with its fundamental role in maintaining the cognitive map, fMRI studies have shown that older people underperformed at navigation tasks requiring an allocentric reference frame, associated with a reduced or completely absent hippocampal activity compared to young adults (Antonova et al., 2009; Moffat et al., 2006). Thus, the hippocampal function decline is traditionally held responsible for the widespread observation of an age-related shift towards egocentric abilities and the discontinued spontaneous use of allocentric strategies by older adults (Bohbot et al., 2012; Harris et al., 2012; Wiener et al., 2013, 2012).

This shift towards response-based strategy preference was nicely demonstrated by Rodgers et al. (2012) who assessed strategy preference of young and aged subjects in a Y-maze, using a strategy dissociation paradigm adapted from rodent experiments initially designed by C. A. Barnes et al. (1980). During training, the subjects learned to approach a goal location in one of the arms from a fixed start arm. When starting from a novel arm during testing, the strategy preference was classified as egocentric when turning to the same egocentric direction as during the learning phase, and as allocentric when choosing the correct goal location. Older adults more often used an egocentric strategy than an allocentric one, whereas younger subjects did not. Even though they become the most privileged option when orienting in a novel environment, route-based strategies were also found to be negatively impacted by age, although to a lesser degree (Head & Isom, 2010; Ruggiero et al., 2016).

2.2.2 Degradation of executive functions

Executive functions, in particular those relying on the frontal and parietal cortices, which are also structurally affected by healthy aging (Sowell et al., 2003), certainly play a role in the general age-related deficits encountered in spatial cognition (Ekstrom et al., 2018). Among these, the capacity of the navigator to monitor its own behavior, adapt its search strategy to the situation, and selectively attend to the most relevant stimuli are essential to ensure efficient wayfinding (Moffat et al., 2007).

2.2.2.1 Metacognition

The aforementioned shift from allocentric to egocentric strategies may be facilitated by the degradation of metacognitive abilities, for which the prefrontal cortex constitutes the major neural basis (Fleming & Dolan, 2012). Indeed, the metacognitive confidence judgment upon its own performance at a task requiring the formation of a cognitive map was found lower for older adults than for young adults (Ariel & Moffat, 2018). This result suggests that the differential engagement of prefrontal processes in metacognition could partially account for robust age-related differences in allocentric strategy use (Zhong & Moffat, 2018).

2.2.2.2 Decision-making

On a different note, observing that older adults' wayfinding impairment manifested from the very first trial of their task, Moffat and Resnick (2002) reported a less efficient search behavior as compared to the younger counterparts (*i.e.*, longer distances traveled and multiple visits of the same spots). This was either interpreted as the implementation of an inappropriate search strategy or the inability to monitor the current behavior during the search, both functions relying on the prefrontal cortex (Moffat, 2009). This claim was further supported by Moffat et al. (2007), who found a correlation between overall navigational performance, working memory tests, and the volume of the prefrontal cortex.

2.2.2.3 Inhibitory control of attention

Together with these concerns, age-related executive declines have also been suggested to adversely affect the allocation of attentional resources.

Many studies report that older adults are more susceptible to distraction by irrelevant visual stimuli due to their degraded ability to exert top-down inhibitory mechanisms (Dempster, 1992; Gazzaley & D'Esposito, 2007; Lustig et al., 2007). This prevents the suppression of the automatic capture of attention by salient task-irrelevant stimuli, negatively affecting their performance in tasks where a lot of visual information is provided (Kramer et al., 2000; Mertes et al., 2017; Schmitz et al., 2010, 2014). Impaired inhibitory capacities can also perturb the extraction of task-relevant information, as numerous distractors may lead to the overload of the working memory, in turn preventing the proper encoding of the stimuli of interest (Gazzaley et al., 2008; Schmitz et al., 2010). This phenomenon resonates with another commonly reported age-related behavior, *hyper-binding*, where older adults demonstrate an increased reliance on non-pertinent information (Campbell et al., 2010; S. Kim et al., 2007).

Strikingly, Lipman (1991) reported that older adults automatically gave a preference to salient over informative landmarks, illustrating how this mechanism can affect visual processing in a navigational context. More recently, older adults were found to be more perturbed than young adults by auditory (Hartmeyer et al., 2017) and visual distractors (*i.e.*, a moving crowd; Merriman et al. 2018) when simultaneously having to decide upon the heading direction to take at intersections. The later experiment illustrates more specifically the age-related reduction in control of goal-directed eye movements described previously by Dowiasch et al. (2015).

2.2.3 Scene processing: between alteration and compensation

Because their discovery is fairly recent, few studies have focused on the possibility that the SSRs may be involved in the decline in visuo-spatial cognition reported in healthy aging. Investigating the SSRs in the context of scene perception and healthy aging, Ramanoël et al. (2015) demonstrated an age-related specific deficit for processing high-spatial frequencies (*i.e.*, edges) in the PPA and the MPA, associated with difficulties in determining the indoor/outdoor component of scenes for older adults. Following these findings, resting-state

magnetic resonance imaging (MRI) evidence revealed an age-related increase in functional connectivity between the OPA and the PPA, as well as preserved white matter integrity between the OPA and the navigation network (Ramanoël et al., 2019). The retrieval of this relatively preserved structural network was interpreted as a compensatory mechanism counterbalancing the degradation of the hippocampus with age. Interestingly, Ramanoël et al. (2020) subsequently reported an elevated activity in the OPA of the older adults when solving a landmark-based Y-maze task compared to young adults, contrasting with the decreased activity in hippocampal and prefrontal areas. Behaviorally, this was associated with a greater reliance on a response-based strategy, further confirming the recruitment of more preserved neural bases in alternation to the degraded structures necessary for building a cognitive map.

On a side note, the RSc, partly overlapping with the MPA in terms of anatomy and function, has also been implicated in spatial navigation deficits experienced by older adults, as the failure of its translating role between egocentric percepts and allocentric representations would fit well with the egocentric shift previously described (Zhong & Moffat, 2018). Accordingly, several studies reported a lower activation in the RSc directly associated with impaired navigational abilities (Antonova et al., 2009; Meulenbroek et al., 2004; Moffat et al., 2006).

2.3 Embodiment of spatial cognition: Multimodal aspects in aging

The widespread use of structural and functional MRI in spatial cognition paradigms has often hindered the possibility of collecting insights on the neural bases of spatial navigation in its entirety because perceptual (other than visual) and motor aspects are omitted. Nonetheless, the isolated characterization of multisensory integration, postural, and locomotor control has yielded crucial insights on how aging may perturb the interactions between sensory, cognitive, and executive abilities at stake during natural navigation.

2.3.1 Multisensory integration

Although humans rely extensively on vision, other types of sensory information, such as auditory, vestibular, and proprioceptive, are all at play during navigation (Arleo & Rondi-Reig, 2007). Critically, the perceptual information available during navigation differentially modulates young and older adults' behavior. In young adults, several studies have reported similar performance during path integration (*i.e.*, the capacity to keep track of one's position on a trajectory through the integration of rotational and translational displacements provided by self-motion cues) when participants relied on visual optic flow only, vestibular inertial information only, or vestibular and proprioceptive afferents conjointly (Adamo et al., 2012; Mahmood et al., 2009; Wiener et al., 2011). In contrast, in older adults, the variety of sensory information available is known to determine their navigational performance (Harris & Wolbers, 2012; Mahmood et al., 2009). Some age-related navigational deficits frequently

observed in desktop-based tasks appear to be mitigated in mobile conditions (immersive virtual reality and real-world settings), which highlights the importance of the availability of multimodal information to improve navigational performance in older adults (Kirasic, 1991; McAvan et al., 2021). These findings emphasize that multisensory integration can at least partially alleviate certain struggles faced by older adults when navigating, by compensating for age-related unisensory degradations (S. L. Bates & Wolbers, 2014). However, older adults sometimes demonstrate an excess in multisensory integration, which typically manifests in difficulties of adjusting the relative weighting of multiple sensory cues appropriately (Kuehn et al., 2018), for example placing less influence on landmark cues as would have been optimal to solve the task (S. L. Bates & Wolbers, 2014).

2.3.2 Postural control & Locomotion

Postural control and locomotion represent essential aspects of spatial navigation that are frequently neglected by brain aging studies. From a perceptual-motor perspective, the up weighting of visual cues and increased VF dependence in older adults can have a drastic impact on their locomotor behavior and stability (Agathos et al., 2015). Evidence also suggests an important role for visuo-podal integration in postural control and mobility (Foisy & Kapoula, 2018; Roll et al., 2002). Strengthening the argument for close ties between visual and locomotor systems, an increasing number of rodent neurobiological studies suggest that visual brain patterns are modulated by motion-related inputs (Parker et al., 2020). Motor-related skills are also tightly intertwined with the attentional and cognitive factors that lie at the heart of spatial navigation. In older adults, attentional resources are neither precisely nor optimally allocated in situations that require intricate multi-tasking capabilities, such as when performing two motor actions simultaneously (Tsang, 2013). During spatial navigation, the attentional resources dedicated to postural control and locomotion can even interfere with the other cognitive processes at play (Agathos et al., 2020; Holtzer et al., 2006). Most strikingly, age-related deficits in balance and locomotion induce an increased fear of falling that in turn shapes older adults' navigable space (Sugovic & Witt, 2013), and it forces them to adapt their walking behavior. Indeed, older navigators tend to walk more slowly, to focus their gaze on the ground, and to avoid obstacles in their peripersonal space. These age-related changes could contribute to suboptimal spatial learning and orientation in older adults. For example, older adults place emphasis on body awareness and stability when walking rather than on the formation of a mental map to orient themselves in the immediate environment (Yogev-Seligmann et al., 2008). Beyond behavioral observations, neuroimaging findings show that age-related reductions in walking speed and increases in gait variability are linked to structural and functional changes in a distributed brain network encompassing prefrontal, frontal, parietal, occipital, cingulate, and thalamic regions (Agathos et al., 2020; Tripathi et al., 2019; Wagshul et al., 2019). Although it is striking that the neural underpinnings of age-related locomotor deficits widely overlap with those of spatial navigation (Li & King, 2019; Moffat, 2009; Zhong & Moffat, 2018), no study has yet tested these abilities concomitantly in older adults.

CHAPTER 3

PATHOLOGICAL AGING & VISUAL RESTORATION THERAPIES

This chapter covers broad aspects of pathological visual aging that are required to understand the visual restoration therapies evaluated in Chapters **10** and **12**. Its goal is not to provide an extensive review of visual pathologies that can be addressed by visual restoration but rather introduce the specifics of the pathology targeted by these approaches (*Retinitis Pigmentosa*; Section **3.1**). Similarly, as the development of visual restoration therapies is not the topic of this thesis, Section **3.2** will briefly present the necessary components of the technology that led to the innovations permitting to restore vision in the cases studied. Eventually, the last section (Section **3.3**) highlights the need to consider the link between the eye and the brain for a fully functional restoration of vision, and it presents how EEG can be used to evaluate the visual functions in a pathological context.

Overall, this chapter aims to demonstrate how complementing current approaches to visual restoration in late-stage *Retinitis Pigmentosa* patients with objective assessments of the cortical response induced by therapies would provide essential and novel insights to better understand the recovered partial perception and guide future iterations to improve their efficacy.

3.1 Pathological visual aging: when the photoreceptors go missing

There are many forms of pathological visual aging impairing visual abilities and ultimately causing blindness. The disease mechanisms can impact any step in the visual pathway, interrupting the transmission of the light to the brain. In this work, the target pathological spectrum was a retinal disease affecting photoreceptors, *i.e.* the light sensitive cells of the retina, at the base of the visual system. The fact that visual perception is disrupted at its earliest stage in these clinical settings is important because it offers the opportunity for restoration therapies to bypass this first layer of malfunctioning cells while having to replicate a relatively simple transformation of light compared to later stages of visual processing.

3.1.1 The light sensor: the retina

The retina constitutes a layered light-sensitive tissue located at the back of the eye, measuring approximately 0.5 mm in thickness. Within the retinal neural network, multiple layers of cellular bodies, along with their dendrites and axons, form a complex arrangement (depicted in Figure **3.1**; Yue et al. 2016).

In a healthy retinal context, light goes through the retinal layers to ultimately stimulate the photoreceptors, *i.e.* cones and rods. Cone cells exhibit distinct light wavelength responsiveness, synergistically generating the basis for chromatic perception. On the other hand, rod cells, sensitive to lower intensities than cones, are predominantly responsible for low-light or nocturnal vision. The photoreceptors transform incoming photons into a neural signal that sequentially progresses through bipolar and ganglion cells to ultimately propagate toward higher-order visual centers in the brain via the optic nerve (consisting in the axons of ganglion cells). Basic computations are performed by bipolar and ganglion cells, by integrating signals coming from clusters of photoreceptors and executing operations like edge detection through center-surround structures. Neural signaling also undergoes lateral modulation, introduced by horizontal cells and amacrine cells, during the initial processing stages that occur within the inner retinal layers.

As depicted in Figure **3.1**, cell distribution profiles manifest marked disparities between the central and peripheral regions of the retina. Cones exhibit heightened packing density in the macular area, whereas rods predominate in the periphery. Signaling within the macula is almost analogous to a dedicated line of transmission from individual cones, while the signal coming from the periphery is aggregated over thousands of photoreceptors (Yue et al., 2016).

3.1.2 The pathology: *Retinitis Pigmentosa*

Within the scope of this project, the primary focus rested upon the evaluation of strategies aimed at restoring visual function in one particular case of pathological visual aging: *Retinitis Pigmentosa* (RP). RP is a group of hereditary diseases associated with the degeneration of photoreceptors, leading to a progressive and irreversible transition into complete

blindness over the course of several decades (Busskamp et al., 2010; Hallum & Dakin, 2021; Hamel, 2006; Hartong et al., 2006). Its global prevalence stands at approximately 1 in 4000 individuals (Hallum & Dakin, 2021; Hamel, 2006). While RP typically presents in a non-syndromic manner, a spectrum of syndromic forms exists, with Usher syndrome ranking among the most prevalent (Hamel, 2006).

Initial symptoms commonly involve night blindness, reflective of impaired rod photoreceptor function. Subsequent progression encompasses the gradual deterioration of peripheral daytime vision, culminating in eventual total blindness upon the disease advancement to central vision (Hamel, 2006; Hartong et al., 2006). Predominantly, the usual form of RP precipitates the degeneration of the retinal outer layers, designated as rod-cone dystrophy. In this process, rod photoreceptors disappear early, while cone photoreceptors persist for a more prolonged duration with a modified malfunctioning morphology (Busskamp et al., 2010). Conversely, the inner retinal layer, encompassing ganglion, bipolar, and amacrine cells, appear to exhibit lesser susceptibility to the degenerative process (Stone et al., 1992). Genetic factors exhibit marked heterogeneity, encompassing over 70 genetic mutations that have been correlated with RP (https://web.sph.uth.edu/RetNet/sum-dis.htm).

Presently, a definitive therapy capable of halting the course of RP remains elusive (Hamel, 2006). Nevertheless, protective measures such as sunlight protection and nutritional interventions have demonstrated potential in retarding disease progression for numerous patients (Hamel, 2006; Hartong et al., 2006). The imminent prospect of therapeutic interventions for RP is considerably anticipated and has instigated intensive research efforts, embracing avenues such as retinal prosthetics, neuroprotective measures, and gene therapy.

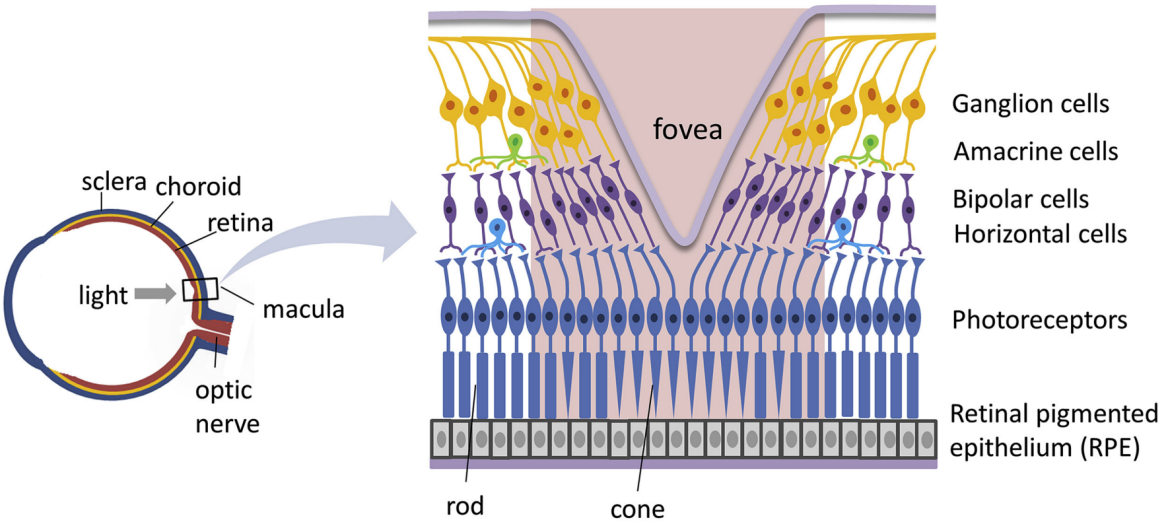

Figure 3.1: Schematic representation of the physiological structures of the eye and the retina. Pink-shaded area represents the macular region. Reused from Yue et al. (2016).

3.2 Restorative approaches to *Retinitis Pigmentosa*

The degeneration of photoreceptors in RP, central in retinal function, precipitates substantial neural reconfiguration (Yue et al., 2016). Nonetheless, despite such reorganization and cell attrition, inner retinal neurons largely retain their ability to transmit signals (S. Y. Kim et al., 2002; Weiland et al., 2011). Preservation of inner retinal functionality lays the foundation for potential vision reinstatement, achievable by establishing stimulation mechanisms that circumvent the compromised photoreceptor layer and directly interface with the enduring inner retinal neurons. Research endeavors in this domain have embraced diverse stimulation modalities, encompassing bio-electronic, optogenetic, photochemical, and more recently, ultrasonic approaches (Yue et al., 2016). To align with the cases studied during this thesis, only electrical and optogenetic approaches will be presented.

3.2.1 Electrical stimulation

As an effective treatment for RP, one of the mainstream approach has been proposed to replace the function of photoreceptors by electrically stimulating the retina's more viable inner layers (Hallum & Dakin, 2021). Phenomenologically, the development of such bioelectrical interfaces stems from experiments conducted by pioneering scientists such as Leroy and Volta in the 18^{th} century who illustrated that electrical stimulation of the visual system could evoke visual percepts (Farnum & Pelled, 2020). The elicited spots of light, denominated as phosphenes, have been depicted as *generally white-to yellow round or oval shapes across the visual field, depending on the location of the stimulation* (Macé et al., 2015). At the microscopic scale that has now been comprehensively studied, electrical stimulation of retinal neurons follows the same basic principles involved in the stimulation of other excitable neurons. The electrical stimulus delivers charge to the cell membrane that depolarizes the neuron and opens voltage-sensitive ion channels. This bypasses the natural presynaptic neurotransmitter excitation and causes the activated neurons to stimulate their postsynaptic targets (Weiland et al., 2016). Therefore, since the rudimentary description of phosphenes, it is now possible to modulate the activity of retinal neurons with selective spatio-temporal patterns thanks to an array of electrodes to allow for an improved representation of visual scenes in prosthetic vision (S. C. Chen et al., 2009).

The most advanced electrical stimulation vision prostheses typically comprise a microelectrode array that is implanted surgically either epiretinally (at the vitreoretinal interface), subretinally (between the photoreceptor layer and choroid), or suprachoroidally. The focus will be placed on epiretinal prostheses, that are the closest to the inner layers of the retinal tissue. More specifically, the electrodes in such implants directly stimulate the retinal ganglion cell layer (Zrenner, 2002).

Currently, the *Second Sight Argus II* prosthesis is the epiretinal implant with the largest number of electrodes that has been approved by both the US FDA and the European Commission (see Figure **3.2A**; L. da Cruz et al. 2016). It has been authorized as a treatment against RP (Mirochnik & Pezaris, 2019). This implant contains 60 electrodes resulting in

the restoration of a VF of approximately 20° diagonally. The Argus II has enabled patients to read, albeit slowly, recognize words, and detect motion, with a maximum visual acuity of 20/1260 (L. da Cruz et al., 2013; Dorn et al., 2013).

3.2.1.1 Limitations of the current epiretinal prostheses

The current visual restoration produced by the retinal implants remains very restricted and incomparable to normal vision experienced by healthy individuals.

Currently, the main technological limiting factor lies in the restricted number of electrodes that can fit into the implant. Increasing the retinal coverage would allow for an increased field of view (FoV), and increasing the electrode density would allow for a better acuity. These two components are key to improving the overall artificial vision for implanted patients (Vagni et al., 2022). However, increasing the number of electrodes is challenging due to the need to accordingly scale the implantable pulse generator and the size of the trans-scleral cable (Thorn et al., 2020). Another challenge to implanting a larger array of electrodes lies in the associated surgical risks and the inadequate fitting of the existing implants to the curvature of the eye (Ferlauto et al., 2018). Another limitation is the deformation of the phosphenes, resulting from the activation of neighboring axons from retinal ganglion cells leading to an elongation of the phosphene (Weitz et al., 2015).

From the patient's perspective, it still takes an extensive amount of time to perform elementary tasks. Indeed, results from clinical trials show that implanted patients take around one minute to recognize letters (Weitz et al., 2015). Moreover, according to L. da Cruz et al. (2013), most patients cannot determine the orientation of gratings and show great difficulty with shape perception. Even the best performing implant recipients have not yet improved above the level of legal blindness. More concerning is the cognitive fatigue elicited by the device, due to the constant effort required for image reconstruction (Chenais et al., 2021; Erickson-Davis & Korzybska, 2021). Clinical trials evaluating the longer-term use of the Argus II device have noted that this was one of the major reason the treatment was abandoned by implanted recipients (L. da Cruz et al., 2016). Critically, it has been argued that favoring the extent of the FoV over a fine resolution may enhance the acceptability of the device in recipients' daily life by having a greater impact on their mobility and on visual search tasks (Ghezzi, 2023).

3.2.1.2 The next generation of implants

To overcome these issues, a new generation of implants is currently under development. A promising device, inspired by intraocular lenses, is the POLYRETINA foldable and photovoltaic wide-field epiretinal prosthesis developed by the team of Diego Ghezzi at EPFL (see Figure **3.2B**; Ferlauto et al. 2018). Photovoltaic technology enables wireless stimulation of the retinal ganglion cells, thus removing the need for implanting a pulse generator and transocular connections. Consequently, the implant is able to embed many more stimulation unit (2215 pixels) covering a theoretical FoV of 46.3° (Ferlauto et al., 2018; Vagni et al., 2022). Furthermore, the increase in the number of electrodes can serve to sharpen visual acuity, with a theoretical maximum in the order of 20/600, higher than any existing prosthesis. Its

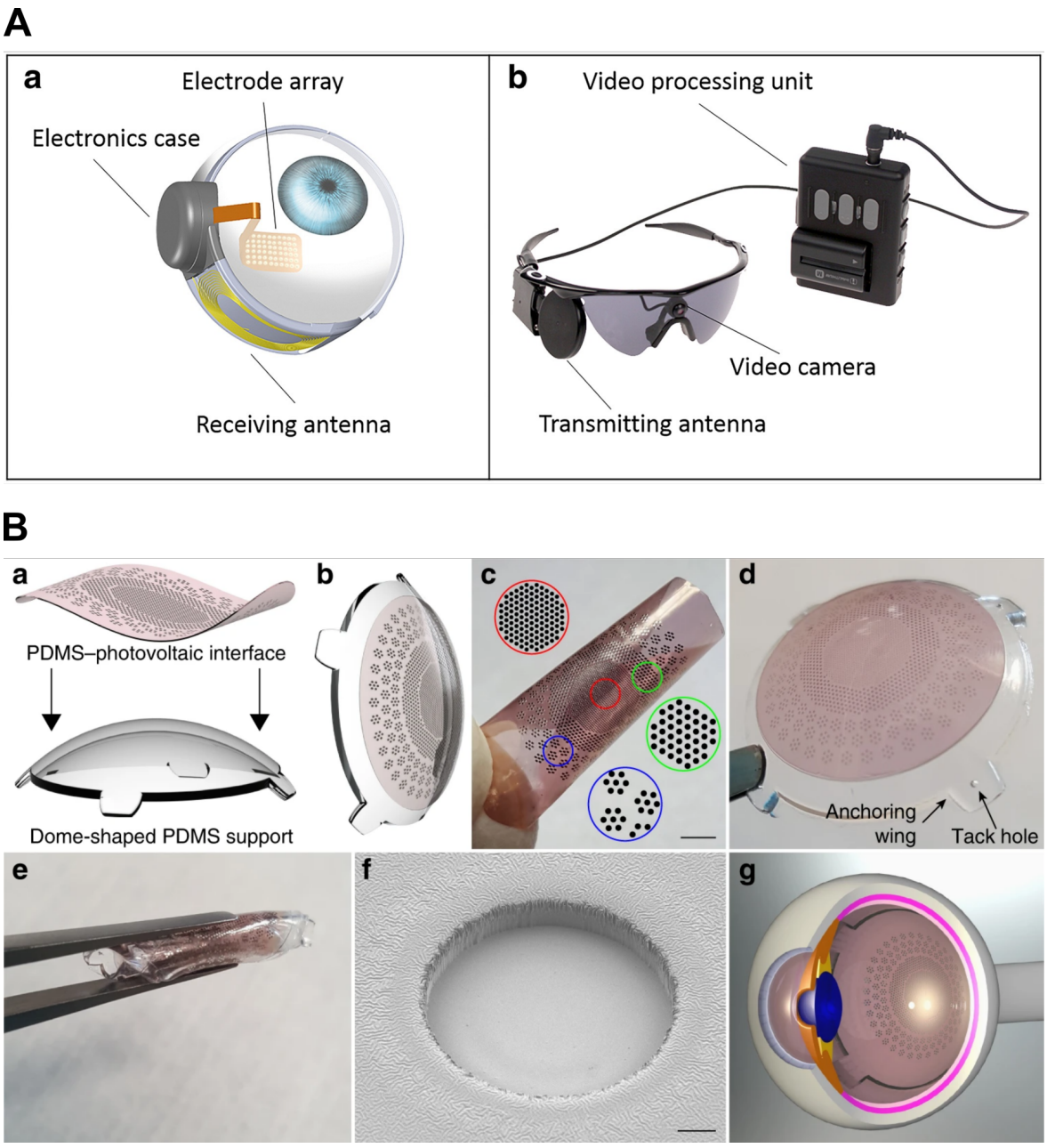

Figure 3.2: Presentation of the Argus II and the POLYRETINA prostheses. **A**. The *Argus II* system. **a**. Implanted components of the system. **b**. External components of the system. Reused from Dagnelie et al. (2017). **B**. POLYRETINA foldable and photovoltaic wide-field retinal prosthesis. **a**. 3D model of the fabricated PDMS-interface and of the dome-shaped PDMS support. **b**. 3D model of the retinal prosthesis after boding the PDMS-interface to the PDMS support. **c**. Fabricated PDMSphotovoltaic interface with pixels arranged in three areas of different sizes and densities: central area (red), diameter of 5 mm, 967 electrodes in hexagonal arrangement, electrode diameter 80 μm and pitch 150 μm, density 49.25 px.mm^{-2}; first ring (green), diameter of 8 mm, 559 electrodes in hexagonal arrangement, electrode diameter 130 μm and pitch 250 μm, density 17.43 px.mm^{-2}; second ring (blue), diameter 12.7 mm, 719 electrodes, electrode diameter 130 μm, density 9.34 px.mm^{-2}. Circles show an enlarged view of the pixel distribution. Scale bar is 2.5 mm. **d**. Picture of POLYRETINA. Four anchoring wings with holes are present for attaching the prosthesis with retinal tacks. **e**. POLYRETINA folded before injection. **f**. Scanning electron microscope image (40° tilted view) of a photovoltaic pixel. Scale bar is 10 μm. **g**. 3D model after epiretinal placement. Reused from Ferlauto et al. (2018).

foldable structure also enables it to implant it with a smaller scleral incision while being adaptive to the curvature of the eye (Ferlauto et al., 2018; Vagni et al., 2022).

Short-term *in vivo* validation has recently been conducted on Göttingen mini-pigs, successfully linking the recovery of light sensitivity to the activation of the POLYRETINA prosthesis, via the electro-retinogram recordings (Vagni et al., 2022). Given the numerous developments required before considering human clinical trials, the benefits of this implant have been proposed to be studied using simulated prosthetic vision, which proves to be a powerful tool to investigate the key functions of prosthesis, in order to identify in advance the parameters that still need to be optimized before *in vivo* testing on human participants (Macé et al., 2015). This will be addressed in Chapter **12**.

3.2.2 Optogenetics

One of the most recent technologies envisioned to have a large impact on visual restoration therapies is optogenetics. This approach relies on the expression of an *optogene* encoding a light-activated channel or pump in the remaining cells of the retina to make them sensitive to light. The combination of this technology with adeno-associated viral vectors permits to target the expression of the optogene to specific cell types (Busskamp et al., 2010). The benefit of the approach is that it can theoretically target any cell in the retina, provided the existence of promoters specific to this cell type for the viral vector, and it is independent of the mutation causing the degeneration, as opposed to gene-based therapies.

Attempts to restore visual function with optogenes targeted to cones, bipolar cells, or ganglion cells have been successful in animal models of RP, up until the observation of behavioral responses to visual cues (Bi et al., 2006; Busskamp et al., 2010; Lagali et al., 2008). Furthermore, efficient expression of optogenes in cones and ganglion cells has been demonstrated in the retina of nonhuman primates in vivo (Gauvain et al., 2021) and in postmortem human retinas in vitro (Sengupta et al., 2016). The choice of the target cell type depends on the state of retinal degeneration. Cone targeting is expected to produce optimal results, followed by bipolar cells and, lastly, ganglion cells (Sahel et al., 2019). Owing to the pioneering role of the Vision Institute in this field, this project participated in the open-label phase 1/2a PIONEER study, which evaluates the safety and efficacy of a ganglion cell-based optogenetic therapy on human volunteers with advanced RP (see Chapter **10**).

3.2.3 Replacing perception: creating the right stimulation

Unlike healthy photoreceptors, the approaches presented in this section do not respond to natural light but they rather rely on artificial stimulation shaped by an imaging device capturing the world from the perspective of the patient, *i.e.* a head-mounted camera (Hallum & Dakin, 2021). This is also the case for optogenetics, in which the photosensitivity enabled by optogenes still requires to be stimulated with light at the appropriate wavelength and intensity (Sahel et al., 2019). This often takes the form of a cyclops eye camera, worn on customized engineered glasses or goggles (see Figure **3.2A** for example).

A central challenge for these devices is the transmission in real-time of the captured image to signal processing algorithms that shape the stimulation pattern to the specific needs of the restoration therapy. For example, in the case of optogenetics, as mentioned earlier, the stimulation should be adapted to the target cell type as the expected neural input is different between photoreceptors and ganglion cells. The algorithms classically used in computer vision have failed to fulfill these requirements, either by not processing the information quickly enough or by providing limited relevance in daily life settings (N. Barnes et al., 2016; Borda & Ghezzi, 2022; Shire et al., 2012). New solutions are currently under development, such as saliency detection or object recognition algorithms (Wang et al., 2021) or deep-learning approaches. They greatly improve the usefulness of the stimulation in real-world context (*e.g.*, finding objects, avoiding obstacles, Lozano et al. 2020; Sanchez-Garcia et al. 2019) but their real-time performance is still a limiting factor (Borda & Ghezzi, 2022).

In the PIONEER study, they tackled this issue by employing a neuro-morphic camera, that detects changes in intensity, pixel by pixel, as distinct events (Posch et al., 2011). Exposure measurements are initiated and carried out locally by the individual pixel that has detected a change of brightness in its FoV. This results in an asynchronous updating of the scene (*i.e.*, each pixel only change its value when a significant change is measured) highly reducing the temporal redundancy of sequential images thereby facilitating massively parallel operations for real-time processing. This type of camera is often referred to as *biomimetic* as it reproduces the way photoreceptors generate their electrical output upon detection of photons (Posch & Matolin, 2011). Thus, an important consequence to bear in mind about the PIONEER clinical study is that, the stimulation of the retina by the goggles being event-based, in theory, if the patient stands still in front of a static scene, the device stays quiet. Therefore, the efficient use of the goggles requires the patient to make substantial head movements for the camera to trigger stimulation when passing over contrasted objects.

3.3 Putting the brain in the equation

Restoring the normal function of the visual circuits, although essential, does not guarantee the success of the therapeutic approach. Because the eye and brain work together in a coordinated manner to process visual information, it is also important to study how the brain responds to the restored retinal input to ensure behavioral improvements in patients (Chaffiol et al., 2022). Indeed, after prolonged periods of deprivation of normal visual experience, the phenomenon of *neuroplasticity* in the brain may have disrupted the organization of brain regions dedicated to visual processing (Castaldi et al., 2020). Neuroplasticity embodies the ability of the nervous system to flexibly adapt and optimize its finite resources in response to physiological changes, injury, novel environmental demands, and sensory interactions (Pascual-Leone et al., 2005). Compared to early life, adult neuroplasticity is limited, particularly for the visual cortex, which is often described as hardwired after a critical period of development (Castaldi et al., 2020). Critically, in their review, Beyeler et al. (2017) identified a 'tolerance envelope' for adequate stimulation by prosthetic devices. It represents an upper bound on the amount of distortion or information loss in the stimulation that can

be successfully compensated by cortical plasticity of visual processing areas. Therefore, monitoring cortical activity during therapy could provide essential insights to better understand the mechanisms of visual restoration and guide new iterations of therapy towards more efficient designs (Ghezzi, 2023).

As argued by Hallum and Dakin (2021), it is also important to introduce more quantitative measurements to the evaluation of the outcome of these devices in the clinic. Indeed, although exhibiting qualitative benefits from the implant in daily life activities (*e.g.*, reports of "hand motion" or "light perception"), the recipients often do not demonstrate significant improvement at conventional tests (*e.g.*, letter charts) with the partial vision restored by the therapy (Humayun et al., 2016). It is left to researchers and clinicians to develop new methods for visual restoration assessment, including tests of the device that better take into account what it brings to patients in daily life and investigative recordings that provide objective evaluation of the effects of the device on the visual system, even at the subconscious level.

Keeping the methodological perspective of this thesis in mind, the review of the investigation of cortical activity was considered under the prism of EEG, which is the non-invasive neuroimaging technique the most compatible with the wearing of a wide range of head-mounted devices required by these restorative approaches.

3.3.1 EEG-based methods to evaluate vision

3.3.1.1 Visually evoked potentials

Visually evoked potentials (VEPs), consisting of stereotypic changes of electrical activity evoked by visual stimulation and measured at the level of the scalp over the occipital lobe are an important tool for understanding the relationships between physical stimuli, brain activity, and human cognition (Creel, 2019). Of particular interest to study visual perception are the VEPs generated in response to a train of stimuli presented at a fixed rate (*i.e.*, a flicker). Because the responses to such periodic stimuli can be very stable in amplitude and phase over time, those responses have been referred to as the steady-state VEP (Norcia et al., 2015). VEP is a good alternative to measure visual function when psychophysical assessment is difficult or the effects of attention and cognitive load need to be controlled (McGregor et al., 2019; Seiple et al., 2005).

VEPs can be used as an objective measure of visual acuity thanks to the sweep VEP paradigm, where the flickering stimulus is parametrically varied over a range of values (*e.g.*, its spatial frequency or its contrast; Hamilton et al. 2021; Norcia et al. 2015). Once the response evoked by the flickering stimulus disappears from the cortical recordings, it indicates that the tested parameter has reached perception threshold. When reviewing this field of the literature, Hamilton et al. (2021) noted that the measures of visual acuity with this paradigm on patients with retinal diseases followed the trend seen in equivalent studies of normally sighted adults with artificially reduced acuity. It indicates that this protocol holds valid even in a pathological context.

A more recent technique is the multifocal VEP paradigm, that enables to test the perception in specific areas of the VF with a flickering stimulus with local elements mapped to retinotopy (Klistorner et al., 1998). This is a very interesting method for objective evaluation of VF deficits (Seiple et al., 2005), especially for diagnostic purposes, which has previously been validated with a RP model (Parisi et al., 2010).

Although they offer a highly predictable stimulus-response association that is important for precise quantitative assessment of visual functions, VEPs are less efficient when considering patients that have reached late stage of the disease and are considered legally blind. For example, Paranhos et al. (1998) admitted that the practical use of VEPs for acuity evaluation requires the patients to have a preserved central vision. Furthermore, they are impractical to use in a real-world context, when trying to assess the benefit of visual restoration in patients daily life, which should be the ultimate target of these therapies (McGregor et al., 2019). To that end, the study of brain rhythms, which have been characterized in a variety of visual tasks closer to ecological conditions can offer more insights.

3.3.1.2 Alpha rhythm

Thanks to the early report of clear pattern of oscillations in EEG recordings (Berger, 1929), the EEG signal has been extensively studied under a spectral perspective (*i.e.*, by quantifying the power manifested in different frequency bands). Alpha rhythm, in particular, is a commonly admitted correlate of visual processing, considering the large synchronization (*i.e.*, elevated power) observed in this frequency band when healthy individuals close their eyes. It is traditionally defined between 8 and 12 Hz but the 'peak' of alpha rhythm in the EEG spectrum is quite variable across individuals (Klimesch, 1999), explaining some fluctuations in the definition of the limits of the band. Numerous reports indicate its association with the intensity of visual processing, visual attention and object recognition in the occipital region (W. Feng et al., 2017; Freunberger et al., 2008; Romei et al., 2010; Thut et al., 2006; van Dijk et al., 2008; Vanni et al., 1997; Wyart & Tallon-Baudry, 2008).

3.3.2 Cortical correlates of *Retinitis Pigmentosa*

A long history of work has coupled EEG recordings with the assessment of visual function in low-vision patients. Since the 1950*s*, cortical correlates of vision in visually impaired patients with RP have been investigated using EEG.

The seminal studies of visual impairment with EEG were already targeted at RP and focused on the assessment of brain rhythm modulations, especially the alpha band (Francois et al., 1954; Gillespie & Dohogne, 1964; Krill & Stamps, 1960; Streifler & Landau, 1955). They noted an abnormally high rate of resting state recordings in RP patients compared to healthy controls but concluded with mixed results and absence of identification of clear common patterns among patients. This probably owes to the vast genetic heterogeneity of this group of diseases (Krill & Stamps, 1960) and the limited computational power for data analysis at this time.

Consequently, later studies have been more focused on VEPs (Alexander et al., 2005; Hamilton et al., 2021; Papathanasopoulos & Papakostopoulos, 1994; Paranhos et al., 1998; Parisi et al., 2010). They described delayed latencies and smaller amplitudes in pattern-reversal VEPs elicited in RP patients compared to healthy controls, coherent with the impaired transmission of visual stimuli from the retina to cortical areas (Papathanasopoulos & Papakostopoulos, 1994; Paranhos et al., 1998). Additionally, Alexander et al. (2005) were able to link the contrast sensitivity loss with reduced VEP amplitude in a RP population. In the domain of visual restoration, the evaluation of recovered retinotopic mapping in Argus II implanted patients using EEG-based methods was recently described by He et al. (2018) in the form of a conference abstract, with limited disclosure of the results.

A renewal for brain rhythms in low vision and functional recovery research was observed recently. For instance, substantial differences to healthy individuals have been found during visual stimulation of patients with inherited retinal dystrophies using the shape of the EEG power spectral density, in particular in the occipital electrodes (Myers et al., 2017). Posterior alpha and theta activity related to the visual processing of motion has also been used to identify the neural mechanisms of functional sight restoration of congenital blindness (Bottari et al., 2016).

CHAPTER 4

TOWARDS MORE ECOLOGICAL PARADIGMS IN HUMAN NEUROIMAGING

As already acknowledged multiple times in the preceding chapters, there is a high interest in conducting the current neuroimaging investigations outside the current standard laboratory framework. First, the current chapter proposes to define what was understood as an ecological paradigm in this thesis, to underline the general limitations of current neuroimaging literature. Then it pinpoints specific gaps in the spatial navigation, healthy aging and visual restoration literatures that could benefit from more ecological paradigms. Eventually, it introduces the methodological framework that served as a basis to this project, the mobile brain/body imaging (MoBI) approach and, focusing on mobile EEG, it reviews the state-of-the-art studies that already leveraged this methodology to bring new insights in the three fields set forth in this project.

Overall, this chapter highlights that although the tools enabling neuroimaging in ecological conditions are now developed enough to consider a wide range of novel paradigms with scientific-grade control over the experimental parameters, mobile EEG has yet to prove its worth in a variety of fields where mobility could have a substantial influence on study outcomes. Specifically, in the three fields of interest of this thesis, the few preliminary findings call for more ambitious research paradigms to gain more insight into the use of visual landmarks during realistic navigation and the effects of multisensory stimulation on the perception of navigability of real-world scenes by SSRs.

4.1 Ecological paradigms: the current stance

Strictly speaking, an ecological experiment studies its participants in their daily life, with minimal interference from the experimenters in terms of instructions and constraints. While it may be conceivable in some fields of research, in the domain of human neuroscience, especially when considering the use of neuroimaging devices, it is often impossible to conduct experiments in such conditions. Therefore, in the scope of this thesis, what is referred to as ecological is in fact *near-ecological*, meaning that researchers are willing to test sensory or cognitive abilities of their participants in conditions that try to reproduce everyday life situations, albeit with more control over the stimuli of interest and the range of external parameters that may interfere with the tested ability.

4.1.1 Most human neuroimaging studies are static

In the field of human spatial cognition, a large body of studies were conducted with a MRI scanner (Epstein et al., 2017; Taube et al., 2013) due to its unmatched spatial resolution among non-invasive methods. By requiring the participants to lay down in the scanner and refrain movements to ensure good imaging, this instrument imposes enormous constraints on the type of paradigms that can be considered. In this case, most experiments consist in either mental imagery or presentation of a sequence of static visual stimuli with minimal actions from the participant (usually not more than one or two buttons to press). Experiments with a dynamic video display and an interactive task are less common (Auger et al., 2015; Diersch et al., 2021; Ramanoël et al., 2020; Stangl et al., 2018), while still restricting the stimulation to the visual sensory input. In practice, many studies have opted for protocols where the participants perform a task outside the scanner and are then tested on specific (static) aspects of the task while undergoing fMRI (see for example Janzen and van Turennout 2004; Peer and Epstein 2021; Shine et al. 2016, 2019).

Among non-invasive methods, EEG is also a widely used option to investigate cortical correlates of a wide range of behavioral tasks. It suffers from a poor spatial resolution compared to fMRI but offers a fine temporal resolution enabling to decipher more precisely the dynamics of brain activity during spatial behavior (Baker & Holroyd, 2009; Bischof & Boulanger, 2003; C.-T. Lin et al., 2009). However, although EEG does not prevent the participant's motion per se, it is very sensitive to movement-related artifacts. Electrical potentials from muscle contractions (*e.g.*, head movements, eye blinks, or heartbeat, see Jung et al. 2000) generate strong artifactual signals that compromise the extraction of brain-related responses thus reducing the signal-to-noise ratio (SNR). As a consequence, most EEG studies have also resorted to drastic mobility constraints in order to minimize motion-related artifacts. Until recently (see Section **4.3**), experimenters were forced to make participants sit in front of visual stimuli and respond with minimal movements (*e.g.*, finger taps), similarly to fMRI.

In that context, any neuroimaging protocol that introduces additional stimulation modalities (*e.g.*, tactile, vestibular, proprioception) and/or enables some degree of natural move-

ments from the participant (from head to full body movements) is already a significant step towards gaining more insights on how the brain functions in ecological situations.

4.1.2 Virtual reality: a compromise to real-world settings?

With the advance in informatics technology, modern neuroscience has been provided the ideal tool to create entirely customizable virtual environments where experimenters can precisely control the amount of visual information available to participants during the task, while varying relevant parameters systematically to test different conditions of interest. In the past 40 years or so, virtual reality (VR) has therefore become a cornerstone of neuroscientific studies investigating complex behaviors (*i.e.*, not limited to passive perception). Here, VR paradigms are understood as experimental paradigms in which participants experience and navigate a digitally generated 3D environment irrespective of whether they actually move during navigation (stationary *vs.* mobile VR) or how they view it, *i.e.* on a 2D screen or in a head-mounted display (Diersch & Wolbers, 2019). See Figure **4.1** for an illustration of different VR in human cognition research. In the following, the term *desktop-*

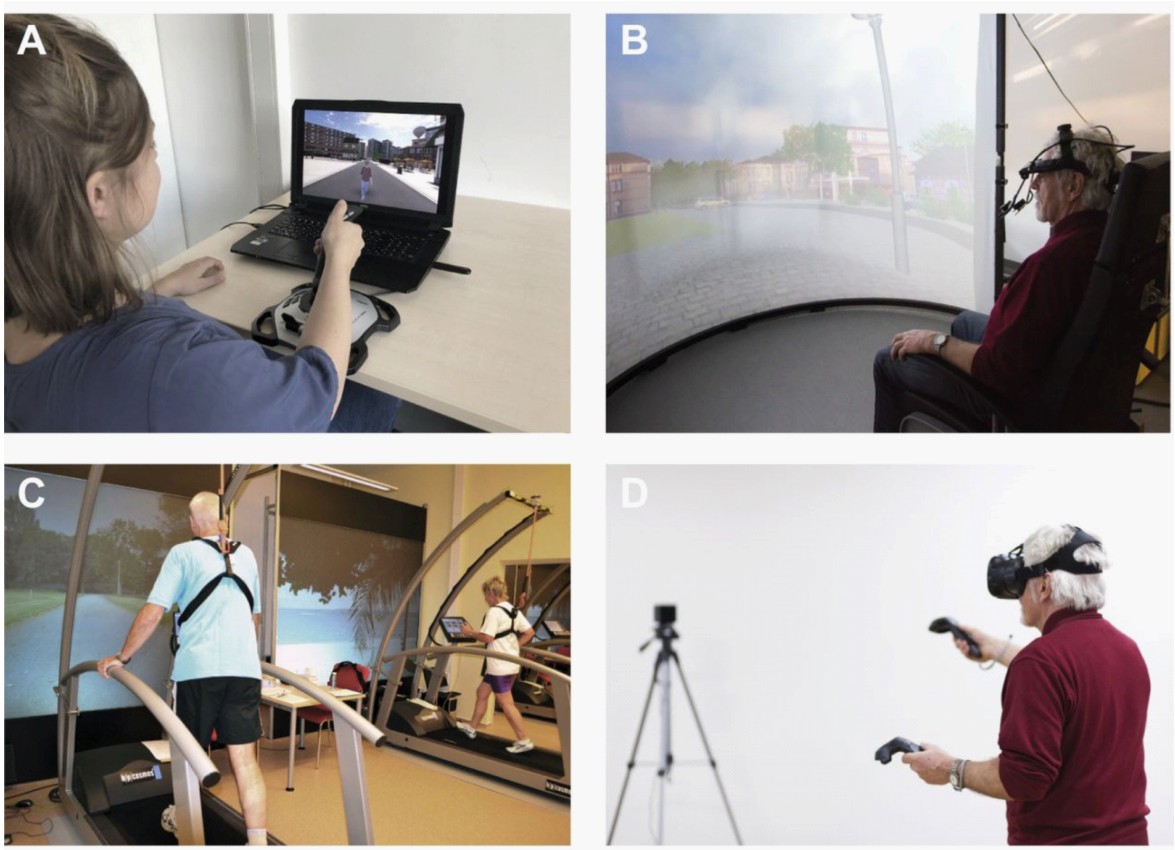

Figure 4.1: VR in human cognition research. Examples of VR setups to study human spatial navigation using **A**. a 2D desktop screen with joystick, **B**. a large-scale screen with eye tracking, **C**. a large-scale screen with a linear treadmill, and **D**. a head-mounted display with motion capture. Note that these setups differ along multiple dimensions, including display size, 2D versus 3D presentation, access to spatial cues, and the correspondence between visual and body-based cues. Each of these parameters will affect immersion into the virtual world, which is generally weakest in **A** and strongest in **D**. Reused from Diersch and Wolbers (2019).

based VR refers to a 2D screen stationary set-up (Figure **4.1A**), while the term *immersive VR* is reserved for head-mounted display mobile set-ups (Figure **4.1D**).

4.1.2.1 Desktop-based VR

Even though computer interfaces are now an inherent part of our daily life, this type of experimental design has poor ecological validity for spatial cognition, notably because it solely relies on optic flow to induce the sensation of movement (Taube et al., 2013). Researchers are making some progress in rendering virtual environments that are more and more realistic and rich detailed (*e.g.*, Diersch et al. 2021; König et al. 2021; Liang et al. 2018; Peer and Epstein 2021) that improve the naturalistic aspects of visual perception.

4.1.2.2 Immersive VR

Enabling a great leap forward, one of the most notable technological innovations in the recent years pertains to the development of increasingly reliable and affordable immersive VR devices. Commercial head-mounted displays now provide a precise coordination of the visual display, with head movements of the participant, thus enabling a near-naturalistic visuo-vestibular integration. Reducing the discrepancy between body-based and visual cues was demonstrated to positively impact on spatial presence (Kober et al., 2012), path integration (Chrastil et al., 2019), route knowledge (Ruddle et al., 2011a), and cognitive map representation (Ruddle et al., 2011b).

The huge advantage of this technology is that it benefits from the same level of control and standardization of all environmental variables than desktop VR (Bohil et al., 2011). VR paradigms further provide the unique opportunity to go beyond reality and imagine experimental manipulations that would otherwise not be possible, such as teleportation between remote places in an environment to investigate the relationship between time and space or distance coding or spatial updating (Bécu et al., 2023; Liang et al., 2021; Vass et al., 2016; Warren et al., 2017). VR also considerably enlarge the extent of the environmental space typically tested in human spatial cognition, both from a visual perspective with distal cues (*e.g.*, Shine et al. 2016) and from a walkable perspective (when coupled to an omnidirectional treadmill; Harootonian et al. 2020; Liang et al. 2018).

Although this represents a technical challenge and additional motion capture recordings, the degree of immersion with head-mounted displays can further be elevated by incorporating an avatar representation in the virtual environment that matches the movements of the participant. Indeed, several illusion studies have demonstrated that synchronous stimulation between sensory sensations (vision combined with proprioceptive, motor, or tactile sensations) successfully evoked a complete feeling of embodiment of a virtual limb or body (Botvinick & Cohen, 1998; Lenggenhager et al., 2007). The development of novel devices successfully reducing the motion-to-image latencies such that it becomes truly undetectable to human perception will definitely help to progress in this direction.

On a very promising note, in a recent study comparing spatial orientation in real-world and immersive VR settings, Pastel et al. (2022) reported a similar behavior in both modalities.

4.1.2.3 Limitations of immersive VR with respect to real-world settings

However, there are still concerns on whether the simulation provided by such devices can fully replace the experience of a real-world environment (Diersch & Wolbers, 2019). Despite unlocking new experimental designs unachievable in real-world settings, immersive VR still does not exactly match some aspects of daily life conditions. It remains a trade-off for the experimenter to decide whether the differences are detrimental to the research question posed by the paradigm.

One main technical limitation is the size of the FoV in the VR headset, which is almost twice as small as the natural FoV (Ghezzi, 2023), which may undermine the importance of peripheral visual processing in naturalistic conditions (Cao & Händel, 2019). Importantly, reduction in the FoV was found to be detrimental to the extraction of geometric information from the environment (Sturz et al., 2013), which was indirectly confirmed by Kimura et al. (2017), who demonstrated that participants were more reliant on landmarks than geometry in immersive VR compared to a real experimental room. Thus, by influencing the type of visual information readily usable for participants, the choice of VR over real-world settings might prove crucial in experiments investigating visuo-spatial strategies in navigation. This may have far-reaching consequences in healthy aging research, where older adults were found to be more dependent on geometrical information to reorient in a real environment than young adults (Bécu et al., 2020a). Hopefully, new devices are already closing the gap with a more natural human FoV.

Another limitation to keep in mind in the influence of the experience with virtual environments, which can explain difference between sub-populations under testing. Indeed, video game experience, which has numerous similarities with the simulation proposed in VR, is deeply correlated to navigational performance in virtual environments (Murias et al., 2016; Richardson et al., 2011). This can be the source of reported gender or age differences in performance if not taken into account properly (Diersch & Wolbers, 2019).

4.2 The need for neuroimaging studies with a more ecological approach

The interest for a more ecological approach in neuroimaging has already been underlined in the preceding chapters. The most important reasons in light of the work conducted during this thesis are summarized in the following.

4.2.1 In visuo-spatial cognition

Most evidently, the benefit of bringing neuroimaging studies closer to ecological situations lies in the multimodal nature of spatial navigation that has already been highlighted multiple times in the previous chapters (Arleo & Rondi-Reig, 2007). Accordingly, the continuous interplay between locomotion and multisensory perception is thought to be a key component of spatial cognition in near-natural conditions, as its absence leads to impaired performance

in various spatial abilities (path integration: Chance et al. 1998; spatial updating: Klier and Angelaki 2008; spatial reference frame computation: Gramann 2013; spatial navigation and orientation: Ladouce et al. 2017; Taube et al. 2013; and spatial memory: Holmes et al. 2018). Mobile brain imaging protocols, by engaging locomotion control processes and enabling the integration of vestibular and proprioceptive cues have already started to yield novel insights on the neural correlates of spatial orientation (Ehinger et al., 2014; Gramann et al., 2021) and attention (Ladouce et al., 2019), modifying the knowledge acquired in stationary settings.

Although introduced from a purely visual perspective, the concept of affordances can also be largely influenced by near-ecological testing conditions. Indeed, as argued in Section **1.2.3.3**, affordances are not only determined by the environmental properties, but are also relative to the agent (Clark, 1999). Therefore, the embodiment of the observer in the scene may play a determinant role in defining what can be afforded or not, especially when considering navigational affordances (Djebbara et al., 2019). Indeed, multiple studies have shown that the visual characteristics of a scene alone were not sufficient to explain the activity in the SSRs (and more particularly the OPA), as the modulation by functional constraints shaped by our daily life experiences was a better predictor of the fMRI signal (Chaisilprungraung & Park, 2021; J. Park & Park, 2020). J. Park and Park demonstrated that a transparent wall, but not a transparent curtain, elicited a different activity in the OPA related to the navigable distance in a corridor while Chaisilprungraung and Park showed that the presence or absence of a bay window had a better correlation with the PPA and OPA activity than the openness of the scene. Interestingly, a recent fMRI study has observed a variability in the activity of the OPA and the PPA depending on the spatial context of the presented scene (Aminoff & Tarr, 2021). Context was manipulated by presenting real-world landscape images as if being viewed through a window or within a picture frame, in order to only affect the functional knowledge related to the scene and not the scene content itself. These regions were more activated in the 3D realistic context, which correlated with better spatial memory of the scene. This may be a sign of predisposition of the SSRs for a space that is navigable, especially considering the responsiveness of the OPA to navigational affordances in general. Investigating these properties in a more ecologically valid context is warranted to elucidate this hypothesis.

4.2.2 In healthy aging

Section **2.1** provided several examples concerning visual perceptual abilities that are perturbed by healthy aging and that may have unforeseen consequences in ecological conditions. For example, the less precise processing of the optic flow (Warren et al., 1989) may be particularly relevant to navigation in mobile conditions, while testing older adults in a more complex and richer visual environment could put more stress on a less flexible visual exploration strategy (Dowiasch et al., 2015) and a failing associative visual system (Head & Isom, 2010).

In addition, Section **2.3** has already underlined many of the motivations for taking into account the interplay between multisensory integration and locomotor aspects with spatial

cognition, in the context of healthy aging. Whereas the binding of multisensory cues remains successful and helpful for older participants especially in path integration paradigms (S. L. Bates & Wolbers, 2014), the decline of physical abilities with age may aggravate the performance of elderly people in spatial navigation tasks by reshaping how they perceive the navigable space (Sugovic & Witt, 2013) and diverting attentional resources from cognitive abilities (Agathos et al., 2020). Since older adults have already been found more sensitive to distractors in visual processing (Gazzaley et al., 2008), the further disturbance in the allocation of attentional resources may prove to be an additional significant impediment for spatial behavior that was not yet well characterized in stationary paradigms.

These considerations advocate for more ecological paradigms to be able to draw conclusions that neither under- nor over-estimate the difficulties encountered by older adults in their daily lives. Beyond behavioral observations, neuroimaging studies testing concomitantly spatial navigation, attentional, and motor abilities would help decipher the neural underpinnings of age-related deficits and disclose the specific role of each brain region within the network of natural processes at play.

4.2.3 In vision restoration

It seems evident to assume that the ultimate goal of visual prostheses is to restore sufficient vision to bring substantial benefits in the daily life of their recipients, especially over orientation and mobility abilities (Ayton et al., 2020). However, current studies often rely on self-reports to evaluate functional visual recovery in more natural conditions which are by nature qualitative, subjective, and non-standardized (Erickson-Davis & Korzybska, 2021). Thus, the insights provided by these evaluations are impractical to use to compare the qualities of different prostheses and more quantitative clinical measures such as acuity, field size, and motion detection are often favored to improve the design of prostheses independently of the real outcome on patients (Borda & Ghezzi, 2022; Hallum & Dakin, 2021). VR tools can help find a middle ground between objective, quantitative assessments in standardized conditions and clinical evaluations that are more generalizable to daily life situations (Borda & Ghezzi, 2022). Introducing more neuroimaging tools into the testing of these devices is also important to better comprehend the neuroplastic mechanisms that are triggered by the implant and to further characterize the cognitive fatigue elicited by the device. Although coming after the numerous technical challenges faced by this field to be able to propose sight restoration solutions, these aspects are far from negligible in the design process of novel prosthetics. Indeed, by demonstrating significant progress in their daily life and trying to alleviate the mental efforts required for its use, they contribute to enhancing the motivation of the recipients to adopt the device, which is currently a substantial issue for the field (Borda & Ghezzi, 2022; Erickson-Davis & Korzybska, 2021; Hallum & Dakin, 2021).

Additionally, it may be noted that considering mobile neuroimaging approaches is an inherent constraint of this kind of evaluations, since, as highlighted in Chapter **3**, the current prostheses require a considerable amount of head movements (because of their narrow FoV) from their users. The use of MRI is also by nature impeded by the metallic elements of

the prosthesis and its accompanying filming device which often do not present magnetic properties compatible with the scanner.

4.3 The Mobile Brain/Body Imaging approach

In order to address these gaps and provide a framework to design mobile experiments that unveil new dimensions of brain signal interpretation, Gramann et al. (2011) introduced the mobile brain/body imaging (MoBI) approach that leverage developments in brain recording techniques, innovations in VR technologies and wearable biometric measurements systems, as well as powerful signal processing tools. These key enablers are first presented in the three following sections. Section **4.4.2** then reviews the main insights that were gained with mobile EEG, focusing on the main fields of application of this thesis.

4.3.1 Brain imaging techniques suitable for mobile conditions

To date, several brain imaging systems have been tested and adopted in mobile conditions: scalp EEG (first report in mobile conditions in Gramann et al. 2010a), functional near-infrared spectroscopy (fNIRS) (first report in mobile conditions in Atsumori et al. 2010), intracranial electro-encephalography (iEEG) (first report in mobile conditions in Aghajan et al. 2017), and even a mobile magneto-encephalography (MEG) system that can be worn like a helmet based on optically pumped magnetometers has recently been successfully developed (Boto et al., 2018). Unfortunately, because of the required surgical intervention, iEEG cannot be considered for systematic use in healthy participants, and its use remains constrained to the chemically resistant epileptic population. Wearable MEG, although a very promising emerging method to non-invasively record brain activity from cortical and subcortical regions, is still dependent on very specific conditions of use (*i.e.*, magnetic shielding of the experimental room) that impede its widespread use. In contrast, the accessible and noninvasive natures of EEG and fNIRS make them ideal candidates for recording large samples of subjects. On the one hand, the strength of mobile fNIRS recordings is that they are based on the BOLD signal, providing a direct comparison with the knowledge obtained with stationary fMRI studies. On the other hand, EEG offers a sub-second timescale window into the dynamics of cognitive processes that can be more adapted to investigate them in natural settings.

For this project and in the following developments, the focus will be put on mobile EEG recordings which represent the majority of studies that provide supporting evidence in the scope of this thesis. More thorough reviews expanding on the advantages and inconvenients between these brain imaging techniques can be found elsewhere (J. L. Park et al., 2018; Stangl et al., 2023). To enable mobile EEG, major technical obstacles related to recording brain signals in motion have been overcome by engineers. For example, the sensitivity of EEG to artifacts has been mitigated through the development of active electrodes and cable shielding (Laszlo et al., 2014). Additionally, lighter amplifiers and wireless capabilities have enabled to record high-quality data without tying the subject to a desk (Oliveira et al., 2016).

4.3.2 Combination with multidimensional biometric recordings

Studying freely moving participants in complex scenarios and real-world settings requires multidimensional recordings of numerous variables, including those considered to be noise or confounds, in order to be able to include these variables in the study design and analyze their impact on human cognition and behavior. Besides mobile neuroimaging data, recording such multidimensional data is possible through the use of modern technological wearable measurement systems that can record behavioral, physiological and environmental influences (Figure **4.2**; Stangl et al. 2023).

The most important features in the field of visuo-spatial cognition are undoubtedly the progress in mobile eye-tracking and motion capture. Accessing the oculomotor behavior of participants can be informative when striving to uncover navigationally relevant information, visual exploration strategies, or movement planning (Bécu et al., 2020a). Similarly, motion capture allows for the investigation of body movements and gait metrics such as walking speed and trajectory efficiency during navigation (Agathos et al., 2020). The co-registration

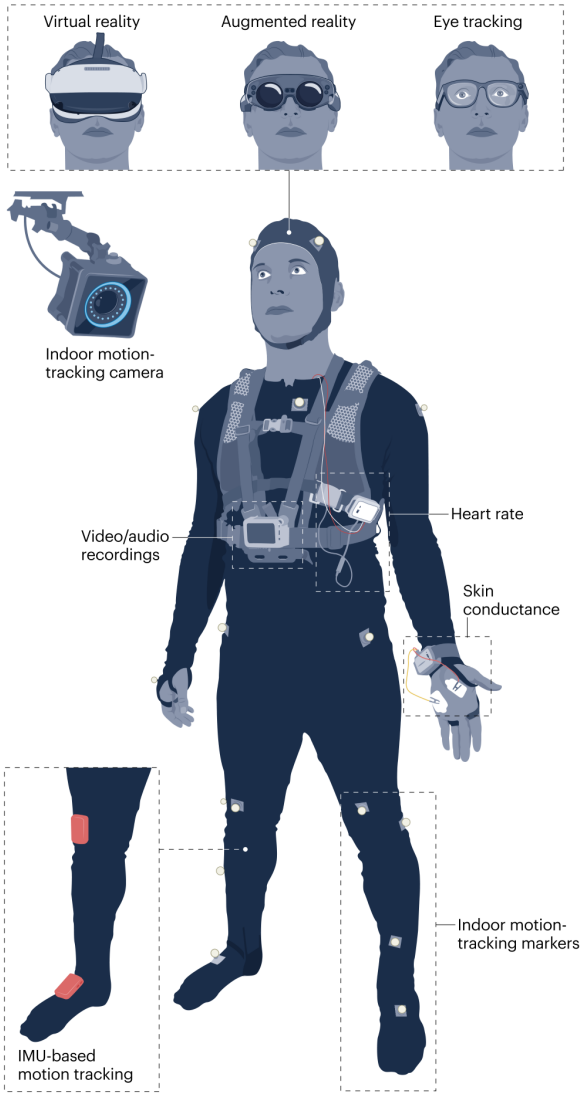

Figure 4.2: Illustration of potential multidimensional recording modalities for mobile cognition studies in humans. All these modalities are ideally recorded synchronously to enable synergistic analyses.
Stimulus presentation technologies. VR & AR head-mounted displays create a controlled virtual environment or integrate digital elements directly into the physical environment.
Oculomotor metrics. Mobile, wearable eye-trackers follow the eye movements and measure the pupils size.
Motion capture modalities. Optical motion-tracking systems continuously capture the position of reflective wearable markers with sub-millimeter resolution through motion-tracking cameras. Alternatively, inertial measurement unit (IMU) systems, using a combination of accelerometers, gyroscopes and magnetometers, track motion of a specific part of the body without the need for cameras.
First-person perspective. Audio and video recordings on the body give access to the environmental cues experienced by the participant.
Physiological parameters. Heart rate, respiration or skin conductance are measurable with wearable systems.
Reused from Stangl et al. (2023).

of brain signals and biometric measures like body and eye movements allows neuroscientists to design mobile experiments that unlock new dimensions of brain signal interpretation (Gramann et al., 2014, 2011; Makeig et al., 2009).

Crucially, the data streams from multiple recording systems need to be synchronized with each other and with the neural recording to allow precise synergistic analyzes. To that purpose, multiple open-source technical solutions have been released to facilitate the synchronous recording of heterogeneous sources of data with different sampling rates and temporal resolutions, such as the Lab Streaming Layer (LSL) protocol (Kothe 2014; see Section **6.2.1** for more details).

4.3.3 Advances in data analysis

Eventually, advances in data processing methods have successfully been applied to EEG recordings to detect and remove aforementioned artifacts. Of utmost importance for this purpose, blind source separation algorithms such as independent component analysis (ICA) can isolate artifactual components from the neural signal (Jung et al., 2000; Makeig et al., 1995, 1997) even with mobile EEG data (Gwin et al., 2010). ICA disentangles the contained information at the electrode level by computing a set of independent components (ICs) that are maximally statistically independent (Bell & Sejnowski, 1995), the decomposition being finer as the number of electrodes increases. Blind source separation additionally eases the solving of the EEG inverse problem *i.e.* finding the spatial origin of EEG signal of interest that emerges from synchronous aspects of local field potentials around parallelly-arrayed cortical cells (Varela et al., 2001). Once components have been extracted from the EEG signal, it is rather simple to perform, one at a time, source localization in accordance with their activation map. Using the dominant model for source localization (*i.e.*, the equivalent current dipole), Delorme et al. (2012) showed there was a clear correlation between ICs having a good dipolar scalp projections and their probability of representing the activity of physiological neural sources. This highlights the relevance of ICA both for artifact removal and for enabling the interpretation of EEG signal with improved spatial resolution.

Protocols typically last longer in mobile settings, as it is more complicated to move from a trial to the other at a rapid pace, and require a higher number of channels to facilitate blind-source separation approaches (Gramann et al., 2021; Nordin et al., 2019, 2020). Consequently, experimenters have to deal with an increasing amount of data which called for automated processing methods to achieve analyzes in a reasonable amount of time and with more objective and standardized parameters (Pedroni et al., 2019). For that purpose, forward leaps in the field of machine and deep learning were instrumental in enabling MoBI, for example in providing automatic labels to the ICs extracted with ICA (Pion-Tonachini et al., 2019). Furthermore, given the increased multidimensionality of the datasets collected, advanced mathematical methods and models (*e.g.*, mixed-effect models, multimodal models and multivariate methods) are continuously adapted and developed to accommodate for the added complexity (Mao et al., 2021; Stangl et al., 2021).

Based on the EEGLAB open-source toolbox for EEG analyzes (Delorme & Makeig, 2004), MoBI developers have made available additional tools to help the mobile EEG community with the import of multimodal recordings accompanying EEG data (Ojeda et al., 2014) and to provide data processing pipelines specifically tuned for mobile EEG recordings (Klug et al., 2022).

4.4 EEG state-of-the-art

In order to set the EEG background of this thesis, this last section first presents the classical approaches for the analysis of EEG recordings that served during this work. Then, the current state of mobile EEG literature in the fields of visuo-spatial cognition, healthy aging, and visual restoration approaches will be reviewed.

4.4.1 Classical approaches to EEG analysis

Once cleaned from artifacts, the signal recorded by EEG comes in the form of a time course of the electrical potential at each electrode (typically expressed in μV). This signal can be analyzed either at the *sensor* (*i.e.*, electrode) level, with very low spatial resolution, or at the *source* level, by attempting to infer the origin of the signal within the brain using a source reconstruction approach. Such an approach relies on modeling the propagation of the electrical current in the brain from the putative source to the electrical sensor (see Section **6.3.2** for more details).

Beyond this choice, there are several types of analysis available to the experimenter. When looking for broad neural activity tied to a predetermined period in the experiment, a spectral decomposition of the time course of the signal (typically a Fourier transform) is the most commonly used option. When examining cortical correlates in response to a specific external stimulus event (usually intentionally introduced in the paradigm), two main approaches are typically used to fully exploit the millisecond timescale of the EEG, depending on the dimension of interest of the data. On the one hand, time domain analysis examines the so-called event-related potentials (ERPs) without any further transformation (see Section **4.4.1.1**). On the other hand, time-frequency analysis, by computing the spectral decomposition over regularly spaced sliding windows, allows the analysis of so-called event-related spectral perturbations (ERSPs; see Section **4.4.1.2**).

4.4.1.1 Event related potentials

ERPs are signatures in the EEG time course that are reliably time-locked to stimulus presentation (*e.g.*, visual, auditory, motor, *etc.*). They are characterized by a strong waveform (up to 20 μV amplitude; Patel and Azzam 2005) with a negative or positive peak that is stable across trial repetitions. The sign of the peak and its latency with respect to stimulus onset are the most important descriptors of an ERP. Sometimes they are also characterized by the amplitude of the peak and the location of the strongest observation on the scalp. They can be

the signature of passive cortical phenomena (*i.e.*, intrinsically linked to the physical parameters of the stimulus), in which case they are called exogenous ERPs, or they can be linked to active cortical processes (*e.g.*, relative to the value of the stimulus to the subject), in which case they are called endogenous. Because they are associated with more complex, slower processes, endogenous ERPs often occur at longer latencies than exogenous ones (Sur & Sinha, 2009). Since ERPs were only a minor focus of the analyses performed in this work, a brief overview of the most common ERPs found in visual processing is proposed here.

Among the exogenous ERPs, the most abundant is the P1 (positive peak at $+100$ ms latency) evoked by any strong stimulus onset. Despite its name, its latency has been reported to be as long as $+250$ ms (Sur & Sinha, 2009). Its largest amplitude is expected at scalp locations around the occipital channels where early visual processing areas are located. The N1 (negative peak following the P1) is a typical marker of visuo-spatial attention (*i.e.*, it has a larger amplitude for attended than for unattended stimuli), which has been linked to discriminative purposes (Luck et al., 2000). Following the N1, the visual P2 component is thought to index the encoding of the stimulus into working memory (Lefebvre et al., 2005). Its peak is typically found over parieto-occipital regions (Freunberger et al., 2007).

The most common endogenous ERP is known as the P300 (positive peak at $+300$ ms latency), first described by Sutton et al. (1965). It seems to be related to the subject's interest in the stimulus. Depending on the stimulus, its latency can span larger values and its scalp location can be quite variable, but it is generally found in parietal, temporal, and frontal regions (Patel & Azzam, 2005).

4.4.1.2 Most frequent interpretations of the frequency bands

With respect to analyses based on the frequency dimension (*i.e.*, broad spectrum or ERSPs), interpretations of the observed patterns have often taken a band-wise approach. The major frequency bands are usually defined as: delta (< 4 Hz), theta (4-8 Hz), alpha (8-12 Hz), beta: (12-30 Hz), and gamma (> 30 Hz). Throughout the long history of the EEG literature, activity in these bands has been ascribed different roles depending on the cortical region involved and the paradigm employed. The consensus on these roles, when relevant to the areas of interest of this work, is reported below.

Delta oscillations are mostly involved in intensive internal cognitive processes, and increased delta synchronization is associated with increased cognitive demands (Güntekin & Başar, 2016). As a possible explanation, Harmony (2013) proposed the hypothesis that sustained delta oscillations inhibit interference that may affect the performance of mental tasks. It should also be noted that oscillations in this band are slow and may rely on the same neural underpinnings as ERPs, particularly the P300 (Güntekin & Başar, 2016).

Theta rhythm is the frequency band most closely associated with spatial cognition, with recurring evidence from animal and human studies for its role in encoding spatial quantities in the medial temporal lobe (Herweg & Kahana, 2018; Kunz et al., 2019). Given the deep location and spatial structure of this region (see Section **1.3.3.3**), these findings have mostly come from intracranial recordings. In addition, theta synchronization has been proposed as a substrate for the integration of perceptual information into decision-making mechanisms

when reported via frontal electrodes over the prefrontal cortex (Cavanagh & Frank, 2014; Womelsdorf et al., 2010).

Alpha rhythm is the dominant oscillatory pattern in the brain. As discussed in Section **3.3.1.2**, it is strongly associated with visual information processing, especially when it is located over occipital regions (Pfurtscheller & Klimesch, 1991). Specifically, occipital alpha desynchronization (*i.e.*, reduced power relative to a reference baseline) is involved in object-based visual attention (W. Feng et al., 2017), top-down control of visual attention (Thut et al., 2006), stimulus discrimination in object detection (Vanni et al., 1997), and object recognition (Freunberger et al., 2008). Alpha oscillations have been theorized to play an inhibitory role in limiting and prioritizing neural processing based on attentional focus (Jensen et al., 2014; Klimesch, 2012).

The beta band has been mainly attributed to the execution or imagination of movement in the sensorimotor cortex (Cevallos et al., 2015; Delval et al., 2020). In other contexts, and more broadly in terms of brain regions, Engel and Fries (2010) have formulated the idea that beta-band activity is associated with the maintenance of the current cognitive state. In this theory, desynchronization in the beta band is likely to be a signature of the disruption of the internal state by the processing of an exogenous stimulus, whereas synchronization should indicate a top-down endogenous effort to attend to the current state of cognition.

Human gamma frequency activity is associated with attention and memory in both sensory and non-sensory areas (Jensen et al., 2007). Particularly over the parieto-occipital region, increased gamma power promotes sharper visuospatial attention (Gruber et al., 1999; Müller et al., 2000). Theoretical models suggest that this frequency band plays an important role in neuronal communication between distant regions and is therefore involved in many complex cognitive processes (Jensen et al., 2007). Interestingly, there appears to be a significant correlation between gamma power and the fMRI blood oxygen level dependent (BOLD) signal (Buzsáki et al., 2012), providing a basis for comparison between the two neuroimaging modalities. However, the highest frequencies are particularly prone to noise contamination, and scalp EEG studies are often limited to analyzing frequencies below 50/60 Hz, while frequencies up to 100 Hz are often reported in animal and intracranial recordings.

4.4.2 Insights from mobile EEG so far

In more than a decade, the MoBI approach has gained considerable momentum and multiple research groups have now integrated mobile brain imaging into their experiments to start filling the knowledge gap between the neural underpinnings of isolated visual stimulation in controlled laboratory settings and ecological brain activity. Out of the scope covered by this thesis but noteworthy, the continuous technological and methodological improvements in this domain keep unlocking new possibilities for researchers to study the brain in a variety of ecological situations (*e.g.*, outdoor walking: Reiser et al. 2019; cycling: di Fronso et al. 2019; on a tightrope: Leroy and Cheron 2020; during space flight: Fiedler et al. 2023).

The state-of-the-art review presented here, in alignment with the interest developed in this project, will focus on the insights brought by mobile EEG in the fields of human visuo-spatial cognition and healthy aging, as no previous neuroimaging studies in near-ecological conditions were found in the domain of visual restoration.

4.4.2.1 In visuo-spatial cognition

For reasons already exposed above, spatial cognition rapidly embraced mobile EEG to extend the findings obtained in static position with more ecological paradigms.

Mobile EEG studies have started to unriddle the complex interaction between visuo-spatial cognition and ambulation at the neural level. The modulation of alpha oscillations recorded during walking reflected increased early sensory processing (X. Chen et al., 2022a) and especially of more peripheral visual inputs (Cao & Händel, 2019). The current locomotion state of the body was also found to affect eye movement patterns; taken together, these results reflect an underlying strategy of optimizing the extraction of sensory information during locomotion (Cao et al., 2020). With respect to cognitive factors required during locomotion, Ladouce et al. (2019) recently employed mobile EEG to understand how participants allocate cognitive resources when tasked with identifying visual targets in moving conditions. They found that the additional cognitive demands during movement, and not the movement *per se*, reduced the attention of participants to the stimuli of interest, as reflected by the P300 ERP (also reported by X. Chen et al. 2022b). A reduction in P300 amplitude was afterwards replicated during free viewing search in real-world settings, compared to gaze-fixed on tablet, confirming the influence of a more complex and dynamical context on the allocation of attention (Ladouce et al., 2022).

Regarding multisensory integration, Ehinger et al. (2014) pioneering study demonstrated that brain rhythms were significantly modulated by the presence of natural vestibular and kinesthetic feedback during spatial orientation. This was recently replicated by Gramann et al. (2021), who reported differences in EEG activity from the RSC between stationary and full-body rotation setups. Their results suggest that a strong desynchronization in the alpha band (8-12 Hz) could be a marker of a sensory mismatch between vision and proprioception during full-body rotations. The latter finding questions previous studies conducted in static conditions that linked this alpha desynchronization with heading computation. Do et al. (2021) prolonged the investigations and showed instead that theta (4-8 Hz) oscillations in the RSC was bound to heading changes during active spatial navigation.

In parallel, multiple brain rhythms have been implicated in encoding the spatial quantities necessary to map the environment in near-ecological conditions. Close to a cognitive map, Snider et al. (2013) demonstrated a structure in theta oscillations mapping the virtual space explored by their participants, reminiscent of place cells and grid cells recordings in the rodent (O'Keefe & Nadel, 1978). A follow-up experiment found an elevated frontal midline theta power for objects that were displaced between two exposures to the environment, indicative of a role in allocentric space template matching (Plank et al., 2015). Building up on intracranial recordings (Bohbot et al., 2017), Liang et al. (2018) showed that frontal-midline low frequency oscillations (below 8 Hz) were signatures of ambulatory movement.

Later, they managed to dissociate spatial and temporal coding, correlating occipital alpha power with the distance covered and frontal midline theta power with the travel time (Liang et al., 2021).

Eventually, some research groups have also started to investigate the perception of the navigable space and its constraints in embodied conditions. Di Marco et al. (2019) demonstrated that the execution of a step was influenced by the egocentric distance perceived by the observer, with faster stepping associated with farther distance. Stronger ERPs were identified over motor regions in far *vs.* near distance cues, interpreted as an action facilitation mechanism by the largest affordances (Tosoni et al., 2021). Mustile et al. (2021) characterized the neural bases of dynamic locomotor control when avoiding obstacles, with sufficient temporal resolution to isolate markers in frontal theta power when apprehending the obstacle and centro-parietal beta power in reaction to the avoidance. In another paradigm interrogating the affordance of a door depending on its width, early visual processing correlates of observation (both ERPs and posterior cingulate alpha-band activity) reflected the degree of passability (Djebbara et al., 2021, 2019). Additionally, the authors reported the dynamic modulation of the activity in the para-hippocampal region by the different affordance levels during the attempt of passing the door (Djebbara et al., 2021). These results underline both the feasibility and the interest in studying the potential actions afforded by a navigable environment to better understand how they interact with perception.

4.4.2.2 In healthy aging

Until now, aging research has extensively relied on the MoBI framework to study the reallocation of attentional resources during dual-task paradigms, with a particular focus on identifying clinical markers of pathological trajectories, and particularly Parkinson's disease (Possti et al., 2021; Roeder et al., 2020). However, until now, the variety of methodological approaches yielded mixed results regarding the neural underpinnings.

When maintaining their balance in a standing position, older adults were found more sensitive to optic flow perturbations and a shift of brain rhythms towards higher frequencies in sensorimotor areas was noticed compared to young participants (B. R. Malcolm et al., 2021). In multitasking conditions (*i.e.*, adding a visual oddball task), they privileged balance stability over cognitive performance, as revealed by increased (*resp.* decreased) activity in sensorimotor (*resp.* occipital) cortices compared to their younger counterparts (Rubega et al., 2021). In contrast, Bohle et al. (2019) reported the absence of a frontal lobe alpha band activity in older adults when confronted to increasingly difficult cognitive task during postural control, in contrast to young participants.

During locomotion, having to perform another motor task (*e.g.*, carrying a glass of water) is more difficult for older adults and elicited more gamma-band oscillations in the frontal lobe for older adults compared to their younger counterparts (Marcar et al., 2014). In turn, Protzak and Gramann (2021) observed a decreased modulation of sensorimotor brain rhythms associated with greater slowing in walking speed in older adults compared to young participants, sign of an adaptive resource allocation strategy. When introducing a cognitive-locomotor interference, however, B. R. Malcolm et al. (2015) had revealed a less flexible

strategy in healthy aging, detrimental to the cognitive performance, correlated with ERP neural markers of increased cognitive load. This was coherent with Protzak et al. (2021), who identified neural markers associated with worsened visual processing during ambulation that were more pronounced in older adults, similarly to Rubega et al. (2021) in postural control.

Eventually, the single mobile EEG study conducted on spatial cognition in the context of healthy aging so far evaluated allocentric spatial memory with resting-state EEG in-between ambulatory learning sessions, and replicated the results found in previous stationary working memory paradigms (Jabès et al., 2021).

CHAPTER 5

OBJECTIVES

To conclude the introduction to this project, this chapter presents the main objectives that stemmed from the reviewed body of literature and that have been addressed by this project. These objectives were divided into three axes. The first axis concerns the development of methodological contributions in the field of mobile EEG. The second axis regroups the experimental work aiming to contribute to the advancement of fundamental scientific knowledge in the field of visuo-spatial cognition in the context of healthy aging. The third axis considers translational applications to the characterization of visual restoration approaches of late-stage *Retinitis Pigmentosa*.

5.1 Methodological axis

I. *Introducing and developing a framework to facilitate mobile EEG recordings in the host laboratory.*

As argued in Section **4.3**, MoBI has multiple prerequisites, on both the technological and the methodological levels, that were new to the host laboratory.

Thus, this objective includes harnessing all the fundamentals to conduct high-density EEG recordings coupled with biometric sensors such as motion capture and eye-tracking, both in immersive VR and real-world conditions. It notably implies the development of relevant software interfaces to synchronize the different streams of data when not readily available from the manufacturer or the open-source scientific community. Additionally, it requires the development of a validated, standardized data analysis pipeline, customized to process mobile EEG recordings, specifically addressing the removal of motion-related artifacts and the extraction of brain-related components.

The achievement of that goal was reliant first on the collaboration with the laboratory of Pr. Klaus Gramann, a pioneer in the MoBI approach, who was of utmost guidance in the adoption of this methodology. Second, it greatly benefitted from the facilities and the expertise of the *StreetLab* company, especially concerning the set-up and usage of the VR system and the complementary behavioral recording modalities.

II. *Validating a source reconstruction approach that enables the study of scene-selective regions with EEG.*

The investigation of SSRs using EEG is a relatively recent development in the literature. Following the seminal work by Groen et al. (2013) and Harel et al. (2016), EEG studies examining temporal properties of scene-selective activity in the brain have primarily focused on analyzing signals recorded from a group of posterior-lateral electrodes (N. E. Hansen et al., 2018; Harel et al., 2020, 2022). In a few cases, investigations were conducted in conjunction with fMRI in order to improve the spatial validity of the conclusions drawn (Kaiser et al., 2020, 2019). Other EEG studies have also reported SSR-related activity based on (1) the proximity of the reconstructed activity locus to the known average location of these regions and (2) the plausibility that the experimental paradigm may activate these regions (Djebbara et al., 2021; Miyakoshi et al., 2021). Nonetheless, these studies lacked individualized source reconstruction models and a functional definition of the SSRs with fMRI, limiting the direct association of their results with these regions.

To address these limitations, the second methodological objective of this project is to enable the recording of SSR activity with the most accurate source localization. It involves implementing a source reconstruction model tailored to each participant and customized for the retrieval of SSRs, building upon the anatomical and functional MRI metadata available from the *SilverSight* cohort. It also requires to set up and to validate a quick and reliable approach for accurately obtaining the electrode locations on the participants' scalp, which had not been previously established at the host laboratory.

5.2 Fundamental axis

I. *Demonstrating the value of the mobile brain/body imaging approach to study landmark-based spatial navigation in more ecological conditions.*

As shown in Section **4.4.2**, there are still few recordings of human brain activity during active spatial navigation based on visual cues. To validate the MoBI approach in this context, it is first important to show that the analysis of the EEG signal can retrieve the brain structures known to be engaged during landmark-based navigation in stationary conditions, while providing new insights from the locomotor aspects of the task. Then, to highlight the added value of this methodology, it is essential to illustrate how the temporal resolution, as well as the synergistic behavioral recordings, help to enrich the interpretation of the brain dynamics along the different phases of navigation.

II. *Studying the impact of healthy aging on visuo-spatial information processing in scene-selective regions with EEG.*

At the interface between the early visual system and the high-hierarchical cognitive regions, SSRs are key elements of visuo-spatial information processing, but knowledge about their properties is largely limited to static scene presentation and suffers from a lack of temporal resolution. EEG neuroimaging would therefore provide access to a range of paradigms not yet available in the literature and would complement our knowledge of these regions. In addition, factoring in the visual impairments accompanying healthy aging, and in particular the reshaping of the use of visual space along the vertical axis is essential to better characterize how the processing of visuo-spatial information in the cortical scene system alters spatial navigation abilities in older adults.

III. *Assessing the influence of embodiment and mobility on the activity of the occipital place area associated with the perception of the walkable distance, and its modulation by age.*

Considering that several experiments conducted in the MRI scanner have demonstrated the influence of the scene context on the activity of the SSRs, especially when it played a role in the navigability of the scene, it seems legitimate to evaluate the effects of real-world presence and multisensory stimulation during scene perception. Given the relationship between the OPA and the perception of navigational affordances, which precisely characterize the possible interactions of the observer with the local space, there is great interest in assessing this specific aspect of scene perception in a more ecological context. Furthermore, since the impact of healthy aging on this domain remains moderate and even beneficial for older adults in some studies, walkable distance perception provides an interesting framework to study the aging of the OPA, which has so far shown signs of preservation with age, in contrast to other declining cortical regions involved in spatial cognition.

5.3 Translational axis

I. *Identifying objective neural markers of visual restoration approaches to Retinitis Pigmentosa.*

On a more translational level, this project aims to demonstrate how mobile EEG could benefit the understanding of perception in the context of pathological visual aging and, more specifically, to provide objective neural markers for the evaluation of visual restoration approaches in *Retinitis Pigmentosa*. First, as argued in Section **3.3**, it is essential to characterize the neural underpinnings of visual recovery in order to assess the reorganization of the cortical visual system in response to therapy. Second, more ecological clinical testing are warranted to evaluate, in a holistic context, whether the visual prosthesis being tested confers significant improvements to its recipients in their daily activities, and at what cost in terms of cognitive fatigue. It is hoped that these investigations will yield quantitative measures of the efficacy and ease of use of the therapeutic device from a brain perspective, in order to help guide the design of future vision restoration solutions and improve outcomes for patients with severe visual impairment.

Part II

Original Contributions

CHAPTER 6

METHODOLOGICAL CONTRIBUTIONS

This chapter encompasses the principal methodological contributions put forward during this project. Section **6.1** provides considerations for conceiving MoBI paradigms in practical applications. These original recommendations are based on the practical knowledge acquired throughout this thesis and focus on aspects not explicitly described in the literature yet, offering guidelines applicable to various mobile EEG protocols.

Moving on, Section **6.2** outlines the core components of the mobile EEG preprocessing pipeline used throughout this thesis. This pipeline was adapted from the BeMoBIL pipeline (Klug et al., 2022), developed by the *Biological Psychology and Neuroergonomics laboratory* in Berlin.

Finally, Section **6.3** describes how the source localization approach designed by Cottereau et al. (2015) was employed to reconstruct the electrical activity originating from the scene-selective regions (SSRs). Complying with the requirements of this procedure, a novel aspect of this project was to validate the use of a depth perception camera to accurately determine the localization of electrodes on the participants' scalp (Section **6.3.1**).

6.1 Practical conception of MoBI paradigms

As highlighted in Chapter **4**, the MoBI framework provides tools for researchers to enable the collection and the fruitful analysis of mobile brain imaging data. Except for the core principle that experimenters should enrich their datasets by co-registering brain recordings with other physiological measures (Gramann et al., 2014), there is little explicit recommendations on how to conceive MoBI experimental paradigms in practice. This section aims to share some practical considerations encountered when designing experiments in this thesis, that seemed general enough to help future protocol designs beyond the scope of this work.

Introduce spatial events. It is widely recognized that various EEG analyses, such as event-related potentials (ERPs) and event-related spectral perturbations (ERSPs), rely on well-defined events for comparison and the aggregation of repetitions to enhance the signal-to-noise ratio (SNR). This requirement becomes even more challenging in mobile EEG experiments, as establishing fixed trial durations for each participant proves arduous under such conditions. In the context of spatial navigation tasks, this issue is further compounded by the inherent variability in walking speed across trials, participants, and especially when comparing distinct populations, such as young and older adults.

To address these challenges, adopting a spatial sequence perspective, rather than a traditional time sequence perspective, can be highly advantageous. In this approach, events serving as reference for the analysis are linked to specific spatial locations within the environment, which remain consistent across trials (*e.g.*, also adopted in Do et al. 2021; Ehinger et al. 2014; M.-H. Lin et al. 2022; Miyakoshi et al. 2021). However, it is important to note that this methodology may not be applicable to all research inquiries, as it necessitates participants reaching all predetermined locations in a fixed order, thereby imposing constraints on the way participants' can explore the spatial environment. This spatial sequence approach was well-suited and fruitful for the mobile experiments conducted in this thesis. A spatial discretization technique was implemented, notably in the Y-maze configuration (Figure **7.2c,d**) and along the path between the observer and the door (Figure **9.1b**). It is noteworthy that the successful implementation of this approach relied on the co-registration of motion capture data with the EEG recording, allowing for precise tracking of the participant's position within the environment.

Avoid dispensable artifacts. Despite the availability of advanced data cleaning techniques for effectively separating brain-related signals from artifacts in mobile recordings (Delorme et al., 2012; Makeig et al., 1995; Nordin et al., 2018; Pion-Tonachini et al., 2019; Richer et al., 2020; Roy et al., 2017; M. Zhao et al., 2021), it remains imperative to prioritize the maximization of raw data quality. Thus, when designing protocols for MoBI, it is recommended to address and control for additional sources of noise that are not directly related to the scientific inquiry, as these factors inevitably diminish the quality of the dataset with respect to the targeted signal of interest.

For instance, in the experiment presented in Chapter **7**, a visual reward was opted for over an auditory reward to indicate the goal location (*i.e.*, the sudden appearance of a gift in

the VR environment). This decision was made to circumvent the introduction of an auditory processing evoked signal on top of the activity of interest bound to learning and memorization processes. This specific compromise was viable due to the experimental context being VR-based, offering high control over the visual stimulation within the protocol, unlike real-world scenarios.

Anticipate participants' comfort. Due to the time-consuming preparation of high-density EEG caps and the necessity to maximize the SNR by accumulating numerous repetitions (a single trial typically lasts between 30 and 60 s when it involves locomotion), mobile EEG experiments focusing on spatial navigation often require extensive experimental sessions. However, limiting the duration of these sessions to a reasonable timeframe of 3 to 4 hours presents challenges in protocol design. In such conditions, ensuring participants' comfort be-

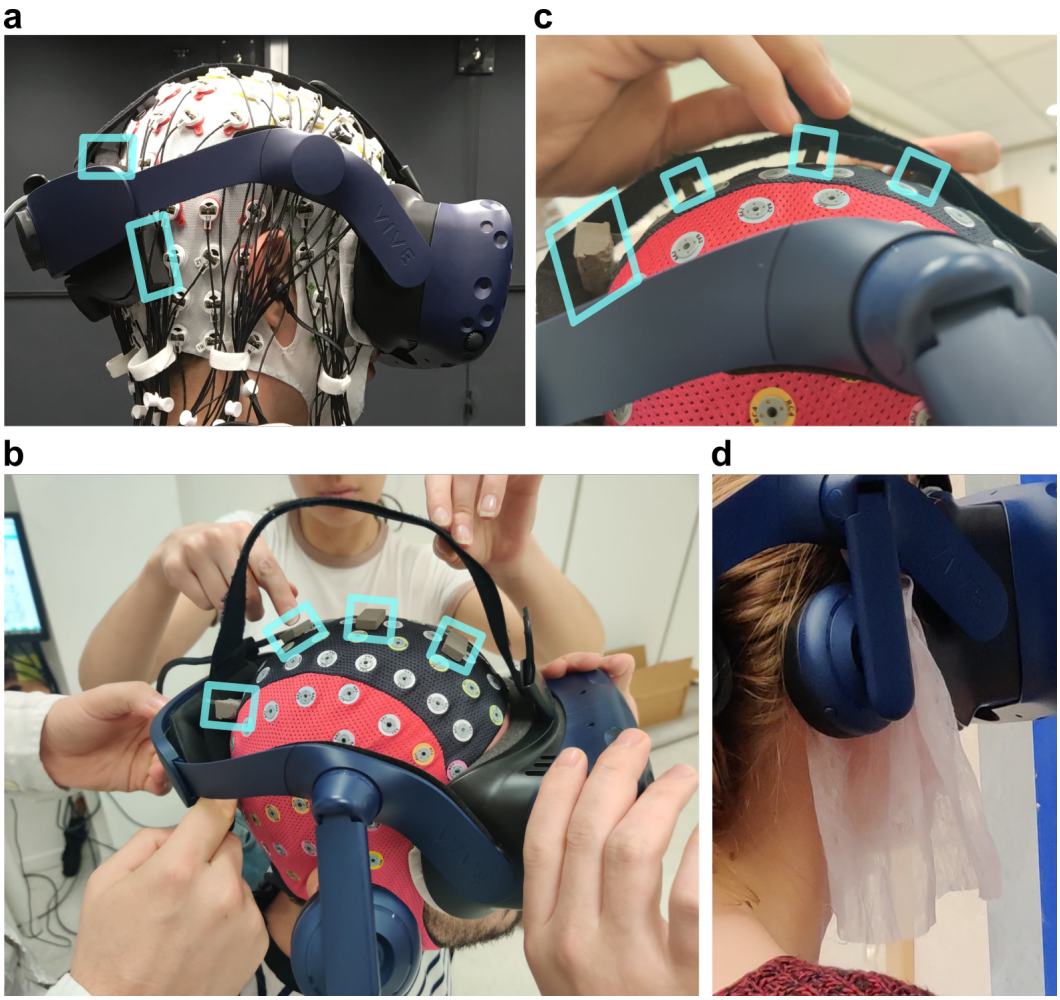

Figure 6.1: Illustration of methods to improve participant's comfort in VR experiments. The VR headset is the HTC Vive Pro head-mounted display. Light blue squares highlight the presence of 'foam spacers' in different set-ups. (**a**) Photograph taken from the experiment described in Chapter **7**. The EEG cap is a 128 channels equidistant layout *actiCAP slim*. (**b-d**) Photographs taken from the experiment described in Chapter **12**. The EEG cap is a 128 channels equidistant layout *waveguard original*. (**b**) Before tightening the superior headband. (**c**) After tightening the superior headband. (**d**) Type of fabric that was placed between frontal electrodes and the skin to alleviate the discomfort caused by the pressure of the VR headset. This photograph shows a piloting step before smaller pieces of fabric were cut out to fit under the cap.

comes crucial, particularly when studying vulnerable populations such as children or older adults. A specific issue addressed in this thesis concerns the compatibility of the EEG cap with other head-mounted devices. Continuous pressure applied by these devices on the electrodes during the task can lead to discomfort and even pain after a few minutes into the session. Apart from the risk of introducing mechanical artifacts in the recording, this discomfort hampers participants' compliance and attention to the task, rendering the recorded data unusable.

This issue arose in experiments involving the eye-tracker used in Chapter **8** and combining EEG with a VR headset (Chapters **7** and **12**). For the eye-tracker, which interfered only with frontal electrodes, a simple solution was implemented by slightly shifting the EEG cap backward, thereby eliminating contact between the electrodes and the forehead resting frame. This adjustment was facilitated by the possibility to acquire precise electrode locations (see Section **6.3.1**), allowing deviations from the standard cap positioning.

Regarding VR experiments, ensuring a comfortable setup requires thorough pilot testing, as it may depend on the specific VR headset and EEG cap used. In this thesis, the HTC Vive Pro head-mounted display (HTC Corporation, Taoyuan, Taïwan) was employed for VR experiments. It comprises two rigid components, the display and the fastening device, which exert pressure on the frontal and posterior electrodes, respectively (Figure **6.1a,b**). The headband connecting them applies pressure to the superior electrodes (Figure **6.1c**). Two different EEG cap models were used: the actiCAP slim (Brain Products, Gilching, Germany) during the first experiment in Berlin (Chapter 7) and the waveguard original (ANT Neuro, Hengelo, The Netherlands) in later experiments conducted at the Vision Institute. The waveguard cap, despite having thinner electrodes, was found to be more uncomfortable under pressure due to its suction-cup design. To alleviate pressure on the posterior and superior electrodes, custom-made rigid 'foam spacers' were inserted between the electrodes and the fastening elements (see Figure **6.1a-c**). On the frontal side, the optimal solution involved shifting the cap backward to create distance between the electrodes and the display frame, similar to the approach taken with the eye-tracker. When this option was unavailable, an alternative was to mitigate the contact between the electrode and the scalp using medical fabric (Figure **6.1d**), which effectively reduced discomfort caused by the waveguard cap's suction-cup design. However, this approach resulted in signal loss from the frontal electrodes and should only be employed when frontal regions are not relevant to the research question.

6.2 Recording and cleaning mobile EEG data

Concurrent analysis with complementary data modalities (Gramann et al., 2014) and increasing noise levels in mobile EEG recordings (Gramann et al., 2010a; Richer et al., 2020) present challenges that traditional EEG processing toolboxes designed for stationary recordings often cannot fully address. To tackle this methodological issue, this thesis draws upon the pioneering work of the *Biological Psychology and Neuroergonomics* laboratory in Berlin, which has made significant efforts to develop an adaptive multimodal data processing pipeline called the BeMoBIL pipeline (Klug et al., 2022). As the BeMoBIL pipeline was still in development at the project's outset, the implementation of EEG processing in this thesis adapts to specific needs encountered during the analyses while adhering to the pipeline's original principles.

6.2.1 Synchronized data collection

Simultaneously recorded multimodal data requires careful considerations starting from the data collection stage. To enable joint analyses, a harmonized and time-synchronized representation of EEG data along with additional data modalities is essential. Achieving time synchrony is particularly challenging in MoBI studies, as datasets often comprise multiple modalities with different sampling rates and temporal resolutions. For example, EEG recording systems typically produce data with highly regular inter-sample intervals, while motion capture data may exhibit irregular temporal intervals between samples.

In this project, following the principles of the BeMoBIL pipeline, synchronized multimodal recordings relied on the Lab Streaming Layer (LSL) protocol (Kothe, 2014). LSL is an open-source data streaming protocol that facilitates the flexible definition and recording of data streams from diverse sources, including EEG amplifiers, motion capture systems, eye-tracking devices, and custom applications running the experimental protocol. LSL is supported in various coding languages such as Matlab, Python, and C#. Utilizing the LSL recorder, the multimodal dataset is stored in the extensible data format (XDF), containing all selected data streams with their respective definitions, samples, and a timestamp for each sample. This approach ensures precise synchronization and facilitates subsequent analyses involving multiple data modalities.

6.2.2 Data cleaning

EEG data processing has been exclusively conducted with MATLAB version R2019a (Mathworks Inc., Natick, MA, USA). Most of the code was based on *EEGLAB* functions and plugins, version 2021.0 (Delorme & Makeig, 2004).

As mentioned earlier (Section **4.3.3**), the fundamental preprocessing concept adopted by the MoBI approach involves decomposing the EEG signal into statistically independent components (ICs) to extract valuable information about their characteristics and differentiate brain originating components from artifact-generated ones. Although a standardized data

processing pipeline is not fully established (Klug et al., 2022; Robbins et al., 2020), there is a growing consensus in the EEGLAB community regarding a common framework for single-subject level preprocessing (`https://eeglab.org/`, see Section **6.2.2.2**). The BeMoBIL pipeline also follows this architecture as a foundation for its methodology. In this project, we built upon this approach, particularly focusing on independent component analysis (ICA), while maintaining a modular framework that enables the integration of new building blocks and the comparison of different implementations of each step to continuously enhance the data processing pipeline.

6.2.2.1 Mathematical detour: Independent Component Analysis

ICA is a mathematical method aiming at untangling a random vector $\boldsymbol{x}$ assumed to be a linear mixture of unknown random vector $\boldsymbol{s}$, such as expressed in Equation **6.1**. Given the observations of $\boldsymbol{x}$ $(\boldsymbol{x}_1,\ldots,\boldsymbol{x}_t)$ and a model with unknown parameters for $\boldsymbol{s}$, the ICA algorithm finds the optimal mixture matrix $\boldsymbol{A}$ and mean $\boldsymbol{c}$ such that the components $[s_1,\ldots,s_N]$ are statistically independent (*i.e.* their mutual information is null: $\forall i,j:\ I(s_i,s_j)=0$). In statistical terms, this extends the component decomposition performed by the better known principal component analysis (PCA) by taking into account all higher-order statistics of the s_i and not only the correlation term (2^{nd} order).

$$\begin{aligned} \boldsymbol{x} &= \boldsymbol{A} * \boldsymbol{s} + \boldsymbol{c} \\ \text{with } \boldsymbol{x} &= [x_1,\ldots,x_N]^T \\ \boldsymbol{s} &= [s_1,\ldots,s_N]^T \end{aligned} \tag{6.1}$$

Thanks to its implementation in powerful algorithms capable of handling large data sets (originally by Bell and Sejnowski 1995), this technique has been advantageously transferred to EEG data processing (Delorme et al., 2007; Makeig et al., 1995, 1997). Indeed, scalp electrodes ($\boldsymbol{x}$) record a mixture of brain and artifacts sources ($\boldsymbol{s}$): the multichannel decomposition performed by ICA allows the identification of those independent sources to remove the artifactual ones and disentangle cortical time courses (statistical independence of random vectors can be interpreted as independence of the signals' time courses), mixed by electrical volume conduction.

Principal limitations of ICA. The principal limitations of ICA arise from certain assumptions made in the mathematical model. One critical assumption is the stationarity of sources ($\boldsymbol{s}$), meaning ICA does not consider any temporal or spatial variations in activity, including slightly moving sources. Another unrealistic assumption is the absence of random noise in the model. However, incorporating noise into the mathematical solving would considerably complicate the process, and the benefits gained from accounting for random noise are negligible compared to the artifacts' amplitudes. Furthermore, the size of the sources space ($\boldsymbol{s}$) is assumed to be the same as the recorded data ($\boldsymbol{x}$), and in the case of EEG recordings, the number of independent components that can be retrieved is strictly limited by the number of electrodes. This implies that if the number of artifacts in the data is too high, they may

overshadow the brain-related sources during ICA processing, particularly those contributing most to the original signal's variance.

In the context of mobile EEG, where artifacts are inevitable, it becomes essential to work with a larger number of electrodes and avoid feeding ICA with data heavily contaminated by artifacts. Given these limitations, the role of pre-cleaning methods before applying ICA is critical to preparing the data for an optimal retrieval of cortical sources.

6.2.2.2 Pipeline architecture work-flow

This section delineates the principal steps employed for the preprocessing of EEG data in this thesis. While each of these steps holds significance, it is acknowledged that some alterations made during the preprocessing phase might not be desirable for subsequent data analysis. For instance, eliminating noisy temporal segments is necessary for ICA, but these segments may still contain valuable information, particularly when combined with motion capture data in later analyses. In order to preserve the data in its original state as much as possible for subsequent analysis, the preprocessing pipeline was not implemented linearly. A flexible approach was adopted to extract relevant information without making definitive changes. This principle is illustrated in a flowchart presented in Figure **6.2**. Particularly, it was deliberately avoided to permanently remove noisy temporal sections (Section **6.2.2.2.7**) to prevent introducing boundaries and associated boundary effects during subsequent filtering procedures. Consequently, certain preprocessing steps had to be applied multiple times (*e.g.*, high-pass filtering and line noise removal) as they were essential for subsequent methodologies, even though not deemed definitive. Throughout the architecture, unless explicitly stated otherwise, the data is treated as a continuous recording, encompassing periods when the subject was not actively engaged in any task.

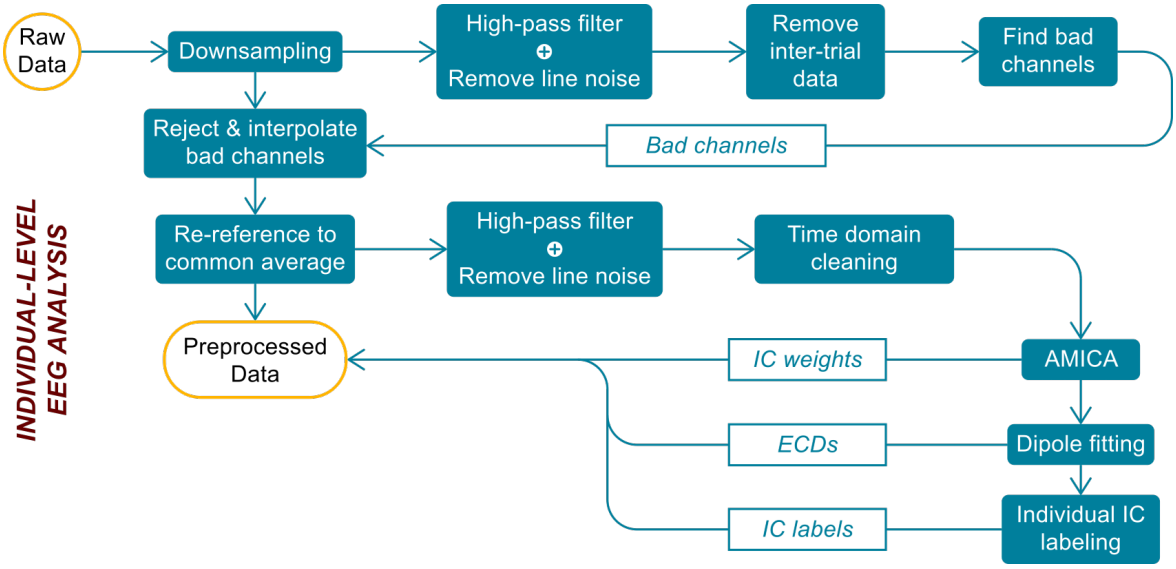

Figure 6.2: Flowchart of the EEG preprocessing pipeline at the individual-level. Modified from Delaux et al. (2021).

6.2.2.2.1 Importing raw data

The raw data is initially extracted from the XDF file using the `load_xdf` function from the *xdfimport* plugin (version 1.18) designed for EEGLAB. To achieve synchronization between data streams with different clocks, especially when originating from different computers, the function utilizes the relative offset information stored in the XDF file. For data streams with regular sampling rates, such as EEG data, slight deviations from the expected regular intervals are corrected, ensuring that the stream aligns with a well-defined regularly spaced dataset. Furthermore, all streams containing quantitative data are resampled to the EEG sampling rate, usually the highest among all streams, to achieve complete synchronization with corresponding samples from each modality at each timestamp. For event streams that do not have regular sampling rates, they are interpreted in the common time frame of reference to provide markers annotating specific time frames in the dataset. The resulting data is stored in a file format compatible with EEGLAB, allowing seamless utilization of the EEGLAB toolbox for further processing.

Initially, these operations were performed through the *MoBILAB* plugin (Ojeda et al., 2014), specifically designed for analyzing and visualizing MoBI data, which was used for Chapter **7** of this thesis. However, due to encountered data recording issues in subsequent experiments and the lack of continuous support for the plugin, custom code was subsequently developed to perform these operations.

An important original development to note is the implementation of a function to address missing EEG data in the XDF file. During experiments, EEG data was both streamed with LSL for synchronization with other modalities and recorded locally without information from other modalities. Sometimes, problems such as Wi-Fi transmission failures, caused the XDF file to be incomplete compared to the local file. To resolve this, a purely data-driven approach was adopted. The function searched for a match between the existing EEG data bits in the XDF file and the data present in the local file, before copying the corresponding neighboring data from the local file to complete the XDF stream. The search process involved sliding a 1-second segment of XDF data across the local data and comparing it with an equal-length window. A match was identified when the mean sample-wise difference between the two windows was below 0.0021μV.

6.2.2.2.2 Down-sampling

To optimize computational efficiency and manage the size of the data sets, down-sampling was performed, reducing the sampling rate to 250 Hz. Notably, relevant brain signals recorded through scalp EEG typically occur at frequencies below 40 Hz. Therefore, down sampling to 250 Hz provides a sufficient margin, ensuring that the data-of-interest range is adequately covered.

6.2.2.2.3 High-pass filtering

Data underwent high-pass filtering for all subsequent processing operations. In the first MoBI experiment (Chapter **7**), the initial threshold value of this filter was set to 1 Hz, using a zero-phase Hamming windowed finite impulse response filter with a 0.5 Hz cutoff fre-

quency and a 1 Hz transition bandwidth. However, in subsequent experiments, the threshold was adjusted based on insights from a sensitivity analysis published by Klug and Gramann (2021). The threshold was increased to 1.75 Hz, utilizing a zero-phase Hamming windowed finite impulse response filter with a 1.5 Hz cutoff frequency and a 0.5 Hz transition bandwidth for improved results.

The rationale behind high-pass filtering is to eliminate slow drifts, which are naturally present in EEG recordings, especially when recorded over extended periods of time. These drifts can hinder the comparison of data across time and typically degrade the performance of certain steps of the pipeline (Bigdely-Shamlo et al., 2015), especially Sections **6.2.2.2.4**, **6.2.2.2.5**, and **6.2.2.2.7**.

6.2.2.2.4 Removing Line Noise

Power line noise, characterized by frequencies at 50 Hz and its harmonics, is a well acknowledged source of artifacts in EEG recordings. Although these frequencies generally lie at the periphery of the range of brain signals of interest, retaining them for later stages of analysis can still negatively affect the performance of cleaning methods. One example is their interference with the effectiveness of ICA in identifying uncontaminated components. To mitigate this interference, the `cleanLineNoise` function from the *PREP* pipeline (version 0.55.4; Bigdely-Shamlo et al. 2015), integrated as an EEGLAB plugin, is used. Unlike simple notch filters, the `cleanLineNoise` function employs a more sophisticated approach based on multi-taper decomposition. This method offers increased accuracy and introduces less distortion in neighboring frequency bands.

During VR experiments involving the VIVE VR headset, an additional noise peak similar to line noise emerged at 90 Hz. To address this, the same method was employed, with the target frequency adjusted accordingly. It is suspected that this additional artifact is likely related to the display refresh rate inside the VR headset, which also operates at 90 Hz. This observation highlights the utmost caution required when employing additional systems in conjunction with EEG recordings to minimize potential confounding artifacts.

6.2.2.2.5 Detecting and interpolating bad channels

Several factors may render certain channels unsuitable for analysis in EEG recordings, such as insufficient electrical connection, electrode displacement during recording, or interactions with the VR headset in the case of VR experiments. Electro-oculography (EOG) channels are excluded from the dataset at this step since they are likely to be considered artifacts. To detect and exclude these problematic channels, portions of the continuous dataset not associated with actual experimental trials are removed to prevent their inclusion in the analysis of abnormal channel behavior. Four criteria are employed for identifying problematic channels:

- *Deviation criterion*. This criterion aims to identify channels with extreme amplitudes, which can be indicative of large artifacts or poor scalp contact.
- *Noisiness criterion*. It involves the detection of channels exhibiting high-frequency power that deviates significantly from the expected $1/f$ power law. Such channels are likely to contain unusable signals.

- *Correlation criterion*. Channels should generally exhibit a high level of correlation due to scalp electrical conduction. Channels with signals deviating significantly from their neighbors are considered dysfunctional.
- *Predictability criterion*. Dysfunctional channels may also show a lack of predictability compared to other channels. If a group of channels behaves abnormally together, this criterion helps to identify them with respect to the previous criterion. The prediction is based on the correlation with other channels, even if they are not spatially adjacent, as scalp volume conduction plays a role in signal distribution.

To conduct this detection process, the `findNoisyChannels` function from the PREP pipeline is employed. Once the problematic channels are identified, their signals are removed from the dataset, and they are reconstructed through spherical interpolation using the neighboring channels, as implemented in the EEGLAB function `pop_interp`.

6.2.2.2.6 Re-referencing

Typically, EEG raw data is initially referenced to a single electrode, as determined by the equipment manufacturer. However, referencing the EEG data to the common average is a common practice to eliminate the mean signal and accentuate the individual differences among channels concerning their average activity. This referencing method also improves the reproducibility of results across different studies. At this step, the EOG channels are not included in the referencing process. To achieve the common average referencing, the EEGLAB function `pop_reref` is used.

6.2.2.2.7 Rejecting noisy temporal segments

In a similar manner to dealing with noisy channels, certain segments of the EEG recording may contain excessive noise, which renders them unsuitable for subsequent analysis. Such noise can result from vigorous subject movements, facial muscle activity, and other factors. The identification and removal of these noisy temporal segments hold particular significance when performing ICA decomposition. Without proper handling, certain periods impacted by general artifacts might be misinterpreted as individual ICs by the ICA algorithm (J. R. da Cruz et al., 2018; Delorme et al., 2012).

In this work, the treatment of noisy temporal segments was not approached uniformly. Two main alternative methods were employed, depending on the complexity and conservativeness required for the specific experimental recording conditions. The first approach was directly inspired by the BeMoBIL pipeline (Klug et al., 2022), while the second approach relied on the APP pipeline (J. R. da Cruz et al., 2018).

BeMoBIL pipeline. The BeMoBIL pipeline incorporates an additional preprocessing step aimed at excluding eye movements before the detection of noisy temporal segments. This strategy is motivated by the fact that eye-related artifacts often lead to large amplitude variations in the EEG signal, effectively concealing other artifacts from many commonly used noise detection metrics. Eye components are identified with ICA decomposition (AMICA, Palmer et al. 2008) and automatic IC labelling (ICLabel, Pion-Tonachini et al. 2019). To

optimize computational efficiency, only a small portion of the data is employed to train the AMICA algorithm, depending on the specifics of the experimental design. Subsequently, eye components are identified based on automatic predictions provided by the ICLabel algorithm (refer to Section **6.2.2.2.10**). Components for which the prediction exceeds the designated threshold only for the Eye class are considered eye components and are removed from the channel-based dataset using the EEGLAB function `pop_subcomp`.

Following the eye component removal, the EEG data undergoes band-pass filtering and is then divided into non-overlapping epochs of 1 second each. For each of these epochs, three distinct measures are computed to assess the level of noisiness:

I. *Mean signal of the epoch* (averaged over channels and time). Higher values indicate general impedance inflation or significant artifacts affecting a substantial proportion of channels.

II. *Channel standard deviation of epoch mean*. This measure gauges channel heterogeneity within the epoch, with larger values indicating that certain channels are individually affected by artifacts during that specific period.

III. *Mahalanobian distance of epoch mean*. Mahalanobian distance (MD) offers a more robust estimate of channel heterogeneity than channel standard deviation (SD) as it considers variances and covariances between channels. Elevated MD values also point to a noisy epoch.

These computed quantities are then combined into a single score using a weighted sum, where the MD is given greater importance $[w(I) = 1; w(II) = 1; w(III) = 2]$. Subsequently, the epochs are sorted based on their respective scores, and a predetermined percentage of the highest-scoring epochs are flagged for removal (*e.g.*, 15% in Chapter **7**). Adjacent noisy epochs are merged to form rejection blocks. Finally, each rejection block is extended by 200 ms on both sides to account for potential artifact contamination from neighboring sections. The implementation of this process was adapted from the original scripts provided by the authors.

APP pipeline. The Automatic Pre-Processing (APP) pipeline, as proposed by J. R. da Cruz et al. (2018), serves as an automatic artifact rejection method specifically designed for high-density EEG data. This pipeline employs robust statistics to achieve effective artifact removal while minimizing the rejection of channels and time segments compared to other approaches (J. R. da Cruz et al., 2018). The utilization of robust statistics, such as biweight estimation of mean and standard deviation, enables a more accurate representation of statistical distributions, thereby avoiding potential errors in identifying abnormal behaviors without assuming normality. Remarkably, the rejection criteria in this pipeline are relative, meaning that outliers are identified based on the subject-specific distribution of the metric used. This adaptability to subject-specific data quality prevents the application of overly stringent thresholds.

The continuous EEG dataset is initially segmented into 1-second windows using the `eeg_regepochs` function in EEGLAB. Each epoch is then evaluated using three metrics to assess its level of noisiness:

- *Mean amplitude difference*. This metric detects epochs affected by large artifacts by examining variations within the epoch window across channels. The difference between the minimum and maximum values for each channel within the epoch is computed, and these channel-wise differences are averaged using the biweight method. Outliers on the right tail of the distribution (indicating extremely high mean amplitude differences) are classified as bad epochs.
- *Global Field Power*. To detect impedance increases due to electrode movements, which cause unusual high amplitudes in the signal, APP calculates the mean global field power (GFP) of the signal over the epoch. GFP quantifies the overall scalp EEG strength based on Lehmann and Skrandies (1980) and is analogous to the spatial SD of the signal at a given time point. Distribution outliers on the right tail (indicating extremely high mean GFP) are flagged as bad epochs.
- *Mean deviation from channel mean*. Alternatively, electrode movements may not generate high perturbations detectable by the previous metric but still significantly contaminate the data. To account for this, the APP pipeline computes the mean deviation from the channel mean (MDCM) for each epoch. Distribution outliers on the right tail (indicating extremely high MDCM) are classified as bad epochs.

Any epoch identified as bad by at least one of these metrics is marked for rejection. Adjacent noisy epochs are merged to form blocks of rejection, and each block is extended by an additional epoch on both sides to account for potential artifact contamination from neighboring sections. The implementation of this process was adapted from the original scripts provided by the authors.

In both approaches, once these identified noisy segments are determined, they are excluded from the dataset, and the remaining segments are concatenated together using the EEGLAB function `pop_select`.

For the sake of thoroughness, a direct comparison between the two approaches was conducted on the ambulatory EEG dataset presented in Chapter **7**, and the results are detailed in Section **D.3**. In summary, the BeMoBIL pipeline demonstrated greater robustness on this dataset. It exhibited higher stability and conservativeness compared to the APP pipeline, effectively rejecting more artifact-laden channels and noisy temporal segments across participants, which was particularly advantageous given the substantial noise present in such ambulatory conditions. However, in experiments involving less movement and greater data quality (as exemplified in Chapter **8**), the APP pipeline was favored to retain as much data as possible for subsequent analyses.

6.2.2.2.8 Performing ICA decomposition

The ICA decomposition was conducted using an adaptive mixture algorithm devised by Palmer et al. (2008) and implemented in the *AMICA* (version 1.5.1) plugin for EEGLAB.This

specific algorithm was found to outperform more than 20 other ICA and blind source separation algorithms, as reported by Delorme et al. (2012).

Prior to applying the AMICA, a PCA was carried out to reduce the dataset to its remaining rank ($r_p = Nchans - Ninterp - chans(p)$, where p denotes participant-wise). Consequently, exactly r_p ICs were obtained after the decomposition process. The optimal decomposition from 2000 iterations of the algorithm was retrieved.

6.2.2.2.9 Fitting equivalent current dipole model

For each extracted IC, an equivalent current dipole (ECD) model was computed based on the scalp activation map using the *DIPFIT* plugin for EEGLAB (version 3.7) (Oostenveld & Oostendorp, 2002). To achieve this, electrode locations were determined either from individual measurements (as explained in Section **6.3.1**, applied in Chapters **8** and **9**), from a file containing the average measurements of participants wearing the same cap (in Chapter **7**), or from standard locations provided by the cap manufacturer (in Chapters **10** and **12**). These electrode locations were then co-registered with a boundary element model (BEM) based on the MNI brain (Montreal Neurological Institute, Montreal, QC, Canada) to estimate dipoles location.

6.2.2.2.10 Selecting Independent Components

In this final step, the ICLabel algorithm (version 1.3, Pion-Tonachini et al. 2019) was initially employed with the *default* option to obtain an automatic class prediction for each IC. The ICLabel model encompasses seven classes, namely: (1) Brain, (2) Muscle, (3) Eye, (4) Heart, (5) Line Noise, (6) Channel Noise, and (7) Other. The algorithm's prediction takes the form of a compositional label, represented by a percentage vector indicating the likelihood of the IC belonging to each of the specified classes. However, given the algorithm's relatively recent development and its lack of validation with mobile EEG data, the labels were manually examined, with a specific focus on potential Brain ICs. This inspection adhered to objective and predefined criteria, which were derived from ICLabel guidelines to ensure consistency in the selection process (see Appendix **B** for detailed information on these selection rules). Subsequently, ICs lacking sufficient evidence of brain-related signals were removed from further analysis.

6.3 Reconstruction of scene-selective regions' activity

As acknowledged previously, the current state-of-the-art of the investigation of SSRs using EEG lacks individualized source reconstruction models and a functional definition of the SSRs with functional magnetic resonance imaging (fMRI), limiting the direct association of the findings with these regions.

To address these limitations, the second major methodological focus of this project was to enable the recording of SSR activity with the most accurate source localization. This involved implementing a fMRI-informed source reconstruction model tailored to each participant, building upon a previously established approach (Cottereau et al., 2012, 2015). An essential preliminary step for this approach was to validate a method for accurately obtaining the electrode locations on the participants' scalp, for which there was no readily available solution at the host laboratory of this project. Consequently, a small comparative study was conducted to investigate the advantages and disadvantages of using a depth perception camera *vs.* a more standard motion capture approach for this purpose (Section **6.3.1**).

Subsequently, Section **6.3.2** presents the implementation of the source reconstruction pipeline, following the methodological details published in Cottereau et al. (2015), with specific considerations for the SSRs. These methodological foundations serve as a basis for the studies presented in Chapters **8** and **9**.

6.3.1 Rapid and reliable acquisition of electrodes' positions

6.3.1.1 Rationale

Accurate electrode positioning is crucial for source localization methods in order to estimate the origin of recorded signals. Many studies opt for standardized cap placement and electrode templates due to time and resource constraints, resulting in models with limited spatial precision (*e.g.*, as in the first study presented in this thesis, see Chapter **7**). However, theoretical investigations have shown that even a small average displacement of 0.5 cm in electrode positioning can introduce an uncertainty of 0.5 to 1.2 cm in the estimation of source location (Akalin Acar & Makeig, 2013; Shirazi & Huang, 2019).

Thus, to enhance the accuracy of source estimation, it is essential to register the actual electrode positions on each participant's head during the experiment. This practice corrects for both individual morphological characteristics (*e.g.*, head size, deviation from a perfect sphere) and placement variability introduced by the experimenter(s). Various techniques are available to obtain the three-dimensional position of the electrodes, a process also referred to as *digitization* in the literature (Koessler et al., 2007; Shirazi & Huang, 2019). Traditional methods utilizing ultrasound and electromagnetism were costly and time-consuming (Koessler et al., 2007). However, recent advancements have focused on improving accessibility and convenience. Photogrammetry and motion capture techniques have gained prominence in the last decade, offering accurate electrode localization in a shorter timeframe (Baysal & Şengül, 2010; Koessler et al., 2010). In the context of mobile EEG experiments,

which already involve extensive experimental sessions and complex setups, it is imperative to adopt a technology that allows for quick acquisition and minimal additional equipment.

To address these requirements, depth perception cameras, also known as *3D scanners*, have emerged as a promising option for electrode digitization (Homölle & Oostenveld, 2019; Shirazi & Huang, 2019; Taberna et al., 2019). These cameras detect the reflections of projected light patterns (infrared or visible) and estimate the object's shape, enabling efficient electrode localization. Consequently, an important methodological aspect of this thesis was to (1) develop the experimental protocol for electrode digitization using a depth perception camera and (2) compare the accuracy of the obtained models to a motion capture-based alternative, which was previously validated in the literature (Shirazi & Huang, 2019).

6.3.1.2 Methods

6.3.1.2.1 Participant

To validate the accuracy of both methods, a comparative accuracy test was conducted on a healthy young human participant from the *SilverSight* cohort to examine the performance in realistic experimental conditions (including potential errors introduced by head movements).

6.3.1.2.2 Materials

The depth perception camera used in the study was the Intel RealSense D435 (Intel, Santa Clara, CA, USA; Figure **6.3a**), which combines depth perception based on infrared sensors with a standard camera for capturing 2D images. This model of depth perception camera was selected due to its close range capability (down to $\sim$30 cm), making it suitable for use in small experimental rooms. The RecFusion software (v2.3.0, ImFusion GmbH, München, Germany) was employed to oversee real-time model construction.

For comparison, the OptiTrack motion capture system (NaturalPoint - Corvallis, OR, USA) was used, tracking the position of a digitizing probe in space (Figure **6.3d**). The probe consisted of a solid object with four fixed reflective markers on the upper part (MSP0001 Digitizing Probe, NaturalPoint). The motion capture setup involved six cameras (OptiTrack Flex 13, NaturalPoint) to map the tracking space, with data acquisition performed using Motive software (v1.7.5, NaturalPoint).

The EEG cap employed was a large-sized 128-channel equidistant layout waveguard original (ANT Neuro, Hengelo, The Netherlands).

6.3.1.2.3 Procedure

Both procedures were conducted sequentially, with the motion capture performed first, to ensure consistent placement of the EEG cap on the head for both methods.

Depth perception camera. The head scan procedure involved rotating the camera around a seated participant wearing the EEG cap. The camera was directed towards the participant's head, and the experimenter slowly moved it up and down during a 360° rotation.This allowed for capturing images from various angles and elevations, ensuring optimal visibility of all electrodes, particularly those located superiorly and in the neck region. Colored stickers

were applied to three anatomical fiducial landmarks on the participant's skull (nasion, helix/tragus junctions of the left and right ears; see Figure **6.3b**) for subsequent co-registration with magnetic resonance imaging (MRI) data (see Section **6.3.2.5**). Post-processing of the obtained model was performed using RecFusion software to enhance colorization, to ensure clear visibility of electrodes and fiducial markers (Figure **6.3b** shows the final rendering). The position of each electrode in 3D space, defined by the fiducial markers, was manually determined using the *get_chanlocs* plugin (v3.00) of the EEGLAB software (v2021.0, Delorme and Makeig 2004, see Figure **6.3c**).

Motion capture. The motion capture system required an initial calibration procedure using Motive software to define the tracking space (approximately $3m \times 3m$) and the horizontal plane in relation to camera positioning. The participant wore the EEG cap and was seated at the center of the tracking space. The digitizing probe and its fixed reflective markers were defined as a rigid body (RB) in the Motive software. To account for head movements,

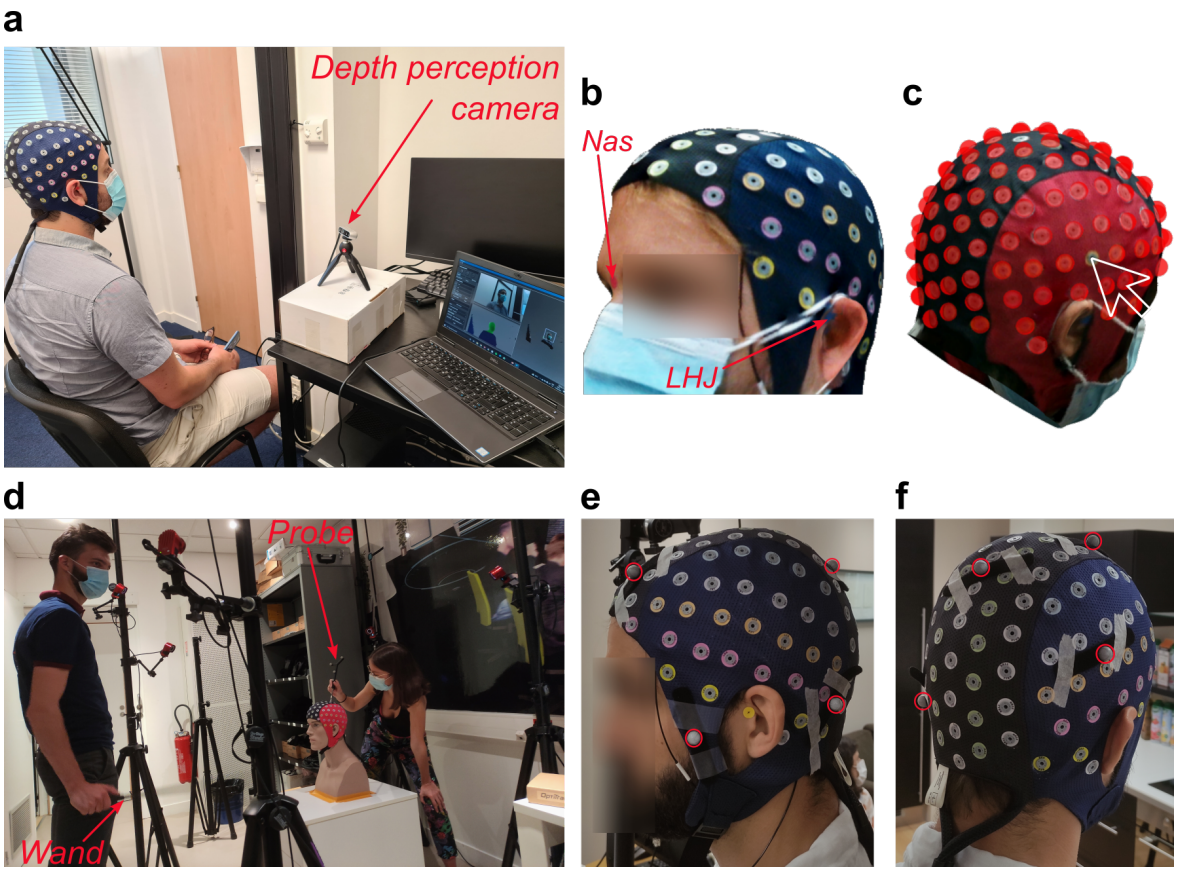

Figure 6.3: Methodology for the digitization of electrodes. (**a**) Depth perception camera initial set-up (before turning around the participant). The computer running RecFusion software for the acquisition can be seen on the bottom right corner. (**b**) Example of colored 3D scan obtained with the RecFusion software after refinement. Anatomical fiducials (Nas: Nasion, LHJ: left helix/tragus junction) indicated with colored stickers are visible on the scan. (**c**) Example of individual electrode pointing using the *get_chanlocs* plugin of EEGLAB. (**d**) OptiTrack motion capture set-up for the digitization of a mannequin head (practice session) using 6 cameras to map the tracking space. An experimenter manipulates the probe to localize each electrode individually. (**e-f**) Placement of the 6 reflective markers (circled in red) on the cap to follow head movements of the participant during the tracking session.

six additional reflective markers (9 mm diameter) were placed on the EEG cap to define a second RB (placement shown on Figure **6.3e-f**).

The digitization process involved an experimenter sequentially inserting the tip of the digitizing probe into each electrode well on the cap, starting with the fiducials. To ensure consistent placement inside the electrode wells, the probe was inserted until it reached a mechanical stop positioned five millimeters away from the tip. This procedure was recorded in the Motive software, with another experimenter waving a wand (a third RB tracked in space with three reflective markers; CS-500 Calibration Wand, NaturalPoint) up and down to mark the timing of each measurement (experimenter on the left in Figure **6.3d**). Post-session data processing by the StreetLab company generated a list of 3D coordinates for the electrodes in the space defined by the fiducial markers. It is important to note that for accurate comparison with the 3D scan, which captures the surface of the electrodes, these coordinates reflected the position of the mechanical stop, rather than the tip itself.

6.3.1.2.4 Evaluation metrics

Each procedure was performed five times, with different experimenters involved in each run, as in Shirazi and Huang (2019). Evaluation metrics were devised to assess the reliability of each method (*i.e.*, variability between runs) as well as the deviation between the two methods (*i.e.*, systematic bias).

Digitization reliability. To evaluate the reliability of each method, the variability of electrode locations across different repetitions of the procedure was analyzed. Firstly, the five digitized locations for each electrode were averaged to determine their centroid. Subsequently, the within-method variability was quantified by calculating the average Euclidean distances between the five digitized points and their centroid for each electrode.

Deviation between methods. The deviation between the two methods was assessed by computing the Euclidean distance between the centroids obtained for each electrode using each procedure.

Centroids displacement. To examine the primary factors contributing to the deviation between the two methods, the displacement of centroids between the procedures was analyzed, taking into consideration both the absolute deviation and the direction. The centroid obtained from the 3D scan was used as the reference point, as it provided electrode locations accompanied by a 3D mesh of the EEG cap surface. This surface information was used to calculate the local *inward vector*, which represents the direction orthogonal to the local tangent plane and points towards the inside of the head for each electrode.

The *angular displacement* for each electrode was quantified by computing the absolute solid angle between the vector connecting the centroid location determined with the depth perception method to the centroid location determined with the motion capture method, and the inward vector. Values close to 0° indicate a displacement that primarily occurs in the inward direction, while values above 90° suggest that the centroid location computed with the motion capture method is located more outward compared to the centroid computed with the depth perception method.

6.3.1.3 Results

6.3.1.3.1 Convenience and timing

The duration of the digitization procedure differed significantly between the depth perception camera and the motion capture system. A single scan using the depth perception camera typically lasted approximately 1 minute, whereas the fastest acquisition observed for the motion capture procedure took around 12 minutes. The depth perception camera approach proved to be more convenient as it was relatively easy to set up in the experimental room, with the exception of requiring adequate lighting conditions (see Section **6.3.1.3.2**). Additionally, it did not necessitate a calibration procedure. In contrast, the OptiTrack motion capture system required a dedicated space for installing the cameras and setting up the tracking area, in a dedicated room.

Regarding post-processing time, the motion capture system offered an advantage as data processing was automated, although human intervention was sometimes necessary for data cleaning. Conversely, the post-processing of the 3D scan obtained from the depth perception camera involved manual intervention by the experimenter, particularly when refining the colorization of the model (see Section **6.3.1.3.2**). The entire post-processing procedure, including subsequent electrode pointing (which is not automated either), typically required between 20 and 50 minutes per scan.

6.3.1.3.2 Quality of the 3D model

Although the fundamental steps of the 3D scanning procedure are relatively straightforward, achieving an accurate model required extensive iterative refinement and expertise. A comprehensive summary of best practices and general tips for optimizing the quality of the 3D model using the RecFusion software is provided in Appendix **C**.

During the acquisition phase, attention to lighting conditions was crucial, aiming for uniform illumination of the head. Careful consideration was also given to objects and colors that could potentially interact with infrared light (*e.g.*, the conductive gel placed inside electrode wells), as they had the potential to disrupt the acquisition process. As a precautionary measure, acquiring at least two 3D scans of the same participant allowed for selecting the best acquisition and ensuring a high-quality final model.

In the post-processing stage, the RecFusion software used 2D images captured at regular intervals during the scan to apply high-resolution texture to the 3D mesh generated from the depth data. However, the *re-texturing* algorithm often required experimenter intervention due to imperfections in its initial iterations, necessitating the discarding of 2D images leading to significant errors (see Figure **6.4** for examples). This iterative process typically accounted for the most time-consuming aspect of the post-processing procedure, taking between 15 and 45 minutes per scan. While it resulted in a satisfactory overall outcome, precise localization of every electrode simultaneously was rarely achieved. Therefore, during the electrode pointing step, electrodes with insufficiently accurate positions on the colored 3D model were flagged and excluded from subsequent source reconstruction. Although this limitation was noteworthy, the number of electrodes affected remained relatively low. For

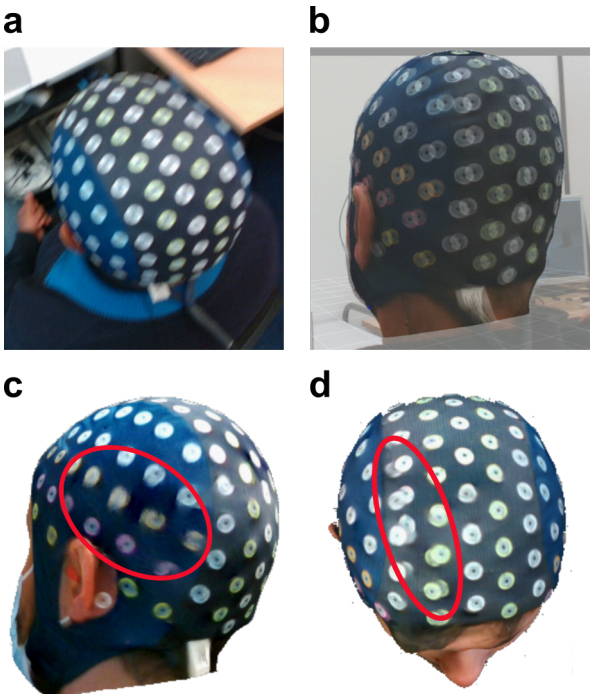

Figure 6.4: Illustration of most common issues encountered during the post-processing stage using the RecFusion software. Please refer to Appendix **C** for a description of the approach taken to address these issues. (**a**) Example of blurry 2D image to be discarded (corresponding to fast movement during acquisition). (**b**) Example of inadequate overlay between the 2D image and the texturing of the 3D model. This kind of discordant image should be discarded as it often leads to texturing errors as exemplified in (**c-d**). (**c**) Example of poor 3D model texturing resulting in blurry electrodes (circled in red). (**d**) Example of poor 3D model texturing resulting in duplicated electrodes (circled in red).

instance, in the experiment described in Chapter **8**, out of the 127 electrodes of interest, an average of 3.8 ± 2.3 (mean $\pm$ SD) electrodes were deemed uncertain in the young adults group ($N = 23$), while the older adults group ($N = 23$) had an average of 8.9 ± 3.4 uncertain electrodes.

6.3.1.3.3 Comparison between procedures

The within-method variability was comparable for both procedures across the five repetitions, with a slight advantage observed for the motion capture method (see Figures **6.5a-b**). The obtained variability for the 127 electrodes of interest was 2.36 ± 0.51 mm (mean $\pm$ SD) for the 3D scan method and 2.23 ± 0.39 mm for the motion capture method. In both cases, the variability did not fall below 1 mm accuracy. The distribution of variability was relatively uniform across electrode locations on the EEG cap for both methods, although the depth perception camera method exhibited slightly higher variability for electrodes in the neck region (see Figures **6.5d-e**). Deviation between the two methods reached higher values, with an average of 3.59 ± 1.11 mm (see Figures **6.5c,f**). The largest deviations, reaching almost 7 mm, were observed for electrodes located at the lowest part of the back of the neck. The electrodes on the frontal left side showed the least deviation between the methods, with an approximate deviation of 1 mm.

Further investigation into the origin of the deviation revealed that, except for electrode LD1 on the frontal left side, the displacement of the centroid determined by the motion capture method in relation to the centroid determined by the 3D scan method was consistently directed towards the inside of the head (below 90°; Figure **6.6a**). Analyzing the angular displacement, it was found that 49% of the electrodes had a displacement below 30°, and 77% of the electrodes had a displacement within an inward cone of 45° (Figure **6.6b**). The

topographic distribution of this variable indicated a clear inward component of displacement in the posterior/occipital zone (Figure **6.6c**), which corresponded to the regions where the largest deviations were observed (Figure **6.5f**).

6.3.1.4 Conclusions

This work successfully achieved its key objectives, validating the use of the tested 3D scanner for subsequent experimental recordings.

Firstly, it provided a quick and efficient method for obtaining electrode positions during experimental sessions. The major advantages of this procedure compared to the motion capture digitizing probe included its rapid acquisition, regardless of the number of electrodes used, versatile setup, absence of calibration requirements, and the possibility of a single experimenter performing the scan. These advantages address critical concerns in mobile EEG experiments, where high-density caps are commonly used, and minimizing participant burden is crucial. Difficulties in obtaining a good scan were identified, relating to the sen-

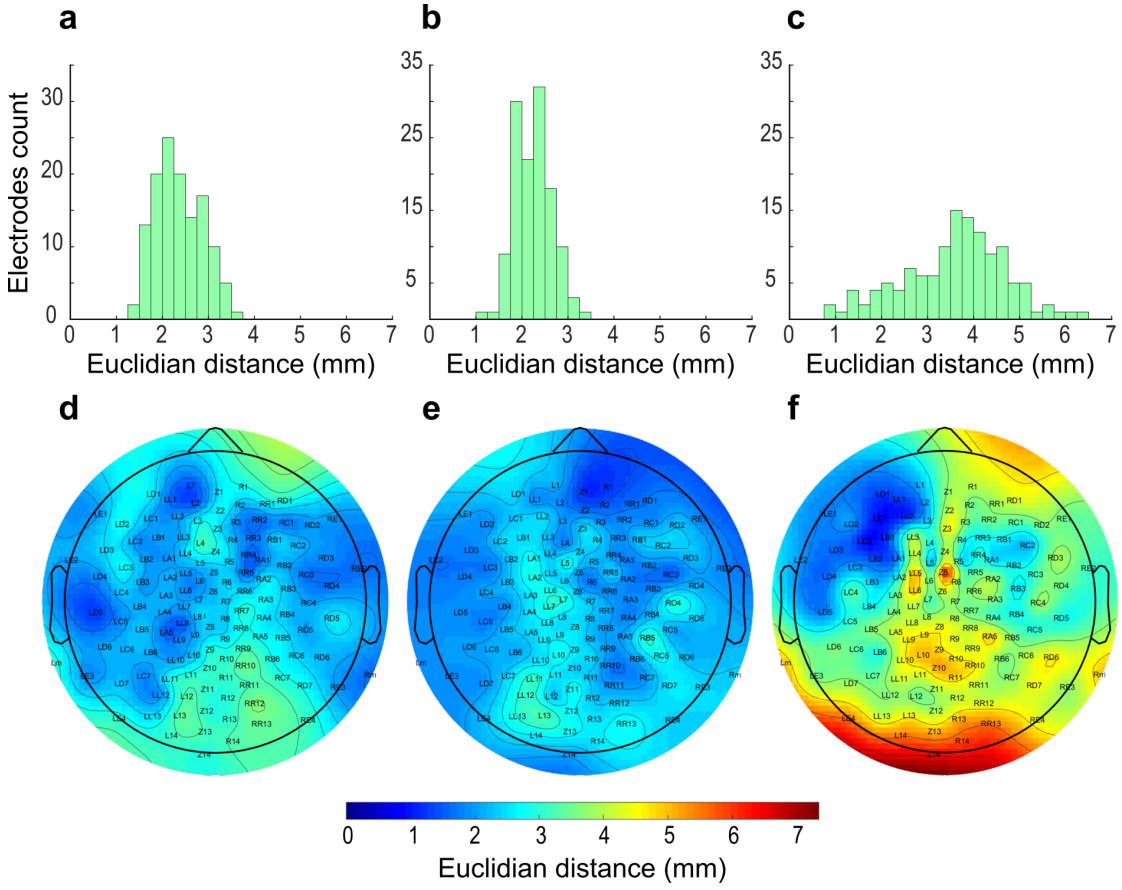

Figure 6.5: Quantitative comparison of electrodes' digitization procedures. (**a**) Histogram count of electrodes according to the variability of the depth perception camera method (computed over 5 repetitions). The variability for the 127 electrodes of interest is reported: 2.36 ± 0.51 mm (mean $\pm$ SD). (**b**) Histogram count of electrodes according to the variability of the digitizing probe method (computed over 5 repetitions). The variability for the 127 electrodes of interest is reported: 2.23 ± 0.39 mm. (**c**) Histogram count of electrodes according to the deviation between methods. The deviation for the 127 electrodes of interest is reported: 3.59 ± 1.11 mm. (**a-c**) 0.25 mm bins are used for the histograms. (**d**) Topographic map of the variability of the depth perception camera method. (**e**) Topographic map of the variability of the digitizing probe method. (**d**) Topographic map of the deviation between methods.

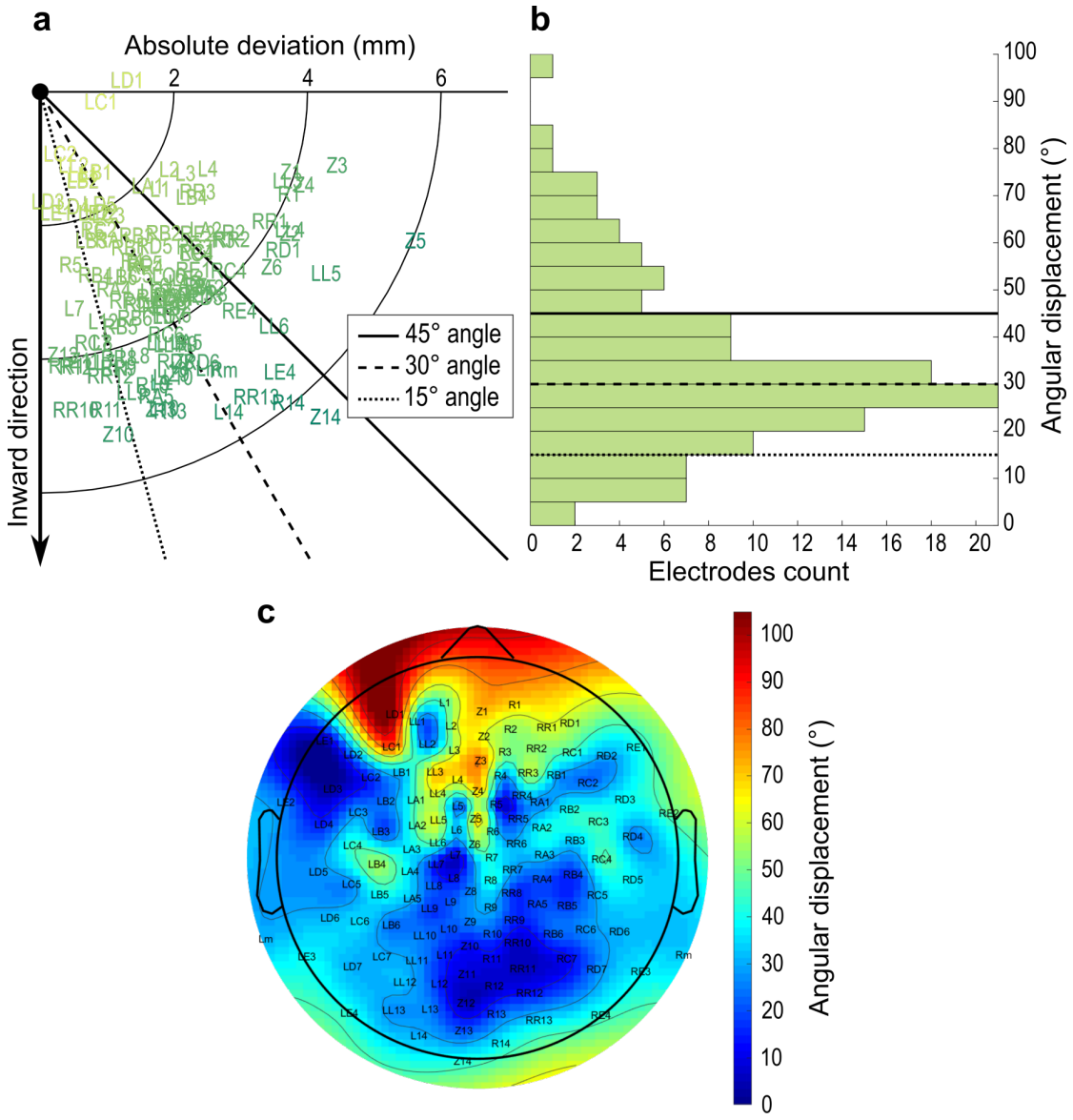

Figure 6.6: Investigation of centroids displacement between digitization methods along the inward direction. (**a**) Polar representation of centroids displacement. Centroid location determined with the depth perception method is represented by the dot at $(0,0)$. Electrode names are placed relatively at the centroid location determined with the motion capture method. Names are colored according to a gradient following the deviation value (light yellow for low deviation and dark green for high deviation). (**b**) Histogram count of electrodes according to their angular displacement (5° bins). 13% of electrodes had an angular displacement below 15°. 49% of electrodes had an angular displacement below 30°. 77% of electrodes had an angular displacement below 45°. (**c**) Topographic map of the angular displacement.

sitivity to lighting conditions and to the experimenter's expertise, but they were addressed with proper training and testing. In the end, reliability analysis demonstrated that variability remained within an acceptable range even when different experimenters performed the scan. In terms of post-processing, the depth perception camera method was found to be more time-consuming compared to the digitizing probe method. A notable drawback was the need to discard a few electrodes that could not be accurately localized, but this was not deemed a major issue thanks to the spatial redundancy of the high-density cap used. These post-processing challenges could potentially be mitigated in future improvements, by using

alternative 3D scanners, such as the Structure sensor[1] (Occipital Inc., Boulder, CO, USA). Indeed, literature examples using this camera did not report such inconveniences, as the 3D model post-processing is automatized with this scanner (Homölle & Oostenveld, 2019; Shirazi & Huang, 2019; Taberna et al., 2019). Additionally, Taberna et al. have proposed an automated detection method for electrode locations on the 3D model, which achieves accurate results and allows for the automation of the electrode pointing step.

Secondly, the performance of the 3D scanner was satisfactory, demonstrating similar reliability compared to the digitizing probe procedure and low deviation between methods in most electrodes. The reliability and deviation values obtained in this study align with previous findings using similar procedures. For example, the study by Shirazi and Huang (2019) on a mannequin head reported a reliability of their 3D scan with a variability of 2.4 ± 0.5 mm, which closely matches the findings in this study (2.36 ± 0.51 mm). According to their analysis, this high level of reliability already significantly improved the localization accuracy of Brodmann areas (BAs) compared to using template electrode locations (91% *vs.* 53% mean accuracy). However, the variability of the motion capture system in Shirazi and Huang's study was quantified at 1.5 ± 0.3 mm, which was lower than the findings in this study (2.23 ± 0.39 mm). It is worth noting that their study used the same probe and motion capture system but had a setup with 22 cameras, which could have reduced the localization error of the system. More likely, the difference in performance between the two studies can be attributed to the ecological conditions in which the data was collected. The current work involved a real participant, and it suggests that the reliability of the motion capture digitization method may degrade under more realistic conditions, even when accounting for head movements. In this work, it resulted in a comparable variability between the two methods, cancelling the precision benefit for the probe digitization procedure. This interpretation is supported by the findings of Taberna et al., who found a systematic accuracy benefit of the 3D scanner procedure over motion capture probing when acquiring data from real participants. One key difference between the procedures is that the motion capture method requires contact with the electrodes by inserting the probe into the electrode wells. Although precautions were taken during the acquisitions, this method is inevitably susceptible to measurement bias due to potential inward displacements, especially for electrodes where the cap does not fit perfectly, such as those in the neck region. The inward displacement analysis reported in this study thus provide further support for the use of the 3D scan procedure, which provides electrode positions that closely align with their actual placement during the experiment. As the deviation was found to be related to inward displacement in a majority of electrodes, this observation may explain most of the difference observed between acquisitions on a mannequin head and a real participant's head, as the cap fits better on the mannequin head and allows for less electrode movement during pointing.

Although this study is limited to a single participant, it provided sufficient experience and insights to confidently utilize the depth perception camera for capturing electrode positions on the scalp of participants. The performance results were convincing enough to justify its

[1]This scanner model was initially selected for the comparative test; however, preliminary testing yielded inconclusive results, possibly due to a defective device.

use in an individualized source reconstruction pipeline, as the alternative option did not offer a significant precision benefit while imposing greater constraints on convenience of usage.

6.3.2 EEG source reconstruction model informed by fMRI localizer

EEG has excellent temporal resolution, but the estimation of the neural sources that generate the signals recorded by the sensors is a difficult, ill-posed problem. The high spatial resolution of fMRI makes it an ideal tool to improve the localization of the EEG sources using data fusion. The original idea set forth by Cottereau et al. (2015) is to use fMRI localizer data to provide source constraints that are based on functional areas defined individually for each participant. To enable the most accurate spatial allocation of EEG activity, this source reconstruction approach was tailored to each participant at every major step in the model. It relied on the combination of the recorded EEG signal with a 3D model of electrode positions, MRI anatomical scans for head and brain structure and a SSR fMRI localizer task (Ramanoël et al., 2020).

6.3.2.1 3D positions of electrodes on the scalp

This step was achieved using the depth perception camera procedure validated previously in Section **6.3.1**. The acquisition and post-processing of the 3D scan was performed exactly as described in Section **6.3.1.2.3**. Electrode positions were acquired prior to the actual experimental session, after cap positioning and before gelling the electrodes.

6.3.2.2 MRI acquisitions

As participants of the *SilverSight* cohort study are also subject to spatial cognition fMRI experiments, MRI anatomical scans and fMRI localizer of the SSRs were conveniently available to build an individual model for each of our participants.

These acquisitions took place at the Quinze-Vingts National Ophthalmology Hospital in Paris, over an extended period of time (from 2017 to 2023) using 2 different MRI scanners depending on the date. Scanners were always equipped with a 64-channel head coil during acquisitions. Earliest data was collected using a 3 Tesla Siemens MAGNETOM Skyra whole-body system (Siemens Medical Solutions, Erlangen, Germany) while most recent data was collected using a 3 Tesla Siemens MAGNETOM Prisma whole-body system (Siemens Medical Solutions, Erlangen, Germany).

For anatomical scans, 2 types of sequences were used: a T1*-weighted MPRAGE 3D sequence (voxel size $= 1 \times 1 \times 1.1$ mm, TR/TE/Angle flip $= 2300$ ms$/2.9$ ms$/900$ ms$/9°$, matrix size $= 256 \times 240 \times 176$; Figure **6.7a**) and a T2-weighted 3D sequence SPACE CAIPI (voxel size $= 1 \times 1 \times 1.1$ mm, TR/TE $= 3140$ ms$/410$ ms, matrix size $= 256 \times 256 \times 176$; Figure **6.7c**). This second sequence provides additional spatial precision to the model (see Section **6.3.2.3**) but was not always available, since it was introduced later in the fMRI experiments routine. For the experiment reported in Chapter **8**, only the model for young adults benefitted from this sequence. However, for the experiment reported in Chapter **9**, almost all participants had this sequence available, with rare exceptions.

A T2*-weighted SMS-EPI sequence (voxel size $= 2.5 \times 2.5 \times 2.4$ mm, TR/TE/Angle flip $= 1000$ ms/30 ms/90°, matrix size $= 100 \times 100$, SMS = 2, GRAPPA = 2) was acquired for the localizer task.

When multiple acquisition sessions were available for a single participant, the complete session (*i.e.*, including both anatomical sequences plus the functional localizer) closest in time to the EEG experimental session was preferred. In some cases where no complete session was available, sequences from separate days were combined, again using the ones closest in time to the experiment. Refer to Ramanoël et al. (2020) for a detailed description of the SSRs localization paradigm.

6.3.2.3 Processing of MRI anatomical images

T1-weighted images were first processed individually for each participant with the FreeSurfer suite (*v.*7.1.1, Fischl et al. 2004) using the *recon-all* command. The latter estimates the interfaces between white matter, gray matter, and cerebrospinal fluid (CSF) and parcellates the brain according to anatomical atlases. The automatically generated surfaces were carefully inspected by an experimenter who subsequently applied manual corrections where necessary (see Figure **6.7b**). Second, the inner skull, outer skull and outer skin surfaces required

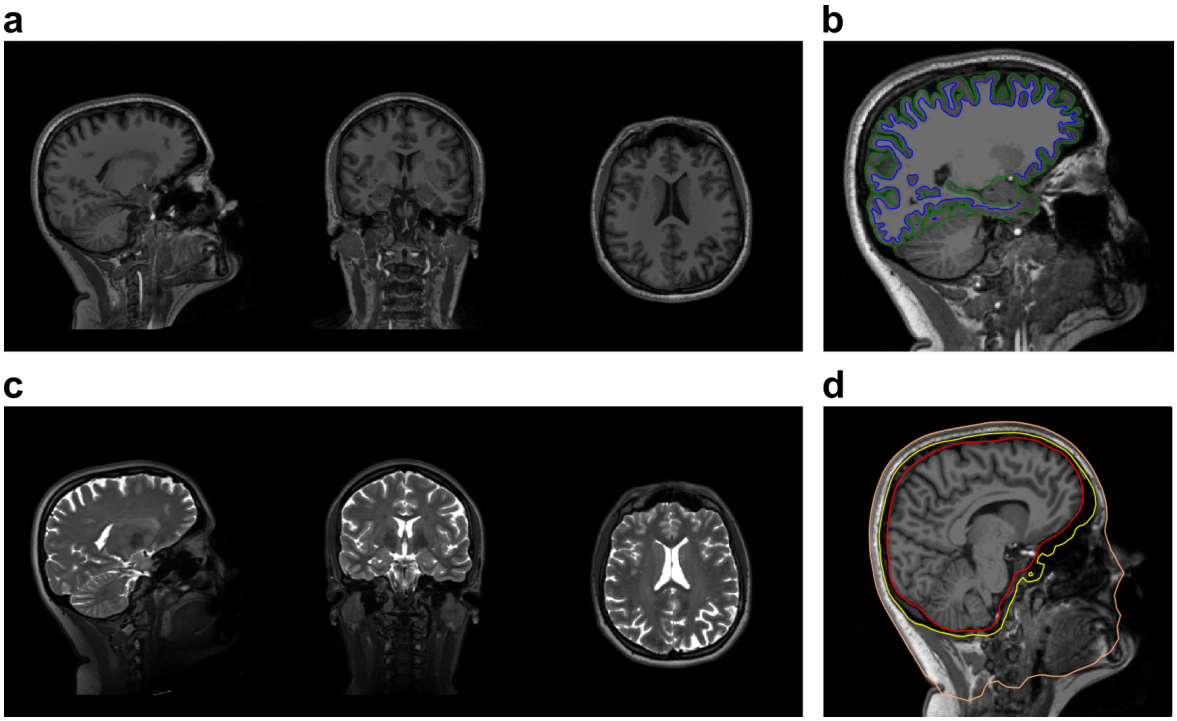

Figure 6.7: Illustration of main processing steps of MRI anatomical images on one of the participants. Visualization in Freeview software (part of FreeSurfer suite). (**a**) Images obtained with T1*-weighted sequence. From left to right: sagittal, coronal and axial view. (**b**) Gray/white matter segmentation overlaid on the T1-weighted image in sagittal view. Blue line: gray/white matter boundary. Green line: gray matter/CSF boundary. Output after manual corrections. (**c**) Images obtained with T2-weighted sequence. From left to right: sagittal, coronal and axial view. (**d**) Definition of the compartments used for the BEM overlaid on the T1-weighted image in sagittal view. Red line: CSF/skull boundary (inner skull surface). Yellow line: skull/skin boundary (outer skull surface). Orange line: skin/air boundary (outer skin surface). Output after manual corrections.

for the three-compartment BEM were computed using the BET tool from the FSL library (Jenkinson et al., 2005; S. M. Smith, 2002). This tool was selected because it enables to combine the T2-weighted images (when available) with the T1-weighted images to improve the automatic estimation. Again, the automatically generated surfaces were checked by an experimenter by an experimenter who subsequently applied manual corrections where required (see Figure **6.7d**).

6.3.2.4 Processing of fMRI localizer task

The localizer task was analyzed using the *SPM12* toolbox implemented in Matlab R2019a (release 7771, Wellcome Department of Imaging Neuroscience, London, UK). Functional images were re-aligned and co-registered to the T1-weighted images. Forward and inverse deformation fields from the individual T1 image to the Montreal Neurological Institute (MNI-152) space were then computed. Finally, all images were normalized using the forward deformation field, the functional images were resampled to a $3 \times 3 \times 3$ mm voxel size (4^{th} degree B-spline interpolation), and were smoothed using an 8 mm full width at half maximum Gaussian kernel. The localizer data was fit to a single participant general linear model for block design. The model included five categories of interest (scenes, faces, objects, scrambled objects, rest) as regressors, convoluted with the *SPM* canonical hemodynamic response function (HRF). The 6 movement parameters were added as regressors of no interest in the model and each voxel time-series was high-pass filtered ($1/128$ Hz cut-off).

The contrast $[Scenes > (Faces + Objects)]$ was used to delineate the para-hippocampal place area (PPA), occipital place area (OPA), and medial place area (MPA) for each participant, according to the following original procedure.

1. For each SSR in each hemisphere, the peak supra-threshold voxel in the contrast t-map closest to reference coordinates provided from Ramanoël et al. (2020) was identified. 'Supra-threshold' voxels were defined using false discovery rate correction for multiple comparisons ($p < 0.05$). The peak coordinates, expressed in the MNI-152 space, used for the study reported in Chapter **8** are presented in Tables **E.1** and **E.2** for the interested reader.
2. A greedy algorithm was run to create the volume of the region of interest (ROI) around this peak voxel according to the following rules:
    - At each iteration, the voxel with the highest t-value while being contiguous to the growing volume is considered to be added to the ROI.
    - This voxel is effectively added only if it is comprised within a 10 mm sphere around the original peak and if it is connected to the gray matter (obtained from the parcellation of white and gray matter performed in Section **6.3.2.3**).
    - The algorithm stops once the volume reaches 60 voxels.
3. Each ROI volume (*i.e.* 3D mask) is reverted to individual space using the inverse deformation field computed earlier and resampled to $1 \times 1 \times 1$ mm voxel size (trilinear interpolation). In this space, each ROI mask contained 1620 contiguous voxels ($= 60 \times 3^3$).

At this stage, a participant-wise mask was obtained for each ROI of each hemisphere. For a practical identification of the ROIs in the source reconstruction model, these masks were overlaid on the source space (see Section **6.3.2.5** for a definition) to identify the ECDs belonging to each ROI (Figure **6.9**), according to the following procedure:

1. Each voxel in the mask was associated with the closest ECD (*i.e.*, the minimal Euclidean distance between the dipole and the center of the voxel), only if this distance was below 2 mm.
2. When two ROIs were too close from each other, it happened that the same ECD belonged to both. In that case, it was removed from both ROIs.
3. Eventually, dipoles without any neighbor (neighboring dipoles are those connected by an edge in the source space mesh) inside the ROI were discarded.

6.3.2.5 Forward model

The forward model refers to the definition of the potential cortical sources of activity and the modelling of the propagation of electrical activity from these sources throughout the brain to characterize of their influence on the signal recorded at the scalp level where the electrodes are placed. It is summarized in the so-called *gain matrix*. It is subject-specific and does not depend on the experimental paradigm.

The forward model was computed using *MNE-Python* tools (v0.23, Gramfort et al. 2013). The source space was defined using the 'midgray' surface (Cottereau et al., 2015), *i.e.*

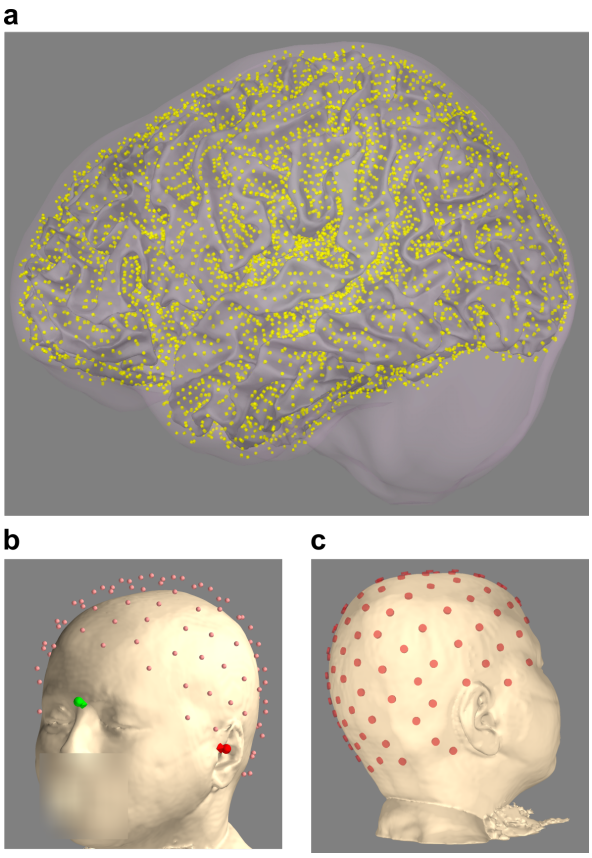

Figure 6.8: Illustration of main forward model steps for an example participant. (**a**) Source space definition. Each yellow arrow depicts an ECD on the midgray surface (10242 per hemisphere). The semi-transparent envelope stands for the inner skull surface (red line on Figure **6.7d**). (**b**) Co-registration of electrodes with the MRI scalp surface based on fiducials alignment. The three fiducials (nasion, left and right helix/tragus junctions) were digitized in the 3D scan (spherical shapes on the figure) and identified anatomically on the surface generated from the MRI T1-weighted images (diamond shapes on the figure). Visible on the figure: nasion (green), left helix/tragus junction (red), electrode positions (pink dots). (**c**) Projection of the electrodes on the scalp surface after co-registration, giving the final locations of the electrodes used in the forward model.

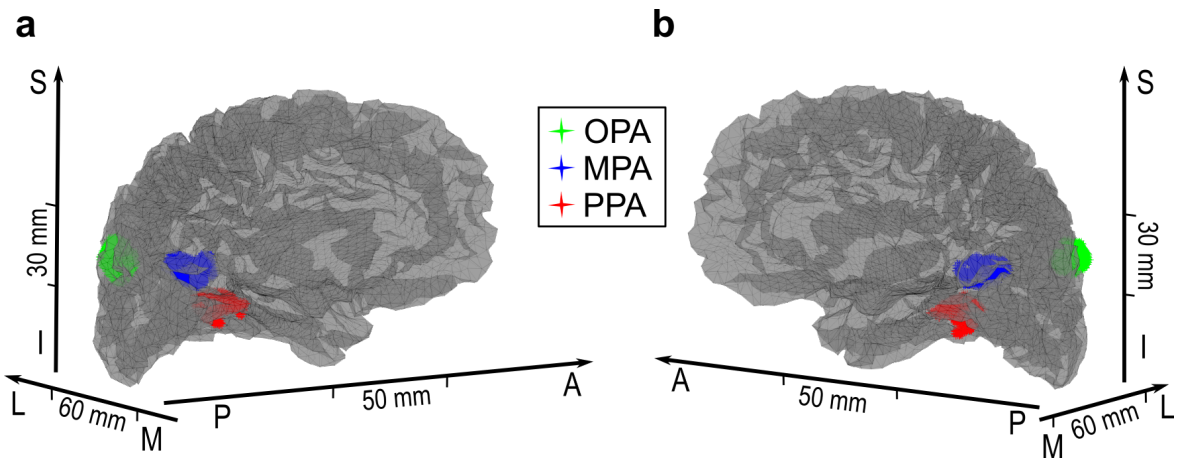

Figure 6.9: Illustration of ROIs definition in the source space for an example participant. The transparent mesh corresponds to the source space (each vertex stands for an ECD). Colored areas display the volume mask computed for each ROI using the fMRI task localizer (see Section **6.3.2.4**). (**a**) Left hemisphere. (**b**) Right hemisphere. Axes abbreviations: A, anterior; P, posterior; M, medial; L, lateral; I, inferior, S, superior.

the surface located halfway in the gray matter (in-between the blue and green surfaces plotted on Figure **6.7b**). A tessellation of this midgray surface with 10242 regularly spaced vertices (hemisphere-wise) served as the basis for our source space (Figure **6.8a**). Each of these vertices held an ECD oriented orthogonally to the cortical surface in order to diminish the number of parameters to be estimated in the inverse procedure (Cottereau et al., 2015; Hämäläinen et al., 1993). Inner skull, outer skull and outer skin surfaces were individually tessellated into 5120 faces meshes defining the boundaries between the CSF and the skull, the skull and the scalp and the scalp and the air, respectively. In the BEM, a standard 0.33 $S.m^{-1}$ conductivity was assigned to brain/CSF and scalp compartments. The skull thickens and densifies across the lifespan, which modifies its electrical properties. Taking the latter into consideration age-dependent conductivity measures were assigned to the skull compartment. There are no charts precise enough to choose a different value for ages close to each other so, following Michel and Brunet (2019) review of the literature, a single value was assigned per age group. Skull conductivity was estimated to 0.02145 $S.m^{-1}$ for young participants (1:15 ratio with the brain/CSF conductivity around 30 years old) and at 0.0099 $S.m^{-1}$ for older participants (1:33 ratio around 75 years old). Electrode positions from the 3D scan were co-registered to the MRI head surface using MNE-python `coregister` function which finds the rigid body transformation that minimizes the distance between fiducials coordinates in both reference frames (Figure **6.8b**). Once in the common reference frame, the electrodes were orthogonally projected onto the outer skin surface (Figure **6.8c**). Ultimately, the source space, the electrical boundaries, and the electrode locations were combined to form the gain matrix.

6.3.2.6 Inverse model

With the theoretical gain matrix modelling the electric field propagation from the cortical sources to the scalp sensors, the inverse problem consists in retrieving the sources activa-

tion based on the signal observed at the electrodes level during the experiment. With 127 sensors against 20484 sources, the mathematical inversion of the gain matrix is an ill-posed problem with an infinite number of solutions. A conventional approach to this issue is to introduce priors, tailored to the research question and the experimental paradigm, on the source distribution to constrain the estimation problem.

The inverse problem was solved using the L2-regularized minimum norm estimation (MNE) (Hämäläinen et al., 1993) with the *FieldTrip-lite* plugin (v20210601, Oostenveld et al. 2011) for EEGLAB. In this case, the inverse solution has a closed form and can be written:

$$\begin{aligned} &\hat{\boldsymbol{J}}(s) = \boldsymbol{R}\boldsymbol{G}'(\boldsymbol{G}\boldsymbol{R}\boldsymbol{G}' + \lambda^2\boldsymbol{C})^{-1}\boldsymbol{M}(s) \\ &\text{with } \boldsymbol{M}(s) \text{ the measurements on the EEG sensors for sample s,} \\ &\hat{\boldsymbol{J}}(s) \text{ the estimated source activity for sample s,} \\ &\boldsymbol{G} \text{ the gain matrix,} \\ &\boldsymbol{R} \text{ the source covariance matrix,} \\ &\boldsymbol{C} \text{ the noise covariance matrix,} \\ &\lambda \text{ the regularization parameter.} \end{aligned} \tag{6.2}$$

Depending on the type of analysis, $\boldsymbol{M}(s)$ represents amplitudes at time t ($s = t$, temporal analysis) or complex Fourier coefficients at time t and frequency f ($s = (t, f)$, time-frequency analysis). Similarly, $\hat{\boldsymbol{J}}(s)$ represents the current density associated with the ECDs at time t for the temporal analysis and the spectral power at time t and frequency f for the time-frequency analysis.

6.3.2.6.1 Introducing priors into the source covariance matrix

The original idea proposed in Cottereau et al. (2015) consists in enforcing local correlation constraints in the source covariance matrix ($\boldsymbol{R}$ in Equation **6.2**) to bias the inverse procedure towards coherent activity within the ROIs. In the absence of any prior on the source distribution, the source covariance matrix $\boldsymbol{R}$ is often equal to the identity matrix. By introducing the knowledge of sources belonging to the functionally defined ROIs into this matrix, the aim is to decrease the tendency of the minimum-norm procedure to smooth activity over very large surfaces and across different functional areas.

To do so, a *local correlation matrix* was constructed for each ROI by identifying first- and second-order neighbors in the source space mesh for each ECD belonging to the ROI. Starting from the identity matrix, a weight of 0.5 and 0.25 was assigned off-diagonal elements corresponding to first- and second-order neighbors, respectively. $\boldsymbol{R}$ is then modified according to these local correlation matrices, resulting in a block-diagonal matrix. This modification of $\boldsymbol{R}$ therefore respects areal boundaries which permits to dissociate the signals from different functional areas, unlike other smoothing methods such as LORETA that apply the same smoothing rule throughout the cortex (Pascual-Marqui et al., 1994). To solve the inverse problem, the Cholesky decomposition of $\boldsymbol{R}$ is used in practice. Owing to the block-diagonal property of $\boldsymbol{R}$, it is advantageous to compute this decomposition on the local

correlation matrices separately, before reuniting them to obtain the Cholesky decomposition of $\boldsymbol{R}$ itself. In some cases, the modification of the off-diagonal elements lead to non semi-definite matrices, which prevents the Cholesky decomposition. To circumvent this issue, the local correlation matrix was first rewritten from its eigenvalue decomposition by setting all the negative eigenvalues to 10e−5 to force it to be semi-definite.

6.3.2.6.2 Optimization of the depth parameter γ

Prior to the inversion procedure, the contribution of each ECD in the gain matrix was normalized to compensate for the bias of the MNE method towards superficial sources (F.-H. Lin et al. 2004; equation 7, parameter $\gamma = 0.95$). The selection of the parameter γ is an inherent aspect of the model and required an optimization process, as no predefined value exists for this parameter due to its dependence on the relative depth of the ROIs in a specific experimental design. The optimization objective involved minimizing the deviation index D (computed on simulated data, as described in Section **6.3.2.7** and Equation **6.3**) for a given (γ, λ) pair. Discrete values of γ (ranging from 0.5 to 1 in increments of 0.05) and λ (ranging from 10^{-4} to 10^2 on a logarithmic scale) were systematically tested. The inclusion of λ in this procedure was necessary since the construction of the cross-talk matrix and the computation of D relied on a full pass through the forward and inverse models, and the outcomes were found to be highly dependent on the value of λ. The optimization process was carried out on a participant-by-participant basis, resulting in a specific γ_{opt} for each participant. Subsequently, the median value of the γ_{opt} distribution was selected as the final value for γ, which was then adopted for the subsequent steps of the inverse model (see Figure **6.10**).

6.3.2.6.3 Cross-validation of regularization parameter

As suggested by Cottereau et al. (2015), the regularization parameter λ was determined using a data-driven, generalized cross-validation approach (Reeves, 1994) based on the singular value decomposition of the gain matrix $\boldsymbol{G}$ and implemented in the *regtools* toolbox for Matlab (P. C. Hansen, 2007). This optimization was run after fixing the depth parameter γ (see earlier). Participant-wise, an optimal λ was computed for each sample s involved in the source reconstruction. The mean optimal λ of the obtained distribution (participant and analysis specific) was chosen as the final value used in Equation **6.2**. This analysis was run prior to solving the inverse problem, such that the optimization of λ did not occur concurrently to the inversion.

6.3.2.6.4 ROI-based analysis

Once the inversion performed, the activity from all sources within each ROI is averaged to form a summary activity per ROI. ROI-based analysis confers several advantages over the conventional whole-brain analysis typically employed in EEG imaging investigations (Cottereau et al., 2015). Primarily, it facilitates a direct comparison of activations among functionally equivalent sources across different subjects. As ROI definitions are used on a subject-basis, co-registering the subject's brain to an anatomical common space is no longer required, thereby avoiding associated challenges in the co-registration process. Moreover,

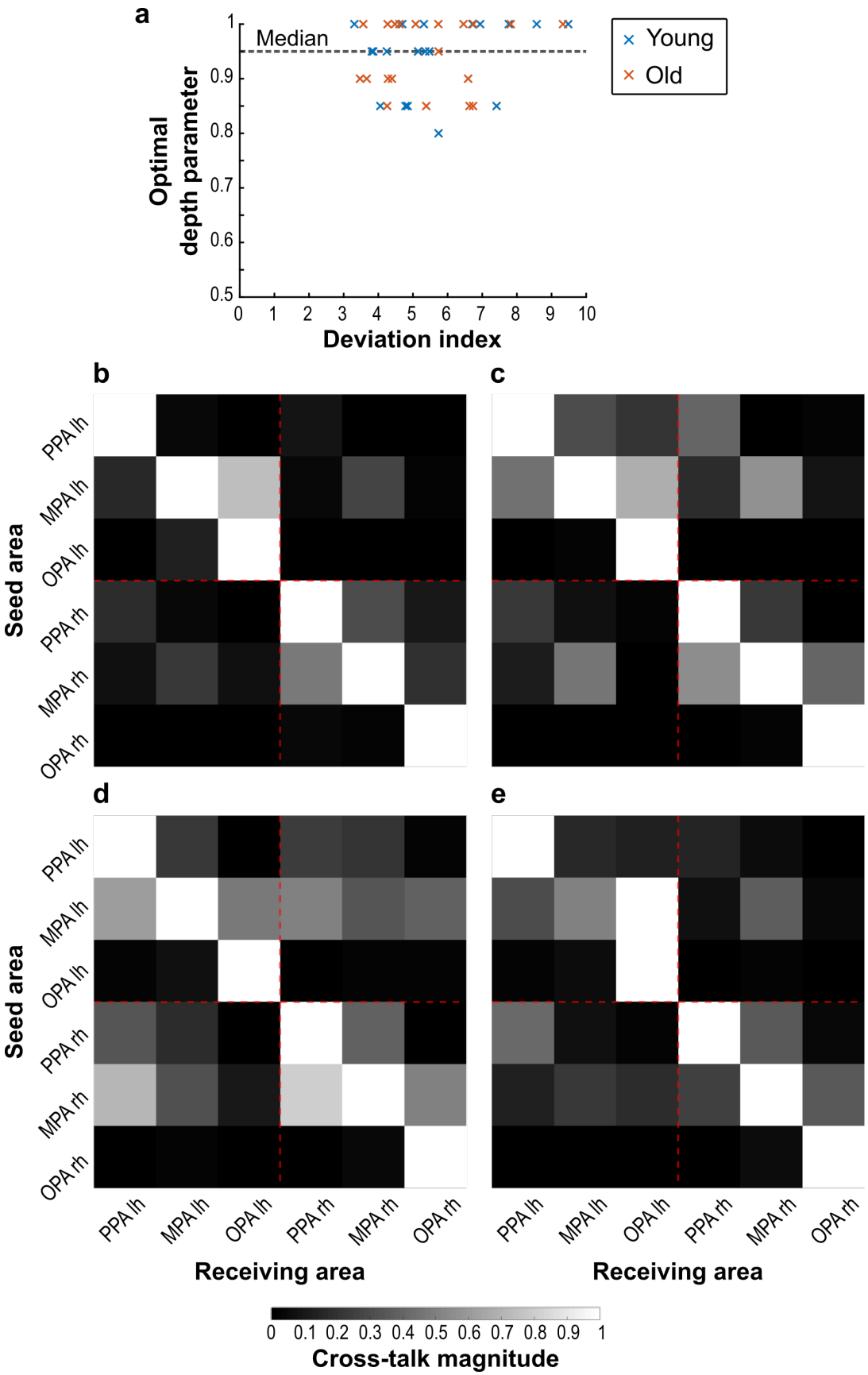

Figure 6.10: Results of the γ optimization procedure. [Continued on next page]

Figure 6.10: [On previous page] These results illustrate the optimization procedure for the experiment described in Chapter **8** (21 young adults and 21 older adults). (**a**) Individual optimal depth parameter (γ_{opt}) plotted against the optimal deviation index (D_{opt}) achieved for each participant. The median γ_{opt} value of 0.95 was chosen for the source reconstruction based on real activations. (**b-e**) Illustration of optimal cross-talk matrices obtained with the optimal (γ, λ) couple at the individual-level. Cross-talk magnitude values are scaled according to the maximum amount of activity recovered in any of the ROIs. (**b**) Cross-talk matrix achieving the lowest deviation among all participants. $D_{opt} = 3.309$, with $\gamma_{opt} = 1$ and $\lambda_{opt} = 10^{-4}$. Young adult. (**c**) Cross-talk matrix achieving the least deviation among all participants. $D_{opt} = 5.079$, with $\gamma_{opt} = 1$ and $\lambda_{opt} = 10^{-4}$. Older adult. (**d**) Cross-talk matrix achieving the least deviation among all participants. $D_{opt} = 6.634$, with $\gamma_{opt} = 0.85$ and $\lambda_{opt} = 10^{-3}$. Older adult. (**e**) Cross-talk matrix achieving the highest deviation among all participants. $D_{opt} = 9.482$, with $\gamma_{opt} = 1$ and $\lambda_{opt} = 10^{-4}$. Young adult.

this method enables a meaningful comparison of EEG findings with results obtained from other studies utilizing different techniques, such as fMRI or single-unit physiology, targeting the same ROIs. Lastly, it considerably simplifies the multiple comparison problem in statistical analyses, as the number of ROIs is typically three orders of magnitude smaller than the number of cortical sources.

6.3.2.7 Evaluation of the model with the cross-talk matrix

In the absence of a ground truth reference, which would require an invasive procedure to determine, evaluating the accuracy of a specific source reconstruction model poses a challenging task. Nonetheless, a partial assessment of the model's reliability can be achieved through numerical simulations (Cottereau et al., 2012). In the context of ROI-based analysis, a convenient approach involves characterizing the model's accuracy using a cross-talk matrix. Cross-talk refers to neural activity erroneously attributed to a specific ROI that is generated by another ROI (Cottereau et al., 2015). Ideally, the cross-talk should be null, ensuring that the model solely retrieves activity from the corresponding active region.

To construct the cross-talk matrix on a participant-by-participant basis, active sources are systematically placed in each ROI while estimating the reconstructed activity in all ROIs after passing through the forward and inverse models once. The cross-talk magnitude is summarized in a matrix (see illustrations on Figure **6.10**), with values scaled according to the maximum amount of activity recovered in any of the ROIs (should be the seed region in principle).

To assess the quality of the cross-talk matrix, a deviation index D was computed using the formula presented in Equation **6.3**. This index quantifies the deviation between the cross-talk matrix and the ideal cross-talk matrix (*i.e.*, the identity matrix), with a weight penalty of 10 applied to diagonal elements smaller than one (indicating that the reconstructed activity should be maximal for the seed ROI).

$$D = 10 \times (\mathrm{N_{ROIs}} - tr(\boldsymbol{C_t})) + \sum_{\forall (i,j),\, i \neq j} c_t(i,j) \tag{6.3}$$

with D the deviation index,

$\boldsymbol{C_t}$ the cross-talk matrix,

$c_t(i,j)$ the cross-talk matrix element at column i and row j.

For all the participants evaluated (see Figure **6.10a**), the cross-talk matrix was deemed satisfactory ($D < 10$), with a strong diagonal pattern (see Figure **6.10b-e**). As depicted on Figure **6.10a**, age was not a significant variable explaining differences between D values, suggesting the model validity was similar for both age groups. Nonetheless, some cross-talk was noted, especially when the seed area was the MPA, which occasionally was not the area with the maximal reconstructed activity after a full pass through the model (like in Figure **6.10e** for the left hemisphere). It was also noted that the cross-talk between the MPA from each hemisphere was often elevated too since this SSR has a very medial location. It was not attempted to further refine the source reconstruction model, but these considerations must be kept in mind as limitations when interpreting the results in the subsequent experiments.

CHAPTER 7

MOBILE BRAIN/BODY IMAGING OF LANDMARK-BASED NAVIGATION WITH HIGH-DENSITY EEG

This chapter presents the first major experimental contribution of this thesis, the proof-of-concept for the application of the MoBI approach to landmark-based navigation in young adults. Mobile EEG investigations permitted to identify a set of brain areas matching state-of-the-art brain imaging literature of landmark-based navigation. Spatial behavior in mobile conditions additionally involved sensorimotor areas related to motor execution and proprioception usually overlooked in static fMRI paradigms. A cortical source near the retrosplenial complex (RSC) was retrieved, in line with the engagement of this region in spatial reorientation. Consistent with its role in visuo-spatial processing and coding, we observed an alpha-power desynchronization while participants gathered visual information. Additionally, transient time-frequency patterns were identified and, thanks to the concomitant motion capture recordings, were attributable to increases in attentional demand (in the alpha/gamma range) or in memory workload (in the delta/theta range).

This work was peer-reviewed and published as a journal article, entitled "Mobile brain/body imaging of landmark-based navigation with high-density EEG", as part of the special issue "Time to move: brain dynamics underlying natural action and cognition" of the European Journal of Neuroscience, released in December 2021 (Delaux et al., 2021). It is transcribed exactly as written in the published version. Supplementary material attached to the published version of the article are presented in Appendix **D**.

Received: 29 May 2020 | Revised: 5 March 2021 | Accepted: 14 March 2021

DOI: 10.1111/ejn.15190

SPECIAL ISSUE ARTICLE

EJN European Journal of Neuroscience FENS WILEY

Mobile brain/body imaging of landmark-based navigation with high-density EEG

Alexandre Delaux[1] | **Jean-Baptiste de Saint Aubert**[1] | **Stephen Ramanoël**[1] | **Marcia Bécu**[1] | **Lukas Gehrke**[2] | **Marius Klug**[2] | **Ricardo Chavarriaga**[3,4] | **José-Alain Sahel**[1,5,6,7] | **Klaus Gramann**[2] | **Angelo Arleo**[1]

[1]Sorbonne Université, INSERM, CNRS, Institut de la Vision, Paris, France

[2]Institute of Psychology and Ergonomics, Technische Universität Berlin, Berlin, Germany

[3]Center for Neuroprosthetics, Ecole Polytechnique Fédérale de Lausanne, Geneva, Switzerland

[4]Zurich University of Applied Sciences, ZHAW Datalab, Winterthur, Switzerland

[5]CHNO des Quinze-Vingts, INSERM-DGOS CIC 1423, Paris, France

[6]Fondation Ophtalmologique Rothschild, Paris, France

[7]Department of Ophthalmology, The University of Pittsburgh School of Medicine, Pittsburgh, PA, USA

Correspondence
Alexandre Delaux and Jean-Baptiste de Saint Aubert, Institut de la Vision, CNRS, INSERM, Sorbonne Université, 17 rue Moreau, 75012 Paris, France.
Emails: alexandre.delaux@inserm.fr; jean-baptiste.de-saint-aubert@inserm.fr

Abstract

Coupling behavioral measures and brain imaging in naturalistic, ecological conditions is key to comprehend the neural bases of spatial navigation. This highly integrative function encompasses sensorimotor, cognitive, and executive processes that jointly mediate active exploration and spatial learning. However, most neuroimaging approaches in humans are based on static, motion-constrained paradigms and they do not account for all these processes, in particular multisensory integration. Following the Mobile Brain/Body Imaging approach, we aimed to explore the cortical correlates of landmark-based navigation in actively behaving young adults, solving a Y-maze task in immersive virtual reality. EEG analysis identified a set of brain areas matching state-of-the-art brain imaging literature of landmark-based navigation. Spatial behavior in mobile conditions additionally involved sensorimotor areas related to motor execution and proprioception usually overlooked in static fMRI paradigms. Expectedly, we located a cortical source in or near the posterior cingulate, in line with the engagement of the retrosplenial complex in spatial reorientation. Consistent with its role in visuo-spatial processing and coding, we observed an alpha-power desynchronization while participants gathered visual information. We also hypothesized behavior-dependent modulations of the cortical signal during navigation. Despite finding few differences between the encoding and retrieval phases of the task, we identified transient time–frequency patterns attributed, for instance, to attentional demand, as reflected in the alpha/gamma range, or memory workload in the delta/theta range. We confirmed that combining mobile high-density EEG and biometric measures can help unravel the brain structures and the neural modulations subtending ecological landmark-based navigation.

KEYWORDS

ecological navigation, mobile EEG, retrosplenial complex, source reconstruction, virtual reality

Edited by: Teodoro Solis-Escalante

Delaux and de Saint Aubert contributed equally (co-first authorship).

Experiment conducted at: FG Biopsychologie und Neuroergonomie (Sekr. KWT-1), TU Berlin, 10623 Berlin, Fasanenstr. 1, Germany.

Analysis carried out at: Institut de la Vision, 17 rue Moreau 75012 Paris, France.

Figure 7.1: Cover of the article "Mobile brain/body imaging of landmark-based navigation with high-density EEG", as published in the European Journal of Neuroscience (Delaux et al., 2021).

7.1 Introduction

Spatial navigation requires active exploration, multisensory integration, as well as the encoding and long-term consolidation of internal models of the world (Arleo & Rondi-Reig, 2007; Epstein et al., 2017; Wolbers & Hegarty, 2010). Thus, the ability to navigate in space encompasses both perceptual and cognitive faculties (Ekstrom et al., 2017; Spiers & Barry, 2015). A large body of work has elucidated the neural bases of wayfinding behavior in both animals and humans, leading to a better understanding of the navigational system across multiple levels (Burgess, 2008; Epstein et al., 2017; Hardcastle et al., 2017; Poulter et al., 2018).

Most investigations of the brain network subtending human spatial navigation rely on fMRI (Epstein et al., 2017; Taube et al., 2013) due to its unmatched spatial resolution among non-invasive methods. However, this technique is not suited for testing participants in unconstrained motion conditions, which limits the study of neural processes involved during natural behavior (Zaitsev et al., 2015). Combining behaviometric and neurometric recordings in ecological (*i.e.*, close to real, natural) conditions is key to modern cognitive neuroscience (Ladouce et al., 2019; Schaefer, 2014), in particular to study spatial cognition (Bécu et al., 2020a; Gehrke & Gramann, 2021; Miyakoshi et al., 2021). With relatively coarse spatial but fine temporal resolution, EEG offers a complementary tool for neuroimaging the brain during spatial behavior (Baker & Holroyd, 2009; Bischof & Boulanger, 2003; C.-T. Lin et al., 2015, 2009; Plank et al., 2010). Although EEG does not prevent the participant's motion per se, it is very sensitive to movement-related artifacts. Electrical potentials from muscle contractions (*e.g.*, head movements, eye blinks, or heartbeat, see Jung et al. 2000) generate strong artifactual signals that compromise the extraction of brain-related responses (*i.e.*, reducing the signal-to-noise ratio; SNR). As a consequence, most EEG studies have constrained the mobility of participants in order to minimize motion-related artifacts (*e.g.*, by making them sit in front of a screen and respond with finger taps only).

Recent technical developments have unlocked the possibility of using EEG brain imaging in a variety of ecological conditions (indoor walking: Ladouce et al. 2019; Luu et al. 2017a; J. L. Park and Donaldson 2019; outdoor walking: Debener et al. 2012; Reiser et al. 2019; cycling: di Fronso et al. 2019; Zink et al. 2016; and dual tasking: Bohle et al. 2019; Marcar et al. 2014). By coupling EEG recordings with other biometric measures (*e.g.*, body and eye movements), the mobile brain/body imaging (MoBI) approach gives access to unprecedented behavioral and neural data analysis (Gramann et al., 2014, 2011; Ladouce et al., 2017; Makeig et al., 2009). In addition, the MoBI paradigm has been successfully combined with fully immersive virtual reality (VR) protocols (Djebbara et al., 2019; Liang et al., 2018; Peterson & Ferris, 2019; Plank et al., 2015; Snider et al., 2013). Immersive VR allows near-naturalistic conditions to be reproduced, while controlling all environmental parameters (Diersch & Wolbers, 2019; J. L. Park et al., 2018; Parsons, 2015; Starrett & Ekstrom, 2018). The reliability of 3D-immersive VR enables the stimulation of visual, auditory, and proprioceptive modalities, while allowing the participant to actively explore and sense the virtual environment (Bohil et al., 2011; Kober et al., 2012). This continuous interplay be-

tween locomotion and multisensory perception is thought to be a key component of spatial cognition in near-natural conditions, as its absence leads to impaired performance in various spatial abilities (path integration: Chance et al. 1998; spatial updating: Klier and Angelaki 2008; spatial reference frame computation: Gramann 2013; spatial navigation and orientation: Ladouce et al. 2017; Taube et al. 2013; and spatial memory: Holmes et al. 2018).

In the present study, we use the MoBI approach to combine high-density mobile EEG recordings and immersive VR in order to study spatial navigation in a three-arm maze (*i.e.*, a Y-maze). Our primary aim is to provide a proof-of-concept in terms of EEG-grounded neural substrates of landmark-based navigation consistent with those found in similar fMRI paradigms (Iaria et al., 2003; Konishi et al., 2013; Wolbers & Büchel, 2005; Wolbers et al., 2004). We chose the Y-maze task because it offers a simple two-choice behavioral paradigm suitable to study landmark-based spatial navigation and to discriminate between allocentric (*i.e.*, world-centered) and egocentric (*i.e.*, self-centered) responses, as previously shown in animals (C. A. Barnes et al., 1980) and humans (Bécu et al., 2020b; Rodgers et al., 2012). Complementarily, a recent fMRI study of ours has investigated the brain activity of regions involved in visuo-spatial processing and navigation in a similar Y-maze task (Ramanoël et al., 2020). This offers the opportunity to comparatively validate the neural correlates emerged through static fMRI experiment against those found by mobile high-density EEG.

The neural substrates of landmark-based navigation form a network spanning medial temporal areas (*e.g.*, hippocampus and para-hippocampal cortex) and medial parietal regions (Epstein & Vass, 2014), such as the functionally defined retrosplenial complex (RSC) (Epstein, 2008). Here, we expect the RSC to play a role in mediating spatial orientation through the encoding and retrieval of visual landmarks (Auger & Maguire, 2018; Auger et al., 2012, 2015; Julian et al., 2018; Marchette et al., 2015; Spiers & Maguire, 2006). The RSC is indeed implicated in the translation between landmark-based representations in both egocentric and allocentric reference frames (Marchette et al., 2014; Mitchell et al., 2018; Shine et al., 2016; Sulpizio et al., 2013; Vann et al., 2009). Our hypothesis also encompasses the role of specific upstream, visual processing areas of the parieto-occipital region involved in active wayfinding behavior (Bonner & Epstein, 2017; Patai & Spiers, 2017). In addition, our paradigm accounts for the role of downstream, higher-order cognitive functions necessary for path evaluation, covering a frontoparietal network (including prefrontal areas, Epstein et al. 2017; Spiers and Gilbert 2015) that codes for overarching mechanisms such as spatial attention and spatial working memory (Cona & Scarpazza, 2019).

Mobile brain imaging protocols also engage locomotion control processes, in which motor areas in the frontal lobe and somatosensory areas in the parietal lobe are typically involved (Gwin et al. 2010; Roeder et al. 2018; Seeber et al. 2014; see Delval et al. 2020 for a recent review). Furthermore, the integration of vestibular and proprioceptive cues made possible by mobile EEG paradigms is likely to influence the observed neural correlates of spatial orientation (Ehinger et al., 2014; Gramann et al., 2018) and attention (Ladouce et al., 2019).

Finally, given the high temporal resolution of EEG, we aim at characterizing how the activity of the structures engaged in active, multimodal landmark-based navigation is modulated by behavioral events, related to either action planning (*e.g.*, observation of the environment, physical rotation to complement mental perspective taking) or action execution (*e.g.*, walking, maintaining balance). We also aim at exploring the differential engagement of brain regions involved in the encoding (learning condition) and the retrieval (control and probe conditions) phases of the task (RSC is implicated in both; Burles et al. 2018; Epstein and Vass 2014; Mitchell et al. 2018).

The purpose of this study is thus to explore the cortical correlates of landmark-based navigation in mobile participants. We first hypothesize that the analysis of the EEG signal will retrieve the above-mentioned brain structures known to be engaged during active spatial navigation based on visual cues. We then expect behavioral events to modulate features of the recorded EEG data, identifiable as transient time-frequency patterns in the involved brain areas, and to interpret them with respect to spatial cognition and locomotion control literature. Finally, we expect to find significant differences in these patterns across the phases of the task, contrasting the cognitive mechanisms involved in context-dependent task solving. We aim to investigate and interpret their condition specificity and their temporality. Under such considerations, this work can help toward a better understanding of context-specific neural signatures of landmark-based navigation.

7.2 Methods

7.2.1 Participants

Seventeen healthy adults (range: 21-35 years old, $M = 26.82$, $SD = 4.85$; 10 women) participated to this study. Fifteen were right-handed and two left-handed. All participants had normal (or corrected to normal) vision and no history of neurological disease. In one recording session, there were abnormalities (discontinuities and absence of events) in the motion capture signal. Thus, we removed one participant from the analysis. The experimental procedures were approved by the local ethics committee (GR_12_20190513, Institute of Psychology & Ergonomics, *Technische Universität Berlin*, Germany) and all participants signed a written informed consent, in accordance with the Declaration of Helsinki. All participants answered a discomfort questionnaire at the end of the experiment, adapted from the simulation sickness questionnaire of Kennedy et al. (1993), which can be found in Supplementary Methods **D.1**. We gave the instructions in English and all participants reported a good understanding of the English language. Each participant received a compensation of either 10€/h or course credits.

7.2.2 EEG system

The EEG system (Figure **7.2a**) consisted of 128 active wet electrodes (actiCAP slim, Brain Products, Gilching, Germany) mounted on an elastic cap with an equidistant layout

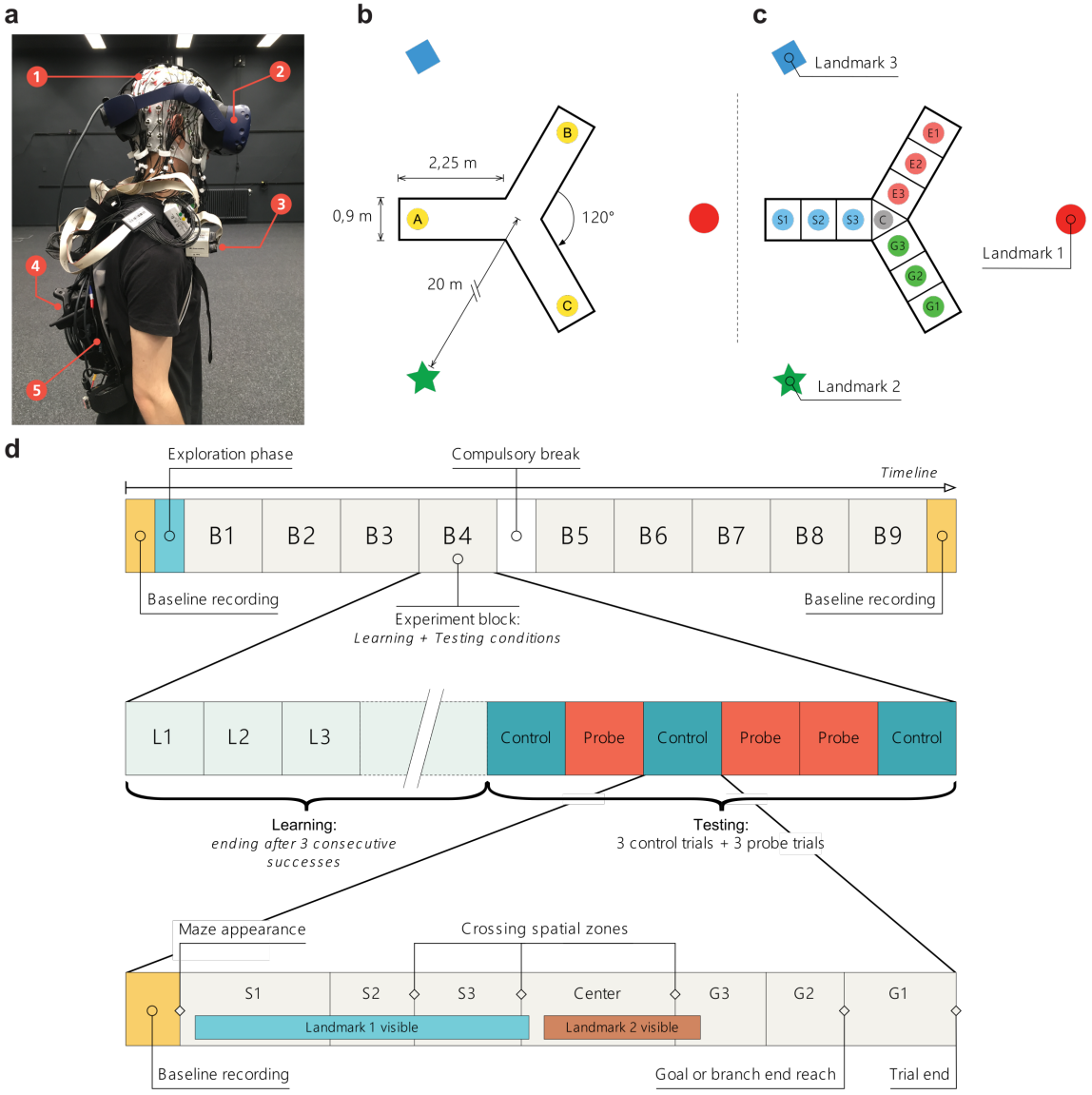

Figure 7.2: Virtual environment, setup, and timeline of the experiment. (**a**) Details of participant's equipment. (1) EEG cap (128 channels); (2) VR Head-mounted display (VIVE Pro); (3) Wifi transmitter for EEG data (Move system); (4) Additional motion capture tracker (VIVE tracker); and (5) Backpack computer running the virtual environment (Zotac PC). (**b**) Virtual environment. Participants explored a virtual equilateral Y-maze. In the learning condition, they always started in the same arm (*e.g.*, A) and they had to find a hidden goal, always placed in the same location (*e.g.*, C). In the testing conditions, the environment and goal location stayed the same but the participant would start from either the same position (A) in control trials or the third arm (B) in probe trials. (**c**) Spatial discretization of the environment (example for a learning trial). We delimited 10 areas in the maze: 'S' stands for starting arm, 'C' for center, 'E' for error arm, and 'G' for goal arm. In the text, when referring to the arm chosen by the participant (either 'E' or 'G'), we use the letter 'F' standing for finish arm. These labels are condition-dependent (different in the probe condition). The names of the landmark depend on the location of starting arm in the learning condition and goal arm. These names are block dependent. (**d**) General timeline of the experiment. The first row represents the general succession of conditions in the experiment. The second row shows an example of the sequence of trials in an experimental block. The third row illustrates the structure of a trial, including a possible course of events: progress across spatial sections and visibility of landmarks depending on participant's head movements. We provide a video of a participant performing the task, along with the reconstruction of the tracker positions, in Video S1 (see Appendix **D**).

(EASYCAP, Herrsching, Germany). The impedance of a majority of the channels was below 25 kΩ (9.5% of the electrodes had an impedance above 25 kΩ). Two electrodes placed below the participant's eyes recorded electro-oculography (EOG). An additional electrode located closest to the standard position F3 (10-20 international system) provided the reference for all other electrodes. The EEG recordings occurred at a sampling rate of 1 kHz. The raw EEG signal was streamed wirelessly (BrainAmp Move System, Brain Products, Gilching, Germany) and it was recorded continuously for the entire duration of the experiment.

7.2.3 Virtual Y-maze and motion tracking

The virtual maze consisted of an equilateral Y-maze (3-armed maze) with three distal landmarks placed outside the maze, 20 m away from the center and visible above the walls (Figure **7.2b**). The landmarks were abstract geometric shapes (*e.g.*, square, circle, star). The wall texture and the light were homogeneous and non-informative. Each arm of the maze was 90 cm wide and 225 cm long. For the sake of analysis, the maze was discretized into 10 zones (3 evenly divided zones per arm and one for the maze center, Figure **7.2c**). These zones were not visible to the participant. Crossing between zones was recorded online without influencing the task flow.

We designed the virtual Y-maze by using the Unity3D game engine (Unity Technologies, San Francisco, California, USA, version 2017.1.1f1 for Windows), and we rendered it using an HTC Vive Pro head-mounted display (HTC Corporation, Taoyuan, Taïwan) with a 90 Hz refresh rate (2 times AMOLED 3.5" 1440x1600 pixels, 615 ppi, and 110° nominal field of view). The HTC was connected to a VR capable backpack computer (Zotac PC, Intel 7^{th} Gen Kaby Lake processor, GeForce GTX 1060 graphics, 32GB DDR4-2400 memory support, Windows 10 OS, ZOTAC Technology Limited, Fo Tan, Hong Kong) running on batteries and controlled remotely (Figure **7.2a**). An integrated HTC Lighthouse motion tracking system (four cameras, 90 Hz sampling rate, covering an 8 x 12 m area) enabled the recording of the participant's head by tracking the HTC Vive Pro head-mounted display. It also enabled the tracking of the torso movements via an additional HTC Vive Tracker placed on the participant's backpack. We virtually translated the position of this tracker to better reflect the real position of the participant's torso by considering his or her body measurements. The torso tracker was also used to trigger spatial events (*e.g.*, reaching the goal, crossing spatial section boundaries). The height of the maze walls and the altitude of landmarks were adjusted to the participant's height (based on the head tracker) to provide each participant with the same visual experience. Each participant wore earphones playing a continuous white noise to avoid auditory cues from the external world. During the disorientation periods (see protocol), relaxing music replaced the white noise. One experimenter gave instructions through the earphones, while monitoring the experiment from a control room. The participant could answer through an integrated microphone. He/she was instructed to refrain from talking while performing the experiment to limit artifacts in the recorded EEG signal. Another experimenter stayed with the participant inside the experimental room to help with potential technical issues and conduct the disorientation, avoiding any interaction

with participants during the task. The EEG signal, motion capture, and all trigger events were recorded and synchronized using the Lab Streaming Layer software (Kothe, 2014).

7.2.4 Experimental protocol

An entire experimental session lasted 3 hours on average and it included preparing the participant with the EEG and VR equipment and running the experimental protocol. The immersion time in VR was between 60 and 90 min.

7.2.4.1 Free exploration phase

Before starting the actual task, the participant explored the Y-maze for 3 min, starting at the center of the maze. He/she was instructed to inspect all details of the environment and to keep walking until the time elapsed. The purpose of this phase was to familiarize the participant to the VR system and the Y-maze environment (including the constellation of landmarks).

7.2.4.2 Navigation task

The navigation task included a learning condition and a testing condition. During learning, the participant began each trial from the *starting* arm (*e.g.*, location A in Figure **7.2b**) and he/she had to find the direct route to a hidden target at the end of the *goal* arm (*e.g.*, location C in Figure **7.2b**). Upon reaching the goal, a reward materialized in front of the participant (3D object on a small pillar representing, for instance, a treasure chest) to indicate the correct location and the end of the current trial. The learning period lasted until the participant reached the goal directly, without entering the other arm, three times in a row. Before each trial, we disoriented the participant to ensure that he/she would not rely on previous trials or the physical world to retrieve his/her position and orientation. To disorient the participant, the experimenter simply walked him/her around for a few seconds with both eyes closed (and the head-mounted display showing a black screen). The testing condition included six trials: three *control* trials and three *probe* trials, ordered pseudo-randomly (always starting with a control, but never with three control trials in a row). In the control trials, the participant started from the same arm as in the learning condition (*e.g.*, location A in Figure **7.2b**). In the probe trials, he/she started from the third arm (*e.g.*, location B in Figure **7.2b**). Before starting a new trial (either control or probe), the participant was always disoriented. Then, he/she had to navigate to the arm where he/she expected to find the goal and stop there (without receiving any reward signal). If the participant went to the incorrect arm, it was considered as an *error*. We present a single trial example of one participant performing the task and we illustrate the motion tracking in the virtual environment in Video S1 (see Appendix **D**).

7.2.4.3 Block repetitions

The sequence *learning condition + testing condition* formed an *experimental block*. Each participant performed nine experimental blocks (Figure **7.2d**). In order to foster a feeling of

novelty across block repetitions, we varied several environmental properties at the beginning of each block: wall texture (*e.g.*, brick, wood, etc.), goal location (*i.e.*, in the right or left arm, relative to the starting arm), reward type (*e.g.*, treasure chest, presents, etc.), as well as the shape (*e.g.*, circle, square, triangle, etc.) and color of landmarks. When changing the environment between blocks, we kept the maze layout and landmark locations identical. The sequence of blocks was identical for all participants, who had to take a compulsory break after the fourth block (Figure **7.2d**). In addition, after the sixth or seventh block, a break was introduced when requested by the participant.

7.2.4.4 EEG baseline recordings

Both before the free exploration period and after the 9^{th} block, the participant had to stand for 3 min with his/her eyes opened in a dark environment. This served to constitute a general baseline for brain activity. Similarly, we recorded the EEG baseline signal (in the dark for a random duration of 2-4 s) before each trial (Figure **7.2d**, bottom). Besides providing a baseline EEG activity specific to each trial, this also allowed the starting trial time (*i.e.*, the appearance time of the maze) to be randomized, thus avoiding any anticipation by the participant.

7.2.5 Behavioral analysis

All analyses were done with MATLAB (R2017a and R2019a; The MathWorks Inc., Natick, MA, USA), using custom scripts based on the EEGLAB toolbox version 14.1.0b (Delorme & Makeig, 2004), the MoBILAB (Ojeda et al., 2014) open source toolbox, and the BeMoBIL pipeline (Klug et al., 2018).

7.2.5.1 Motion capture processing

A set of MoBILAB's adapted functions enabled the preprocessing of motion capture data. The rigid body measurements from each tracker consisted of (x, y, z) triplets for the position and quaternion quadruplets for the orientation. After the application of a 6 Hz zero-lag low-pass finite impulse response filter, we computed the first time derivative for position of the torso tracker for walking speed extraction and we transformed the orientation data into axis/angle representations. An EEGLAB dataset allowed all preprocessed, synchronized data to be collected, and split into different streams (EEG, Motion Capture) to facilitate EEG-specific analysis based on motion markers.

7.2.5.2 Allocentric and egocentric groups

Probe trials served to distinguish between allocentric and egocentric responses by making the participants start from a different arm than the one used in the learning period. We assigned a participant to the *allocentric group* if he/she reached the goal location in the majority of probe trials (*i.e.*, presumably, by using the landmark array to self-localize and plan his/her trajectory). Conversely, we assigned a participant to the *egocentric group* when he/she reached the error arm in the majority of probe trials (*i.e.*, by merely repeating the

right- or left-turn as memorized during the learning period).

7.2.5.3 Time to goal

We assessed the efficacy of the navigation behavior by measuring the 'time to goal', defined as the time required for the participant to finish a trial (equivalent to the 'escape latency' in a Morris Water Maze). In learning trials, it corresponded to the time to reach the goal zone and trigger the reward. In test trials, it corresponded to the time to reach the believed goal location in the chosen arm (*i.e.*, entering the G1 or E1 zone in Figure **7.2c**).

7.2.5.4 Horizontal head rotations (relative heading)

The participant's heading was taken as the angle formed by his/her head orientation in the horizontal plane with respect to its torso orientation, aligned with the participant's sagittal plane. After extracting the head and torso forward vectors from each tracker, computing the signed angle between those vectors' projections in the horizontal plane provided the heading value.

7.2.5.5 Walking speed

The forward velocity component of the torso tracker provided the participant's walking information. For each trial, we computed the mean and SD of the forward velocity, and their average for each participant. To evaluate movement onsets and offsets, we compared motion data recorded during the trials against those recorded during the short baseline period before each trial, considered as a reliable resting state for movements. Movement transitions (onsets and offsets) were based on a participant-specific threshold, equal to the resting-state mean plus 3 times the resting-state SD. The excluded movement periods were those lasting less than 250 ms and during which motion did not reach another participant-specific threshold, equal to the resting-state mean plus 5 times the resting-state SD.

7.2.5.6 Landmark visibility

For analysis purposes, we named the three landmarks as Landmark 1, Landmark 2, and Landmark 3 (Figure **7.2c**) and we tracked their visibility within the displayed scene. The participant had a horizontal field of view of 110° and a vertical field of view of 60°. Whenever a landmark appeared in the viewing frustum[1] (*i.e.*, in the region of virtual space displayed on the screen) and it was not occluded by any wall, it was considered as visible by the participant. Given the restrained horizontal field of view and the configuration of the VR environment, perceiving more than one landmark at the same time was unlikely.

7.2.5.7 Zone-based behavioral analysis

The maze discretization (Figure **7.2c**) provided a coherent basis for analyses across trials and participants. To ensure consistency in the comparison between trials, we selected those trials

[1] In 3D virtual reality and computer graphics, the viewing frustum is defined as the region of virtual space displayed on the screen, and it is a coarse imitation of the 'cone of vision' in natural viewing. It takes the form of a truncated rectangular pyramid, defined by the horizontal and vertical field of view and by near and far bounds.

where the participant followed a straightforward pattern (zone-crossing sequence: S1 → S2 → S3 → C → G3 → G2 → G1). We thus discarded all trials in which the participant went backward while navigating (*e.g.*, during learning, when his/her first choice was toward the error arm, and he/she had to come back to the center in order to go toward the goal arm). To further ensure homogeneity, we also excluded those trials in which the time to goal was unusually long (*i.e.*, by computing the outliers of the time to goal distribution across all participants). These selection criteria kept 1289 (of a total of 1394) trials for analysis (see Supplementary Table **D.1** for details about the distribution of trials across participants). Finally, we computed offline an additional event corresponding to the first walking onset of the participant in S1 (see *Walking speed* paragraph above for movement detection) which was inserted in the delimiting sequence of zone-crossing events. For the sake of simplicity, we used the notations 'staticS1' for the period preceding this event, and 'mobileS1' for the one that follows, before the participant enters S2. Hence, the complete sequence for each trial was, *e.g.*, staticS1 → mobileS1 → S2 → S3 → C → G3 → G2 → G1.

7.2.5.8 Motion capture statistics

The above zone-based discretization framed the analysis of the motion capture metrics mentioned above: walking speed, standard deviation of horizontal head rotations, and landmark visibility. For each trial, we first averaged the value of each motion variable over the period between two events of the zone sequence. Then, for each participant, we averaged these values across trials of the same condition.

To better characterize the participants' behavior in the maze, we investigated how these metrics would depend on the condition, the spatial zone, the landmark (for landmark visibility only), and the different combinations of those factors. Concerning walking speed and standard deviation of horizontal head rotations, we tested the hypothesis that participants would walk slower and make larger head movements in specific zones of the maze related to the challenge posed by the experimental condition (*e.g.*, taking information in S1 during Learning and stopping in C to look at the constellation during Probe). Concerning landmark visibility, we tested the hypothesis that participants would make a differential use of the three landmarks (*i.e.*, preference for one or two) and that attendance to a landmark would depend on the condition and the location of the participant in the maze (*e.g.*, realignment with a preferred landmark at the center specific to Probe condition). We used fixed model between factors analyses of variance (ANOVAs; balanced design) to assess differences and interactions between conditions, zones, and landmarks in those dependent variables. Specifically, for the landmark visibility, we used a three-way ANOVA with the factors: *condition* (Learning, Control, Probe), *landmark* (Landmark 1, Landmark 2, Landmark 3), and *zone* (*e.g.*, staticS1, mobileS1, S2, S3, Center, F3, F2). Note that 'F', standing here for *finish* arm, can be either 'G' for *goal* or 'E' for *error* as used in Figure **7.2c**, depending on the trial outcome. For the walking speed and the standard deviation of horizontal head rotations, we used a two-way ANOVA with the factors *condition* and *zone*. The alpha level for significance was set at 0.01 (more conservative level taking into account that we are computing three simultaneous ANOVAs on the same dataset). When a significant main effect or interac-

tion was found, we used pairwise *t*-tests (with Tukey's honest significant difference criterion method for multiple comparison correction) to unravel individual differences between factor or interaction terms.

7.2.6 EEG data analysis overview

Figure **7.3** shows the outline of the data preprocessing and analysis steps.

7.2.7 Individual EEG analysis

7.2.7.1 Processing

We used the BeMoBIL pipeline to preprocess and clean the EEG data (Klug et al., 2018). This pipeline is fully automated and designed to improve SNR in large-scale mobile EEG datasets, which ensures full replicability of the procedure. We first downsampled the data to 250 Hz, applied a 1 Hz high-pass filter to suppress slow drifts in EEG data (zero-phase Hamming windowed finite impulse response filter with 0.5 Hz cut-off frequency and 1 Hz transition bandwidth), and removed spectral peaks at 50 Hz and 90 Hz, corresponding to power line frequency and VIVE headset refreshing rate, respectively (implemented by the `cleanLineNoise` function from the PREP pipeline, Bigdely-Shamlo et al. 2015). We identified noisy channels with automated rejection functions, setting parameters numerical values according to default recommendations from Bigdely-Shamlo et al. (2015). We then reconstructed the removed channels by spherical interpolation of neighboring channels and applied re-referencing to the common average. In a subsequent time-domain cleaning, we detected and removed segments with noisy data. We present more details on the implementation of the cleaning steps in Supplementary Methods **D.2**.

On the cleaned dataset, we performed an independent component analysis (ICA) using an adaptative mixture independent component analysis (AMICA) algorithm (Palmer et al., 2008), preceded by a principal component analysis (PCA) reduction to the remaining rank of the dataset taking into account the number of channels interpolated and the re-referencing to the common average. For each independent component (IC), we computed an equivalent current dipole (ECD) model with the DIPFIT plugin for EEGLAB (version 3.0) (Oostenveld & Oostendorp, 2002). For this purpose, we used a common electrode location file obtained from the average of previous measures on participants wearing the same cap. We co-registered this file with a boundary element head model based on the MNI brain (Montreal Neurological Institute, MNI, Montreal, QC, Canada) to estimate dipole location. In this article, the spatial origin of an IC is approximated with the location of its associated dipole.

We opted for the BeMoBIL pipeline after comparing it against the APP pipeline (J. R. da Cruz et al., 2018), which proved to be less robust for our dataset. We based this conclusion on different metrics, by evaluating each artifactual detection step (number of channels removed, proportion of time samples excluded) and by assessing the performance of the subsequent ICA (mutual information reduction and remaining pairwise mutual information, Delorme et

al. 2012). In particular, the BeMoBIL pipeline proved to be more stable and conservative than the APP pipeline (rejecting more artifactual channels and noisy temporal segments, both more consistently across participants). We detail the comparison and its results in Supplementary Methods **D.3** and Supplementary Figure **D.4**, respectively.

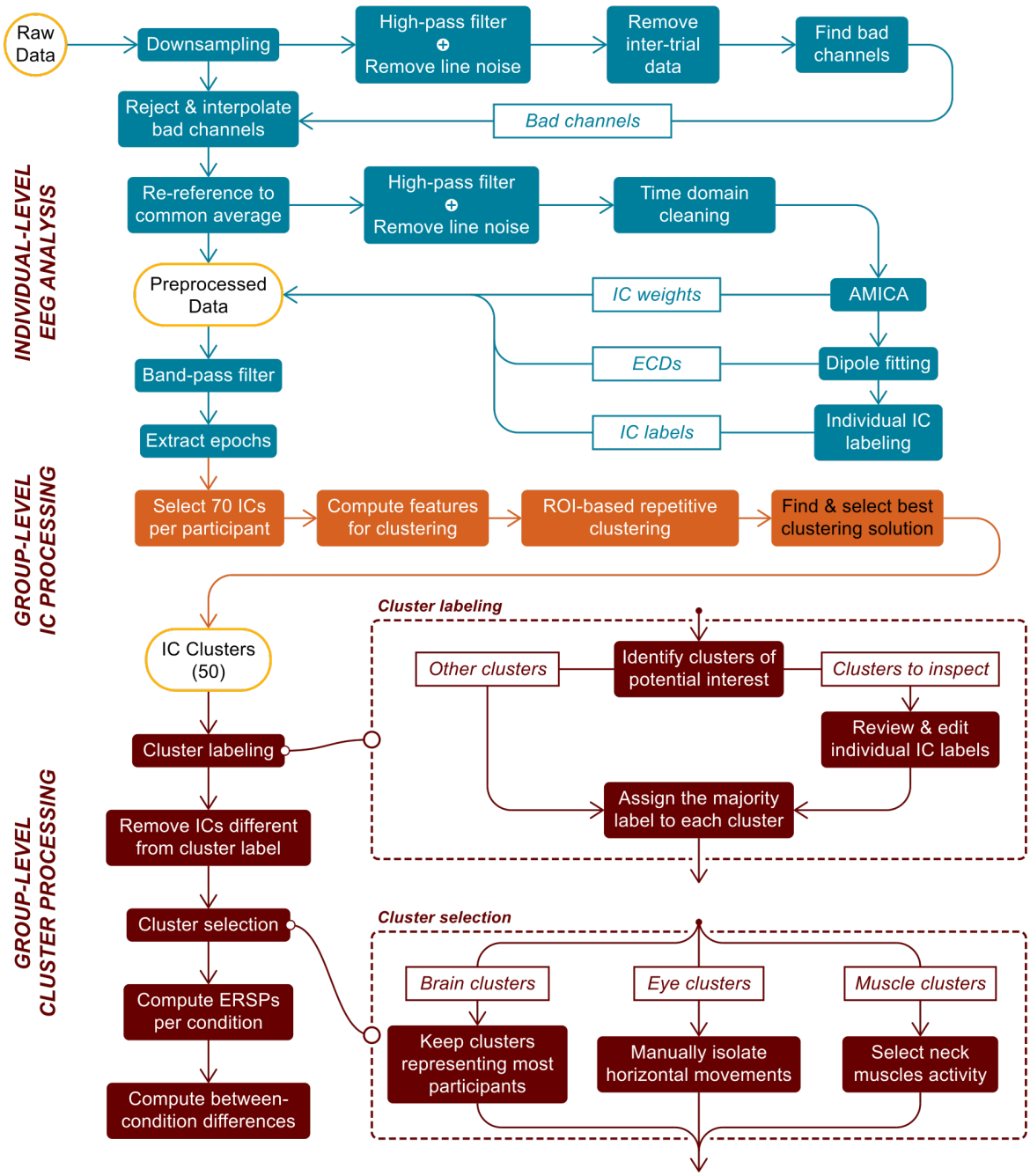

Figure 7.3: Flowchart of the EEG processing pipeline. We first preprocessed EEG data at the individual level (in blue) and, in particular, decomposed the channel data into independent components (ICs) with an adaptative mixture ICA (AMICA) algorithm. We then selected 70 ICs per participant for the clustering procedure (in orange). Finally, we labeled and selected the clusters of interest for an ERSP analysis per condition (in brown). The 'Cluster selection' process is described in the 'EEG cluster analysis' section of the Results.

7.2.7.2 Individual IC labeling

We used the ICLabel algorithm (version 1.1, Pion-Tonachini et al. 2019) with the `default` option to give an automatic class prediction for each IC. The model supporting this algorithm considers seven classes: (1) Brain, (2) Muscle, (3) Eye, (4) Heart, (5) Line Noise, (6) Channel Noise, and (7) Other. The prediction takes the form of a compositional label: a percentage vector expressing the likelihood of the IC to belong to each of the considered classes. Then, it compares each percentage to a class-specific threshold to form the IC label. We used the threshold vector reported by Pion-Tonachini et al. (2019) for optimizing the testing accuracy. Considering the recentness of this algorithm and the fact it has never been validated on mobile EEG data, we refined the labeling process to increase its conservativeness on Brain ICs. After the initial categorization by the algorithm, we automatically examined the ECD of ICs passing the Brain threshold and we rejected all ICs whose ECD was either located outside brain volume or exhibiting residual variance over 15% (commonly accepted threshold for dipolarity, see Delorme et al. 2012) and we put them in the 'Other' class. Residual variance quantifies the quality of the fit between the actual topographic activation map and the estimated dipole projection on the scalp. Among the remaining ones, we distinguished two cases: (1) if the IC label was uniquely 'Brain', we automatically accepted it; (2) if the IC label was hybrid (multiple classes above threshold), we manually inspected the IC properties to assign the label ourselves according to the ICLabel guidelines (`https://labeling.ucsd.edu/tutorial/labels` - an example can be found in Supplementary Figure **D.3**). To all ICs below brain threshold, we assigned unique labels based on their highest percentage class.

7.2.8 Group-level EEG analysis

In order to retain maximal information for further processing, for each participant we copied the ICA results (decomposition weights, dipole locations, and labels) back to the continuous version of the dataset (*i.e.*, the dataset before time domain cleaning in the BeMoBIL pipeline). We first band-pass filtered the data between 1 Hz (zero-phase Hamming windowed finite impulse response high-pass filter with 0.5 Hz cut-off frequency and 1 Hz transition bandwidth) and 40 Hz (zero-phase Hamming windowed finite impulse response low-pass filter with 45 Hz cut-off frequency and 10 Hz transition bandwidth). We then epoched each dataset into trials, starting at the beginning of the baseline period and ending at the time of trial completion. For each IC and each trial, we computed the trial spectrum using the *pwelch* method (1s Hamming windows with 50% overlap for power spectral density estimation). We baselined the spectrum with the average IC spectrum over all baseline periods using a gain model.

We additionally computed single-trial spectrograms using the `newtimef` function of EEGLAB (1 to 40 Hz in linear scale, using a wavelet transformation with three cycles for the lowest frequency and a linear increase with frequency of 0.5 cycles). Using a gain model, we individually normalized each trial with its average over time (Grandchamp & Delorme, 2011). Separately for each participant, we calculated a common baseline from the average

of trial baseline periods (condition specific) and we subsequently corrected each trial with the baseline corresponding to its experimental condition (gain model). At the end, power data were log-transformed and expressed in decibels. To enable trial comparability, these event-related spectral perturbations (ERSPs) were time-warped based on the same sequence of events as for the zone-based analysis.

7.2.8.1 Component clustering

To allow for a group-level comparison of EEG data at the source level (ICs), we selected the 70 first ICs outputted by the AMICA algorithm, which corresponded to the ICs explaining most of the variance in the dataset (Gramann et al., 2018). This ensured the conservation of $90.6 \pm 1.8\%$ (mean $\pm$ SEM) of the total variance in the dataset while greatly reducing computational cost and mainly excluding ICs with uncategorizable patterns. We conducted this selection independently of the class label for each IC. We applied the repetitive clustering region of interest (ROI) driven approach described in Gramann et al. (2018). We tested multiple sets of parameters to opt for the most robust approach and we present here the selected one (the detailed procedure for this comparison can be found in Supplementary Methods **D.4** and its results in Supplementary Table **D.3**). We represented each IC with a 10-dimensional feature vector based on the scalp topography (weight = 1), mean log spectrum (weight = 1), grand average ERSP (weight = 3), and ECD location (weight = 6). We compressed the IC measures to the 10 most distinctive features using PCA. We repeated the clustering 10000 times to ensure replicability. According to the results from parameters comparison (see Supplementary Methods **D.4**), we set the total number of clusters to 50 and the threshold for outlier detection to 3 SD in the k-means algorithm. This number of clusters was chosen inferior to the number of ICs per participant to favor the analysis of clusters potentially regrouping ICs from a larger share of participants and therefore more representative of our population. We defined $[0, -55, 15]$ as the coordinates for our ROI, a position in the anatomical region corresponding to the retrosplenial cortex (BA29/BA30). We set the first coordinate (x) to 0 because we did not have any expectation for lateralization. Coordinates are expressed in MNI format. We scored the clustering solutions following the procedure described in Gramann et al. (2018). For each of the 10000 clustering solutions, we first identified the cluster whose centroid was closest to the target ROI. Then, we inspected it using six metrics representative of the important properties this cluster should fulfill (see Supplementary Table **D.3** detailing the comparison procedure results). In order to combine these metrics into a single score using a weighted sum (same weights used to choose the best of the 10000 solutions), we linearly scaled each metric value between 0 and 1. We eventually ranked the clustering solutions according to their score and selected the highest rank solution for the subsequent data analysis.

7.2.8.2 Cluster labeling

We then inspected the 50 clusters given by the selected clustering solution. We first used the individual IC class labels to compute the proportion of each class in the clusters. As the clustering algorithm was blind to the individual class labels, most clusters contained

ICs with heterogeneous labels. Bearing in mind that the ICLabel algorithm has not been validated on mobile EEG data yet, we suspected that the observed heterogeneity could, to a certain extent, owe to individual labeling mistakes. We therefore performed a manual check (identical to the hybrid case in the *Individual IC labeling* section above) of individual IC labels in specific clusters exhibiting a potential interest for the analysis. These clusters were those with at least 20% of Brain label, those with at least 50% of Eye label, and those located in the neck region with at least 50% of Muscle label. Indeed, both eye and muscle activity are inherent to the nature of the mobile EEG recordings and their analysis can inform us on participants' behavior (Gramann et al., 2014), similarly to horizontal head rotations and landmark visibility variables, with a finer temporal resolution. We finally labeled every cluster from their most represented class after correction, only when this proportion was above 50%. Eventually, within each of the labeled clusters, we removed the ICs whose label did not coincide with the cluster label.

7.2.8.3 Clusters analysis

We computed single-trial ERSPs as for the clustering procedure. To get the cluster-level ERSP, we took the arithmetic mean of the power data first at the IC level (including the baseline correction), then at the participant level, and finally at the behavioral group level. At the end of these operations, we log-transformed the power data to present results in decibels. We performed statistical analysis comparing ERSP activity between trial type (learning, control, probe), using a non-parametric paired permutation test based on maximum cluster-level statistic (Maris & Oostenveld, 2007) with 1000 permutations. For each permutation, we computed the F-value for each 'pixel' (representing spectral power at a given time-frequency pair) with a 1×3 ANOVA. As the ANOVA test is parametric, we used log-transformed data for statistical analysis as ERSP sample distribution has a better accordance with Gaussian distribution in that space (Grandchamp & Delorme, 2011). We selected samples with F-value above 95^{th} quantile of the cumulative F-distribution and clustered them by neighborhood. The cluster-level F-value was the cumulative F-value of all samples in the cluster. We then formed the distribution of observed maximum clustered F-values across permutations to compute the Monte Carlo p-value for the original repartition. As a *post hoc* test, we repeated the same analysis for each pair of conditions, with t-values instead of F-values and two-tailed t-test instead of ANOVA. We finally plotted ERSP differences only showing samples significant for both the three conditions permutation test and the inspected pairwise permutation test. The significance level was $p < 0.05$ for all tests in this case.

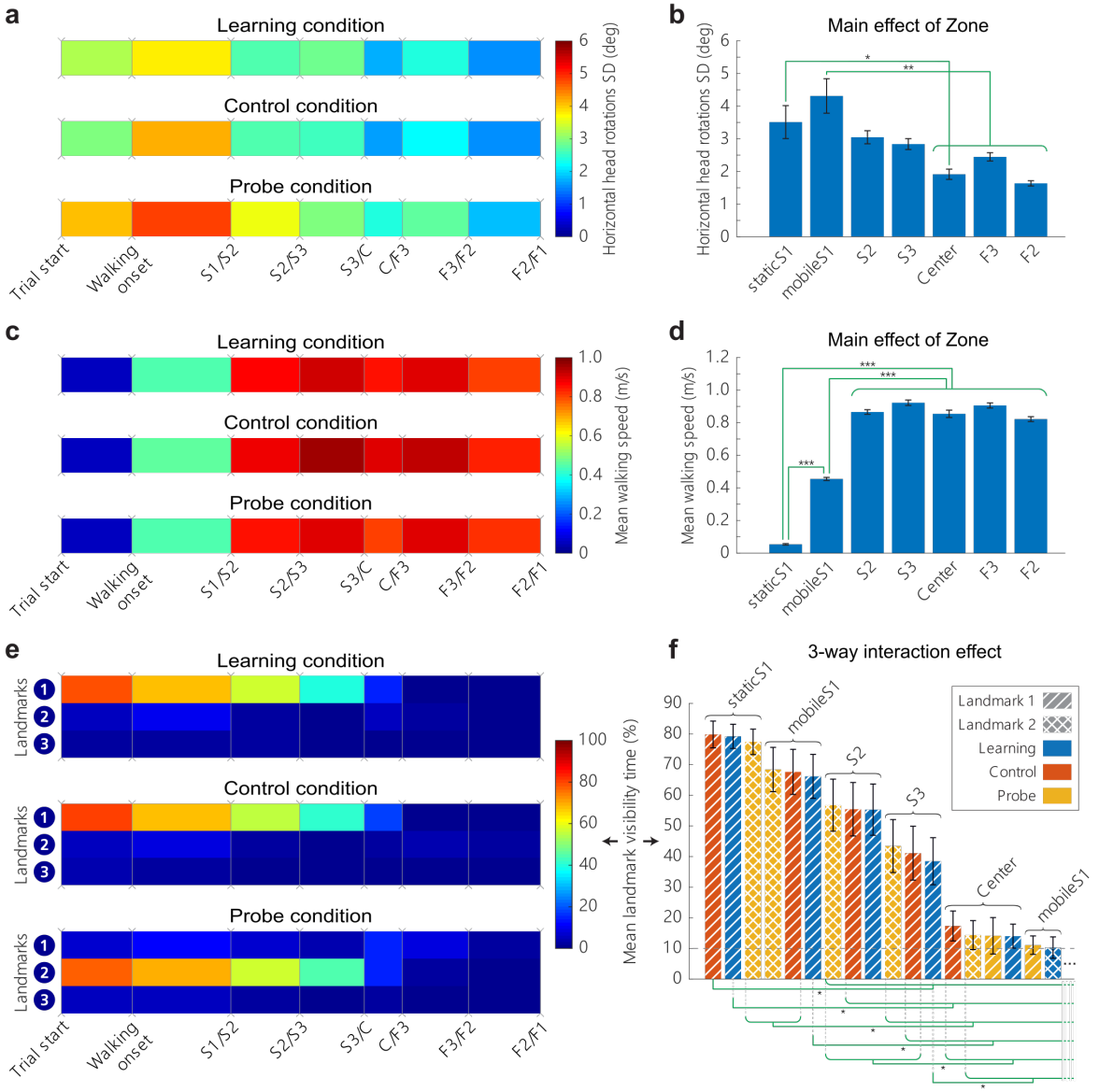

Figure 7.4: Behavioral metrics - Walking speed, horizontal head rotations variability, and landmark visibility for the allocentric group. (**a**) Average standard deviation of horizontal head rotations, computed from the difference between head and torso orientation. (**b**) Main effect of Zone on horizontal head rotations variability $F(6;273) = 8.99$, $p < 0.00001$. (**c**) Average instantaneous walking speed. (**d**) Main effect of Zone on walking speed $F(6;273) = 472.15$, $p < 0.00001$. (**e**) Average landmark visibility. The color code corresponds to the percentage of time each landmark was visible at the screen. (**f**) Three-way interaction effect of Zone, Condition, and Landmark on landmark visibility. Each bar shows average landmark visibility (sorted in descending order) for a specific combination of zone (labeled), condition (color), and landmark (texture). We present only combinations associated with at least 10% landmark visibility (17 combinations out of 63). (**a**, **c**, **e**) We divided each trial according to the same sequence of events: walking onset, followed by the first passage in the starting arm (S) then in the finish arm (F), being either the *goal* or the *error* arm. Events are horizontally spaced according to the median duration between each event. All three plots represent data in the learning, control, and probe conditions, averaged between separating events across all trials and blocks for all 14 allocentric participants. (**b**, **d**, **f**) Mean value with standard error of the mean (black bars). We present the summary of the significant differences (green braces) found in post-hoc analysis (computed on a pairwise basis, then grouped when similar). For figure (**f**), we found no pairwise significant differences within the group of combinations not shown (below 10%). $^{***}p < 0.0001$, $^{**}p < 0.001$, $^{*}p < 0.01$

7.3 Results

7.3.1 Behavioral results

7.3.1.1 Goal-oriented navigation performance

During control trials, all participants successfully solved the Y-maze task by consistently choosing the goal arm (Supplementary Figure **D.1a**, left). During the probe trials, 14 participants navigated to the correct goal arm (*i.e.*, allocentric response), whereas 2 participants went to the error arm (*i.e.*, egocentric response; **D.1a**, right).

In terms of time to goal, all participants learned rapidly to locate and navigate to the goal position: after the first learning trial, in which goal finding was merely random, the mean time to goal of the allocentric group plateaued at around 6 s (Supplementary Figure **D.1b**, left). During control trials, the mean time to goal of allocentric participants remained constant and identical to the plateau reached at the end of the learning condition (Supplementary Figure **D.1b**, middle). In the probe trials, the mean time to goal of the allocentric group increased slightly by ~ 1 s as compared to the control condition (Supplementary Figure **D.1b**, right). Overall, the interindividual variability remained very low, reflecting the simplicity of the navigation task.

7.3.1.2 Spatial behavior across conditions and maze zones

We sought to characterize the exploratory behavior as a function of the protocol conditions (Condition factor) as well as of the zones in the Y-maze (Zone factor, see Figure **7.2c**). Hereafter, only the analyses on the allocentric group are presented as only two participants adopted an egocentric behavior (expectedly, Bécu et al. 2020b; see Supplementary Figure **D.2** for the individual behavior of egocentric participants).

7.3.1.2.1 Horizontal head rotations

First, we assessed the searching behavior by quantifying the horizontal head rotations variability (Figure **7.4a,b**). We did not observe any effect of Condition ($F(2;273) = 2.69$, $p = 0.069$), whereas we found a significant effect of the Zone on horizontal head rotations variability ($F(6;273) = 8.99$, $p < 0.00001$). Post-hoc analysis indicated that horizontal head rotations variability was higher at the beginning of the trajectory in comparison to the center of the maze (staticS1 versus C, $t(2) = 3.67$, $p < 0.01$; mobileS1 versus C, $t(2) = 5.5$, $p < 0.00001$). There was no interaction between Condition and Zone for this metric ($F(12;273) = 0.13, p = 0.99$).

7.3.1.2.2 Walking speed

Second, we analyzed the walking speed across different conditions and zones (Figure **7.4c,d**). We found a significant main effect of Zone ($F(6;273) = 472.15$, $p < 0.00001$). Post-hoc analysis revealed that the participants spent more time, and exhibited a slower walking speed at the beginning of the starting arm (*i.e.*, in zone S1, both before and after walking onset, $t(2) < -15$, $p < 0.00001$, for all pairwise comparisons involving either staticS1 or

mobileS1). We observed a tendential, but not significant, main effect of Condition on the walking speed ($F(2;273) = 3.91$, $p = 0.021$, which did not survive the multiple comparisons correction). There was no interaction effect between Condition and Zone ($F(12;273) = 0.45$, $p = 0.94$).

7.3.1.2.3 Landmark visibility

Third, we tested the visibility of the landmarks depending on the condition, zone, and landmark (Figure **7.4e**) and we observed a three-way interaction between all factors ($F(24;819) = 25.31$, $p < 0.00001$). Post-hoc analysis (Figure **7.4f**) revealed a clear tendency for landmarks being visible in the starting arm of the maze (as opposed to the center zone and the finish arm), modulated by the condition and the landmark attended. Figure **7.4f** shows the landmark visibility of [Condition; Zone; Landmark] combinations in descending order, and we can notice steps of combination triplets with the same Zone factor (from staticS1 to C only), in the order in which they are visited by the participants. The consistent pattern in each triplet shows a preferred landmark for each condition: Landmark 1 for learning and control trials, and Landmark 2 for probe trials. A slight deviation from the dominant pattern is that the mean visibility of Landmarks 1 & 2 in Center zone during probe trials is found at the same level (Figure **7.4f**), although not statistically different from the visibility of any landmark in any condition in the same zone. All additional statistical results (main effects, two-way interactions) are presented in Supplementary Table **D.2**.

7.3.2 EEG cluster analysis

7.3.2.1 Independent component selection

To give an overview of the IC inspection and selection process, we provide IC and cluster counts at different steps of our procedure (see Figure **7.3**). In total, we extracted 1943 ICs of the whole dataset (16 participants). First, at the individual IC labeling step, we relabeled 204 of 394 ICs initially labeled as 'Brain' (*i.e.*, automatic rejection based on RV threshold and manual inspection of hybrid cases). Starting from 1120 input ICs, the clustering algorithm placed 1047 ICs in valid clusters (73 outliers). Then, to complete the cluster labeling step, we selected 35 'clusters of interest' out of the 50 output clusters. We reviewed 755 ICs and edited the label in 207 of them. Eventually, we removed a total of 414 ICs in disagreement with their cluster label, leaving 40 $\pm$ 2 ICs per participant (mean $\pm$ SEM) for the final analysis (all clusters included).

7.3.2.2 Cluster description

Of the 50 clusters, we obtained: 2 Eye, 24 Muscle, 12 Brain, 1 Heart, 1 Channel Noise, 0 Line Noise, and 4 Other clusters. The last 6 clusters did not contain a class represented by at least 50% of the ICs.

7.3.2.2.1 Eye clusters

The two eye clusters contained a mixture of components linked to horizontal and sometimes vertical eye movements. We manually separated these two categories, easily identifiable at the IC level, and we focused on the largest 'Horizontal Eye' cluster (Figure **7.5a**). In all

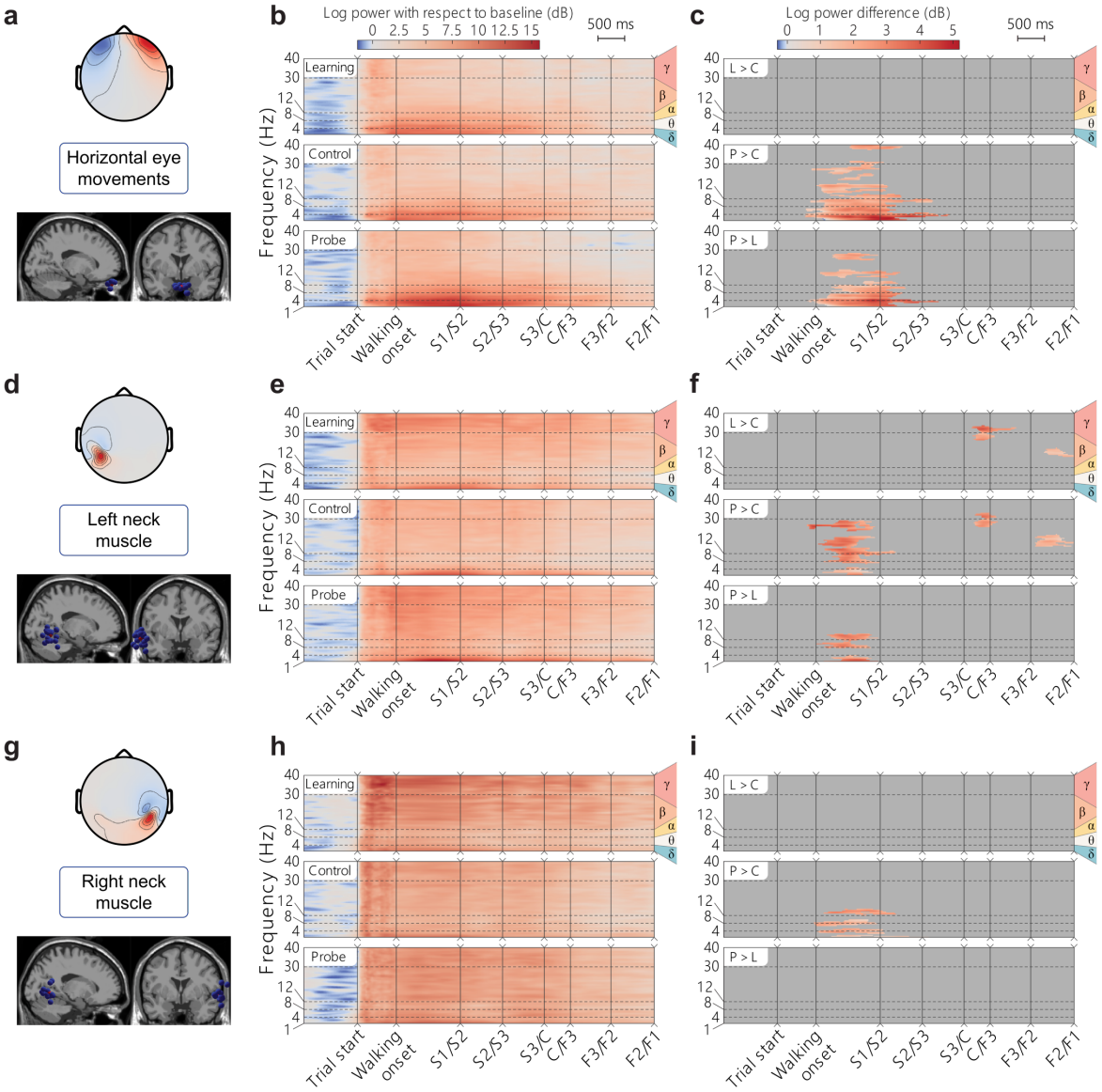

Figure 7.5: Horizontal eye movements and neck muscle clusters for the allocentric group. (**a**, **d**, **g**) Topographical map of the average cluster components' projection at the scalp level and sagittal view of all ICs in the cluster (blue spheres) with the position of the centroid (red sphere). (**b**, **e**, **h**) ERSP average per condition. We first averaged the data at the participant level, then at the group level. (**c**, **f**, **i**) ERSP pairwise differences between conditions. Plotted values represent the average of participant-wise ERSP difference between the two conditions compared. We masked differences not satisfying the statistical threshold in the permutation test (*i.e.*, $p > 0.05$). For all the ERSP plots, the Y axis displays the delta, theta, alpha, beta, and gamma frequency bands and the X axis represents the time-warped sequence of main events in the trial. We horizontally spaced the events according to the median duration between them. 'L > C': difference between Learning and Control, 'P > C': difference between Probe and Control, and 'P > L': difference between Probe and Learning. (**a**-**c**) Horizontal eye movements cluster. (**d**-**f**) Left neck muscle cluster. (**g**-**i**) Right neck muscle cluster.

conditions, the ERSPs showed a significant increase in horizontal eye movements relative to baseline recordings, during which eyes were supposedly at rest (Figure **7.5b**). The power increase was particularly pronounced before reaching the Center zone, especially in the lower frequencies (1-5 Hz). The significant differences between conditions reflected the increased eye-exploration behavior in the probe condition, mostly before leaving the starting zone S1 (Figure **7.5c**).

7.3.2.2.2 Neck muscle clusters

We identified the neck muscle clusters (out of 24) most likely to reflect sternocleidomastoid activity based on their topographic activation map and associated dipole location. Two neck

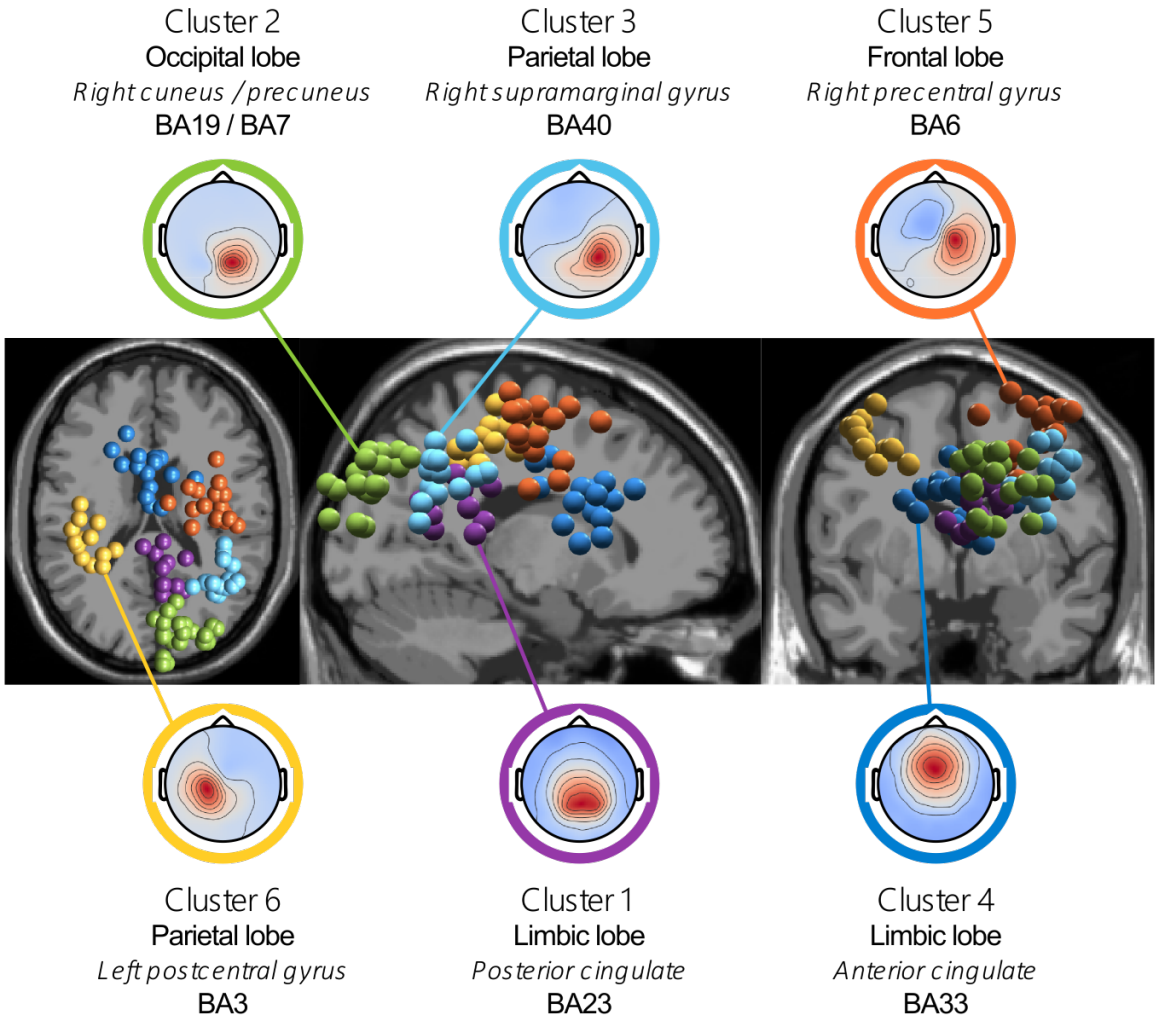

Figure 7.6: Brain cluster 3D localization and mean channel activation maps. Spatial location of brain clusters retained for analysis (from left to right: transverse view, sagittal view, and coronal view). Each IC is represented by a sphere located at its corresponding dipole location. For each cluster, we plotted all ICs, irrespective of their associated participant's behavioral group. We used MRI scans from the standard MNI brain for representation. Topographies show the mean channel activation map associated with each cluster. The centroids of the clusters are located in or near the posterior cingulate (Cluster 1 - 12 ICs, 12 participants), the right cuneus (Cluster 2 - 22 ICs, 12 participants), the right supramarginal gyrus (Cluster 3 - 15 ICs, 11 participants), the anterior cingulate (Cluster 4 - 15 ICs, 12 participants), the right precentral gyrus (Cluster 5 - 17 ICs, 13 participants), and the left postcentral gyrus (Cluster 6 - 13 ICs, 11 participants). Detailed information on the location of the cluster centroids is provided in Supplementary Table **D.4**.

muscle clusters (one on each side) were selected (Figure **7.5d,g**). The ERSPs of both clusters revealed an increased activity of the muscles with respect to the baseline period, across all frequency bands (Figure **7.5e,h**). The muscle activity in both clusters (high beta and gamma band >20 Hz; Pion-Tonachini et al. 2019) was the greatest after maze appearance and it faded out as the participants walked through the maze. For the left-side cluster, power in mobileS1 was significantly greater in the probe condition than in the other conditions (Figure **7.5f**), like for the Eye cluster. We also found a significantly increased muscle activity in the learning and probe conditions as compared to control at the center of the maze and just before the end of the task (Figure **7.5f**). For the right-side cluster, the learning condition seemed to be associated with higher and more sustained activity, but the difference with other conditions was not significant in high frequencies (Figure **7.5h,i**).

7.3.2.2.3 Brain clusters

Concerning the brain clusters, we kept only those containing ICs coming from at least 9 of the 14 allocentric participants ($\sim 65\%$), to ensure that they were representative enough of our sample population (detailed information about the 12 brain clusters is reported in Supplementary Table **D.4**). This sorting left 6 clusters for analysis. Using the Talairach client (Lancaster et al., 2000), we computed the closest gray matter region to each brain cluster centroid. As shown in Figure **7.6**, the 6 selected clusters of interest were located in or near BA23 in the posterior cingulate (Cluster 1: $[8,-47,25]$), BA19 in the right cuneus overlapping with BA7 in the right precuneus (Cluster 2: $[15,-82,35]$), BA40 in the right supramarginal gyrus (Cluster 3: $[39,-51,33]$), BA33 in the anterior cingulate (Cluster 4: $[-2,9,22]$), BA6 in the right precentral gyrus (Cluster 5: $[33,-9,52]$), and BA3 in the left postcentral gyrus (Cluster 6: $[-37,-28,49]$). These coordinates ($[x,y,z]$) are in Talairach units.

7.3.2.3 Brain cluster activity

The analyses of the 6 selected brain clusters are presented in Figures **7.7** and **7.8** (clusters 1-3 and 4-6, respectively).

7.3.2.3.1 Alpha band activity (8-12 Hz)

The average ERSP analysis for posterior parieto-occipital clusters (1-3) showed a marked alpha (8-12 Hz) desynchronization (power suppression of 3 dB or more) starting after trial onset in all conditions (Figure **7.7b,e,h**). This power suppression slowly faded away or narrowed down around 9 Hz when the participant left the first section of the maze. The desynchronization was less marked in the precentral and the postcentral gyri, but it was sustained throughout the trial, except for the control condition (significant difference found for the precentral gyrus near the central zone of the maze, see Figure **7.8f**). In the anterior cingulate, we intermittently observed a similar but reduced alpha power suppression (difference of 1 dB with respect to baseline, Figure **7.8b**).

7.3.2.3.2 Gamma band activity (>30 Hz)

We found that gamma (>30 Hz) synchronization was strongly enhanced in this navigation task, with clusters 1-4 (posterior and anterior cingulate, cuneus, and supramarginal gyrus) presenting amplitudes greater than baseline in this frequency band, consistently throughout the maze (Figures **7.7** and **7.8**). Nonetheless, a power increase in this frequency band was found between trial start and the center, especially in the probe condition (significant differences found in the mobileS1 zone for cuneus, supramarginal gyrus, and anterior cingulate

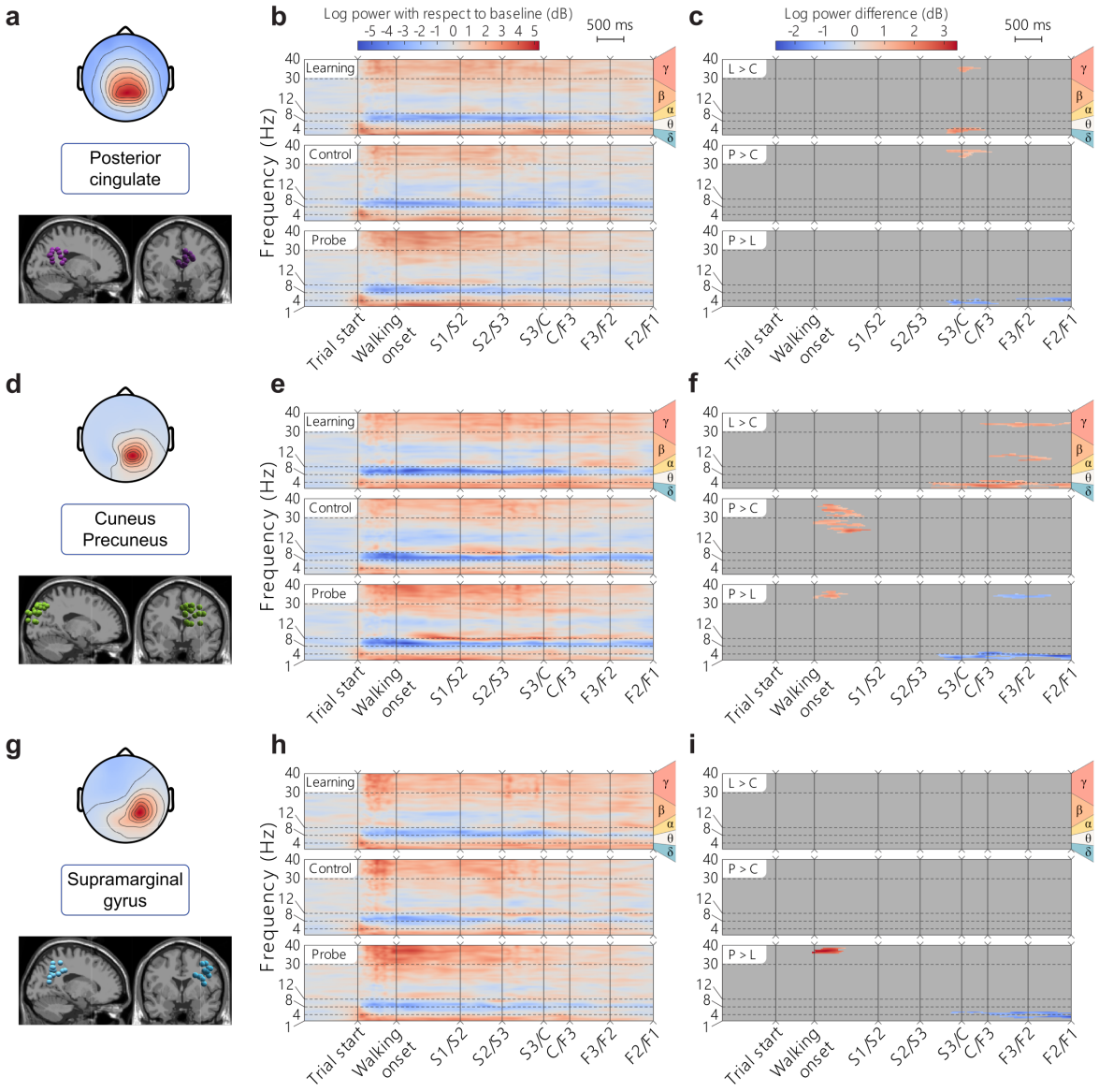

Figure 7.7: Detailed analysis of brain clusters 1-3 for the allocentric group. (**a**, **d**, **g**) Topographical map of the average cluster components' projection at the scalp level (top) and sagittal/frontal views of all ICs in the cluster (bottom). (**b**, **e**, **h**) ERSP average per condition. (**c**, **f**, **i**) ERSP pairwise differences between conditions. 'L > C': difference between Learning and Control, 'P > C': difference between Probe and Control, 'P > L': difference between Probe and Learning. (**a**-**c**) Cluster 1 - Posterior Cingulate. In the allocentric group, this cluster contains 10 ICs from 10 different participants. (**d**-**f**) Cluster 2 - Right Cuneus/Precuneus. In the allocentric group, this cluster contains 21 ICs from 11 different participants. (g-i) Cluster 3 - Right Supramarginal Gyrus. In the allocentric group, this cluster contains 13 ICs from 9 different participants

clusters). A comparison between conditions also demonstrated a reduced gamma activity upon reaching the center in the control condition in the posterior cingulate and an increased gamma power in the learning condition in the cuneus in the finish arm.

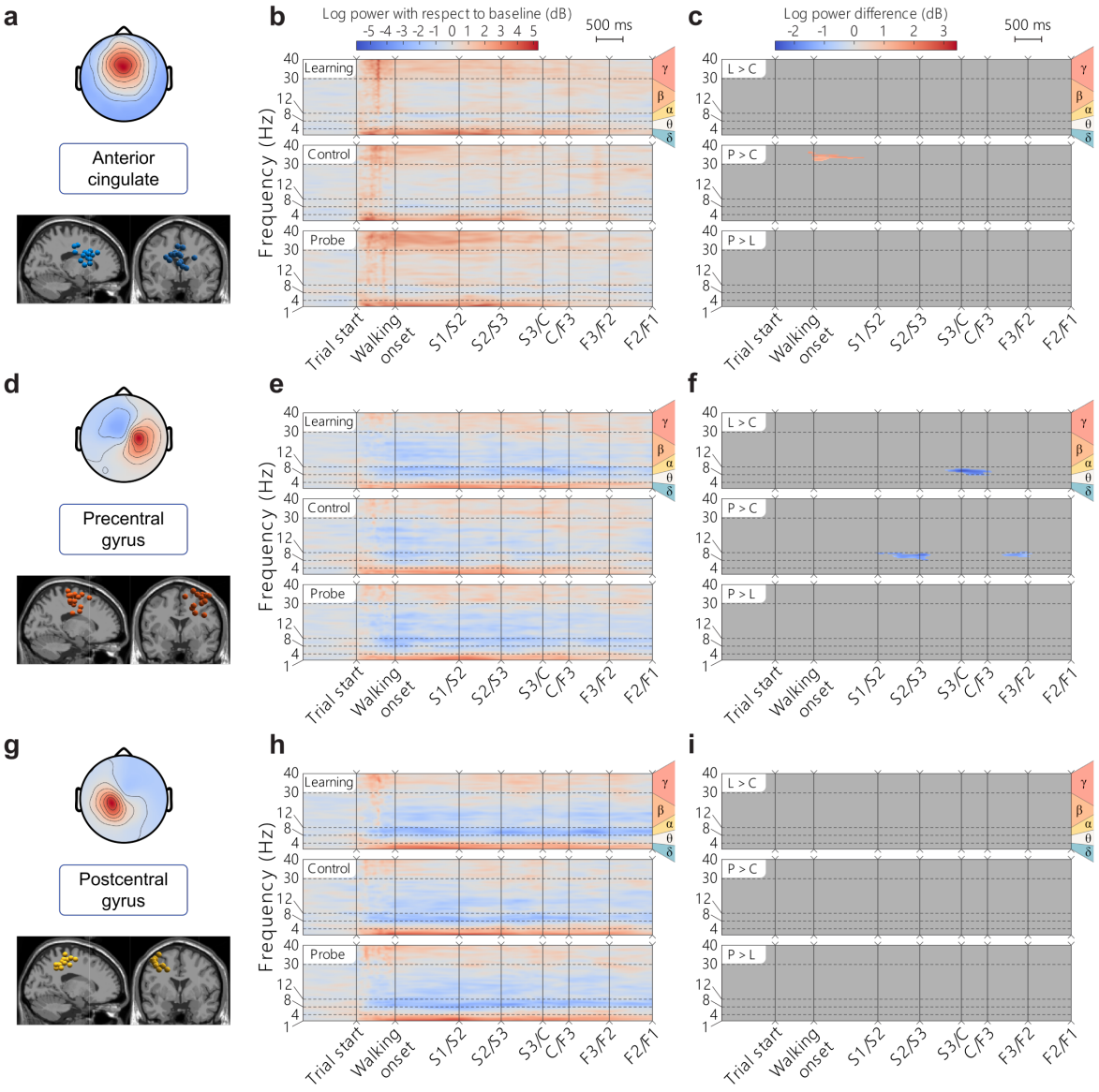

Figure 7.8: Detailed analysis of brain clusters 4-6 for the allocentric group. The layout is the same as in Figure **7.7a,d,g** Topographical map of the average cluster components' projection at the scalp level (top) and sagittal/frontal views of all ICs in the cluster (bottom). (**b**, **e**, **h**) ERSP average per condition. (**c**, **f**, **i**) ERSP pairwise differences between conditions. 'L > C': difference between Learning and Control, 'P > C': difference between Probe and Control, 'P > L': difference between Probe and Learning. (**a**-**c**) Cluster 4 - Anterior Cingulate. In the allocentric group, this cluster contains 14 ICs from 11 different participants. (**d**-**f**) Cluster 5 - Right Precentral Gyrus. In the allocentric group, this cluster contains 15 ICs from 11 different participants. (**g**-**i**) Cluster 6 - Left Postcentral Gyrus. In the allocentric group, this cluster contains 12 ICs from 10 different participants

7.3.2.3.3 Delta and theta band activity (<8 Hz)

Finally, we observed modulations of low-frequency rhythms (delta range 1-4 Hz, theta range 4-8 Hz), with sustained greater delta amplitudes in the starting arm in all brain clusters and a strong transient theta burst at the beginning of the trial in posterior parieto-occipital clusters (1-3). The brain activity in these frequency bands proved to be condition specific for these clusters, with a generally higher power for the learning condition along the finish arm (Figure **7.7c,f,i**).

7.4 Discussion

This work brings together the technology and data analysis tools to perform simultaneous brain/body imaging during landmark-based navigation in fully mobile participants. Our behavioral results show that a majority of young adults can rapidly learn to solve the Y-maze by using an allocentric strategy, confirming previous findings in similar landmark-based navigation studies (Bécu et al., 2020b; Kimura et al., 2019). We find that allocentric participants have the capacity to flexibly reorient by observing landmarks at the beginning of the trial (consistent with the more precise gaze dynamics described in Bécu et al. 2020b). The analysis of high-density EEG data shows that exploitable neural signals are extracted from various brain regions (posterior cingulate, cuneus/precuneus, supramarginal gyrus, anterior cingulate, precentral gyrus, and postcentral gyrus) that replicate and extend previous neuroimaging findings from a similar fMRI study (Ramanoël et al., 2020). Overall, the identified brain structures represent an extended ensemble of areas involved in the high-level processing of visual information, in spatial representation, and in motor planning necessary to navigate.

7.4.1 Task-solving behavior

The zone-based analysis reveals a common task-solving behavior in allocentric participants, starting by an observation period at the beginning of the trial (slow speed, high variability in horizontal heading, and maximal visibility of landmarks) followed by navigation to the chosen arm. We found minimal head rotations after reaching the center of the maze and no significant deceleration, indicating the initial observation period to be the main source of visual information for the participants. This interpretation was also supported by the analysis of horizontal eye movement and neck muscle activity clusters, which exhibited greater activity at the beginning of the maze (Figure **7.5b,e,h**). Interestingly, between-condition contrasts revealed an accentuation of this pattern in the probe condition (Figure **7.5c,f**), probably reflecting a higher need for information gathering at an unfamiliar starting point.

The landmark visibility analysis confirmed that navigators may rely extensively on the landmark appearing straight ahead at the beginning of the task, which differs in the probe condition (Landmark 2) from the other conditions (Landmark 1). This suggests that the participants were mainly capable of reorienting with the information gathered from this landmark only, even in the probe condition. We found additional tendencies for this metric (see

last columns of Figure **7.4f**), such as (a) a similar visibility for the two predominant landmarks at the center during probe condition and (b) an increased visibility for the second most visible landmark (relative to each condition) with respect to the third during the initial observation period in the learning and probe conditions. None of these observations were applicable to the two egocentric participants (Supplementary Figure **D.2e-f**). Therefore, these findings might reflect a perceptual mechanism helping to bind multiple landmarks in a single representation of the environment, specific to the allocentric participants' strategy.

7.4.2 Anatomical substrates of the clusters retrieved

We hypothesized that the analysis of brain dynamics in fully mobile individuals would retrieve structures involved in active, multimodal landmark-based spatial navigation. Here, we contrast our results against those from static neuroimaging paradigms. First, we expected the RSC to play a central role in solving the Y-maze, as this task requires landmark-based reorientation. Accordingly, we found a cluster located in or near the posterior cingulate cortex (cluster 1), encompassed by the RSC (Julian et al., 2018). fMRI studies have consistently shown that the human RSC encodes heading direction (Marchette et al., 2014; Shine et al., 2016) anchored to local visual cues, like stable landmarks, by using a first-person perspective (Auger & Maguire, 2018; Auger et al., 2012; Marchette et al., 2015). Moreover, the RSC is embedded in a network of somatosensory areas that were also partially retrieved in our cluster analysis. In particular, the precuneus (cluster 2) is involved in several aspects of spatial cognition, such spatial attention, spatial working, long-term memory, and the representation of landmarks, in association with RSC during navigation (Cona & Scarpazza, 2019). Also, in line with the mobile aspects of our paradigm, several studies have highlighted the role of the precuneus in the integration and coordination of motor behavior during navigation (Navarro et al., 2018). Around the centroid of the cluster associated with the precuneus, we note that the ICs forming the cluster are distributed across the anatomical boundaries between occipital and parietal cortices. This region spans areas mediating visuo-spatial processing, such as the occipital place area (OPA), which is sensitive to navigable pathways in a perceived scene (Bonner & Epstein, 2017; Patai & Spiers, 2017).

Our EEG analysis also retrieved three clusters associated with the supramarginal gyrus (cluster 3), the anterior cingulate cortex (cluster 4), and the precentral gyrus (cluster 5). The supramarginal gyrus, which belongs to the somatosensory cortex, plays a role in the mnemonic components of spatial navigation (Sneider et al., 2018; van der Linden et al., 2017). In addition, as it is encompassed within the inferior parietal lobule, the supramarginal gyrus is involved in spatial attention (Cona & Scarpazza, 2019). The anterior cingulate cortex subserves high-level cognitive functions such as route planning (C.-T. Lin et al., 2015; Spiers & Maguire, 2006) as well as its re-evaluation and updating based on internal monitoring, more specifically with respect to error detection and spatial reorientation (Javadi et al., 2019). As for the right precentral gyrus cluster, we report its centroid in BA6 although the spatial extent of its ICs spans toward more frontal areas. Considering this limited spatial precision, we speculate a putative contribution from the supplementary motor area proper

and the right middle frontal gyrus, both overlapping with BA6. The former is recruited in motor planning (Simon et al., 2002) and motor execution of self-initiated movements (Cona & Semenza, 2017), consistent with the mobile aspect of our task. The latter is involved in spatial attention and spatial working memory, specifically in BA6 (Cona & Scarpazza, 2019). Finally, our brain analysis retrieved postcentral gyrus activity (cluster 6), encompassing the primary somatosensory cortex, and thus most likely to be involved in the processing of proprioception (Rausch et al., 1998).

7.4.3 Functional analysis of the clusters' activity

7.4.3.1 Gamma band activity (>30 Hz)

An objective of this work was to couple brain and body imaging during spatial navigation. Complementing the behavioral findings, the analysis of transient time-frequency EEG patterns shows a strong gamma band synchronization in posterior parieto-occipital clusters, especially in the starting arm (Figure **7.7b,e,h**), which coincides with the increased eye movement related activity observed in the same spatial area (low frequencies in Figure **7.5b**). In line with findings showing that increased gamma power in parieto-occipital region promotes sharper visuo-spatial attention (Gruber et al., 1999; Jensen et al., 2007; Müller et al., 2000), this cortical activity pattern supports our interpretation of the participants' behavior. We reported significant differences when the participant starts walking in the probe condition compared to the learning and control conditions (in the cuneus/precuneus, Figure **7.7f**, and supramarginal gyrus, Figure **7.7i**). This pattern may reflect a greater attentional demand triggered by the visual conflict between the probe and the other conditions, forcing the participant to actively reorient. Statistical analyses conducted on eye and muscle clusters also revealed a more active state (more frequent eye movements and increased muscle activity) when the participant starts walking during probe trials. The greater involvement of posterior parietal cortex (especially the precuneus) during this crucial reorientation moment is coherent with the fMRI evidence linking it to the navigationally relevant representation of landmarks, when participants are moving with respect to stable objects (Cona & Scarpazza, 2019). The mobile EEG literature of locomotion control more often reports activity bound to steady-state gait cycle events (*e.g.*, Castermans et al. 2014; Gwin et al. 2011; Luu et al. 2017b; Wagner et al. 2016, 2014) , making it difficult to compare with our experimental design. Several works presenting results contrasting a walking condition with a standing baseline condition described a desynchronization in the high beta band (25-35 Hz) in the sensorimotor cortex (Seeber et al., 2014, 2015; Wagner et al., 2012), which does not concur with our findings (Figure **7.8e,h**). Nonetheless, Bulea et al. (2015) report high gamma band synchronization (30-50 Hz) when comparing active walking to quiet standing in the posterior parietal area, which better aligns with our results (Figure **7.7b,e,h**). However, locomotor control can only be a part of the interpretation as it does not explain the specific activity observed in the probe condition.

7.4.3.2 Alpha band activity (8-12 Hz)

Our ERSP analysis shows a desynchronization in the alpha band, spanning almost all clusters (except the anterior cingulate), with different temporal dynamics. In the sensorimotor cortex (post-central and pre-central gyri), the desynchronization extends to the low beta band, it starts a few moments before movement onset, and it is sustained throughout the whole maze traversal (Figure **7.8e,h**). This pattern advocates for a mere signature of locomotion, as reported in numerous mobile EEG studies comparing walking and standing (Bulea et al., 2015; Presacco et al., 2011; Seeber et al., 2014). Further supporting the idea that such activity is a neural correlate of ambulation, no differences between conditions were found in postcentral gyrus (Figure **7.8i**). Interestingly, the precentral gyrus exhibited a modulation of activity around the center of the maze where alpha desynchronization was less pronounced in the control condition as compared to others (Figure **7.8f**). The precentral gyrus is known to be associated with movement planning (Navarro et al., 2018; Wagner et al., 2014). Alpha power suppression has been linked to increased activity in motor regions (Pfurtscheller & Klimesch, 1991), such that this activity pattern could reflect a more passive execution of the turn in a situation in which the participant can straightforwardly repeat the learning condition. Although this purely ambulatory feature extends to more posterior parietal areas (Bulea et al., 2015), the temporal dynamics of the alpha power in our parieto-occipital clusters (*i.e.*, an almost immediate desynchronization after trial start and a subsequent fading across maze traversal, Figure **7.7e,b,h**) suggests a different interpretation. According to the meta-analysis from Cona and Scarpazza (2019), the precuneus and the inferior parietal lobule are embedded in a fronto-parietal network mediating spatial attention. Thus, the fading of the desynchronization might reflect a progressive decrease in spatial attention, as sufficient visual information is being gathered. As participants seem to make their decision early in the task, they should reach their maximal degree of alertness in the first sections of the maze and let it drop afterwards. Echoing this interpretation, several EEG studies of spatial navigation associated alpha power in the parietal cortex to spatial learning (Gramann et al., 2010b; C.-T. Lin et al., 2015), with significant task-related modulations.

In an experiment reporting the modulation of RSC activity in passive simulated navigation, those participants who relied on an allocentric reference frame demonstrated a sustained alpha power decrease during straight segments and a strong alpha power increase during absolute heading rotation (Chiu et al., 2012; C.-T. Lin et al., 2015, 2018). For our posterior cingulate cluster, such heading discriminant activity is neither observed at the starting position where head movements are maximal (relative to the body) nor near the central zone of the maze (relative to the global environment, *i.e.*, the landmarks) (Figure **7.7b**). Partially explaining these diverging results, Gomez et al. (2014) reported a stronger RSC activation during on-the-spot rotation as compared to continuous movement, tempering the heading computation role of RSC when translational movements are involved. Additionally, the alpha desynchronization elicited by a desktop-based rotation is absent when performed physically (Gramann et al., 2018), which shows the important influence of vestibular and proprioceptive cues in modulating RSC activity. Thus, assuming that our posterior cingulate

cluster is bound to RSC activity, our results provide additional evidence that the involvement of RSC in heading calculation has been overestimated with respect to ecological navigation. The dynamics of the posterior cingulate cluster in the alpha frequency band are more in accordance with a memory role serving the encoding/retrieval of the egocentric percepts into the allocentric representation (Mitchell et al., 2018; Vann et al., 2009). Indeed, the fact that alpha desynchronization occurred during the observation of the environment suggests the association of RSC with the encoding/decoding of landmark-based information. This interpretation fits with the tendency of our cluster to be localized in the dorsal part of the posterior cingulate, which is known to play a role in spatial recall tasks in opposition to the ventrolateral part, more likely to be activated during tasks proposing passive viewing or active navigation without the need to respond, perform spatial computation, or self-localize (Burles et al., 2018).

7.4.3.3 Delta and theta band activity (<8 Hz)

We observe a strong delta band synchronization (<5 Hz) in all clusters, lasting the whole traversal of the maze, which has been previously reported as a motion-related artifact (Castermans et al., 2014; Gwin et al., 2010; Presacco et al., 2011). However, the presence of condition-specific modulations in posterior parieto-occipital clusters casts a doubt on this interpretation. During the learning condition, statistical analyses demonstrated a sustained delta/theta synchronization in the finish arm (starting in the center zone, Figure **7.7c,f,i**). Possibly elucidating this feature, a previous study of spatial working memory in mobile conditions observed a similar theta synchronization seconds prior to the stimulus presentation in posterior cingulate and somatosensory association areas (Kline et al., 2014). Arguing that theta power modulations can be related to memory encoding and maintenance, this may be the signature of a learning mechanism, preparing to encode the outcome of the learning trial at the end of the finish arm. However, unlike Kline et al. (2014), we do not find subsequent theta desynchronization on stimulus presentation (goal appearance). Another deviation from the artifactual hypothesis is that the delta/theta synchronization seems specific to the starting arm for the anterior cingulate cortex (Figure **7.8b**), coinciding with participants' decision-making period as indicated by behavioral analyses. This may reflect the increased spatial working memory demand required for route planning, as previous studies reported increased theta power in the frontal cortex during more cognitively demanding navigation periods (Caplan et al., 2003; Kahana et al., 1999; C.-T. Lin et al., 2015). Closer to the interrogations posed by the present task, Ferguson et al. (2019) found the anterior cingulate to mediate a reinforcement learning role by eliciting a reward when allocentric navigators were shown previously learned cues predicting the goal location. In addition, we observed theta bursts of activity (4-8 Hz) closely time-locked to the beginning of the task in most clusters (mainly in the posterior cingulate, Figure **7.7b**, and supramarginal gyrus, Figure **7.7h**). This pattern of activity may be framed within a postural control interpretation: as the environment suddenly appears to the participant, his/her balance control system, previously deprived of any visual information, needs to be updated based on the novel visual cues (Flückiger & Baumberger, 1988; Horak & Macpherson, 2011). Strikingly, theta bursts of activity were similarly de-

scribed immediately following spontaneous loss of balance from walking on a beam (Sipp et al., 2013) and sudden visual perturbations to standing or walking balance (Peterson et al., 2018). These bursts were noticeable in posterior cingulate and posterior parietal areas, associated with vestibular sensing (M. Kim et al., 2017) and resolving visual conflicts (Peterson et al., 2018), respectively.

7.4.4 Limitations

Source reconstruction was performed using an electrodes' location template and average MRI anatomical data, which limited its spatial accuracy. Thus, the interpretations proposed in this work should be treated with caution. The use of subject-specific data to build the head model would help increase the accuracy of source localization algorithms (Akalin Acar & Makeig, 2013; Shirazi & Huang, 2019) and it would eventually enable more robust interpretations of the neural correlates of spatial behavior.

Although the methods employed here to clean the EEG signals have been previously validated in the literature (Nordin et al., 2019; Richer et al., 2019), there is never complete guarantee that the results are artifact free. In particular, the muscular activity associated with microsaccades has been shown to resist standard cleaning methods (Hassler et al., 2011; Yuval-Greenberg et al., 2008) and it could in principle be contributing to the brain ICs in the gamma frequency band (Yuval-Greenberg et al., 2008). However, the influence of this type of artifact is meaningful in experimental setups favoring the accumulation of microsaccades at a fixed latency with respect to the synchronizing event (*e.g.*, fixation of a visual target; Yuval-Greenberg et al. 2008) and the probability that this applies to our setup is low.

Gait-related artifact contamination is another well-known pitfall of ambulatory studies (Castermans et al., 2014). Walking induces small motions of electrodes and cables that can have a large impact on the signal-to-noise ratio. Typically, the spectral signature of such artifacts contains elevated power amplitudes at the stepping frequency (between 0.5 and 1 Hz for normal walking speeds) and its harmonics, as well as a power modulation pattern time-locked to gait cycle especially marked below 20 Hz (Castermans et al., 2014; Snyder et al., 2015). Therefore, as already acknowledged, the low frequencies (between 1 and 5 Hz) power increase observed consistently through our clusters may reflect this type of contamination. Yet, motion artifacts were found negligible during treadmill walking at moderate speeds such as those adopted by participants in our study (Gwin et al., 2010; Nathan & Contreras-Vidal, 2016). Also, the wireless property of our EEG system (as in Nathan and Contreras-Vidal 2016) provides additional robustness to gait-related artifacts by minimizing cable sways, identified as major artifactual causes (Symeonidou et al., 2018).

Considering the recent publication of the ICLabel algorithm, our work provides some practical insights on how to integrate this promising tool into the MoBI approach. At first, the automatic IC classification has proven to be very useful to deal with large numbers of components. However, through the manual inspection of a large proportion of the automatically assigned labels, we uncovered and corrected a substantial amount of discrepancies between the algorithm and the experimenter's opinion, thus adopting a semi-automated procedure.

Even if human categorization of ICs can be variable and error prone (Pion-Tonachini et al., 2019), we believe that these discrepancies also stem from complex artifact patterns present in mobile EEG. However, resorting to the experimenter's judgment is not desirable for future studies as it impairs replicability, and it is very time-consuming for high-density recordings. Future works should explore the flexibility of interpretation offered by the compositional label, for example, by adapting the probability thresholds to better tailor the algorithm's output to the characteristics of the data being processed.

7.5 Conclusion & Future works

This study provides a proof-of-concept about the possibility of imaging the neural bases of landmark-based spatial navigation in mobile, ecological set-ups. First, the presented EEG analysis identifies a set of brain structures also found in fMRI studies of landmark-based spatial cognition. Second, our approach reveals the role of brain areas involved in active, fully engaging spatial behavior (such as clusters in the sensorimotor cortex related to motor execution and proprioception), whose contribution is usually overlooked in static fMRI paradigms. We present new insights onto the cortical activity mediating successful spatial reorientation when visual, proprioceptive, and vestibular sensory inputs are coherent. Specifically, alpha band desynchronization in the posterior cingulate when participants gather visual information provides further support to the idea that RSC plays an important role at the interface between perception of landmarks and spatial representation. Despite showing few effects of experimental condition, our results illustrate the benefit, in terms of deciphering neural dynamics within the course of a trial, of fine temporal resolution brain imaging paired with meaningful behavioral markers during spatial navigation.

The methodology associated with the MoBI approach remains quite new, and such experiments help to identify vectors of improvement. At the preprocessing stage, further characterization of the parameters and robustness comparison with other pipelines (such as Automagic, Pedroni et al. 2019) would be beneficial. Complementary steps such as sliding window approaches for isolating transient artifacts using principal component analysis and/or canonical correlation analysis can improve source separation compared to ICA alone (Artoni et al., 2017; Nordin et al., 2020). Adding simultaneous noise and neck electromyographic recordings have also been shown to successfully assist the identification and removal of motion-related artifacts (Nordin et al., 2019, 2020). Concerning the gathering of insights on strategy-specific behaviors, additional improvements of the protocol are also desirable. Using a passively guided traversal of the maze as a baseline to contrast with the main task may help to disentangle the neural correlates of locomotion control and active landmark-based spatial navigation. The addition of an eye-tracking system embedded in the VR head-mounted display would also bring further insights on the differential role of visuo-spatial cues (Bécu et al., 2020a).

CHAPTER 8

THE VERTICAL POSITION OF NAVIGATIONAL CUES DRIVES SCENE-SELECTIVE OSCILLATORY DYNAMICS THROUGHOUT ADULTHOOD

This chapter presents the second major experimental contribution of this thesis, the study of the impact of healthy aging on visuo-spatial information processing in scene-selective regions (SSRs) with EEG. Building up on numerous reports of vertical heterogeneities in perceptual tasks, with a lower visual field (VF) preference in healthy aging, this paradigm interrogates the influence of the vertical position of navigational cues on visuo-spatial processing in a dektop-based virtual environment. The paradigm was not conducted in immersive VR because it already introduces the novelty of the source reconstruction method for the SSRs. Behavioral, oculomotor and EEG correlates of navigation were investigated. This study sheds light on the importance of considering vertical positioning as a fundamental property of objects in scenes. It seems to drive oscillatory dynamics in scene-selective regions and cues in the upper field may hinder navigational behavior in older adults who exhibit a systematic downward gaze bias and a deficit in top-down modulation of attentional mechanisms.

This work was conducted jointly with Marion Durteste, PhD student at the *Aging in Vision and Action* laboratory, who was in charge of the behavioral and oculomotor analyses. An article associated with this work is currently in preparation so the most up-to-date draft version is transcribed here. It was posted on the *bioRχiv* server (preprint ID: 2023.10.16.562507) on October 17^{th}, 2023. When already introduced in Chapter **6**, methodologically redundant sections were omitted. Supplementary material is provided in Appendix **E**.

8.1 Authors

Alexandre Delaux*,[1], Marion Durteste*,[1], Ainhoa Ariztégui[1], Benoit R. Cottereau[2,3], Denis Sheynikhovich[1], Stephen Ramanoël[1,4] & Angelo Arleo[1].

* These authors contributed equally to the manuscript.

1. Sorbonne Université, INSERM, CNRS, Institut de la Vision, 17 rue Moreau, F-75012 Paris, France
2. CerCo UMR 5549, CNRS Université Toulouse III, Toulouse, France
3. IPAL, CNRS IRL 2955, Singapore
4. Université Côte dAzur, LAMHESS, Nice, France

8.2 Abstract

Position is a key property that allows certain objects in the environment to attain navigational relevance. Symmetrical processing of object position along the horizontal meridian remains an unchallenged assumption of the spatial navigation literature. Nonetheless, a growing body of research reports vertical heterogeneities in perceptual tasks and recent evidence points towards a lower visual field (VF) preference in healthy aging. Factoring in the vertical position of objects to better apprehend spatial navigation abilities across the lifespan is essential. The occipital place area (OPA), para-hippocampal place area (PPA), and medial place area (MPA) are ideal candidates to support the processing of the vertical location of navigational cues. Indeed, they play intricate roles in scene processing and spatial cognition that may interact with their underlying retinotopic codes. In this study, a sample of 21 young and 21 older participants completed a desktop-based task requiring them to navigate using objects at different vertical locations. We equipped them with an eye tracker and a high-density EEG cap. We used a fMRI-informed source-reconstruction algorithm to study the OPA, PPA and MPA with high spatial and temporal precision. Older adults exhibited a lower performance than young adults across environments. The first main result pertains to striking age-related disparities in beta/gamma band synchronization. The latter could reflect deficient top-down attentional mechanisms during navigation and explain performance deficits in aging. The second finding relates to the vertical position of objects useful to orient. Older adults displayed a systematic gaze bias for objects in the lower half of the screen. Moreover, in both age groups, we revealed a differential pattern of theta and beta band activity in environments that only contained relevant cues in the upper field. This study sheds light on the importance of considering vertical positioning as a fundamental property of objects in scenes. It drives oscillatory dynamics in scene-selective regions and cues in the upper field may hinder navigational behavior in older adults who exhibit a systematic downward gaze bias. We argue that the OPA, PPA, and MPA are key nodes of the network that parses information across the vertical hemifields for efficient navigation.

8.3 Introduction

High-resolution visual input is essential to forming accurate spatial representations that support successful wayfinding behavior in humans (Ekstrom, 2015). In natural settings, objects often hold sufficiently detailed visuo-spatial information to serve as anchors for positional or directional knowledge thereby guiding future actions (Zhong & Moffat, 2016). One question that has sparked much debate in the field pertains to the properties which allow certain objects, among the abundance of incoming visual information, to attain navigational relevance (Chan et al., 2012). Intrinsic visual features that make objects useful for spatial navigation include size, color, and distinctiveness (Auger & Maguire, 2018; Auger et al., 2012; Miller & Carlson, 2011; Stankiewicz & Kalia, 2007). Notwithstanding the contribution of these characteristics, non-physical properties such as location also play a decisive role in using a specific object as a spatial reference. A wealth of research has demonstrated that the position of objects in an environment conditions spatial behavior. For example, the most recognizable and useful stimuli for navigation are those located at decision points (Janzen, 2006) or in close proximity to the goal (Waller & Lippa, 2007). Additionally, spatial representations differ according to the distance of objects with respect to the navigator. While proximal cues may be easier to rely upon as they engage action-based memories of learned trajectories, distal information enables the formation of precise cognitive maps (Foo et al., 2005; Hartley et al., 2003; Hurlebaus et al., 2008; Jabbari et al., 2021).

The undifferentiated processing of objects with respect to their location across the horizontal meridian nonetheless remains an unquestioned assumption in the literature (Hafed & Chen, 2016). We argue that position within the upper and the lower VFs represents an underappreciated cornerstone of visual information usage for spatial navigation. First, upper-lower inhomogeneities are pervasive across a wide array of perceptual and cognitive tasks. On the one hand, the lower VF allows for better visual acuity, contrast sensitivity, spatial attention, and motion processing of stimuli (Carrasco et al., 2001; Lakha & Humphreys, 2005; Levine & McAnany, 2005; Regan et al., 1986; Rezec & Dobkins, 2004; Skrandies, 1987). The upper VF, on the other hand, favors abilities such as visual search, change detection and categorical processing (Niebauer & Christman, 1998; Pflugshaupt et al., 2009; Previc & Naegele, 2001; Rutkowski et al., 2002). Second, the environment imposes differing constraints with respect to the type of information available for navigational purposes across the horizontal meridian. Monuments, immovable objects and wayfinding signage are typical components of the upper VF whereas moving stimuli, obstacles, and spatial layout information appear predominantly in the lower VF (Greene, 2013; Groen et al., 2017). In natural settings, one can therefore expect these vertical asymmetries to modulate both gaze dynamics and orienting of attention (Jóhannesson et al., 2018). The above arguments provide solid grounds to factor in vertical position to the extensive literature on how object properties tie in with spatial behavior.

Wayfinding skills in the elderly are increasingly considered in light of the visual impairments that accompany healthy aging. Visuospatial processing declines in older age and modifies the way in which older adults sample the outside world and encode navigationally

relevant visual information (Dowiasch et al., 2015; Kimura et al., 2019; Ramanoël et al., 2020; Zhong & Moffat, 2016). For example, a recent study found that healthy older adults' orientation capabilities are rescued when geometry, instead of salient objects, is available to guide behavior (Bécu et al., 2023). Interestingly, accumulating evidence is pointing towards a possible influence of verticality on visuospatial function in healthy older adults. Vertical anisotropies in visual search appear to undergo significant changes throughout adulthood, shifting progressively to a lower VF dominance (Brennan et al., 2017; J. Feng et al., 2017). Moreover, older adults have been found to gaze preferentially at the ground when reorienting in ecological laboratory settings (Bécu et al., 2020a) and to show impaired spatial memory specifically for upper VFs objects (Durteste et al., 2023). Such reshaping of the use of visual space in healthy aging could have drastic consequences on the navigational relevance of objects located in the upper half of scenes.

At the neural level, the processing of scene layout and visual information contained within an environment has mainly been ascribed to the ventromedial posterior network of scene-selective regions (SSRs). The occipital place area (OPA), para-hippocampal place area (PPA) and medial place area (MPA) endorse distinct functions in this three-scene cortical system (Dilks et al., 2022). The OPA underpins the processing of obstacles, available paths and egocentric motion thereby facilitating immediate visually guided navigation (Bonner & Epstein, 2017; Ferrara & Park, 2016; Kamps et al., 2016a). The PPA, by exploiting spatial layout as well as objects and their respective associations, is mostly responsible for the rapid categorization of a scene (Bilalić et al., 2019; Harel et al., 2016). Finally, neural activity in the MPA (or retrosplenial cortex; see Silson et al. 2016) enables the bridging of local and global reference frames to support more complex map-based navigation (Auger et al., 2015; Marchette et al., 2014; Persichetti & Dilks, 2019). The established roles of the SSRs in scene viewing and spatial cognition have been posited to interact with underlying retinotopic codes (Steel et al., 2023; Uyar et al., 2016). Indeed, the OPA, PPA and MPA inherit some of the retinotopic organization from early visual cortex, and they exhibit preferences for designated areas of the VF. The OPA and PPA display striking vertical biases for the lower and upper VFs, respectively, while the MPA harbors a more general contralateral bias (Silson et al., 2015, 2016). The above findings make the OPA and PPA ideal candidates to support the encoding of the vertical position of objects during navigation. Research examining SSRs in healthy aging is scarce, but new evidence is pointing at a preserved connectivity and an increased activity of the OPA (Ramanoël et al., 2020, 2019). This result stands in contrast with the age-related alterations reported in the PPA and MPA (Ramanoël et al., 2015; Zhong & Moffat, 2018). No study has yet investigated whether such unequal aging of the cortical scene systems could alter the processing of information within the upper and lower VFs of older adults in the context of navigation.

In the present study, we first test the hypothesis that the vertical position of objects modulates spatial navigation performance and does so differentially in young and older adult populations. Second, we sought to establish whether SSRs in both age groups exhibit preferences for specific object positions, in line with their retinotopic biases. Most findings relating to SSR properties stem from experiments relying on the brief presentation of static

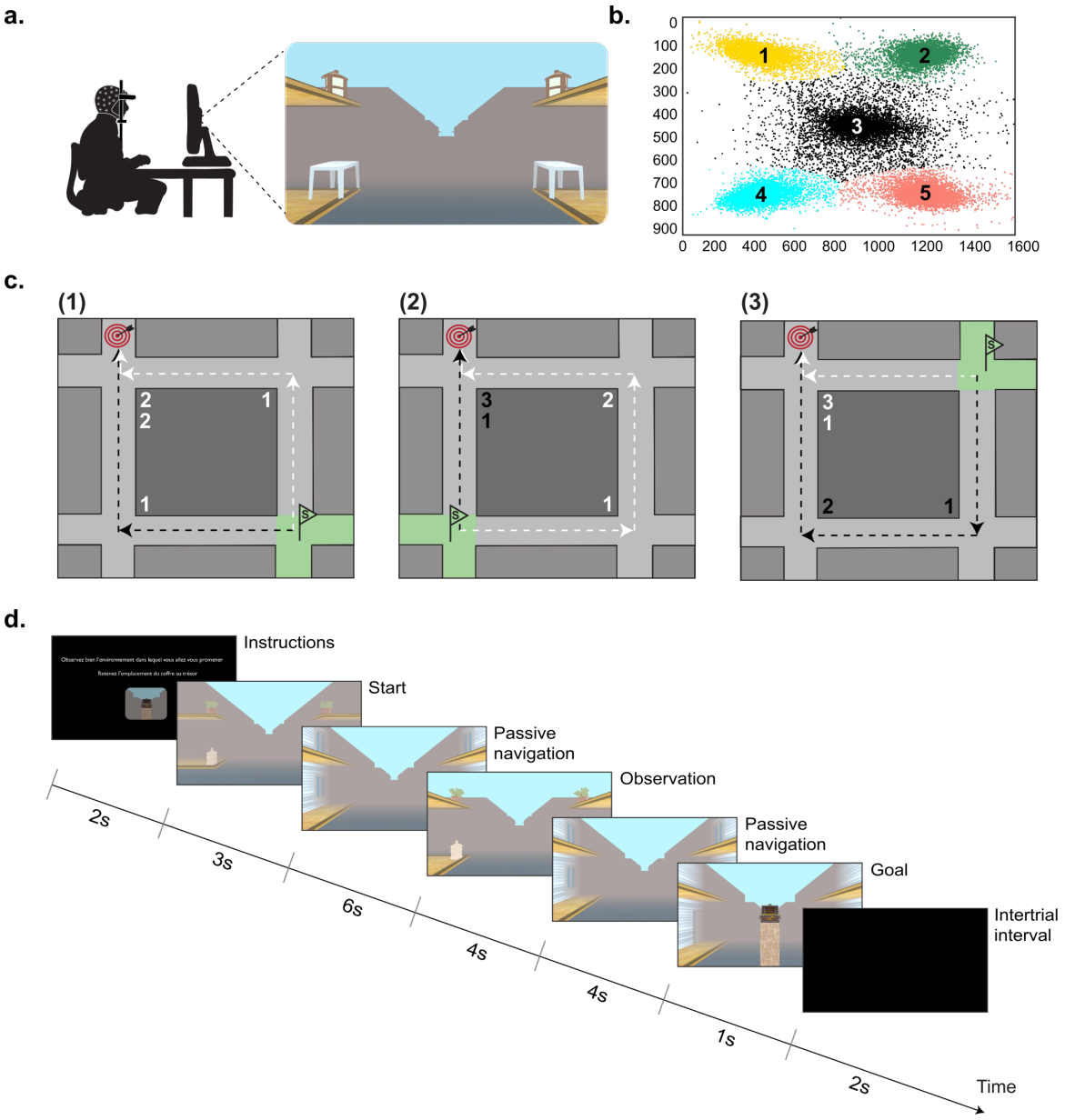

Figure 8.1: Experimental paradigm and definition of the areas of interest (AOIs). **a**. The participant, equipped with a 127-electrode EEG cap, is seated in front of a monitor with his head positioned on a head-mounted eye tracker. The screen displays a navigational task in a square-like virtual environment. **b**. Results from the gaussian mixture model (GMM) clustering analysis of fixation data at intersections during the encoding phase. All data points are depicted. The GMM defined five AOIs: top left (1), top right (2), center (3), bottom left (4), and bottom right (5). For data analysis, AOIs 1 and 2 are merged (upper AOI) and AOIs 4 and 5 are merged (lower AOI). Screen coordinates are in pixels. **c**. Schematic top view of the square-like layout of the virtual environment. The target represents a goal position, in the continuity of the top left intersection, within a specific instance of the environment. The green flags and green colored intersections mark the 3 starting positions associated with that goal. Each starting position is associated with two possible trajectories to the goal, that correspond to two distinct starting orientations. (1) If the participant starts from the bottom right intersection, it can take two routes that each pass through two intersections. (2, 3) If the participant starts from the bottom left or top left intersection, it can take two routes, one that passes through a single intersection and one that passes through three intersections. **d**. Schematic representation of a single encoding trial. Subjects navigate passively throughout the virtual environment and pause for 4 seconds at each intersection to encode the objects. The trial ends upon reaching the goal.

scene images (Epstein & Baker, 2019), thus hindering the possibility to study top-down influences on their activity. We deemed it important that our paradigm allowed for unrestricted visual exploration and for scene processing in a navigational context. In this regard, we designed a desktop-based virtual navigation task coupled to an eye tracker that explored the behavioral and oculomotor patterns during orientation with cues of varying vertical location. To record cerebral activity pertaining to SSRs, we used source-localized EEG. Recent EEG works successfully extracted the timing at which SSRs became sensitive to scene features underlining the added value of this technique in elucidating the underlying temporal dynamics (Harel et al., 2022; Kaiser et al., 2020, 2019). To optimize the signal recovered from the OPA, PPA and MPA in participants, we opted for a region of interest (ROI) analysis using an individualized source reconstruction model informed with fMRI (Cottereau et al., 2015).

8.4 Methods

8.4.1 Participants

A total of 24 young and 23 older adults from the French *SilverSight* cohort took part in the experiment (Lagrené et al., 2019). All subjects met the cohort inclusion criteria: normal cognitive performance on a battery of neuropsychological tests including the Mini-Mental State Examination (Folstein et al., 1975), the 3D mental rotation test (Vandenberg & Kuse, 1978) and the perspective-taking task (Kozhevnikov & Hegarty, 2001), no history of sensory, neurological, or psychiatric disorder, and normal or corrected-to-normal eyesight. We excluded 3 young participants and 1 older participant because their fMRI were of poor quality and thus not usable for the EEG source reconstruction analysis. One other older participant was removed from analyses as he struggled to stay awake during the spatial navigation task. The final analyzable group comprised 21 young, 7 females and 14 males (29.0 ± 4.27 years-old [$mean \pm$ SD]), and 21 older adults, 11 females and 10 males (75.8 ± 3.79 years-old). Of note, 1 young adult had eye tracking data of poor quality and 3 young adults were missing data for the 3D mental rotation task; they were thus removed from these particular analyses. Each participant provided their written informed consent, and the study was approved by the Ethics Committee "*CPP Ile de France V*" (ID_RCB 2015-A01094-45, CPP N: 16122).

8.4.2 Virtual environment

We designed the virtual town with Unity3D v2019.2 (Unity Technologies, Inc. San Francisco, California, USA) for the purpose of this experiment. The virtual environment consisted of a series of 4 intersections arranged in a square-like layout (Figure **8.1c**). Streets lined with identical buildings connected the four-way intersections, rendering them indistinguishable from one another. Every intersection comprised 4 corner balconies and 4 corner sidewalks, with an object placed at each of these 8 positions. Notably, all balcony items and all sidewalk items in any given intersection were strictly identical in order to limit the per-

ceptual and mnemonic load. Therefore, a unique set of 2 items unambiguously characterized an intersection (Figure **8.1a**). Participants' visibility was restricted to the front 4 objects of an intersection with the addition of gray fog (Figure **8.1a**).

The specific configuration of objects in the virtual environment defined three separate conditions (*UP*, *DOWN* and *MIX*). The UP, DOWN, and MIX conditions differed by the position of navigationally relevant objects at intersections: on balconies only, on sidewalks only or on both (Figure **8.2a**). Across intersections of an UP environment, the balcony items were different from each other while the sidewalk items were identical. Across intersections of a DOWN environment, the balcony items were identical while the sidewalk items were different. Finally, across intersections of a MIX environment, both balcony and sidewalk objects differed.

We selected objects included in the virtual environments from 3D Warehouse, a website for pre-made 3D models (`http://3dwarehouse.sketchup.com/`), and from the Unity Asset Store. Congruency with the virtual town was the main criterion for object selection. To reduce saliency differences between items, we normalized their height to 1 virtual meter and homogenized their color and texture. Specifically, we took special care in attenuating vibrant colors and textures. Before launching the experiment, 5 examiners rated objects according to their recognizability. We discarded and replaced items judged to be poorly recognizable. We created 9 instances of the virtual environment (3 per condition) with this set of objects. We did not reuse items across different instances, and we presented the same 9 instances to each participant.

8.4.3 Virtual navigation task

Participants performed a reorientation paradigm in the previously described virtual town. Their overall task consisted in learning the location of a goal in order to retrieve it from different starting positions throughout the environment. The goal changed position across the various instances of the environment (see Section **8.4.2**) but was always situated in the continuity of one of the 4 streets making up the square-like layout. A single goal position and 6 possible starting zones characterized an environment. Six different trajectories could therefore lead to the goal: 2 that passed through one intersection, 2 that passed through two intersections, and 2 that passed through three intersections (Figure **8.1c**).

A single condition comprised an encoding phase and a test phase. During the encoding phase, subjects navigated passively towards the goal with a forward speed of 5 $m.s^{-1}$ and a turning speed of approximately $67°.s^{-1}$. They watched first-person videos of a single-intersection trajectory, a two-intersection trajectory, and a three-intersection trajectory through the environment, in a randomized order. These videos ensured that participants passed through every intersection at least once. The videos marked a 4-second pause at the starting position and at the level of each intersection for participants to encode the objects (Figure **8.1d**). To succeed in the task, participants had to learn the position of the goal with respect to the objects present at each intersection. Once the 3 routes had been shown, participants were tested on their reorientation ability. During the test phase, subjects navigated

passively through the 6 possible routes. The video paused upon reaching an intersection and subjects decided whether they needed to go straight, left, or right using the keypad. A correct answer led to navigation resuming, while a wrong decision triggered a sound that notified the participant to retry. Subjects could not move along the route until the correct direction had been chosen. Upon finding the goal, a black screen appeared, and the next video started after a 2-second delay. The first three videos shown during the test phase were always the same as those presented during the encoding phase. The last three test videos corresponded to the remaining three possible trajectories, unexplored during the encoding phase. Such a design served to reduce the difficulty of the task by reinforcing the learning of specific routes.

8.4.4 Procedure

While we placed the conductive gel, subjects read the paper instructions and watched a demonstration of the paradigm. The demonstration video showed the entire course of a condition, with the encoding and test phases. During the simulated test phase, correct and wrong decisions were made in order for participants to assimilate the two types of feedback. Notably, the virtual environment used for the demonstration was strictly identical to the one used for the actual task except for the objects at intersections which were replaced by colored cubes. We also presented participants with a map of the global layout of the environment to facilitate learning, particularly in older adults (Allison & Head, 2017). Following the EEG preparation and paradigm familiarization phase, the experimental session began with a 5- or 9-point grid eye tracking calibration depending on the subject's fixation stability. The gaze patterns of the dominant eye were sampled at 500 Hz throughout the experiment.

Subjects performed a total of 9 different conditions as the experiment comprised 3 blocks, each divided into UP, DOWN, and MIX conditions. A block always ended with the MIX condition but could start with an UP or a DOWN condition. Such a configuration mitigated the possibility that subjects starting with the MIX condition would apply the same strategy to perform the UP and DOWN conditions. We counterbalanced the presentation order of the UP and DOWN conditions across blocks and subjects to avoid a potential bias linked to the starting condition. Note that eye tracking calibration was repeated at the beginning of each block, before launching the navigational task, to limit the amount of drift and allow participants to remove their head from the chin rest.

Once the 3 conditions within a block ended, subjects performed a recognition task. The latter acted as an evaluation of the level of item encoding. Participants saw 6 objects that they had encountered in the previous virtual environments, 2 from each condition, and 6 new objects (*i.e.*, distractors). We presented one item at a time on a black screen, and we randomized their order of presentation. Subjects responded with the keypad whether they believed to have seen the object in one of the three previous environments or not. A pause followed the recognition paradigm, and we adapted its duration to each participant's individual needs. The experimental session ended with a questionnaire probing subjects' strategy use and object selection during the reorientation task (Supplementary Figure **E.5**).

8.4.5 Apparatus and setting

The virtual navigation task was displayed on a 23 inches Dell monitor with a 1600×900 pixel resolution, subtending 49° in width and 30° of visual angle in height. Subjects' head was positioned 57 cm from the screen on a head-mounted monocular eye tracker (EyeLink 1000 Tower Mount, SR Research Ltd., Canada). The center of the screen was adjusted to be at participant eye-level. Answers were recorded via a numeric keypad (KKmoon) placed on the table in front of participants and adjusted individually for optimal visibility. Subjects wearing progressive lenses removed them for the duration of the task as they could have biased the use of visual information within the upper and lower VFs. The experimental session took place in a dark room devoid of light, except from that coming from the monitor.

The EEG recording system comprised 127 active wet electrodes mounted on an elastic cap with an equidistant arrangement (waveguard original - ANT Neuro, Hengelo, The Netherlands). An electrode located closest to the standard Cz position (10-20 international system) provided the reference for all other electrodes and an additional one on the left earlobe served as electrical ground reference. After placing the cap on the participant's head, we collected the fiducial and electrode positions with the depth perception camera approach presented in Section **6.3.1**. Prior to recording for the experimental session, we lowered the impedance of the electrodes with the scalp below 20 kΩ. We acquired raw EEG data with eego mylab software (v1.9.1, ANT Neuro) at a 1 kHz sampling rate, continuously within each block. To simultaneously record all streams of data (eye tracking, EEG and protocol events), we used the Lab Streaming Layer protocol (Kothe, 2014) and the LabRecorder software (v1.13.0) to collect them into a single XDF file per block.

8.4.6 Data analysis

8.4.6.1 Behavior

Data were extracted from the XDF files of each participant using the `pyxdf` library in Python 3.8. Analyses were conducted using *R* version 4.0.3 in RStudio version 2022.12.0+353 (*R* Core Team, 2020; RStudio Team, 2022). To assess participants' navigational performance, we computed the number of errors per intersection during the navigational task. This number could vary from 0 to 2, 2 being the total number of wrong directions at a single intersection. We also reported the number of errors made during the recognition task. Using the answers from the post-experiment questionnaire, we grouped participants into two categories: those who used a mental map to orient (from the beginning or at some point during the experiment) and those who never did. As an exploratory analysis, we also classified participants according to the reported number of objects they relied upon for orientation at each intersection: individuals who selected a subset of objects *vs.* those who relied on all 4 objects. We used one linear mixed model to evaluate the influence of age group, sex, condition, and strategy on performance and a second to test the impact of trajectory type (repeated *vs.* new) on behavior. We chose the random and fixed effects structures based on the Akaike information criterion (AIC) goodness-of-fit statistic. We carefully inspected the normality of residuals

from these models. We also verified using linear regression whether neuropsychological performance as assessed by the Corsi block-tapping, 3D mental rotation, and perspective-taking tasks were associated with performance on the virtual navigation task.

8.4.6.2 Eye-tracking

We conducted all analyses on gaze patterns from the encoding and test phases separately. One young participant had eye tracking data of poor quality and was therefore excluded from the following analyses. We focused solely on the static observation periods at all intersections. The observation period during the test phase depended on the time it took for participants to choose the correct direction. In order to reduce interindividual variability, we restricted our analysis to the first 4 seconds upon arrival at the intersection even when participants took longer to make their decision. We chose a 4-second window in line with the observation phase of the encoding phase. We did not analyze the eye movements during the dynamic parts of videos. The detection algorithm supplied by SR Research classified eye movements into fixations, saccades, and blinks (EyeLink 1000 User Manual, 2005 - 2009). We further processed the data by removing fixations that were shorter than 80 ms or that fell outside the computer screen. We used a gaussian mixture model (GMM) to cluster fixation data into specific areas of interest (AOIs) for young and older adults separately. We fitted a GMM with $N = 5$ components to the encoding and test fixation data, as they had the lowest bayesian information criterion (BIC) value. We subsequently labeled each fixation according to the AOI it belonged to, and we visualized the results. For both encoding and test data, we found an AOI at each of the four object positions and an AOI in the center of the screen (Figure **8.1b**).

Before examining fixation statistics associated with the AOIs, we discarded fixations that fell too far from the center of their attributed AOI. In other words, we removed fixations with coordinates situated outside the ellipse forming the 99^{th} percentile of the Mahalanobian distance (computed for each AOI with the parameters found by the GMM). We merged the left and right AOIs into 'upper' and 'lower' AOIs as we did not have any hypotheses pertaining to left-right asymmetries (see Figure **8.1b**). We measured 3 metrics at each intersection: (1) the proportion of time spent looking at each AOI (*i.e.*, the sum of all fixation durations), (2) the first fixated AOI per intersection, and (3) the vertical meridian asymmetry (VMA) related to total dwell time (DT) using the following formula:

$$\mathrm{VMA(DT)} = 200 * \frac{\mathrm{DT_{lower\ AOI}} - \mathrm{DT_{upper\ AOI}}}{\mathrm{DT_{lower\ AOI}} + \mathrm{DT_{upper\ AOI}}} \tag{8.1}$$

The vertical meridian asymmetry (VMA) computes the difference in dwell time (DT) between the lower and upper AOIs, it can thus decipher a possible vertical gaze bias. Indices that are close to 0 indicate no asymmetry in DT between the upper and lower AOIs. Indices that are below 0 reflect an asymmetry in DT with more time spent looking at the upper AOI than at the lower AOI. Indices above 0, on the other hand, highlight that more time was spent looking at the lower AOI than at the upper AOI. We ran linear mixed models to assess the impact of age group, sex, and condition on the 3 eye movement parameters.

The latter were summary variables per block and per condition for each participant. We included participant and block as random intercepts in all models, and we compared fixed effect structures, starting with the most complex, using the AIC.

8.4.7 EEG

We processed and analyzed the EEG data using Matlab R2019a (Mathworks Inc., Natick, MA, USA) and standalone toolboxes.

8.4.7.1 Source reconstruction modeling

We followed the procedure described in Section **6.3.2**. In this analysis, the T2-weighted sequence was available for the young group only. Concerning the functional definition of SSRs, we present the peak coordinates for each young and older participant into Supplementary Tables **E.1** and **E.2**.

8.4.7.2 EEG processing

We followed the procedure described in Section **6.2**, using the APP pipeline for time-domain cleaning.

On the cleaned-with-ICA full dataset (*i.e.*, data from all trials, regardless of whether they were labeled as artifactual periods earlier), we ran a final artifact check with the APP pipeline. We used this analysis to automatically flag any epoch containing at least one data point classified as an artifact by both runs of the APP pipeline. These data points contain transient artifacts that were sufficiently strong to be detected prior to independent component analysis (ICA) but that were not satisfyingly dealt with after removal of non-brain independent components (ICs). Before epoching the dataset we applied a bandpass filter between 1.25 Hz and 42 Hz (zero-phase Hamming windowed finite impulse response filters: high-pass filter with 1 Hz cut-off frequency and 0.5 Hz transition bandwidth and low-pass filter with 47.25 Hz cut-off frequency and 10.5 Hz transition bandwidth). We then epoched the dataset into $[-2, +4]$ second fixed time windows centered around the event of arriving at an intersection. We considered all intersections excluding start positions. We discarded epochs that were previously flagged as well as those that did not contain any fixations. We present the detailed count of epochs included in the EEG analysis in Supplementary Tables **E.3** and **E.4**.

For the following analyses, we used functions from the *FieldTrip-lite* plugin (v20210601, Oostenveld et al. 2011) for EEGLAB. At the epoch level, we first computed event-related spectral perturbations (ERSPs) for each channel (with a 25 Hz sampling rate in the temporal domain and with a linear scale between 2 and 40 Hz for the spectral domain) using the `ft_freqanalysis` function. The latter was based on a frequency-wise combination of Morlet wavelets of varying cycle widths (*superlet* method: Moca et al. 2021). We discarded data from electrodes for which the position was not determined with sufficient confidence on the 3D model. Then we proceeded to solving the inverse problem with the complex Fourier coefficients as inputs using the `ft_sourceanalysis` function and the minimum norm es-

timation (MNE) method. To summarize activity from the OPA, PPA and MPA, we averaged power estimations over all dipoles included in the ROI and combined its contribution from both hemispheres. Finally, at the epoch level, we divided the activity by its arithmetic mean over the course of the epoch.

8.4.7.3 Group-level analysis

The group-level analysis focused on 4 main variables of interest: (1) age group, (2) condition, (3) the interaction between age and condition and (4) ROI. Since we used a mixed-effects modeling approach on the epoch-based description of the data: there was no within-subject averaging. We performed separate analyses for the encoding and the test phases of the experiment.

We used the period during which participants are transported along the street before the arrival at the intersection (*i.e.*, prestimulus period) as a baseline for cortical activity during scene observation. We defined the baseline activity independently for each variable of interest, frequency and subject, and we computed it as the grand average of the prestimulus period from all epochs. We removed baseline activity from each epoch data using a gain (*i.e.*, divisive) model. We then randomly drew samples from the prestimulus period to build surrogate baseline epochs and statistically compare real epochs with baseline-level activity.

We used log-transformed data for statistical analysis as ERSP sample distribution has a better accordance with Gaussian distribution in that space (Grandchamp & Delorme, 2011). To investigate the specificity of ERSPs to the variables of interest within each ROI (age, condition, and their interaction), we performed a statistical analysis using a non-parametric unpaired permutation test based on the maximum cluster-level statistic with 1000 permutations (Maris & Oostenveld, 2007). We used linear mixed-effects modeling to evaluate the statistical significance at the 'pixel' level (spectral power at a given time-frequency pair) for a given permutation. In the encoding model, we considered participants and instances of the virtual environment as random intercepts and age, condition, sex, block, VMA and the interaction between age and condition as fixed effects (see Equation **8.2**). In the test model, we kept the same random effects structure and we included trial type (repeated *vs.* new), number of errors and their respective interaction with age as additional fixed effects (see Equation **8.3**).

$$\begin{aligned}\mathrm{ERSP}(f,t) \sim\ & \mathrm{Age} * \mathrm{Condition} + \mathrm{Sex} + \mathrm{Block} + \mathrm{VMA} \\ & + (1|\mathrm{ID}) + (1|\mathrm{Environment}) + (\mathrm{Condition} - 1|\mathrm{ID})\end{aligned} \tag{8.2}$$

$$\begin{aligned}\mathrm{ERSP}(f,t) \sim\ & \mathrm{Age} * \mathrm{Condition} + \mathrm{Sex} + \mathrm{Block} + \mathrm{VMA} + \mathrm{TestTrialType} + \#\mathrm{Error} \\ & + \mathrm{Age} : \mathrm{TestTrialType} + \mathrm{Age} : \#\mathrm{Error} \\ & + (1|\mathrm{ID}) + (1|\mathrm{Environment}) + (\mathrm{Condition} - 1|\mathrm{ID})\end{aligned} \tag{8.3}$$

We fit a model for each pixel, and we evaluated the contribution of the variable of in-

terest to the model by computing its associated F-statistic. For variables with more than 2 levels, we also extracted pairwise F-statistics. We selected pixels with an F-value above the 95^{th} quantile of the cumulative F-distribution and we clustered them by neighborhood. The cluster-level F-value was the cumulated F-value from all pixels included in the cluster. We then formed the distribution of observed maximum clustered F-values across permutations to compute the Monte Carlo p-value for the original repartition. We performed a paired permutation test to assess the statistical significance of ERSP activity for each level of the variables of interest with respect to its corresponding surrogate baseline. Here, we considered participants as random intercepts and original *vs.* surrogate epochs as a fixed effect (see Equation **8.4**). We set the initial significance level to $p < 0.05$, and Bonferroni-corrected for variables with more than 2 levels.

$$\text{ERSP}(f,t) \sim \text{EpochType} + (1|\text{ID}) + (\text{EpochType} - 1|\text{ID}) \tag{8.4}$$

In a follow-up analysis, we sought to investigate the time-resolved spectral activity across ROIs and age groups for all frequency bands: delta/theta (2-8 Hz), alpha (8-12 Hz), beta (12-30 Hz) and gamma (30-40 Hz). We averaged the ERSPs over the spectral dimension at the epoch level, yielding a time-course of mean spectral activity for each frequency band, ROI and age group. To study the influence of ROI in each age group on this signal, we performed a non-parametric paired permutation test based on the maximum cluster-level statistic (Maris & Oostenveld, 2007) with 1000 permutations. To evaluate the statistical significance at the sample level for a given permutation (mean spectral power at a given time), we used linear mixed-effects modeling for each age group independently. We considered participants and instances of the virtual environment as random intercepts and ROI, condition, sex, block, VMA, trial type, number of errors and the interaction between ROI and condition as fixed effects (see Equation **8.5**).

$$\begin{aligned}\text{ERSP}(f,t) \sim\ & \text{ROI} * \text{Condition} + \text{Sex} + \text{Block} + \text{VMA} + \text{TestTrialType} + \#\text{Error} \\ & + (1|\text{ID}) + (1|\text{Environment}) + (\text{Condition} - 1|\text{ID}) + (\text{ROI} - 1|\text{ID})\end{aligned} \tag{8.5}$$

We fit a model for each sample, we estimated the F-statistic for ROI and we extracted pairwise F-statistics. We selected the samples with an F-value above the 95^{th} quantile of the cumulative F-distribution and clustered them by neighborhood. The cluster-level F-value was the cumulated F-value of all samples included in the cluster. Using the distribution of observed maximum clustered F-values across permutations, we found the Monte Carlo p-value for the original repartition. We set the significance level to $p < 0.00104$, Bonferroni-corrected for 24 (2 models $\times$ 4 frequency bands $\times$ 3 pairwise comparisons) two-sided comparisons.

8.5 Results

To elucidate the role of the vertical position of information for spatial navigation, we asked 42 participants (21 young and 21 older adults) to perform a desktop-based virtual navigation task as we tracked their gaze patterns and EEG signals. Participants' task was to learn the position of a goal in a square-like environment using the objects situated on the balconies and sidewalks at each intersection (Figure **8.1a,c,d**). During the encoding phase, they watched videos of three trajectories to the goal. During the test phase, they viewed footage of multiple routes in the same environment and pressed a key upon arriving at each intersection to indicate the direction to the goal. We varied the position of navigationally relevant information across three different conditions. In the *UP* condition, only objects situated on balconies could be used to orient, while in the *DOWN* condition, only objects situated on sidewalks could be used. In the *MIX* condition, on the other hand, both balcony and sidewalk items were relevant for navigation. The experiment comprised 3 blocks, each divided into UP, DOWN, and MIX conditions (see Figure **8.2a**) and concluded with an object recognition task.

To test our hypotheses, we compared young and older subjects' behavioral performance, eye movement parameters and EEG activity across the three conditions of encoding and test phases of the navigational task. We used a GMM on participants' fixation data to precisely delineate the upper and lower AOIs and to conduct statistics on these regions (Figure **8.1b**). We investigated dynamic cortical correlates of scene observation in the three ROIs (OPA, PPA, MPA) using ERSPs analysis on source-reconstructed EEG data. We looked for significant patterns in the ERSPs and their variations across age groups and conditions within each ROI. Guided by the main contrasts of the latter results, we conducted follow-up analyses to delineate ROI differences per age group within specific frequency bands.

8.5.1 Navigational behavior varies as a function of age but not condition

We assessed participants' performance on the spatial navigation task by computing the number of errors made during the test phase and by identifying the strategy used to reorient (mental map users *vs.* non mental map users). Across all three conditions, the average performance of young adults (0.22 ± 0.22 errors per intersection [mean $\pm$ SD]; $t(62) = -28.67$, $p < 0.001$, d $= 3.61$) and the average performance of older adults (0.74 ± 0.19 errors per intersection; $t(62) = -11.27$, $p < 0.001$, d $= 1.42$) were significantly above the chance level of 1 error per intersection. A chi-square test of independence revealed that there was a significant association between age and strategy ($\chi^2(1,\ N = 42) = 16.43$, $p < 0.001$). A significantly greater proportion of young participants ($19/21$) reported being mental map users compared with older participants ($5/21$). A second chi-square test showed a significant relationship between age and object selection ($\chi^2(1,\ N = 42) = 11.76$, $p < 0.001$). Older adults reported relying on the 4 objects at intersections ($15/21$) in significantly greater proportion than young participants ($3/21$) who were more inclined to select a subset of objects.

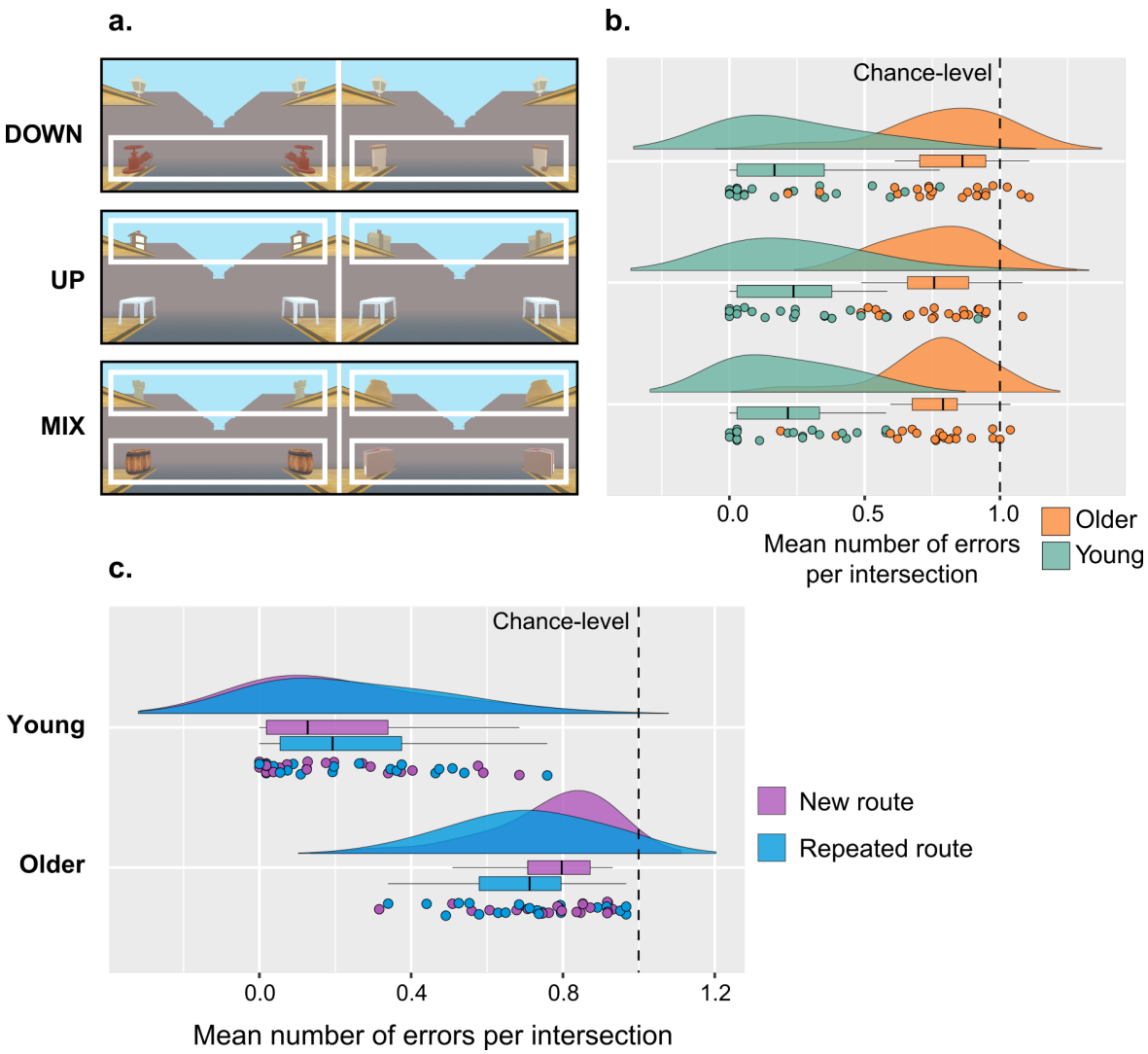

Figure 8.2: Conditions presentation and mean number of errors per intersection depending on the age group, the condition and the trial type. **a**. Screenshots of two intersections of a DOWN, UP, and MIX condition. The white boxes highlight the objects that are navigationally relevant in each condition. Note that in a MIX condition all objects are helpful to orient. **b**. Distributions of the mean number of errors per intersection according to the condition in young and older adults. Age has a significant influence on navigational performance ($F(1,37) = 28.57$, $p < 0.001$, $\eta_p^2 = 0.44$, 95% CI $= [0.20, 0.61]$). **c**. Distributions of the mean number of errors per intersection for a new or repeated route in young and older adults. Older adults perform better on repeated routes than on new routes ($t(208) = 1.57$, $p = 0.0096$, $d = 0.37$, SEM $= 0.18$).

We then ran a linear mixed model aimed at explaining the number of errors with participants as random intercepts and age, sex, condition, and strategy as fixed effects. Interactions between age, condition and strategy were discarded as they resulted in worse model fits. First, we found that age had a significant influence on navigational performance ($F(1,37) = 17.98$, $p < 0.001$, $\eta_p^2 = 0.33$, 95% CI $= [0.10, 0.53]$; Figure **8.2b**) with older subjects making more errors than young subjects per intersection (older: 0.74 ± 0.19; young: 0.22 ± 0.22). Moreover, there was a main effect of sex on the mean number of mistakes per intersection made during the test phase ($F(1,37) = 12.95$, $p < 0.001$, $\eta_p^2 = 0.26$, 95% CI $= [0.054, 0.47]$) with more errors reported in females (0.6 ± 0.27 errors per in-

tersection) than in males (0.39 ± 0.33 errors per intersection). We also found an influence of strategy on navigational performance ($F(1,37) = 10.97$, $p = 0.0021$, $\eta_p^2 = 0.23$, 95% CI $= [0.037, 0.44]$). Across age groups, individuals who did not use a mental map to reorient (0.74 ± 0.18 errors per intersection) displayed significantly worse performance than those who did (0.28 ± 0.27 errors per intersection). The linear mixed model did not reveal any evidence for an effect of condition on navigation performance ($F(2,208) = 0.50$, $p = 0.61$, $\eta_p^2 = 0.0048$, 95% CI $= [0.00, 0.033]$). We ran a second linear mixed model with participants as random intercepts to investigate the impact of repeated *vs.* new test trials on behavioral performance. Our results indicated that there was a significant interaction between age and type of test trial on performance ($F(1,208) = 8.38$, $p = 0.0042$, $\eta_p^2 = 0.039$, 95% CI $= [0.0040, 0.10]$; Figure **8.2c**). We found a significant difference between repeated and new routes in older adults only ($t(208) = 1.57$, $p = 0.0096$, $d = 0.37$, SEM $= 0.18$), with new routes leading to a greater average number of mistakes (0.77 ± 0.16 errors per intersection) compared with repeated routes (0.70 ± 0.18 errors per intersection).

Finally, we assessed associations between performance on the spatial navigation task and neuropsychological test scores. The overall linear regression models for the perspective-taking ($R^2 = 0.65$, $F(2,39) = 35.61$, $p < 0.001$) and 3D mental rotation tasks ($R^2 = 0.64$, $F(2,36) = 31.76$, $p < 0.001$) were statistically significant. We found that lower performance on the perspective-taking ($\beta = 0.073$, $p = 0.011$, $\eta_p^2 = 0.15$, 95% CI $= [0.0087, 0.36]$) and on the 3D mental rotation ($\beta = -0.37$, $p = 0.022$, $\eta_p^2 = 0.14$, 95% CI $= [0.0014, 0.35]$) tasks were associated with a significantly greater number of navigational errors across all participants.

8.5.2 Adapting gaze patterns to the condition is impaired in older age

8.5.2.1 Gaze patterns during the encoding phase

We first examined participants' gaze patterns across all 4-second observation periods of the encoding phase. We ran separate linear mixed models to study the effects of age, condition, and sex on DT in the lower, upper, and central AOI. Regarding the proportion of time spent looking at the lower AOI, we found little evidence for main effects of age ($F(1,38) = 1.25$, $p = 0.27$, $\eta_p^2 = 0.032$, 95% CI $= [0.00, 0.20]$) or sex ($F(1,38) = 3.67$, $p = 0.063$, $\eta_p^2 = 0.088$, 95% CI $= [0.00, 0.29]$). However, we uncovered a significant influence of condition on DT in the lower AOI ($F(2,317) = 3.60$, $p = 0.020$, $\eta_p^2 = 0.022$, 95% CI $= [0.00, 0.060]$). Post-hoc comparisons showed a significant difference between the DOWN and MIX conditions ($t(317) = -2.90$, $p = 0.035$, $d = 0.24$, SEM $= 0.13$), with longer time spent looking at the lower AOI in the MIX condition ($37.02\% \pm 11.73\%$ [mean $\pm$ SD]) than in the DOWN condition ($34.12\% \pm 12.77\%$) across all participants. We then examined the upper AOI and we found no evidence that age ($F(1,38) = 0.83$, $p = 0.37$, $\eta_p^2 = 0.021$, 95% CI $= [0.00, 0.17]$) or sex ($F(1,38) = 0.74$, $p = 0.40$, $\eta_p^2 = 0.010$, 95% CI $= [0.00, 0.15]$) significantly predicted DT in that area. There was a significant main effect of condition on DT in the upper AOI ($F(2,315) = 6.03$, $p = 0.0027$, $\eta_p^2 = 0.037$, 95% CI $= [0.0049, 0.083]$). Post-hoc Tukey testing revealed that upper DT was signifi-

cantly different between the MIX and UP conditions ($t(315) = 3.70$, $p = 0.0040$, $d = 0.31$, SEM $= 0.13$) and between the MIX and DOWN conditions ($t(315) = -3.13$, $p = 0.018$, $d = 0.24$, SEM $= 0.13$). Participants spent longer fixating the upper AOI during the MIX condition ($35.34\% \pm 13.46\%$) than during the UP ($31.30\% \pm 12.80\%$) and DOWN conditions ($32.11\% \pm 13.73\%$).

Finally, there was little evidence to support a main effect of age ($F(1,38) = 0.0004$, $p = 0.98$, $\eta_p^2 = 0.00$, 95% CI $= [0.00, 0.00]$) on central DT. We nonetheless found that sex ($F(1,38) = 4.55$, $p = 0.040$, $\eta_p^2 = 0.11$, 95% CI $= [0.00, 0.31]$) and condition ($F(2,315) = 13.21$, $p < 0.001$, $\eta_p^2 = 0.077$, 95% CI $= [0.028, 0.14]$) had significant influences on time spent looking at the central AOI. We uncovered that central DT in male participants ($35.65\% \pm 14.81\%$) was superior to central DT in female participants ($27.15\% \pm 16.90\%$). Post-hoc comparisons also showed significant differences in central DT between the MIX and UP conditions ($t(315) = -6.17$, $p < 0.001$, $d = 0.41$, SEM $= 0.13$) and between the MIX and DOWN conditions ($t(315) = 6.16$, $p < 0.001$, $d = 0.40$, SEM $= 0.13$), with all participants fixating the central AOI longer during the UP ($34.14\% \pm 17.50\%$) and DOWN conditions ($33.77\% \pm 16.23\%$) than during the MIX condition ($27.64\% \pm 14.38\%$). We ran another linear mixed model to investigate the influence of age, sex, and condition on the VMA for DT. The VMA computes the vertical asymmetry in the distribution of time spent looking at the AOIs. We found no evidence for main effects of age ($F(1,38) = 2.02$, $p = 0.16$, $\eta_p^2 = 0.050$, 95% CI $= [0.00, 0.23]$), sex ($F(1,38) = 0.34$, $p = 0.57$, $\eta_p^2 = 0.012$, 95% CI $= [0.00, 0.19]$), or condition ($F(2,317) = 0.19$, $p = 0.83$, $\eta_p^2 = 0.0012$, 95% CI $= [0.00, 0.013]$) on the VMA for DT. The distribution of time spent looking across the upper and lower AOIs remains stable across conditions. One-sample Wilcoxon signed rank tests (WSRTs) showed that the mean VMA per condition per block was significantly different from zero in older participants ($V(182) = 11387$, $p < 0.001$, $median = 18.52$, 95% CI $= [10.07, 26.76]$, $r = 0.31$) but not in young participants ($V(178) = 7768$, $p = 0.68$, $median = -2.00$, 95% CI $= [-11.31, 6.85]$, $r = 0.031$).

Finally, we ran linear mixed models to study the proportion of first fixations across all intersections of the encoding phase directed towards the lower, upper, or central AOIs. We stress that the term first fixation refers to the very first fixation upon arrival at each intersection, *i.e.*, the first fixated AOI at each intersection. We found no evidence to support a significant influence of age ($F(1,39) = 0.0002$, $p = 0.99$, $\eta_p^2 = 0.00$, 95% CI $= [0.00, 0.00]$), sex ($F(1,39) = 1.66$, $p = 0.20$, $\eta_p^2 = 0.041$, 95% CI $= [0.00, 0.21]$) or condition ($F(2,325) = 1.10$, $p = 0.33$, $\eta_p^2 = 0.0068$, 95% CI $= [0.00, 0.031]$) on the proportion of first fixations directed towards the lower AOI. Moreover there was no evidence for statistically significant main effects of sex ($F(1,39) = 0.63$, $p = 0.43$, $\eta_p^2 = 0.016$, 95% CI $= [0.00, 0.16]$) or condition ($F(2,323) = 1.42$, $p = 0.24$, $\eta_p^2 = 0.0087$, 95% CI $= [0.00, 0.035]$) on the proportion of first fixations located in the upper AOI. We found that age ($F(1,39) = 5.22$, $p = 0.028$, $\eta_p^2 = 0.12$, 95% CI $= [0.00, 0.32]$) and the interaction between age and condition ($F(2,323) = 3.56$, $p = 0.030$, $\eta_p^2 = 0.022$, 95% CI $= [0.00, 0.059]$; Figures **8.3a-b**) significantly predicted the proportion of upper first fixations. Young participants had a greater proportion of first fixations directed towards the upper AOI than

did older participants across conditions (young: $34.57\% \pm 23.84\%$ [mean $\pm$ SD]; older: $21.93\% \pm 22.14\%$). Furthermore, post-hoc tests revealed an absence of significant pairwise comparisons for the interaction of age and condition. There was no evidence to indicate that sex ($F(1,39) = 0.28$, $p = 0.60$, $\eta_p^2 = 0.0072$, 95% CI $= [0.00, 0.14]$) significantly pre-

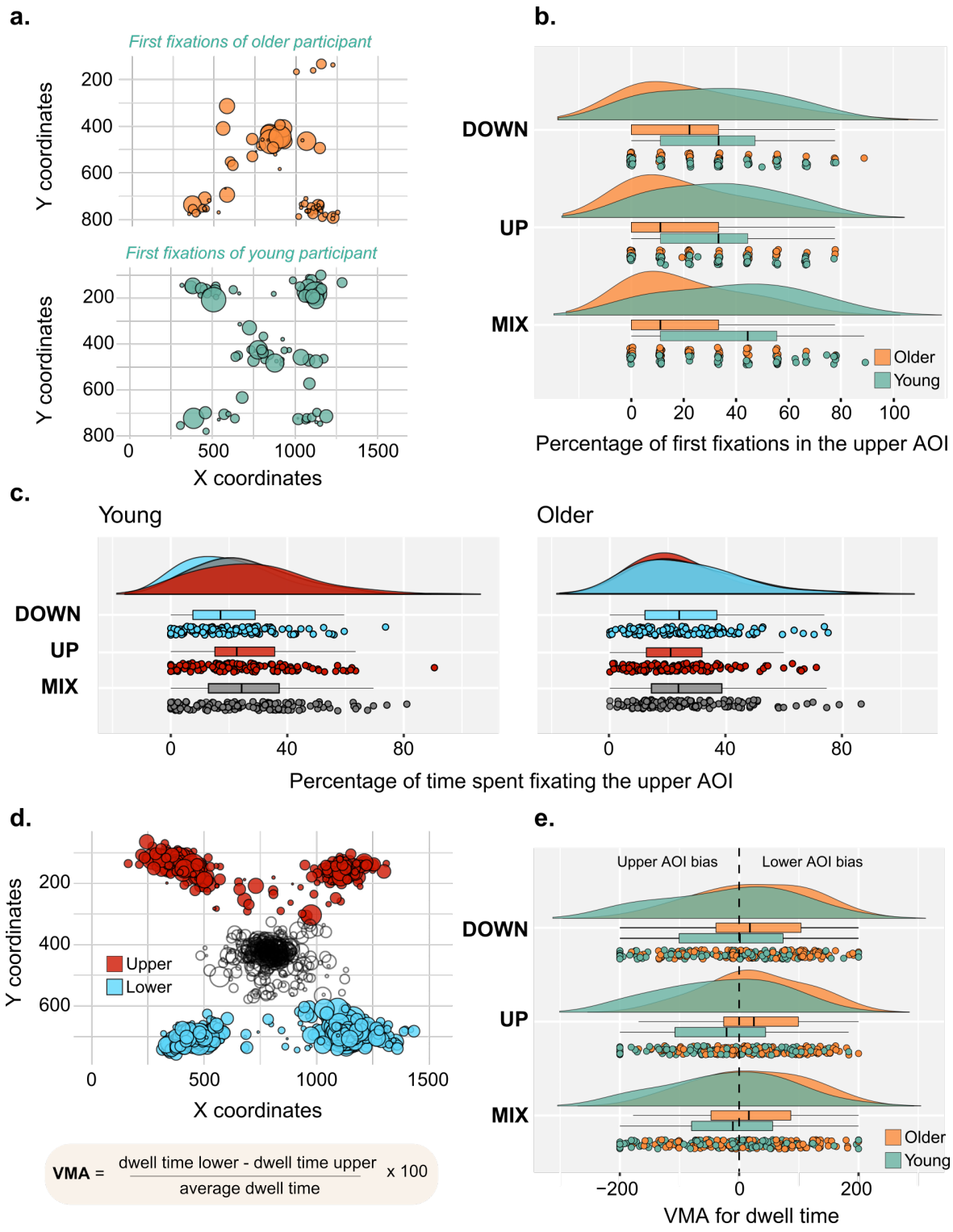

Figure 8.3: Eye movement parameters in young and older participants. [Continued on next page]

Figure 8.3: [On previous page] **a**. Depiction of all first fixations at the start of intersections during the encoding phase for an example older participant and an example young participant. Dots represent fixations and their size covaries with the duration of the fixation. **b**. Distributions of the percentage of first fixations situated in the upper AOI in young and older adults across conditions during the encoding phase. Age is a significant predictor of first fixations in the upper AOI ($F(1,39) = 5.22$, $p = 0.028$, $\eta_p^2 = 0.12$, 95% CI = $[0.00, 0.32]$). **c**. Distributions of the percentage of time spent fixating the upper AOI in young and older adults across conditions during the 4 seconds after arriving at the intersection in the test phase. There were significant differences in upper DT between the DOWN and MIX conditions ($t(677) = -7.76$, $p < 0.001$, $d = 0.47$, SEM = 0.13) and between the DOWN and UP conditions ($t(677) = -5.75$, $p < 0.001$, $d = 0.35$, SEM = 0.13) in young adults only. **d**. Depiction of all fixations during the 4 seconds after arriving at the intersection in the test phase for an example participant. The VMA computes the difference in DT between the lower and upper AOIs. Indices that are close to 0 indicate no asymmetry in DT between the upper and lower AOIs, indices that are superior to 0 indicate a bias for the lower AOI, and indices that are inferior to 0 indicate a bias for the upper AOI. Dots represent fixations and their size covaries with the duration of the fixation. **e**. Distributions of the VMA for DT in young and older adults across conditions during the test phase. Age is a significant predictor of the VMA ($F(1,38) = 4.70$, $p = 0.036$, $\eta_p^2 = 0.11$, 95% CI = $[0.00, 0.31]$).

dicted the proportion of first fixations situated in the central AOI. However, we did reveal main effects of age ($F(1,39) = 7.65$, $p = 0.0086$, $\eta_p^2 = 0.16$, 95% CI = $[0.012, 0.37]$) and condition ($F(2,323) = 3.72$, $p = 0.025$, $\eta_p^2 = 0.023$, 95% CI = $[0.00, 0.060]$). Older participants looked at the central cluster at the start of each intersection to a significantly greater extent than young participants (young: $39.18\% \pm 18.69\%$; older: $53.43\% \pm 22.76\%$). We also found the interaction between age and condition to be significant ($F(2,323) = 3.71$, $p = 0.022$, $\eta_p^2 = 0.022$, 95% CI = $[0.00, 0.060]$). Post-hoc Tukey tests showed a significant age-related difference in the proportion of central first fixations during the UP condition only ($t(55) = 17.47$, $p = 0.023$, $d = 0.89$, SEM = 0.19). Indeed, older participants fixated the central AOI at the start of UP intersections to a greater extent than did young participants (young: $38.24\% \pm 16.57\%$; older: $56.11\% \pm 23.18\%$). We also found a significant difference between the DOWN and MIX conditions in young adults ($t(323) = 8.60$, $p = 0.012$, $d = 0.45$, SEM = 0.18). Young participants had a significantly greater proportion of first fixations located in the central AOI during the DOWN condition ($43.94\% \pm 21.62\%$) than during the MIX condition ($35.34\% \pm 16.64\%$).

8.5.2.2 Gaze patterns during the test phase

We then focused our analysis on participants' gaze patterns across all pre-decision intervals of the test phase. The latter correspond to the periods between arrival at the intersection and pressing a key to indicate the correct direction of travel. They were restricted to a maximum of 4 seconds even if participants took longer to make a decision.

We ran separate linear mixed models to test the influence of age, condition, and sex on the proportion of time spent looking at the upper, lower, and central AOIs. We found no evidence to support a main effect of age ($F(1,38) = 0.072$, $p = 0.79$, $\eta_p^2 = 0.0019$, 95% CI = $[0.00, 0.10]$) on the proportion of upper DT. There were, however, statistically significant influences of sex ($F(1,38) = 4.69$, $p = 0.037$, $\eta_p^2 = 0.11$, 95% CI = $[0.00, 0.31]$), condition ($F(2,677) = 10.76$, $p < 0.001$, $\eta_p^2 = 0.031$, 95% CI = $[0.0093, 0.059]$), and the interaction between age and condition ($F(2,677) = 8.56$, $p < 0.001$, $\eta_p^2 = 0.025$, 95% CI =

[0.0058, 0.051]; Figure **8.3c**) on the proportion of time spent fixating the upper AOI. Indeed, DT in the upper AOI was superior in female participants ($30.05\% \pm 17.84\%$ [mean $\pm$ SD]) than in male participants ($21.37\% \pm 14.65\%$). Post-hoc Tukey tests showed that there were significant differences in upper DT between conditions in young adults only, between the DOWN and MIX conditions ($t(677) = -7.76$, $p < 0.001$, $d = 0.47$, SEM $= 0.13$) and between the DOWN and UP conditions ($t(677) = -5.75$, $p < 0.001$, $d = 0.35$, SEM $= 0.13$). Young participants spent less time fixating the upper AOI during the DOWN condition ($20.58\% \pm 15.03\%$) than during the MIX ($28.34\% \pm 17.84\%$) and UP conditions ($26.12\% \pm 16.61\%$). Examining lower DT, we found no evidence for significant main effects of age ($F(1,38) = 4.09$, $p = 0.050$, $\eta_p^2 = 0.097$, 95% CI $= [0.00, 0.30]$) or sex ($F(1,38) = 1.76$, $p = 0.19$, $\eta_p^2 = 0.044$, 95% CI $= [0.00, 0.22]$). We nonetheless revealed that condition was a significant predictor of the proportion of time spent in the lower AOI ($F(2,679) = 3.22$, $p = 0.041$, $\eta_p^2 = 0.0094$, 95% CI $= [0.00, 0.027]$). There were significant differences in lower DT between the DOWN and MIX conditions ($t(679) = -2.49$, $p = 0.031$, $d = 0.14$, SEM $= 0.091$) across all participants. They spent more time looking at the lower AOI during the MIX condition ($28.13\% \pm 17.45\%$) than during the DOWN condition ($25.63\% \pm 17.84\%$). Moreover, the linear mixed model analyzing DT in the central AOI revealed no evidence that age was a significant predictor ($F(1,38) = 1.99$, $p = 0.17$, $\eta_p^2 = 0.050$, 95% CI $= [0.00, 0.23]$). However, we found main effects of sex ($F(1,38) = 7.06$, $p = 0.011$, $\eta_p^2 = 0.16$, 95% CI $= [0.0086, 0.37]$), condition ($F(2,677) = 17.67$, $p < 0.001$, $\eta_p^2 = 0.050$, 95% CI $= [0.021, 0.084]$), and the interaction between age and condition ($F(2,677) = 10.30$, $p < 0.001$, $\eta_p^2 = 0.030$, 95% CI $= [0.0085, 0.057]$) on central DT. Male participants spent significantly more time fixating the central AOI than did female participants (male: $55.21\% \pm 20.96\%$; female: $38.91\% \pm 21.45\%$). In addition, post-hoc pairwise comparisons showed central DT differences between the DOWN and MIX conditions ($t(677) = 11.98$, $p < 0.001$, $d = -0.52$, SEM $= 0.13$) and between the DOWN and UP conditions ($t(677) = 7.49$, $p < 0.001$, $d = -0.31$, SEM $= 0.13$) in young adults only. Indeed, young participants spent significantly more time looking at the central AOI during the DOWN condition ($59.34\% \pm 23.77\%$) than during the MIX ($47.35\% \pm 22.33\%$) and UP conditions ($52.15\% \pm 23.25\%$). To complement the analyses regarding DT proportions, we ran a linear mixed model examining the influence of age, sex, and condition on the VMA for DT. Whereas we found no evidence to suggest main effects of sex ($F(1,38) = 0.43$, $p = 0.51$, $\eta_p^2 = 0.011$, 95% CI $= [0.00, 0.15]$) or condition ($F(2,670) = 0.37$, $p = 0.69$, $\eta_p^2 = 0.0011$, 95% CI $= [0.00, 0.0089]$) on the VMA, we did show that age ($F(1,38) = 4.70$, $p = 0.036$, $\eta_p^2 = 0.11$, 95% CI $= [0.00, 0.31]$; Figures **8.3d-e**) was a significant predictor of the VMA. The VMA in older adults (23.74 ± 88.20) was significantly higher than the VMA in young adults (-20.35 ± 101.72), underlining a greater fixation bias towards the lower AOI in older age. One-sample WSRTs revealed that the mean VMA per condition per block was significantly different from zero in young ($V(178) = 5736$, $p = 0.023$, *median* $= -17.67$, 95% CI $= [-32.34, -2.42]$, $r = 0.17$) and in older participants ($V(183) = 11029$, $p < 0.001$, *median* $= 24.76$, 95% CI $= [11.65, 37.40]$, $r = 0.27$).

We ran additional linear mixed models to study the proportion of first fixations across all intersections of the test phase situated in the lower, upper, or central AOIs. We reported no statistical evidence for main effects of age ($F(1,39) = 1.09$, $p = 0.30$, $\eta_p^2 = 0.027$, 95% CI $= [0.00, 0.19]$), sex ($F(1,39) = 0.48$, $p = 0.49$, $\eta_p^2 = 0.012$, 95% CI $= [0.00, 0.15]$) or condition ($F(2,327) = 2.57$, $p = 0.078$, $\eta_p^2 = 0.015$, 95% CI $= [0.00, 0.048]$) on the proportion of first fixations located in the lower AOI. Regarding first fixations towards the upper AOI, we found no evidence to support influences of age ($F(1,39) = 0.33$, $p = 0.57$, $\eta_p^2 = 0.0083$, 95% CI $= [0.00, 0.14]$) or sex ($F(1,39) = 1.71$, $p = 0.20$, $\eta_p^2 = 0.042$, 95% CI $= [0.00, 0.22]$). However, we did reveal that condition predicted the proportion of upper first fixations ($F(2,327) = 6.35$, $p = 0.0020$, $\eta_p^2 = 0.037$, 95% CI $= [0.0056, 0.083]$). Post-hoc Tukey testing revealed significant differences between the DOWN and UP conditions ($t(325) = -5.16$, $p = 0.0026$, d= 0.23, SEM $= 0.13$) as well as between the DOWN and MIX conditions ($t(325) = -4.18$, $p = 0.020$, $d = 0.20$, SEM $= 0.13$). Across age groups, participants directed less first fixations towards the upper AOI during the DOWN condition ($21.62\% \pm 19.81\%$ [mean $\pm$ SD]) than during the UP ($26.56\% \pm 23.46\%$) and MIX conditions ($25.80\% \pm 22.88\%$). Finally, while we did not find any evidence for a main effect of age ($F(1,39) = 0.20$, $p = 0.66$, $\eta_p^2 = 0.0051$, 95% CI $= [0.00, 0.13]$) or sex ($F(1,39) = 0.42$, $p = 0.52$, $\eta_p^2 = 0.011$, 95% CI $= [0.00, 0.15]$), we uncovered a main effect of condition ($F(2,325) = 13.72$, $p < 0.001$, $\eta_p^2 = 0.078$, 95% CI $= [0.029, 0.14]$), and a significant interaction between age and condition ($F(2,325) = 5.53$, $p = 0.0044$, $\eta_p^2 = 0.033$, 95% CI $= [0.0036, 0.076]$) on the proportion of first fixations situated in the central AOI. Post-hoc Tukey testing showed differences between the DOWN and UP conditions ($t(323) = 13.26$, $p < 0.001$, $d = 0.51$, SEM $= 0.18$) and between the DOWN and MIX conditions ($t(323) = 10.89$, $p < 0.001$, $d = 0.43$, SEM $= 0.18$) in young adults only. At the start of each intersection, young participants had a greater proportion of fixations that were situated in the central AOI during the DOWN condition ($57.59\% \pm 26.75\%$) than during the UP ($44.87\% \pm 23.46\%$) and MIX conditions ($46.70\% \pm 24.17\%$).

8.5.3 EEG activity in SSRs differs across age groups and conditions

To enable the most accurate spatial allocation of EEG activity, we relied on a fMRI informed source reconstruction model tailored to each participant (Cottereau et al., 2012, 2015). Individual data included MRI anatomical scans for head and brain structure, a fMRI localizer task for SSRs (Ramanoël et al., 2020) and a 3D model of electrode positions co-registered with the anatomical MRI data. We solved the inverse problem using the L2-regularized MNE model (Hämäläinen et al., 1993).

We conducted an ERSP analysis time-locked to the event of arriving at an intersection ($t = 0$ ms) and grouped by principal frequency bands (delta: < 4 Hz, theta: 4-8 Hz, alpha: 8-12 Hz, beta: 12-30 Hz, gamma: > 30 Hz). We averaged the source-reconstructed power spectrum from both hemispheres to summarize bilateral ROI activity, as we did not have any hypothesis on lateralized effects. We reported average ERSPs baselined with the activity preceding the arrival at the level of an intersection. This baseline corresponds to partici-

pants passively navigating through a street that is devoid of any relevant spatial information. We computed ERSP statistical differences with permutation tests based on the maximum cluster-level statistic (Maris & Oostenveld, 2007) using 1000 permutations. We set the initial significance level to $p < 0.05$, and Bonferroni-corrected for variables with more than 2 levels.

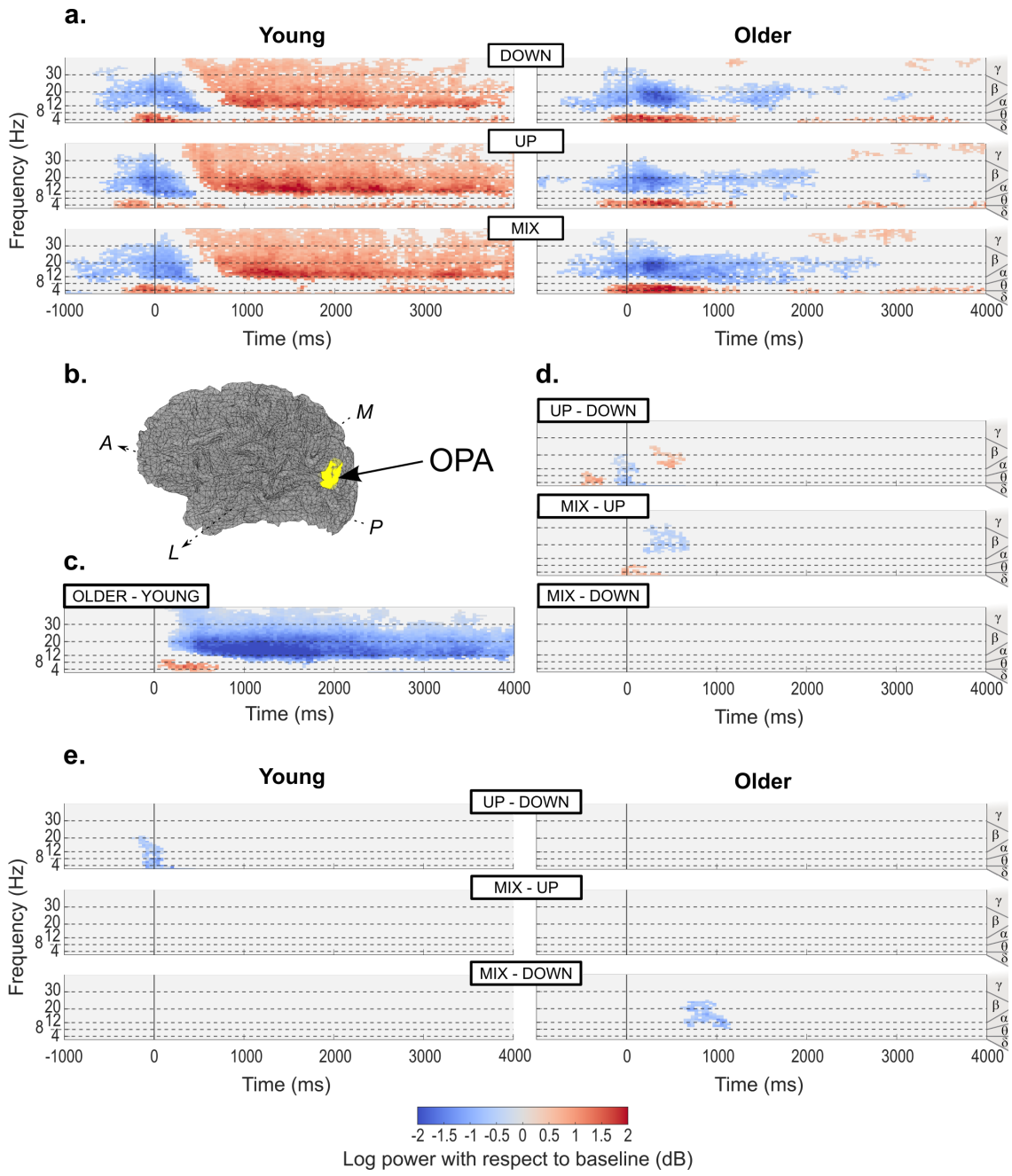

Figure 8.4: ERSP activity time-locked to the event of arriving at an intersection in the test trials, reconstructed in the OPA. [Continued on next page]

Figure 8.4: [On previous page] Activity merged from both hemispheric locations after source reconstruction. We examined delta (δ; < 4 Hz), theta (θ; 4-8 Hz), alpha (α; 8-12 Hz), beta (β; 12-30 Hz) and gamma (γ; > 30 Hz) frequency bands. We investigated all statistical differences with permutation tests based on the maximum cluster-level statistic using 1000 permutations. We used linear mixed-effects modeling to evaluate the statistical significance at the 'pixel' level (spectral power at a given time-frequency pair) for a given permutation. **a**. Average activity per age group and condition baselined with the 2 seconds period prior to arrival at the intersection. We only display activity statistically different from surrogate baseline distribution ($p < 0.05$). **b**. Illustration of the localization of the left OPA overlaid on left hemisphere source space (midgray surface) in one young participant. A: Anterior; P: Posterior; M: Medial; L: Lateral. **c**. Differences between age groups, irrespective of conditions. We indicate the direction of the difference above each graph (*e.g.* for the graph entitled 'OLDER-YOUNG', we subtracted the average signal for the young adults from the average signal for the older adults, such that a positive difference means more power in the older group than in the young group and a negative difference means less power in the older group than in the young group). We only display statistically significant differences ($p < 0.05$). **d**. Differences between conditions, irrespective of age groups. We only display statistically significant differences ($p < 0.0083$, Bonferroni-corrected for 3 two-sided comparisons). **e**. Differences between conditions within each age group. We only display statistically significant differences ($p < 0.0041$, Bonferroni-corrected for 6 two-sided comparisons).

8.5.3.1 Encoding trials

The investigated ERSP activity during the encoding trials relates to the perception of the intersection and the objects contained within it. We allowed participants a fixed 4-second static observation period at each intersection to give them enough time to scan the whole scene and encode the spatial relationships between intersections (see Figure **8.1b**). We found ERSP activity during the encoding trials to be highly similar to that associated with the test trials, particularly with regards to the patterns of average activity and age-related differences. Worthy of note, there are half as many trials in the encoding phase as in the test phase, which increases statistical power in the latter. We therefore chose to only present results relative to test trials and we refer the interested reader to the Supplementary Figures **E.1**, **E.2**, and **E.3** for a thorough description of ERSP activity during the encoding phase.

8.5.3.2 Test trials

The investigated ERSP activity during test trials relates to the observation phase at the intersection prior to the navigational decision. Therefore, this static observation and decision period depended on the time it took for participants to choose the correct direction. To be consistent with the fixed observation time during the encoding trials, we inspected the first 4 seconds of cortical activity following arrival at the intersection.

8.5.3.2.1 ERSP activity in the ROIs

First, we found a sustained synchronization in the delta/theta frequency band (2-8 Hz) across all ROIs in both age groups, starting 250 ms before event onset and sustained over the 4-second window (Figures **8.4a**, **8.5a**, **8.6a**). It was more pronounced during the first second of observation, particularly in the older adult group. Indeed, we reported a significant increase in synchronization in the theta band between $+100$ ms and $+750$ ms after arrival at the intersection in the OPA (Figure **8.4c**) and MPA of older participants (Figure **8.6c**).

In all ROIs, we also observed significant differences in the lower frequency band between the conditions irrespective of the age group. In the OPA only, the theta synchroniza-

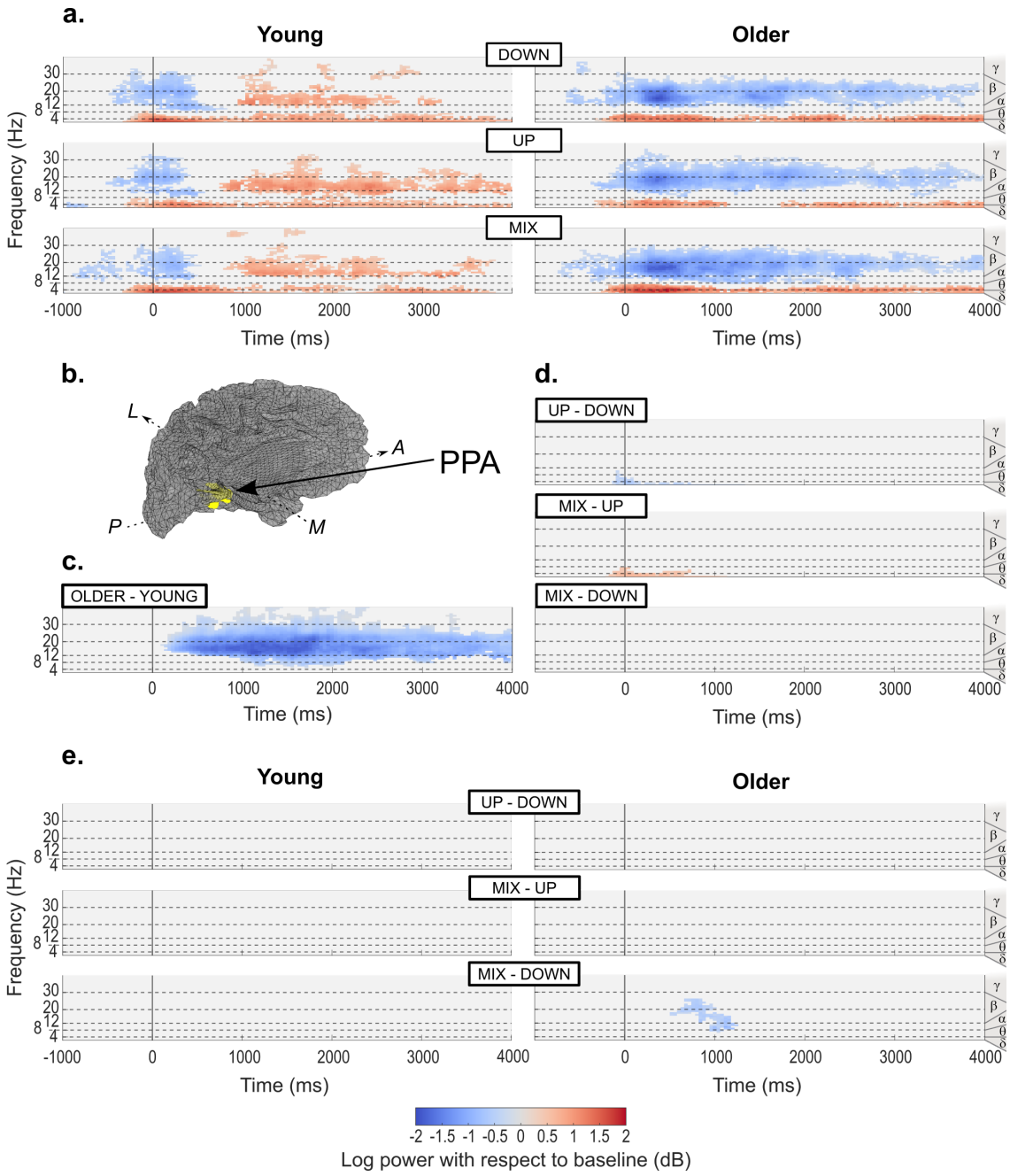

Figure 8.5: ERSP activity time-locked to the event of arriving at an intersection in the test trials, reconstructed in the PPA. For further details, see Figure **8.4** legend. **a**. Average activity per age group and condition baselined with the 2 seconds period prior to arrival at the intersection. We only display activity statistically different from surrogate baseline distribution ($p < 0.05$). **b**. Illustration of the localization of the left PPA overlaid on left hemisphere source space (midgray surface) in one young participant. A: Anterior; P: Posterior; M: Medial; L: Lateral. **c**. Differences between age groups, irrespective of conditions. We only display statistically significant differences ($p < 0.05$). **d**. Differences between conditions, irrespective of age groups. We only display statistically significant differences ($p < 0.0083$, Bonferroni-corrected for 3 two-sided comparisons). **e**. Differences between conditions within each age group. We only display statistically significant differences ($p < 0.0041$, Bonferroni-corrected for 6 two-sided comparisons).

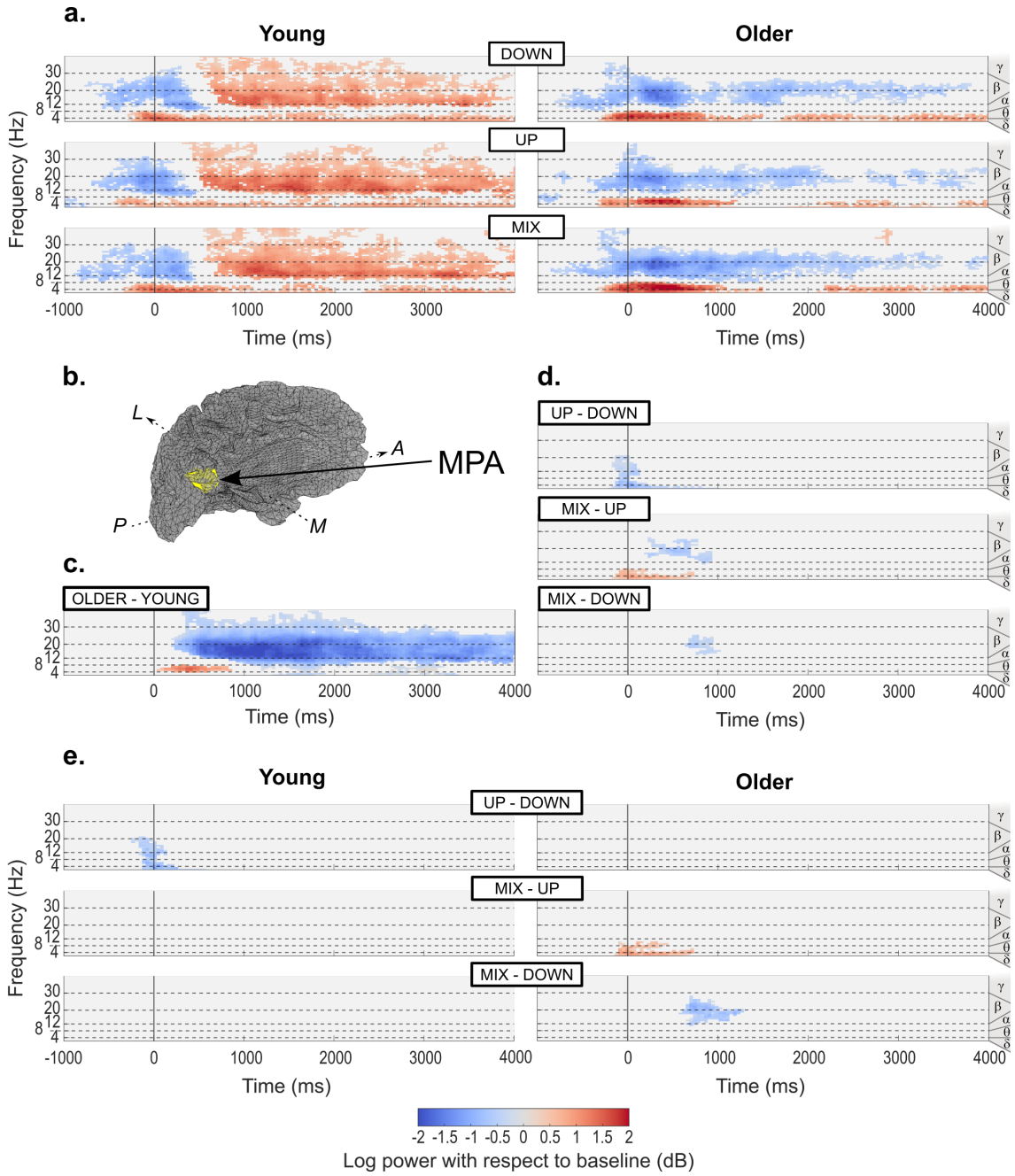

Figure 8.6: ERSP activity time-locked to the event of arriving at an intersection in the test trials, reconstructed in the MPA. For further details, see Figure **8.4** legend. **a**. Average activity per age group and condition baselined with the 2 seconds period prior to arrival at the intersection. We only display activity statistically different from surrogate baseline distribution ($p < 0.05$). **b**. Illustration of the localization of the left MPA overlaid on left hemisphere source space (midgray surface) in one young participant. A: Anterior; P: Posterior; M: Medial; L: Lateral. **c**. Differences between age groups, irrespective of conditions. We only display statistically significant differences ($p < 0.05$). **d**. Differences between conditions, irrespective of age groups. We only display statistically significant differences ($p < 0.0083$, Bonferroni-corrected for 3 two-sided comparisons). **e**. Differences between conditions within each age group. We only display statistically significant differences ($p < 0.0041$, Bonferroni-corrected for 6 two-sided comparisons).

tion started earlier, 500 ms prior to arriving at the intersection, in the UP condition than in the DOWN condition (Figure **8.4d**). We also found a significant decrease of delta/theta synchronization upon reaching the intersection in the UP condition with respect to DOWN and MIX conditions in all ROIs (Figures **8.4d**, **8.5d**, **8.6d**). This effect lasted until +750 ms in the PPA (Figure **8.5d**) and MPA (Fig. 6d), but stopped at around +250 ms in the OPA (Figure **8.4d**). When analyzing differences between the conditions within each age group, we revealed a significantly lower synchronization in the UP condition than in the DOWN condition between −100 ms and +250 ms in the OPA (Figure **8.4e**) and MPA of young participants (Figure **8.6e**). Finally, we noted a significantly stronger synchronization in the MIX condition than in the UP condition up until +750 ms in the MPA of older adults only (Figure **8.6e**).

Commonly to both age groups and all ROIs (Figures **8.4a**, **8.5a**, **8.6a**), we found a strong desynchronization spanning the beta band between −500 ms and +500 ms around the event of arriving at the intersection. Notably, after +200 ms this desynchronization was significantly more pronounced in older adults than in young adults for all ROIs (Figures **8.4c**, **8.5c**, **8.6c**). While the beta desynchronization continued after +500 ms in the older group, we observed an inversion leading to a strong power synchronization in the young group (Figures **8.4a**, **8.5a**, **8.6a**). This age-related divergence between activity patterns remained consistent until the end of the 4-second window (Figures **8.4c**, **8.5c**, **8.6c**). In the three ROIs of young participants, and particularly in the OPA, a significant low gamma band (30-40 Hz) synchronization accompanied the age-specific beta band synchronization (Figures **8.4a**, **8.5a**, **8.6a**). This activity remained significantly more synchronized in young adults than in older adults between +500 ms and +2500 ms (Figures **8.4c**, **8.5c**, **8.6c**).

Differences between conditions were more specific to the ROI in this range of frequencies than in lower frequencies. In the OPA (Figure **8.4d**) and MPA (Figure **8.6d**), we found a significantly greater desynchronization in the low beta band (12-20 Hz) for the UP condition than for the DOWN condition around the synchronizing event. Breaking down the analysis within age groups, we reported that this significant difference was mostly attributable to young participants (Figures **8.4e**, **8.6e**). In the OPA just before +500 ms, we also noted a significantly greater beta band desynchronization in the DOWN and MIX conditions compared to the UP condition (Figure **8.4d**). In the MPA between +500 ms and +1000 ms, there was a significantly more pronounced beta band desynchronization in the MIX condition than in the UP and DOWN conditions (Figure **8.6d**). Finally, we found a more sustained beta band desynchronization in the MIX condition than in the DOWN condition between +500 ms and +1000 ms, in the OPA, PPA and MPA of older participants (Figures **8.4e**, **8.5e**, **8.6e**).

8.5.3.2.2 Mean ERSP activity per frequency band across ROIs

In a follow-up analysis of activity during the test phase, we sought to compare time-resolved spectral activity between ROIs. We grouped the ERSP activity by frequency band: delta/theta (2-8 Hz), alpha (8-12 Hz), beta (12-30 Hz), and low gamma (30-40 Hz). Within each frequency band we averaged the ERSPs over the spectral dimension, yielding a time-course of mean spectral activity for each ROI across conditions. Using an independent model for

each age group, we then performed pairwise statistical analysis with paired permutation tests based on the maximum cluster-level statistic using 1000 permutations. We set the significance level to $p < 0.00104$, Bonferroni-corrected for 24 two-sided comparisons. We displayed results pertaining to the alpha band in Supplementary Figure **E.4** due the absence of significant activity observed in this frequency range in the previous analysis.

In the lowest frequencies, we observed a strong increase in power synchronization around the time of arrival at the intersection across all ROIs and in both age groups (Figures **8.7a-b**). In the OPA and MPA only, we found the peak of synchronization to be significantly higher and sharper in young participants compared to older participants (Figures **8.4c**, **8.6c**). In the young group, we reported the delta/theta burst of activity to be earlier and more transient in the OPA than in other ROIs (Figure **8.7a**). The synchronization in this region fell significantly below that found in the PPA and MPA during the first 1.5 seconds of observation (Figure **8.7a**). In the older group, the peak width and latency was similar across ROIs but the amplitude of the power synchronization was significantly higher in the MPA than in the OPA and PPA (Figure **8.7b**). Moreover, we found that in older participants there was a sustained delta/theta synchronization until the end of the observation window that was significantly more important in the PPA and MPA than in the OPA (Figure **8.7b**).

In the beta band, we observed a strong desynchronization starting 1 second prior to the arrival at the intersection and peaking at around $+250$ ms in both age groups (Figures **8.7c-d**). The peak of desynchronization was slightly delayed but deeper in older adults than in young adults across all ROIs (Figures **8.4c**, **8.5c**, **8.6c**). However, this early beta desynchronization was less pronounced in the PPA than in the OPA and MPA in both age groups (Figures **8.7c-d**). After $+750$ ms, in older participants the beta desynchronization slowly went back to baseline, particularly in the OPA and MPA (Figure **8.7d**). In young participants, we noted an inversion around $+500$ ms, leading to a strong beta synchronization in all ROIs (Figure **8.7c**). Although the activity pattern after $+500$ ms was more similar between the OPA and the MPA, we reported significant differences between all pairs of ROIs until the end of the observation window (Figure **8.7c**). Overall, the beta synchronization was strongest in the OPA and weakest in the PPA, with an intermediate activity in the MPA (Figure **8.7c**).

In the low gamma band, we previously reported a significant synchronization shortly after the arrival at the intersection that was specific to the OPA and MPA of young participants (Figures **8.4a**, **8.5a**, **8.6a**). The low gamma band activity was significantly more synchronized in the OPA than in the MPA and PPA for the whole course of the observation period in young participants (Figure **8.7e**). Gamma synchronization in the MPA was significantly stronger than in the PPA during the $[+500; +2500$ ms$]$ period (Figure **8.7e**). We revealed a similar trend in the older participant group, albeit on a smaller scale (Figure **8.7f**). Gamma synchronization was strongest in the OPA and weakest in the PPA, with the MPA in between (Figures **8.7e-f**).

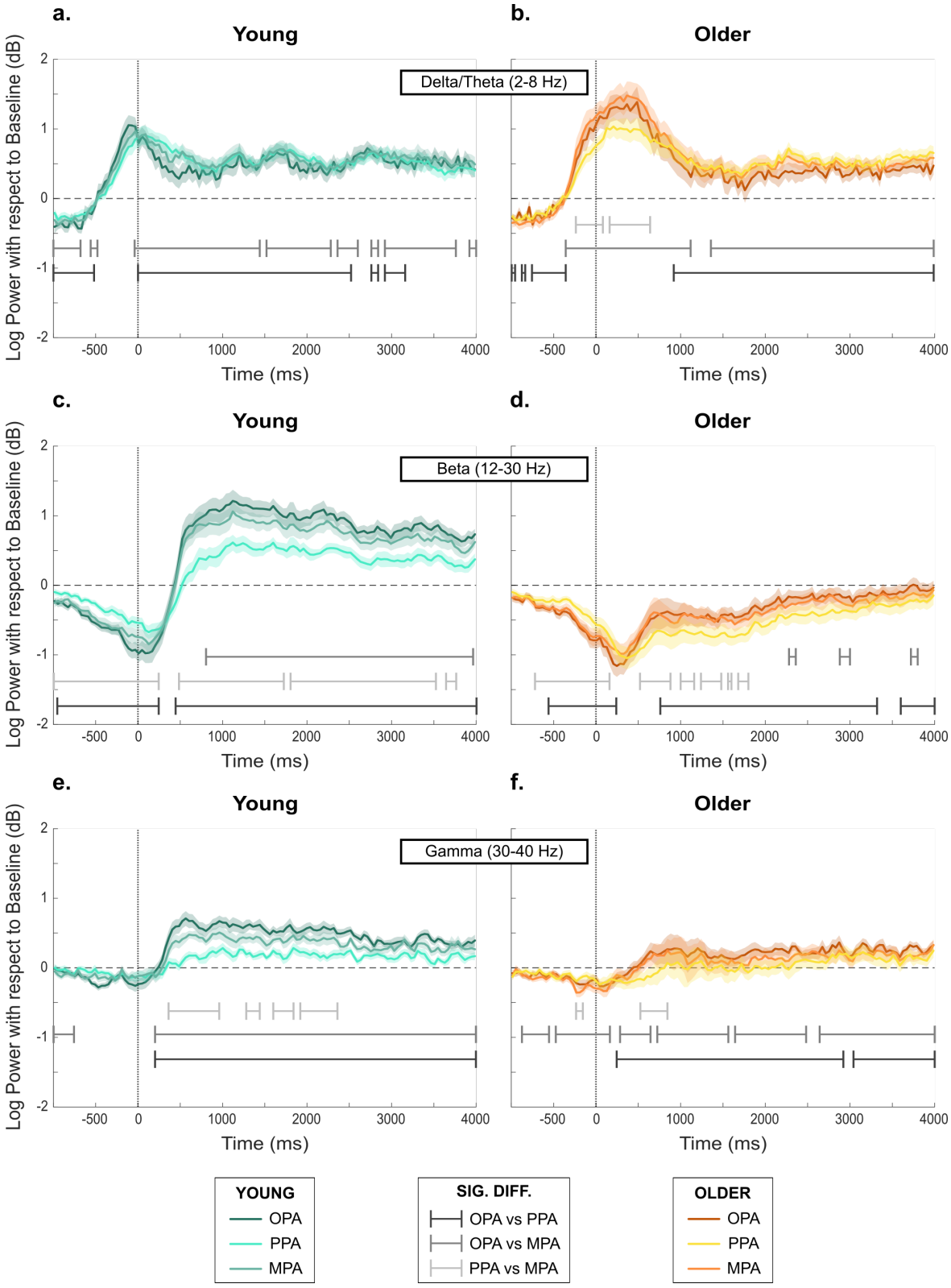

Figure 8.7: Mean ERSP activity per ROI and frequency band in the test trials across age groups. [Continued on next page]

Figure 8.7: [On previous page] Bold lines represent the mean ERSP activity per ROI, averaged on the spectral dimension and across all test trials in the corresponding age group. Shaded areas represent the standard error of the mean computed with average subject traces in each age group ($N = 21$ for each age group). The signal is time-locked to the event of arriving at an intersection ($t = 0$ ms). We investigated all statistical differences with paired permutation tests based on the maximum cluster-level statistic using 1000 permutations. To evaluate the statistical significance at the sample level (mean spectral power at a time point) for a given permutation, we used linear mixed-effects modeling. We examined pairwise differences between ROIs for each age group (6 comparisons). Significant differences reflect clusters with a Monte Carlo p-value below 0.00104 (Bonferroni-corrected for 24 two-sided comparisons) **a**. ERSP activity averaged over the delta/theta band (2-8 Hz) in the young group. **b**. ERSP activity averaged over the delta/theta band in the older group. **c**. ERSP activity averaged over the beta band (12-30 Hz) in the young group. **d**. ERSP activity averaged over the beta band in the older group. **e**. ERSP activity averaged over the low gamma band (30-40 Hz) in the young group. **f**. ERSP activity averaged over the low gamma band in the older group.

8.6 Discussion

This work brings together an unprecedented set of tools to shed light on how the vertical position of objects ties in with navigational behavior in young adulthood and healthy aging. We found that young adults' equivalent performance across conditions echoed with an adaptation of their gaze patterns to the position of relevant cues in the environment. On the contrary, older adults displayed impaired navigational behavior in all conditions and a systematic oculomotor bias for objects in the lower AOI. Source-reconstructed EEG activity revealed extensive age-related differences in the OPA, PPA and MPA. Moreover, we found that the SSRs of young and older adults displayed theta and beta band specificities for environments that contained relevant cues only in the upper AOI.

8.6.1 Healthy aging is associated with a downward bias in gaze dynamics

We first revealed similar behavioral performance in young participants across conditions. We argue that young adults' navigational behavior is malleable to variations in the vertical location of relevant objects. This finding is coherent with recorded gaze metrics. Indeed, the distribution of first fixated AOIs highlighted that young adults divided their initial fixations equivalently between lower, central and upper portions of the screen throughout the encoding phase. Along the same lines, young participants spent less time looking at the upper AOI in the DOWN condition than in the other two conditions during the test trials, conveying the idea that their gaze patterns adapted to the condition. These results are in accordance with research showing that the cognitive demands of the task at hand drive the oculomotor patterns in young adulthood (de Condappa & Wiener, 2016; Grzeschik et al., 2019; Jovancevic-Misic & Hayhoe, 2009). For example, young adults spend more time gazing at landmarks located at decision points than at non-relevant objects (Hamid et al., 2010). In line with numerous accounts of navigational deficits in healthy aging, we found that older adults made significantly more errors on the task than their younger counterparts (Lester et al., 2017; Lithfous et al., 2013; Moffat, 2009). We reported that strategy correlated with behavior and that few older participants used a map-based strategy to get their bearings in the square-shaped vir-

tual environment. They also displayed better wayfinding skills on repeated routes than on new ones suggesting a sequence-based route learning strategy. A large body of literature has indeed established that difficulties in creating and using cognitive maps for orientation are characteristic of healthy aging (Allison & Head, 2017; Moffat et al., 2006; Wiener et al., 2020, 2012), particularly in environments devoid of geometric information (Bécu et al., 2023). The unsuccessful map use in aging may have not been the only contributing factor to such navigational impairments. Indeed, older individuals reported using all 4 objects at intersections, confirming previous research that directing gaze patterns towards the informative part of a scene is frequently impacted in aging (Grzeschik et al., 2019; Hilton et al., 2020). We hypothesize that older participants experienced visual working memory overload as navigationally irrelevant objects competed with relevant ones (Gazzaley et al., 2008; Schmitz et al., 2010). Such behavioral deficits resonate with the observed stereotyped oculomotor behavior. Older participants' first fixations preferentially targeted the central AOI during the UP condition, neglecting the upper AOI. Moreover, the VMA index revealed that older adults spent more time looking at the lower half of the screen regardless of the condition. In contrast to young participants who modulated their attentional focus according to vertical position of relevant cues in the test phase, older participants displayed a systematic downward gaze bias. Past studies revealed that older people tend to focus on lower portions of a visual scene during locomotion (Bécu et al., 2020a; Uiga et al., 2015). In real-life settings, fixations directed towards the lower field could aid in anticipating stepping patterns, planning trajectories and encoding the geometric layout of the space. Moreover, recent work shed light on an age-related spatial memory deficit that was specific to the upper VF (Durteste et al., 2023). We speculate that the observed vertical shift, apparent both in natural and desktop-based conditions, could represent a default state aimed at minimizing task error in aging.

8.6.2 A specific neural pattern in scene-selective regions during the UP condition

The EEG signatures around the time of arrival at the intersection were equivalent in both age groups. We found strong beta desynchronization along with the transient theta synchronization in all ROIs, in line with a previous study that had participants recalling spatial relationships between objects (Rondina II et al., 2019). We thus argue that this pattern of cortical activity reflects visual processing of a scene and the objects contained within it. According to the status quo theory, beta band desynchronization in sensory areas is a sign of disruption of the internal state by a strong exogenous stimulation (Engel & Fries, 2010). Moreover, multiple reports demonstrate that transient parietal and medial temporal theta synchronization accompany the processing of landmarks in paradigms assessing spatial cognition (Kober & Neuper, 2011; White et al., 2012). Across both age groups, we also observed that the pattern of theta synchronization and beta desynchronization was different in the UP condition than in the DOWN and MIX conditions. This result hints at a specificity of the UP condition; the absence of navigationally relevant objects in the lower half of a

scene seems to impact the activity of SSRs. With regards to the fact that all 3 conditions contained an equal quantity of visual information, we emphasize that the vertical position of information useful for navigation modulates cortical signals in scene-selective systems. The vertical retinotopic preferences of the OPA and PPA cannot explain the latter finding as all three ROIs exhibited similar EEG signatures during the UP condition (Silson et al., 2015). Nonetheless, early stages of visual processing are tuned to the typical vertical position of objects within the VF (Kaiser et al., 2018). For example, the upper VF provides orienting information from distal and large immovable objects whereas the lower VF frequently contains smaller objects and obstacles (Greene, 2013; Groen et al., 2017; Hafed & Chen, 2016; Saleem, 2020). In our paradigm, we removed distal information by introducing fog which forced participants during the UP condition to orient using proximal objects on balconies. It is therefore conceivable that such condition-associated differences emerged from the atypical scene grammar of intersections in the UP condition. We highlight that this pattern was consistent between age groups, in accordance with a recent report providing evidence for a robust object-scene congruency effect in the OPA and PPA across the lifespan (Rémy et al., 2020). Further research should seek to elucidate the mechanisms that confer the UP condition its specificity.

8.6.3 Age-related differences in oscillatory dynamics reflect discrepancies in attentional processing

Despite these initial similarities, after +500 ms, we reported striking disparities in cortical activity patterns between young and older participants across conditions. The young group displayed a sudden and sustained beta/gamma synchronization which was absent in the older group. This activity has been associated with tasks that require an effort to maintain the current cognitive state (Deiber et al., 2007; Engel & Fries, 2010). A previous study has also shown that beta band synchronization over the occipital cortex is a marker of visual attentional processes and that healthy older adults demonstrate a specific reduction of this oscillatory pattern (Gola et al., 2013). Similarly, there is converging evidence that gamma oscillations in parieto-occipital regions promote sharper visuospatial attention (Jensen et al., 2007). We interpret this age-specific beta/gamma synchronization as a sign of top-down modulation, possibly highlighting the reactivation of pre-existing visual representations (Osipova et al., 2006). In our opinion, the absence of such a component in the activity of SSRs in older adults might relate to their inability to compare incoming visual information with internal spatial representations. In the older group, instead of the sudden beta synchronization, we found the initial beta desynchronization and delta/theta synchronization to persist until the end of the time window. The intensity of cognitive processing positively correlates with delta power (Güntekin & Başar, 2016; Harmony, 2013). In addition, evidence points towards the amplitude of theta synchronization in temporal regions being associated with impaired, more effortful, spatial encoding (Fellner et al., 2016; Rondina II et al., 2019). We speculate that the EEG signals in the older group compared with the young group demonstrate prolonged, and stronger bottom-up processing evoked by the

arrival at the intersection. The sustained synchronized theta power and desynchronized beta power observed in older participants resonate with a recent study putting forward the possibility that this activity underpins the recollection of superfluous contextual details (Strunk et al., 2017). In further support of this hypothesis, we noted the greatest beta desynchronization in the condition characterized by the higher number of relevant objects for navigation in the older group (*i.e.*, the MIX condition). Healthy aging correlates with an increased reliance on non-pertinent information, a process known as hyper-binding (Campbell et al., 2010; S. Kim et al., 2007). Hyper-binding originates from a failure of the inhibition mechanisms that regulate attention. Taken together, these results shed light on age-related modifications of attentional mechanisms that may have impeded efficient visual processing and ultimately hindered the formation of adequate spatial representations in older participants.

8.6.4 Three distinct scene-selective systems

The present study aligns with extensive research highlighting functional dissociations between the OPA, PPA and MPA (Dilks et al., 2022; Epstein & Baker, 2019). We did not find any evidence for age-related modulations of lower frequencies in the PPA. The PPA processes scene content and layout as the natural statistics of a scene explain a large proportion of its variance (Aminoff & Durham, 2023; Bonner & Epstein, 2021; Chaisilprungraung & Park, 2021; Dwivedi et al., 2021). The comparable delta/theta synchronization in the PPA across age groups lends credence to the idea that older adults can adequately extract visual information that is devoid of navigational purpose. In the OPA and MPA, however, we noted a stronger delta/theta synchronization in older adults compared to young adults. The OPA is a major node in the network facilitating immediate visually guided navigation (Dilks et al., 2022). The conclusions from previous fMRI studies converge to suggest that OPA activity increases with age in response to spatial navigation difficulties (Lithfous et al., 2018; Ramanoël et al., 2020). In a more complex cognitive task requiring the formation of a mental map, older adults demonstrated an elevated recruitment of the OPA and MPA in tandem (Diersch et al., 2021). Although we lack converging evidence across brain regions, the BOLD response and theta power have been positively correlated during human navigation in the para-hippocampal cortex (Ekstrom et al., 2009). In this light, we speculate that the increased theta synchronization in the OPA and MPA of older adults fits with the fMRI literature and confirms a compensatory role for the OPA during spatial navigation in healthy aging. In the younger group, we also noticed that the peak of theta synchronization was earlier and more transient in the OPA than in the other ROIs. This finding is consistent with the claim that the OPA can rapidly extract local scene information in order to guide deliberate gaze exploration during prolonged scene viewing (G. L. Malcolm et al., 2018; Suzuki et al., 2021). Our study thus emphasizes the distinct roles of the PPA and OPA, and it provides further confirmation of the OPA's function in automatic scene parsing for immediate navigational purposes (Harel et al., 2022). Further distinguishing the 3 SSRs, we reported the late stage synchronization of higher frequencies in young adults to be ROI-specific. Indeed, the OPA and PPA exhibited the most and least synchronized activity respectively, while the

MPA found itself in the middle. We argue that this continuum of synchrony may correlate with the amount of connectivity with other brain areas at intersections, as gamma band oscillations structure communication between regions (Fries, 2015; Lachaux et al., 2005) In a recent study, researchers observed that the retrosplenial cortex, but not the para-hippocampal region, cooperated actively with the hippocampus and prefrontal cortex during map-based navigation (Qi et al., 2022). Despite a paucity of research delving into the connectivity of the OPA, its role in identifying immediately navigable paths is essential to inform navigational decisions (Bonner & Epstein, 2017, 2018; Patai & Spiers, 2017). It thus seems reasonable to speculate that the OPA communicates with an extended cerebral network (Baldassano et al., 2016; Ramanoël et al., 2019). We stress that shedding light on how neural oscillations in the scene-selective systems mediate the use of spatial representations for wayfinding is a critical next step in the field (Kunz et al., 2019).

8.7 Limitations & Perspectives

From a methodological standpoint, we must highlight that although the source reconstruction model provides a fine-tuned localization of SSRs, spatial precision is incomparable to that of an fMRI study. This is particularly true for deep cortical regions as increasing depth correlates with a decrease in synchronization of the highest frequency band. It is conceivable that the lesser synchronization reported in high frequencies for the PPA may stem from its location in deep structures of the brain. We note that this drawback does not affect low frequency bands. A second methodological consideration pertains to the choice of baseline for the EEG analysis. The baseline corresponded to a period devoid of task-relevant visual information, when participants moved passively along the street. We thus compare the intersection observation period to a phase that called for optic flow processing. The latter may have confounded reported differences between ROIs as the OPA represents self-motion information to a greater extent than the MPA and PPA (Kamps et al., 2016a; Sulpizio et al., 2020). Optic flow emanates primarily from the lower VF which may have primed the processing of objects on sidewalks (Saleem, 2020). Furthermore, young adults were quicker than older adults to make the correct navigational decision in the test phase, such that they resumed to passive navigation within the 4-second window more often. We acknowledge that age-related differences in EEG activity may have been influenced in part by this behavioral disparity.

A final limitation to this study relates to task design. Indeed, we believe that the difficulty of the paradigm prevented behavioral differences between conditions from emerging in older participants. Interestingly, top performers in the older group made fewer navigational errors in the DOWN and MIX conditions than in the UP condition. We put forward the hypothesis that, with an easier wayfinding task, the vertical shift in gaze behavior would have translated into a greater difficulty to orient in the UP condition in aging. Future studies could design an immersive task that would increase the availability of multisensory cues and as a consequence facilitate performance in older adults (Adamo et al., 2012). Finally, a virtual reality or real-world protocol in combination with mobile EEG would confer greater ecolog-

ical validity while preserving access to the neural correlates of spatial cognition (Delaux et al., 2021; Djebbara et al., 2021; Do et al., 2021; Liang et al., 2021).

8.8 Conclusion

The present study reached two main conclusions. First, it revealed age-related disparities in beta/gamma band synchronization concurring with a deficient regulation of attentional mechanisms during navigation in aging. Second, it highlighted the need to consider vertical position as an essential object property for spatial navigation throughout adulthood. Older adults exhibited a systematic bias for downward fixations. We stress that vertical biases in eye movements in healthy aging may have detrimental consequences on wayfinding abilities as relevant cues are not uniformly distributed across the VF. A gaze bias for the lower portion of a scene may prevent the formation of adequate spatial representations by hindering the capacity of older adults to anchor their position to larger immovable landmarks. Finally, in both age groups, orienting with objects situated in the upper portion of the screen modified neural activity in SSRs. We argue that the OPA, PPA, and MPA have a significant role to play in parsing information across vertical hemifields. Further research is required to confirm this coding property across imaging modalities and to elucidate its behavioral correlates across the lifespan.

Chapter 9

Perception of the Walkable Distance throughout Adulthood

Following-up on the study of visuo-spatial cognition in healthy aging, this chapter aims at unraveling the brain correlates of scene understanding in mobile conditions, combining the MoBI approach developed in Chapter **7** and the individualized source reconstruction method to investigate the EEG signal coming from the SSRs designed in Chapter **8**.

It focused on the perception of navigational affordances, and more precisely on the walkable distance between the observer and a door at the end of a path. To emphasize embodiment and foster multi-sensory integration in this paradigm, participants were asked to walk the distance after the estimation. It was hypothesized that the OPA activity captured by mobile EEG would be modulated by the perceived distance, as in (J. Park & Park, 2020). The impact of healthy aging was also evaluated at the same time, further investigating the signs of preservation of both egocentric distance estimation (Bian & Andersen, 2013; Sugovic & Witt, 2013) and the activity of the OPA during spatial cognition in older adults (Ramanoël et al., 2020).

The final analyses of this experiment are still ongoing, and this section has not been framed into a journal article yet. When already introduced in previous chapters, methodologically redundant sections were omitted.

9.1 Contributors

Alexandre Delaux[1], Ilaria Selle[1], Marion Durteste[1], Benoit R. Cottereau[2,3] & Angelo Arleo[1].

1. Sorbonne Université, INSERM, CNRS, Institut de la Vision, 17 rue Moreau, F-75012 Paris, France
2. CerCo UMR 5549, CNRS Université Toulouse III, Toulouse, France
3. IPAL, CNRS IRL 2955, Singapore

9.2 Introduction

The decline in cognitive abilities, including spatial navigation, is a common experience among older adults, even in the absence of major pathologies (Salthouse, 2019). Spatial navigation encompasses complex cognitive functions that allow individuals to perceive and comprehend scenes, recognize places, and perform actions within them (Lester et al., 2017). Therefore, the decline in navigational abilities can significantly impact the autonomy and social participation of older individuals (Burns, 1999; Lester et al., 2017; Moffat, 2009).

Despite the significance of egocentric distance perception in everyday life (*e.g.*, to avoid static and moving obstacles while navigating), healthy aging research on this topic is scarce and based on low sample sizes (Bian & Andersen, 2013; Sugovic & Witt, 2013). Asking their participants to verbally estimate the distance separating them from an object, both studies reported a similar pattern in young adults, *i.e.* underestimation accompanied by foreshortening. Even if older adults gave higher estimations in both cases, in one study they were more accurate than their younger counterparts (Bian & Andersen, 2013) and in the other they overall overestimated the distance (Sugovic & Witt, 2013). Egocentric distance overestimation in aging was hypothesized to emerge from declined physical abilities influencing older adults' perception of their environment in the light of their less efficient way of performing movements and actions (Sugovic & Witt, 2013). However, looking at the path integration literature, older adults underestimate traveled distances in desktop-based virtual reality paradigms, where only visual cues are available (Adamo et al., 2012; Harris & Wolbers, 2012). All these evidence point to a key mediating role for multisensory integration when studying this ability, which is often reported as particularly strong in older adults (S. L. Bates & Wolbers, 2014).

At the cortical level, the SSRs are acknowledged to play a crucial role in scene perception and spatial representation (Epstein & Baker, 2019). Among the three SSRs, the OPA is thought to be the most predominantly involved in visually-guided navigation (Dilks et al., 2022). Notably, the OPA was described to be responsive to qualitative and quantitative aspects of navigational affordances, *i.e.* navigable paths, present into a scene (Bonner & Epstein, 2017; Persichetti & Dilks, 2018). One particular form of navigational affordance that is typically important in ecological situations is the egocentric distance, *i.e.* the distance in front of the observer that is free of obstacles (*i.e.*, navigable). The OPA was found to be sensitive to this concept in multiple experiments (Chaisilprungraung & Park, 2021; Kang

& Park, 2023; J. Park & Park, 2020; Persichetti & Dilks, 2016). In a fMRI study, J. Park and Park (2020) demonstrated that the activity of the OPA specifically encoded the length of a corridor in front of the observer. By subsequently introducing transparent navigability constraints (*i.e.*, a glass wall or a transparent curtain) dissociating the length of the corridor from the reachable space, they further demonstrated that the OPA activity was more sensitive to the actual navigable distance rather than reflecting the perceived depth of the corridor. However, it must be noted that the paradigms of these studies did not focus the attention of the participant on distance perception, as they presented static images of scenes with a distracting task to accomplish in the scanner.

The study of the SSRs with EEG is relatively recent but it gains momentum in order to get more insights on the dynamic properties of scene processing. Some groups have already started to investigate affordance perception with this methodology. Focusing on a group of posterior-lateral electrodes previously validated to be associated with scene processing correlates (Harel et al., 2016), Harel et al. (2022) were able to associate the characteristics of the event-related potential (ERP) elicited by scene presentation with the number of affordances in the scene. Using mobile EEG, Djebbara et al. (2021) retrieved a cluster of activity near the OPA in an experiment where participants had to judge whether they could pass a door frame in immersive VR. No investigations of this kind were yet conducted in a healthy aging context.

Therefore, given the assumed important role of the OPA in affordance perception and the interest in studying distance estimation in a more ecological context in aging, we designed an immersive experimental paradigm to analyze scene processing in a real-life scenario and explore its dynamics during actual movements, using the MoBI approach. On the recorded EEG, this study will employ an individualized, fMRI-based, source reconstruction model previously validated to assess the electrical activity coming from the SSRs with a particular focus on the OPA.

9.3 Methods

9.3.1 Participants

We recruited a total of 38 participants from the *SilverSight* cohort (Lagrené et al., 2019). All participants met the cohort inclusion criteria: normal cognitive performance on a battery of neuropsychological tests, no history of sensory, neurological, or psychiatric disorder, and normal or corrected-to-normal eyesight. Participants were divided into 2 age groups, 20 young adults (28.2 ± 3.5 years old [$mean \pm$ SD], 9 women) and 18 older adults (77.0 ± 3.9 years old, 7 women). Each participant provided their written informed consent, and the study was approved by the Ethics Committee "*CPP Ile de France V*" (ID_RCB 2015-A01094-45, CPP N: 16122).

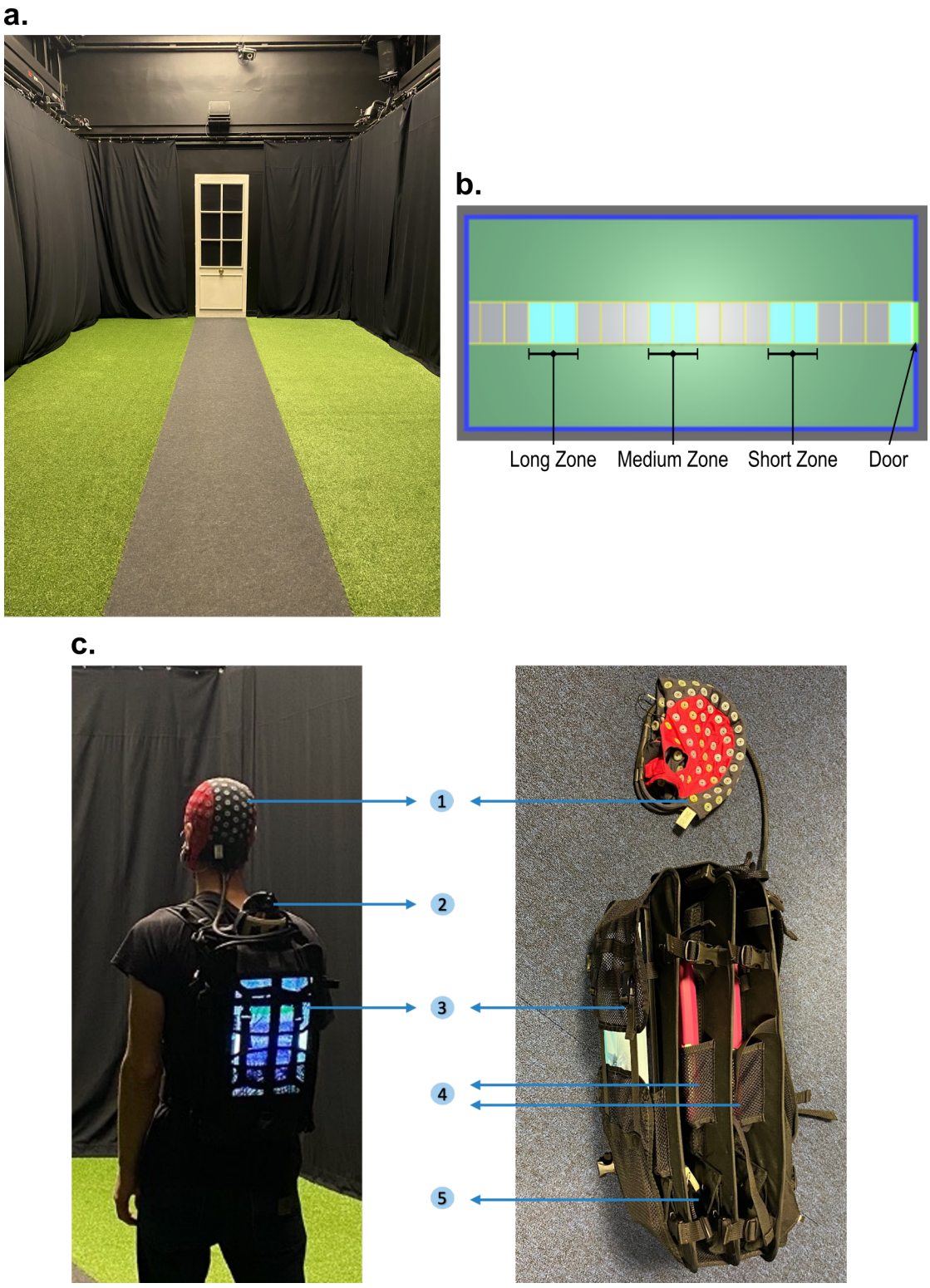

Figure 9.1: Experimental set-up. **a**. View of the experimental room from the end of the path, facing the door. **b**. Top view of the room, as modeled in the virtual environment for motion capture. At the center is the path leading to the door (in gray). Starting zones for each condition are represented in blue. The door is at the far right in green. Each yellow rectangle represents a 50×95 cm rectangle on the actual path. **c**. Details of the participant's equipment. (1) EEG cap (128 electrodes); (2) Motion capture tracker (VIVE tracker). The backpack carried by the participant (of about 3.5 kg) contained (3) the tablet allowing to record the EEG signals and (4) 2 amplifiers connected by (5) a synchronization cable.

9.3.2 Real-world environment

We implemented the experimental environment in a rectangular space measuring 9.1m × 4.5m, designed to resemble a garden within the *Rue Artificielle* experimental platform at *StreetLab*, within the Vision Institute. To recreate the ambiance of an outdoor garden, we arranged an 8.5 meter straight path using a gray carpet, complemented by artificial grass covering the remaining area and placed a physical door at the end (Figure **9.1a**). In order to maintain uniform lighting and eliminate potential landmarks that could aid participants in spatial orientation and distance estimation, we covered the walls with black curtains. We provided participants with indoor shoes to prevent any stains on the carpet that could inadvertently provide spatial cues. Additionally, we maintained consistent lighting conditions, including brightness and color temperature, by utilizing the lighting control system of the *StreetLab* platform. To facilitate real-time tracking of participants' positions using a motion capture system, we constructed a virtual model of the experiment room (Figure **9.1b**) using Unity 3D software (version 2019.2.1). One experimenter remained in the room with the participant to ensure safety and assist during the disorientation phase, while the other experimenter operated from an adjacent control room to administer the different phases of the protocol. To maintain silence between them and prevent inadvertent information transfer to participants regarding their positioning within the room, we established communication between experimenters using a VR controller and a dedicated vibration system.

9.3.3 Protocol

Participants performed a task within the previously described room, aiming to estimate the distance to the door and subsequently walk along the path leading to it. Prior to each trial, participants underwent a disorientation phase where their eyes were closed, and they were guided by one of the experimenters to a new starting position, following a non-straight path and making a few turns. Once participants were positioned at the designated distance from the door, the experimenter provided them with instructions on how to orient their head (directly facing the door) and stance (positioning their feet at mid-width of the walkway). These instructions aimed to ensure consistency between participants and trials. The trial commenced when the experimenter pressed the button on the VR controller, initiating a series of instructions for the participants. Each trial comprised four distinct phases: the *Baseline* phase, the *Observation* phase, the *Question* phase, and the *Exploration* phase (Figure **9.2a**). The Baseline phase, lasting for 1 second, was initiated by the room experimenter when the participant was in the correct trial condition, standing with their eyes still closed. Then, the Observation phase commenced with a beep tone, signaling the participant to open their eyes and observe the scene for 5 seconds. Afterward, a second instruction prompted the participant to evaluate the distance, marking the beginning of the Question phase. During this phase, the participant verbally expressed their estimation of the distance to the door in meters and centimeters, which the experimenter in the control room transcribed. After a 5-second interval, the participant received the instruction to start walking, commencing the Exploration phase, during which they could walk the straight path toward the door at their

preferred pace. Upon reaching the last 50 centimeters of the path, oral feedback was provided, indicating the conclusion of the trial and prompting the participant to close their eyes again for the disorientation phase.

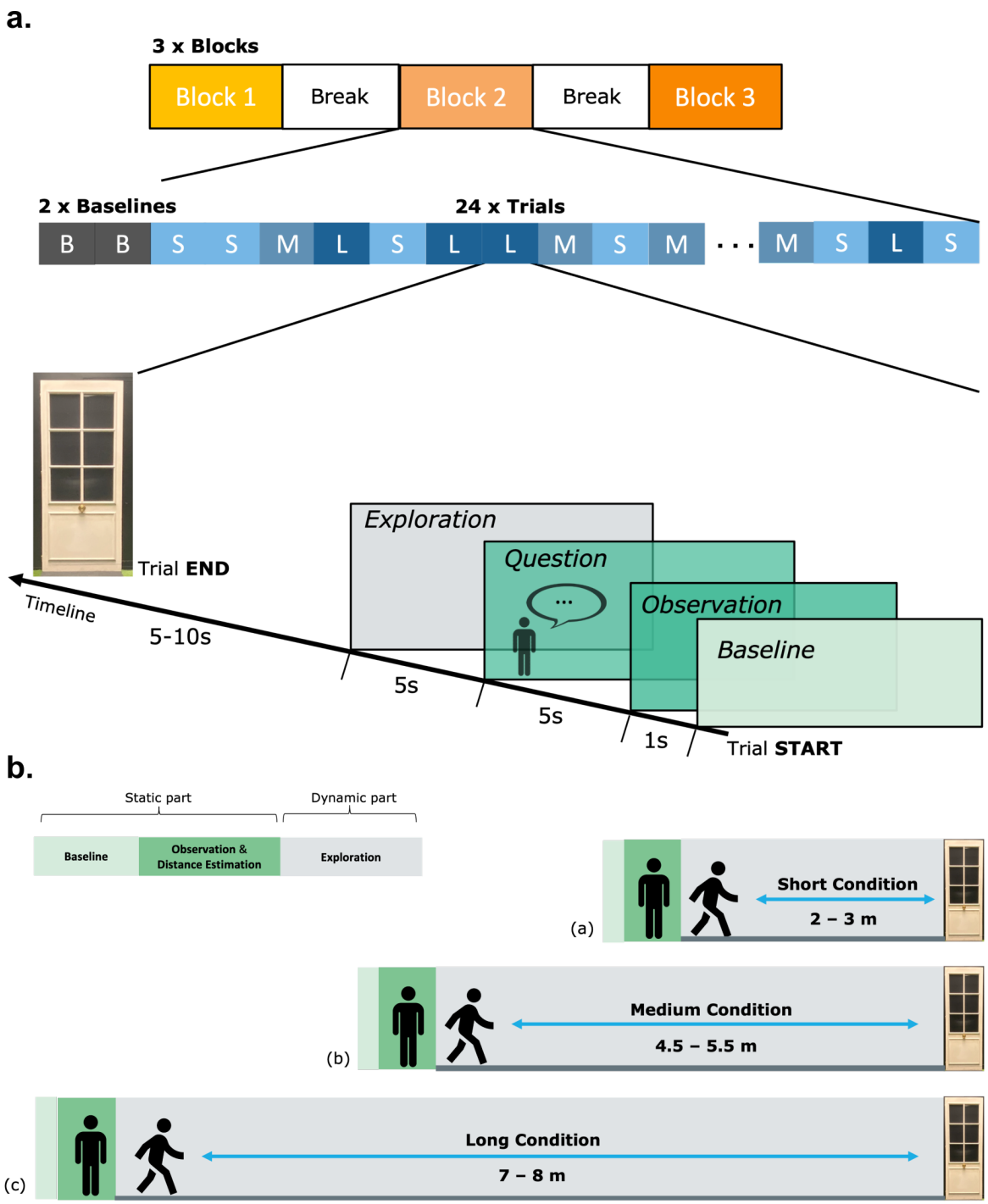

Figure 9.2: Experimental protocol. **a**. Experiment timeline. The first row represents the succession of blocks in the experiment. The second row shows an example of the sequence of trials in an experimental block. "S" stands for Short condition, "M" for Medium condition, "L" for Long condition. The third row shows the succession of phases in a trial. **b**. Experimental conditions. (a) *Short* trial (*i.e.*, starting in the 2-3 m interval from the door); (b) *Medium* trial (*i.e.*, starting in the 4.5-5.5 m interval from the door); (c) *Long* trial (*i.e.*, starting in the 7-8 m interval from the door).

9.3.4 Procedure

After positioning the EEG cap on the participant's head, we took a 3D scan to capture the precise placement of the electrodes, and then we filled the electrode wells with conductive gel. During this phase, participants were provided with written instructions for the task and familiarized themselves with the associated sounds and instructions. A motion tracker was attached to their backpack to track their movements accurately. At this stage, the door was intentionally concealed, and no information regarding the scale of the room was given to the participants. The task paradigm comprised three conditions (Figure **9.2b**), each representing different navigational distances with one-meter-wide intervals: Short (2-3 meters from the door), Medium (4.5-5.5 meters from the door), and Long (7-8 meters from the door). At the end of each trial, the experimenter in the room received information about the next trial condition through the VR controller, allowing them to randomly position the participant within the protocol-defined interval for that condition.

The task was organized into three blocks, each consisting of 26 trials: 8 trials for each condition and 2 baseline trials (Figure **9.2a**). The baseline trials required participants to walk straight in the dark room with their eyes open, devoid of any visual stimuli, and these recordings were specifically designed to isolate gait-specific patterns for subsequent EEG analyses. The order of conditions within each block was pseudo-randomized for each participant at the beginning of the task, ensuring that the same condition did not appear consecutively more than three times to mitigate potential learning effects on distance estimation. At the end of the experimental session, participants were asked to complete a brief questionnaire to provide additional insights into their overall task experience, including factors such as comfort, difficulty, and personal strategies utilized to solve the task.

9.3.5 Equipment and setting

The EEG recording system utilized in the experiment consisted of a cap with 128 equidistantly arranged electrodes (waveguard original; ANT Neuro, see Figure **9.1c**). The reference electrode was placed closest to the standard C_z position, while an additional electrode was positioned under the left eye to capture the electro-oculography (EOG) signal. A separate electrode on the left earlobe served as the electrical ground reference. Conductive gel was applied to each electrode to optimize electrical contact and minimize impedance, with efforts made to reduce impedance below 20 kΩ. The EEG cap was connected to two amplifiers (eego Mylab; ANT Neuro), and data were acquired using eego software at a sampling rate of 500 Hz. After placing the cap on the participant's head, fiducials and electrode positions were collected with the depth perception camera approach presented in Section **6.3.1**. To track the participant's position and trigger spatial events during the experiment, a motion tracker (HTC, VIVE tracker) was attached to their backpack (Figure **9.1c**). All data streams, including EEG, motion capture, and experimental events, were synchronized using the LSL protocol (version 113). These streams were then collected and stored in a single file using LabRecorder (version 1.13.0-b13).

9.3.6 Data analysis

9.3.6.1 Behavior

MATLAB (version R2021b) was used for the behavioral analysis. Upon analyzing the post-experiment Questionnaire, it was revealed that the majority of participants attempted to refine their estimations by counting the number of steps taken during the Exploration phase. To maintain consistency in the analysis across a homogeneous group of subjects, the 4 participants who did not adopt this strategy were excluded from the analysis. Therefore, we only analyzed the data from 17 young adults (28.3 ± 3.6 years old, 8 women) and 17 older adults (77.3 ± 3.8 years old, 6 women).

To evaluate participants' performance, we conducted a comprehensive analysis. Initially, we employed a linear mixed model to examine the impact of age group, sex, condition, block, and the interaction between block and condition on (1) the distance estimate (d_e) and (2) the error in comparison to the true distance (d_t). These models treated subjects as random-effect grouping factors and were fitted using maximum likelihood estimation and type III sum of squares. The selection of random and fixed effects structures was based on the Akaike information criterion (AIC) for good model fit, and we verified the normality of residuals. To ensure unbiased regression coefficients and standard errors, we assessed collinearity among factors using variance inflation factors (VIFs). We employed an F-test analysis to identify significant fixed effects and subsequently performed an ANOVA with the Satterthwaite correction. Variables with a p-value of 0.05 or less were considered statistically significant. To account for multiple comparisons, we conducted pairwise comparison tests with the Holm-Bonferroni correction applied.

9.3.6.2 Detection of eye-opening

We conducted an analysis of the signal recorded by the EOG electrode to identify the precise moment when participants opened their eyes during the observation phase, following the oral instruction. To achieve this, we developed a custom, semi-automated procedure, inspired by Sharma et al. (2020) and illustrated in Figure **9.3**.

First, we reversed the polarity of the EOG signal. Next, we applied a band-pass filter between 0.75 Hz and 5 Hz (zero-phase Hamming windowed finite impulse response filters: high-pass filter with 0.75 Hz cut-off frequency and 0.5 Hz transition bandwidth and low-pass filter with 6 Hz cut-off frequency and 2 Hz transition bandwidth) to the continuous EOG signal, allowing us to detect transient peaks indicative of eyelid-related events (*i.e.*, eye-opening, eye closing, or blinking). The signal was then epoched around each Observation instruction event, creating windows of $[-2, 4]$ seconds. For each epoch, we selected the most prominent[1] peaks as candidates for eye-opening events, using the `findpeaks` function in Matlab and considering peaks with a prominence above 90% of the maximal amplitude observed in the epoch.

To better distinguish between different eye events and include more low-frequency components, a second band-pass filter was applied to the EOG signal, this time between 0.05 Hz

[1] Refer to Matlab documentation for the mathematical definition of prominence.

and 5 Hz (zero-phase Hamming windowed finite impulse response filters: high-pass filter with 0.025 Hz cut-off frequency and 0.05 Hz transition bandwidth and low-pass filter with 6 Hz cut-off frequency and 2 Hz transition bandwidth). Under this filtering, eye-opening events exhibited a descending step signature at the latency of the peak detected with the previous filtering (as depicted in Figure **9.3**).

The most probable eye-opening event was automatically defined as the peak associated with the most negative difference between the mean post-peak amplitude and the mean pre-peak amplitude, calculated within a $[-0.4, 0.4]$ seconds window around the peak. This automatic definition was further validated or adjusted by the experimenter through meticulous manual inspection of the signal (Figure **9.3**). Trials presenting significant artifacts or challenges in determining the eye-opening event were excluded from the analysis to ensure data integrity.

9.3.6.3 EEG

Source reconstruction modeling. Source reconstruction modeling was performed according to the procedure described in Section **6.3.2**. In this analysis, the T2-weighted sequence was available for a majority of older adults (10 out of 17).

EEG processing. EEG processing was performed according to the procedure described in Section **6.2**, using the BeMoBIL pipeline for time-domain cleaning with a 10% predetermined percentage for removal. Data analysis was focused on the observation period to inspect scene presentation neural dynamics. Before epoching the dataset we applied a band-pass filter between 1.25 Hz and 42 Hz (zero-phase Hamming windowed finite impulse response filters: high-pass filter with 1 Hz cut-off frequency and 0.5 Hz transition bandwidth and low-pass filter with 47.25 Hz cut-off frequency and 10.5 Hz transition bandwidth). Epochs were taken around the eye-opening event resulting from the procedure presented in Section **9.3.6.2** within a $[-1, 2]$ seconds window. Epochs exhibiting excessive noise (*i.e.*, containing more than 25% of bad samples as detected during time-domain cleaning) or lacking a clear eye-opening event were not considered.

For the event-related spectral perturbation (ERSP) analysis, we proceeded as in Chapter **8**. We used functions from the *FieldTrip-lite* plugin (v20210601, Oostenveld et al. 2011) for EEGLAB. At the epoch level, we first computed ERSPs for each channel (with a 25 Hz sampling rate in the temporal domain and with a linear scale between 2 and 40 Hz for the spectral domain) using the `ft_freqanalysis` function. The latter was based on a frequency-wise combination of Morlet wavelets of varying cycle widths (*superlet* method: Moca et al. 2021). We discarded data from electrodes for which the position was not determined with sufficient confidence on the 3D model. Then, we proceeded to solve the inverse problem with the complex Fourier coefficients as inputs using the `ft_sourceanalysis` function and the minimum norm estimation (MNE) method. To summarize activity from the OPA, PPA, and MPA, we averaged power estimations over all dipoles included in the region of interest (ROI) and combined its contribution from both hemispheres. Finally, at the epoch level, we divided the activity by its arithmetic mean over the course of the epoch.

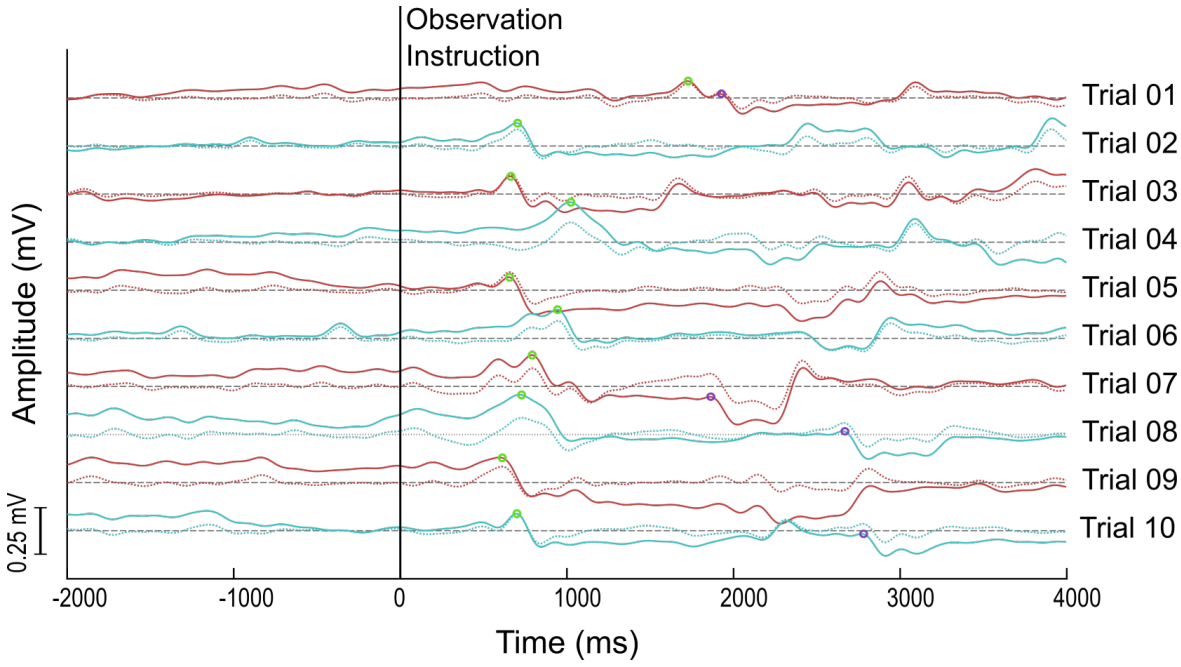

Figure 9.3: Illustration of the eye-opening definition procedure on the EOG signal. Ten trials are plotted for an example young participant. For each trial, the signal was epoched around the Observation instruction event with a $[-2, 4]$ seconds window. Dotted lines: EOG signal band-pass filtered between 0.75 Hz and 5 Hz used for peak detection. Solid lines: EOG signal band-pass filtered between 0.05 Hz and 5 Hz used for eye-opening definition (descending step signature). Green circles show the definition of eye-opening events confirmed with manual inspection. Purple circles show the automatic definition of eye-opening events by the algorithm that were not selected by the experimenter upon manual inspection.

9.3.7 Group-level analysis

The group-level analysis was framed as in Chapter **8**. The group-level analysis focused on 4 main variables of interest: (1) age group, (2) condition, (3) the interaction between age and condition and (4) ROI. We used a pre-stimulus period of 1 second before participants' eye-opening as a baseline. We removed this activity from each epoch data using a gain (*i.e.*, divisive) model. We then randomly drew samples from the pre-stimulus period to build surrogate baseline epochs and statistically compare real epochs with baseline-level activity. We used log-transformed data for statistical analysis. To investigate the specificity of ERSPs to the variables of interest within each ROI (age, condition, and their interaction), we performed a statistical analysis using a non-parametric unpaired permutation test based on the maximum cluster-level statistic (Maris & Oostenveld, 2007) with 1000 permutations. We used linear mixed-effects modeling to evaluate the statistical significance at the 'pixel' level for a given permutation. In the model, we considered participants as random intercepts and age, condition, sex, trial#, and pairwise interactions between age, condition, and trial number as fixed effects (see Equation **9.1**). Additionally, we performed a paired permutation test to assess the statistical significance of ERSP activity for each level of the variables of interest with respect to its corresponding surrogate baseline as in Equation **8.4**. We set the initial significance level to $p < 0.05$, and Bonferroni-corrected for variables with more than 2 levels.

$$\begin{aligned}\text{ERSP}(f,t) \sim\ & \text{Age} * \text{Condition} + \text{Sex} + \text{Trial\#} \\ & + \text{Age} : \text{Condition} + \text{Age} : \text{Trial\#} + \text{Condition} : \text{Trial\#} \\ & + (1|\text{ID}) + (\text{Trial} - 1|\text{ID}) + (\text{Condition} - 1|\text{ID})\end{aligned} \tag{9.1}$$

9.4 Results

9.4.1 Behavior

To get an overview of the behavioral results, we present the distance estimates (d_e) and the relative estimation errors on Figure **9.4**. The relative estimation error was computed as the difference between the true distance and the estimated distance ($d_t - d_e$). Hence, a negative error corresponds to an overestimation of the distance, and respectively, a positive error transcribes an underestimation of the distance.

To investigate comprehensively these results in statistical terms, we fitted each variable with a linear mixed model and, for factors that exhibited a significant effect ($p < 0.05$) in the Satterthwaite ANOVA with more than 2 categories, we analyzed specific pairwise contrasts. We found a significant main effect of the condition on the distance estimates ($F(2;34) = 10.497, p < 0.001$; Figure **9.4a-c**). Post-hoc comparisons confirmed that the distance was perceived differently in all conditions, coherently with the true distance. Specifically, distance estimates in the Short condition were significantly lower than distance estimates in the Medium condition which were in turn significantly lower than distance estimates in the Long condition. The gender was also a significant predictor of the distance estimate given by participants ($F(1;34) = 22.31, p < 0.001$; Figure **9.4b**) as women gave lower estimates than men on average. The distance estimate was neither significantly modulated by the block index ($F(2;34) = 0.26, p = 0.771$; Figure **9.4a**) or the age group ($F(1;34) = 1.50, p = 0.229$; Figure **9.4c**). A significant interaction was found between the block index and the condition ($F(4;2278) = 10.123, p < 0.001$). For this interaction, we specifically tested two types of *post hoc* contrasts: (1) between conditions within the same block (2) between the 1^{st} and 3^{rd} blocks for the same condition. All contrasts of type (1) returned significant, similar to the main effect of the condition. For contrasts of type (2), we only reported a significant difference between the 1^{st} and 3^{rd} blocks for the Short Condition ($F(1,47.45) = 9.17, p = 0.011$; Medium: $F(1,47.45) = 1.05\text{e}{-6}, p = 0.999$; Long: $F(1,47.45) = 1.10, p = 0.599$).

Similarly, we found a significant main effect of the condition on the relative estimation error ($F(2;34) = 8.568, p < 0.001$; Figure **9.4d-f**). Post-hoc comparisons indicated that the estimation error was significantly different in the Long condition compared to the Short and Medium conditions ($F(1;34) = 13.82, p = 0.008$ and $F(1;34) = 17.11, p = 0.003$, respectively). The difference in estimation error between Short and Medium conditions was not statistically significant ($F(1;34) = 6.55, p = 0.106$). Overall, the relative estimation error followed a decreasing trend when the true distance increased, ending up in average overesti-

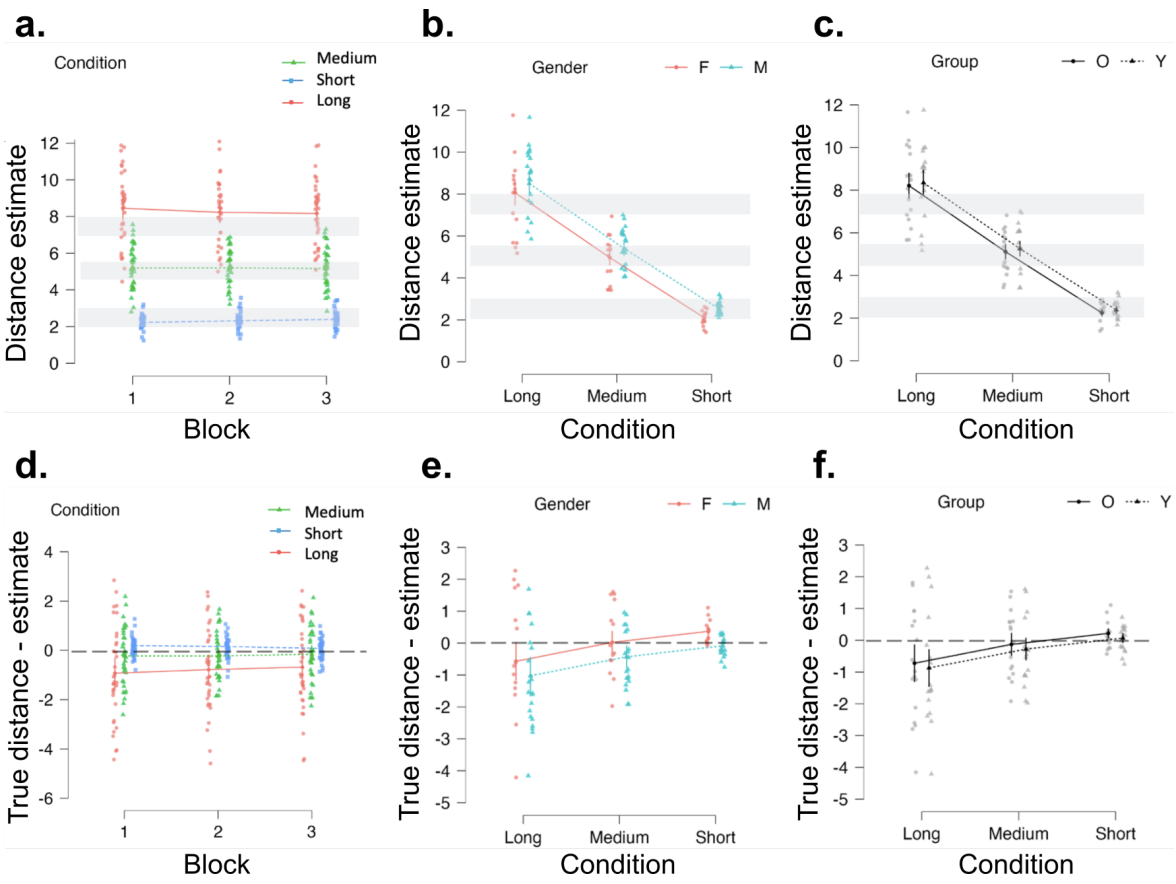

Figure 9.4: Summary of distance estimates and relative estimation errors. Bars exhibit the 95% confidence interval (CI). **a**. Average distance estimate (d_e) within blocks split by conditions. **b**. Average distance estimate within conditions split by gender. 'F' stands for Female, 'M' for Male. **c**. Average distance estimate within conditions split by age group. 'O' stands for Older, 'Y' for Young. **a-c**. Individual dots in the background represent participant-wise mean distance estimate. The gray areas correspond to the range of departure distances for each condition. **d**. Average relative estimation error (distance estimate subtracted from true distance; $d_t - d_e$) within blocks split by conditions. **e**. Average relative estimation error within conditions split by gender. **f**. Average relative estimation error within conditions split by age group. **d-f**. Individual dots in the background represent participant-wise mean relative estimation error. The horizontal gray line corresponds to the absence of error.

mation in the Long condition. The gender was also a significant predictor of the estimation error given by participants ($F(1;34) = 27.47, p < 0.001$; Figure **9.4e**) as women made higher relative errors than men on average. This resulted in women making lower overestimation errors in the Long condition but greater underestimation errors in the Short condition compared to men. Again, the estimation error was neither significantly modulated by the block index ($F(2;34) = 0.319, p = 0.728$; Figure **9.4d**) or the age group ($F(1;34) = 3.071, p = 0.088$; Figure **9.4f**). We conducted the same investigation of the significant interaction between the block index and the condition ($F(4;2278) = 7.109, p < 0.001$) as above. The contrasts of type (1) revealed a significant difference in the 1^{st} block between Short and Medium conditions ($F(1,40.11) = 8.82, p = 0.045$) and between Short and Long conditions ($F(1,35.69) = 19.22, p = 0.001$). In the 2^{nd} block, differences were found between Medium and Long conditions ($F(1,45.19) = 16.62, p = 0.003$) and between Short and Long condi-

tions ($F(1,37.43) = 14.08, p = 0.007$). In the 3^{rd} block, significant differences were found between the Medium and Long conditions ($F(1,39.40) = 12.37, p = 0.011$) and between the Short and Long conditions ($F(1,35.69) = 8.88, p = 0.045$). No significant differences were found for the contrasts of type (2) indicating no significant variation of the estimation error across blocks in any of the conditions.

9.4.2 ERSP activity during scene observation

We examined ERSP activity during the static observation phase, focusing on cortical activity beginning 1 second prior to eye-opening and extending for a period of 2 seconds.

First, in the alpha band (8-12 Hz), we observed a strong desynchronization, regardless of the age group, the condition or the ROI (Figures **9.5a**, **9.6a**, and **9.7a**). In older participants, this desynchronization manifested at the latency of eye-opening, while it began around +250 ms for the younger participants. In the OPA and the PPA only, this difference in onset of alpha oscillations between the two age groups proved statistically different (Figures **9.5c** and **9.6c**). In the long-lasting effects of this desynchronization, starting around +1250 ms after eye-opening, we revealed a difference in alpha band activity between the Medium and the Long conditions, in the MPA only (Figure **9.7d**). The pattern differed upon the age group, with the MPA of young participants exhibiting a more important desynchronization in the Long condition than in the Medium condition, while older adults displayed the inverted trend (Figure **9.7e**)

Regardless of the age group, the condition or the ROI, the alpha desynchronization extended to the beta band (12-30 Hz), although with a decreased intensity (Figures **9.5a**, **9.6a**, and **9.7a**). Similarly to the alpha desynchronization, it manifested sooner in older adults (at the latency of eye-opening) than in younger participants (around +250 ms), with statistical significance of this early onset exhibited only in the OPA (Figure **9.5c**). Age group comparison demonstrated a significantly greater beta-band desynchronization in the OPA for young participants compared to older adults, starting around +250 ms and sustained throughout the window of analysis (Figure **9.5c**). A similar age-related significant difference manifested in the MPA, but it was more transient and restricted to the end of the window of analysis, around +1750 ms (Figure **9.7c**). We found no significant effect of the condition over this frequency band.

In the OPA only, we report transient gamma (30-40 Hz) synchronization starting around +1000 ms, which seemed more pronounced when the distance in front of the participant was shorter (Figure **9.5a**). However, we found no statistical difference between the conditions to indicate this trend to be robust (Figure **9.5d**).

Eventually, we observed a synchronization in the delta/theta frequency band (2-8 Hz) across all ROIs from −250 ms to +500 ms in all age groups, with a slightly more pronounced effect in the older group (Figures **9.5a**, **9.6a**, and **9.7a**), although not found significant (Figures **9.5c**, **9.6c**, and **9.7c**). Beyond this period, the activity pattern inverted and we observed a significant desynchronization in the theta band (4-8 Hz) similarly across all ROIs, age groups and conditions, to the exception to the OPA, where the young adults ex-

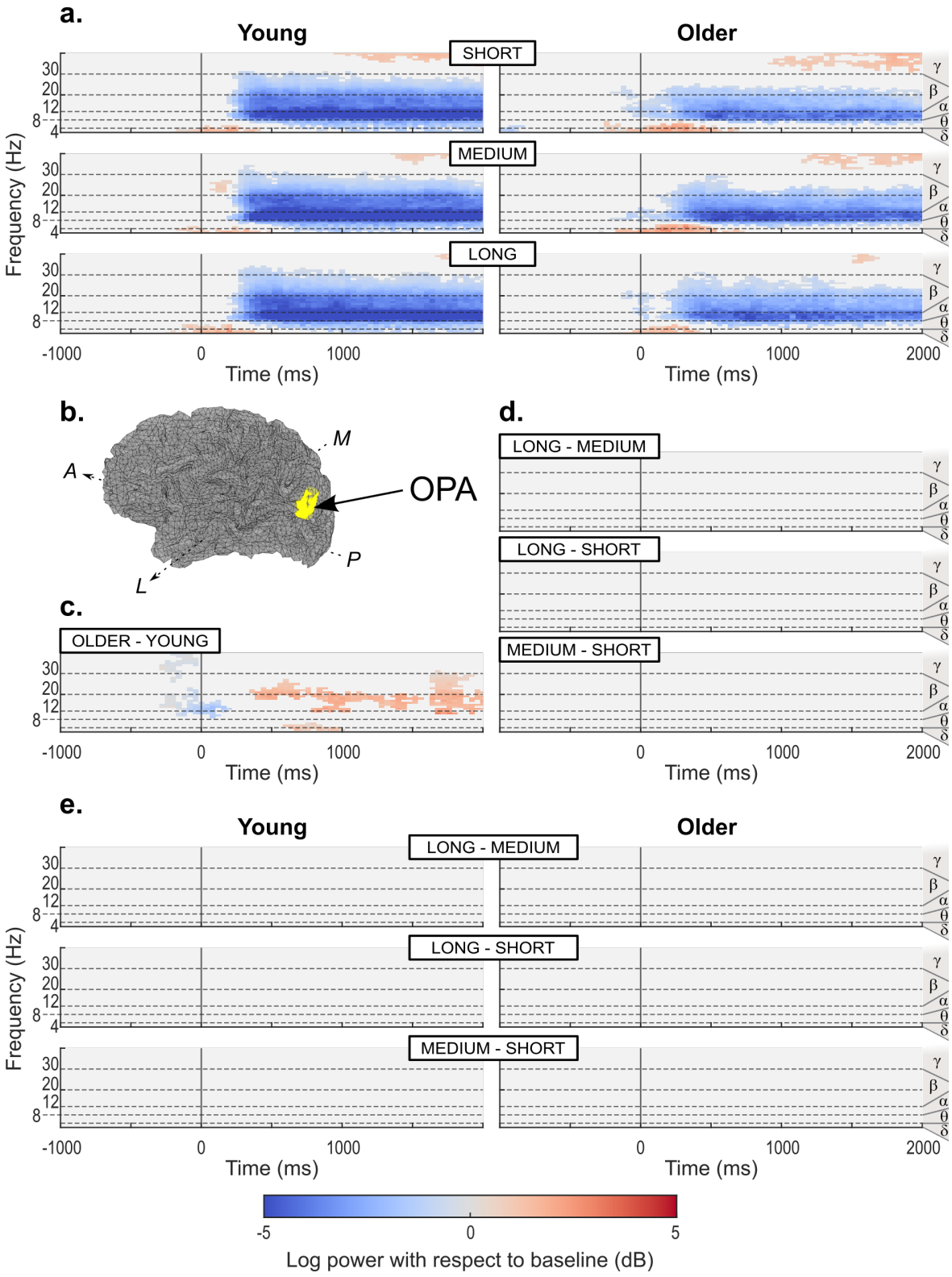

Figure 9.5: ERSP activity time-locked to the eye-opening event, reconstructed in the OPA. [Continued on next page]

Figure 9.5: [On previous page] Activity merged from both hemispheric locations after source reconstruction. We examined delta (δ; < 4 Hz), theta (θ; 4-8 Hz), alpha (α; 8-12 Hz), beta (β; 12-30 Hz) and gamma (γ; > 30 Hz) frequency bands. We investigated all statistical differences with permutation tests based on the maximum cluster-level statistic using 1000 permutations. We used linear mixed-effects modeling to evaluate the statistical significance at the 'pixel' level (spectral power at a given time-frequency pair) for a given permutation. **a**. Average activity per age group and condition baselined with the 1-second period prior to the eye-opening. We only display activity statistically different from the surrogate baseline distribution ($p < 0.05$). **b**. Illustration of the localization of the left OPA overlaid on left hemisphere source space (midgray surface) in one young participant. A: Anterior; P: Posterior; M: Medial; L: Lateral. **c**. Differences between age groups, irrespective of conditions. We indicate the direction of the difference above each graph (*e.g.* for the graph entitled "OLDER-YOUNG", we subtracted the average signal for the young adults from the average signal for the older adults, such that a positive difference means more power in the older group than in the young group and a negative difference means less power in the older group than in the young group). We only display statistically significant differences ($p < 0.05$). **d**. Differences between conditions, irrespective of age groups. We only display statistically significant differences ($p < 0.0083$, Bonferroni-corrected for 3 two-sided comparisons). **e**. Differences between conditions within each age group. We only display statistically significant differences ($p < 0.0041$, Bonferroni-corrected for 6 two-sided comparisons).

hibited a significantly enhanced desynchronization than older participants in the $+500$ ms and $+1000$ ms window following eye-opening (Figure **9.5c**).

9.5 Discussion

9.5.1 Behavior

The behavioral results allowed us to validate our paradigm, which was designed to assess distance perception abilities throughout adulthood. As expected, participants perceived the relative distance changes between conditions, and their estimates increased relative to the actual distance from the door. Thus, we were able to validate our experimental design, as the 3 starting intervals were contrasting enough for participants to induce a difference in the perception of the 3 navigable distances at the behavioral level. This encouraged us to further investigate the EEG activity associated with each condition to look for correlates of navigable distance perception.

However, in contrast to the existing literature (Bian & Andersen, 2013; Sugovic & Witt, 2013), we did not find a significant age-related effect on distance perception. We can formulate two hypotheses regarding this discrepancy with previous findings.

The first hypothesis concerns the population sample. In Bian and Andersen (2013), the results are drawn from a sample of 8 young adults and 9 older adults. In Sugovic and Witt (2013), they had a slightly larger number of subjects, but the age differences between the groups were larger than in our sample (Young group: $N = 12$, mean $= 20.27$ years; older group: $N = 12$, mean $= 81.38$ years old), which may have exacerbated age-related differences. In addition, they recruited older adults from an assisted living facility, suggesting to some degree a lack of autonomy in daily living, whereas our older participants were all recruited from the *SilverSight* cohort, where they had to comply with an extensive battery of tests certifying that they did not suffer from any visual or cognitive pathology. Another strength of our study is the number of repetitions, 24 per condition, whereas the two ref-

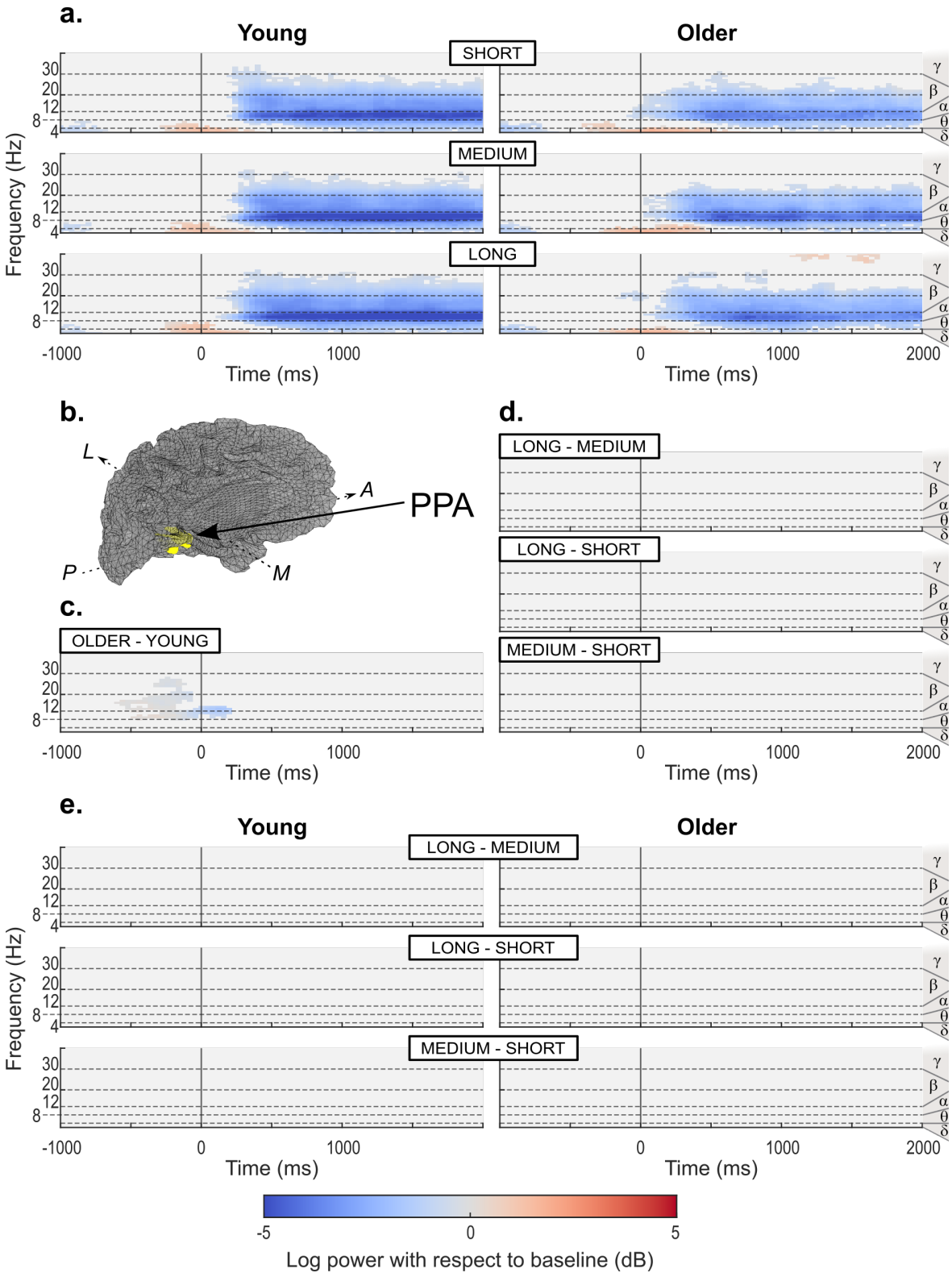

Figure 9.6: ERSP activity time-locked to the eye-opening event, reconstructed in the PPA. [Continued on next page]

Figure 9.6: [On previous page] For further details, see Figure **9.5** legend. **a**. Average activity per age group and condition baselined with the 1-second period prior to the eye-opening. We only display activity statistically different from the surrogate baseline distribution ($p < 0.05$). **b**. Illustration of the localization of the left PPA overlaid on left hemisphere source space (midgray surface) in one young participant. A: Anterior; P: Posterior; M: Medial; L: Lateral. **c**. Differences between age groups, irrespective of conditions. We only display statistically significant differences ($p < 0.05$). **d**. Differences between conditions, irrespective of age groups. We only display statistically significant differences ($p < 0.0083$, Bonferroni-corrected for 3 two-sided comparisons). **e**. Differences between conditions within each age group. We only display statistically significant differences ($p < 0.0041$, Bonferroni-corrected for 6 two-sided comparisons).

erence studies asked their participants to estimate distance only once per condition. This allows for more robust estimates, especially since we did not observe any evolution of the estimates between the first and the last block (although in some individual cases learning may be present at a finer timescale in the first block).

The second hypothesis involves multisensory integration, as a distinctive feature of this experiment with respect to comparable literature is the opportunity for participants to walk the estimated distance and thus compare their static visual estimate with the feedback coming from optic flow as well as vestibular and proprioceptive information. This aspect, tied to the multiple repetitions of the task, allows for a strategy of improvement across trials, which was reported by all participants included in these results (*e.g.*, trying to find a correspondence between the estimate and the number of steps to the door). Because path integration paradigms conducted under mobile conditions, which allows for multisensory integration, have often reported similar good performance between age groups (Adamo et al., 2012; Allen et al., 2004), this could be an important factor in explaining the undetectable differences between age groups in this experiment.

In general, for both age groups, we found a strong pattern of mean overestimation only in the long condition when comparing the true distance to the estimated distance. In contrast to the foreshortening pattern described previously (Bian & Andersen, 2013; Sugovic & Witt, 2013), the deviation from the correct estimate increased with distance, but in favor of overestimation instead of underestimation. Furthermore, since we notice a small tendency to underestimate short distances, our results are more consistent with a central tendency effect, in which estimated distances cluster around the mean of the stimulus set, previously observed in distance reproduction paradigms (Petzschner & Glasauer, 2011; Robinson & Wiener, 2021). Our results also show greater variability in estimation error with increasing distance (see Figure **9.4e-f**), which is also commonly reported in the path integration literature (Harootonian et al., 2020). These similarities again suggest a strong influence of multisensory integration in this paradigm. Because our participants relied heavily on step-counting strategies, we speculate that the observed pattern of increasing distance overestimation may result from the cumulative sum of overestimation errors at the single-step level. Indeed, Kluft et al. (2017) showed that both young and older adults had a similar tendency to overestimate their stepping ability.

Finally, it is interesting to note that gender had a significant effect on the distance estimation models. Specifically, men showed a systematic bias to overestimate more than

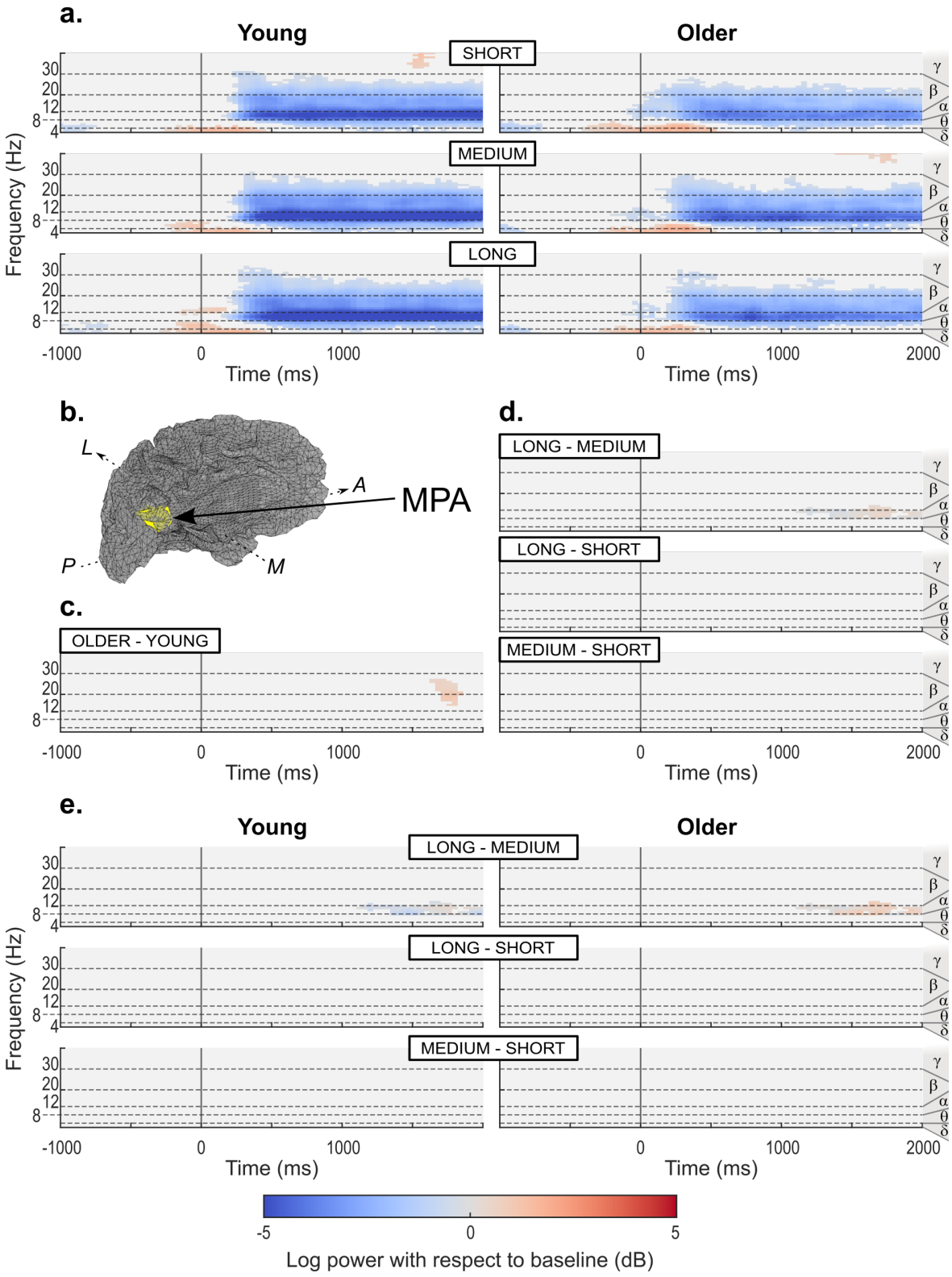

Figure 9.7: ERSP activity time-locked to the eye-opening event, reconstructed in the MPA. [Continued on next page]

Figure 9.7: [On previous page] For further details, see Figure **9.5** legend. **a**. Average activity per age group and condition baselined with the 1-second period prior to the eye-opening. We only display activity statistically different from the surrogate baseline distribution ($p < 0.05$). **b**. Illustration of the localization of the left MPA overlaid on left hemisphere source space (midgray surface) in one young participant. A: Anterior; P: Posterior; M: Medial; L: Lateral. **c**. Differences between age groups, irrespective of conditions. We only display statistically significant differences ($p < 0.05$). **d**. Differences between conditions, irrespective of age groups. We only display statistically significant differences ($p < 0.0083$, Bonferroni-corrected for 3 two-sided comparisons). **e**. Differences between conditions within each age group. We only display statistically significant differences ($p < 0.0041$, Bonferroni-corrected for 6 two-sided comparisons).

women in all conditions. No gender difference in this ability had previously been reported, although gender differences are pervasive in the spatial cognition literature, often associated with better performance for male participants than for females (Saucier et al., 2002; Voyer et al., 1995). Potentially providing a clue for the interpretation of our result, Kober and Neuper (2011) reported increased correlates of sensorimotor integration in females compared to males, although tested under very different conditions (*i.e.*, spatial navigation in a maze using landmarks in desktop-based VR).

9.5.2 EEG

The ERSP analysis was performed on the observation period that was tied to scene perception from a static position with respect to the door in front of the participant. We took special care to detect the actual eye-opening event of the participants in order to capture the correlates of visual processing and to correctly define the pre-stimulus baseline where the participants had their eyes closed.

The most striking result from the ERSP analysis is the common desynchronization of the alpha band with respect to the closed-eye baseline, which is a well-known signature of visual processing in the occipital lobe (Klimesch, 1999; Pfurtscheller et al., 1994). This signature was found across all SSRs and all age groups. The main difference between age groups was related to the onset of alpha-band desynchronization, which occurred later in young adults, about 250 ms after eye-opening detection, especially in the OPA and PPA. This observation could reflect a more rapid mobilization of cognitive resources by older adults than by young adults, as already suggested by Missonnier et al. (2011), especially in low-demand cognitive tasks.

Alpha desynchronization in the SSRs was accompanied by beta desynchronization. Strikingly, Liang et al. (2021) reported a similar oscillation pattern over the parieto-occipital region that was modulated by the distance traveled by the participants. Although our results are limited to a static observation phase, it is likely that distance estimation involves mental imagery of the distance traveled to the door. In that case, our results may highlight the precursor implication of SSRs in the physical experience of space, consistent with the central role of vision in navigation (Ekstrom, 2015). In addition, beta-band desynchronization showed a significant age-related difference during scene viewing, particularly in the OPA. Under the mental reproduction of travel hypothesis, this could reflect the association of beta power with temporal reproduction duration (Kononowicz & van Rijn, 2015), as older adults

have a slower walking speed than young adults (the same distances take longer to travel). This mental reproduction hypothesis is also supported by the retrieval of delta/theta oscillations, which are frequently found in spatial coding of movement, especially in intracranial hippocampal recordings (Aghajan et al., 2017; Bohbot et al., 2017; Bush et al., 2017; Vass et al., 2016).

However, in contrast to the behavioral results, the EEG analysis did not reveal many differences between conditions. We found a significant difference between the Long and Medium conditions only in the late phase of scene viewing and only in the MPA. There is currently no evidence in the literature to help interpret this pattern. These results did not replicate the fMRI results presented in J. Park and Park (2020). Because they used much greater distance intervals than in this experiment, it may be that the relative variation between the starting positions was not enough to find significant differences between the conditions in the activity of the OPA. Moreover, since J. Park and Park (2020) relied on a multivariate pattern analysis to investigate the correlation of OPA activity with the observed navigable distance, it is possible that the univariate EEG analysis performed here did not provide sufficient detail to reveal the affordance encoding in the OPA. It is interesting to note that in another fMRI study close to this question, Bonner and Epstein (2017) reported that the univariate analysis of OPA activity was not sufficient to reveal a significant correlation with navigational affordances, and only their multivariate analysis revealed a positive association. Therefore, it may be an interesting future perspective to perform multivariate analysis on the activity of the SSRs by keeping the activity specific to each dipole in the ROI instead of averaging the source reconstructed activity. Encouragingly, the trend observed for gamma-band synchronization, which seemed to gradually intensify with closer distances to the door, especially in the OPA, may be the sign of a correlation between perceived distance and univariate EEG activity. Indeed, it is often argued that gamma activity is the EEG signature that correlates most strongly with the fMRI blood oxygen level dependent (BOLD) signal (Buzsáki et al., 2012).

In contrast to Harel et al. (2022), who found a significant scaling of P2 amplitude with the number of affordances in the presented scene, we did not have time to perform an ERP analysis because it relied on the precise timing of eye-opening, which was obtained late in the analysis. This shows that univariate ERP analysis of the EEG signal recorded from the SSRs, and in this case more specifically from the OPA, can reveal substantial differences between affordance levels. A similar investigation in our study may be a promising avenue, although concerns have been raised about combining source localization and ERP analysis (Nunez & Srinivasan, 2006).

9.6 Conclusion & Immediate perspectives

As suggested by the behavioral results of this paradigm, incorporating the multisensory aspects of spatial cognition profoundly affects how we judge spatial distance and moderates age-related differences in a healthy aging context. So far, however, the additional evidence brought by the EEG analysis remains rather limited. The most satisfying aspect is that the

OPA seems to be the most involved among the 3 SSRs, in line with the specificity of this region for navigational affordances reported in the literature.

For immediate future analyses, we plan to investigate the cognitive correlates of approaching the door to further investigate whether these regions might be involved in spatial coding during real-time execution of the movement. In addition, as mentioned above, to explain the lack of consistent modulation of brain signals by condition, alternative approaches such as an ERP or/and multivariate analysis will be considered to fully explore the coding of affordances in the OPA reported in previous studies. Finally, as we have unraveled a strong alpha desynchronization, it may be appropriate to adopt a frequency modulation approach for this band, as it has been successfully correlated with distance and duration coding in previous reports (Cao & Händel, 2019; Liang et al., 2021).

CHAPTER 10

CORTICAL MARKERS OF VISUAL RECOVERY AFTER OPTOGENETIC THERAPY

This chapter regroups the experimental investigations associated with the EEG ancillary study of the PIONEER clinical trial, the major translational contribution of this thesis. This open-label phase I/IIa clinical study is designed to evaluate the safety and efficacy of an investigational treatment for patients with advanced non-syndromic *Retinitis Pigmentosa* (RP) that combines injection of an optogenetic vector with the wearing of light-stimulating goggles. The study is multi-centric (London, Paris, and Pittsburgh), however the results reported contain only recordings from Paris center patients. The goal of the EEG ancillary study is to investigate and quantify the visual restoration elicited by the therapy with neural markers.

The case study of the first patient to show significant progress following therapy has been reported, peer-reviewed and published as a journal article, entitled "Partial recovery of visual function in a blind patient after optogenetic therapy", in Nature Medicine, released in May 2021 (Sahel et al., 2021). It is transcribed in Section **10.1** exactly as written in the published version. Supplementary material attached to the published version of the article are presented in Appendix **F**. More precisely, the contribution of this thesis to that publication covered:

1. The adaptation of the existing behavioral protocol to the requirements of an EEG experiment quantifying visual perception.
2. The collection of the experiment on the subject (third test).
3. The conduction of the EEG data analysis (*i.e.*, data preprocessing, features extraction, training the decoder and perform the statistical analysis of the results).
4. The writing of the EEG sections of the manuscript (*i.e.*, methods, results, discussion).

Section **10.2** describes the experimental developments made since the publication of this article. These included testing new patients responding favorably to therapy and adapting the existing protocol to enrich the interpretation of the recorded brain activity. This work is still ongoing, and the results reported here require further consolidation.

10.1 Partial recovery of visual function in a blind patient after optogenetic therapy

nature medicine

ARTICLES

https://doi.org/10.1038/s41591-021-01351-4

Check for updates

Partial recovery of visual function in a blind patient after optogenetic therapy

José-Alain Sahel[1,2,3,4]✉, Elise Boulanger-Scemama[3,4], Chloé Pagot[5], Angelo Arleo[1], Francesco Galluppi[6], Joseph N. Martel[2], Simona Degli Esposti[7], Alexandre Delaux[1], Jean-Baptiste de Saint Aubert[1], Caroline de Montleau[5], Emmanuel Gutman[5], Isabelle Audo[1,3], Jens Duebel[1], Serge Picaud[1], Deniz Dalkara[1], Laure Blouin[6], Magali Taiel[6] and Botond Roska[8,9]✉

Optogenetics may enable mutation-independent, circuit-specific restoration of neuronal function in neurological diseases. Retinitis pigmentosa is a neurodegenerative eye disease where loss of photoreceptors can lead to complete blindness. In a blind patient, we combined intraocular injection of an adeno-associated viral vector encoding ChrimsonR with light stimulation via engineered goggles. The goggles detect local changes in light intensity and project corresponding light pulses onto the retina in real time to activate optogenetically transduced retinal ganglion cells. The patient perceived, located, counted and touched different objects using the vector-treated eye alone while wearing the goggles. During visual perception, multichannel electroencephalographic recordings revealed object-related activity above the visual cortex. The patient could not visually detect any objects before injection with or without the goggles or after injection without the goggles. This is the first reported case of partial functional recovery in a neurodegenerative disease after optogenetic therapy.

[1]Sorbonne Université, Institut National de la Santé et de la Recherche Médicale, Centre National de la Recherche Scientifique, Institut de la Vision, Paris, France. [2]Department of Ophthalmology, The University of Pittsburgh School of Medicine, Pittsburgh, PA, USA. [3]Institut National de la Santé et de la Recherche Médicale-Centre d'Investigation Clinique 1423, Centre Hospitalier National d'Ophtalmologie des Quinze-Vingts, Paris, France. [4]Département d'Ophtalmologie, Fondation Ophtalmologique Rothschild, Paris, France. [5]Streetlab, Institut de la Vision, Paris, France. [6]GenSight Biologics, Paris, France. [7]National Institute for Health Research Moorfields Biomedical Research Centre at Moorfields Eye Hospital and UCL Institute of Ophthalmology, London, UK. [8]Institute of Molecular and Clinical Ophthalmology Basel, Basel, Switzerland. [9]Department of Ophthalmology, University of Basel, Basel, Switzerland. ✉e-mail: sahelja@upmc.edu; botond.roska@iob.ch

Figure 10.1: Cover of the article "Partial recovery of visual function in a blind patient after optogenetic therapy", as published in Nature Medicine (Sahel et al., 2021).

10.1.1 Introduction

Retinitis Pigmentosa (RP) is a progressive, inherited, monogenic or rarely digenic (Kajiwara et al., 1994) blinding disease caused by mutations in more than 71 different genes (`https://web.sph.uth.edu/RetNet/sum-dis.htm`). It affects more than 2 million people worldwide. With the exception of a gene replacement therapy for one form of early-onset RP caused by mutation in the gene *RPE65* (Russell et al., 2017), there is no approved therapy for RP.

Optogenetic vision restoration (Bi et al., 2006; Busskamp et al., 2010; Lagali et al., 2008) is a mutation-independent approach for restoring visual function at the late stages of RP after vision is lost (Roska & Sahel, 2018; Sahel et al., 2019; Sahel & Roska, 2013; Scholl et al., 2016). The open-label phase 1/2a PIONEER study (*ClinicalTrials.gov* identifier: NCT03326336; the clinical trial protocol is provided in the Supplementary Text) was designed to evaluate the safety (primary objective) and efficacy (secondary objective) of an investigational treatment for patients with advanced nonsyndromic RP that combines injection of an optogenetic vector (GS030-Drug Product (GS030-DP)) with wearing a medical device, namely light-stimulating goggles (GS030-Medical Device (GS030-MD)). The proof of concept for GS030-DP and the GS030-DP dose used in the PIONEER clinical trial were established in nonhuman primate studies (Gauvain et al., 2021; Picaud et al., 2019).

The optogenetic vector, a serotype 2.7m8 (Dalkara et al., 2013) adeno-associated viral vector encoding the light-sensing channelrhodopsin protein *ChrimsonR* fused to the red fluorescent protein *tdTomato* (Klapoetke et al., 2014), was administered by a single intravitreal injection into the worse-seeing eye to target mainly foveal retinal ganglion cells (Gauvain et al., 2021). The fusion protein *tdTomato* was included to increase the expression of *ChrimsonR* in the cell membrane (Gauvain et al., 2021). The peak sensitivity of *ChrimsonR-tdTomato* is around 590 nm (amber color) (Klapoetke et al., 2014). We chose *ChrimsonR*, which has one of the most red-shifted action spectra among the available optogenetic sensors because amber light is safer and causes less pupil constriction (Gauvain et al., 2021) than the blue light used to activate many other sensors. The light-stimulating goggles capture images from the visual world using a neuromorphic camera that detects changes in intensity, pixel by pixel, as distinct events (Posch et al., 2011). The goggles then transform the events into monochromatic images and project them in real time as local 595 nm light pulses onto the retina (Supplementary Figure **F.1**).

10.1.2 Results

10.1.2.1 Safety of the optogenetic vector and light-stimulating goggles

In this article, we describe the partial recovery of vision in one participant of the PIONEER study. At the inclusion in the study, this 58-year-old male, who was diagnosed with RP 40 years ago, had a visual acuity limited to light perception. The worse-seeing eye was treated with 5.0×10^{10} vector genomes of optogenetic vector. Both before and after the injection, we performed ocular examinations and assessed the anatomy of the retina based on optical

coherence tomography images, color fundus photographs and fundus autofluorescence images taken on several occasions over 15 visits spanning 84 weeks according to the protocol (Supplementary Figure **F.2**). We monitored potential intraocular inflammation according to the international guidelines of the Standardization of Uveitis Nomenclature Working Group (SUN working group, 2005; Trusko et al., 2013) (further details are provided in the clinical trial protocol). In addition, we assessed vital signs at each visit and performed a general examination and electrocardiogram before and after the injection. There was no intraocular inflammation, no changes in the anatomy of the retina and no ocular or systemic adverse events over the follow-up period (details of the findings are shown in the Supplementary Section **F.1** and Supplementary Figures **F.3-F.6**). The treated eye retained light perception over the 84 weeks of testing.

We tested the light-stimulating goggles on the patient three times before vector injection (Supplementary Figure **F.2**). The patient did not report any change of vision or photophobia on any of these occasions. Four and a half months after the injection, we started systematic visual training using the light-stimulating goggles (Supplementary Figure **F.7**). Training was not started sooner because the expression of *ChrimsonR-tdTomato* in foveal ganglion cells stabilizes between two and six months after injection in nonhuman primates (Gauvain et al., 2021). Seven months after the start of visual training, the patient began to report signs of visual improvement when using the goggles.

10.1.2.2 Partial recovery of visual function

We analyzed the visual improvement under three conditions with three psychophysical tests. The conditions were: (1) both eyes open without the light-stimulating goggles (natural binocular); (2) untreated eye covered, treated eye open without the goggles (natural monocular); and (3) untreated eye covered, treated eye open and stimulated with the goggles (stimulated monocular).

The first test consisted of perceiving, locating and touching a single object placed on a white table (80×80 cm^2 or $67.2^\circ \times 50.9^\circ$ visual angle, calculated based on distance from

Stimulus	Natural binocular: both eyes open without the light-stimulating goggles			Natural monocular: untreated eye covered, treated eye open without the light-stimulating goggles			Stimulated monocular: Non-treated eye covered, treated eye open and stimulated with the light-stimulating goggles		
	Perceive	**Locate**	**Touch**	**Perceive**	**Locate**	**Touch**	**Perceive**	**Locate**	**Touch**
Notebook, contrast = 40%	0/1	0/1	0/1	0/1	0/1	0/1	4/4	4/4	4/4
Notebook, contrast = 55%	0/1	0/1	0/1	0/1	0/1	0/1	4/5	4/5	4/5
Notebook, contrast = 100%	0/1	0/1	0/1	0/1	0/1	0/1	4/4	4/4	4/4
Staple box, contrast = 40%	0/1	0/1	0/1	0/1	0/1	0/1	3/6	3/6	2/6
Staple box, contrast = 55%	0/1	0/1	0/1	0/1	0/1	0/1	2/5	2/5	1/5
Staple box, contrast = 100%	0/1	0/1	0/1	0/1	0/1	0/1	1/4	1/4	1/4

Table 10.1: First test: finding the notebook or staple box. In natural conditions, no test repetition was performed because the patient was unable to complete the task. He could not see anything and did not want to try again.

the eye) along an imaginary line 40 cm in front of the patient (60 cm distance from the eye), either 20 cm to the right or to the left (18.4° visual angle relative to the middle) or in the middle (Supplementary Figure **F.8**). The object was either large, that is, a 12.5×17.5 cm^2 notebook ($10.8° \times 10.3°$), or small, that is, a 3×5.5 cm^2 staple box ($2.8° \times 3.7°$), shown one by one in three different grayscale contrasts (notebook and staple box: Michelson contrast = 40, 55 and 100%; notebook: root mean square (RMS) contrast = 0.41, 0.53 and 0.80; staple box: RMS contrast = 0.13, 0.16 and 0.21) in random order. During the first test, the patient was unable to perceive any of the objects under natural binocular or natural monocular conditions; therefore, he did not attempt to locate or touch them (Table **10.1** and Supplementary Video 1). In contrast, in the stimulated monocular condition, the patient perceived the presence of, located and touched the larger object in 92% (36 out of 39) of the trials (Table **10.1** and Supplementary Video 1). We performed a multivariable logistic regression analysis for success in performing the tasks, with object size (large or small), contrast (low = 40%, medium = 55% or high = 100%) and task (perceive, locate or touch) as the explanatory variables. The success rate was dependent on the size of the object, with a significantly higher rate of successful trials with the larger object than with the smaller one (36% [16/45]; $p < 0.001$, likelihood-ratio test for the effect of object size). The success rate was similar for objects at different contrasts (low = 67% [20/30]; medium = 57% [17/30]; high = 63% [15/24]; $p = 0.29$, likelihood-ratio test for the effect of contrast), suggesting that even objects at lower contrasts generated enough retinal activity for perception. Finally, the success rate was similar for the different tasks (perceive, 64% [18/28]; locate, 64% [18/28]; touch, 57% [16/28]; $p = 0.73$, likelihood-ratio test for the effect of task), suggesting that once the object was perceived, the patient could coordinate his motor system with the percept.

The second test included perceiving, counting and locating more than one object, that is, either two or three tumblers (Supplementary Figure **F.9**). The patient was asked to determine how many objects were placed on the white table and point to them without touching. Each tumbler (6 cm diameter and 6 cm height, 5.5° and 8.1° at 40 cm, 4.2° and 5.8° at 66 cm) was positioned in 1 of 6 possible positions along two imaginary lines: at 40 cm in front of the patient (60 cm distance from the eye), either 20 cm to the right or to the left (18.4° relative to the middle) or in the middle; or at 66 cm in front of the patient (80 cm distance from the eye), either 20 cm to the right or to the left (14°) or in the middle. The objects

Stimulus	Natural binocular: both eyes open without the light-stimulating goggles			Natural monocular: untreated eye covered, treated eye open without the light-stimulating goggles			Stimulated monocular: Non-treated eye covered, treated eye open and stimulated with the light-stimulating goggles		
	Perceive	Locate	Touch	Perceive	Locate	Touch	Perceive	Locate	Touch
Tumblers, contrast = 40%	0/1	0/1	0/1	0/1	0/1	0/1	4/6	4/6	4/6
Tumblers, contrast = 55%	0/1	0/1	0/1	0/1	0/1	0/1	5/7	5/7	5/7
Tumblers, contrast = 100%	0/1	0/1	0/1	0/1	0/1	0/1	3/6	3/6	2/6

Table 10.2: Second test: counting and locating tumblers. In natural conditions, no test repetition was performed because the patient was unable to complete the task. He could not see anything and did not want to try again.

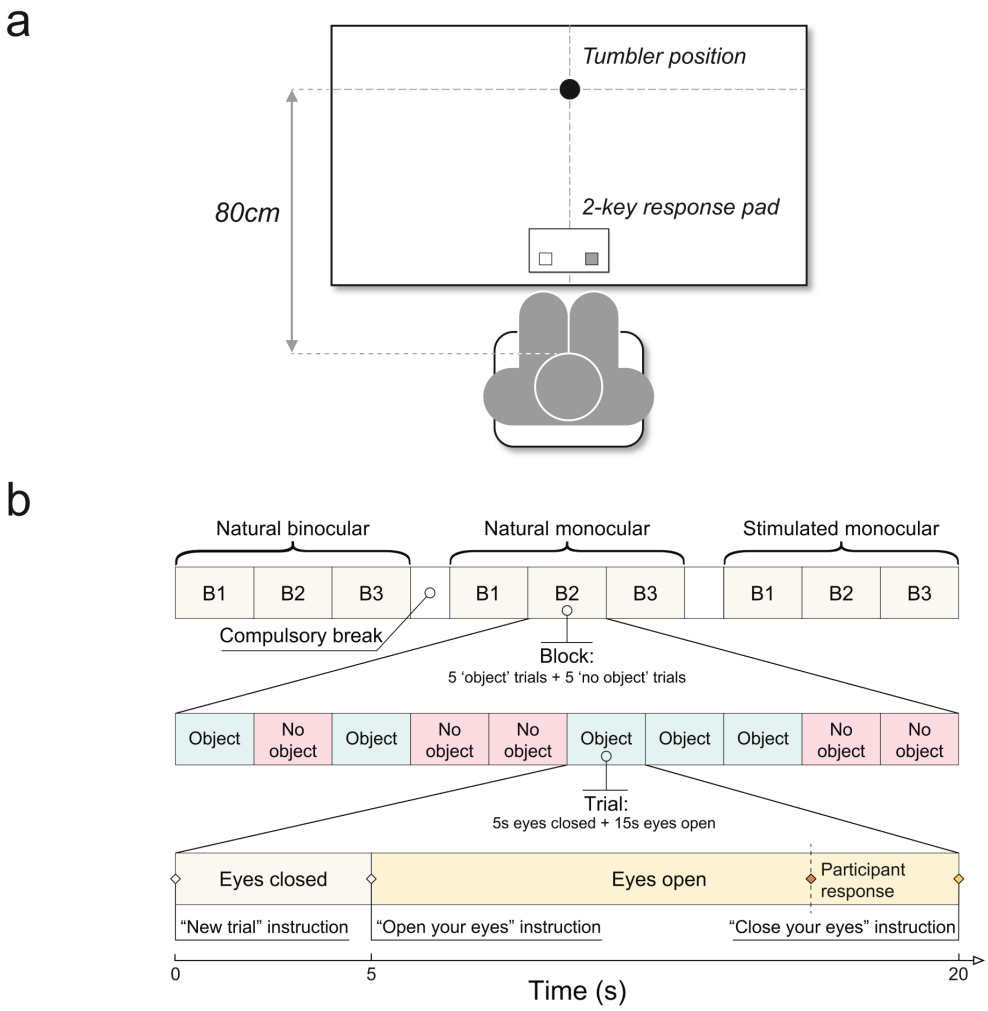

Figure 10.2: Visual task coupled with electro-encephalography (EEG) recordings. [Continued on next page]

Figure 10.2: [On previous page] **a**. Visual detection task. The patient had to assess the presence or absence of a tumbler (6×6 cm^2) on a white table (Michelson contrast = 55%) through a two-key response pad. The tumbler was positioned 80 cm in front of the patient. **b**. Experimental protocol. The entire experiment involved two sessions, with a total of 183 randomized object/no-object trials for a total duration of about 140 minutes. Each recording session included three conditions: natural binocular; natural monocular; and stimulated monocular. Each condition was divided into three blocks consisting of ten trials each: five object trials and five no-object trials (tumbler removed from the table). Each trial lasted 20 s. The patient was instructed to close his eyes during the first 5 s (while the experimenter placed/removed the tumbler on/from the table). The patient was then asked to open his eyes and was given 15 s to determine visually whether the tumbler was present on the table. **c**. Experimental setup. Behavioral responses and brain activity were simultaneously recorded during the visual test. EEG data analysis focused on the activity recorded from the occipital channels O_1, O_z and O_2.

were shown at three contrasts (Michelson contrast = 40, 55 and 100%; RMS contrast = 0.29, 0.33 and 0.41) in random order. In this test, similar to the results of the first test, the patient was unable to perceive the objects under natural binocular or natural monocular conditions; therefore, he did not attempt to count or locate them (Table **10.2** and Supplementary Video 2). In contrast, in the stimulated monocular condition, the patient perceived the objects in 63% of the trials [12/19]. Furthermore, he correctly counted and located them in most of the trials (count, 63% [12/19]; locate, 58% [11/19]; Table **10.2** and Supplementary Video 2). As in the first test, the success rate was similar for objects at different contrasts (low = 67% [12/18]; medium = 71% [15/21]; high = 44% [8/18]; $p = 0.20$, likelihood-ratio test for the effect of contrast).

10.1.2.3 Neural correlates of vision recovery

To investigate the link between partial vision recovery and neuronal activity, we performed a third test that combined the assessment of vision with a noninvasive brain recording technique, extracranial multichannel EEG, which provides a readout of neuronal activity across the cortex (Figure **10.2**). This technique is more suitable than functional magnetic resonance imaging since the metallic components of the goggles are incompatible with the magnetic field generated by a magnetic resonance imaging scanner. We analyzed EEG traces in the eyes-open and eyes-closed states separately for each of the three conditions (natural binocular, natural monocular and stimulated monocular). A tumbler (6 cm diameter and 6 cm height, 4.2° and 5.8°, Michelson contrast = 55%, RMS contrast = 0.33) was placed or not placed on a white table in front of the patient and the patient had to assess its presence or absence. When present, the tumbler was always placed at the same position (66 cm in front

	Natural binocular: both eyes open without the light-stimulating goggles			**Natural monocular: untreated eye covered, treated eye open without the light-stimulating goggles**			**Stimulated monocular: Non-treated eye covered, treated eye open and stimulated with the light-stimulating goggles**		
Trial	**Answer: yes object**	**Answer: no object**	**No answer**	**Answer: yes object**	**Answer: no object**	**No answer**	**Answer: yes object**	**Answer: no object**	**No answer**
Object trial	3/30	0/30	27/30	2/30	2/30	26/30	21/32	2/32	9/32
No-object trial	3/30	1/30	26/30	2/30	1/30	27/30	3/31	5/31	23/31

Table 10.3: Third test: visual detection task (coupled with EEG recordings).

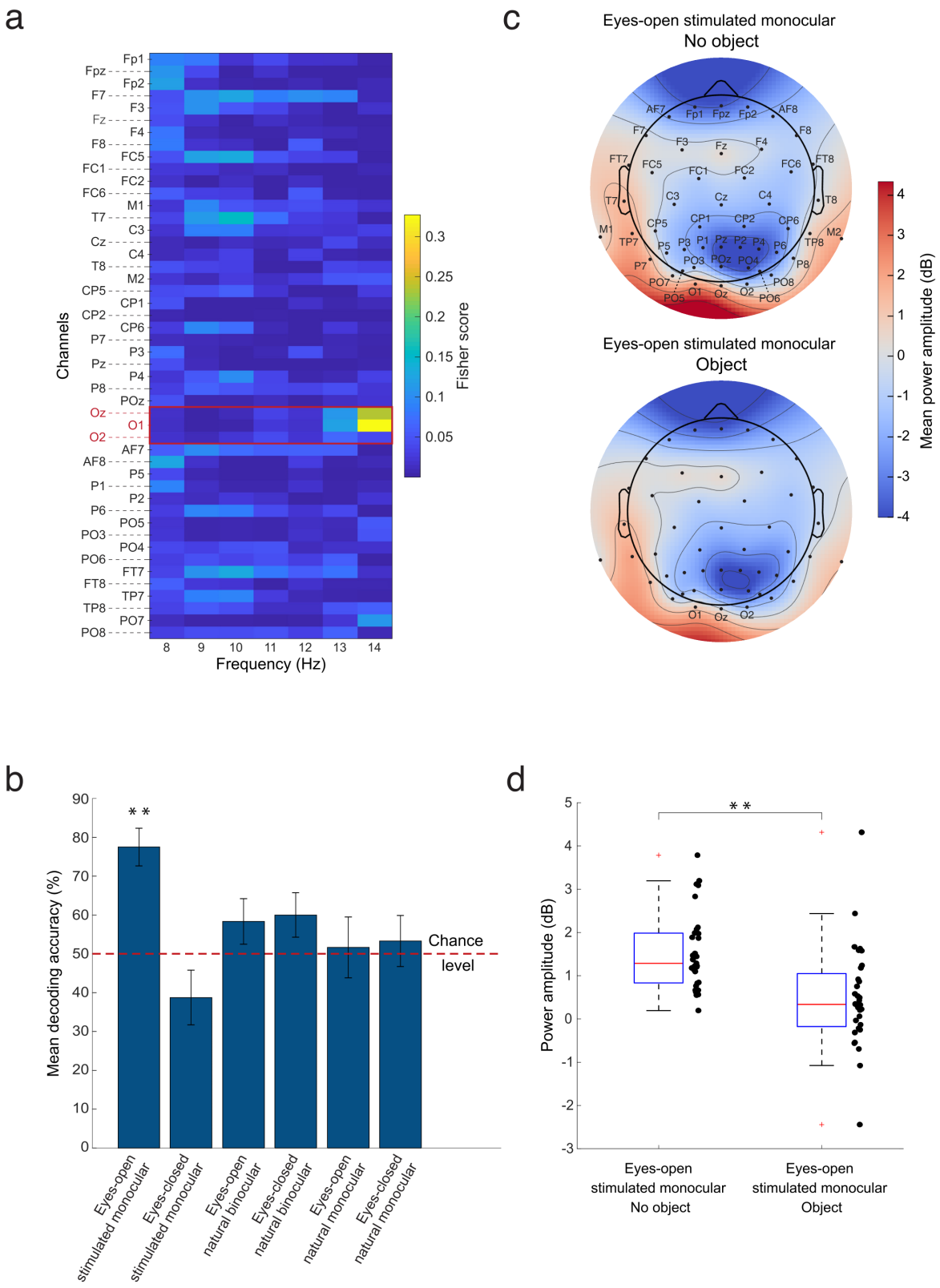

Figure 10.3: Decoding EEG data based on power spectrum amplitude modulation of occipital alpha oscillations. [Continued on next page]

Figure 10.3: [On previous page] **a**. Fisher scores for object versus no-object discrimination during the eyes-open periods in the stimulated monocular condition, calculated from power amplitude over all EEG channels for the alpha band (8-14 Hz). Only features from the occipital channels O_1, O_z and O_2 (red) were given as input to the binary decoder. **b**. Mean decoding accuracy evaluated by k-fold cross-validation on eyes-open and eyes-closed periods during stimulated monocular (63 trials), natural binocular (60 trials) and natural monocular (60 trials) conditions. The error bars indicate the SEM ($N = 20$ folds). For a given condition, the data points indicate the decoding accuracy for each fold. Data points are distributed across discrete levels according to the number of randomized testing trials per fold. One-sided, one-sample Wilcoxon signed rank test against chance level (50%). The outcomes for each condition were: eyes-open stimulated monocular $V(19) = 199$, $p = 1.79 \times 10^{-4}$, $r = 0.895$, CI $= [0.773, +\infty]$; eyes-closed stimulated monocular $V(19) = 66.5$, $p = 0.933$, $r = 0.108$, CI $= [-0.357, +\infty]$; eyes-open natural binocular $V(19) = 140.5$, $p = 0.082$, $r = 0.479$, CI $= [0.091, +\infty]$; eyes-closed natural binocular $V(19) = 142$, $p = 0.073$, $r = 0.352$, CI $= [-0.051, +\infty]$; eyes-open natural monocular $V(19) = 111.5$, $p = 0.408$, $r = 0.640$, CI $= [0.282, +\infty]$; eyes-closed natural monocular $V(19) = 124$, $p = 0.233$, $r = 0.621$, CI $= [-0.266, +\infty]$. **c**. Topographic representation of the mean power amplitude at 14 Hz over the eyes-open period in the stimulated condition averaged across trials. Top: no-object trials. Bottom: object trials. A lower power amplitude indicates a desynchronization of alpha oscillations in the visual areas, which is a signature for increased cortical excitability (Romei et al., 2008; Vandewalle et al., 2018), near-threshold stimulus perception (Ergenoglu et al., 2004; Vandewalle et al., 2018) and information transfer to downstream ventral object-selective regions (Zumer et al., 2014). **d**. Modulation of the power spectrum amplitude in the alpha band (that is, average signal in the occipital channels O_1 and O_z at 14 Hz) enabling the decoding of object versus no-object trials in the stimulated eyes-open condition. The horizontal red bars indicate the median, the blue boxes delimit the 1^{st} and 3^{rd} quartiles and the error bars encompass all non-outlier data (outliers shown by red crosses). Individual data points are shown on the right. Two-sided Mann-Whitney U-test, object ($N = 32$) versus no-object ($N = 31$) trials, $W = 792.5$, $p = 4.71 \times 10^{-5}$, $r = 0.598$, CI $= [0.382, 0.752]$. For all tests, $**p < 0.001$. CIs are 95%.

of the patient, 80 cm from the eye). We conducted a multivariable logistic regression analysis for correct assessments with condition (stimulated versus natural) and object presence (yes or no) as the explanatory variables. The rate of correct assessments was significantly higher under stimulated monocular (41% (26 out of 63)) than natural binocular or monocular conditions (5.8% (7 out of 120) for both conditions; $p < 0.001$, likelihood-ratio test for the effect of condition; Table **10.3**).

To localize the neuronal activity with the highest information content about the visual object across the cortex, we performed a spectral analysis of the recorded signals across the 48 EEG channels in the alpha-band (8-14 Hz) in the eyes-open stimulated monocular condition. We found that the highest discriminant power for the object/no-object trials was located above the occipital cortex contralateral to monocular stimulation, with the most informative features corresponding to channels O_1 and O_z at 14 Hz (Figure **10.3a**). We then trained a linear binary decoder with the mean alpha-power amplitudes of the occipital channels to discriminate object versus no-object trials. In the stimulated monocular condition and eyes-open state, the decoder reached a mean accuracy of 78% ($\pm$4.8 [SEM]), which was significantly above chance level (Figure **10.3b**; 20-fold cross-validation, one-sided, one-sample Wilcoxon signed rank test, $p < 0.001$). By contrast, the accuracy of decoders remained at chance level when trained under the eyes-closed state of the stimulated monocular condition, as well as under both eyes-open and eyes-closed states of the natural binocular and natural monocular conditions (Figure **10.3b**; eyes-closed stimulated monocular, $39 \pm 7.1\%$, $p = 0.93$; eyes-open natural binocular, $58 \pm 5.9\%$, $p = 0.08$; eyes-closed natural binocular, $60 \pm 5.7\%$, $p = 0.07$; eyes-open natural monocular, $52 \pm 7.1\%$, $p = 0.41$; eyes-closed natural

monocular, $53 \pm 6.6\%$, $p = 0.23$). Leave-one-out cross-validation testing provided similar decoding results (eyes-open stimulated monocular, 75%; eyes-closed stimulated monocular, 41%; eyes-open natural binocular, 55%; eyes-closed natural binocular, 62%; eyes-open natural monocular, 55%; eyes-closed natural monocular, 55%). The above-chance accuracy of the decoder trained with the occipital EEG signals recorded during the eyes-open stimulated monocular condition stemmed from a modulation of the 14 Hz alpha-power spectrum amplitude as a function of the presence/absence of the object (Figure **10.3c**). Object-triggered optogenetic stimulation led to a significant power decrease (that is, a desynchronization) of occipital 14 Hz alpha oscillations (Figure **10.3d**; two-sided Mann-Whitney U-test, object versus no-object trials, $p < 0.001$).

10.1.3 Discussion

In this study, we present the first evidence that injection of an optogenetic sensor-expressing gene therapy vector combined with the wearing of light-stimulating goggles can partially restore visual function in a patient with RP who had a visual acuity of only light perception.

The results of all three visual and visuomotor tests suggest that optogenetic retinal stimulation triggered by the visual scene induced visual perception. Moreover, the visual process leading to the percept was effective enough to enable the patient to orient toward the object and perform the visuomotor task of reaching for it. The first and second tests were performed five months before the third visual test (Supplementary Figure **F.2**), suggesting that the gain in visual function was stable over this period.

In addition to the visual and visuomotor tests, we obtained further evidence of vision recovery in that the EEG recording of occipital cortex signals was modulated by the presence or absence of a visual object. A large body of work has coupled EEG recordings with the assessment of visual function in low-vision patients. Since the 1950*s*, cortical correlates of vision in visually impaired patients with RP have been investigated using EEG, through the assessment of alpha rhythm modulations (Ebe et al., 1964; Francois et al., 1954; Gillespie & Dohogne, 1964; Krill & Stamps, 1960; Streifler & Landau, 1955), as well as using visually evoked potentials (Alexander et al., 2005; Hamilton et al., 2021; Paranhos et al., 1998; Parisi et al., 2010). Furthermore, other characteristics of the EEG signal have been used to investigate the neural correlates in low-vision patients or patients with functional visual recovery. For instance, substantial differences to healthy individuals have been found during visual stimulation of patients with inherited retinal dystrophies using the shape of the EEG power spectral density, in particular in the occipital electrodes (Myers et al., 2017). Posterior alpha and theta activity related to the visual processing of motion has also been used to identify the neural mechanisms of functional sight restoration (Bottari et al., 2016).

In this study, the EEG recordings suggested that retinal activity evoked by the optogenetic stimulation of the retina propagates to the primary visual cortex and modulates its activity. This cortical activity, quantified as changes in amplitude of the local EEG alpha power, conveys sufficient information to allow object versus no-object stimulations to be decoded on a single-trial basis. Our findings are consistent with the involvement of occipital

alpha rhythm fluctuations in object-based visual attention (W. Feng et al., 2017) and processing (Vanni et al., 1997), top-down control of visual attention (for example, to mediate forthcoming visual stimulation processing Romei et al. 2010; Thut et al. 2006; van Dijk et al. 2008; Wyart and Tallon-Baudry 2008), stimulus discrimination in object detection (Vanni et al., 1997) and object recognition (Freunberger et al., 2008). Our analysis of the EEG power spectrum shows that visual object-triggered optogenetic stimulation induces desynchronization of occipital EEG oscillations in the upper alpha range, as shown by a significant decrease in the 14 Hz power amplitude compared to the absence of the object. Alpha-power decrease in visual areas has been associated with increased cortical excitability (Romei et al., 2008; Vandewalle et al., 2018), near-threshold stimulus perception (Ergenoglu et al. 2004; Vandewalle et al. 2018) and transfer of information to ventral object-selective regions (Zumer et al., 2014). Thus, occipital alpha desynchronization induced by visual object-triggered optogenetic stimulation is likely a neurophysiological confirmation of the individual's partially recovered visual perception.

In attempts to detect the presence of objects during the visual tests, the patient adopted a head-scanning strategy when using the light-stimulating goggles. There are two possible reasons for this. Either the field of optogenetic activation was too small to detect objects not aligned with the camera center or there was no spatial resolution within the area of the retina that expressed the optogenetic sensor. Based on experiments in nonhuman primates (Gauvain et al., 2021), we estimated the region of optogenetic expression in human retina to be 8.20° of visual angle (2.5 mm diameter retinal disc). Moreover, using the same vector and injection method reported in this article, electrophysiological experiments in nonhuman primate retinas demonstrated spatial resolution within the foveal ganglion cell array (Gauvain et al., 2021). Therefore, we hypothesize that the patient's need to scan the scene with the goggles to detect an object was due to the relatively small area of the field of optogenetic activation.

The three visual tests were performed in an indoor laboratory (Streetlab) according to a preestablished protocol. We also examined whether the patient could recognize patterns during locomotion outside on the street. In the stimulated monocular condition but not in the natural binocular condition, the patient spontaneously reported identifying crosswalks, and he could count the number of white stripes. Subsequently, the patient testified to a major improvement in daily visual activities, such as detecting a plate, mug or phone, finding a piece of furniture in a room or detecting a door in a corridor but only when using the goggles. Thus, treatment by the combination of an optogenetic vector with light-stimulating goggles led to a level of visual recovery in this patient that was likely to be of meaningful benefit in daily life.

Interestingly, while performing the psychophysical tests under stimulated monocular condition, the patient reported 'vertical vibrations' when perceiving an object (Supplementary Video 1). The patient did not report vibrations when wearing the light-stimulating goggles before the injection, suggesting that optogenetic activation was responsible for this phenomenon. We hypothesize that the vibrations are caused by the use of an event-based camera that provides localized light pulses at each pixel where the camera detects changes

in contrast. When the camera scans through an object, synchronized light pulses are sent to the eye, which may be perceived by the individual as 'vibrations'. We have no explanation yet why the patient reported the vibrations as 'vertical'.

The red fluorescent protein *tdTomato* encoded by the injected vector could, in theory, be visualized by a scanning laser ophthalmoscope. However, visualization of red fluorescent probes using scanning laser ophthalmoscopy is not yet approved for clinical use. Should this be approved in the future, direct visualization of the cells expressing the fusion protein *ChrimsonR-tdTomato* could prove particularly useful to monitor vector transfection and to individually tailor the size and location of the light beam projected by the device.

Taken together, the psychophysical and neurophysiological evidence presented in this article suggest that the optogenetic stimulation of human retinal ganglion cells by a light-projection system linked to a camera is a promising way to partially restore vision in blind patients affected with advanced RP.

10.1.4 Methods

10.1.4.1 Study design

PIONEER is a multicenter, phase 1/2a, open-label, non-randomized, dose-escalation study to evaluate the safety and tolerability of an adeno-associated viral vector, GS030-DP, administered via a single intravitreal injection to the worse-seeing eye of patients with non-syndromic RP, and ensuing light stimulation via light-stimulating goggles (GS030-MD). The secondary objective of the study is to evaluate visual and visuomotor function with and without the light-stimulating goggles. The clinical trial protocol, including patient selection criteria, is provided in the Supplementary Text. Before initiation, the PIONEER study protocol was approved by the *Agence Nationale de Sécurité du Médicament et des Produits de Santé*, the US Food and Drug Administration, the Medicines and Healthcare products Regulatory Agency and the following national/local ethics committees and institutional review board: *Comité de Protection des Personnes Île-de-France III*; North East-York Research Ethics Committee; and Human Research Protection Office at the University of Pittsburgh. Study participants provided written informed consent before enrollment, according to CARE guidelines and in compliance with the Declaration of Helsinki 2013. The individual participating in the experiments described in this report was a 58-year-old man. The study design includes three dose-escalation cohorts (5.0×10^{10}, 1.5×10^{11} and 5.0×10^{11} viral genomes per eye) of three participants each and an extension cohort treated at the highest tolerated dose. After each cohort is completed, a data safety monitoring board reviews safety data and recommends escalation to the next dose. As of the end of 2020, seven patients had received a single intravitreal injection of GS030-DP in their worse-seeing eye: three patients in each of the first two cohorts and one patient in the third cohort. Because of COVID-19, only one patient from the first cohort, the patient described in this article, could perform sustained ($N = 15$) post-injection training sessions. So far, the pandemic has prevented any functional assessment of the combined therapy in the other treated patients. Genotypic studies were performed in all patients of the study. The reported patient has two pathogenic

alleles on the *USH2A* gene (NM_206933.2) that were identified by targeted next-generation sequencing (Audo et al., 2012) and segregation analysis using samples from his parents. The first pathogenic allele is on exon 13 *c.2299del p.(Glu767Serfs*21)* (Eudy et al., 1998) and was inherited from his father. The second pathogenic allele is a complex allele with exon 22 *c.4714 C>T p.Leu1572Phe* (Song et al., 2011) and exon 50 *c.9882 C>G p.Cys3294Trp* (Nishiguchi et al., 2013), which was inherited from his mother.

10.1.4.2 Assessment of intraocular inflammation

We used standardized assessment of intraocular inflammation according to the international guidelines of the Standardization of Uveitis Nomenclature Working Group, such as the assessment of the anatomic location, severity and clinical evolution (activity) of anterior and intermediate uveitis (Nussenblatt et al., 1985; SUN working group, 2005; Trusko et al., 2013) (Supplementary Section **F.1**).

10.1.4.3 GS030-DP

GS030-DP consists of a serotype 2.7m8 (Dalkara et al., 2013) adeno-associated viral vector expressing the fusion protein ChrimsonR-tdTomato13 under the control of the CAG promoter (*AAV2.7m8-CAG-ChrimsonR-tdTomato*). A human growth hormone 1 polyadenylation signal sequence was inserted in the 3' end of the construct. Similar to other adeno-associated viruses, GS030-DP is replication-defective and contains single-stranded DNA. Capsid 2.7m8 was created by inserting a 10-mer peptide in the capsid of AAV2 (Dalkara et al., 2013).

AAV2.7m8-CAG-ChrimsonR-tdTomato was suspended in phosphate buffer including 0.001% Pluronic F-68. The GS030-DP suspension was dispensed into individual vials and stored at ≤ -70 °C until use. An aliquot of 100 μL of GS030-DP (5.0×10^{10} vector genomes) was administered via intravitreal injection once into the worse-seeing eye.

10.1.4.4 GS030-MD

The external medical device GS030-MD consists of two hardware units connected by a high-speed link. The first unit (head unit) is a pair of goggles hosting a camera and a light-projection system. The goggles are connected to the second unit (processing unit) that runs the software (Supplementary Figure **F.1**).

Each pixel of the camera (Posch et al., 2011) continuously records the light intensity in a local region of the natural scene, with a dynamic range of 120 dB. If the change in light intensity crosses a threshold, the camera signals an event, which is represented by the coordinates of the pixel at which the change was recorded. The events are asynchronous in time and 33346 camera pixels are used for event detection. The camera pixels are then mapped to the pixels of the light-projection system, which projects the image onto a circular retinal area of 10° of visual angle. A light pulse at a given projected image pixel, which corresponds to an event, has an onset precision of 0.694 ms (1440 Hz) and is 16.6 ms long (60 Hz). The image is binary, that is, each individual pixel is either ON or OFF. A stimulus pixel is ON in a given image if the corresponding camera pixel signaled an event; otherwise it is OFF. The light-

projection system uses a light-emitting diode light source (595 nm peak wavelength, 15 nm half width, tailored to activate *ChrimsonR* close to the peak of its action spectrum) that is projected onto an array of individually switchable micromirrors (digital micromirror device) mounted on the goggles. A given micromirror of the array can be either in the ON or OFF position, leading to light reflectance or no light reflectance. This results in a binary pixelated image stream that is projected onto the retina. Note that the stimulation at different contrasts is not the same since the probability of an event being generated by a pixel in the camera varies with the contrast of the stimulus (Posch & Matolin, 2011). The light-stimulating goggles output a maximum radiative flux of 1.3 mW, which corresponds to a retinal irradiance of 13 mW.cm^{-2} (4×10^{16} photons.cm^{-2}.s^{-1}) for a pupil size of 6 mm. This is 51 times below thermal safety thresholds set by ophthalmological standards (ISO, 2007). Note that the pupil of the patient was not dilated when wearing the goggles and the assumed 6 mm pupil size corresponding to a dilated pupil was only used to calculate an upper limit for retinal irradiance. The light-stimulating goggles can create a retinal irradiance ranging from a minimum of 4×10^{14} photons.cm^{-2}.s^{-1} to 4×10^{16} photons.cm^{-2}.s^{-1}. This range was chosen because preclinical studies in nonhuman primates indicated that *ChrimsonR*-expressing foveal retinal ganglion cells were activated starting at 10^{15} photons.cm^{-2}.s^{-1} (Gauvain et al., 2021). The maximal corneal irradiance of the light-stimulating goggles is 4.7 mW.cm^{-2}, which is 850 times below the thresholds set by ophthalmological standards for the anterior segment and 127 times below the thresholds set by the American National Standard for Safe Use of Lasers Z136.1 standard (LIA, 2014) for pigmented iris illumination. When using 595 nm light, the photochemical damage threshold of the retina (ICNIRP, 1997), expressed in retinal irradiance (E^{max}) at 6 mm pupil size and at $t \geq 10000$ s, is 880 mW.cm^{-2}. This value is 67 times higher than the maximal retinal irradiance of 13 mW.cm^{-2} produced by the light-stimulating goggles at the same pupil size. As a precautionary measure and with approval from regulatory agencies, the use of the device was limited to 4 hours per day in the context of this clinical trial. The light-stimulating goggles were classified by the IEC 62471 standard (IEC, 2014) in the risk group 'exempt', indicating that they do not constitute a photobiological hazard. The maximum irradiance provided by the device was well tolerated by the patient. The patient tested the goggles three times before the injection was administered and did not report any photophobia.

10.1.4.5 Visual training

Training of participants was performed at *Streetlab*, a center of naturalistic vision rehabilitation platforms dedicated to the evaluation of vision and training in low-vision patients. The first step of visual training was to teach the patient, who had lost vision two years before enrollment in the clinical trial and had divergent strabismus in his treated eye, to become aware of the direction of his gaze and to control his eye movements to be able to look straight into the light beam projected by the goggles. With a visual acuity limited to light perception, the patient was able to learn how to align his gaze with the light beam of the goggles even before any improvement in vision. Visuomotor exercises were initially performed without the goggles, then with the goggles in simple exercises and eventually in

daily life (Supplementary Figure **F.7**): (1) oculomotor exercises without goggles. Each visit started with ocular relaxation exercises, which were followed by fixation exercises, ocular pursuit exercises and eye-hand coordination exercises; (2) oculomotor exercises with goggles (simple exercises). Training with the goggles was initiated four and a half months after the injection and included four types of exercises: (a) camera-target alignment exercises. The objective was to make the patient aware of the position of the camera on the goggles; (b) eye-beam-target alignment exercises. The objective was to train the patient to look with his treated eye straight into the light beam projected by the goggles once a target was aligned with the camera; (c) scanning exercises. The objective was to learn head-scanning and eye-movement strategies during target search with the camera of the goggles. Using fine head movements, the patient had to localize a contrasting target, follow its contours and identify its shape. With the same scanning technique, the patient also had to locate multiple targets one after the other; (d) eye-hand coordination exercises. The objective was to learn how to associate the visual perception of a target with its physical location. The patient first had to visually locate a target and then touch it. In addition, he had to follow the edge of a target with the camera, identify its shape and eventually touch the target; (3) Oculomotor exercises with goggles (daily life exercises). Daily life exercises were conducted at *Streetlab* starting seven months after the injection. Ten months after the injection, the patient agreed to use the goggles during locomotion outside.

10.1.4.6 Visual tests

The first two functional vision tests described in the main text each lasted for 30 minutes and the trials were randomized according to object type, contrast and location. Before each of the two tests, the objects and their possible locations were verbally described to the patient once. Before each trial, the patient sitting at the table had to close his eyes when the experimenter prepared the test to prevent the patient from localizing the object(s) in advance. In addition, the experimenter was careful not to make any noise when placing the object(s) on the table. Foam was placed under each object to avoid any sound during placement. The experimenter always stood on the same side of the patient when placing objects on the table. After placing the object, the experimenter moved back to their original position about 1 meter away from the patient. For trials without objects, the experimenter pretended to put something on the table. The objects and settings specific to the two psychophysical tests were not used during the visual training sessions. However, the patient was trained to implement strategies to perceive, locate and touch objects of different sizes, shapes and contrasts.

10.1.4.7 Image contrast

Image contrast was assessed using two measures. Michelson contrast was measured as $(I_{max} - I_{min})/(I_{max} + I_{min})$, where I_{max} is the intensity of the table and I_{min} that of the object. RMS contrast was measured as the SD of the image pixel intensities in a circle 21 cm in diameter, which included the object in the middle. The local illumination associated with the different RMS values was as follows. First test (notebook): RMS contrast $= 0.80$, local luminance 51.90 Cd.m^{-2}; RMS contrast $= 0.53$, local luminance 59.23 Cd.m^{-2}; RMS contrast

$= 0.41$, local luminance 63.94 Cd.m^{-2}. First test (staple box): RMS contrast $= 0.21$, local luminance 94.92 Cd.m^{-2}; RMS contrast $= 0.16$, local luminance 93.83 Cd.m^{-2}; RMS contrast $= 0.13$, local luminance 94.14 Cd.m^{-2}. Second test (tumbler): RMS contrast $= 0.41$, local luminance 82.91 Cd.m^{-2}; RMS contrast $= 0.33$, local luminance 85.11 Cd.m^{-2}; RMS contrast $= 0.29$, local luminance 83.28 Cd.m^{-2}. Third test (tumbler): RMS contrast $= 0.33$, local luminance 85.11 Cd.m^{-2}.

10.1.4.8 Extracranial EEG recordings

10.1.4.8.1 Visual detection task

The third visual test was adapted to simultaneous behavioral and EEG recordings (Figure **10.2**). The task was to detect the presence of an object (tumbler) placed 80 cm in front of the patient (Figure **10.2a,c**; Michelson contrast = 55%). Unlike the other two visual tasks, object location was fixed and the patient was informed before the beginning of the experiment that the object position would not change throughout the experiment. The patient acknowledged the presence or absence of the object by means of a two-key response pad, but he was not forced to answer. The protocol included a total of 183 randomized object/no-object trials distributed across three conditions: natural binocular; natural monocular; and stimulated monocular (60, 60 and 63 trials, respectively). The experiment was split into two sessions of approximately 70 minutes each (see Figure **10.2b** for the detailed protocol of each session). Each trial lasted 20 s. During the first 5 s, the patient was instructed to close his eyes while the experimenter silently placed or did not place an object on the table (thus avoiding visual and auditory cues). The patient was then instructed to open his eyes, search for the object and provide an answer within 15 s. The between-trial time interval was set according to the participant's pace.

10.1.4.8.2 EEG data acquisition and preprocessing

A 64-channel EEG cap with passive electrodes (Waveguard original, standard 10/10 system; ANT Neuro) connected to an eego mylab amplifier (ANT Neuro) was used to record time-dependent cortical activity (Figure **10.2c**). EEG signals were recorded from 48 electrodes (out of 64) distributed at a higher density in the occipital area. Data were acquired with the eego software v1.9.1 (ANT Neuro) and preprocessed with the EEGLAB toolbox of MATLAB (R2019a-20a) via the following pipeline. Raw recordings were first high and low-pass-filtered (1 and 40 Hz, respectively). Artifactual channels were then removed and interpolated. Independent component analysis was performed to decompose the EEG signals into statistically independent components, which were then labeled using the ICLabel algorithm (Pion-Tonachini et al., 2019) to probabilistically assign the origin of their signals to brain, muscles, heart, eyes or artifactual sources. Finally, the most likely brain-related independent components were selected and used to reconstruct data into the electrode space before the analyses.

10.1.4.8.3 Spectral analysis of EEG data and decoding

Spectral EEG analyses were conducted to identify power spectrum signatures in the alpha frequency range (8-14 Hz), which is associated with the intensity of visual processing in the occipital region (W. Feng et al., 2017; Vandewalle et al., 2018). A binary decoder was trained to discriminate object *versus* no-object trials based on the alpha-band power amplitudes over the occipital channels (O_z, O_1, and O_2; Figure **10.2c**). EEG data recorded during the eyes-open periods of the stimulated condition were used for training, after signal power amplitude normalization across trials (frequency $\times$ channel pairwise, independently) for feature comparability. The Fisher score was used to quantify the discriminant power of each spectral feature:

$$\text{Fisher score} = \frac{\sum_c (\mu(c) - \mu)^2}{\sum_c \sigma(c)} \tag{10.1}$$

where $\mu(c)$ and μ indicate the means of the observations within the class c and over all classes, respectively and $\sigma(c)$ is the variance of the observations within the class c. By computing the ratio between the separability of means across all classes and the overall spread around their means, the Fisher score provided a discriminability index between classes (two in the case of the binary decoder used in this study). The six most informative features (that is, the features with the highest Fisher scores) were fed into the decoder in increasing number, leading to multiple instances of the decoder. For each instance, k-fold cross-validation (20-fold) and leave-one-out cross-validation procedures were then used to assess the decoding accuracy on testing samples (that is, data unseen by the decoder during training). Finally, the optimal number of features was determined based on the instance with the best decoding accuracy. As a control, the decoder was also trained and tested on data extracted from the eyes-closed periods of the stimulated condition and from the eyes-open and eyes-closed periods of the natural conditions for classification comparison purposes.

10.1.4.9 Statistical analyses

Statistical analyses of behavioral data were conducted in R v.4.0.3. Likelihood-ratio tests for the effects of explanatory variables in multivariable logistic regressions were used to compare the data in Tables **10.1-10.3**. A likelihood-ratio test was used to check whether the patient's counting performance was above chance level in Table **10.2**. Statistical analyses of EEG data were conducted in JASP v.0.11.1. All tests on EEG data assumed independence between the samples of each distribution and normality was assessed using the Shapiro-Wilk test to apply either parametric or non-parametric tests. A one-sided, non-parametric test (one-sample Wilcoxon signed rank test) was employed for each decoder separately to determine whether classification accuracy was above chance level (50%). A two-sided non-parametric test (Mann-Whitney U-test) was used to investigate the spectral power modulation in the object and no-object trials.

10.2 Current developments of the ancillary study

10.2.1 Contributors

Alexandre Delaux*,1, Jean-Baptiste de Saint Aubert*,1, Chloé Pagot[2], Francesco Galluppi[3] & Angelo Arleo[1].

* These authors contributed equally to the project.

1. Sorbonne Université, INSERM, CNRS, Institut de la Vision, 17 rue Moreau, F-75012 Paris, France
2. Streetlab, Institut de la Vision, Paris, France.
3. GenSight Biologics, Paris, France.

10.2.2 Introduction

Building upon the case study reported in the published article, this section presents the most recent developments of the visual detection task (third test of Sahel et al. 2021). This task was initially designed as a behavioral experiment and subsequently adapted for EEG recordings. It became evident that several limitations existed within the paradigm that warranted addressing before proceeding with other patients from the clinical cohort.

Foremost, enhancing the protocol with a larger number of trials would bolster the robustness of the EEG signal analysis. The limited number of trials was compounded by the participant's freedom to choose not to report whether the object was detected during the task, leading to an unpredictable ratio of trials in which the subject would provide an answer. To ensure consistency, responses were mandated after a fixed visual search period, accompanied by the introduction of a confidence rating. As no notable distinctions were observed between the two natural conditions (monocular and binocular), solely the monocular conditions were retained, allowing a focused examination of the stimulation effect (natural monocular *vs.* stimulated monocular). Consequently, the total number of trials per condition within a session was increased from 30 to 40 (Figure **10.4a**).

Given the patient' unrestrained head movements during the task, there existed the possibility that the patient could miss the object for entire trials, thereby never getting the chance to report it. This uncertainty in head movements necessitated incorporating supplementary behavioral recordings alongside EEG data and participant responses.

These adaptations were meticulously tested and gradually integrated through several pilot sessions. The overarching objective of these ongoing developments is twofold: to validate the previously presented findings with a larger number of patients tested and, if feasible, to further refine our comprehension of the underlying neural mechanisms of partial vision recovery.

10.2.3 Adaptations to the visual task protocol

10.2.3.1 Forced choice paradigm

In the version of the visual detection task employed in Sahel et al. (2021), the participant's response rate posed a notable challenge. Specifically, the participant provided an answer in less than 50% of the trials during the stimulated condition and in less than 12% of trials across both natural conditions. This inconsistency in response rates presents difficulties in conducting meaningful comparisons across different conditions and renders a significant portion of trials non-analyzable in terms of behavioral outcomes. Moreover, when considering the task's application to multiple patients, the variability in response rates across subjects could potentially hinder reliable inter-subject comparisons. To address these issues, a modification was introduced wherein the patient's response was made mandatory for all trials in both conditions. This adjustment ensured that a response was always given, thus ameliorating comparability across conditions and subjects. Additionally, a confidence rating was implemented to augment the assessment process (discussed in Section **10.2.3.2**).

Furthermore, patients were instructed to withhold their responses until the conclusion of the dedicated visual search period (Figure **10.4a**), deviating from the earlier version where they could respond at any point during this period. This deliberate decoupling of perceptual and cognitive processes from the motor response phase harmonizes trial procedures and decreases the introduction of artifacts in the EEG data for the main period of interest. However, it does come at the cost of diminishing insight into the precise decision time within each trial.

10.2.3.2 Confidence ratings

Enforcing mandatory responses from the patient introduces a challenge in deciphering the underlying perceptual evidence that prompts the decision to respond with 'Present' or 'Absent'. In light of this, a confidence rating measure was introduced immediately subsequent to the button press. In this measure, patients are required to verbally express a numerical value ranging from 1 (indicating a completely arbitrary response) to 5 (representing an absolutely certain response).

Confidence ratings are recognized to offer an additional layer of information about the subject's perceptual decisions, augmenting the understanding of visual perception (Maniscalco & Lau, 2016). This concept of perceptual confidence falls within the realm of meta-perception, perhaps one of its most studied facets (see Mamassian 2020 for a review). The utilization of confidence measurements can not only refine but also expand the scope of our comprehension of partial visual recovery in patients undergoing the treatment. Notably, the neurological foundations of perceptual confidence have been extensively explored (Yeung & Summerfield, 2012). Although this work will not tackle these aspects, the combination of this confidence measure with EEG recordings holds the potential to yield an even deeper comprehension of the accumulated perceptual evidence within this context.

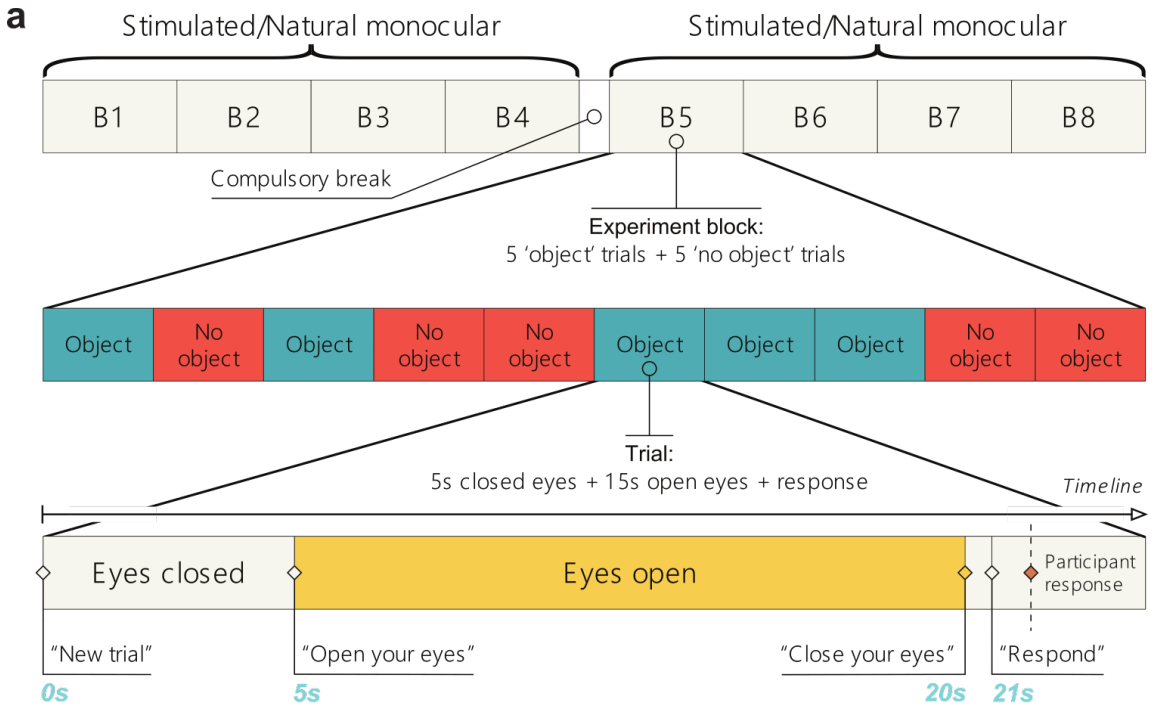

b

Figure 10.4: Protocol of the visual detection task coupled with EEG recordings. **a**. Experimental protocol. A session includes two conditions: natural monocular; and stimulated monocular. Each condition is divided into four blocks consisting of ten trials each: five object trials and five no-object trials (tumbler removed from the table). Patients are instructed to close their eyes during the first 5 s of the trials. Patients are then asked to open their eyes, are given 15 s to determine visually whether the tumbler is present on the table, and are then instructed to close their eyes. A second later, they are asked to provide their answer through a two-key response pad, and to specify the level of confidence in their answer by a number between 1 and 5 (see Section **10.2.3.2**). **b**. Experimental setup. Behavioral responses, motion capture, and brain activity were simultaneously recorded during the test.

10.2.3.3 Re-alignment procedure

Another constraint of the initial version of the task stemmed from the unconstrained visual search. Indeed, considering the goggles' limited field of view (FoV) (10° diameter) and the importance of stimulating the goggles with changing contrasts, patients often adopted a visual search strategy involving a lot of head movements. As a result, it was noticed that, in some trials of the stimulated condition, the object failed to come within the FoV of the camera. In the revised version of the task, the experimenter, leveraging visual feedback from the computer operating the goggles, provided assistance to patients in aligning the camera of the goggles with the object's location. This was performed at the beginning of each trial in the stimulated condition, irrespective of whether the upcoming trial was an object or no-object trial. This procedural enhancement is consistent with the primary objective of the task, which aims at assessing the capacity to discern the presence or absence of an object at a predetermined position, rather than gauging the ability to precisely locate it.

Comparable efforts were undertaken to replicate this procedure in the natural condition. However, the absence of real-time feedback on the patient's head orientation hindered the same degree of re-alignment accuracy. Nonetheless, steps were taken to ensure that, at the onset of each trial, the patient's head orientation was generally directed toward the central area of the table. It is pertinent to acknowledge that while the patients' residual vision is very limited, the natural condition did not have to cope with the additional constraint of the 10° camera FoV.

The incorporation of a chin-rest was disregarded to allow patients the freedom to engage in uninhibited head movements, facilitating their ability to detect the object. However, the re-alignment procedure introduced to address this issue does not preclude patients from swiftly shifting the focus of the camera away from the object's location during the 15-second observation interval. As such, it became important to assess when the tumbler was in the FoV of the camera throughout the course of the trial.

10.2.3.4 Following head movements in real time

To obtain a more comprehensive understanding of the visual perspective experienced by the patient during the experiment, a crucial addition to the original protocol was to incorporate a motion capture system (visible of Figure **10.4b**). This system enabled the tracking of the patient's head position and, more importantly, the position of the goggles. This additional tracking was essential to precisely quantify the duration of exposure of the goggles to the target object. The objective was to gain deeper insights into the behavioral success of the therapy and the associated neural correlates.

By monitoring the goggles' position and orientation, the intention was to assess the amount of time the goggles' camera pointed towards the target object during the visual search. As explained in Section **10.2.3.3**, this quantitative measurement was in part meant to help discern whether the failure to detect the object was attributable to the goggles not capturing it during the visual exploration. These fine-grained measurements of tumbler visibility are hoped to contribute to a more nuanced interpretation of the patients' behavioral performance in the task.

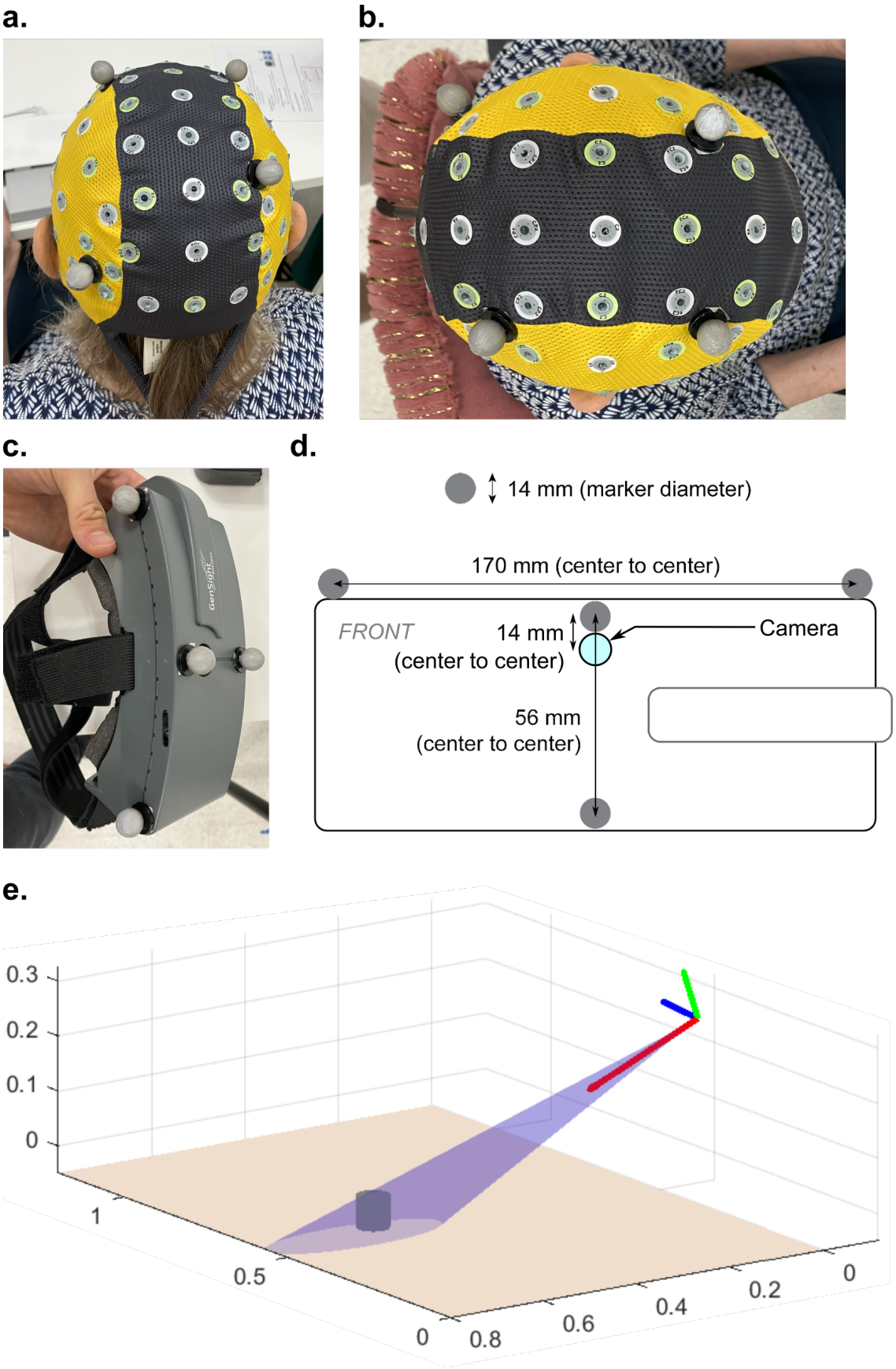

Figure 10.5: Placement of motion capture markers and illustration of the modeling. [Continued on next page]

Figure 10.5: [On previous page] **a-b**. Placement of motion capture markers on the EEG cap to define the head rigid body. **a**. Back view. **b**. Top view. **c**. Placement of motion capture markers on the goggles to define the goggles rigid body. **d**. Schematic of the placement of motion capture markers on the goggles, with measurements. **e**. Illustration of the modeling of the main elements of the experiment. The red, green and blue arrows represent the forward, upward and rightward directions of the goggles, respectively. They are centered on the goggles' camera lens. The *cone of vision* (in transparent blue) was simulated with a 10° solid angle diameter, starting from the camera lens, and aligned with the forward direction. The tumbler (in gray) was modeled as a cylinder of 6 cm diameter and 6 cm height and was placed according to measurements taken at the beginning of the first block of the stimulated condition. The table surface (shown in light brown) is 80 cm by 120 cm. Axes are expressed in meters.

10.2.4 Updated methods

10.2.4.1 Participants

A total of 7 sessions of the modified protocol were performed with 3 different patients of the clinical study cohort, including the patient who was already reported in Sahel et al. (2021). All recordings occurred in *StreetLab* facilities at the Vision Institute in Paris. However, an infrared stroboscopic effect caused by the motion capture system disrupted the goggles' normal functioning and was only detected and solved after the 6^{th} recording session. Therefore, only the last session, devoid of interference, could be analyzed and presented here. Compared to the previous report, this session was recorded with a new patient (P1002), a 72-year-old woman diagnosed with RP 33 years ago.

10.2.4.2 Motion capture

10.2.4.2.1 Materials

The OptiTrack motion capture system (NaturalPoint - Corvallis, OR, USA) was used to track the positions of two custom-defined rigid bodies (RBs), using infrared reflective markers (Figure **10.5a-d**). The first RB was affixed to the patient's head using four adhesive markers. Two markers were symmetrically placed on the lateral axis at the front of the cap, while a third marker was positioned more centrally on the right-hand side, and the fourth marker was situated over the temporo-occipital zone on the left-hand side of the cap (Figure **10.5a-b**). This RB was consistently defined and tracked throughout the entire duration of the experiment.

In the stimulated condition of the experiment (when the patient wore the goggles), a second RB was tracked, attached to the goggles themselves. This RB also comprised four adhesive markers: two symmetrically placed at the top of the goggles, and the other two located on the frontal part of the device, along the central axis, one at the top and one at the bottom (Figure **10.5c-d**). Precise measurements were taken to accurately determine the position of the camera lens relative to the markers (Figure **10.5d**).

The motion capture setup involved six cameras (OptiTrack Flex 13, NaturalPoint) to cover the tracking space (Figure **10.4**), and data acquisition was performed using Motive software (v1.7.5, NaturalPoint).

10.2.4.2.2 Procedure

The motion capture system necessitated an initial calibration process using Motive software to establish the tracking space and the horizontal plane relative to camera positioning (performed without the patient). This calibration procedure set the $[0,0,0]$ origin of the tracked space on the left-hand side corner of the table, closer to the patient. At the start of the first block of each condition, the precise measure (in the motion capture space) of the tumbler location was captured using an additional reflective marker.

To ensure synchronization with EEG data and experimental events, the motion capture data was streamed in real-time from the Motive software using the Lab Streaming Layer (LSL) (Kothe, 2014), which was implemented in custom python scripts. The streamed data included the 3D position of each individual marker, organized by RB.

10.2.4.2.3 Analysis

The analysis was conducted in Matlab R2019a.

Preprocessing. The motion capture data was imported from the XDF file and synchronized with the EEG data, after which it was resampled to a frequency of 250 Hz. Subsequently, a data-driven approach based on the relative position of the markers was employed to assign roles to each marker within each RB. During this process, any missing or artifactual samples resulting from recording noise were identified and subsequently removed or interpolated. Following that, the data was low-pass filtered at 6 Hz using a zero-phase Hamming windowed finite impulse response filter with 7 Hz cut-off frequency and 2 Hz transition bandwidth.

Rigid body definition. The position and orientation of the RBs were determined based on the positions of their respective markers. For the head RB, the position was computed as the center of mass of the 4 markers. Its rightward axis was defined by the normalized vector connecting the 2 frontal markers, while the frontward axis was determined as the unit vector orthogonal to the rightward axis, lying in the plane containing the 3 markers on the top of the cap. To ensure an orthonormal basis, the upward axis was obtained as the cross-product of the two previously defined axes.

Regarding the goggles RB, its axes were established first. The upward axis was defined using the unit vector connecting the 2 frontal markers, and the frontward axis was computed as the cross-product of this vector and the normalized vector connecting the 2 markers on the upper part of the device. The rightward axis was then determined as the cross-product of the two axes mentioned earlier, ensuring orthogonality. The position of the goggles rigid body was taken as the center of the camera lens, achieved through a translation of 14 mm along the downward axis from the upper frontal marker. For a visual representation, refer to Figure **10.5d-e**.

Tumbler visibility index computation. Following that, a *cone of vision* was created to model the FoV of the device. This cone originates from the position of the goggles RB, *i.e.*, the camera lens, and follows its frontward axis. The width of the cone was set to a 10° solid

angle, in line with the theoretical FoV of the goggles. The tumbler was represented as a cylinder, placed upright at the previously recorded position, with dimensions as closely resembling the real object as possible (6 cm diameter and 6 cm height). The modeling is illustrated on Figure **10.5e**.

In order to determine the visible portion of the tumbler from the goggles at any given moment during the experiment, a volumetric approach was employed. The volume intersection between the tumbler body and the cone of vision was computed relative to the tumbler volume, indicating the percentage of the tumbler filmed by the goggles in real-time. This approach provided a measure of the tumbler's visibility from the perspective of the goggles throughout the experiment.

10.2.4.3 EEG

10.2.4.3.1 EEG acquisition and preprocessing

A 64-channel EEG cap with passive electrodes (waveguard original, standard 10/10 system; ANT Neuro) connected to an eego mylab amplifier (ANT Neuro) was used to record time-dependent cortical activity. Data was acquired with the eego software v1.9.1 (ANT Neuro) and streamed in real-time using the LSL protocol (Kothe, 2014). The LabRecorder software (v1.13.0) was used to collect all streams (EEG, motion capture and events from the protocol) into a single XDF file per block.

EEG processing was performed according to the pipeline described in Section **6.2**, using the APP pipeline for time-domain cleaning. Before epoching, the dataset was bandpass filtered between 0.75 Hz and 45 Hz (zero-phase Hamming windowed finite impulse response filters: high-pass filter with 0.5 Hz cut-off frequency and 0.5 Hz transition bandwidth and low-pass filter with 50.625 Hz cut-off frequency and 11.25 Hz transition bandwidth). Epochs were taken around the eye-opening instruction event with a $[-5, 15]$ seconds window. Negative time samples encompassed the *eyes closed* (EC) period while positive time samples delineated the *eyes open* (EO) period. For each period separately, the power spectral density was estimated between 1 Hz and 40 Hz, trial by trial, with the *pwelch* method (1 s sliding window with 80% overlap). Then the power spectral density was normalized using a gain model (divided by the average across trials), per condition.

10.2.4.3.2 Classification

Two types of spectral activity decoders were considered in this analysis: an *object* decoder aimed at discriminating between object and no-object trials, as in the previous study, and an *answer* decoder enabled by the novel forced choice paradigm, aimed at discriminating between 'Present' and 'Absent' answers given by the patient. Both decoders employed a linear discriminant classifier and used power spectral densities [channel $\times$ frequency] as features, with different possible selections of channels and frequency ranges.

Two groups of channels of equivalent size were defined as channels of interest: occipital channels (O_1, O_z, O_2) and frontal channels (F_1, F_z, F_2). Occipital channels were selected for their implication in visual processing and to provide a direct comparison with the results reported for the first patient (Sahel et al., 2021). They are especially expected to be

discriminant for the object decoder. Electrodes over the frontal lobe record correlates of decision-making and are therefore expected to be particularly discriminant for the answer decoder. Indeed, the frontal cortex, especially the prefrontal cortex, is known to play a central role in perceptual decision-making processes (Hanks & Summerfield, 2017; Heekeren et al., 2008; Rushworth et al., 2011). In terms of frequency ranges, the alpha band [8-14 Hz] was expected to be involved in the visual processing (W. Feng et al., 2017; Vandewalle et al., 2018), while the theta band [4-8 Hz] was hypothesized to be related to answer discriminability, as it is proposed to be a substrate for decision-making mechanisms in the frontal lobe (Cavanagh & Frank, 2014).

Before classification, the Fisher score (see Equation **10.1**) was used to measure the discriminant power of each feature. The ten most informative features, based on the highest Fisher scores, were used incrementally in the decoder, resulting in multiple instances of the decoder. Each instance underwent leave-one-out cross-validation to assess decoding accuracy on unseen data, with corrections made to account for unbalanced classes to avoid bias towards the most represented class (*e.g.*, when there were more 'Present' than 'Absent' answers). The optimal number of features and decoder were determined based on the instance with the best decoding accuracy.

Four *object* decoders were compared, depending on the training data: the main decoder of interest trained on the eyes open period during the stimulated condition, and control decoders trained on the eyes open period of the natural condition, the eyes closed period of the stimulated condition, and the eyes closed period of the natural condition. Due to the absence of 'Present' answers in the natural condition for this patient, only two instances of the *answer* decoder were considered: the main decoder trained on the eyes open period during the stimulated condition, and the control decoder trained on the eyes closed period of the stimulated condition.

To assess the statistical significance of the obtained classification accuracies, they were compared to results obtained with a random decoder on the same data. Random decoding was repeated 20000 times to create a distribution of randomly achieved accuracy. The one-sided p-value of each decoder was determined by the proportion of random decoding

	Natural monocular: untreated eye covered, treated eye open without the light-stimulating goggles		**Stimulated monocular: Non-treated eye covered, treated eye open and stimulated with the light-stimulating goggles**	
Trial	**Answer: 'Present'**	**Answer: 'Absent'**	**Answer: 'Present'**	**Answer: 'Absent'**
Object trial	0/20	20/20	20/20	0/20
No-object trial	0/20	20/20	10/20	10/20

Table 10.4: Visual detection task: P1002 behavioral results. Answers are summed over the course of 4 blocks in each condition.

accuracies superior to the decoder accuracy in this distribution. The significance level was set at $p < 0.05$.

10.2.5 New Results

10.2.5.1 Behavior

For all trials under the natural monocular condition, the patient responded that the object was absent (40/40), with the lowest possible confidence rating. With the goggles' stimulation, the patient reported detecting the object in all object trials (20/20), with a 2.3 average confidence rating, but also in half of the no-object trials (10/20), with a 1.9 average confidence rating. Overall, the patient performed significantly better than chance under stimulation (Table **10.4**; 75% accuracy; Fisher exact test, $p = 4.36e{-}4$). These results are consistent with those previously reported in Sahel et al. (2021). The confidence ratings also confirm the patient's difficulty in confidently asserting the absence of the object under the stimulated condition: all 'Absent' answers under stimulation, although all correct rejections, were rated with the lowest mark (Figure **10.6a**). However, confidence ratings did not significantly differ between correct detections, *i.e.*, answer 'Present' in object trials, and false positives, *i.e.*, answer 'Present' in no-object trials (Figure **10.6b**; two-sided Mann-Whitney U-test, correct detections versus false positive, $p = 0.56$).

10.2.5.2 Motion capture

Figure **10.7** presents the results of the visibility analysis based on the motion capture data. The plots demonstrate that in all trials, the tumbler was in the FoV of the camera for a

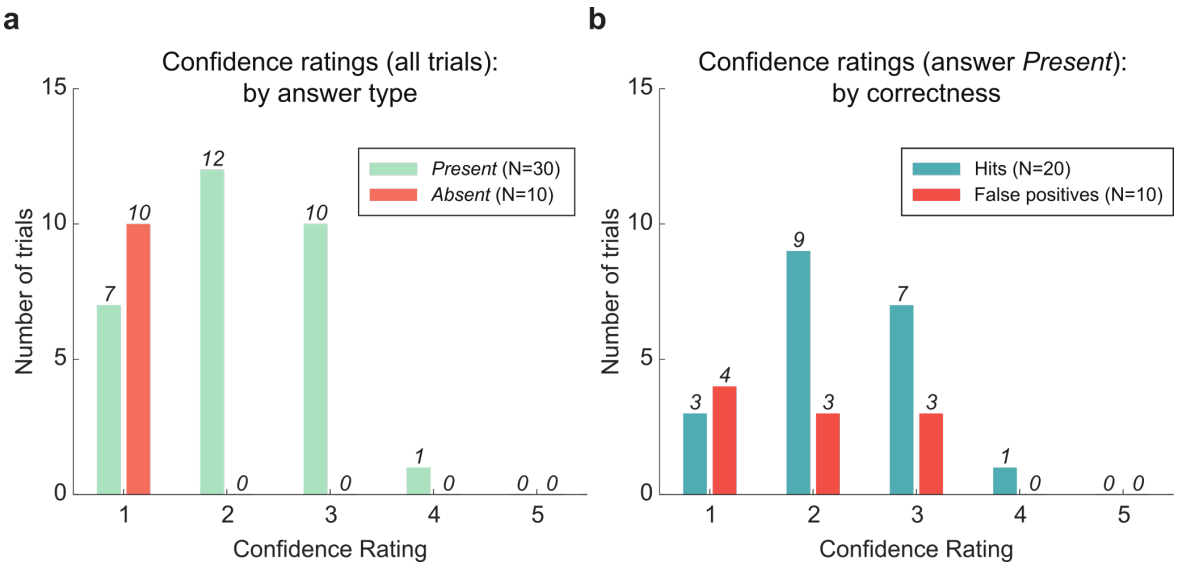

Figure 10.6: P1002: Confidence ratings under the stimulated monocular condition. **a**. Confidence ratings over all trials, by answer type. **b**. Confidence ratings over trials where the subject's answer was 'Present', by correctness of the answer. The patient had to rate their confidence level after each answer, by providing a number ranging from 1 (the answer was random) to 5 (the answer is certain).

significant amount of time, providing enough exposure for the patient to be able to assess its presence.

A striking difference between the eyes closed and the eyes open periods is the variability of the index across time. Indeed, as intended by the repositioning of the patient in front of the tumbler at the beginning of each trial, the percentage of visibility is quite high and stable during the eyes closed period. Then, as soon as the visual search is allowed, large variations appear, often between 0% and 100%. This phenomenon is associated with the sweeping behavior of the patient, who intentionally makes head movements around the object location to make it appear and disappear from the goggles FoV in order to elicit striking events in the eye projection. This sweeping behavior is key to the successful detection of the object and was already observed with the first patient.

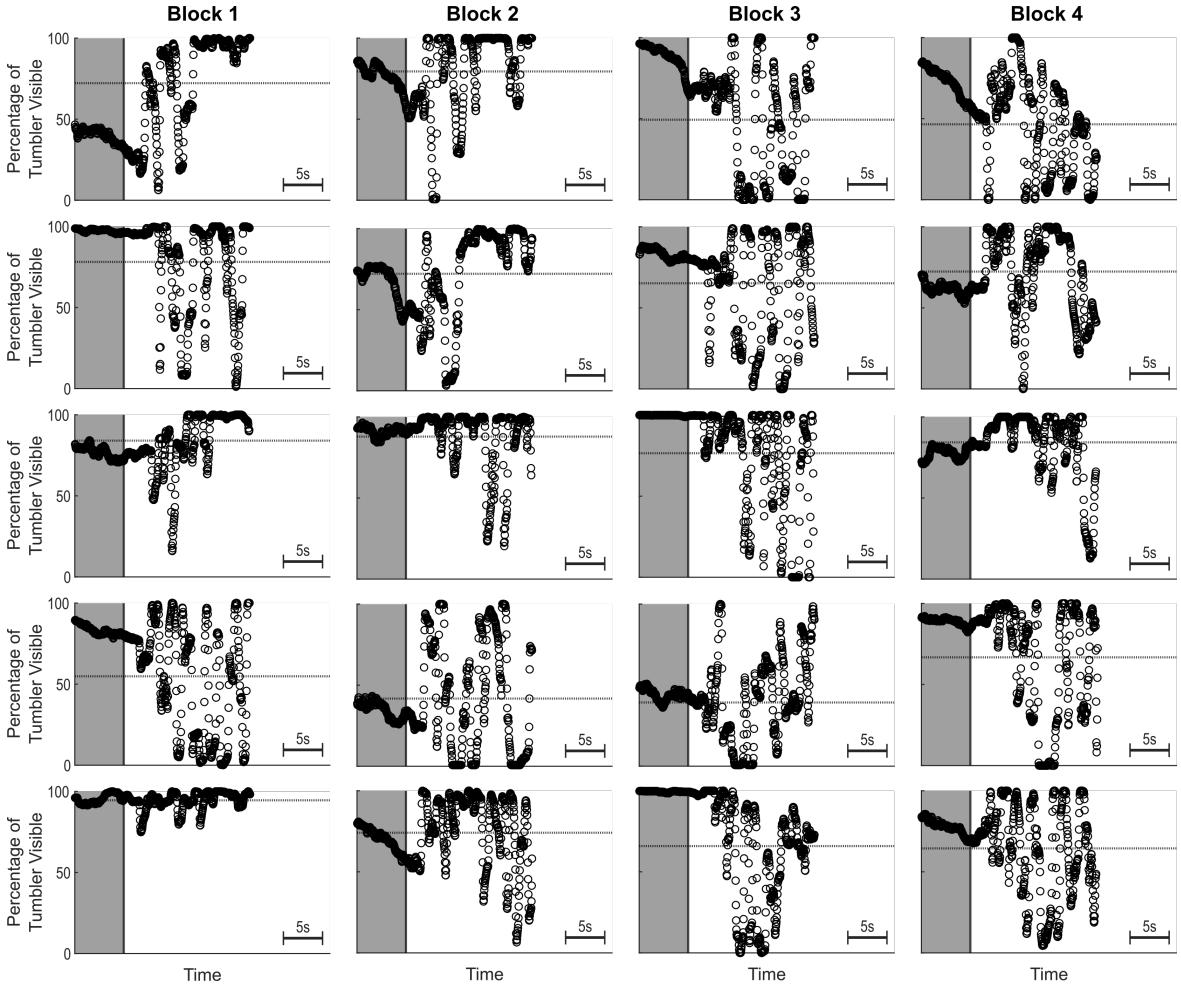

Figure 10.7: P1002: Percentage of visibility of the tumbler for all object trials in the stimulated monocular condition. In all of these trials, the patient provided a positive response (answered 'Present'). One plot per trial. Each column corresponds to a block. Descending rows correspond to chronological order of the trials. Sampling rate for the plots: 31.25 Hz. The grayed zone indicates the eye closed period. The dotted line marks the mean visibility in the eyes open period.

10.2.5.3 EEG classification

10.2.5.3.1 Object decoder

In contrast to the previous findings, no discernible pattern of object presence discriminability was observed across the occipital channels (O_1, O_z, O_2) within the alpha band [8-14 Hz] (Figure **10.8a**). However, certain features exhibited substantial discriminability (Fisher score around 0.3) in more parietal electrodes (P_3 , P_1, P_z) at higher frequencies within the beta band (around 22 Hz). The most discriminant feature was identified on the O_1 channel at 1 Hz (Fisher score = 0.34, Figure **10.8a**). Given the absence of significant discriminant features within the alpha band, the decoders were trained using features from the designated channels of interest without constraining the frequency range (Figure **10.8b-c**).

Across the occipital channels, the primary decoder (EO-Stimulated) achieved a statistically significant accuracy (72.5%, $p = 0.0011$); however, this was also matched by all control decoders (EO-Natural: 63.95%, $p = 0.0421$; EC-Stimulated: 67.5%, $p = 0.0102$; EC-Natural: 74.08%, $p = 0.001$; Figure **10.8b**). The main decoder's accuracy primarily stemmed from 1-2 Hz frequency features on the O_1 and O_z channels (optimal accuracy achieved with 5 features). For the EO-Natural decoder, the highest accuracy was achieved with 1 feature at 10 Hz. In the case of the EC-Stimulated decoder, the best accuracy resulted from 1 feature at 1 Hz. The EC-Natural decoder reached its peak accuracy with 2 features at 21-22 Hz.

Regarding the frontal channels, the primary decoder did not attain a statistically significant accuracy (55%, $p = 0.2382$), and the control decoders faced a similar situation, except for the one trained on the eyes closed period of the natural condition (EO-Natural: 43.42%, $p = 0.8015$; EC-Stimulated: 55%, $p = 0.2382$; EC-Natural: 69.34%, $p = 0.008$; Figure **10.8c**). For this last decoder, the optimal accuracy was realized using 3 features at 22 Hz.

10.2.5.3.2 Answer decoder

Examining the Fisher score map reveals two distinct patterns of discriminability power (Figure **10.9a**). Firstly, a theta band component (4-6 Hz) encompasses a substantial number of frontal electrodes while also extending to parieto-occipital ones (notably O_1, O_z, and O_2). Secondly, a beta band component centered around 22 Hz is prevalent mostly over frontal channels, yet it also extends to the parieto-occipital region. This second component aligns with the pattern previously observed for the object decoder. Consistent with the preceding analysis, the decoders were trained using features from the designated channels of interest without constraining the frequency range (Figure **10.9b-c**).

Across the occipital channels, the primary decoder (EO-Stimulated) did not achieve a statistically significant accuracy (58.33%, $p = 0.1716$), and this held true for the control decoder as well (EC-Stimulated: 41.67%, $p = 0.8265$; Figure **10.9b**).

Conversely, over the frontal channels, the main decoder did attain a statistically significant accuracy (65%, $p = 0.277$), unlike the control decoder (EC-Stimulated: 43.33%, $p = 0.8247$; Figure **10.9c**). The accuracy of the primary decoder mainly stemmed from fea-

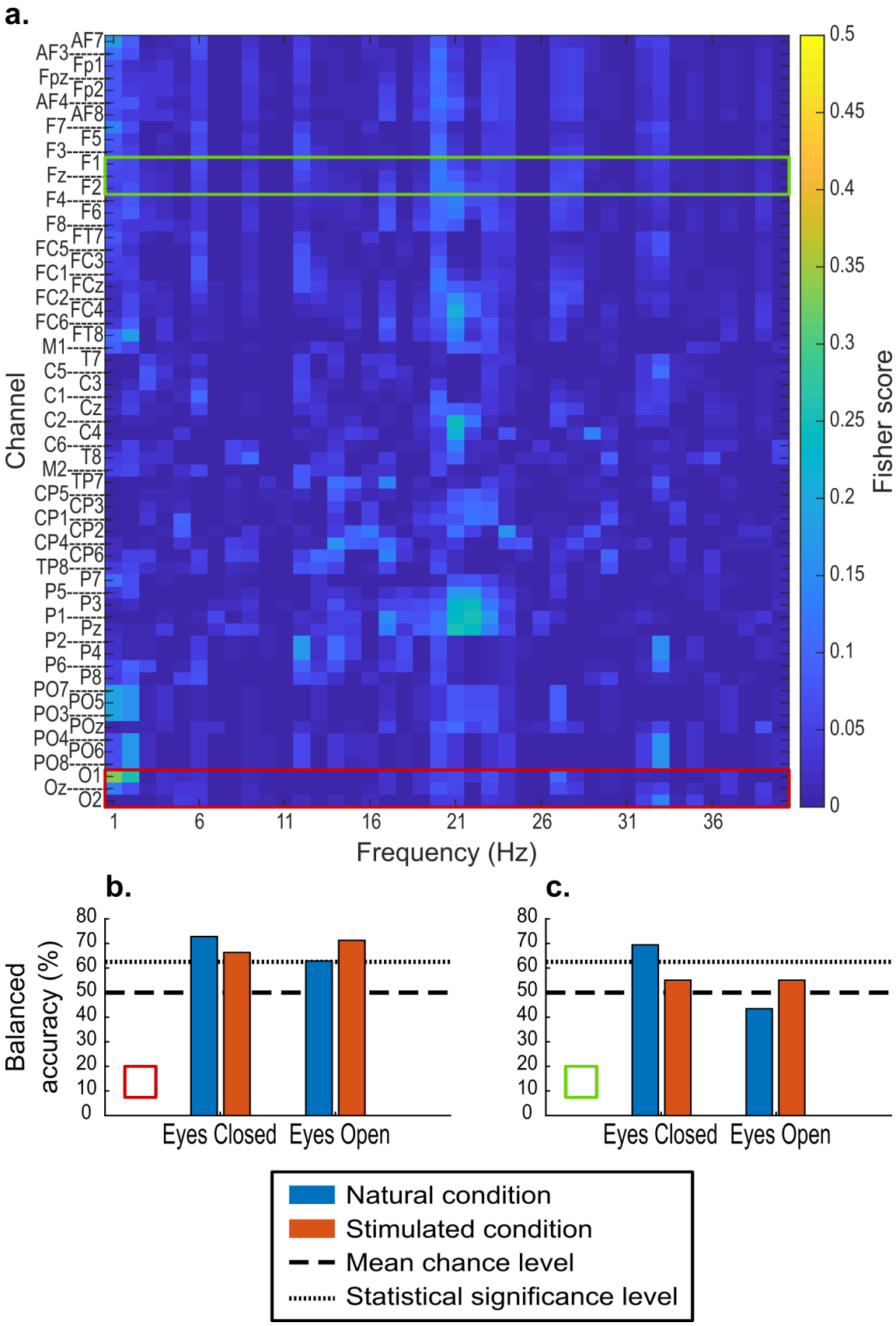

Figure 10.8: P1002: Results of the *object* decoder. [Continued on next page]

Figure 10.8: [On previous page] **a**. Map of the Fisher score depending on the feature for the object decoder trained over the eyes open periods of the stimulated condition. The maximum Fisher score attained is 0.34. Channels are ordered by area, with the most frontal on the upper part of the map and the most occipital on the lower part of the map. **b**. Between decoder comparison of the best achieved balanced accuracy results, using at most the 10 best features from the occipital channels (O_1, O_z, O_2), highlighted in red on **a**. **c**. Between decoder comparison of the best achieved balanced accuracy results, using at most the 10 best features from the frontal channels (F_1, F_z, F_2), highlighted in green on **a**. **b-c**. The mean decoding accuracy is the average accuracy obtained on the testing set by leave-one-out cross validation. Chance level and significance level ($p = 0.05$) are obtained from the comparison with a random decoder (see Section **10.2.4.3.2**).

tures at 5 Hz and 22 Hz frequencies on the frontal channels (optimal accuracy achieved with 3 features).

10.2.6 Discussion of the EEG results

The primary objective of this revised version of the object detection task was to replicate the findings obtained with the first case report (Sahel et al., 2021), specifically, to discern whether the presence or absence of a visual object influences the EEG signal over the occipital cortex during stimulation.

With the inclusion of this new patient, it was confirmed that the occipital EEG signal indeed conveys information regarding the presence or absence of the object, as demonstrated by the improved performance of the main decoder trained on the EO-stimulated periods, surpassing the significance threshold of chance classification. However, it was intriguing to note that the driving features behind this result were not primarily derived from the alpha frequency band, but instead, manifested partly in very low frequencies (1-2 Hz). This observation may be attributed to substantial inter-subject variability in visual recovery, notwithstanding that visual alpha oscillatory activity has previously been found to be absent only in patients who were congenitally blind (Bottari et al., 2016), a scenario distinct from this study. Notably, oscillations within the lowest frequency range, commonly referred to as the delta band, have been associated with the slowest components of event-related potentials (ERPs) (Güntekin & Başar, 2016). In this context, it is plausible that the opening of the patient's eye, now systematically aligned with the object location at the beginning of each trial, elicits an ERP-like response distinct between object and no-object trials. Alternatively, it might suggest a potential contribution of artifacts to the decoding process. Thus, this possibility is tempered by the fact that the optimal classification was achieved through the integration of multiple features (5), rather than a singular feature.

A noteworthy discovery arising from the object decoder trained with occipital features pertains to the fact that control decoders achieved accuracy levels above chance, with the decoder trained on EC-Natural data even matching the accuracy of the primary decoder. This observation diverges from the outcomes obtained with the first patient (Sahel et al., 2021). In the EO-Natural periods, it's conceivable that residual vision might still impart object-related information to early occipital cortices, despite not facilitating conscious perception, as supported by behavioral results. Nevertheless, while the extent of residual vision can differ among patients in the clinical cohort, the stage of disease progression makes this

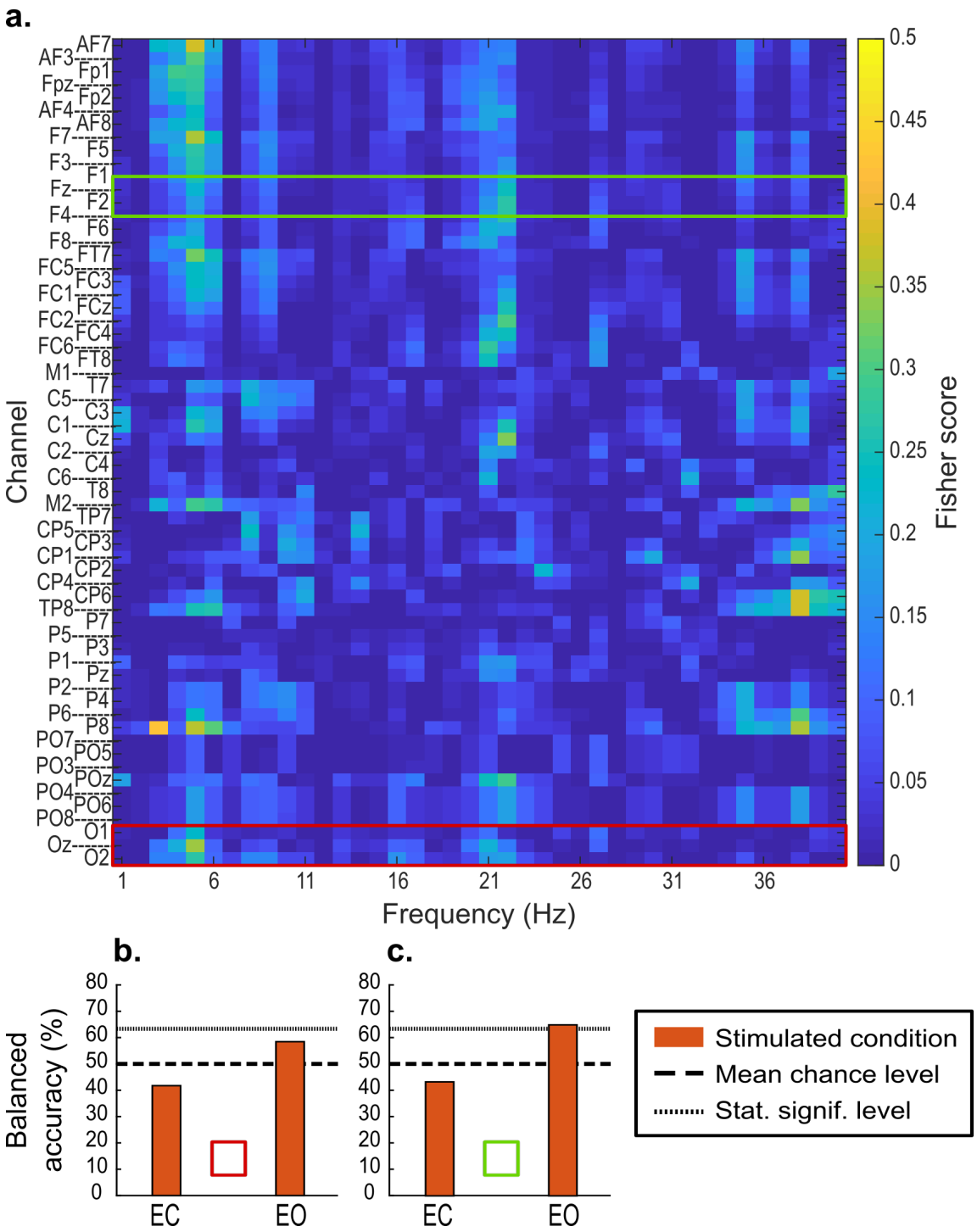

Figure 10.9: P1002: Results of the answer decoder. **a**. Map of the Fisher score depending on the feature for the answer decoder trained over the eyes open periods of the stimulated condition. The maximum Fisher score attained is 0.42. Channels are ordered by area, with the most frontal on the upper part of the map and the most occipital on the lower part of the map. **b**. Between decoder comparison of the best achieved balanced accuracy results, using at most the 10 best features from the occipital channels (O_1, O_z, O_2), highlighted in red on **a**. **c**. Between decoder comparison of the best achieved balanced accuracy results, using at most the 10 best features from the frontal channels (F_1, F_z, F_2), highlighted in green on **a**. **b-c**. No decoders were run on the natural condition because the patient always answered 'Absent'. The mean decoding accuracy is the average accuracy obtained on the testing set by leave-one-out cross validation. Chance level and significance level ($p = 0.05$) are obtained from the comparison with a random decoder (see Section **10.2.4.3.2**).

explanation quite unlikely. Conversely, the fact that peak accuracy was realized with a singular feature raises suspicions of an artifact-based origin. Within the EC-Stimulated periods, an intriguing possibility to consider is the potential of the light stimulation intensity within the goggles to transmit partial information through the subject's eyelid. The intensity of light stimulation is meticulously adjusted for each patient to optimize both behavioral performance and comfort. For this patient, the intensity setting during the recording session was twice that of the first patient's. However, as revealed by the motion capture analysis, the patient's stability during the eyes closed periods suggests that few visual events were evoked by the goggles, thereby diminishing the validity of this proposition. Lastly, in the EC-Natural periods, it appears that only an artifact-based explanation could be ascribed to the elevated decoding accuracy. Notably, all external cues were rigorously controlled across trials of all conditions, including auditory cues, as the experimenter meticulously maintained identical gestures irrespective of trial type and the tumbler was equipped with soft pads to muffle noise.

Considering the answer decoder, the primary intent was to isolate markers of higher-level cognitive processes that influence responses and underlie the decision-making process. As explained earlier, this decoder cannot be compared to the data of the first patient due to disparities in task design. As anticipated, the decoder of interest trained on frontal signals during EO-Stimulated periods exhibited better-than-chance results, while the control decoder (EC-Stimulated), along with both decoders trained on occipital signals, did not achieve similar success. The prominently discriminative theta component encompassing a majority of frontal channels, particularly the more lateral ones not employed for decoding, implies the reliance on neural activity orchestrating choice-relevant perceptual information and its integration to inform decision (Womelsdorf et al., 2010). Frontal theta activity has indeed been proposed as a pivotal mechanism governing cognitive control (Cavanagh & Frank, 2014), which may assume heightened significance when partial visual perception is facilitated via stimulation. Further dissection of the characteristics of this signal is warranted to gain a deeper comprehension of its role within the decision-making process during the task. Specifically, the phase-locked dynamics of frontal theta are also posited to serve as a potential mechanism for organizing brain activities across large spatial distances (Buzsáki & Draguhn, 2004; Uhlhaas et al., 2010) particularly between mid-frontal and distant sites (Fries, 2005).

A shared discriminative feature spanning both the object and answer decoders, as well as across occipital, frontal, and parietal channels, is apparent within the beta frequency band around 22 Hz. Intriguingly, beta band activity has been proposed to contribute to the maintenance of the present cognitive state across various tasks (Engel & Fries, 2010). Within the monkey brain, beta band activity has been shown to mediate top-down interactions between frontal and parietal regions during visual search tasks (Buschman & Miller, 2007, 2009). In a human study, the amplitude of beta band oscillations predicted the response to visual motion within posterior parietal and prefrontal areas, alongside large-scale interactions between these regions (Donner et al., 2007). Consequently, within this experimental context, the beta band oscillations around 22 Hz could potentially be interpreted as an indicator of

shared activity across the network of brain regions involved in processing visual perceptions until the response is formulated.

10.2.6.1 Limitations

Despite the concerted efforts devoted to refining both the protocol design and the rigorous analysis of the captured neural activity, the present study remains encumbered by several limitations. Firstly, the total number of trials conducted within a single session (80) remains relatively modest considering the demanding nature of the decoding analysis. In the prior study, the combination of two consecutive sessions spanning two days was adopted to augment the trial count, albeit at the cost of stricter control over the EEG recording parameters such as electrode positioning and signal quality, which can vary across sessions. Further escalation of the trial count per session appears feasible only through the potential reduction of trial duration, notably the visual search period.

Secondly, the comprehensive understanding of the distinctive decoding outcomes observed in the context of control conditions, particularly during eyes closed periods, remains unsatisfactorily unanswered. This complexity further accentuates the need for an extended data collection phase involving a more substantial pool of patients from the clinical cohort. In contrast, the task refinements introduced through iterative piloting sessions are extensively validated, endowing the experimental setup with enhanced command over procedural dynamics, a more intricate comprehension of behavioral nuances, and a more stringent utilization of the captured EEG signal. However, the analysis itself has unveiled substantial deviations when juxtaposed with outcomes from the first reported case study, warranting a more exploratory analysis encompassing varying frequency bands and distinct cerebral regions to investigate between-subject variability.

10.2.6.2 Perspectives

This study will be advanced along several trajectories. Primarily, a larger group of patients is expected to perform the task, with the intent to amass an expanded dataset that could potentially enable group-level analyses. Secondly, as mentioned above, a more in-depth analysis of the current data discussed here will be undertaken. In particular, the combined analysis of the motion capture data with the time-domain EEG data can give access to the visual-related brain activity at events like the appearance and disappearance of the object in the camera FoV. Deciphering the EEG signatures of such events holds potential to augment the comprehension of the mechanisms underpinning object detection during stimulation, potentially catalyzing advancements in patient rehabilitation protocols.

Concomitant with the ongoing exploration of the visual detection task, an entirely novel task is concurrently being designed and subjected to pilot testing. Based on a visually evoked potential (VEP) paradigm, this novel task endeavors to accomplish two principal goals: firstly, to gain insights on the consistency of the visual areas' response to strong, repeated visual events; and secondly, to quantitatively gauge the extent to which spatial frequency or orientation information of a visual object is conveyed to visual areas by the therapeutic approach. Substantive methodological refinements specific to this task are currently underway,

encompassing the use of a custom high-density cap designed to densify electrode coverage over the occipital lobe, alongside synchronized recordings of the intensity of the light projected by the goggles onto the eye.

Part III

Additional Contributions

CHAPTER 11

AGING BRAIN DYNAMICS FROM SCENE-SELECTIVE REGIONS DURING SPATIAL REORIENTATION

This chapter presents an additional contribution to the study of visuo-spatial processing bound to reorientation in healthy aging, providing complementary insights to the findings of Chapter **8**. Conducted at the LAMHESS (Université Côte d'Azur, Nice, France), the experimental paradigm could not benefit from the mobile EEG equipment and set-up at the Vision Institute, thus it does not contribute much to improve the ecological validity set forth in this thesis. Nonetheless, using desktop-based VR, the paradigm explores scene processing in a spatial reorientation context, requiring spatial navigation processing from participants upon presentation of the image, which is more ecological than many of the studies in the literature concerning the SSRs. Using EEG recordings, it investigates the dynamical brain activity attributable to the SSRs at the scalp-level in healthy aging, through ERP and ERSP analyses. Age-related navigational difficulties were accompanied by differences in the neural dynamics associated to high-level visual processing. Specifically, older adults exhibited cognitive markers of slower cognitive processes for the utilization of the landmarks, reduced inhibitory control of attention, and working memory impairments.

This work was conducted by Clément Naveilhan, PhD student at the LAMHESS (Université Côte d'Azur, Nice, France). He is supervised by Dr. Stephen Ramanoël, a former member of the *Aging in Vision and Action* laboratory. We conceived the paradigm together, and I advised them on the EEG aspects of their experiment, both for the experimental design and the analysis.

An article associated with this work is currently in preparation so the most up-to-date draft version is transcribed here. The structure and tone of the writing of this chapter follows the formatting of the target journal (Neurobiology of Aging).

11.1 Authors

Clément Naveilhan[1], Alexandre Delaux[2], Marion Durteste[2], Jerome Lebrun[3], Raphaël Zory[1,4], Angelo Arleo[2] & Stephen Ramanoël[1,2].

1. Université Côte d'Azur, LAMHESS, Nice, France.
2. Sorbonne Université, INSERM, CNRS, Institut de la Vision, 17 rue Moreau, F-75012 Paris, France.
3. Université Côte d'Azur, Laboratoire I3S, CNRS, Nice, France.
4. Institut Universitaire de France (IUF), Paris, France

11.2 Introduction

Spatial navigation represents a complex behavior that enables us to orient and move in our environment. Although it may appear easy due of its daily use, successful navigation requires intricate cognitive processes such as integration of sensory cues, working memory, or path integration (Wolbers & Hegarty, 2010) underpinned by a large and highly interconnected cerebral network (Ekstrom et al., 2014, 2017). Healthy aging is causally involved in decrements of spatial navigation abilities, older adults experiencing difficulties to navigate in both familiar and unfamiliar environments (Barrash, 1994). These changes in navigation capabilities reduce older adults' autonomy and mobility (Burns, 1999), resulting in an increased risk of progression of age-related disorders such as Alzheimer's disease (Gelfo et al., 2018). Considering the general aging of the population, particularly in northern countries, it is essential to gain a better understanding of the factors contributing to age-related navigational deficits and their neural correlates.

In a recent review on spatial navigation tasks and MRI, Li and King (2019) reported structural and functional brain correlates of age-related decline of spatial capabilities. The authors emphasized a marked deficit for older adults in allocentric navigation (*i.e.*, world-centered) consistently with previous studies (Colombo et al., 2017; Lester et al., 2017). Moreover, they reported an association between the allocentric spatial deficit and other brain regions implicated in spatial processing, such as the para-hippocampal gyrus, retrosplenial cortex and prefrontal cortex. In their review Li and King (2019) also reported a preserved navigational performance for older adults when using an egocentric strategy (*i.e.*, body-centered) relying more on the posterior parietal cortex (Lithfous et al., 2013). These findings emphasize the importance of hippocampus-dependent deficits, but also the need to consider extra-hippocampal contributions to age-related decline and their possible functional compensation mechanisms (Snytte et al., 2022; Zhong & Moffat, 2018). Others neuroimaging modalities such as EEG reported similar age-related decline in navigation using an allocentric spatial reference frame. For example, Lithfous et al. (2014) reported in an event-related potentials (ERPs) study, an age-related increase of the P2 component amplitude and delayed P2 latency over parietal electrodes (P_7 and P_8) associated with impaired performances in allocentric spatial condition only. They suggested that the parietal P2 component may reflect

the mechanisms underlying the age-related decline in spatial processing and emphasized the need for further studies to include other elements of navigation such as spatial memory or spatial visual cue processing. Interestingly, the parietal P2 component has also recently been proposed to reflect the visual processing of high-level scene information, which is an important cognitive process for an efficient navigation (Harel et al., 2016, 2022).

The ability to perceive and integrate visuo-spatial information such as salient landmarks is indeed essential to orient and navigate in space efficiently. This is particularly important for humans who depend predominantly on their visual system to perceive their surroundings (Ekstrom, 2015; Foo et al., 2005). Furthermore, greater visual attention is devoted to salient landmarks, which subsequently serve as crucial reference points for successful navigational behavior (de Condappa & Wiener, 2016; Hamid et al., 2010; Wenczel et al., 2017). Their use for navigation as recently been proposed to be the key mechanism behind age related decline in allocentric processing (Bécu et al., 2023). In this study, young and older adults performed a Y-maze paradigm in immersive virtual reality (VR) and, after a learning phase, had to reorient themselves using either landmarks or geometric cues. Their results suggest that the well reported age-related decrements of allocentric navigation abilities for older adults might rather reflect difficulties in navigating with the help of landmarks, highlighting the importance to investigate this navigation modality in the context of aging. In this sense, a subset of high-level visual regions is speculated to support the mechanisms responsible for integrating visual inputs with the egocentric or allocentric representations of the surrounding environment. This system comprises the para-hippocampal place area (PPA) which is involved in encoding the spatial significance of objects presented as landmarks and place recognition; the medial place area (MPA), a key region of the scene processing and navigational network for the translation of information between spatial reference frames; and the occipital place area (OPA), involved in the encoding of environmental boundaries and supporting first-person vision-guided navigation (Epstein & Baker, 2019; Julian et al., 2018). In the context of aging, several fMRI studies suggested that these scene-selective regions need to be carefully considered in order to investigate decline of navigational abilities. Notably, reduced activity in the PPA has been revealed to underpin age-related differences in the categorization of high spatial frequency contents of visual scenes (Ramanoël et al., 2015). Furthermore, the neural specificity and distinctiveness of the PPA and retrosplenial complex (RSC) have been shown to decline with age and to predict individual source and spatial memory abilities (Koch et al., 2020; Srokova et al., 2020). Remarkably, functional connectivity between the OPA and PPA has been found to be increased in healthy aging (Ramanoël et al., 2019) highlighting significant age-related modifications to visual processing in regions linked to spatial navigation. These results were complemented with fMRI acquisitions during a Y-maze reorientation task using 3D objects as landmarks (Ramanoël et al., 2020). The authors reported lower brain activation of the hippocampus, prefrontal and cerebellum but also an increased parietal activity over the OPA region in older adults. Critically, this age-related higher parietal activity was reported during reorientation task involving landmark processing and navigation but not for free navigation only.

Despite these results providing foundation for investigating the role of visual aging on

spatial abilities, the knowledge about the neural mechanisms subtending age-related navigational decline is scarce. Notably, the temporal dynamic of this pattern remains poorly unexplored, fMRI not allowing to investigate brain dynamic at the millisecond scale (Glover, 2011). To address this, the present study proposes to navigate the maze of aging by investigating age-related effects on brain dynamics using EEG recorded from electrodes imputable to high-level visual brain regions (Harel et al., 2016; Kaiser et al., 2020) during a landmark desktop-based spatial reorientation task. We hypothesized that, reflecting a possible compensatory mechanism supported by OPA activity (Ramanoël et al., 2020), older adults would exhibit a higher parietal P2 component amplitude during reorientation compared to young adults. In addition, we hypothesized that higher brain activity will be more present during reorientation task compared to passive perception. Considering age effect over vision (Faubert, 2002) and reduced capacity for fine processing (Ramanoël et al., 2020, 2015), we also modulated the perceptual difficulty, varying landmark size. We hypothesized that older adults would be more impaired in this condition, with an increased activity of our investigated brain regions, reflected in a more pronounced increase of the P1 and P2 components for older adults in the small landmark condition. To complete these ERP results and gain more insights in the underlying cognitive processes, we also computed event-related spectral perturbations (ERSPs) (for a comprehensive exploration of the techniques and uses of time-frequency analysis see Gable et al. (2022)), focusing on theta (3-8 Hz) and alpha (8-12 Hz) bands, previously reported as decreased in older adults and associated with deficits in spatial memory and cognitive mapping (Lithfous et al., 2015). This same theta activity being also reduced in high-performing older and young adults compared to low-performing older adults (Lithfous et al., 2018), supporting the relationship between theta oscillations and spatial memory (Bohbot et al., 2017; Chrastil et al., 2022; Jacobs, 2014). Here we hypothesized that older adults would exhibit increased theta activity and reduced alpha during reorientation.

11.3 Methods

11.3.1 Participants

We recorded brain activity using EEG from 30 young participants and 32 healthy older participants. We excluded 2 older participants from the analysis because their performance during the navigation task was below chance level, suggesting poor understanding of the task. In addition, 4 other participants (2 older and 2 young participants) were also excluded due to excessive artifacts assessed by signal-to-noise ratio calculation completed by a careful visual inspection. Analyses were finally conducted on 28 young participants (mean age: 23.93 years old; SEM = 0.64; range : 19-36; 14 women) and 28 older adults (mean age: 71.25 years old; SEM = 1.01; range : 61-81; 18 women) mainly right-handed. Participants had no history of neurological or psychiatric disorders and reported normal or corrected-to-normal vision. They were assessed for cognitive impairment with the GRECO French version of the Mini Mental State Examination (MMSE) (Kalafat et al., 2003) using the proposed 26 cut-

off to ensure their healthy cognitive status. They also completed a computerized version of the Spatial Orientation Test (SOT) (Friedman et al., 2020) and a French version of a spatial navigation questionnaire (De Beni et al., 2014). See Table **11.1** for a summary. The experiment was approved by local Ethical Committee (CERNI-UCA n°2021-050) and participants provided informed consent before starting the experiment.

	Groups				
	Mean (± SEM)				
Sex (M/F)	Young 14/14	Older 10/18	p-value	Effect size	95% CI
Age (years)	23.93 (±0.64)	71.25 (±1.01)	< 0.001	$r_{rb} = 1.00$	$[7.68; 13.29]$
Education level	4.11 (±0.29)	2.57 (±0.46)	0.007	$r_{rb} = 0.41$	$[-1.31; -0.19]$
MMSE	29.18 (±0.17)	29.11 (±0.21)	0.972	$r_{rb} = 0.01$	$[-0.52; 0.52]$
SOT	32.63 (±4.67)	58.28 (±5.69)	< 0.001	$r_{rb} = 0.54$	$[0.35; 1.50]$

Table 11.1: Demographic information about the participants and their performance at the cognitive evaluations. A Mann-Witney U-test was used to assess the difference between age groups for each measure. M: Male ; F: Female.

11.3.2 Stimuli & procedure

Visual stimuli were created using Unity Engine (Unity Technologies version 2019.2.0.0f1) and were presented on a iiyama ProLiteB2791HSU screen (1920×1080, 30-83 kHz) placed at eye level and at 60 cm distance from the participants. Stimuli were presented via the open-source software PsychoPy (v2022.13), implemented on a computer Dell Precision 7560 (Intel Xeon W-11955). The retinal visual angle of the landmarks in the far condition was 2.59° on average, while it was 1.27° in the near condition. The environment was adapted from a previous fMRI experiment on healthy aging (Ramanoël et al., 2020). It was a three-arm maze (*i.e.*, a Y-maze) consisting of three corridors: one branch containing a goal, materialized by a gift box, two identical starting branches and three 3D objects positioned at the intersection to be used as landmarks (*i.e.*, a cube, a sphere, and a pyramid).

The experimental paradigm was divided in 3 tasks: *Learning*, *Reorientation*, and *Control* (Figure **11.1**). First, during the *learning task*, participants were passively displaced through the maze. They were instructed to memorize the path to the goal hidden at the end of one corridor using the 3D objects of the intersection. Then, during the *reorientation task*, participants were presented images of the intersection taken from the videos, and they were instructed to indicate, as quickly and accurately as possible, the location of the goal using directional keys (left or right). Participants were presented snaps in a pseudo-randomized order taken from either a condition near the intersection or from a far condition to modulate the perceptual difficulty. Each image was presented for a duration of 3 seconds followed by distinct auditory feedbacks depending on success or failure in trial. Then participants performed the *control task*, consisting in the passive perception of images of the intersection,

but this time, all 3 objects were identical (3 spheres, 3 cubes, or 3 pyramids). They were instructed to carefully look at the objects and at the fixation cross presented between the different images. To avoid a too important weariness, we varied environment properties: wall texture and goal location, leading to the presentation of 15 different combinations pseudo-randomized across participants. This sequence of learning, reorientation and control task was repeated 3 times leading to the presentation of 60 videos, 300 reorientation trials and 180 control trials for a total acquisition duration of 49 minutes.

11.3.3 Recording & Analysis

11.3.3.1 EEG recording

The EEG recording was sampled at 500 Hz, digitized with 24 bits of resolution, from 64 Ag/AgCl electrodes mounted in a cap (waveguard original) connected to an amplifier (eego mylab, ANT Neuro). Data were online referenced to CP_z electrode, using AF_z as ground. Electrodes impedance was kept below 20 kΩ (under 10 kΩ in most cases, and for our region of interest (ROI)), which was well below recommended maximum of 50 kΩ for high-impedance eego amplifiers. Synchronization of the EEG recording, and the events of presentation of the stimuli was ensured by the Lab Streaming Layer (LSL) software LabRecorder (version 1.13).

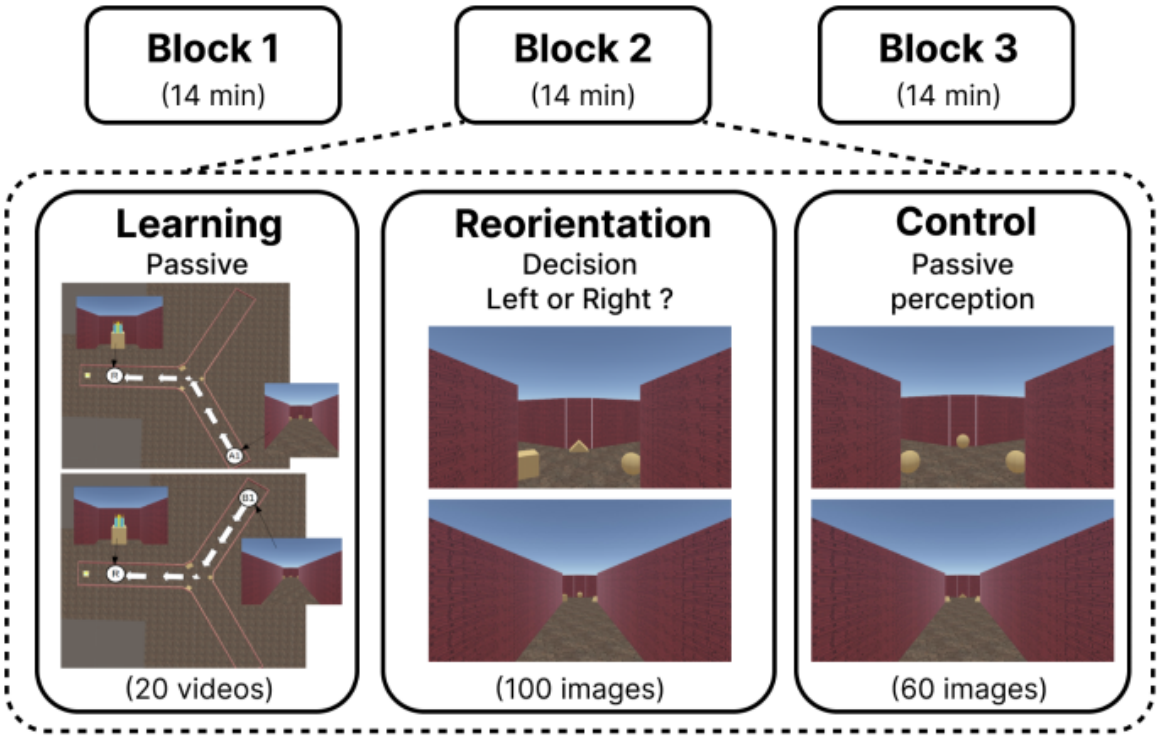

Figure 11.1: Presentation of the paradigm and stimuli used for the different phases. Blocks were the same between participants but presented in a pseudo-randomized, with different wall textures. A short break was proposed to all participants between blocks.

11.3.3.2 EEG preprocessing

The off-line preprocessing procedures were performed with MATLAB (R2021a; The MathWorks Inc., Natick, MA, USA) using customs scripts based on the EEGLAB toolbox version 14.1.0b (Delorme & Makeig, 2004) and adapted from a processing pipeline previously used (Delaux et al., 2021). We first down sampled the data to 250 Hz, and corrected time points for software delay using trigger time added to a fixed delay of 50 ms for hardware delay. We automatically removed line noise using the recently developed algorithm *Zapline-Plus* (Klug & Kloosterman, 2022). Then, using default parameters proposed in the *PREP* pipeline (Bigdely-Shamlo et al., 2015), we automatically identified and rejected noisy channels. On average, 4.25 channels were rejected (SD = 0.39). Those channels were then reconstructed by spherical interpolation of neighboring channels, and data were re-referenced to the common average. Artifacts were automatically rejected using the Artifact Subspace Reconstruction (ASR) (Kothe & Jung, 2015) which use clean portions of data to determine thresholds for rejecting components. We used an ASR cutoff parameter of 20, corresponding to the proposed optimal range between 10 and 100 (Chang et al., 2020).

Then, on the cleaned dataset, we temporally high passed with a 1.5 Hz filter (Klug & Gramann, 2021) before applying an ICA using the *AMICA* algorithm (Palmer et al., 2008). Next, dipoles were reconstructed using ECD model reconstruction (*DIPFIT*; Oostenveld and Oostendorp 2002). Then, we used *ICLabel* algorithm (Pion-Tonachini et al., 2019) to classify components according to 7 classes, using default percentage for classification. On average, we kept 14.64 components (SD = 0.67) corresponding to brain activity. Next, we applied a band-pass filter to the data using a finite impulse response filter with a Hamming window. We chose a lower cutoff frequency of 0.3 Hz (with 0.5 Hz transition bandwidth, 0.55 Hz pass band edge and 1650 order) to remove slow drifts, and an upper cutoff frequency of 80 Hz (20 Hz transition bandwidth, 80 Hz pass band edge and 42 order) to attenuate high-frequency noise and muscle artifacts.

Finally, preprocessed data were segmented into epochs ranging from -200 ms before to 600 ms after stimulus onset for all conditions, using a buffer of 1000 ms before and after epoch for frequency domain analysis. Epochs were extracted of the analysis whenever less than 90% of the period was clean. On average, we kept 76.56% of epochs (mean epochs kept per subject: 367.50; SD = 2.60), and there was no difference between age groups regarding number of epochs extracted ($t(1,43.33) = 0.820$, $p = 0.417$).

11.3.3.3 ERP analysis

Analyses were restricted to electrodes previously associated to scene selective regions (Harel et al., 2016; Kaiser et al., 2020), corresponding to P_6-P_8-PO_8 for the right hemisphere and P_5-P_7-PO_7 for the left hemisphere. Further data analysis was conducted using custom MATLAB scripts with *Fieldtrip* toolbox functions (Oostenveld et al., 2011). For ERPs, baseline was identified from -200 ms to image appearance corresponding to the minimum recommended of 10% to 20% overall epoch length (Luck, 2014), and mean baseline activity were subtracted from the data. Peak amplitude was calculated using mean amplitude, corresponding to the average of the most positive value surrounded by 2 lower values (Luck,

2014). Considering the reported effect of aging on peak latency (Kropotov et al., 2016; Mueller et al., 2008), we decided to calculate for each age group, P1, N1 and P2 latency using the grand average of each group. Then, we took a window around this value taking 50 ms before and after grand average peak latency, and extracted, individual's components latencies and amplitudes.

11.3.3.4 Time-frequency analysis

Time-frequency analysis were decomposed using the *superlet* approach (Moca et al., 2021), a spectral estimator using sets of increasingly constrained bandwidth wavelets to achieve time-frequency super-resolution. To this end, we used *Fieldtrip* function `ft_freqanalysis` to decompose between 1 and 80 Hz, using a width of 2 and a gaussian width of 3, with an increasing order scaling from 1 to 80. Once the decomposition done, we computed ERSPs. We used the decibel conversion to baseline normalize power values, taking a baseline between -250 ms to -50 ms because of temporal smearing (see Cohen 2014 for more details).

11.3.3.5 Statistical analysis

For ERSPs, dealing with multiple comparison problem, we applied non-parametric cluster based permutation test using Monte-Carlo estimate (Maris & Oostenveld, 2007) implemented in the *Fieldtrip* toolbox. After comparison, we chose the most robust and least conservative method among different modalities, which involved 10000 permutations with weighted cluster mass (Hayasaka & Nichols, 2004) and a cluster-level alpha of 0.005 to account for multiple comparisons.

All other statistical analyses were then performed using *R* Statistical Software (version 4.2.1, *R* Foundation for Statistical Computing, Vienna, Austria) with *R* studio (version 2022.07.02+576). After comparing different models using the Akaike information criterion (Akaike, 1974), we decided to use linear mixed model implemented in the *lme4 R* package (D. Bates et al., 2014), with participants as random intercept. Then we used the implemented `anova` function to compute a type III ANOVA with Satterthwaite's method. Results reported are estimated marginal means computed with *emmeans* package in *R*, using a type III sum of squares, and post-hoc Tukey's honestly significant difference were finally performed. To ensure normality of residuals and homoscedasticity, both were cautiously inspected visually using quantile-quantile plots and boxplots, respectively.

11.4 Results

11.4.1 Behavioral results

We reported age-related difference on navigational performance (Figure **11.2**). First, considering accuracy, we only reported a main effect of Age ($F(1,54) = 6.63$, $p = 0.013$, $\eta_p^2 = 0.11$, 95% CI $= [0.00, 0.28]$), with a lower accuracy for older adults ($93.4 \pm 0.94\%$ [mean $\pm$ SEM]) compared to young adults ($96.8 \pm 0.94\%$). There was no effect of Condition ($F(1,54) = 0.527$, $p = 0.47$) nor interaction ($F(1,54) = 0.136$, $p = 0.71$).

Considering reaction time, we found a main effect of Age ($F(1,54) = 40.97$, $p < 0.001$, $\eta_p^2 = 0.43$, 95% CI $= [0.24, 0.58]$) with a higher reaction time for older adults (1162 ± 35.2 ms) compared to young adults (843 ± 35.2 ms). We also found main effect of Condition ($F(1,54) = 52.47$, $p < 0.001$, $\eta_p^2 = 0.48$, 95% CI $= [0.30, 0.63]$) with a higher reaction time for the far condition (1020 ± 25 ms) compared to the near condition (985 ± 25 ms). We did not observe any interaction between Age and Condition ($F(1,54) = 1.48$, $p = 0.229$).

11.4.2 ERP results for near and far conditions during Reorientation phase

In this first analysis we compared near and far condition, investigating the interaction of age with perceptual complexity during a reorientation task (Figure **11.3**).

11.4.2.1 P1, N1, and P2 amplitudes

First, we considered the age effect comparing young *vs.* old. We reported no main effect for the P1 amplitude ($F(1,54.17) = 2.57$, $p = 0.11$), but a higher amplitude for young compared to older adults when considering only the right hemisphere ($t(67) = -3.02$, $p = 0.018$, d $= 1.29$, 95% CI $= [0.43, 2.15]$). We reported an increased N1 amplitude (*i.e.*, more negative) for older adults compared to young adults ($F(1,54.09) = 28.92$, $p < 0.001$, $\eta_p^2 = 0.35$, 95% CI $= [0.16, 0.51]$). We also observed a decreased P2 amplitude for older adults compared to young adults ($F(1,54) = 7.36$, $p < 0.001$, $\eta_p^2 = 0.12$, 95% CI $= [0.01, 0.29]$) but this age effect was restricted to the right hemisphere ($t(68) = -4.58$, $p < 0.001$, d $= -1.82$, 95% CI $= [-2.62, 1.00]$), with no difference for the left hemisphere ($t(68.3) = -0.53$, $p = 0.95$).

Next, we considered the effect of the condition comparing near *vs.* far. We reported a higher P1 amplitude for the far condition compared to the near condition ($F(1,159.25) =$

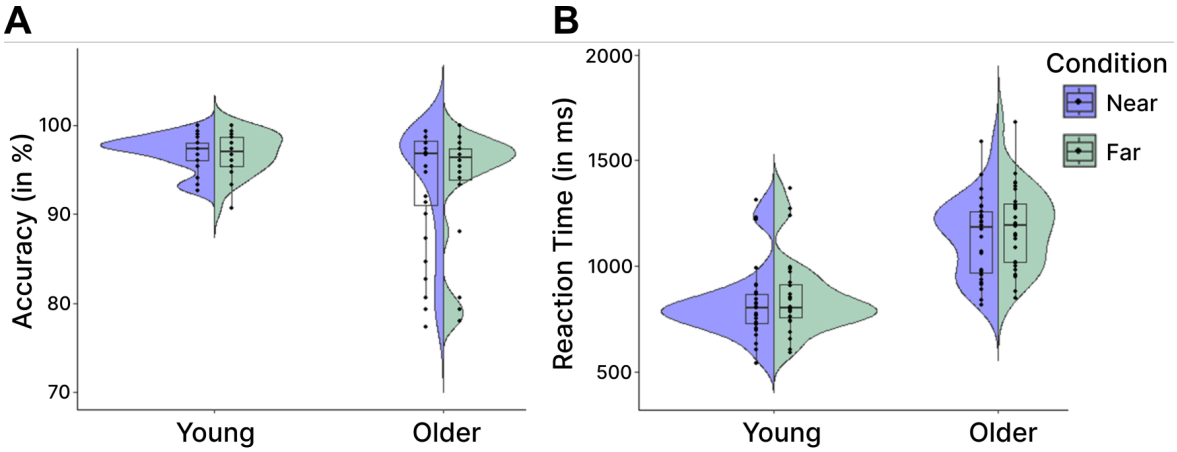

Figure 11.2: Performance of participants at the reorientation task. Results are grouped by Age and Condition for comparison purposes. Individual points represent the average for each participant. **A**. Accuracy computed as the percentage of reorientation errors over all trials. **B**. Reaction time between the presentation of the stimulus and the recorded response.

4.91, $p = 0.028$, $\eta_p^2 = 0.03$, 95% CI $= [0.00, 0.10]$). There was neither modulation of the N1 ($F(1,159) = 3.43$, $p = 0.066$), nor of the P2 amplitudes ($F(1,162) = 1.70$, $p = 0.19$).

Finally, we investigated lateralization effect comparing right *vs.* left hemisphere. We observed a similar pattern for P1 ($F(1,159.77) = 33.74$, $p < 0.001$, $\eta_p^2 = 0.17$, 95% CI $= [0.08, 0.28]$) and P2 ($F(1,162) = 122.29$, $p < 0.001$, $\eta_p^2 = 0.43$, 95% CI $= [0.32, 0.52]$), with a higher amplitude in the right hemisphere. Considering N1, we observed the opposite, with a greater amplitude in the left hemisphere ($F(1,159.79) = 15.15$, $p < 0.001$, $\eta_p^2 = 0.09$, 95% CI $= [0.02, 0.18]$), but this effect was restricted to young adults ($t(160) = -5.13$, $p < 0.001$, d $= -0.99$, 95% CI $= [-1.39, -0.60]$), older adults presenting similar N1 activity for both hemispheres ($t(159) = -0.32$, $p = 0.99$).

11.4.2.2 P1, N1, and P2 latencies

Considering age effect, we reported later peaks for older adults regarding the P1 ($F(1,54.35) = 13.12$, $p < 0.001$, $\eta_p^2 = 0.19$, 95% CI $= [0.04, 0.37]$), the N1 ($F(1,53.92) = 37.24$, $p < 0.001$, $\eta_p^2 = 0.41$, 95% CI $= [0.21, 0.56]$) and the P2 ($F(1,54) = 130.25$, $p < 0.001$, $\eta_p^2 = 0.71$, 95% CI $= [0.57, 0.79]$). The effect for the P1 was restricted to the far condition ($t(77) = 4.76$, $p < 0.001$, d $= 1.57$, 95% CI $= [0.90, 2.24]$) as we reported no age-difference for the near condition ($t(77) = 1.85$, $p = 0.26$).

Considering the condition effect, we reported a delayed P1 for the far condition compared to the near ($F(1,159.53) = 20.89$, $p < 0.001$, $\eta_p^2 = 0.12$, 95% CI $= [0.04, 0.21]$).

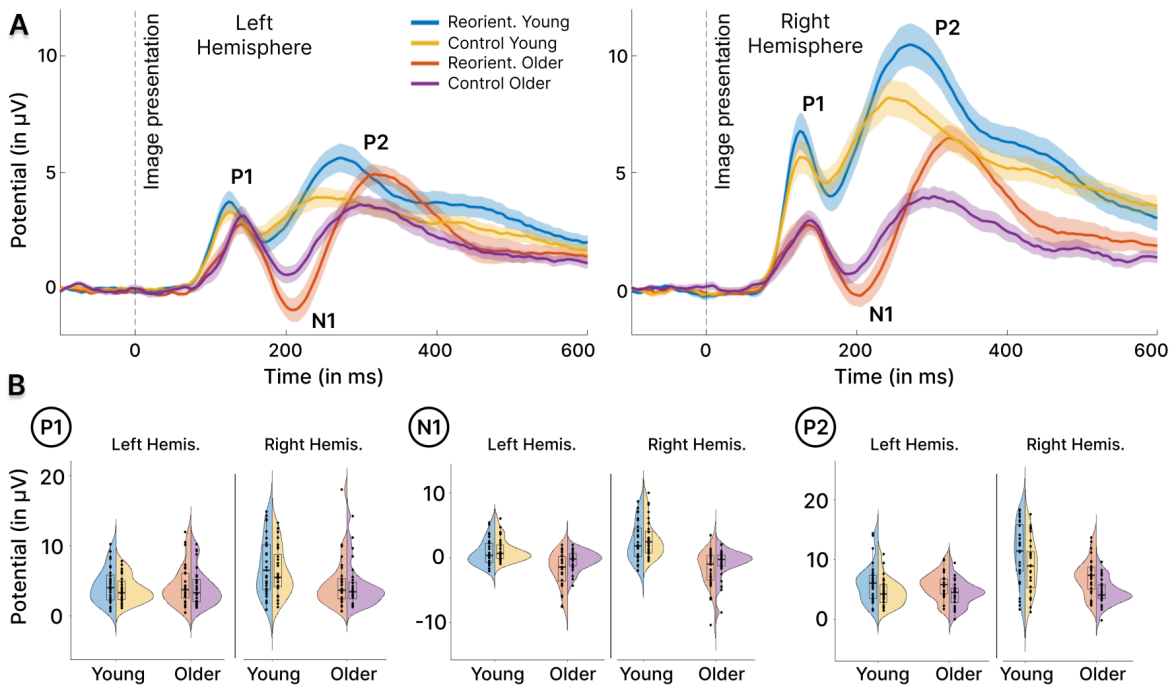

Figure 11.3: ERP results for near and far conditions during Reorientation phase. **A**. Grand-average ERPs, considering Age (Young/Older), Condition (Near/Far) and Hemisphere (Left/Right) as variables, individually baseline corrected. Activity averaged over P_6-P_8-PO_8 electrodes for the right hemisphere and over P_5-P_7-PO_7 electrodes for the left hemisphere. **B**. Split violin plot of extracted individual amplitudes for P1, N1 and P2 component. Statistics were computed using these values.

This effect was neither present for the N1 ($F(1,159.28) = 1.85$, $p = 0.544$), nor the P2 ($F(1,162) = 1.52$, $p = 0.22$). This condition effect for the P1 was only present for older adults ($t(159) = 5.80$, $p < 0.001$, d $= 1.10$, 95% CI $= [0.71, 1.49]$) with no difference for young adults ($t(159) = 0.70$, $p = 0.90$).

Finally, for the lateralization, we found no effect for the P1 ($F(1,160.32) = 3.76$, $p = 0.054$) or the N1 ($F(1,160.32) = 3.76$, $p = 0.054$). For the P2, we reported a later peak for the right hemisphere compared to the left one ($F(1,160.42) = 3.64$, $p = 0.058$, $\eta_p^2 = 0.02$, 95% CI $= [0.00, 0.09]$).

11.4.3 ERP results comparing Reorientation and Control phases

For this second analysis we isolated the effect of the Reorientation phase compared to a passive perception of similar scenes allowing the dissociation between scene perception and reorientation (Figure **11.4**). To this end, the results presented below correspond to merged results for the near and far condition. Beforehand, we have ensured that considering them separately gave the same pattern of results.

11.4.3.1 P1, N1, and P2 amplitudes

First, we considered age effect comparing young and older adults. We reported no effect for the P1 amplitude ($F(1,54.06) = 2.15$, $p = 0.15$), and a higher N1 amplitude for older adults

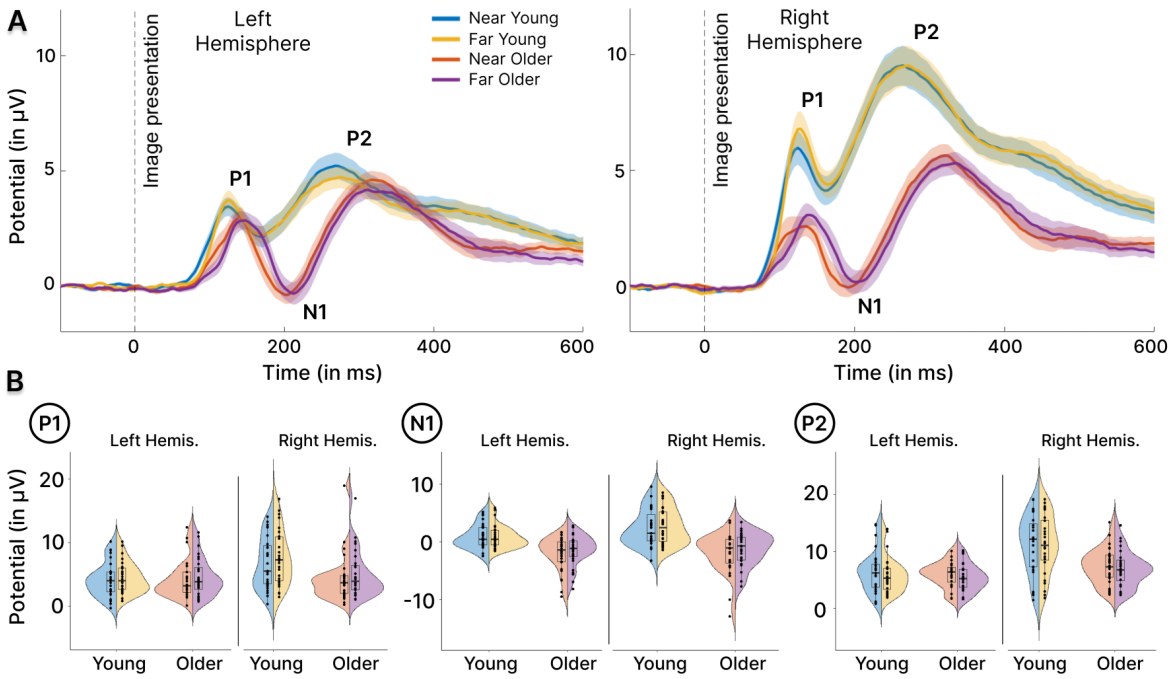

Figure 11.4: ERP results comparing Reorientation and Control phases. **A**. Grand-average ERPs, considering Age (Young/Older), Phase (Reorientation/Control) and Hemisphere (Left/Right) as variables, individually baseline corrected. Activity averaged over P_6-P_8-PO_8 electrodes for the right hemisphere and over P_5-P_7-PO_7 electrodes for the left hemisphere. **B**. Split violin plot of extracted individual amplitudes for P1, N1 and P2 component. Statistics were computed using these values.

($F(1,54.08) = 31.82$, $p < 0.001$, $\eta_p^2 = 0.37$, 95% CI = $[0.18, 0.53]$). We found the opposite pattern for the P2, with a higher amplitude for young adults ($F(1,84) = 10.33$, $p = 0.002$, $\eta_p^2 = 0.16$, 95% CI = $[0.02, 0.34]$).

Then, considering the task, comparing reorientation and control (*i.e.* passive perception). We found a similar pattern, with higher amplitude for the reorientation task for P1 ($F(1,161.14) = 4.32$, $p = 0.040$, $\eta_p^2 = 0.03$, 95% CI = $[0.00, 0.09]$), N1 ($F(1,161.16) = 13.90$, $p < 0.001$, $\eta_p^2 = 0.08$, 95% CI = $[0.02, 0.17]$) and P2 ($F(1,162) = 44.38$, $p < 0.001$, $\eta_p^2 = 0.22$, 95% CI = $[0.11, 0.32]$). Only considering the N1 amplitude, the effect was restricted to older adults ($t(159) = 3.98$, $p < 0.001$, d = 0.75, 95% CI = $[0.37, 1.14]$), as young adults displayed no difference for this component amplitude between reorientation and control ($t(161) = 1.30$, $p = 0.57$).

Finally, considering laterization, comparing left and right hemisphere. We reported a similar pattern for positive components, with a higher amplitude in the right hemisphere for P1 ($F(1,161.14) = 32.22$, $p < 0.001$, $\eta_p^2 = 0.17$, 95% CI = $[0.07, 0.27]$) and P2 ($F(1,162) = 95.95$, $p < 0.001$, $\eta_p^2 = 0.37$, 95% CI = $[0.26, 0.47]$). Those results were only observed for young adults, as older adults displayed neither lateralization effect for P1 ($t(161) = -0.58$, $p = 0.94$) nor for the P2 component ($t(162) = -2.43$, $p = 0.12$). For the N1, we found the opposite result, with a higher amplitude for the left hemisphere ($F(1,161.16) = 14.83$, $p < 0.001$, $\eta_p^2 = 0.08$, 95% CI = $[0.02, 0.18]$), once again only for young adults ($t(159) = -5.94$, $p < 0.001$, d = -1.13, 95% CI = $[-1.52, -0.73]$) with no lateralization for older adults ($t(161) = 0.51$, $p = 0.96$).

11.4.3.2 P1, N1, and P2 latencies

First, we reported a similar pattern for age differences over the different components, with a later peak for the P1 ($F(1,54.06) = 12.12$, $p < 0.001$, $\eta_p^2 = 0.18$, 95% CI = $[0.04, 0.36]$), the N1 ($F(1,53.87) = 47.88$, $p < 0.001$, $\eta_p^2 = 0.47$, 95% CI = $[0.28, 0.61]$) and P2 components ($F(1,54) = 154.14$, $p < 0.001$, $\eta_p^2 = 0.74$, 95% CI = $[0.62, 0.82]$). The age difference for the P1 was only present for the left hemisphere ($t(69.8) = 4.16$, $p < 0.001$, d = 1.58, 95% CI = $[0.81, 2.35]$), as we reported no age-related modulation of the P1 for the right hemisphere ($t(70) = 2.36$, $p = 0.10$) When comparing reorientation and control task, there was no difference for the P1 latency ($F(1,161.15) = 0.08$, $p = 0.77$). We observed a similar pattern for the 2 others components, with a later peak for reorientation task for the N1 ($F(1,161.01) = 9.34$, $p = 0.003$, $\eta_p^2 = 0.05$, 95% CI = $[0.01, 0.14]$) and P2 ($F(1,162) = 58.59$, $p < 0.001$, $\eta_p^2 = 0.27$, 95% CI = $[0.16, 0.37]$). For the lateralization, comparing left and right hemisphere, we reported a later P1 peak for the left hemisphere ($F(1,161.15) = 4.96$, $p = 0.027$, $\eta_p^2 = 0.03$, 95% CI = $[0.00, 0.10]$), with a similar pattern for the N1 component ($F(1,161.01) = 6.31$, $p = 0.013$, $\eta_p^2 = 0.04$, 95% CI = $[0.00, 0.11]$). Considering P2 we reported no difference between left and right hemisphere ($F(1,162) = 1.17$, $p = 0.28$). The P1 later peak was only observed for young adults ($t(161.2) = 7.42$, $p < 0.001$, d = 1.41, 95% CI = $[1.00, 1.81]$) as we did not observe any difference for older adults ($t(161) = 0.22$, $p = 0.99$).

11.4.4 ERSP results comparing Reorientation and Control phases

Finally, in this third analysis we examined brain oscillations by computing ERSPs. This technique allows additional information for the underlying cognitive process to be captured beyond ERPs (Herrmann et al., 2014).

Then, considering these ERSPs (Figure **11.5A**), we reported for all results a similar pattern with an increased synchronization in low frequency bands, delta/theta (1-8 Hz) arising 50 ms before image presentation for young adults and lasting up to +400 ms and up to +500 ms for older adults in the reorientation task. This synchronization was followed up by a desynchronization in higher frequency bands alpha (8-13 Hz) and beta (13-30 Hz). There is also a much more diffuse difference in the average frequencies for the control task in the two hemispheres. We then computed cluster-based permutation test on those results (Figure **11.5B**). We reported for older adults, a decreased synchronization in alpha/beta band, starting from +200 ms and lasting until +1000 ms, results not significant in the left hemisphere, with just a cluster at +200 ms that might result from delayed activity for older adults as observed in ERP results. We also reported in the same context, a decreased synchronization in delta (1-3 Hz) band for older adults, starting from −50 ms before image presentation up to +200 ms. Older adults also exhibited an increase in theta (3-8 Hz) synchronization, with a burst starting just after +200 ms and lasting up to +400 ms, and a decrease in high beta band synchronization for the reorientation task and in the right hemisphere only.

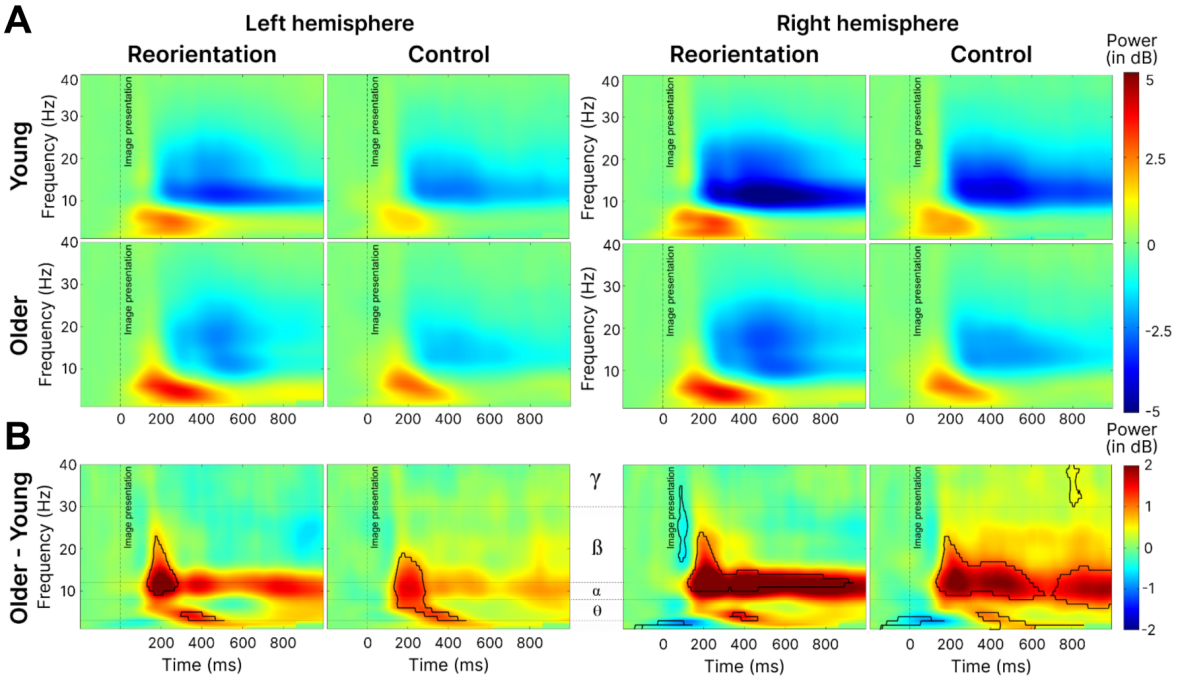

Figure 11.5: ERSP results comparing Reorientation and Control phases. **A**. Grand-average ERSPs, considering Age (Young/Older), Phase (Reorientation/Control) and Hemisphere (Left/Right) as variables, using decibel baseline (−150 to −50 ms) normalization. Activity averaged over P_6-P_8-PO_8 electrodes for the right hemisphere and over P_5-P_7-PO_7 electrodes for the left hemisphere. **B**. ERSP activity of Older minus Young adults. The black line corresponds to cluster-based permutation tests results with $p < 0.05$.

11.5 Discussion

We conducted an EEG study to investigate age-related differences in landmark-based navigational performance and their neural correlates. Consistent with previous studies and our main hypothesis, we reported that older adults experienced reduced navigational abilities, evidenced by slower and less precise reorientation performances. However, contrary to our initial hypothesis, reducing landmark size did not aggravate the impairment of older adults. Age-related navigational difficulties were accompanied by differences in the neural dynamics associated to high-level visual processing. Precisely, older adults exhibited slower cognitive processes for the utilization of the landmarks, as evidenced by the delayed latencies of the P1, N1 and P2 components of the EEG. Moreover, in older adults, the right hemisphere displayed decreased P1 and P2 amplitudes, which corresponded to lower delta and higher alpha-beta power, respectively. These findings may indicate that older adults experience reduced inhibition of irrelevant information and impairments in working memory. Additionally, older adults exhibited enlarged N1 amplitude in both hemispheres, accompanied by higher levels of theta power, which could reflect higher activity in scene-selective regions (SSRs) during a reorientation task based on landmarks with a possible bilateral compensatory mechanism.

11.5.1 Behavior

The behavioral data indicated better performances for young adults, with a lower reaction time and a higher percentage of recovered paths. Those results are consistent with the literature, who provide great evidence for age-related decrements in spatial navigation abilities but also in reaction time. Increasing perceptual difficulty (lowering landmark size), we observed an increase in reaction time, this increase being the same for young and older adults. Previous studies also found a faster reaction time to physically larger targets, and this pattern is well documented since a long time (Osaka, 1976; Plewan & Rinkenauer, 2017; Sperandio et al., 2009). Interestingly, older adults do not seem to be more impaired than young adults when increasing perceptual difficulty. A possible explanation is that our manipulation of perceptual difficulty is not sufficient to observe a difference between age groups (*i.e.*, the difference in object size is not sufficient), or that there is no interaction effect between age and perceptual difficulty during a reorientation task. This absence of difference in behavior is also in line with our EEG results, that reported no interaction effect between perceptual difficulty and age, except for a later P1 peak amplitude for older adults in the far condition (*i.e.*, smaller landmark) compared to the near one. These results are discussed in the following. Concerning accuracy, using a similar Y-maze paradigm, previous work also reported a higher navigation error rate for older adults (Ramanoël et al., 2020), in line with an important literature of age-related impairments in navigation abilities (Lester et al., 2017).

11.5.2 Lateralization

For young adults we found a clear lateralization of brain activity, with a higher right hemisphere activation than left hemisphere. Those results are in line with (Harel et al., 2016, 2022) who also found a higher amplitude for the right hemisphere, recording only from young adults during a passive scene perception. This is also consistent with early split-brain investigations (Sperry, 1974) and positron emission tomography studies who provided evidences for a right hemisphere dominance for spatial task (Courtney et al., 1996; Sergent et al., 1992; E. E. Smith et al., 1995), spatial working memory and spatial selective attention proposed to be driven by a right-hemisphere dominant network (Awh & Jonides, 2001). This lateralization was decreased for older adults for P1 and P2 components, with a decrease in amplitude for older adults only in the right hemisphere. This effect seems to be also present in the ERSPs, even if we did not conduct statistics to compare hemispheric activity. This age-related decrease of right hemisphere engagement is consistent with Learmonth et al. (2017). Using a 'tachistoscopic line bisection' task adapted from McCourt (1999) where participants had to indicate which side of a line was shorter, they recorded EEG and reported a decreased right hemisphere lateralization for older adults. They prudently interpreted those results in regard of the HAROLD model of cognitive aging (Cabeza, 2002). They emitted the possibility that their results might be due to neurodegeneration, highlighting the lack of neuropsychological examination in their study. Since in our experiment participants were selected based on a MMSE criterion (> 26), our results reinforce the hypothesis of right hemisphere engagement decrease with healthy aging during a visuo-spatial task as proposed by the right hemi-aging model, which seems to be more applicable to posterior regions (Dolcos et al., 2002).

11.5.3 N1 component and theta activity

Interestingly, considering only the left hemisphere, we found a higher N1 amplitude for older adults, whereas P1 and P2 were identical in both age groups. De Sanctis et al. (2008) also found a similar pattern, interpreted as a bilateral involvement of ventral stream visual area in aging whereas in young adults it was restricted to left hemisphere. They used orthographic stimuli known to be left lateralized. These results were also replicated by Finnigan et al. (2011), interpreting this bilateral N1 as a greater degree of attentional enhancement for older adults interpreted as a possible compensatory mechanism. Using spatial stimuli, proposed in the literature as right lateralized, we observed an exact opposite pattern (*i.e.*, a right lateralized N1 for young and bilateral for older). We also reported for older adults only, an increased N1 amplitude bilaterally for reorientation task compared to passive perception. In the context of spatial navigation, Baker and Holroyd (2009, 2013) investigated this N1 component (labelled NT170 in their work) over posterior areas and proposed it was an index of spatial navigation, originating from the para-hippocampal system. They confirmed these EEG source localization results later with fMRI recordings (Baker et al., 2015), using the same reward-related feedback stimuli. The authors also reported an increase of theta activity during the period of this NT170 peak, consistent with other findings (Kahana et al., 1999),

results that we also replicated. Indeed, comparing reorientation task between age groups, we found an increase in theta synchronization for older adults, with a burst occurring after 200 ms, in the time window of the N1 component. The proposed role of this component is also supported by the fact that we observed no significant change in its amplitude when increasing the perceptual difficulty. These results are consistent with previous findings reporting a discrimination effect equally large for easy and difficult discriminations (Vogel & Luck, 2000). Taken together those results highlight the role of the N1 component in landmark based spatial navigation, providing evidence for an increased bilateral activity recorded over electrodes related to SSRs for older adults. Regarding the proposed compensatory role of SSRs during a spatial task in older adults (Ramanoël et al., 2020, 2019), we can cautiously interpret this N1 as a possible compensatory mechanism for healthy older adults (Zhou et al., 2023), originating from high-level visual brain regions, even if our results do not allow us to attribute this activity to a specific brain region.

11.5.4 P1 component and delta activity

Considering P1 amplitude, we found a decreased amplitude for older adults only in the right hemisphere. This component is proposed in the literature to be modulated by spatial attention, interpreted as a sensory gain control for the suppression of task irrelevant processing and information (Hillyard et al., 1998; Luck et al., 2000), directing the flow of information, to task relevant neuronal structures (Klimesch et al., 2011). Those findings are consistent with findings from Gazzaley et al. (2008), who reported a decrease for older adults of top-down deficit suppression of irrelevant information in a visual task. As supported by Gazzaley et al. (2008), our results also seem to reconcile the two leading cognitive aging hypotheses, with an inhibitory deficit (*i.e.*, decreased P1 amplitude) and the processing speed hypothesis (*i.e.*, increased P1 latency) for older adults. Additionally, when modulating perceptual difficulty we found that P1 amplitude increases with perceptual difficulty, with a higher P1 peak amplitude for lower size stimulus compared to larger one. Interestingly, we did not find any interaction of perceptual difficulty and age on P1 amplitude, both age groups were similarly affected. But, considering P1 latency, we reported only for older adults, a later peak in the far condition compared to the near condition. This time, these results seem to be more in line with the proposed speed hypothesis, older adults taking more time to inhibit irrelevant stimuli when perceptual difficulty is increased. They also highlight the importance of P1 latency over P1 amplitude as a reliable ERP indicator of attentional decline in cognitive aging (Finnigan et al., 2011). Delving more into this difference, a follow-up analysis reported a similar interaction for the passive perception task, with older adults exhibiting a later P1 peak for the far condition compared to the near condition. Finally, the other components are not affected by the perceptual difficulty, suggesting that after this later P1 older adults might exhibit a compensatory mechanism allowing them to make up for the delay in this P1, as reported in our behavioral data also, but our data does not allow us to conclude anything about this point.

Considering now the ERSPs, we found decreased delta oscillations for older adults just before and up to 200 ms after image presentation, with a higher difference (*i.e.*, a higher effect size) between age groups for reorientation task. Those results are consistent with the inhibition role of P1, as delta oscillations are also proposed to reflect inhibition (Harmony, 2013), results that are interpreted as an impairment for older adults to inactivate irrelevant brain networks during a visual task. In this same time window, we also reported, only for the comparison of the activity during reorientation between age groups in the right hemisphere, a decrease of high beta band activity. This band was proposed to reflect difficulty and deficits for older adults in sustaining attentional process (Gola et al., 2013). This age-related decrement in inhibition is present even for a passive scene perception, as we observed a decreased P1 for older adults also in the control task, with a similar increase for both age groups when adding the reorientation task. Taken together, these results propose that older adults are impaired at inhibiting irrelevant information during a visual task, even during a passive perception. This effect is observable even before image presentation, consistent with other findings (Walker et al., 2022) and is a major concern for more ecological navigation context where distractors are omnipresent (Heft, 1996).

11.5.5 P2 component and alpha/beta desynchronization

Considering the P2 component, we reported an increased amplitude for reorientation task compared to passive perception. During the reorientation task, participants had to engage working memory systems to take the right decision relative to information acquired few minutes earlier during the learning task. This posterior P2 component was indeed proposed as mediating information between memory systems, as a way to compare inputs and information stored in working memory (Cepeda-Freyre et al., 2020; Freunberger et al., 2007; Lefebvre et al., 2005), consistent with the proposed role of the parietal cortex in working memory retrieval (Berryhill & Olson, 2008; Cabeza et al., 2008). Our reported absence of difference in P2 amplitude between near and far conditions for both age groups also support the memory contribution of this component, the cognitive load being the same in both conditions. Older adults exhibited lower amplitudes compared to young adults, consistent with findings from Finnigan et al. (2011). We can interpret this decrease of P2 amplitude for older adults as related to working memory impairments for spatial information with cognitive aging (Klencklen et al., 2012). This age-related decrease of spatial information processing is also supported by our ERSP results, with a decrease of alpha/beta desynchronization for older adults, only in the right hemisphere and mainly for the reorientation task. Using a memory task (Karlsson & Sander, 2023) also found an age-related decrease of alpha-beta desynchronization, and in regard of the literature, interpreted it as representing a reduced processing capacity for older adults contributing to their episodic memory decline. We reported similar results with a spatial reorientation task, emphasizing the importance of working memory decline in older adult's navigation impairment. One remaining question is why P2 amplitude during passive perception task was similarly affected by age as during the reorientation task. We cannot exclude that participants realized an *N*-back task during the

passive scene presentation, as reported by few of them during the experiment, trying to infer rules from the randomized image presentation, which, to a lesser extent, also involved their episodic memory.

11.5.6 Limitations & Perspectives

One of the main limitations of our results is that, we did not isolate one component and ultimately, we cannot exclude that the results observed for the P2 or N1 are influenced by previous peaks modulations (Luck & Handy, 2005). To address this and investigate landmark based reorientation task like we did, we could have either increase conditions but leading to lower signal-to-noise ratio, or simplify even more our task, decreasing its ecological validity. Thus, it would be interesting to conduct further studies trying to modulate individually each component even if in an aging study context this might not be possible to investigate a spatial reorientation process. Another limitation is that after correcting for multiple comparisons, we did not find any correlations between behavioral and EEG data using participants averages over trials. This can be explained by the relative ease of our task (especially for young participants), inherent to our design to investigate aging, not allowing to capture enough variability in accuracies. Finally, given the motor impairments of older adults (Agathos et al., 2020), using mobile EEG with a virtual reality or real-world protocol would enhance the ecological validity of measuring the neural correlates of spatial cognition (Delaux et al., 2021) and is required to better understand age-related impairments in spatial navigation (Ramanoël et al., 2022).

CHAPTER 12

EFFECT OF THE FIELD OF VIEW UNDER SIMULATED PROSTHETIC VISION EVALUATED WITH MOBILE EEG

Using the MoBI approach, the work presented in this chapter proposes to evaluate the cognitive load elicited by the simulated prosthetic vision (SPV) of the POLYRETINA implant in an ecological task. The prosthetic vision was simulated under three distinct fields of view (FoVs): a 20° field of view that is the current standard for epiretinal implants (*i.e.*, the Argus II), a 45° field of view that is the theoretical expanse reached by the novel POLYRETINA prosthesis, and a 110° field of view that serves as a control for normal vision. Although the generalizability of the results presented suffer from a low sample size of 8 participants, the outcome of this experiment provided promising insights to evaluate the benefits the POLYRETINA implant could bring to the patients once tested in clinical settings. Indeed, the widening of the FoV to 45° made a significant difference for performing near-ecological tasks that matter for the daily life of the potential receivers. The combination with EEG recordings was a difficult challenge, but the main analysis enabled to retrieve cortical signatures of visual processing, attentional processes, and cognitive load.

This work was conducted by Louise Placidet during her Master's thesis at the *Aging in Vision and Action* laboratory. She was supervised by Sandrine Hinrichs, PhD student of Diego Ghezzi's laboratory at EPFL, on all aspects relative to the POLYRETINA implant and the simulated prosthetic vision, and I was her advisor on the mobile EEG aspects, both for the experimental design and the analysis. This project was conducted over a limited time period and no additions were made to her report posterior to the end of her internship, thus the analysis is limited, was run under exploratory perspectives, and the conclusions should be taken as preliminary.

12.1 Contributors

Louise Placidet[1,2], Sandrine Hinrichs[1], Jacob Thomas Thorn[1], Alexandre Delaux[2], Angelo Arleo[2] & Diego Ghezzi[1].

1. School of Engineering, École Polytechnique Fédérale de Lausanne, Medtronic Chair in Neuroengineering, Center for Neuroprosthetics and Institute of Bioengineering, Chemin des Mines 9, 1202 Geneva, Switzerland

2. Sorbonne Université, INSERM, CNRS, Institut de la Vision, 17 rue Moreau, F-75012 Paris, France

12.2 Introduction

From a theoretical perspective, the innovations brought by the POLYRETINA prosthesis, especially its expanded field of view (FoV) and enhanced resolution, hold substantial promise for patients suffering from acquired blindness. The objective of this work is to anticipate the impact of these advancements in the daily life of patients. More specifically, it intends to assess whether the augmentation of the prosthesis FoV engenders notable enhancements in recipients' autonomy during their interactions with their surroundings and concurrently mitigates the cognitive load associated with the device's use. This research project builds upon a previous evaluation of the POLYRETINA prosthesis (Thorn et al., 2020), wherein the FoV was established as the most influential parameter contributing to enhanced performance across a range of realistic tasks, encompassing object recognition, word reading, and street navigation.

Considering the long list of prerequisite assessments before being ready to embark in clinical trials, simulated prosthetic vision (SPV) emerges as a practical tool for investigating pivotal functionalities attainable by the POLYRETINA prosthesis on healthy human participants. This innovative methodology can be particularly useful to identify and tune the parameters that will be crucial in the design of the prosthesis (Ferlauto et al., 2018; Macé et al., 2015; Vagni et al., 2022). SPV typically relies on a virtual reality (VR) or augmented reality device to replace the natural vision with an emulation of the artificial visual perception that the implant is designed to engender (see Figure **12.1**; S. C. Chen et al. 2009). Here, the simulated artificial visual experience is tailored in line with the parameters characterizing the POLYRETINA implant. Under this simulation, it is possible to conduct experiments allowing for a better comprehension of the psychophysical aspects of the prosthetic vision (Macé et al., 2015).

Numerous research investigators have resorted to SPV, owing to the restrictive access to testing in clinical settings (Macé et al., 2015). To ensure the fidelity and realism of the SPV in replicating the visual perceptions encountered by implant recipients, standardized simulation frameworks have been meticulously formulated. In order to mitigate any potential disparities between the simulated vision and actual visual experience of implant recipients, factors such as phosphene luminance, mapping procedures, and rendering techniques were

carefully designed (S. C. Chen et al., 2009). To stay as close as possible to future clinical assessments, the artificial vision is simulated only on the dominant eye of participant, where the prosthesis would be implanted.

At the cognitive level, the central objective of this project is to address the issue of cognitive fatigue, frequently observed in recipients of retinal implants, a phenomenon conventionally documented in clinical trials (Chenais et al., 2021; Erickson-Davis & Korzybska, 2021). This fatigue often serves as a catalyst for the rejection of prosthesis usage (L. da Cruz et al., 2016), and it is hoped that expanding the FoV could alleviate the cognitive load elicited by the device. It was intended to conduct these investigations in conditions mirroring real life settings to draw conclusions closer to daily life activities.

The framework of cognitive load theory posits human cognitive architecture as consisting of three processors and their corresponding memory elements, namely the perceptual, cognitive, and sensorimotor processors (Kumar & Kumar, 2016). This cognitive framework is characterized by both a capacity and a temporal limitation when processing incoming information (Hossain & Yeasin, 2014). Within this theoretical construct, the *cognitive load* is defined as the demand imposed on the cognitive resources of the mind during the execution of a task (Kumar & Kumar, 2016). Three distinct subtypes of cognitive load have been suggested: the intrinsic load, the extraneous load, and the germane load (Kumar & Kumar, 2016). Intrinsic cognitive load pertains to the inherent complexity of the task itself, with due consideration for the learner's expertise level. Germane cognitive load involves the allocation of resources to process and construct patterns of ideas. The third subtype, extraneous cognitive load, is attributed to the manner in which information is presented. Given that the variable that will be manipulated in this experiment will be the FoV, the EEG measurements are anticipated to reflect correlates of extraneous cognitive load.

The prevailing consensus concerning the EEG signatures of cognitive load posits the implication of the frontal and parietal regions, specifically within the alpha (8-12 Hz) and the theta (4-8 Hz) frequency bands (Holm et al., 2009; Hossain & Yeasin, 2014; Klimesch, 1999; Kumar & Kumar, 2016). To delve into more details, heightened cognitive load is expected to be associated with an elevated power (*i.e.*, a synchronization) in theta frequency range over the frontal lobe. Conversely, reductions in spectral power (*i.e.*, a desynchronization) within the alpha band over the parietal lobe has been observed in situations of increased cognitive load. Marginally, it should be noted that the modulation of EEG relative to heightened cognitive demands as also been reported in other frequency bands (Gevins & Smith, 2003; Kumar & Kumar, 2016). Indeed, the beta frequency band (12-30 Hz) can also serve as an indicator of mental workload, particularly discernible within the temporal and occipital lobes (Gevins & Smith, 2003; Kumar & Kumar, 2016; Strube et al., 2021). In a similar vein, the gamma frequency band (above 30 Hz) has also been associated with effortful mental activity and the representation of sensory information processing (Gevins & Smith, 2003; Kumar & Kumar, 2016; Strube et al., 2021). Closer to the purpose of this experiment, a preceding investigation of cognitive load elicited by the navigational environment in visually impaired people reported alpha desynchronization in more complex and dynamic environment, when the cognitive load was the highest (Klimesch, 1999). Gevins and Smith (2003) also high-

light the importance of designing tasks in naturalistic settings as they deeply influence the signature of cognitive load. In such conditions, paying attention to the level of cognitive load during the baseline phase is crucial, as otherwise the comparison with the real stimulus of interest may be attenuated.

Using the mobile brain/body imaging (MoBI) approach, this work proposes to evaluate the cognitive load elicited by the SPV of the POLYRETINA implant in an ecological situation under three distinct FoVs: a 20° FoV that is the current standard for epiretinal implants, a 45° FoV that is the theoretical expanse reached by the novel prosthesis, and a 110° FoV that serves as a control for normal vision. This value is lower than the FoV of a healthy individual but was the maximal extent achievable with the VR head-mounted display. The introduction of this last condition will enable to assess whether there still is a substantial improvement to achieve beyond the 45° FoV. It is hypothesized that the expansion of the FoV will result in (1) a greater ease at the task manifested by an improved performance and/or faster execution (2) a decreased cognitive load during the task, associated with a lower synchronization in the theta band over frontal electrodes and a lower desynchronization in the alpha band over parietal electrodes.

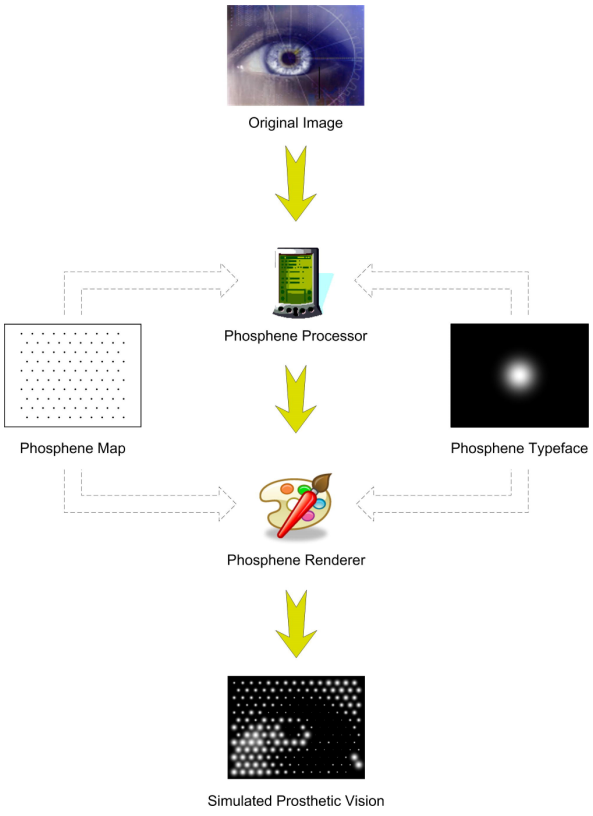

Figure 12.1: Diagram of the pipeline used for SPV. At the phosphene processor, the original image is filtered and phosphenized based on the selected phosphene typeface and phosphene map. The output of the phosphene processor is visualized at the phosphene renderer module using the selected phosphene map and typeface to produce the final SPV. Solid arrows indicate the path of the visual information. Arrows with dotted outlines indicate flow of the accessed parametric information. Reused from (S. C. Chen et al., 2009).

12.3 Methods

12.3.1 Participants

Eight young adults from the *SilverSight* cohort (Lagrené et al., 2019) took part in the experiment (29.0 ± 4.1 years old [*mean* $\pm$ SD]). All participants met the cohort inclusion criteria: normal cognitive performance on a battery of neuropsychological tests, no history of sensory, neurological, or psychiatric disorder, and normal or corrected-to-normal eyesight. They had no prior experience with SPV. Each participant provided their written informed consent, and the study was approved by the Ethics Committee "*CPP Ile de France V*" (ID_RCB 2015-A01094-45, CPP N: 16122).

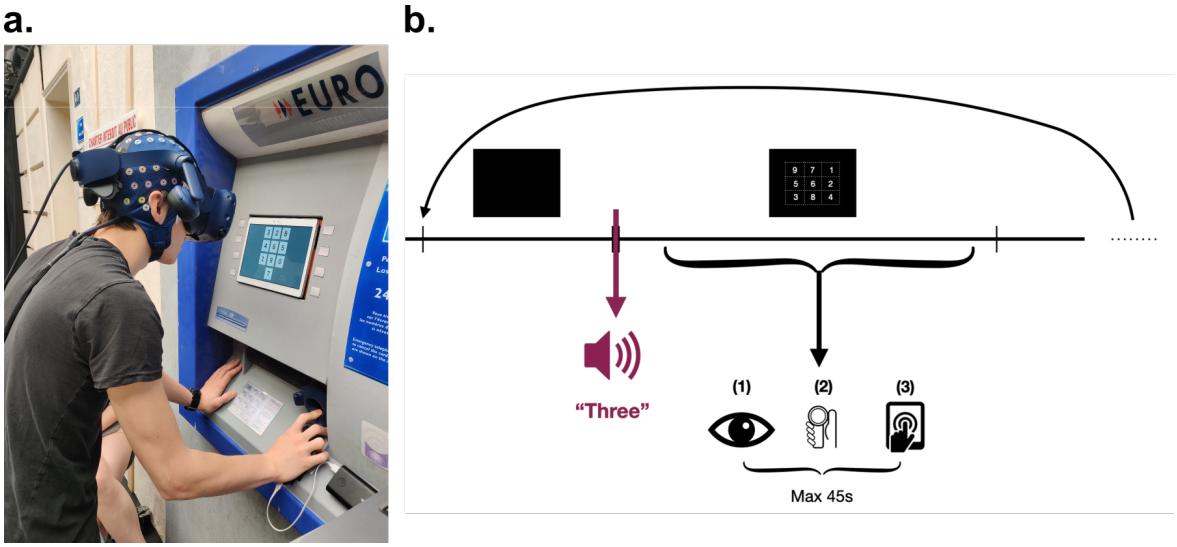

Figure 12.2: Experimental setting and course of a trial. **a**. Illustration of a participant performing the task. The participant is in a starting position, with both hands placed systematically at the same locations. His right hand is placed in advance over the VR controller trigger used to indicate when the digit is found. **b**. Diagram of the course of a trial. For each trial, the participant receives an oral instruction to perform a visual search towards a target digit on the screen. A button press (outside the screen) was first required to indicate the digit was found. Only then the participant is invited to touch the screen at the location of the digit. All these actions had to completed under 45 seconds after the start of the trial.

12.3.2 Paradigm

The experiment was designed to disentangle the EEG correlates of a visual search task under 3 distinct conditions relative to the FoV of the SPV: 20°, 45° and 110° (see Figure **12.3b**). This experiment had a within-subjects design and all participants performed the task under the 3 conditions. In order to propose a task mimicking a daily-life scenario, the paradigm rationale was to propose a task where participants had to interact with a cash dispenser, *i.e.* recognizing digits to enter a credit card password (Figures **12.2a** and **12.3a**).

12.3.3 Protocol

Before the main experimental session, participants practiced with the SPV in a familiarization task, introducing them to the mechanics of the experiment. During the familiarization, they were exposed to the three FoVs, starting from the largest to the smallest one. For each FoV, they had to first identify the location of an empty grid on the screen of the cash dispenser (**12.3**, left column). This enabled them to locate the grid in the environment, as well as to adjust their position with respect to the dispenser, under the different FoVs. Then, a grid containing three symbols placed randomly was presented to enable the participants practice performing the visual search with these symbols (**12.3**, central column).

For the main experimental session, participants started a trial in front of the cash dispenser, wearing the VR head-mounted display without any visual input. They were standing or sitting according to what was most comfortable for them. They were asked to place both hands at pre-defined locations on the cash dispenser. Specifically, to minimize response delay, their right hand rested on a VR controller trigger that would serve to indicate the time as the button press, and the participants were asked to interact with the screen only with their right hand.

At the beginning of each trial, an automatic oral instruction randomly gave them a digit to find, ranging from 0 to 9. As soon as the instruction was given, the SPV turned on, and their task was to identify the location of this digit on the screen of the dispenser as quickly as possible. The screen displayed a grid containing all digits from 0 to 9 whose positions were randomized at each trial to avoid learning across trials (Figure **12.3**, right column). The FoV of the SPV was also randomized at the trial level. As soon as they detected the target digit, they were instructed to press the trigger placed under their right hand from the beginning of the trial. The introduction of this step allowed to have a more precise estimation of the latency at which visual identification occurred. It was only after this that they could touch the screen at the location of the digit they detected to confirm the validity of their answer. Each trial was limited in time to 45 seconds after the target digit was announced. Participants performed 36 trials per condition for a total of 118 trials. Between each trial, a 5 seconds pause was enforced (*i.e.*, black screen display in the headset) to give some rest to participants from the SPV and give the opportunity to change the FoV for the following trial. During the experiment, longer, self-paced pauses were authorized upon subject request at any time between 2 trials.

12.3.4 Materials

12.3.4.1 Experimental setting

The experiment took place in the *Rue Artificielle* platform of *StreetLab* facilities. This room featured a realistic cash dispenser machine embedded in a wall (see Figure **12.2a**). The original screen of the dispenser was replaced by a tablet to display the stimuli with a resolution of 1920×1200 pixels. The protocol for the familiarization task and the experimental task was created using Unity3D (Unity Technologies, Inc. San Francisco, California, USA). The

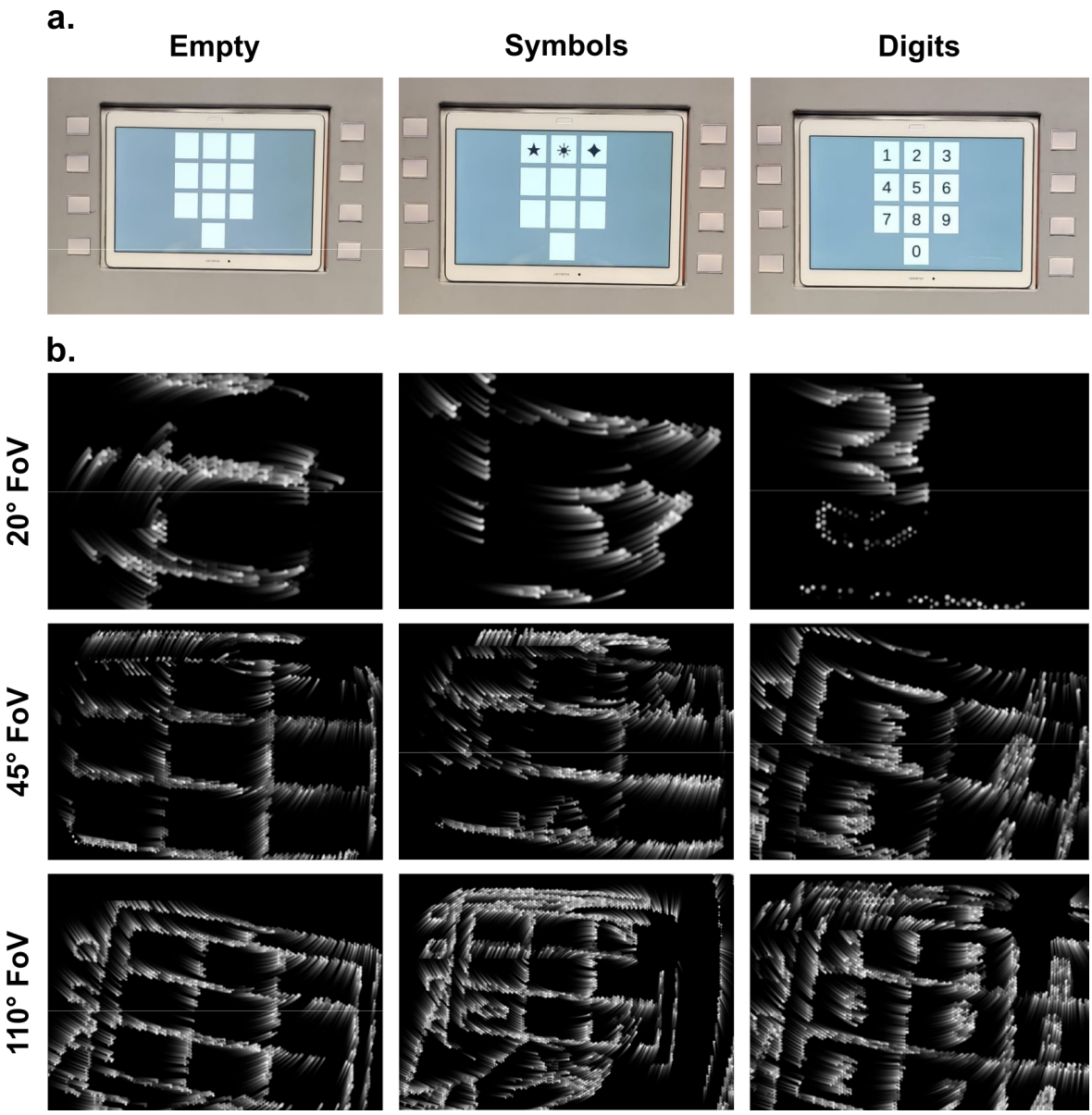

Figure 12.3: Illustration of the various stimuli encountered during the experiment. **a**. Touch screen embedded in the dispenser, displaying the stimuli. From left to right: the empty grid used at the beginning of the familiarization phase to help the participant locate the screen, 3 randomly located symbols used in the familiarization phase, full grid with digits used during the trials. **b**. View of the stimuli from the SPV rendering at different FoVs. First row: 20° FoV. Second row: 45° FoV. Third row: 110° FoV. Columns are arranged like in **a**.

size of symbols and digits was set to 100 pt. This size was large enough to be seen by participants under artificial vision (Figure **12.3b**), while still remaining close to real life conditions. During the experiment, each time the screen was touched, the displayed grid automatically reset and the location of the digits was reshuffled for the next trial.

12.3.4.2 VR equipment

Simulated prosthetic vision was rendered using an HTC Vive Pro Eye head-mounted display (HTC Corporation, Taoyuan, Taiwan), which offered a 90 Hz refresh rate, with a nominal FoV of 110°. This headset is equipped with a camera to film the environment from the point

of view of the participant, from which the SPV was derived in real-time. This headset is also embedded with an eye-tracking device providing gaze data to evaluate the oculomotor behavior of the participant inside the headset. The VR headset was connected to a VR-capable backpack computer (HP Z VR backpack). An HTC Vive controller was attached with velcro on the cash dispenser and its trigger was used as the button to be pressed by the participant.

12.3.4.3 EEG equipment

The EEG recording system comprised 127 active wet electrodes mounted on an elastic cap with an equidistant arrangement (waveguard original - ANT Neuro, Hengelo, The Netherlands). An electrode located closest to the standard C_z position (10-20 international system) provided the reference for all other electrodes and an additional one on the left earlobe served as electrical ground reference. The EEG cap was positioned laterally and longitudinally according to standard anatomical reference points for each participant. Prior to recording for the experimental session, the impedance of the electrodes were lowered below 20 kΩ.

Small pieces of fabric were used to alleviate the pain building up at the level of the frontal electrodes (see Figure **6.1d**). As a result, no signal could be recorded from 6 of the frontal electrodes (LD1, LL1, LC1, RD1, RR1 and RC1).

Raw EEG data was acquired with eego mylab software (v1.9.1, ANT Neuro) at a 500 Hz sampling rate (except for the first 2 participants where the sampling rate was 1 kHz) continuously during the experiment. The Lab Streaming Layer protocol (Kothe, 2014) and the LabRecorder software (v1.13.0) was used to simultaneously record all streams of data (EEG data, gaze data, SPV events and protocol events) and collect them into a single XDF file per block.

12.3.5 Data analysis

The data was processed and analyzed using Matlab R2019a (Mathworks Inc., Natick, MA, USA) and EEGLAB functions and plugins, version 2021.0 (Delorme & Makeig, 2004).

12.3.5.1 Behavioral analysis

12.3.5.1.1 Visual search duration

The first metric of interest relates to the time taken by participants to perform the task, defined by the latency of the digit touching with respect to the start of the trial (triggered by the oral instruction of the target digit). This duration is later referred to as *total time*. When the participant did not finish the trial in the allowed time, this duration was assigned a value of 45 seconds. A finer analysis of this duration was undertaken by further subdividing it into 2 durations delimited by the button press. The duration between the start of the trial and the button press, associated with the visual search, was named *detection time* and the duration between the button press and the touch of the digit on the screen, referred to as *press time*.

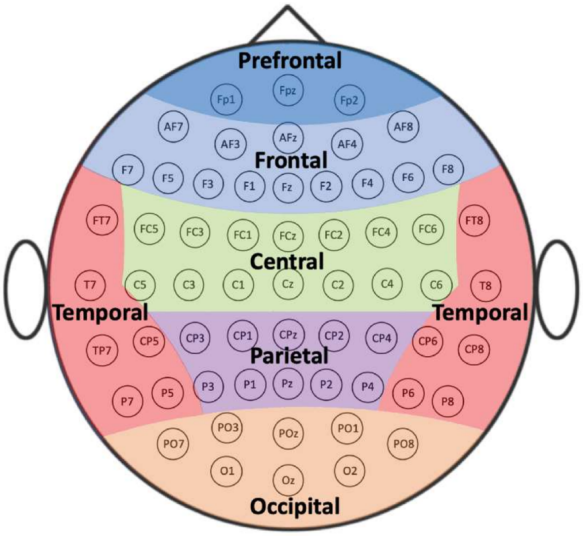

Figure 12.4: Definition of the main regions of interest on the 128 equidistant layout waveguard original EEG cap. The segmentation between the regions was inspired from the definition on conventional EEG caps in the 10/5 international system (Alsuradi et al., 2020).

12.3.5.1.2 Accuracy of the visual search

Another metric of interest was the accuracy of participants at the visual search task, *i.e.* the number of trials where they correctly pointed the digit on the screen within the allowed time. In other words, the trial was considered failed if the participant pressed the button and did not touch the target digit, or if the time limit went up before having time to touch the screen.

12.3.5.2 Gaze analysis

The recorded gaze data corresponded to $[x, y]$ normalized coordinates of the binocular fixation point, expressed in the world reference (*i.e.*, taking into account both eye and head movements). In particular, participant's oculomotor behavior along the dispenser's grid was evaluated during the visual search. After cleaning the data (*i.e.*, detection and interpolation of missing samples), the length of the path taken by the eye was used as a metric to compare the effect of the different FoVs on the visual search. To compute this metric, the Euclidean distance between two consecutive samples was summed over the course of a trial.

No other gaze metrics were analyzed due to the time constraints of the project. However, potential future analysis could also investigate metrics based on the number of fixations, or saccades *etc*.

12.3.5.3 EEG analysis

12.3.5.3.1 EEG processing

EEG processing was performed according to the procedure described in Section **6.2**, using the BeMoBIL pipeline for time-domain cleaning. Before epoching the dataset we applied a band-pass filter between 0.5 Hz and 45 Hz (zero-phase Hamming windowed finite impulse response filters: high-pass filter with 0.75 Hz cut-off frequency and 0.5 Hz transition bandwidth and low-pass filter with 50.625 Hz cut-off frequency and 11.25 Hz transition bandwidth).

Data analysis was focused on the visual search period, *i.e.* from the beginning of the trial

to the button press or until the time allowed for the trial was up. The inter-trial period preceding each trial served as a baseline with no visual stimulation. The mean power spectrum was extracted over these periods for each channel and trial using the `spectopo` function of EEGLAB.

12.3.5.3.2 Group level

For the multi-subject analysis, the arithmetic mean of the power spectrum over all trials was computed for each channel, frequency, condition (20° FoV, 45° FoV, 110° FoV and baseline) and participant. At the end of these operations, the data was log-transformed to present results in decibels.

For statistical analyses comparing the power spectrum between conditions, the non-parametric paired permutation test based on maximum cluster-level statistic approach by Maris and Oostenveld (2007) was implemented using 1000 permutations. In this study, a sample relates to a given channel-frequency pair. To form statistical clusters, all electrodes separated with a solid angle lower than 20° in the spherical coordinate system provided by the manufacturer were considered as spatial neighbors. To facilitate the interpretations, when presenting the results electrodes have been grouped by brain regions(Figure **12.4**), customized for the specific cap used in this experiment (not following the $10/5$ international system).

First, the analysis targeted the pairwise differences between each FoV and the baseline condition with t-test and t-values as the sample-wise statistical test. This allowed evaluating significant EEG signatures, reflecting the brain signals specific to artificial vision with respect to the absence of visual input. Second, the analysis targeted the differences between the 3 FoVs with analysis of variance (ANOVA) and F-values as the main sample-wise statistical test and t-test and t-values for post-hoc pairwise comparisons. This allowed identifying existing disparities between the EEG signatures of the three conditions of interest. Third, the mean spectra of the 20° and 45° FoVs were baselined with the mean spectrum of the 110° FoV, serving as a reference. The statistical analysis was then conducted between these baseline corrected 20° and 45° FoVs conditions with t-test and t-values as the sample-wise statistical test. For all these comparisons, condition differences were plotted only showing samples significant for both the three conditions permutation test and the inspected pairwise permutation test. The significance level on the Monte Carlo p-value was set to $p < 0.05$ for all tests.

12.4 Results

12.4.1 Behavior

The first metric considered in this study was the time taken by participants to complete the task under different FoV conditions. A brief and rapid adaptation to the task was observed across all three FoV conditions, but no significant overall learning curve was evident (Figure **12.5a**). The total time taken for each trial, including those where the digit was not found,

was analyzed. The average total time was computed across all trials and participants for each FoV (Figure **12.5b**).

Since the data distribution was non-parametric, a Kruskal-Wallis test was employed to assess the differences across the FoV conditions, and it revealed a significant difference

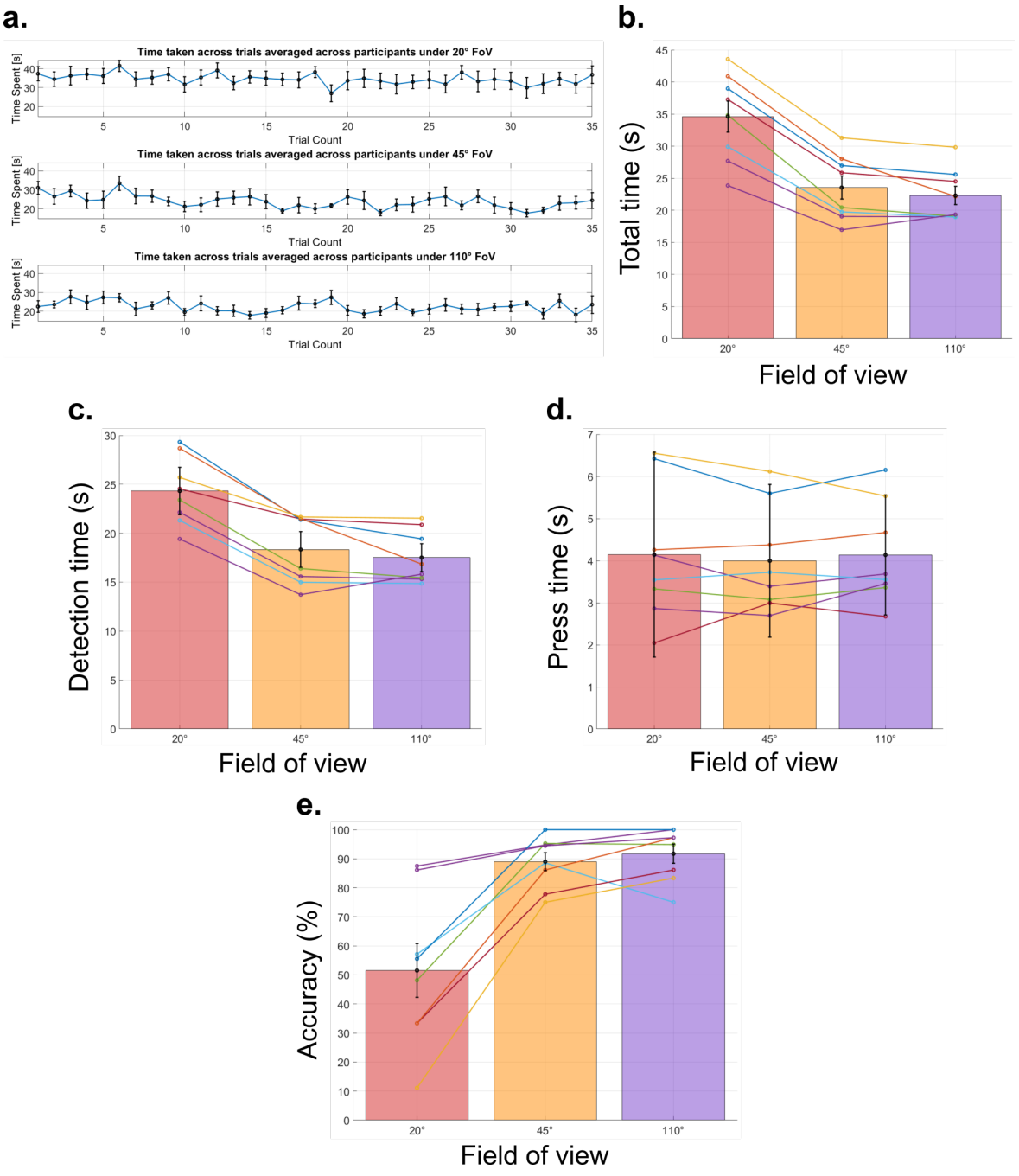

Figure 12.5: Behavioral metrics across conditions. **a**. Total time per trial in chronological order, by condition. The plot displays the mean total time across participants and error bars indicate the standard error of the mean (SEM). Top row: 20° FoV, middle row: 45° FoV, bottom row: 110° FoV. **b**. Average total time per condition. **c**. Average detection time per condition. **d**. Average press time per condition. **e**. Average accuracy per condition. **b-e**. Red bar: 20° FoV, yellow bar: 45° FoV, purple bar: 110° FoV. Black line indicates the mean across all participants while the error bars represent the SEM. Colored lines show individual participants.

($\chi^2(2,23) = 10.89$, $p = 0.0043$). Subsequent post-hoc multiple pairwise comparisons were conducted with a Bonferroni correction to further investigate the significant differences. The results showed that the total trial time was significantly increased when the FoV was restricted to 20° compared to the 45° ($p = 0.036$) and 110° ($p = 0.0056$) FoVs (medians: 20°, $\sim$ 36 s; 45°, $\sim$ 23 s; 110°, $\sim$ 20 s). However, no significant difference was found in the total trial time between the 45° and 110° FoVs ($p = 1$).

Breaking down the analysis, the Kruskal-Wallis test revealed significant differents across the three conditions for the detection time ($\chi^2(2,23) = 10.38$, $p = 0.0056$; Figure **12.5c**). Post-hoc multiple pairwise comparisons with a Bonferroni correction indicated that the detection time was significantly increased when the FoV was restricted to 20° compared to the 45° ($p = 0.036$) and 110° ($p = 0.008$) FoVs (medians: 20°, 23.98 s; 45°, 18.88 s; 110°, 16.33 s). However, no significant difference was observed between the 45° and 110° FoVs ($p = 1$). However, a similar Kruskal-Wallis test on the press time showed no statistically significant difference between the three respective FoVs ($\chi^2(2,23) = 0.1$, $p = 0.95$; Figure **12.5d**).

The investigation of the participants' performance at identifying the correct digit within the allowed time yielded coherent results with the analysis of the durations (Figure **12.5e**). The accuracy of participants was notably lower for the 20° FoV compared to the wider FoVs. Using a Kruskal-Wallis test, a significant effect was observed across the three conditions ($\chi^2(2,23) = 10.91$, $p = 0.0043$). Subsequent post-hoc multiple pairwise comparisons with a Bonferroni correction revealed a significant difference in accuracy between the 20° and 45° conditions ($p = 0.034$) as well as between the 20° and 110° conditions ($p = 0.0058$, medians: 20°, 51.85%; 45°, 91.51%; 110°, 96.05%). However, there was no significant difference in accuracy between the 45° and 110° FoVs ($p = 1$).

12.4.2 Eye-tracking

Gaze trajectories on the touch screen grid were analyzed on a trial-by-trial basis to investigate differences in gaze behavior across the three FoV conditions. The length of the eye path was used as a summary metric to assess the variations in visual search under each FoV.

The data distribution was sufficiently normal to employ a parametric test. Thus, a 1×3 ANOVA was conducted, revealing a significant main effect of the condition ($F(2,308) = 7.87$, $p = 0.0005$). Post-hoc pairwise t-tests further demonstrated significant differences in the length of the eye path between the 20° FoV and both the 45° FoV (p = 0.0027) and the 110° FoV ($p = 0.0057$). However, there was no significant difference between the 45° and 110° conditions ($p = 0.3799$).

This pattern closely resembles the findings in the behavioral analysis, and it is likely that the two are highly correlated, given that trials in the 20° condition took much longer to complete, naturally resulting in elongated eye paths during the visual search.

12.4.3 EEG

The permutation analysis serves as an exploratory method to investigate the EEG signatures that emerged during the visual search and to examine their differences across the conditions. A crucial objective of this analysis is to discern whether neural markers indicative of cognitive load are present in this paradigm and whether they correlate with the observed behavioral and oculomotor outcomes, which suggest a significant advantage of larger FoVs.

12.4.3.1 Comparison with the baseline

First, the average power spectrum associated with each FoV was compared to the power spectrum recorded during the corresponding inter-trial baselines where no visual stimulation was provided. The results are illustrated on Figure **12.6**.

Two main clusters emerge across these three heat maps. The first corresponds to a strong desynchronization appearing around the upper alpha frequency (10-12 Hz) and extending to the beta band. This signal is present across all three FoVs, and across most of the electrodes (Figure **12.6a-c**). The desynchronization is more pronounced for 20° and 110° (on average around -8 dB) than for the 45° condition (on average -5 dB). Second, a significant desynchronization in the delta frequency band can be noticed for all three conditions, spanning a large portion of electrodes (Figure **12.6a-c**). Again, it is less notable for the 45° FoV than for the other FoVs.

12.4.3.2 Comparison between the fields of view

Pairwise comparisons of the 3 conditions are illustrated by the heat maps presented on Figure **12.7**, using the same permutation analysis. The reporting of results was driven by the most important patterns observed and is not exhaustive.

When comparing the narrowest FoVs (20° & 45°) with the widest FoV (45°), similar clusters are retrieved. Indeed, on both heat maps, the spectral power in the theta band was elevated in the smallest FoVs compared to the largest FoV over the frontal electrodes (RD_1, RD_2, RD_3, LL_1, R_1, L_1) (Figure **12.7b-c**, highlighted in blue). The cluster is larger and displays a greater amplitude difference when comparing the 20° condition to the 110° condition (mean difference: 0.7 dB) than when comparing the 45° condition to the 110° condition (mean difference: 0.51 dB).

On the contrary, these heat maps demonstrated a lower alpha activity in the smallest FoVs compared to the largest FoV over a group of central electrodes (R_{10}, R_9, Z_9) (Figure **12.7b-c**, highlighted in red). Again, the cluster is larger and displays a greater amplitude difference when comparing the 20° condition to the 110° condition (mean difference: -0.97 dB) than when comparing the 45° condition to the 110° condition (mean difference: -0.73 dB).

12.4.3.3 Comparison between restricted fields of view corrected for visual perception

The last analysis consisted in comparing the two restricted FoVs corrected with a control condition (*i.e.* 110°, corresponding to an almost natural FoV) to remove the correlates of visual perception. With such baseline correction, the goal is to isolate the significant clusters

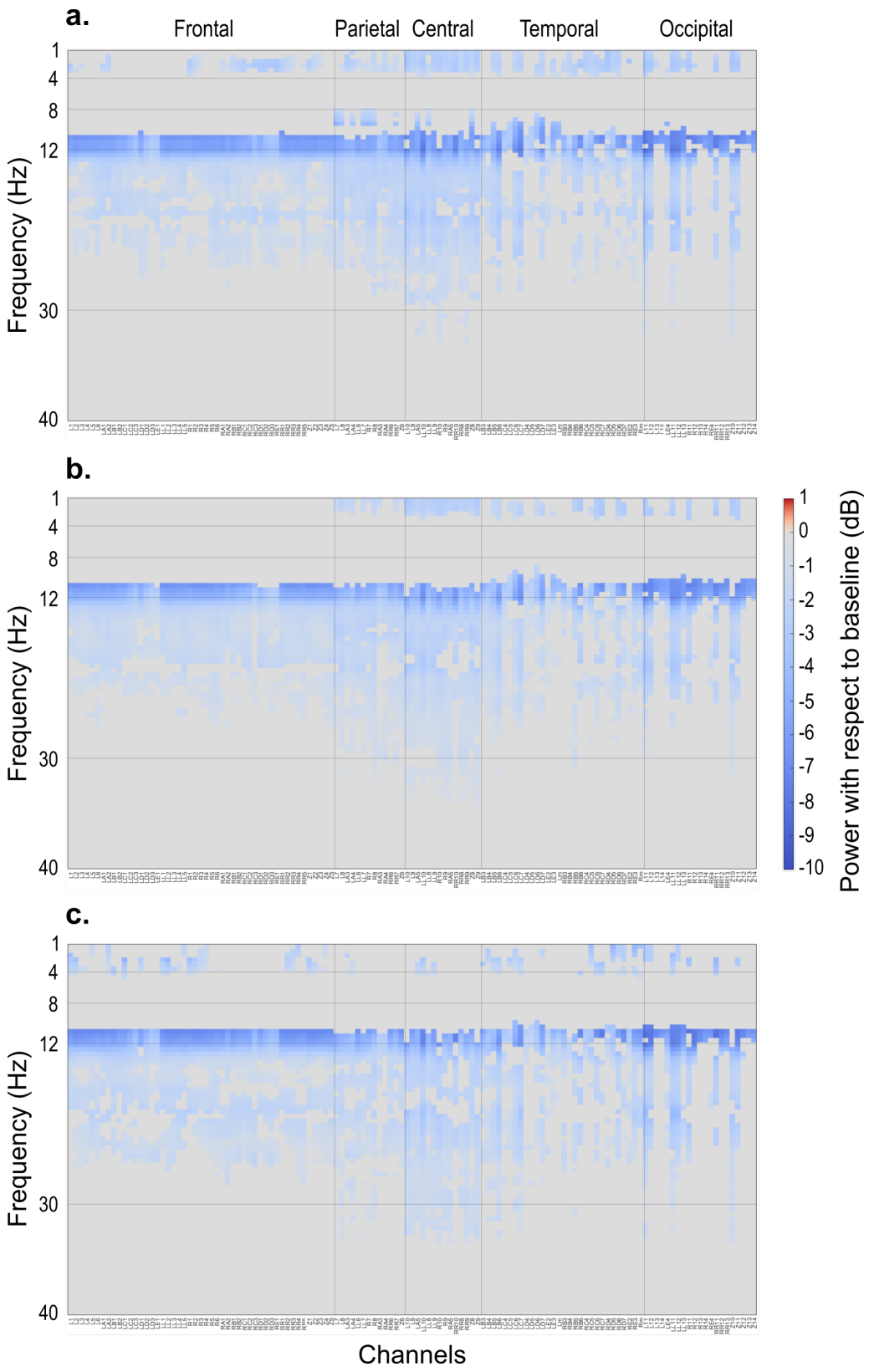

Figure 12.6: Results of the permutation analysis on the comparison of each FoV with its corresponding baseline. The horizontal axis displays the electrodes, grouped by brain regions (see Figure **12.4**). The vertical axis displays frequency bands: delta [1-4 Hz], theta [4-8 Hz], alpha [8-12 Hz], beta [12-30 Hz] and gamma [30-40 Hz]. **a**. 20° FoV. **b**. 45° FoV. **c**. 110° FoV.

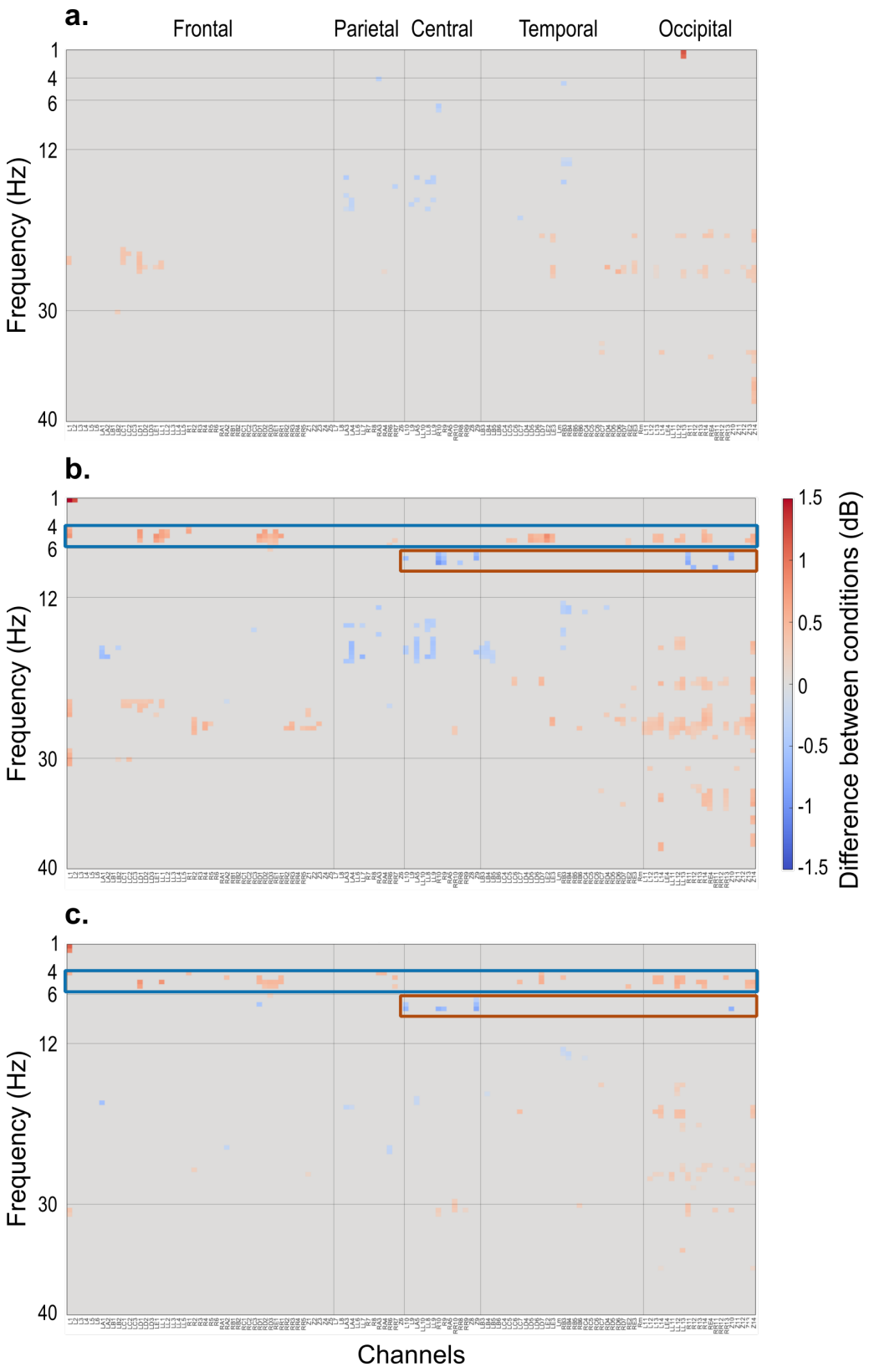

Figure 12.7: Results of the permutation analysis on the comparison between each pair of FoVs. Similar layout to Figure **12.6**. **a**. 20° FoV - 45° FoV. **b**. 20° FoV - 110° FoV. **c**. 45° FoV - 110° FoV. The blue squares highlight significant synchronization in the theta band. The red squares highlight significant desynchronization in the alpha band.

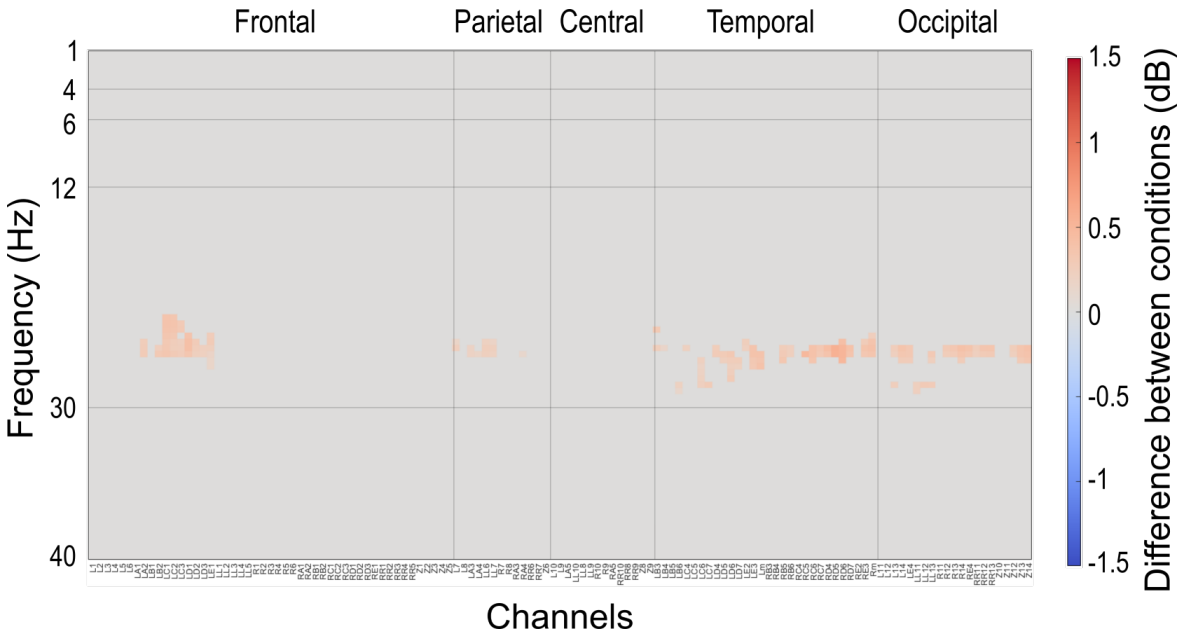

Figure 12.8: Results of the permutation analysis on the comparison between restricted FoVs corrected for visual perception. Similar layout to Figure **12.6**. Difference between 20-110 and 45-110 baselined conditions.

that are not related to vision but rather that might be signatures of different cognitive loads. The 110° condition is acknowledgedly not the ideal baseline since the visual stimulation is quite different from the narrowest FoVs, but it was the most adequate period that could fulfill this role. The heat map exhibiting the statistical differences between the 20-110 power spectrum and the 45-110 power spectrum is presented on Figure **12.8**.

A clear difference spanning across a wide range of electrodes (mostly frontal, temporal and occipital) is visible in the beta band (24-26 Hz; Figure **12.8**).

12.5 Discussion

Unanimously across behavioral and oculomotor metrics, the visual search was significantly more efficient when the participants benefitted from a larger FoV. Under the 45° and the 110° FoVs, they took less time to complete the task, travelled shorter eye distances and achieved a higher success rate compared to the 20° FoV. Very interestingly for the purpose of this study, the 45° and the 110° FoVs were indiscernible from a statistical point of view, suggesting a drastic improvement when the FoV is extended from 20° to 45°, but not when expanding further beyond 45°. The benefit of larger FoVs was manifest only during the visual search phase, and not for touching the digit once found. Although the ecological task was limited to the finding of a single digit in less than 45 s, this holds the promise that the theoretical FoV of the POLYRETINA implant can make a substantial difference for the future patients.

12.5.1 Cortical activity elicited by the simulated prosthetic vision

When considering the cortical activity elicited by the SPV during the visual search period with respect to the baseline deprived of visual input, the EEG signatures were similar across all conditions.

First, a generalized desynchronization in the upper alpha frequency was reported, coherent with the processing of sensory-semantic information described by Klimesch (1999). In particular, the presence of this desynchronization over the occipital electrodes confirms that the SPV recruited the same structures as what would be observed under normal vision.

Second, a significant desynchronization in the delta band was identified. Harmony et al. (1996) have linked oscillations in the delta band to the modulation of top-down attentional processes, with increasing power associated with increased internal focus. Under this light, the reported activity suggests the lack of top-down modulation during the visual search and instead a strong drive of bottom-up sensory processing, which is likely to be particularly enhanced in this demanding task with a very unnatural stimulation for healthy participants. This explanation goes hand in hand with the presence of generalized desynchronization in the beta band (extension of the first cluster) which was also hypothesized to be related to external bottom-up disruptive stimulation to the internal status quo (Engel & Fries, 2010).

All-in-all, this analysis expectedly reveals a strong effect of the SPV on the visual system and cortical processes dedicated to interpret the incoming information.

12.5.2 Absolute differences between the fields of view

The respective comparison between the most restricted FoVs (20° and 45°) with the widest FoV (110°) revealed a significant theta band synchronization over the frontal electrodes and a significant alpha band synchronization over the centro-parietal electrodes. This pattern of activity corresponds to the expected signature of increased cognitive load (Holm et al., 2009; Hossain & Yeasin, 2014; Klimesch, 1999; Kumar & Kumar, 2016) during the most restricted FoVs. Interestingly, this pattern is enhanced when comparing the narrowest to the largest FoV than when comparing the intermediate to the largest. However, no significant presence of this pattern could be reported between the 20° and the 45° FoVs.

Delving into a more exploratory interpretation of the results, it can be noticed that the comparison of the FoVs also elicited signatures over the occipital electrodes, particularly between the 20° and the 110° FoVs (Figure **12.7b**). This similarly takes the form of a desynchronization in the alpha band accompanied by a synchronization in the theta band. This pattern over the occipital electrodes was reported by Klimesch (1999) as a signature of visual information processing. It is also notable in the comparison between the 45° and the 110° FoVs (Figure **12.7c**), although to a lesser degree. That is an expected signature since the amount of stimulation is directly proportional to the width of the FoV, thus giving a higher quantity of information to process at the same time by the visual system.

In addition, occipital electrodes also exhibit a beta band synchronization in all pairwise comparisons of the FoVs (the wider FoV is always subtracted to the smaller in the comparison). Interpreting this under the scope of attentional mechanisms, it coherently indicates that

narrower FoVs trigger more top-down processes relatively to wider FoVs (Engel & Fries, 2010; Gola et al., 2013). The increasing demand on attentional resources may be a compensatory mechanism for the decreasing amount of information available when restricting the FoV.

The comparison of the 3 FoVs established signatures of cognitive load and attention that were modulated by the condition. Although they confirmed the trend for a more effortful processing while reducing the width of the FoV, in contrary to the behavioral results, the absence of clear distinction in activity between 20° and 45° suggests that the widening of the FoV beyond 45° may be necessary to significantly alleviate the cognitive load experienced by patients.

12.5.3 Difference between the field of view of type of prosthesis relative to 'normal' vision

The final part of this analysis considered the two most restricted FoVs, which are associated with each type of prothesis, corrected them with the activity associated with a 'normal', unrestricted FoV. The difference emerged mostly in the beta band over occipital channels, but with much lower absolute amplitudes than the previous comparison. In line with the previous interpretations, this is thought to reflect differences in attentional processes, with a more top-down attentional drive under the most restricted FoV (Engel & Fries, 2010; Gola et al., 2013).

12.5.4 Limitations

The central limitation of this study lies in the small number of participants as well as in the limited number of trials for each participant. Indeed, given the absence a restriction of movements to keep the task as ecologically valid as possible, a significant proportion of trials had to be discarded from the analysis due to the prominent presence of artifacts in the EEG signal. Moreover, it must be acknowledged that the experiment was very difficult to complete for the participants. First, they reported a notable tiredness created by the SPV itself, onto which was superimposed the exhaustion created by the cognitively demanding nature of task. Second, despite the resources deployed to relieve the pain on the frontal electrodes with smooth fabric partially increasing the endurance of the participants, the discomfort gradually increased and settled across the experiment. An interesting perspective for future experiments would be to introduce several testing sessions. This would enable to consider more trial repetitions for each condition and participant while keeping single sessions shorter to avoid the discomfort generated by a prolonged simultaneous wearing of the EEG cap and the VR head-mounted display.

Lastly, the discrepancy between the behavioral and the EEG results interrogates. Indeed, whereas the benefit of the 45° FoV with respect to the 20° FoV was evident from the behavioral metrics, there were no clear signatures of cognitive load relief between these FoVs. Apart from the lack of repetitions that has a detrimental impact on the power of the statistical

tests employed, it can be hypothesized that the interindividual variability frequently observed in the peak of alpha and theta oscillations (Klimesch, 1999) failed to disclose a coherent cognitive load effect at the group level. In future developments, it would be interesting to pursue a more comprehensive single-subject analysis to investigate this hypothesis. The third analysis, hoped to accentuate the cognitive differences between the two restricted FoVs, probably suffered from the limited available choices for the baseline. Indeed, the power spectrum associated with the 110° FoV was not entirely satisfactory because it differed from the more restricted FoVs not only from a cognitive perspective but also by the amount of visual information to process (demonstrated in the second analysis). Future studies should consider introducing a more adapted baseline in the protocol. To precisely control for the perceptive aspects specific to each FoV, the baseline could for example require the participant to stare at a digit without having to search for it (*e.g.*, the location would be known in advance, or the digit would directly be simulated in the SPV), under each FoV. By subtracting the spectrum of this baseline to the one extracted for the task of interest, one could expect to better isolate the cognitive components of the visual search, enabling a finer comparison of the cognitive load elicited under each FoV.

12.6 Conclusion

Although the results presented in this project suffer from limitations hindering the generalizability of the conclusions drawn here, the outcome of this experiment provides promising insights to evaluate the benefits the POLYRETINA implant could bring to the patients once tested in clinical settings. Indeed, the widening of the FoV to 45° makes a significant difference for performing near-ecological tasks that matter for the daily life of the potential receivers. This further validates the use of SPV to explore the influence of important parameters in the design of visual prostheses. The combination with EEG recordings was a difficult challenge that still requires some adaptations to be perfected, but the main analysis enabled to retrieve signatures expected from the literature (visual processing, attentional processes, cognitive load), giving further insights to understand the cortical mechanisms associated with the improvements provided by a larger FoV.

Part IV

General Discussion

CHAPTER 13

DISCUSSION ON THE METHODOLOGICAL AXIS

13.1 Achievements

The first methodological objective of this work was to develop mobile EEG tools at the *Aging in Vision & Action* laboratory to study the human brain in near-ecological conditions, within the mobile brain/body imaging (MoBI) framework. It was built on the know-how and the knowledge gained during the implementation of the initial experiment conducted in the *Biological Psychology and Neuroergonomics* laboratory (Chapter **7**). The latest EEG equipment adapted to mobile conditions (active electrodes, cable shielding, lightweight amplifiers, and wearable backpack, from *ANT Neuro*) with the biometric measurement facilities of the *StreetLab* company were successfully combined in a mobile EEG platform, at the service of the laboratory's research interests. For the purpose of this project, it allowed 3 different protocols to be carried out (Chapters **9**, **10**, and **12**) and some more not covered in the scope of this thesis. Both immersive virtual reality (VR) and real-world experiments were conducted, in a variety of paradigms that allowed to investigate research questions in different fields. On several levels, this work illustrated the advantage of fine temporal resolution brain imaging paired with meaningful behavioral markers extracted from motion capture or eye-tracking modalities when trying to decipher the dynamics of the task-related cortical processes.

Following the lead of the BeMoBIL pipeline (Klug et al., 2022), the EEG data analysis tools necessary to process the recordings issued by these protocols were developed in a modular fashion to allow for flexible reuse across different experimental designs (Section **6.2**), benefiting to the two other works not conducted in mobile conditions (Chapters **8**, and **11**). The key to its reusability was that the overall pipeline included many automatic processing tools, with visual reports at each major step, while providing external control over the most important parameters for the analysis. In the remaining step that required experimenter oversight (*i.e.*, the independent components labeling step), guidelines were written down to help the analyst make correct and consistent decisions. Finally, the data collected during the first experiment was subjected to a pipeline comparison approach (Section **D.3**), which

provided very valuable insights for the rest of the project and allowed the selection of the most appropriate preprocessing modules in the subsequent analyses.

The second methodological objective of this work was to enable the recording of scene-selective region (SSR) activity with EEG using the most accurate source localization method. It built on the methodology set forth by Cottereau et al. (2012) and detailed in Cottereau et al. (2015), taking advantage of the opportunity to use the MRI metadata collected as part of the *SilverSight* cohort. This goal was successfully achieved (Section **6.3.2**), and validated both methodologically (Section **6.3.2.7**) and experimentally by yielding unprecedented insights into the dynamic activity of SSRs.

In the process of achieving this goal, an important prerequisite was the adoption and the validation of an efficient and rapid method for the acquisition of electrode positions during the placement of the EEG cap on the scalp of participants. Although methodological comparative studies had already been conducted (Homölle & Oostenveld, 2019; Shirazi & Huang, 2019; Taberna et al., 2019), no previous reports were found in the literature on the use of the specific model of depth perception camera available in the laboratory. Therefore, a direct comparison of the performance and the convenience of this solution against a more conventional technique was performed. Despite being limited to a single subject, this comparison repeated the measurement several times for each method with different experimenters and yielded satisfactory results for the purposes of this project. It even pointed out a potential limitation of the standard technique, namely the issue of moving the electrode inward while pointing at it, which is problematic, as the measurement then do not capture the actual position of the electrodes during the experiment. The depth perception method does not suffer from this problem because it does not involve contact with the electrodes during the measurements. Interestingly, this issue may have been overlooked due to the lack of testing of these methods on real participants (reference comparative studies are often conducted on a mannequin head), which has some variability and inconsistency regarding the fit of the EEG cap to the head.

13.2 Implications

First, it is hoped that the methodological developments from this project will encourage new scientific efforts to conduct more ecological experiments to better understand the functioning of the brain in all its complexity. Started more than 10 years ago, the MoBI approach is now being used in a growing number of experiments (Stangl et al., 2023), and the continuous improvement of the tools needed to design such paradigms is an important parameter to foster the adhesion of the scientific community to this attractive but not easy to implement methodology. Because it did not focus solely on methodological aspects, this project did not make significant direct contributions to making the data analysis tools more accessible to the non-expert community (Klug et al. 2022 have a much greater impact in this regard). However, the successful replication of the implementation of the MoBI approach, as well as the sharing of experimental design tips (Section **6.1**) can facilitate the consideration of more ecological paradigms by researchers new to the field.

On the same page, although the small comparative study reported here was not yet published, the expected scientific publications resulting from this work are a good example of the successful use of depth perception cameras for the purpose of electrode digitization. This more affordable yet efficient solution could help democratize a more accurate recording of electrode positions during EEG experiments. It would arguably be of great value to EEG research in general. First, to improve source reconstruction models, which, regardless of the model, greatly benefit from increased precision in sensor location (Akalin Acar & Makeig, 2013; Shirazi & Huang, 2019). In fact, some recent studies still do not report having registered the position of the electrodes at the participant level (for example Djebbara et al. 2021; Do et al. 2021), thus hindering the accuracy of the sources of activity discussed in their results. Although EEG suffers from a low spatial resolution, the inclusion of these measurements could improve the validity of the results, increase their replicability, and mitigate criticism of source reconstruction approaches. Second, it could also be helpful in situations, such as those encountered during this project, where the experimental setup benefits from moving the cap to a different position than the standard one (*e.g.*, to increase the participant's comfort). It allows for flexible positioning of the cap while maintaining group-level comparability in the analysis (*i.e.*, by establishing a common reference space based on fiducials).

Finally, although the source reconstruction methods presented here are difficult to reproduce in the majority of laboratories, this project also opened new perspectives for the study of SSRs with EEG, more precisely linking cortical dynamics to these brain regions. For researchers who have the possibility to record both fMRI and EEG, it offers an interesting alternative to the difficult endeavor of recording these two modalities simultaneously (Scrivener, 2021), or to have participants perform the same task twice (once in the scanner and once with the EEG cap, as in Kaiser et al. 2020, 2019), which is a limiting factor if the experiment involves a learning component or requires a high degree of naïveness to the task.

13.3 Limitations & Perspectives

While the methods developed in this thesis provide successful implementations of either the MoBI approach or fMRI-informed source reconstruction, they still lack full automation that would allow for standardized reusability across the scientific community (Klug et al., 2022). Currently, the preprocessing step that relies most on the subjective judgment of the experimenter is the selection of independent components (ICs). Although the *IClabel* algorithm has recently contributed to significant progress in this respect (Pion-Tonachini et al., 2019), the experience with careful manual inspection of IC properties in this project revealed substantial inaccuracies in the automatic assignment of labels, when selecting the class with the highest probability. The main hypothesis to explain this discrepancy is the lack of training of the algorithm on data from mobile EEG experiments, which contain many more sources of artifacts than datasets from stationary experiments. To address this issue, a recent initiative, ICMoBI, was launched to specifically target the automatic classification of ICs on mobile EEG datasets, based on the same machine learning and collaborative labeling principles as

ICLabel. The datasets collected during this thesis have been shared to contribute to this effort and the results of this project are eagerly awaited to eventually achieve full automation of IC selection in MoBI paradigms.

Similarly, additional efforts should be made to reduce the involvement of manual inspection in the source reconstruction pipeline, especially at the MRI segmentation stage. In this respect, the steady progress of machine learning algorithms, particularly those based on deep learning models, is a promising lead to improve the performance of current approaches to reduce this time-consuming burden for experimenters (see for example Audelan and Delingette 2021; Brusini et al. 2020).

On another note, to further enrich the depth of the analyses, future work could explore the multiple model option of the adaptative mixture independent component analysis (AMICA) algorithm (Palmer et al., 2008). It was not considered in this project due to its computational cost. It does, however, permit to bypass the unrealistic assumption of source stationarity over the course of the recording made by the classical independent component analysis (ICA) decomposition. As a nice example of how this analysis can be useful, Hsu et al. (2018) demonstrated the possibility to accurately identify the dynamic alternation of sleep stage from of a continuous sleep recording thanks to AMICA. For a successful implementation, the experimenter should first predefine different cognitive states of interest (*e.g.*, the encoding phase, the retrieval phase, *etc.*) during which source stationarity is assumed and identify the time periods when they are expected to be active. At the output of the AMICA procedure, each fitted model is associated with an instantaneous probability of being active, which then allows the reconstruction of state alternation over time.

Finally, outside the scope of this work, augmented reality (AR) is a promising emergent modality that, in principle, allows paradigms to be constructed in real-world environments while maintaining a high degree of control over stimulus presentation, particularly in the field of visual neuroscience. With respect to VR, it may provide greater ecological validity, as the richness and complexity of virtual environments are often limited compared to the real-world, and a recent study suggested that it promotes participant engagement (Maidenbaum et al., 2019). Applications to visuo-spatial cognition and landmark-based navigation are fairly straightforward, as the most basic functionality of AR is to place 3D virtual objects in the real environment, thus enabling infinite manipulations of the visual information available to the participants for orientation (Stefanucci et al., 2022; Y. Zhao et al., 2023). The drawback of VR's limited field of view is also partially mitigated by the fact that commercial AR solutions now come in the form of glasses that do not deprive users of their peripheral visual field (such as the Microsoft HoloLens or the Dream Glass), although no stimulus can be placed at extreme eccentricities. Several pioneering studies have already begun to pave the way for combining AR with EEG, investigating attentional processes (Vortmann et al., 2019), face recognition (Krugliak & Clarke, 2022) or visual processing during walking (X. Chen et al., 2022a, 2022b).

CHAPTER 14

DISCUSSION ON THE FUNDAMENTAL AXIS

14.1 Achievements

First, this thesis presents a successful implementation of the MoBI approach to study landmark-based spatial navigation in immersive VR (Chapter **7**). Focusing on healthy young participants relying on an allocentric reference frame, a set of brain structures comparable to the fMRI-based literature was retrieved, in particular the posterior cingulate, anatomically close to the retrosplenial complex (RSC). As revealed by the fine-grained temporal resolution of EEG and complementary motion capture analysis, the dynamics of activity in this area was consistent with its proposed role in integrating visual perception of landmarks into internal spatial representations. In addition, sensorimotor areas usually overlooked in static paradigms were found to be engaged by the mobile nature of the experiment. In summary, this proof-of-concept provided new insights into the cortical activity that mediates successful spatial reorientation when visual, proprioceptive, and vestibular sensory inputs are coherent.

Second, continuing the investigation of the visuospatial abilities involved in landmark navigation (Chapter **8**), this project focused on the SSRs, key cortical regions at the interface between the early visual system and high-hierarchical cognitive regions such as the hippocampus. Using the vertical position of informative landmarks in the environment, this paradigm showed that forcing orientation to proximal objects in the upper part of the visual field (VF) significantly modulated activity reconstructed in the SSRs. This finding was robust across both age groups and should probably be interpreted in light of the grammar violation expected from natural scenes. In addition, a parallel analysis of eye fixations and event-related spectral perturbations (ERSPs) reconstructed in the SSRs revealed a downward gaze bias in older adults, combined with a time-frequency signature of deficient regulation of the attentional mechanisms necessary to efficiently retrieve the useful navigational information from a scene. Overall, this study highlights the need to consider the vertical position of visuospatial information in the environment to better understand the wayfinding problems observed in healthy aging.

These findings are consistent with the results of the experiment presented in Chapter **11**, which also investigated the EEG correlates of reorientation in a healthy aging context. In a simpler design, but with increased statistical power due to a larger number of trials, event-related potential (ERP) and ERSP analyses of the scalp signal attributable to SSRs similarly revealed delayed and more effortful visuospatial processing, disrupted by impaired suppression of task-irrelevant stimuli.

Taken together, these studies provided further evidence for the detrimental effects of healthy aging on orientation performance based on visual cues. By complementing the tasks with EEG neuroimaging, which is able to unravel the cortical dynamics associated with visuo-spatial processing, they emphasized the critical role of the SSRs in a navigational context and how the disruption of attentional control perturbs their function with aging.

Third, to better understand how visuo-spatial perception is embedded in the multisensory framework experienced under ecological conditions, a specific test of the activity of SSRs related to the perception of walkable distance was conducted (Chapter **9**). The preliminary results of this paradigm suggest a significant impact of multisensory integration in reducing age-related differences classically reported when this ability is tested with only the visual input available. The current EEG analysis does not have the statistical power to reproduce the modulation of SSRs activity by the depth of the path in front of the observer found in the reference fMRI study. Further investigations of the data are warranted to confirm whether this null finding can be overcome with more detailed analyses, or whether other aspects of the paradigm may be responsible for this discrepancy.

14.2 Implications

In line with the initial motivation to push cognitive neuroscience towards more ecological paradigms, several results in this fundamental axis confirmed the added value of studying human spatial cognition under mobile conditions that provide the full multisensory experience to participants.

Consolidating the results first provided by Ehinger et al. (2014), our findings provide further evidence that alpha-band oscillations in the RSC were erroneously associated with a role in heading computation, due to the absence of vestibular stimulation in the original findings (Chiu et al., 2012; C.-T. Lin et al., 2015, 2018). In support of this hypothesis, independent mobile EEG experiments supporting these conclusions were published simultaneously (Do et al., 2021; Gramann et al., 2021). With the last paradigm, another robust finding on perceptual abilities, *i.e.*, the foreshortening of egocentric distance estimation by young adults (Bian & Andersen, 2013; Sugovic & Witt, 2013), seems to be contradicted when participants are allowed to perform a validation of their estimation with multisensory integration. These misinterpretations are a major argument for the field to question the established findings for which the visual input should not be the sole contributor when considering natural spatial behavior.

The second paradigm conducted in this project also offers a novel perspective on how neural correlates of spatial cognition may depend on the natural statistics of our environment. Taking into account the expectations that our brains form about ecological stimuli is a fairly recent addition to neuroimaging paradigms, but has shown striking effects on visual processing (Kaiser & Cichy, 2018a, 2018b; Kaiser et al., 2020, 2018). In this case, it was hypothesized that the discrepancy in finding proximal, informative landmarks in the upper VF disrupts the stereotyped processing of visuo-spatial information. Even if there are no significant behavioral consequences, raising awareness in the neuroscientific community of such expectancy effects, which are unlikely to be restricted to vision since it is generally accepted that our brains learn by aggregating probabilities (Hebb, 1949), could help in the design of future ecological paradigms that either exploit or avoid these biases.

Ultimately, this project has helped to highlight several aspects of healthy aging that should be more fully considered in future research and, in some cases, could even provide concrete guidelines for designing public spaces that would be more helpful to older adults regarding their wayfinding abilities.

The results presented in this thesis, by confirming the age-related bias for the lower part of the visual environment observed in several other paradigms (Bécu et al., 2020a; Brennan et al., 2017; Durteste et al., 2023; J. Feng et al., 2017), invite to reconsider the role of the vertical position of information that should serve for navigation. To facilitate the wayfinding of older adults, who often report a feeling of disorientation in large and complex environments (*e.g.*, a train station or a shopping mall; O'Malley et al. 2022; Phillips et al. 2013), it would be interesting to analyze the positioning of signage in these places to understand whether it could be a significant aggravating factor. If this is the case, it could provide an interventional lever for urban planning to be more inclusive for older people.

Furthermore, the main findings of the studies included in this project support the long-standing description of attentional control deficits in healthy aging (Campbell et al., 2010; Dempster, 1992; Lustig et al., 2007). Grzeschik et al. (2019) had already uncovered such mechanisms in the context of spatial navigation with behavioral and oculomotor metrics, but the novelty of this work lies in its association with cortical dynamics supporting the impaired performance in orienting in the virtual environment. Indeed, the data reported here highlight the influence of top-down attentional processes on the encoding and retrieval of visual information necessary for reorientation, mediated in particular by a late component in the beta/gamma band of SSRs activity. This accumulation of evidence may promote adaptations in the visual environment of older adults, such as assisted living facilities, by reducing the amount of potentially distracting information to facilitate navigation.

14.3 Limitations & Perspectives

Based on the fundamental investigations presented in this thesis, several options for future studies of visuo-spatial cognition in healthy aging can be suggested, always pushing further the ecological validity of the paradigms.

Relative to the Y-maze paradigm, which was intended here more as a proof-of-concept for ecological neuroimaging recordings of landmark-based spatial behavior, new avenues of research could be proposed to extend this work. To further demonstrate the potential of mobile EEG in such a paradigm, it would be interesting to contrast cerebral activity between participants with radically different behavior in the maze. In our sample of young adults, only 2 used an egocentric reference frame compared to 14 allocentric users, so such an analysis could not be performed. Inclusion of a larger sample of young adults pre-screened for their behavioral response, or comparison with older adults, in whom a much larger proportion are observed to adopt an egocentric strategy (Bécu et al., 2023), would be warranted to elucidate the differences between the neural circuits involved in the two contrasting behaviors. These differences have been widely discussed in the fMRI literature, and a recent finding in a very similar paradigm suggested a specific role for SSRs in this age-related process (Ramanoël et al., 2020). Complemented by the source reconstruction methodology targeting these regions of interest validated in this project, the continuation of this work in this direction would provide a good opportunity to confirm the central role of these cortical regions in visuo-spatial integration during naturalistic behavior, upstream of the hippocampal structures classically singled out for such age-related deficits.

Regarding the paradigm in which the influence of the vertical position of landmarks is studied, it would be very interesting to extend the investigations to more ecological conditions, for example in an immersive virtual environment. In this case, will older adults benefit from multisensory integration to restore their overall performance on the task with respect to young adults? Or, will the age-related exacerbation of cognitive-motor interference (B. R. Malcolm et al., 2015; Protzak et al., 2021; Rubega et al., 2021) further impair their navigational behavior? In the second case, postural and locomotor control demands in realistic mobile conditions may have a greater impact in the condition where only landmarks in the upper part of the environment are informative. Indeed, as recently reported by Bécu et al. (2020a) and Bécu et al. (2023), older adults who are impaired in using landmarks for orientation also show a downward gaze bias. However, it is interesting to note that in these studies (and especially in Bécu et al. 2023), landmarks are almost exclusively located in the upper part of the visual environment, making it impossible to determine whether the impairment in using landmarks is caused by the downward gaze bias or whether the gaze bias emerges as a solution to a prior inability to use the information provided by landmarks in general (*i.e.*, by looking for geometric information at ground level). With a paradigm similar to the one proposed here, where the position of the useful landmarks is varied along the vertical axis, it would be possible to disentangle these two hypotheses.

Alternatively, at the neural computations level, to extend the natural scene grammar hypothesis, a modification of this paradigm could be proposed to compare the influence of the depth of the upper landmark position with respect to the observer on the activity of the SSRs. Indeed, it would be particularly informative to study whether distal landmarks located in the upper part of the VF, which are much more common in our daily life, would restore the activation of these brain regions to the same level as for the lower proximal landmarks, thereby confirming the natural statistics hypothesis, or whether the results would be similar to those

found here, calling for exploring deeper explanations of the specificity of the processing of information in the upper VF in the SSRs.

Finally, with respect to the walking distance estimation paradigm, the speculation about the influence of multisensory integration should be further tested with protocol adaptations that play only on this dimension of the paradigm. Two levels could be considered: first, by removing the possibility to compare the initial visual estimation with the proprioceptive feedback in order to remove the path integration component; second, by comparing the results obtained with a 'static scene' presentation in VR (*i.e.*, eliciting the sensation of looking at a picture instead of a 3D world, similar to the manipulations done in Aminoff and Tarr 2021), where the physical presence in the environment would be discarded.

Chapter 15

Discussion on the Translational Axis

15.1 Achievements

The methodological framework at the core of this project also contributed to translational applications, specifically by participating in two projects evaluating visual prostheses for the treatment of late-stage *Retinitis Pigmentosa* (RP).

The first project, the *PIONEER* clinical trial, was an opportunity to work with real patients benefiting from optogenetic therapy coupled with light-stimulating goggles. As the study included near-ecological paradigms to test the abilities of the treated patients in daily activities, a mobile EEG approach was ideally suited to investigate the cortical correlates of the patients performing the tasks. Even though the task examined here did not involve ambulatory movements, the patients needed the freedom to move their heads a lot while searching for the object on the table. In addition, the presence of the stimulation goggles was a concerning source of artifacts for the EEG recordings, which had to be taken into account in the data preprocessing pipeline, similar to a VR headset. In the first case report (Section **10.1**), EEG analysis showed that optogenetic stimulation elicited an occipital alpha rhythm typical of natural visual processing, and that it was more desynchronized by the presence of the object than by its absence. This was an important step in demonstrating the efficacy of the therapeutic approach in reactivating visual pathways at the cortical level. However, although the behavioral gains were evident for the patient, no EEG correlates of conscious perception of the object could be reported, probably due to some choices in the protocol design.

Following these initial findings, protocol modifications were proposed to circumvent the aforementioned limitation and, in line with the philosophy of the MoBI approach, motion capture of head movements was added to the paradigm to expand the possibilities for analysis. Convergence on this updated version of the protocol took some time, and results from only one additional patient could be reported in this thesis (Section **10.2**). Despite the good performance of the task, this new case did not provide the same clear results as the first one. In particular, the expected occipital alpha rhythm did not seem to be involved in the perception of the object. Nonetheless, the presence of the object on the table could be significantly

predicted from the signal recorded on occipital channels at a different frequency band. Furthermore, a signature of response prediction was revealed, implicating the theta rhythm in the frontal region, a well-documented signature of decision-making. Although the protocol update does not allow a full comparison between these two cases, these results illustrate that the cortical correlates of partial visual recovery induced in these late-stage RP patients can be quite variable. This may be a reflection of the diversity of individual trajectories of neuroplasticity at stake for the brain to harness the novel type of visual stimulation induced by optogenetic therapy.

The second project, the collaboration with Diego Ghezzi's team on the POLYRETINA implant, was more upstream in terms of therapeutic design, experimentally evaluating the impact of the improved features (in particular the enlarged field of view) of this prosthesis using simulated prosthetic vision (SPV). The methodological framework of this project was in line with their motivation to evaluate the benefits of their novel design for the performance of daily activities, with an ecological intent. Although limited to a few participants, their preliminary study was rich in insights for this project. First, it highlighted specific pitfalls in the design of mobile EEG protocols, such as participant comfort with a VR headset. Second, it demonstrated the potential of mobile EEG to provide correlates of visual, attentional, and cognitive load processes during SPV. In terms of cognitive load, which remains a major challenge for the long-term adoption of visual prostheses (Borda & Ghezzi, 2022; Erickson-Davis & Korzybska, 2021), it revealed clear patterns of relief under the 'natural' field of view (FoV) compared to the restricted prosthetic FoVs.

15.2 Implications

Due to the relatively recent maturity of the significant successes in the field of vision restoration, neuroimaging findings related to the functional rehabilitation of visual function in humans are still largely absent from the literature (except for Castaldi et al. 2016: an fMRI study of the visual response elicited by the Argus II device). In this context, this work is expected to have a pioneering impact, paving the way for more objective assessments of visual recovery using cortical measurements.

Although not essential for evaluating the concrete gain in visual function and overall autonomy provided by the prosthesis, cortical measurements provide additional insight into the physiological pathways reactivated by the therapeutic approach. These insights may provide access to unconscious, stimulus-driven aspects of visual processing that bypass the cognitive processes that allow the patient to formulate a conscious response. These processes may depend on many external factors (*e.g.*, a bias toward a stereotyped response, lack of attention, fatigue) that interfere with objective assessment of visual recovery. Our first case report provides a good example of this, as the patient was often not confident enough in his perception to formulate a response, but cortical correlates showed significant modulation of EEG activity by the presence of the object. At critical stages in the development of a therapy, such recordings may be of crucial value in supporting the early identification of markers of visual recovery before the patient can actually report it.

In addition to pure visual processing, the second study showed how cortical measures can serve as an objective assessment of cognitive load while using the device. All previous investigations of the cognitive load induced by the use of these prostheses have relied on subjective self-reports (Erickson-Davis & Korzybska, 2021), so this analysis opens up new possibilities for systematically quantifying this load between different conditions of use, different participants, and different devices. Interestingly, the SPV study highlighted a discrepancy between the performance benefits, which became apparent as soon as the FoV was increased to 45°, and the evidence of cognitive load relief, which was not observed until the FoV reached 110°. By illustrating the possibility that behavioral improvements are not necessarily associated with reduced cognitive effort, this decoupling between behavioral and cortical measures is an important further motivation to pursue research endeavors that include cortical markers of visual recovery.

An important complementary value of this work is that it demonstrates the feasibility of using an ergonomic solution to measure brain activity, allowing a wide range of tasks to be considered without compromising the ecological validity of tests used to evaluate functional rehabilitation. As it is now an important concern in the field of vision rehabilitation to take more account of outcomes in everyday settings (Ghezzi, 2023; Hallum & Dakin, 2021), this is a good feature to convince clinicians who might be reluctant to be forced to make a trade-off between cortical measurements and ecological value. In addition, the mobile EEG approach offers many more possibilities than other technologies by being much less conservative about the properties of the device being tested: the MRI scanner and MEG require control of the magnetic properties of the materials used, and fNIRS can quickly become cumbersome on the participant's head, limiting the use of a VR headset, for example. Thus, on a larger scale, EEG evaluations could be used to objectively compare a variety of therapeutic solutions without imposing strong additional constraints on their design.

15.3 Limitations & Perspectives

The EEG studies associated with the *PIONEER* clinical trial are still ongoing and several development paths are being considered. The first priority is to administer the updated version of the object detection protocol to the first patient as well as to a larger group of patients (currently 3 additional patients included in the clinical trial are responding well to the therapy and seem suitable for testing). This will allow for further investigation of the individual variability of the cortical correlates of visual search.

In addition, to fully exploit the methodological framework developed during this thesis, mobile EEG recordings could be extended to the more ecological tasks proposed to patients in the clinical trial, such as detecting a door while walking along a wall, or following a white line on the floor. Again, coupled with motion capture to reconstruct the visual input provided by the goggles and the patient's position in space, it could be used to investigate correlates of vision in successful *vs.* unsuccessful trials, but also to provide more insight into the cognitive load experienced by patients with this device (see last paragraph for more details).

To further investigate the influence of the therapy on neuroplasticity, it would be necessary to perform the neuroimaging protocols prior to the surgical intervention and the training with the glasses. Such a reference record of the patients' abilities and their neural correlates would be invaluable to monitoring their progress during training and quantifying the changes in their brain activity. It is also the most robust control for canceling out the contribution of residual vision in post-treatment recordings (Hallum & Dakin, 2021). As planned in the latest version of the clinical protocol, this will hopefully be the case for future enrolled patients who have not yet been injected with the optogenetic viral vector.

A fundamental future development for the evaluation of optogenetic therapy would be to record the necessary information to reconstruct the stimulation from the goggles to the treated eye as well as the position of the eye in real time. In fact, one limitation that currently hinders the study of cortical correlates at a finer time scale is the poor control of visual input to the retina. This is difficult to infer from the external stimuli because the images captured by the camera undergo significant spatial transformations and are projected with a delay of $\sim$100 ms due to computational processing (Posch & Matolin, 2011; Posch et al., 2011). Binding these additional data streams to the EEG data, as advocated by the MoBI approach, would significantly enrich the investigations and allow to fully exploit the temporal resolution of the EEG recordings. It would also be useful to have full control over the stimulation algorithm of the device to design protocols that require precise timing of stimuli (*e.g.*, visually evoked potentials). For the *PIONEER* clinical trial, unlocking these recordings is not a technical issue, but rather a matter of strict regulatory oversight of any modifications to the medical device. It is hoped that such approvals will be obtained in future submissions of the clinical trial protocol.

Better exploitation of the temporal resolution of EEG would also serve to assess cognitive load on a finer time scale (Antonenko et al., 2010). With the appropriate protocol design, it could be possible to identify particular moments in a task that are particularly intense, or to monitor the dynamic evolution of cognitive fatigue in patients over the course of the experiment. While the data analysis pipeline proposed in this project is only suitable for offline processing (*i.e.*, once the experiment is over), an interesting future avenue of research could also involve real-time feedback, either to the experimenter (who could, for example, adjust the difficulty of the task or propose a break) or to the patients themselves. This last option, known in the literature as *neurofeedback*, is an established method of self-regulating one's own brain activity in order to directly modify the neural mechanisms underlying cognition, which has already been used in various clinical contexts (Enriquez-Geppert et al., 2017). In fact, the tools to consider these approaches are emerging, as EEG-based brain-computer interfaces facilitating closed-loop neuroimaging under ecological conditions are a very active research topic (Minguillon et al., 2017; Zabcikova et al., 2022), with an increase in performance since the advent of deep learning models (X. Chen et al., 2022). Proof-of-concepts assessing various cognitive variables, such as attention (Tuckute et al., 2021) or stress levels (Minguillon et al., 2018), have now demonstrated the potential of this methodology.

Chapter 16

Conclusion

Emphasizing the idea that for a more realistic study of both behavioral and neural correlates, human cognition should be studied through ecological experiments, the primary intent of this doctoral work was to contribute to the development of neuroimaging tools that allow experimental protocols to come closer to the multimodal aspect of everyday activities. By adopting, enriching, and leveraging the mobile brain/body imaging framework in a variety of paradigms, both in virtual reality and in real-world settings, it has demonstrated the feasibility and validity of this approach for the study of EEG correlates associated with visuo-spatial cognition in healthy and pathological aging contexts. To this end, the combination of fine temporal resolution brain imaging with behavioral markers extracted from motion capture and eye-tracking was instrumental. It is hoped that such efforts will contribute to making the neuroscience community aware of the rich set of tools available to build more naturalistic protocols without compromising too much control over experimental parameters.

On a fundamental level, applying this methodology to the field of visuo-spatial cognition, the results presented in this work highlight the value of the multisensory stimulation enabled by mobile environments in the way they challenge previous findings and interpretations related to brain activity during spatial behavior. By proposing a novel approach to accurately study the scene-selective regions with EEG, this project focused on these cortical regions that are central to the transformation of visual percepts into useful spatial information, and whose activity has not been properly characterized in dynamic, navigational contexts. The findings from the study of scene-selective regions correlates of navigation in a richer visual environment highlight the importance of considering the natural statistics of daily life environments for understanding neural processing. Taking into account healthy aging, this research highlights the differences in visual information processing and attentional control experienced by older adults that affect their ability to navigate in complex environments. The characterization of specific biases along the vertical axis of the visual field may suggest potential strategies for the design of public spaces and signage to aid navigation for older adults.

The methodological framework developed in this project also has practical applications in translational research, specifically in evaluating the efficiency of visual prostheses for restorative approaches in late-stage *Retinitis Pigmentosa* in everyday settings. As neuroimaging evidence for functional visual rehabilitation in humans remains limited, the results presented in this project pave the way for objective assessment of visual recovery using cortical measurements, providing insight into physiological pathways reactivated by therapy. EEG recordings open access to unconscious aspects of visual processing that may not be captured by subjective self-reports, allowing early identification of markers of visual recovery. By providing novel insights into the cortical correlates of patients actively using the device in ecological tasks, it is hoped that this work will contribute to a better understanding of the neuroplasticity induced by therapy. In doing so, it will be useful in guiding future innovative solutions aimed at reversing severe visual impairment and blindness.

Overall, benefiting from a highly collaborative scientific framework, this thesis has had the opportunity to demonstrate the versatility of the mobile brain/body imaging approach across multiple domains of visual neuroscience. It unraveled brain dynamics during space perception, orientation, and functional visual rehabilitation in situations mimicking naturalistic activities to promote findings readily applicable to people's everyday lives.

Part V

APPENDIX

APPENDIX A

LIST OF CONTRIBUTIONS

Journal articles

DELAUX* A., de Saint Aubert* J.-B., Ramanoël S., Bécu M., Gehrke L., Klug M., Chavarriaga R., Sahel J.-A., Gramann K., Arleo A. (2021). Mobile brain/body imaging of landmark-based navigation with high-density EEG. *European Journal of Neuroscience*, **54**(12), pp. 8256-8282. doi 10.1111/ejn.15190

Sahel J.-A., Boulanger-Scemama E., Pagot C., Arleo A., Galluppi F., Martel J. N., Degli Esposti S., DELAUX A., de Saint Aubert J.-B., de Montleau C., Gutman E., Audo I., Duebel J., Picaud S., Dalkara D., Blouin L., Taiel M., Roska B. (2021). Partial recovery of visual function in a blind patient after optogenetic therapy. *Nature Medicine*, **27**(7), pp. 1223-1229. doi 10.1038/s41591-021-01351-4

Ramanoël S., Durteste M., DELAUX A., de Saint Aubert J.-B., Arleo A. (2022). Future trends in brain aging research: Visuo-cognitive functions at stake during mobility and spatial navigation. *Aging Brain*, **2**:100034. doi 10.1016/j.nbas.2022.100034

DELAUX* A., Durteste* M., Ariztégui A., Cottereau B. R., Sheynikhovich D., Ramanoël S., Arleo A. (preprint, 2023). Age-related disparities in oscillatory dynamics within scene-selective regions during spatial navigation. *bioRχiv*. doi 10.1101/2023.10.16.562507

Durteste M., Liebi L. R., Sapoval E., DELAUX A., Arleo A., Ramanoël S. (preprint, 2023). Scene-selective regions encode the vertical position of navigationally relevant information in young and older adulthood. *bioRχiv*. doi 10.1101/2023.10.18.562731

DELAUX A., Selle I., Durteste M., Ramanoël S., Sheynikhovich D., Arleo A. (in preparation). Modulation of the perception of walkable distance with age in a real-world situation.

DELAUX A., Ariztégui A., Arleo A. (in preparation). Validating the Intel RealSense D435 depth camera for rapid and reliable acquisition of electrodes' positions.

Sahel J.-A., Boulanger-Scemama E., Pagot C., Arleo A., Galluppi F., Martel J. N., Degli Esposti S., DELAUX A., de Saint Aubert J.-B., de Montleau C., Gutman E., Audo I., Duebel J., Picaud S., Dalkara D., Blouin L., Taiel M., Roska B. (in preparation). Follow-ups on the partial recovery of visual function in a blind patient after optogenetic therapy.

Naveilhan C., DELAUX A., Durteste M., Lebrun J., Zory R., Arleo A., Ramanoël S. (in preparation). Brain dynamics of aging in high visual regions during a spatial reorientation task.

International conferences

de Saint Aubert* J.-B., DELAUX* A., Ramanoël S., Bécu M., Gehrke L., Klug M., Chavarriaga R., Sahel J.-A., Gramann K., Arleo A. (2021). Cortical and behavioral correlates of active landmark-based navigation with high-density EEG. Poster presentation by de Saint Aubert J.-B. at *NeuroFrance 2021*, virtual meeting.

Sahel J.-A., Audo I., Boulanger-Scemama E., Pagot C., Arleo A., Galluppi F., Martel J. N., Degli Esposti S., DELAUX A., de Saint Aubert J.-B., de Montleau C., Gutman E., Duebel J., Picaud S., Dalkara D., Blouin L., Taiel M., Roska B. (2021). Partial recovery of visual function in a blind patient after optogenetic therapy for non-syndromic Retinitis Pigmentosa. Oral presentation by Sahel J.-A. at *the* 24^{th} *annual meeting of the American Society of Gene + Cell Therapy (ASGCT)*, virtual meeting.

DELAUX* A., de Saint Aubert* J.-B., Ramanoël S., Bécu M., Gehrke L., Klug M., Chavarriaga R., Sahel J.-A., Gramann K., Arleo A. (2021). Mobile brain imaging of active landmark-based navigation using immersive virtual reality and high-density EEG. **Poster presentation by DELAUX A.** at *the* 49^{th} *meeting of the European Brain and Behaviour Society (EBBS)*, Lausanne, Switzerland.

Martel J. N., Sahel J.-A., Boulanger-Scemama E., Degli Esposti S., Pagot C., Arleo A., Galluppi F., DELAUX A., de Saint Aubert J.-B., de Montleau C., Gutman E., Audo I., Duebel J., Picaud S., Dalkara D., Blouin L., Taiel M., Roska B. (2021). Optogenetics in the Clinic: Safety and Efficacy Updates on the Phase I/II Clinical Trial PIONEER. Poster presentation by Martel J. N. at *the* 39^{th} *annual scientific meeting of the American Society of Retina Specialists (ASRS)*, San Antonio, TX, USA.

Sahel J.-A., Audo I., Boulanger-Scemama E., Pagot C., Arleo A., Galluppi F., Martel J. N., Degli Esposti S., DELAUX A., de Saint Aubert J.-B., de Montleau C., Gutman E., Duebel J., Picaud S., Dalkara D., Blouin L., Taiel M., Roska B. (2022). Optogenetics in the Clinic: Safety and Efficacy Updates on the Phase 1/2 Clinical Trial PIONEER. Oral presentation by Sahel J.-A. at *the* 45^{th} *Annual Macula Society meeting*, Berlin, Germany.

DELAUX* A., Durteste* M., Ariztégui A., Abderrahmane Benziane B., Cottereau B. R., Ramanoël S., Arleo A. (2022). Functional implications of vertical coding biases in scene-selective regions on spatial orientation: Evidence from source localized EEG recordings. **Poster presentation by DELAUX A.** at *the Federation of European Neuroscience Societies (FENS) forum 2022*, Paris, France.

Ramanoel S., Durteste M., DELAUX A., Habas C., Arleo A. (2022). The neural underpinnings of visual information processing for spatial navigation in healthy aging. Oral presentation by Ramanoel S. at *the 22nd conference of the European Society for Cognitive Psychology (ESCOP)*, Lille, France.

Sahel J.-A., Audo I., Boulanger-Scemama E., Pagot C., Arleo A., Martel J. N., Degli Esposti S., DELAUX A., de Saint Aubert J.-B., de Montleau C., Gutman E., Duebel J., Picaud S., Dalkara D., Galluppi F., Taiel M., Roska B. (2022). Optogenetics in the Clinic: Safety and Efficacy Updates on the Phase 1/2 Clinical Trial PIONEER. Oral presentation by Sahel J.-A. at *the American Academy of Ophtalmology meeting (AAO)*, Chicago, IL, USA.

DELAUX* A., Durteste* M., Ariztégui A., Cottereau B. R., Ramanoël S., Arleo A. (2023). How aging of the Occipital Place Area impacts EEG correlates of spatial orientation. **Poster presentation by DELAUX A.** at *the Organization for Human Brain Mapping (OHBM) 2023 annual meeting*, Montréal, Canada.

Naveilhan C., DELAUX A., Durteste M., Lebrun J., Zory R., Arleo A. Ramanoël S. (2023). Age-related differences in early electrophysiological markers of visuospatial processing during reorientation. Poster presentation by Naveilhan C. at *the Organization for Human Brain Mapping (OHBM) 2023 annual meeting*, Montréal, Canada.

Durteste M., Liebi L., Sapoval E., DELAUX A., Ramanoël S., Arleo A. (2023). The occipital place area encodes the vertical position of navigationally relevant information. Poster presentation by Durteste M. at *the Organization for Human Brain Mapping (OHBM) 2023 annual meeting*, Montréal, Canada.

Ramanoël S., Naveilhan C., DELAUX A., Durteste M., Saulay-Carret M., Zory R., Arleo A. (2023). How visual aging impacts spatial navigation abilities: a neurocognitive approach. Oral presentation by Ramanoël S. at *Ulysseus Research Summit: Towards innovations in ageing and well-being*, Nice, France.

National conferences

Naveilhan C., DELAUX A., Durteste M., Lebrun J., Zory R., Arleo A. Ramanoël S. (2022). Top-down modulation of brain visual coding of navigational affordances during spatial decision task. Oral presentation by Naveilhan C. at *the 17th Journée Scientifique des Jeunes Chercheurs en Psychologie (JSJC)*, virtual meeting.

Naveilhan C., DELAUX A., Durteste M., Lebrun J., Zory R., Arleo A. Ramanoël S. (2023). Age related differences in theta-alpha bands synchronization during spatial orientation. Poster presentation by Naveilhan C. at *Journées d'Étude du Vieillissement (JEV) 2023*, Tours, France.

APPENDIX B

RULES FOR THE SELECTION OF BRAIN INDEPENDENT COMPONENTS

Given ICLabel's relatively recent development (Pion-Tonachini et al., 2019) and its lack of validation with mobile EEG data, the labels outputted by the algorithm were manually examined, with a specific focus on potential Brain independent components (ICs). Candidate ICs were selected based on a preview of their scalp topography and the percentage attributed to the most likely class by ICLabel. In particular, ICs with an elevated likelihood of belonging to the Brain and Other classes were further inspected with the methodology detailed below. Indeed, in theory the Other class regroups ICs for which no signature of the main classes were found by the algorithm but in practice it was frequent to find brain-related ICs with only slightly odd characteristics that fooled the algorithm.

To determine whether a specific candidate IC exhibited enough characteristics of brain-related signal while avoiding heavy noise interference, a systematic inspection of IC properties (as shown in Figure **B.1**) was performed using the following procedure. Each property was assessed sequentially, and objective criteria were employed to grade each IC ($+1$ if positive criterion was met, or -1 if a negative criterion was present). The sum of these grades determined the classification of the IC: if the sum was positive, the IC was classified as belonging to the Brain class and retained; if the sum was negative, the IC was rejected. In cases where the sum of grades equaled 0, the percentage for the Brain class provided by ICLabel was compared to 50% to make the final decision on whether to reject the IC (accepted above 50% rejected otherwise). Additionally, certain criteria, indicating significant flaws, were considered so important that their presence automatically triggered the rejection of the IC.

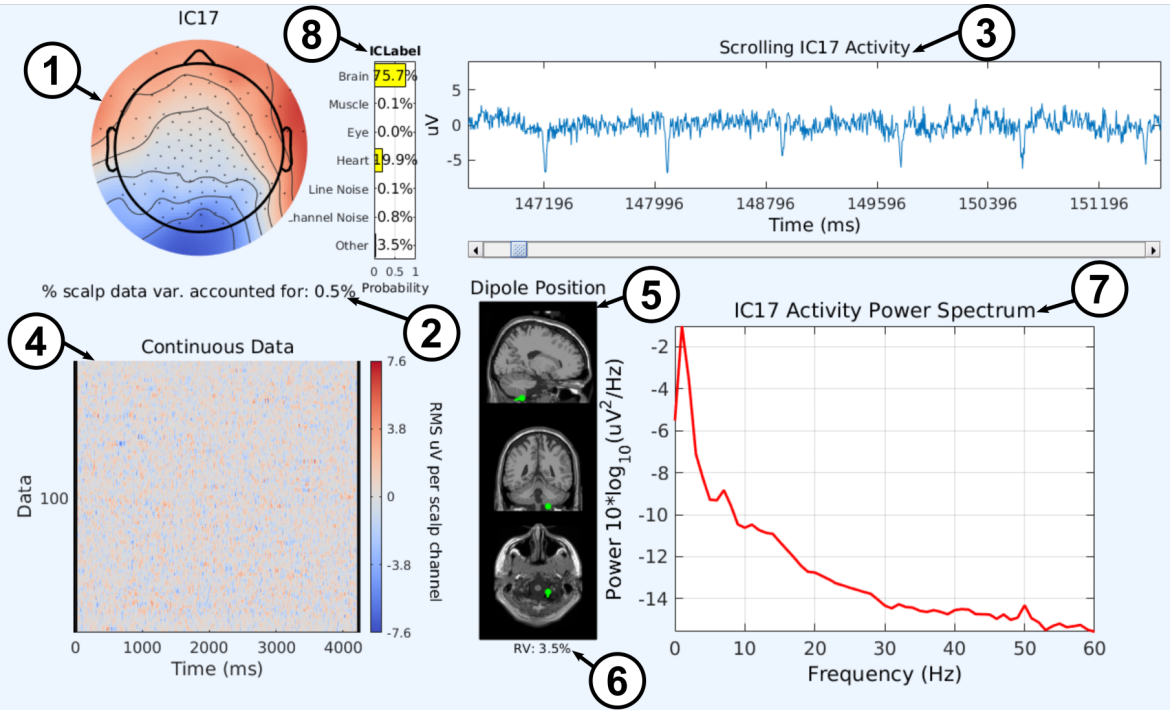

Figure B.1: Illustration of IC properties for manual inspection. **(1) Scalp topography.** Black dots represent electrode positions. This shows what effect the IC process has on each electrode. White represents no effect, where red and blue show positive and negative contributions, respectively. Note: colors far from any electrodes are susceptible to extrapolation artifacts. **(2) Percent data variance accounted for.** Percent data variance accounted for describes how much of the original variance in the channel data can be attributed to this component. Among other things, this measure is useful for determining the relative power of each component. **(3) Component time series.** This plot shows a scrollable segment of activity from the component. It provides a clear view to identify heart beats or eye movements. **(4) Event-related potential image.** The event-related potential (ERP) Image shows all the activity of the independent component process across the entire dataset. As the data is not epoched, it shows the entire data folded into a square with the beginning of the recording at the top left and the end of the recording at the bottom right. **(5) Dipole model plot.** Shows the estimated location of brain equivalent current dipole (ECD) best fitting the IC scalp topography for a one dipole model. The top row shows a sagittal view at the estimated location of the dipole. The middle row shows a coronal view and the bottom row an axial view. **(6) Residual variance.** residual variance (RV) tells how much variance in the scalp topography is left over after subtracting the projected topography of the model ECD from the IC scalp topography. This value provides a measure of how "dipolar" the scalp topography is. **(7) Activity power spectrum.** This plot shows the power spectrum of the IC activity averaged across the entire dataset. **(8) ICLabel compositional label.** ICLabel considers 7 classes: (1) Brain, (2) Muscle, (3) Eye, (4) Heart, (5) Line Noise, (6) Channel Noise, and (7) Other. The prediction takes the form of a compositional label: a percentage vector expressing the likelihood of the IC to belong to each of the considered classes. This panel was extracted with the `pop_prop_extended` EEGLAB function.

List of criteria

These criteria were derived from ICLabel guidelines and personal experience with the data.

On scalp topography (1)

- Checkerboard pattern $\rightarrow$ *reject*
- Heavy contribution of a single channel or not very smooth pattern $\rightarrow -1$

On component time series (3)

- Eye movements $\rightarrow$ *reject*
- Heartbeats $\rightarrow$ *reject*

On ERP image (4)

- Very regular pattern of red and blue $\rightarrow$ *reject*
- All white except a few spots (very transient artifacts) $\rightarrow -1$

On dipole model plot and RV (5&6)

- Localization way out of the head $\rightarrow$ *reject*
- RV above 50% $\rightarrow$ *reject*
- RV above 30% $\rightarrow -1$
- RV below 10% $\rightarrow +1$

On activity power spectrum (7)

- $1/f$ shape absent (excluding 50 Hz peak) $\rightarrow$ *reject*
- Clear α or β bumps 10% $\rightarrow +1$

On ICLabel compositional label (8)

If the *Line Noise* label is clearly winning, estimate the proportions of the other labels without it (all frequencies above $\sim$ 40 Hz will be filtered out for later analyses).

- Brain label below 25% $\rightarrow -1$
- Brain label above 75% $\rightarrow +1$

APPENDIX C

TIPS FOR RECFUSION USAGE

Redacted with the help of Ainhoa Ariztégui and Arnaud Kasteler (Master students).

During the scan

When recording a scan, be aware of the following guidelines:

- Adjust the lighting parameters of the room.
- Position the participant so that the zone of the head that is the least important for the analysis (usually the face) is facing the camera in the starting position (it is often the worst reconstructed).
- Apply the "shaving" technique following the shape of the head with the camera with up and down movements, while making sure to keep the camera as parallel as possible to the scanned area, and keeping the head within the camera's field of view.
- Make a complete turn around the head in order to have (at least) a clear picture of these different areas:
  - A front view (to have a good view of the Nasion sticker).
  - A back view
  - A left profile view
  - A right profile view
  - A top view
- At the end of the scan, check that the 3D shape of the head is correct by clicking on the white square at the top.
- Make sure that there are not many apparent duplications of electrodes and that the scan is satisfactory overall before saving it.
- Always perform (at least) 2 scans, changing the experimenter (if several are present).

Post-processing

For post-processing, here are the steps to follow:

1. **Color**. Adjust the *Brightness* and *Contrast* sliders to get the best possible rendering with a good visualization of the EEG cap electrodes.
2. **Clean**. If there are unwanted residues, click on *select largest component* (the residues should appear in red) then click on *Clean* to remove them.
3. **Crop**. Crop the participants 3D model in the box with *Translate* and *Rotate*. Once satisfied, click on *Crop* (do NOT check *Discard data inside box* which deletes the contents of the box).
4. **Smooth**. If by clicking on the white square at the top, the shape of the head seems somewhat irregular, you can try to "smooth" the model, for a better rendering.
5. **Re-texture**. Launch a first re-texturing.

Once the first re-texturing is complete:

- If the rendering is close to perfection (all electrodes are in focus and the reconstruction is coherent) $\rightarrow$ save!
- If the image still shows some defects, here are 2 alternative options using the **Keyframes** menu:
    1. Click on the eye to view each photo individually; if there is a blurred or out-of-area photo (see Figure **6.4a**), remove it from the images used for 3D reconstruction by unchecking it in *Use for texturing*. Once you've made a first round of all the photos, click on *Re-texture* again. Once the 3D reconstruction has been completed, look at each image again, adjusting the *Transparency* to around 50% to see if any image is offset from the model (see Figure **6.4b**), then click on *Re-texture* again. If necessary, walk around the model to see if an area has been incorrectly reconstructed. If so, look at the images in the area concerned and uncheck any opposing frames. Repeat the procedure until you obtain the best 3D rendering. It's best to click on *Re-texture* each time you remove an image, and alternate between the two models with *Undo* and *Redo* to determine whether the reconstruction is better with or without the image. Remember to inspect the entire model, as adding or removing an image may have an impact on the reconstruction beyond the area present on the image.
    2. Click on the eye to view each photo individually, uncheck all photos in *Use for texturing* at first, then go through again to select only one or two good photos per angle of view, then click on *Re-texture* again. Once the 3D reconstruction has been completed, go around the model to see if any areas have been missed. If so, check off an additional image that best fills the missing area, then click on *Re-texture* again. Repeat the protocol until you obtain the best 3D rendering.

APPENDIX D

SUPPLEMENTARY MATERIAL
MOBILE BRAIN/BODY IMAGING OF LANDMARK-BASED NAVIGATION WITH HIGH-DENSITY EEG

This appendix chapter presents the supplementary material attached to the published version of the article reported in Chapter **7**. They are transcribed the same way they were accepted by the journal, the original document is available online. A supplementary video (Video S1), illustrating a single trial associated with the offline motion capture reconstruction, was also made available online.

Participant	Behavioral group	Total number of trials	Learning Trials	Control Trials	Probe Trials
P01	Allocentric	86 (91)	33 (37)	26 (27)	27 (27)
P02	Allocentric	85 (89)	32 (35)	27 (27)	26 (27)
P03	Allocentric	88 (90)	34 (36)	27 (27)	27 (27)
P04	Allocentric	80 (88)	27 (34)	26 (27)	27 (27)
P05	Egocentric	80 (84)	26 (30)	27 (27)	27 (27)
P06	Egocentric	80 (84)	27 (30)	27 (27)	26 (27)
P07	Allocentric	73 (86)	25 (32)	27 (27)	21 (27)
P08	Allocentric	81 (84)	27 (30)	27 (27)	27 (27)
P09	Allocentric	79 (88)	26 (34)	26 (27)	27 (27)
P10	Allocentric	81 (89)	27 (35)	27 (27)	27 (27)
P11	Allocentric	78 (84)	25 (30)	27 (27)	26 (27)
P12	Allocentric	81 (89)	28 (35)	27 (27)	26 (27)
P13	Allocentric	82 (90)	28 (36)	27 (27)	27 (27)
P14	Allocentric	79 (88)	27 (34)	27 (27)	25 (27)
P15	Allocentric	76 (85)	22 (31)	27 (27)	27 (27)
P16	Allocentric	80 (85)	26 (31)	27 (27)	27 (27)
Total Allocentric group		1129 (1226)	387 (470)	375 (378)	367 (378)
Global dataset		1289 (1394)	440 (530)	429 (432)	420 (432)

Table D.1: Repartition of the trials per participant kept for the zone-based and EEG analyses. We indicate in parentheses the initial number of trials before rejection. We discarded outlier trials that did not comply with the chosen sequence of events and those lasting too long to be consistently incorporated in the analysis. The effective duration cut-off (computed from the distribution of escape latency) was 12956 ms.

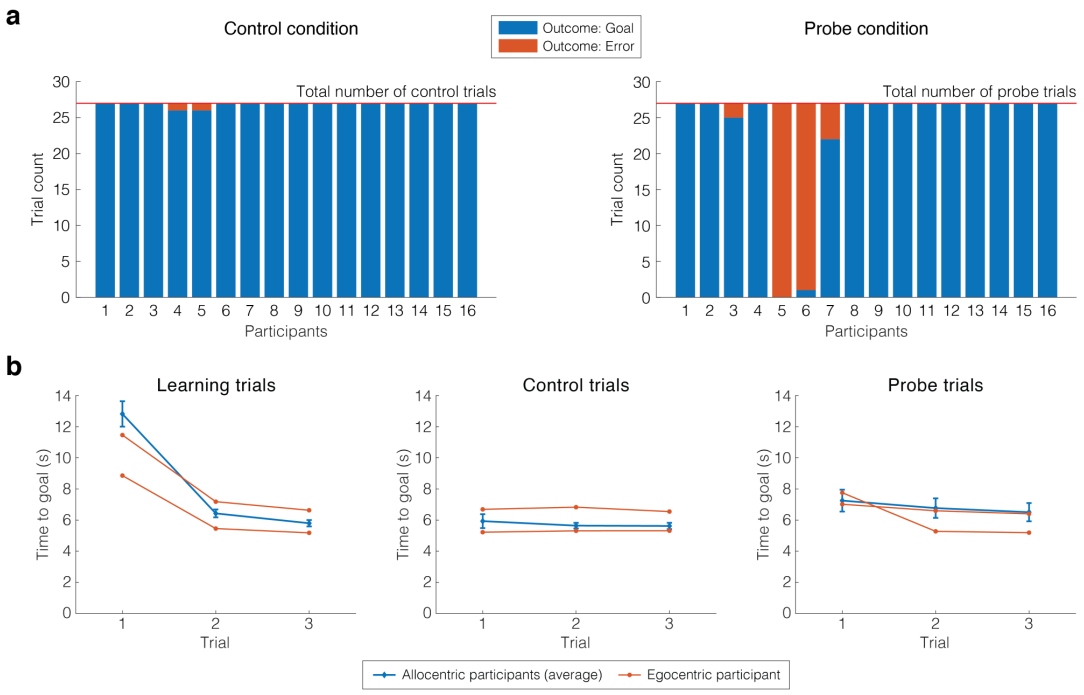

Figure D.1: Behavioral results - Group behavior across trials. (**a**) Strategy assignment. Outcome of the control (left) and probe (right) trials showing the participant-wise count of Goal and Error arm choices. Each test part of the experiment (control and probe conditions) comprised a total of 27 trials across blocks. Probe trial outcomes were used to assign each participant a strategy preference: 14 participants had a majority of allocentric responses (choosing the Goal arm in probe trials) and 2 participants had a majority of egocentric responses (choosing the Error arm in probe trials). (**b**) Group-level time to goal per condition. The evolution of the time to goal across trials, presented for each condition (learning, control, probe) and averaged across blocks. Data were averaged across participants in the allocentric group (bars indicate standard error of the mean). For the two egocentric participants, individual data are showed. For the learning trials, we considered the first 3 trials, irrespectively of their outcome.

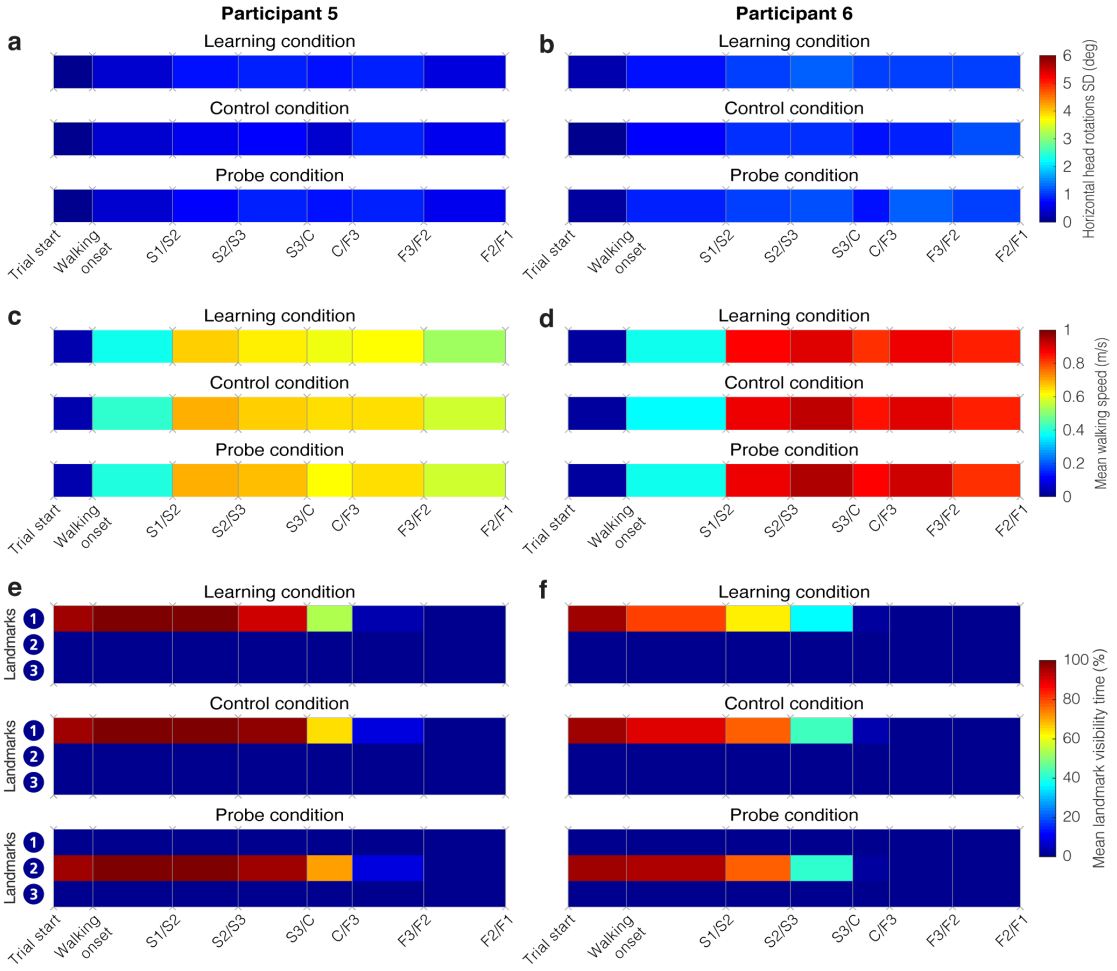

Figure D.2: Behavioral metrics - Walking speed, horizontal head rotations variability, and landmark visibility for the egocentric participants. (**a**,**c**,**e**) Participant 5. (**b**,**d**,**f**) Participant 6. For all plots, we divided each trial according to the same sequence of events: walking onset, followed by the first passage in the starting branch (S) then in the finish branch (F), being either the *goal* or the *error* branch. Events are horizontally spaced according to the median duration between each event. All plots represent data in the learning, the control and the probe conditions, averaged between separating events across all trials and blocks for each egocentric participant. (**a**,**b**) Average standard deviation of horizontal head rotations. (**c**,**d**) Average instantaneous walking speed. (**e**,**f**) Average landmark visibility. Color code corresponds to the percentage of time each landmark was visible at the screen.

Factor	Degrees of freedom	F-statistic	p-value
Main effects			
Condition	$(2; 819)$	1.61	0.2
Zone	$(6; 819)$	95.43	$< 1e{-5}$
Landmark	$(2; 819)$	263.50	$< 1e{-5}$
2-way interaction effects			
Condition & Zone	$(12; 819)$	0.13	1
Condition & Landmark	$(4; 819)$	181.26	$< 1e{-5}$
Zone & Landmark	$(12; 819)$	23.54	$< 1e{-5}$
3-way interaction effect			
Condition & Zone & Landmark	$(24; 819)$	25.31	$< 1e{-5}$

Table D.2: Complete output of the 3-way ANOVA test on Landmark visibility. Effects and interactions for which the p-value was found below 0.01 were followed by post-hoc analyses involving pairwise t-tests between groups, corrected for multiple comparisons with Tukeys honest significant difference criterion method.

D.1 Motion Sickness questionnaire

All participants answered a motion sickness questionnaire at the end of the experiment, adapted from Kennedy et al. (1993). They had to rate the following symptoms as none, slight, moderate, or severe.

- General Discomfort
- Fatigue
- Eye Strain
- Headache
- Difficulty Focusing
- Salvation Increasing
- Sweating
- Nausea
- Difficulty concentrating
- Fullness of Head

D.2 BeMoBIL pipeline - Klug et al. (2018)

D.2.1 Bad channels detection

EOG channels are excluded from the dataset at this step since they are likely to be considered as artifacts by the pipeline. Additionally, in preparation for the detection of bad channels, we removed portions of the continuous dataset that were not part of the actual trials to avoid taking them into account for the detection of abnormal channel behavior. To that purpose, 4 criteria are inspected:

- **Deviation criterion**. Find channels with extreme amplitudes. Extreme amplitudes are the sign of channels affected by large artifacts, suffering from poor contact with the scalp, *etc*...
- **Noisiness criterion**. Find channels with large high-frequency power. The signal of interest obeys a $1/f$ power function, therefore channels exhibiting abnormal power in the high-frequency band are likely to contain unusable signal.
- **Correlation criterion**. Find channels lacking correlation with any other channels. Because of scalp electrical conduction, channels should have a high level of correlation. When a channel has a signal very different from its neighbors, it is likely to be dysfunctional.
- **Predictability criterion**. Find channels lacking predictability by other channels. When group of channels are dysfunctional together, they might pass the previous criterion. A prediction drawn from other channels (not necessarily next to each other) should also respect a certain level of correlation with the original channel (again because of volume conduction).

We implemented this step with the `findNoisyChannels` function, taken from the PREP pipeline (Bigdely-Shamlo et al., 2015). We set parameters numerical values according to default recommendations from Bigdely-Shamlo et al. (2015).

D.2.2 Noisy temporal segment detection

The detection and removal of noisy temporal segments is particularly important for ICA decomposition as some periods affected by general artifacts may be interpreted as single ICs by the ICA algorithm (J. R. da Cruz et al., 2018; Delorme et al., 2012). Some portions of the continuous dataset were irrelevant to the scientific questions of this experiment (*e.g.*, disorientation phases). In our experiment, they are not necessarily noisier than other portions: for example, in disorientation phases, the participant walks but keeps his eyes closed and head relatively steady. This may be a particularly interesting situation to isolate artifacts generated by walking that will be similarly observed in the trials, in a messier situation. Hence, the possibility to use these portions was kept open (if they are not rejected by the noisiness detection), unlike for bad channels detection.

The BeMoBIL pipeline introduces an additional step before the actual detection of noisy temporal segments: artifacts are isolated and excluded from eye movements. The motivation for this lies in the fact that eye related artifacts yield large amplitude variations in the signal, hiding other artefacts to most metrics used for noisiness detection. Eye components are identified with ICA decomposition (AMICA, Palmer et al. 2008) and automatic IC labelling (ICLabel, Pion-Tonachini et al. 2019). To save computational time, we selected a smaller portion of the data to train the AMICA algorithm. This portion corresponded to the exploration phase plus the long baselines. We chose these phases because (1) they are equally defined for all participants; (2) their total duration (9 min) seemed suitable for training the ICA model in reasonable computational time; (3) they should provide examples of a variety of eye-related artifacts: blinks and slow eye movements when the participant finds himself immersed in the dark, large and fast eye movements, saccades to objects (paired with head movements) in the exploration phase. Eventually, we rely on the prediction given by the ICLabel algorithm to automatically identify eye components. Any IC for which the prediction exclusively exceeds the 'Eye' threshold is considered as an eye component. All eye components contribution to the channel-based dataset are removed with the `pop_subcomp` function from EEGLAB.

After this step, we band-pass filter the continuous stream between 1 and 40 Hz and then epoch the data into non-overlapping windows of 1 s. For each of these epochs, we compute 3 different quantities to evaluate their noisiness.

I. **Mean signal of the epoch** (averaged over channels and time). Large values point towards general impedance inflation or large artifacts affecting a large proportion of channels.

II. **Channel standard deviation (SD) of epoch mean**. This is a simple measure of channel heterogeneity in the epoch. Large values indicate that some channels are affected by artifacts at an individual level in this period of time.

III. **Mahalanobian distance (MD) of epoch mean**. MD is a more robust estimation of channel heterogeneity than channel SD since it considers the variances and covariances between channels. Large values are also indicative of a noisy epoch.

Those quantities form a single score computed with a weighted sum giving more importance to the MD [w(I) = 1; w(II) = 1; w(III) = 2]. Then the epochs are sorted according to their score and the 15% highest scores are pinned for removal. Neighboring noisy epochs are merged to form blocks of rejection. Finally, each block is extended by 200 ms on both sides to account for artifact contamination of neighboring sections. We set parameters numerical values according to default recommendations from the authors of the pipeline.

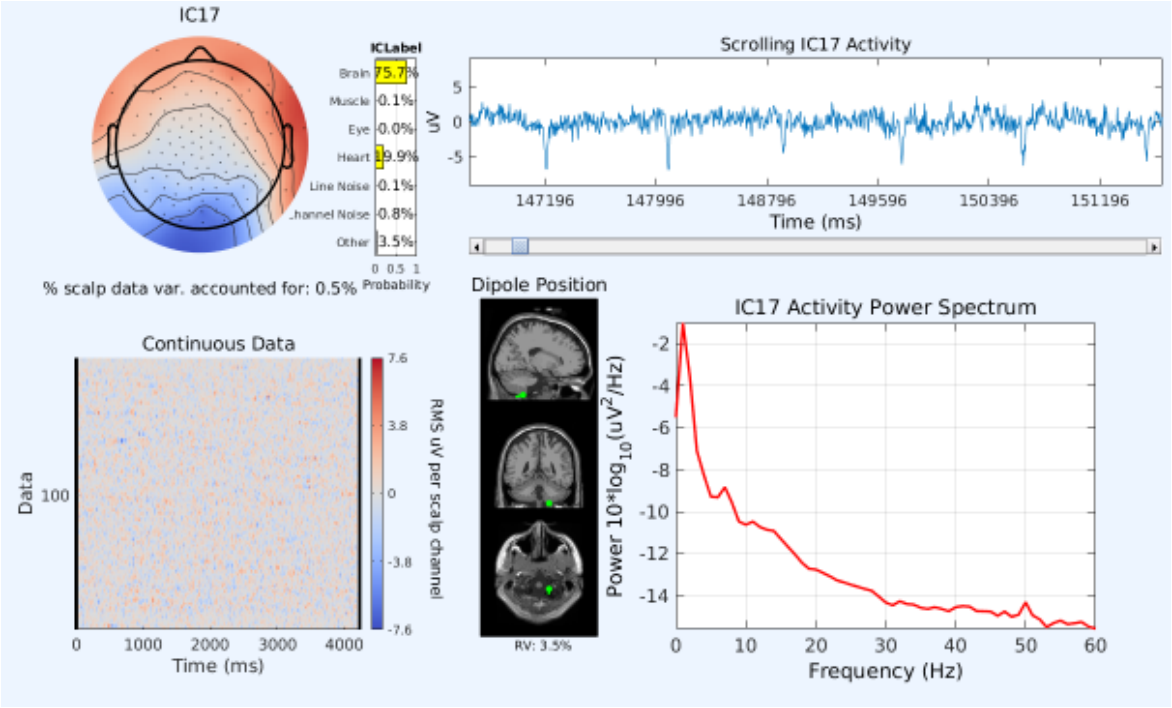

Figure D.3: Example of IC manual inspection during the assignment of IC labels. This IC from participant P09 would have been assigned to the Brain class without manual inspection. The IC was eventually labelled 'Heart' by the experimenter (heart beat clearly identifiable, gradient shape activation map and very deep equivalent current dipole). This panel was extracted with the `pop_prop_extended` EEGLAB function.

D.3 Pipeline comparison

D.3.1 Pipeline evaluation

To compare the performance of the BeMoBIL and the APP (J. R. da Cruz et al., 2018) pipelines, we evaluated different metrics of the preprocessing process.

First, we inspected cleaning metrics: number of channels removed, percentage of data assigned to noisy temporal segments, percentage of brain labels among the retrieved ICs and the meaningfulness of these ICs quantified by the explained percentage of variance in the overall decomposition.

Second, as introduced by Delorme et al. (2012), we chose 2 metrics to evaluate how well ICA achieved its independent decomposition objective.

- Mutual information reduction (MIR). It measures the difference between the mutual information in the original dataset (EEG channels) and the mutual information in the post-ICA dataset (ICs).
- Mean remaining pairwise mutual information (PMI). The mutual information between a pair of ICs averaged over all pairs.

We employed non-parametric statistical tests to evaluate the pipelines against each other. When directly comparing the 2 main pipelines, we used the Wilcoxon signed rank test (WSRT) to assess the equality of medians (paired observations) and the Brown-Forsythe test (BFT) to assess the equality of spreads around median. We set the alpha level for significance at $p < 0.01$ for more conservative results.

D.3.2 Comparison results

We present the principal metrics for pipelines comparison on Figure **D.4**.

We first inspected the outcome of the cleaning steps where pipelines implemented different methods. There was no significant difference (WSRT: $p = 0.12$) between the median number of channels removed by each pipeline (Figure **D.4a**), around 5 channels per subject. However, we found that the artefactual channel detection performed by the BeMoBIL pipeline was significantly more regular across subjects, with a distribution exhibiting a lower spread along the median than APP pipeline (BFT: $p = 0.005$). Moreover, the pipelines performed very different channel rejections: excluding the 3 subjects where the APP pipeline did not find any channels to reject, the median common percentage of rejection (expressed with respect to the pipeline rejecting less channels) is 33%. A detailed inspection of individual rejection criteria shows that the different implementation of similar criteria has a great impact: the deviation criterion as defined in the APP pipeline is significantly more sensitive than in the BeMoBIL pipeline (WSRT: $p = 2e{-}4$; Figure **D.4c**) while we observe the opposite effect for the implemented correlation criterion ($WSRT$: $p = 3e{-}3$, Figure **D.4d**).

On the contrary, we observed a significantly different cleaning behavior between pipelines at the bad temporal segment detection step (Figure **D.4b**). The APP pipeline rejected a median of about 5% of the total recording time per subject, against 17.5% for the BeMoBIL

pipeline (WSRT: $p = 3e{-}5$). The variability around this median is also significantly different between the pipelines (BFT: $p = 2e{-}5$) with a greater variability from APP than from BeMoBIL. A median of 80% of the time portions rejected by the APP pipeline were also rejected by the BeMoBIL pipeline.

Subsequently, we investigated the effect of each pipeline on the efficiency of ICA algorithm, measured by the reduction of mutual information. On a pairwise level, the mean remaining PMI (Figure **D.4e**) revealed a significantly greater performance of ICA after cleaning the data with the BeMoBIL pipeline than with the APP pipeline (WSRT: $p = 3e{-}5$). We observe the same tendency at the scale of the global dataset (MIR, Figure **D.4f**) but with no significant difference (WSRT: $p = 0.14$).

In conclusion, the BeMoBIL pipeline demonstrated more robustness and conservativeness than the APP pipeline in the artefact detection steps. The underlying adaptability proposed by APP pipeline is not advisable as its performance proved to be very inconsistent across participants. When released, this pipeline had not been tested on mobile data (J. R. da Cruz et al., 2018) and the particularities of such recordings, prone to withhold a large spectrum of unusual artifacts (related to gait, large head movements, cable pulling,...) had not been considered. More importantly, according to the mutual information reduction metrics, the BeMoBIL pipeline provided a better preparation for the ICA decomposition than APP pipeline, enabling a greater independence between the resulting ICs.

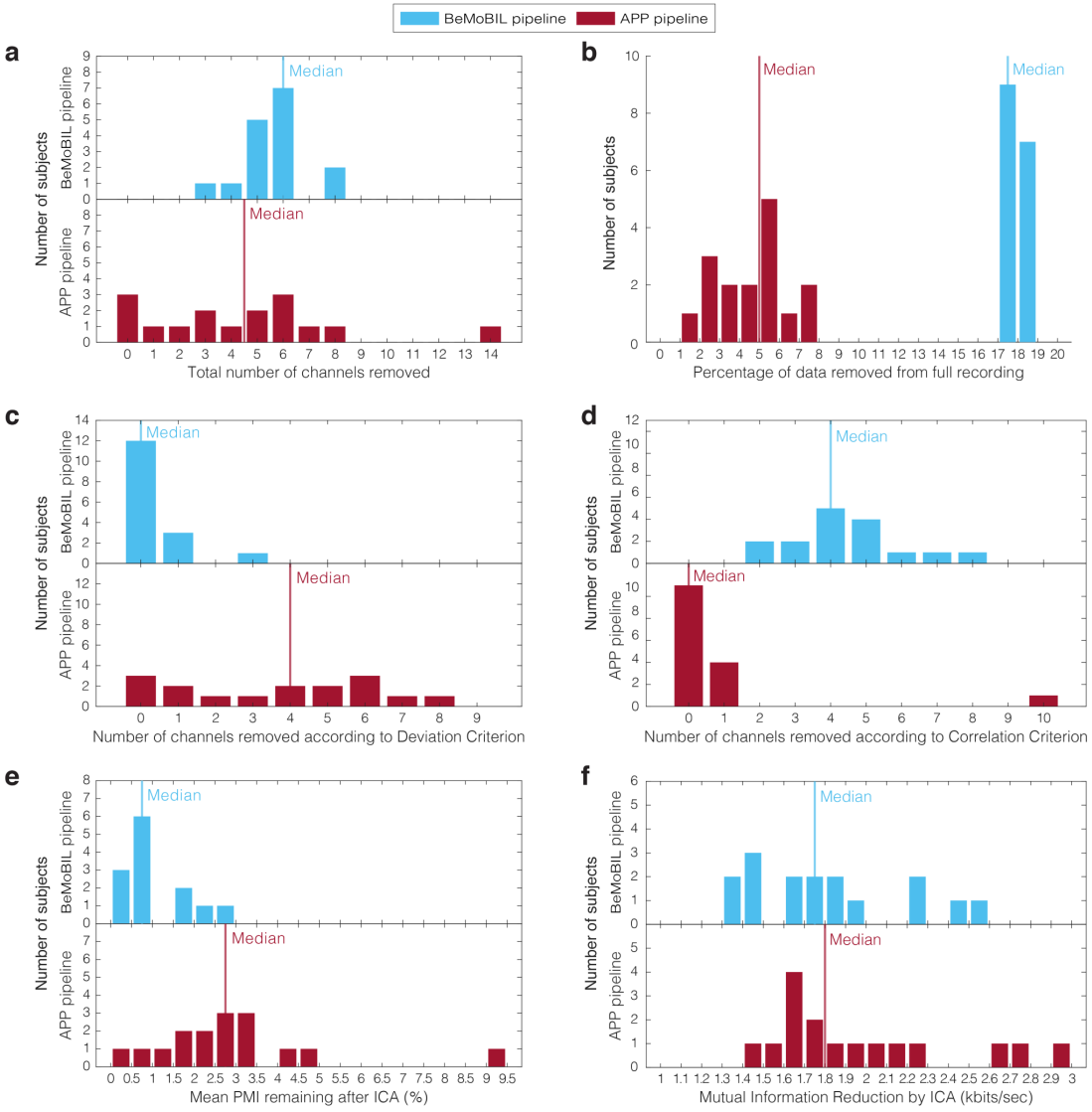

Figure D.4: Pipeline comparison metrics. (**a**) **Artefactual channels outcome.** Histogram plots showing the distribution of number of artefactual channels identified by each pipeline for each subject ($N = 16$). WSRT (BeMoBIL-APP): $U = 77.5$; $p = 0.12$. BFT: $F(1;30) = 9.10$; $p = 0.005$. Subfigures (**c**) and (**d**) show the detail of this identification depending on the criteria used: the *deviation criterion* (**c**) and the *correlation criterion* (**d**) are implemented differently in the pipelines. (**b**) **Temporal artefacts detection outcome.** Histogram plots showing the distribution of the percentage (with respect to total recording time) of time segments detected as artefactual by each pipeline for each subject ($N = 16$). WSRT (BeMoBIL-APP): $U = 136$; $p = 3e{-}5$. BFT: $F(1;30) = 24.28$; $p = 2e{-}5$. (**e**) **Remaining pairwise mutual information after ICA decomposition.** Histogram plots showing the distribution of the mean remaining PMI for the ICA decomposition after each pipeline. For each subject, we first computed the PMI of all pairs (separately in the channel and the component spaces) and then averaged over all pairs in each space. Remaining PMI is the ratio of ICs mean over channels mean, presented as a percentage. WSRT (BeMoBIL-APP): $U = 0$; $p = 3e{-}5$. BFT: $F(1;30) = 2.37$; $p = 0.13$. (**f**) **Mutual information reduction achieved by ICA decomposition.** Histogram plots showing the distribution of the MIR for the ICA decomposition after each pipeline. MIR is the difference of global mutual information contained in the dataset between the IC representation and the channel representation. WSRT (BeMoBIL-APP): $U = 39$; $p = 0.14$. BFT: $F(1;30) = 0.19$; $p = 0.67$.

D.4 Choice of the clustering design parameters

D.4.1 Designs definition - Parameters inspected

To inspect the influence of k-means clustering algorithm parameters, we compared four sets of parameters: number of formed clusters could alternatively be 50 or 60 and threshold for outliers was either 3 or 4 SD. Setting the number of clusters below the number of ICs per participant is common practice (Gramann et al., 2018; Luu et al., 2017b; Nordin et al., 2019) as there is no guarantee for the activity associated with a cortical region to be represented by a unique IC. Additionally, we evaluated the best clustering solution with respect to four different possible retrosplenial complex (RSC) coordinates as region of interest (ROI). We took the first location (RSC1, $[0, -45, 10]$) from Gramann et al. (2018), the second one (RSC2, $[0, -56, 9]$) from C.-T. Lin et al. (2015), the third one (RSC3, $[0, -47, 7]$) from Shine et al. (2016) and we chose the last one close to the anatomical region BA30 (RSC4, $[0, -55, 15]$). We set the first coordinate (x) to 0 because we did not have any expectation for lateralization. Coordinates are expressed in MNI format.

D.4.2 Metrics for ranking solutions within design

For each design, we scored the clustering solutions following the procedure described in Gramann et al. (2018). For each of the 10000 clustering solutions, we first identified the cluster whose centroid was closest to the target ROI. Then, we inspected it using 6 metrics: (1) number of participants represented in the cluster, (2) ratio of ICs per participant, (3) cluster spread (normalized to the number of ICs in the cluster), (4) mean residual variance (RV), (5) distance between cluster centroid and ROI coordinates and (6) Mahalanobian distance to the median of the solutions. We combined these metrics (after normalization) in a single score using a weighted sum [w1=2, w2=-3, w3=-1, w4=-1, w5=-3, w6=-1] and eventually clustering solutions were ranked according to their score.

D.4.3 Metrics for design comparison

We compared designs (*i.e.* set of parameters) based on the evaluating metrics for their highest rank solution and the stability of these metrics across the 11 best ranking solutions. We computed a design score out of the evaluation metrics for the highest rank solution, normalized across the 16 designs, with the same weights (Equation **D.1**). For each metric, we also assessed how stable the value of the highest rank solution was among the 10 following solutions found with the same design parameters, using the variability index in Equation **D.2**. We summarized the overall variability with a single score computed from the weighted average of the variability for each measure (Equation **D.3**). Finally, we selected the design with 50 clusters, 3 SD as threshold for outliers and RSC4 set of coordinates for target ROI.

D.4.3.1 Equation D.1

Summary solution score.

$$
\begin{aligned}
SCORE(\boldsymbol{D}_i) &= \sum_{j=1}^{6} \boldsymbol{w}_j \times \boldsymbol{M}_j^{normalized} \\
\text{with } \boldsymbol{D}_i &= \text{design } i, \\
\boldsymbol{M}_j^{normalized} &= \text{measure } j \text{ normalized across designs}, \\
\boldsymbol{w}_j &= \text{ weigth for measure } j
\end{aligned}
\tag{D.1}
$$

D.4.3.2 Equation D.2

Variability index assessing the stability of a best rank solution measure across the following best ranked solutions.

$$
\begin{aligned}
VAR_{11}(\boldsymbol{M}_i) &= 100 \times \frac{mean_{j=2\rightarrow 11}(|\boldsymbol{M}_i(\boldsymbol{Sol}_j) - \boldsymbol{M}_i(\boldsymbol{Sol}_1)|)}{\boldsymbol{M}_i(\boldsymbol{Sol}_1)} \\
\text{with } \boldsymbol{M}_i &= \text{measure } i, \\
\boldsymbol{Sol}_j &= \text{solution of rank } j
\end{aligned}
\tag{D.2}
$$

D.4.3.3 Equation D.3

Summary variability index.

$$
\begin{aligned}
VAR(\boldsymbol{D}_i) &= \frac{\sum_{j=1}^{6} |\boldsymbol{w}_j| \times VAR_{11}(\boldsymbol{M}_j)}{\sum_{j=1}^{6} |\boldsymbol{w}_j|} \\
\text{with } \boldsymbol{D}_i &= \text{design } i, \\
\boldsymbol{M}_j &= \text{measure } j, \\
\boldsymbol{w}_j &= \text{ weigth for measure } j
\end{aligned}
\tag{D.3}
$$

D.4.4 Choice of clustering parameters

We present the scores comparing the different clustering parameters in supplementary Table 3. Increasing the SD threshold (σ in the table) for outliers unequivocally yield worse solutions for this dataset, mainly due to the fact that the 1 : 1 ratio between number of ICs and number of participants is lost. Within designs with 3 SD threshold, RSC1 set of coordinates outputted very singular solutions, with fewer participants than other ROIs and associated with a high variability score indicating that those solutions were not representative of the pool of best ranks solutions for these designs. The solutions coming from designs with other ROIs were generally more stable. RSC2, RSC3 and RSC4 solutions retrieved almost identical clusters but the set of coordinates consistently closest to the centroid of this cluster was RSC4. We therefore opted for a design with this parameter. The remaining 2 designs (50 or 60 clusters with 3 SD and RSC4) were associated to similar scores (highest ones amongst the 16 designs) and variability scores (low variability in each case). We eventually chose the

50 clusters design to favor the analysis of bigger clusters, potentially regrouping ICs from a larger share of participants and therefore more representative of our population. Choosing the RSC coordinates without any reference, has to be put in perspective with the high variability across literature of RSC functional location (Epstein, 2008) and the poorer spatial resolution of source localization with respect to fMRI scans.

Design			Measures															
Nb. of clusters	σ	ROI	Nb. of Participants		Mean IC/Part.		Cluster spread		Mean RV (%)		Centroid-ROI distance		Mahalanobis distance		*SCORE*		*VAR*	
			BEST	VAR_{11}	BEST	VAR_{11}	BEST	VAR_{11}	BEST	VAR_{11}	BEST	VAR_{11}	BEST	VAR_{11}	value	rank	value	rank
60	3	RSC1	5	66	1	0	171.6	20.4	3.29	10.6	8.05	48.9	29.63	43.8	-3.681	3	32.145	16
60	3	RSC2	12	2.5	1	1.5	215	1.7	4.36	1.3	18.11	1.6	9.75	5.9	-3.744	4	2.117	1
60	3	RSC3	12	18.3	1	0.8	215	6.6	4.36	7.8	18.86	13.8	9.16	92	-3.844	7	16.99	13
60	3	RSC4	12	2.5	1	1.5	215.5	1.7	4.11	6.7	13.23	1.9	11.66	15.5	-2.98	1	3.575	2
50	3	RSC1	9	27.8	1	3.3	213.3	2.2	3.58	22.8	12.86	23.7	25.22	40.9	-3.798	6	18.404	14
50	3	RSC2	12	0.8	1	7.4	215	2.2	4.36	2.2	18.11	2.4	10.46	10.7	-3.768	5	4.207	5
50	3	RSC3	12	2.5	1	5	215	1.5	4.36	2.5	18.86	3.3	16.83	18.2	-4.103	8	4.745	7
50	3	RSC4	12	0.8	1	7.4	215	2.2	4.36	2.2	13.1	1.3	10.84	10.1	-2.985	2	3.855	4
60	4	RSC1	12	5.8	1.083	2.2	246.5	7.4	3.87	13.5	14.19	11.1	11.76	9.8	-4.828	10	7.48	10
60	4	RSC2	13	7.7	1.077	0.6	224.8	2.4	4.52	1.2	17.98	1.7	21.47	21	-5.512	13	4.255	6
60	4	RSC3	12	4.2	1.083	2.1	246.5	8	3.87	14.9	16.84	7.4	11.98	7.6	-5.258	12	6.109	8
60	4	RSC4	13	7.7	1.077	0.6	224.8	2.4	4.52	1.2	12.98	0	19.47	21.2	-4.649	9	3.811	3
50	4	RSC1	11	11.8	1.091	5	238.9	17.1	3.75	16.4	13.63	15.5	18.42	36.5	-5.24	11	14.108	12
50	4	RSC2	13	13.1	1.154	4.2	234	8.7	4.49	4.6	18.46	7.6	24.33	16.3	-7.214	16	8.282	11
50	4	RSC3	8	40	1.125	4.8	255	20.6	4.18	12.3	11.02	44.4	16.58	41.8	-6.13	15	27.483	15
50	4	RSC4	13	9.2	1.154	6.4	234	11.4	4.49	4	13.19	2.7	12.4	13.3	-5.974	14	6.761	9

Table D.3: Measures for the best solution outputted by each clustering design. The first 3 columns introduce the clustering design parameters (see Section **D.4.1**), namely the target number of clusters, the outliers' threshold and the ROI coordinates. The middle 6 columns show the evaluation of each design along a single metric, as presented in the Section **D.4.2**. BEST sub-column corresponds to the metric value associated to the best of the 10000 solutions for the given design parameters. VAR_{11} sub-column corresponds to a variability index assessing the stability of a best rank solution measure across the following 10 best ranked solutions (see Equation **D.2**). The last 2 columns present summary scores aggregating the weighted contribution of all metrics to the ranking of design parameters. *SCORE* column corresponds to the summary solution score (see Equation **D.1**) and *VAR* column corresponds to the summary variability index (see Equation **D.3**). The rank sub-column evaluates the ordering of clustering parameters according to the given summary column (ranked from 1 to 16 with 1 associated to the best performance).

Clust. ID	Nb. allo. part.	Nb. allo. ICs	Mean Position			Mean dist. to centroid (mm)	Mean RV	SD RV	Talairach Client: Closest Gray Matter region						Kept for later analysis
			x	y	z				Level 1	Level 2	Level 3	Level 4	Level 5	Range (mm)	
1	10 (12)	10 (12)	7.67	-46.84	24.47	13.6	4.4%	2.4%	Right Cerebrum	Limbic Lobe	Posterior Cingulate	Gray Matter	Brodmann area (BA) 23	2	YES
2	11 (12)	21 (22)	15.19	-81.61	35	9.8	6.4%	2.4%	Right Cerebrum	Occipital Lobe	Cuneus	Gray Matter	BA 19	0	YES
3	9 (11)	13 (15)	38.96	-50.54	32.91	10.9	7.3%	4.1%	Right Cerebrum	Parietal Lobe	Supramarginal Gyrus	Gray Matter	BA 40	4	YES
4	11 (12)	14 (15)	-2.38	9.63	21.89	15.6	3.5%	3.1%	Left Cerebrum	Limbic Lobe	Anterior Cingulate	Gray Matter	BA 33	2	YES
5	11 (13)	15 (17)	33.26	-9.74	52.04	14.6	7.1%	5.1%	Right Cerebrum	Frontal Lobe	Precentral Gyrus	Gray Matter	BA 6	1	YES
6	10 (11)	12 (13)	-37.34	-27.53	48.87	11.7	6.5%	4.4%	Left Cerebrum	Parietal Lobe	Postcentral Gyrus	Gray Matter	BA 3	0	YES
7	8 (9)	10 (11)	-10.5	-55.98	39.15	10.7	5.4%	2.1%	Left Cerebrum	Parietal Lobe	Precuneus	Gray Matter	BA 7	2	NO
8	8 (8)	8 (8)	26.04	29.69	26.2	14.3	5.2%	2.0%	Right Cerebrum	Frontal Lobe	Middle Frontal Gyrus	Gray Matter	BA 9	4	NO
9	8 (8)	11 (11)	1.33	-30.51	60.23	11.5	7.1%	5.1%	Right Cerebrum	Frontal Lobe	Paracentral Lobule	Gray Matter	BA 6	3	NO
10	8 (10)	11 (13)	4.28	-17.39	0.35	15.4	5.2%	4.2%	Right Cerebrum	Sub-lobar	Thalamus	Gray Matter	*	0	NO
11	7 (8)	7 (8)	-30.74	-58.97	23.64	13.1	6.9%	3.0%	Left Cerebrum	Temporal Lobe	Middle Temporal Gyrus	Gray Matter	BA 39	3	NO
12	5 (7)	5 (7)	55.87	-20.08	-27.43	14.4	9.6%	1.9%	Right Cerebrum	Temporal Lobe	Fusiform Gyrus	Gray Matter	BA 20	1	NO

Table D.4: Selection among the 12 Brain clusters. For the rest of the analysis, we chose to keep only the clusters containing ICs from at least 9 out of the 14 allocentric participants ($\sim 65\%$). This table presents all 12 brain clusters retrieved from the clustering procedure described above. In the order of the columns from left to right: (1) Cluster ID (clusters 1 to 6 are presented in Figures **7.7** and **7.8** in the main document), (2) Number of allocentric participants (*resp.*, in parenthesis, total number of participants) presenting at least one IC in the cluster, (3) Number of ICs accumulated by allocentric (*resp.*, in parenthesis, all participants in the cluster), (4) Mean position of the cluster centroid in Talairach coordinates, (5) Mean distance of the cluster ICs to the centroid (mm), (6) Mean residual variance (%), (7) Standard deviation to the residual variance (%), (8) Closest gray matter region as located by the Talairach Client (Lancaster et al., 2000), (9) Decision to keep the clusters for the rest of the analysis. Cluster 1 to 6 were kept.

APPENDIX E

SUPPLEMENTARY MATERIAL
THE VERTICAL POSITION OF NAVIGATIONAL CUES DRIVES SCENE-SELECTIVE OSCILLATORY DYNAMICS THROUGHOUT ADULTHOOD

This appendix chapter presents the supplementary material planned to be attached to the work reported in Chapter **8**. It notably contains the event-related spectral perturbation (ERSP) activity in the scene-selective regions (SSRs) during the encoding trials, the results of the follow-up analysis in the alpha band, as well as complementary information about the participants.

E.1 Supplementary Results

E.1.1 ERSP activity in the ROIs

We conducted an ERSP analysis time-locked to the event of arriving at an intersection ($t = 0$ ms) and grouped by principal frequency bands (delta: < 4 Hz, theta: 4-8 Hz, alpha: 8-12 Hz, beta: 12-30 Hz, gamma: > 30 Hz). To summarize bilateral region of interest (ROI) activity, we averaged the source-reconstructed power spectrum from both hemispheres. We reported

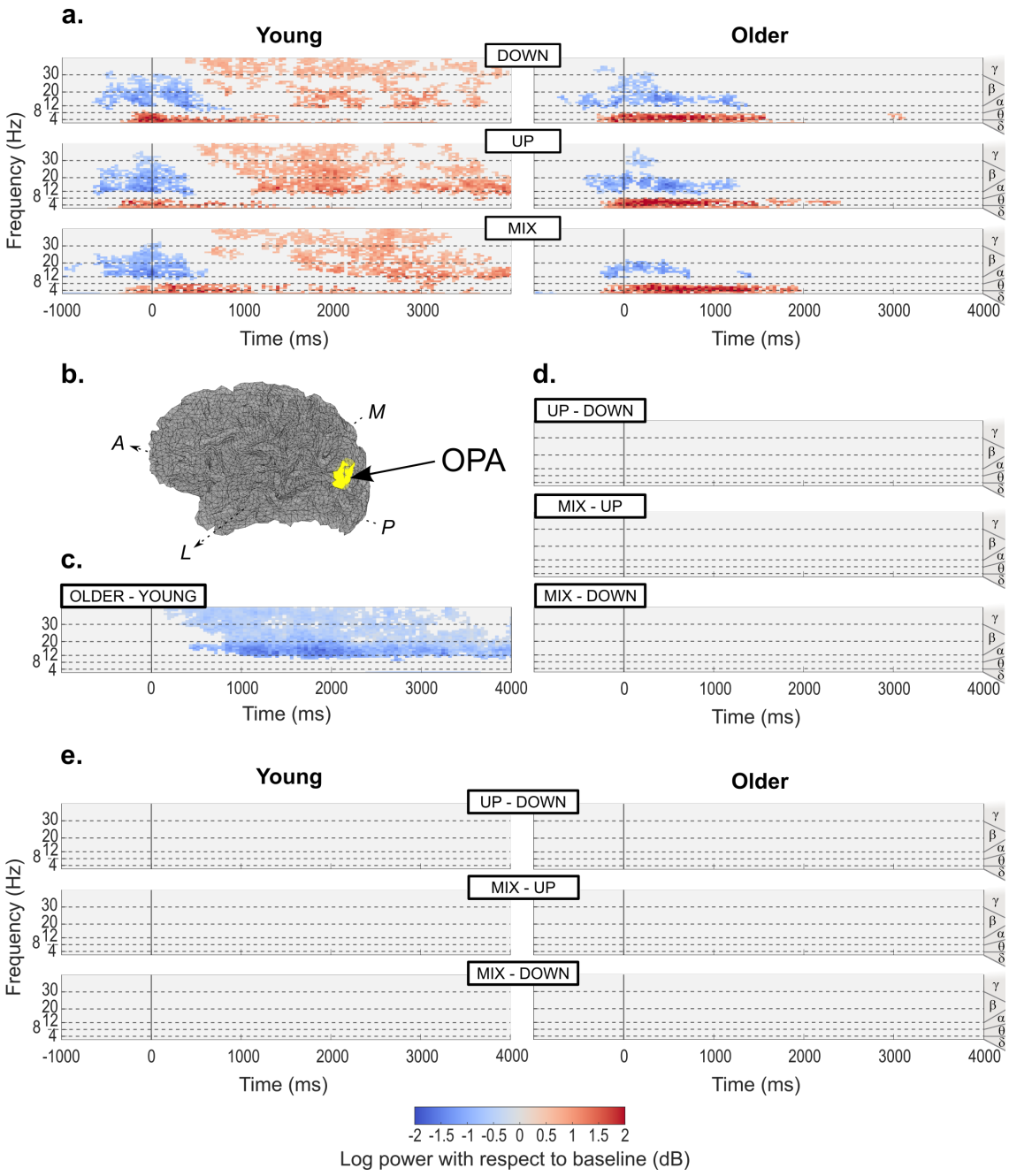

Figure E.1: ERSP activity time-locked to the event of arriving at an intersection in the encoding trials, reconstructed in the OPA. [Continued on next page]

Figure E.1: [On previous page] Activity merged from both hemispheric locations after source reconstruction. We examined delta (δ; < 4 Hz), theta (θ; 4-8 Hz), alpha (α; 8-12 Hz), beta (β; 12-30 Hz) and gamma (γ; > 30 Hz) frequency bands. We investigated all statistical differences with permutation tests based on the maximum cluster-level statistic using 1000 permutations. We used linear mixed-effects modeling to evaluate the statistical significance at the "pixel" level (spectral power at a given time-frequency pair) for a given permutation. **a**. Average activity per age group and condition baselined with the 2 seconds period prior to arrival at the intersection. We only display activity statistically different from surrogate baseline distribution ($p < 0.05$). **b**. Illustration of the localization of the left OPA overlaid on left hemisphere source space (midgray surface) in one young participant. A: Anterior; P: Posterior; M: Medial; L: Lateral. **c**. Differences between age groups, irrespective of conditions. We indicate the direction of the difference above each graph (*e.g.* for the graph entitled "OLDER-YOUNG", we subtracted the average signal for the young adults from the average signal for the older adults, such that a positive difference means more power in the older group than in the young group and a negative difference means less power in the older group than in the young group). We only display statistically significant differences ($p < 0.05$). **d**. Differences between conditions, irrespective of age groups. We only display statistically significant differences ($p < 0.0083$, Bonferroni-corrected for 3 two-sided comparisons). **e**. Differences between conditions within each age group. We only display statistically significant differences ($p < 0.0041$, Bonferroni-corrected for 6 two-sided comparisons).

average ERSPs baselined with the activity preceding the arrival at the level of an intersection. This baseline corresponds to participants passively navigating through a street that is devoid of any relevant spatial information. We computed ERSP statistical differences with permutation tests based on the maximum cluster-level statistic (Maris & Oostenveld, 2007) using 1000 permutations. We set the initial significance level to $p < 0.05$, and Bonferroni-corrected for variables with more than 2 levels.

E.1.1.1 Encoding trials

The investigated ERSP activity during the encoding trials relates to the perception of the intersection and the objects contained within it. We provided a fixed 4-second static observation period at each intersection to give participants enough time to scan the whole scene and encode the spatial relationships between intersections (Figure **8.1d**).

We found a strong synchronization in the delta/theta frequency band (2-8 Hz) across all ROIs in both age groups, starting 250 ms before event onset and sustained until $+2000$ ms (Figures **E.1a**, **E.2a**, and **E.3a**). In the MPA, this activity was significantly more pronounced for older adults compared to young adults. Indeed, we reported an increase in theta synchronization around the first second of observation, between $+400$ ms and $+1400$ ms (Figure **E.3c**). We observed no significant differences between conditions for this range of frequencies in any of the ROIs, neither across groups nor within groups (Figures **E.1d,e**, **E.2d,e**, and **E.3d,e**).

Commonly to both age groups and all ROIs (Figures **E.1a**, **E.2a**, and **E.3a**), we found a desynchronization in the beta band between -500 ms and $+500$ ms, around the event of arriving at the intersection. In the PPA, this desynchronization started slightly later, at around -250 ms, and it was mostly restricted to the lower beta band (12-20 Hz, Figure **E.2a**). The beta desynchronization persisted after $+500$ ms in the older group for all ROIs. In the young group, however, we observed an inversion leading to a power synchronization in the OPA and MPA and an interruption of the desynchronization in the PPA (Figures **E.1a**, **E.2a**, and **E.3a**). Notably, this significant age-related difference in the beta band was sustained until the end

of the 4-second window in the three ROIs (Figures **E.1c**, **E.2c**, and **E.3c**). Although in the PPA it remained mostly localized to the lower beta band (Figure **E.2c**), in the OPA and

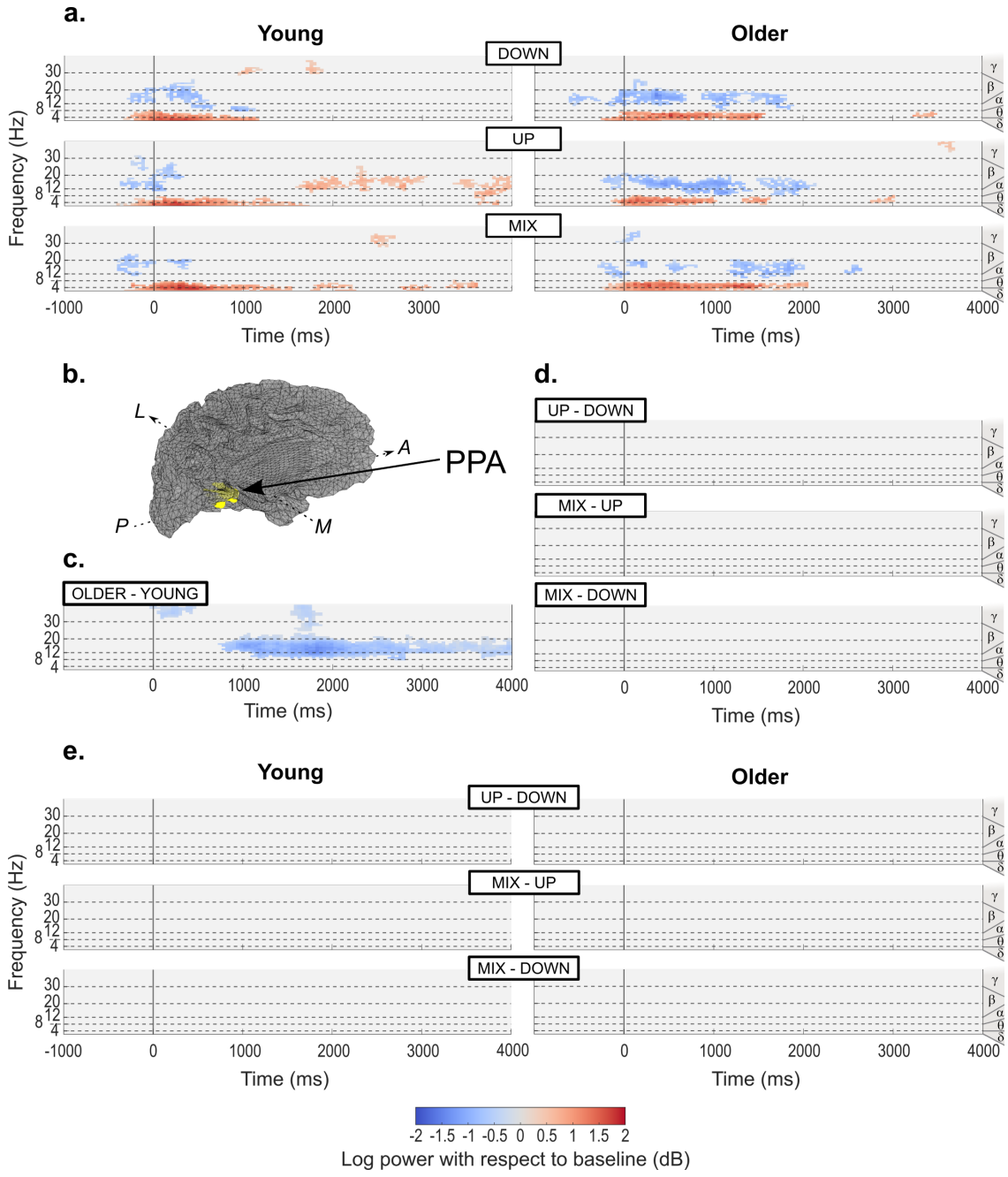

Figure E.2: ERSP activity time-locked to the event of arriving at an intersection in the encoding trials, reconstructed in the PPA. For further details, see Figure **E.1** legend. **a**. Average activity per age group and condition baselined with the 2 seconds period prior to arrival at the intersection. We only display activity statistically different from surrogate baseline distribution ($p < 0.05$). **b**. Illustration of the localization of the left PPA overlaid on left hemisphere source space (midgray surface) in one young participant. A: Anterior; P: Posterior; M: Medial; L: Lateral. **c**. Differences between age groups, irrespective of conditions. We only display statistically significant differences ($p < 0.05$). **d**. Differences between conditions, irrespective of age groups. We only display statistically significant differences ($p < 0.0083$, Bonferroni-corrected for 3 two-sided comparisons). **e**. Differences between conditions within each age group. We only display statistically significant differences ($p < 0.0041$, Bonferroni-corrected for 6 two-sided comparisons).

MPA it extended to the low gamma band (30-40 Hz; Figures **E.1c** and **E.3c**). The low gamma band activity remained significantly more synchronized in young participants than

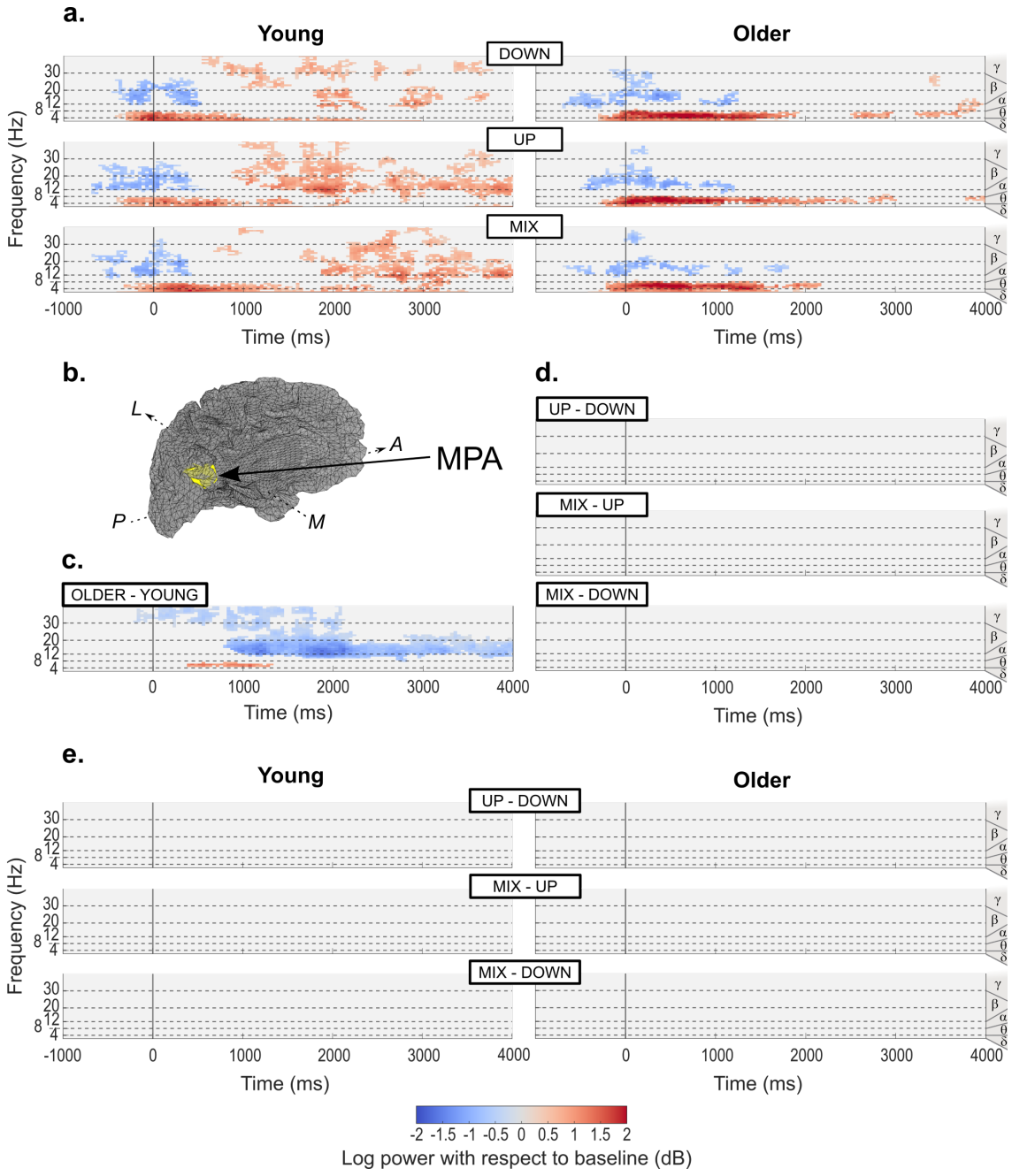

Figure E.3: ERSP activity time-locked to the event of arriving at an intersection in the encoding trials, reconstructed in the MPA. For further details, see Figure **E.1** legend. **a**. Average activity per age group and condition baselined with the 2 seconds period prior to arrival at the intersection. We only display activity statistically different from surrogate baseline distribution ($p < 0.05$). **b**. Illustration of the localization of the left MPA overlaid on left hemisphere source space (midgray surface) in one young participant. A: Anterior; P: Posterior; M: Medial; L: Lateral. **c**. Differences between age groups, irrespective of conditions. We only display statistically significant differences ($p < 0.05$). **d**. Differences between conditions, irrespective of age groups. We only display statistically significant differences ($p < 0.0083$, Bonferroni-corrected for 3 two-sided comparisons). **e**. Differences between conditions within each age group. We only display statistically significant differences ($p < 0.0041$, Bonferroni-corrected for 6 two-sided comparisons).

in older participants from event onset until +3500 ms in the OPA (Figure **E.1c**), and from event onset until +2000 ms in MPA (Figure **E.3c**). We observed no significant differences between conditions, whether across groups or within groups, for this range of frequencies in any of the ROIs (Figures **E.1d,e**, **E.2d,e**, and **E.3d,e**).

E.1.1.2 Test trials

E.1.1.2.1 Mean ERSP activity per frequency band across ROIs

In a follow-up analysis of activity during the test phase, we sought to compare time-resolved spectral activity between ROIs. We grouped the ERSP activity by frequency band: delta/theta (2-8 Hz), alpha (8-12 Hz), beta (12-30 Hz) and gamma (30-40 Hz). Within each frequency band we averaged the ERSPs over the spectral dimension, yielding a time-course of mean spectral activity for each ROI across conditions. We then performed pairwise statistical analysis with permutation tests based on the maximum cluster-level statistic using 1000 permutations. We set the significance level to $p < 0.000104$, Bonferroni-corrected for 24 two-sided comparisons. Here, we display results pertaining to the alpha band due the low activity observed in this frequency range (Figure **E.4**).

In the alpha band, we observed a strong desynchronization starting 1s prior to arrival at the intersection and peaking at around +250 ms in the young group (Figure **E.4a**). This early

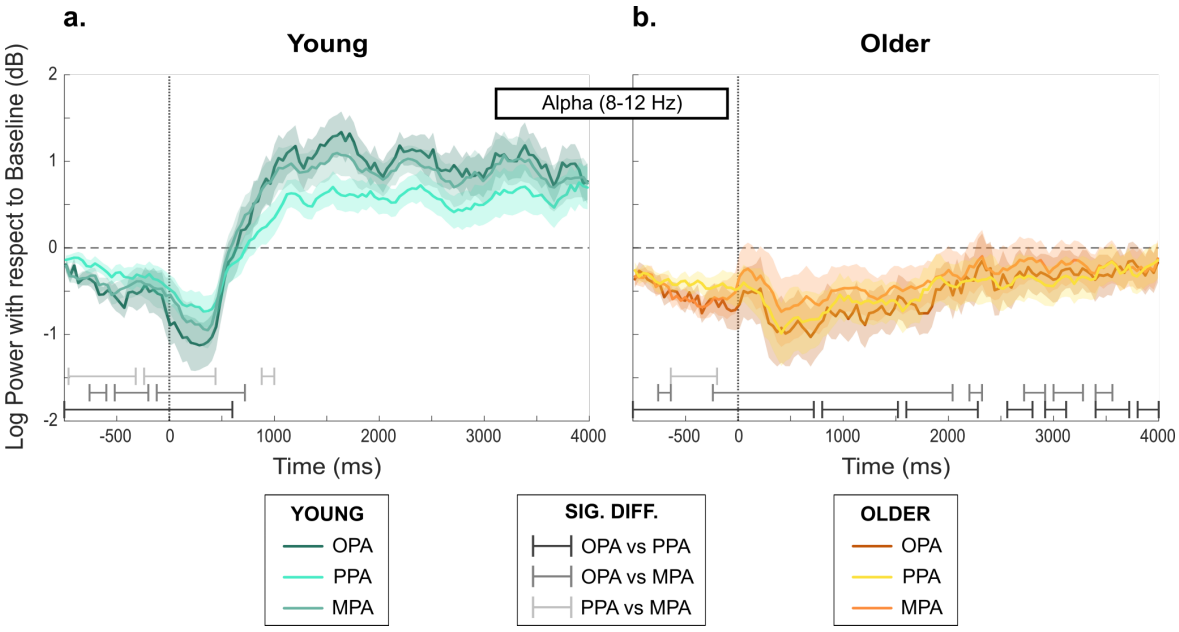

Figure E.4: Mean ERSP activity per ROI in the alpha band (8-12 Hz) in the test trials across age groups. Bold lines represent the mean ERSP activity per ROI, averaged on the spectral dimension and across all test trials in the corresponding age group. Shaded areas represent the standard error of the mean computed with average subject traces in each age group ($N = 21$ for each age group). The signal is time-locked to the event of arriving at an intersection ($t = 0$ ms). We investigated all statistical differences with paired permutation tests based on the maximum cluster-level statistic using 1000 permutations. To evaluate the statistical significance at the sample level (mean spectral power at a time point) for a given permutation, we used linear mixed-effects modeling. We examined pairwise differences between ROIs for each age group (6 comparisons). Significant differences reflect clusters with a Monte Carlo p-value below 0.00104 (Bonferroni-corrected for 24 two-sided comparisons) **a**. ERSP activity in the young group. **b**. ERSP activity in the older group.

alpha desynchronization differed across SSRs. It was the least pronounced in the PPA, and the most pronounced in the OPA, with the MPA in-between (Figure **E.4a**). Alpha activity in the older group was desynchronized over the entire 4-second window, with a peak around +500 ms (Figure **E.4b**). Desynchronization was overall more pronounced in the OPA than the MPA, particularly in the first 2 seconds after arrival at the intersection (Figure **E.4b**). Similarly to young adults, the PPA was less desynchronized than the OPA and MPA in the 1-second period prior to arriving at the intersection (Figure **E.4b**).

E.2 Supplementary Methods

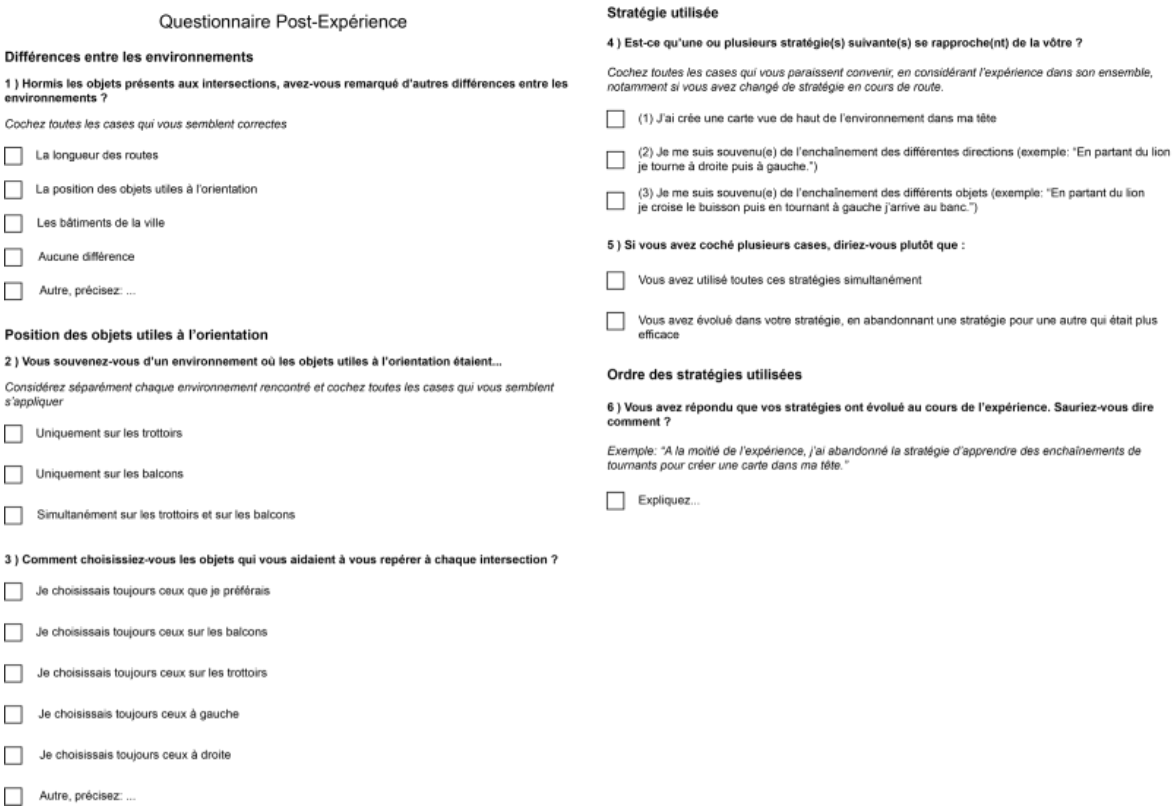

Questionnaire Post-Expérience

Différences entre les environnements

1) Hormis les objets présents aux intersections, avez-vous remarqué d'autres différences entre les environnements ?

Cochez toutes les cases qui vous semblent correctes

- ☐ La longueur des routes
- ☐ La position des objets utiles à l'orientation
- ☐ Les bâtiments de la ville
- ☐ Aucune différence
- ☐ Autre, précisez: ...

Position des objets utiles à l'orientation

2) Vous souvenez-vous d'un environnement où les objets utiles à l'orientation étaient...

Considérez séparément chaque environnement rencontré et cochez toutes les cases qui vous semblent s'appliquer

- ☐ Uniquement sur les trottoirs
- ☐ Uniquement sur les balcons
- ☐ Simultanément sur les trottoirs et sur les balcons

3) Comment choisissiez-vous les objets qui vous aidaient à vous repérer à chaque intersection ?

- ☐ Je choisissais toujours ceux que je préférais
- ☐ Je choisissais toujours ceux sur les balcons
- ☐ Je choisissais toujours ceux sur les trottoirs
- ☐ Je choisissais toujours ceux à gauche
- ☐ Je choisissais toujours ceux à droite
- ☐ Autre, précisez: ...

Stratégie utilisée

4) Est-ce qu'une ou plusieurs stratégie(s) suivante(s) se rapproche(nt) de la vôtre ?

Cochez toutes les cases qui vous paraissent convenir, en considérant l'expérience dans son ensemble, notamment si vous avez changé de stratégie en cours de route.

- ☐ (1) J'ai crée une carte vue de haut de l'environnement dans ma tête
- ☐ (2) Je me suis souvenu(e) de l'enchaînement des différentes directions (exemple: "En partant du lion je tourne à droite puis à gauche.")
- ☐ (3) Je me suis souvenu(e) de l'enchaînement des différents objets (exemple: "En partant du lion je croise le buisson puis en tournant à gauche j'arrive au banc.")

5) Si vous avez coché plusieurs cases, diriez-vous plutôt que :

- ☐ Vous avez utilisé toutes ces stratégies simultanément
- ☐ Vous avez évolué dans votre stratégie, en abandonnant une stratégie pour une autre qui était plus efficace

Ordre des stratégies utilisées

6) Vous avez répondu que vos stratégies ont évolué au cours de l'expérience. Sauriez-vous dire comment ?

Exemple: "A la moitié de l'expérience, j'ai abandonné la stratégie d'apprendre des enchaînements de tournants pour créer une carte dans ma tête."

- ☐ Expliquez...

Figure E.5: Post-experiment questionnaire (in French) given to participants as a Google form. The first section (*Différences entre les environnements*) relates to differences between environments and whether participants perceived them. The second section (*Position des objets utiles à lorientation*) relates to the position of objects at intersections and whether participants displayed any preferences. The third section (*Stratégie utilisée*) relates to the strategy employed by participants to find the goal. Finally, we only displayed the fourth section (*Ordre des stratégies utilisées*) to participants who had changed strategy during the experiment and asked them to explain this shift.

Participant	**ROI**					
YOUNG	**PPA**		**OPA**		**MPA**	
	R	L	R	L	R	L
1	[30, −34, −13]	[−30, −40, −10]	[36, −82, 32]	[−36, −85, 32]	[15, −52, 23]	[−18, −61, 20]
2	[18, −40, −10]	[−27, −43, −10]	[33, −88, 23]	[−39, −82, 26]	[15, −58, 8]	[−18, −61, 8]
3	[27, −40, −13]	[−24, −49, −7]	[36, −85, 26]	[−33, −85, 14]	[15, −52, 11]	[−18, −58, 14]
4	[24, −40, −13]	[−24, −46, −7]	[36, −76, 38]	[−27, −85, 32]	[18, −52, 17]	[−18, −55, 14]
5	[24, −40, −10]	[−24, −46, −7]	[36, −76, 35]	[−30, −85, 32]	[24, −55, 14]	[−24, −55, 8]
6	[27, −52, −7]	[−24, −52, −10]	[36, −79, 17]	[−30, −88, 20]	[18, −49, 11]	[−15, −55, 11]
7	[27, −46, −7]	[−30, −43, −7]	[33, −82, 23]	[−33, −82, 26]	[18, −52, 17]	[−15, −58, 20]
8	[27, −37, −13]	[−24, −43, −13]	[30, −85, 32]	[−33, −88, 29]	[18, −55, 20]	[−18, −61, 20]
9	[24, −46, −7]	[−24, −49, −16]	[36, −76, 23]	[−36, −82, 20]	[15, −49, 14]	[−15, −55, 17]
10	[27, −40, −10]	[−27, −43, −7]	[45, −76, 29]	[−39, −79, 26]	[21, −55, 17]	[−18, −58, 20]
11	[27, −52, −7]	[−24, −49, −10]	[36, −82, 32]	[−33, −82, 32]	[21, −58, 23]	[−15, −61, 20]
12	[27, −46, −7]	[−27, −46, −7]	[33, −79, 26]	[−33, −76, 20]	[21, −58, 14]	[−18, −52, 8]
13	[27, −40, −13]	[−24, −49, −13]	[42, −79, 26]	[−39, −82, 23]	[21, −52, 17]	[−21, −61, 14]
14	[24, −46, −10]	[−27, −49, −10]	[45, −76, 17]	[−36, −85, 29]	[27, −49, 11]	[−24, −61, 20]
15	[33, −58, −7]	[−27, −55, −7]	[39, −73, 20]	[−36, −79, 23]	[21, −55, 14]	[−18, −58, 14]
16	[27, −43, −13]	[−21, −40, −10]	[39, −79, 26]	[−39, −76, 20]	[21, −55, 17]	[−18, −52, 8]
17	[24, −43, −13]	[−24, −46, −10]	[39, −82, 14]	[−39, −82, 14]	[15, −52, 8]	[−15, −55, 8]
18	[27, −46, −7]	[−24, −49, −7]	[33, −82, 26]	[−30, −82, 23]	[21, −58, 20]	[−18, −55, 17]
19	[27, −43, −10]	[−27, −46, −4]	[39, −79, 23]	[−33, −85, 23]	[21, −55, 14]	[−18, −55, 11]
20	[30, −46, −7]	[−30, −43, −10]	[33, −76, 35]	[−33, −79, 32]	[21, −52, 17]	[−18, −55, 17]
21	[27, −49, −16]	[−27, −46, −13]	[45, −76, 17]	[−42, −79, 20]	[18, −58, 20]	[−18, −55, 17]

Table E.1: Coordinates $[X, Y, Z]$ in the Montreal Neurological Institute (MNI)-152 space of the peak voxel (highest t-value) for the right (R) and left (L) scene-selective regions: PPA, OPA, and MPA for each young participant included in the study.

Participant	**ROI**					
OLDER	**PPA**		**OPA**		**MPA**	
	R	L	R	L	R	L
22	$[24,-40,-10]$	$[-27,-43,-10]$	$[33,-79,32]$	$[-33,-82,35]$	$[18,-52,17]$	$[-18,-61,23]$
23	$[30,-43,-10]$	$[-27,-43,-13]$	$[48,-79,17]$	$[-51,-76,11]$	$[18,-55,11]$	$[-27,-61,17]$
24	$[27,-52,-10]$	$[-27,-37,-16]$	$[36,-85,29]$	$[-30,-88,29]$	$[21,-55,17]$	$[-18,-58,20]$
25	$[27,-40,-10]$	$[-24,-37,-13]$	$[42,-79,23]$	$[-36,-82,23]$	$[18,-49,20]$	$[-12,-52,14]$
26	$[24,-40,-10]$	$[-24,-40,-13]$	$[36,-76,26]$	$[-33,-82,26]$	$[12,-52,11]$	$[-12,-55,8]$
27	$[24,-43,-10]$	$[-30,-37,-10]$	$[33,-85,32]$	$[-39,-82,29]$	$[18,-55,20]$	$[-21,-58,23]$
28	$[27,-37,-13]$	$[-27,-40,-10]$	$[45,-73,20]$	$[-33,-79,20]$	$[18,-52,17]$	$[-15,-61,17]$
29	$[30,-49,-4]$	$[-21,-40,-7]$	$[36,-85,32]$	$[-36,-85,29]$	$[15,-52,17]$	$[-21,-61,14]$
30	$[30,-34,-13]$	$[-27,-43,-10]$	$[39,-73,17]$	$[-33,-82,23]$	$[24,-55,20]$	$[-21,-61,20]$
31	$[30,-55,-10]$	$[-27,-40,-13]$	$[33,-76,26]$	$[-36,-85,26]$	$[27,-58,20]$	$[-18,-55,20]$
32	$[21,-40,-10]$	$[-24,-49,-13]$	$[36,-79,32]$	$[-33,-85,29]$	$[18,-55,20]$	$[-15,-58,20]$
33	$[27,-43,-13]$	$[-21,-43,-13]$	$[30,-82,26]$	$[-21,-88,29]$	$[18,-58,23]$	$[-12,-61,14]$
34	$[24,-37,-10]$	$[-21,-37,-13]$	$[36,-79,26]$	$[-30,-85,23]$	$[18,-55,20]$	$[-15,-70,14]$
35	$[27,-40,-10]$	$[-27,-46,-7]$	$[36,-79,29]$	$[-33,-79,23]$	$[18,-55,20]$	$[-15,-61,14]$
36	$[24,-49,-10]$	$[-24,-43,-13]$	$[36,-85,29]$	$[-39,-85,29]$	$[12,-52,14]$	$[21,-58,20]$
37	$[27,-49,-13]$	$[-27,-52,-16]$	$[33,-82,35]$	$[-33,-79,35]$	$[21,-49,14]$	$[-18,-55,17]$
38	$[30,-40,-7]$	$[-24,-43,-4]$	$[39,-79,20]$	$[-36,-79,23]$	$[15,-49,11]$	$[-18,-52,11]$
39	$[30,-49,-10]$	$[-27,-43,-10]$	$[42,-82,23]$	$[-33,-79,26]$	$[12,-55,17]$	$[-15,-61,14]$
40	$[33,-34,-13]$	$[-24,-43,-7]$	$[39,-73,35]$	$[-36,-76,23]$	$[15,-55,11]$	$[-9,-55,8]$
41	$[27,-52,-7]$	$[-24,-46,-7]$	$[36,-82,29]$	$[-30,-88,26]$	$[21,-52,14]$	$[-18,-58,8]$
42	$[24,-55,-10]$	$[-27,-43,-7]$	$[30,-82,23]$	$[-30,-85,23]$	$[18,-55,17]$	$[-18,-55,23]$

Table E.2: Coordinates $[X,Y,Z]$ in the MNI-152 space of the peak voxel (highest t-value) for the right (R) and left (L) scene-selective regions: PPA, OPA, and MPA for each older participant included in the study.

Num epochs in encoding	UP	MIX	DOWN	Total
YOUNG	344	347	346	1037
OLD	350	343	349	1042
Total	694	690	695	2079

Table E.3: Number of epochs in the encoding phase used for the ERSP analysis, detailed by age group and condition.

Num epochs in test	UP	MIX	DOWN	Total
YOUNG	633	631	632	1896
OLD	663	672	675	2010
Total	1296	1303	1307	3906

Table E.4: Number of epochs in the test phase used for the ERSP analysis, detailed by age group and condition.

APPENDIX F

SUPPLEMENTARY MATERIAL
PARTIAL RECOVERY OF VISUAL FUNCTION IN A BLIND PATIENT AFTER OPTOGENETIC THERAPY

This appendix chapter presents the supplementary material attached to the published version of the article reported in Section 10.1. They are transcribed the same way they were accepted by the journal. Supplementary Videos (1 & 2), illustrating vision tests 1 & 2 respectively are also available online.

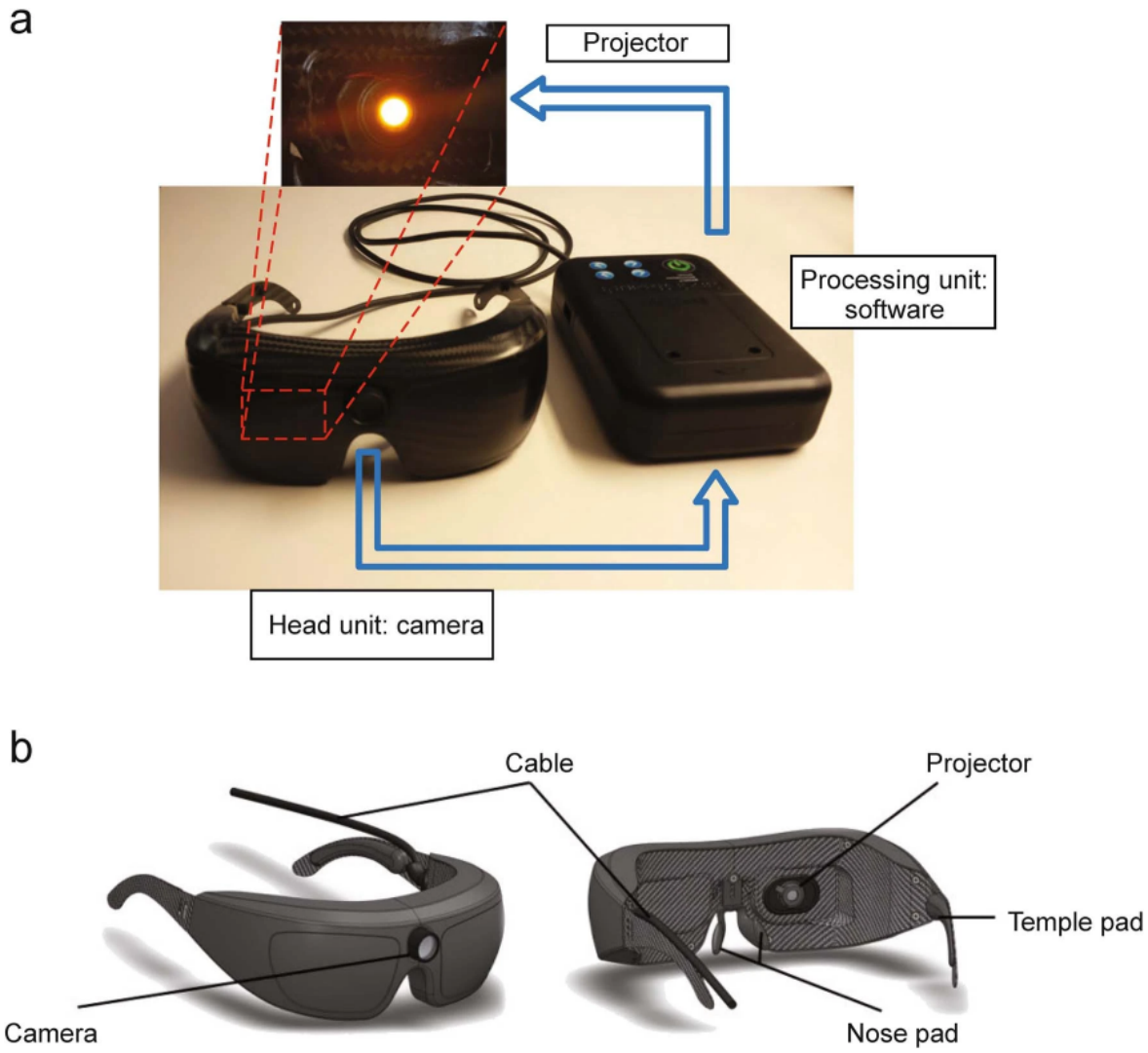

Figure F.1: Light-stimulating goggles. **a**. GS030-MD consists of two units connected by a high-speed link. The head unit (left) hosts the camera which acquires the natural scene in a stream of asynchronous address-events representing pixel coordinates of local relative light intensity changes. The processing unit (right) encodes the visual stream in real time and creates binary images that are sent to the projector in the head unit. The projector, which is also mounted on the head unit (top), is placed in front of the eye. **b**. Front and rear view of the head unit. The camera is placed at the center facing the outside world. The projector is placed in front of the treated eye, facing the eye, and can be moved horizontally so as to be placed precisely in front of the treated eyes pupil, since inter-pupillary distance varies between patients.

F.1 Safety Assessment

To assess safety, we performed combinations of five different tests during 15 patient visits over a period of 84 weeks. There were four visits before vector injection, one visit at injection, and ten visits after injection. The timing of the visits (in weeks) relative to vector injection was -4, -3, -2, -1, 0, 1, 2, 4, 9, 13, 17, 25, 38, 52, and 80, as shown in Supplementary Figure **F.2**.

(1) We performed ocular examinations at every visit. This consisted of slit-lamp examination before and after pupil dilation of eyelids, eyelashes, palpebral and bulbar conjunctiva, cornea, anterior chamber, lens, and vitreous; tonometry measurement of intraocular pressure before pupil dilation; and funduscopy after pupil dilation. On each of the 15 visits, the results of the ophthalmic examinations were as follows: Keratic precipitates: not present; Anterior chamber: calm; Anterior chamber cell grade: 0 (scale from 0 to 4+, based on the recommendation of SUN working group 2005); Anterior chamber flare grade: 0 (from 0 to 4+, SUN Working Group); Vitreous: normal; Vitreous cells grade: 0 (scale from 0 to 4+, SUN Working Group). There were no ocular adverse events.

(2) We examined the anatomy of the retina using spectral-domain optical coherence tomography (OCT) at weeks -4, -3, -2, 1, 2, 4, 9, 13, 17, 25, 38, 52, and 80. The OCT images from all follow-up visits after injection were graded by the reading center (Coimbra Ophthalmology Reading Center) as similar (grade 0) to those from visits before injection (Grades: 0-Approximately the same, 1-Better, 2-Worse, 3-Not applicable). Note that there were similar hypo-reflective cyst-like spaces in both the fellow eye and the treated eye both before and after injection (Supplementary Figures **F.3-F.6**). The hypo-reflective cyst-like spaces 2 are not considered as "true" intraretinal cysts and are commonly observed in late-stage RP as a consequence of outer retinal degeneration (degenerative loss of outer retinal cells).

(3) We examined the anatomy of the retina on color fundus photographs (CFPs) at weeks -4, 25, and 52. On CFP images (and at funduscopy), retinal vasculature with retinal vessel attenuation was visible (as part of the degenerative condition) before and after injection. There was no sign of vasculitis at any time point. Optic disc pallor and bone spicule hyperpigmentation were noted in both eyes before injection and this did not change after injection. Vitreous haze based on CFPs was grade 0 (scale of 0 to 4+, National Institutes of Health grading system; Nussenblatt et al. 1985).

(4) We examined the anatomy of the retina on fundus autofluorescence (FAF) images at weeks -4, 25, and 52, and we found no changes, as assessed by the investigator and graded by the reading center (Coimbra Ophthalmology Reading Center). The evaluation of the reading center at each of these three visits was: hypofluorescence compatible with bone spicule hyperpigmentation, no central hyperautofluorescence, and no parafoveal hyperautofluorescent ring.

(5) We performed a general physical examination and a 12-lead electrocardiogram at weeks -4 and 52. Vital signs (systolic and diastolic blood pressure, pulse rate) were recorded at weeks -4, 0, 1, 2, 4, 9, 13, 17, 25, 38, 52, and 80. The results f the physical examinations, vital signs, and 12-lead electrocardiograms were normal on all occasions. 3 In summary,

there were no ocular or systemic adverse events at any of the visits. In addition, there were no self-reported adverse events, anomalies, or changes in health status of the patient at any time.

The OCT, CFP, and FAF images obtained are available to readers as a downloadable directory.

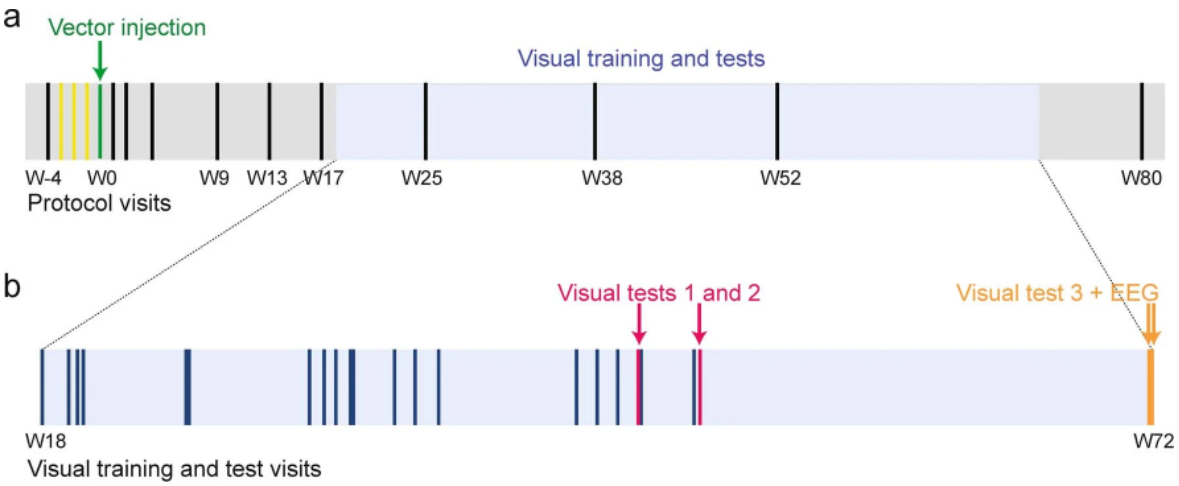

Figure F.2: Timeline of protocol visits, visual training visits, and test visits. **a**. Timeline of protocol visits. Each vertical line corresponds to a visit described in the clinical trial protocol. The visit (week (W) 0) at which the subject was injected is shown in green. The light-stimulating goggles were tested before injection on W-3, W-2, and W-1, shown in yellow. Protocol visits included ocular and general examinations. The time period at which visual training and the three visual tests occurred is shown in light blue. **b**. Timeline of visual training and visual test visits, which corresponds to the light blue region on **a**. Each dark blue line corresponds to a visual training visit (19 visits, thick lines indicate two closely spaced visits). Visual tests 1 and 2 were both run on the two visits shown in red, visual test 3 and EEG were run on the two visits shown in orange.

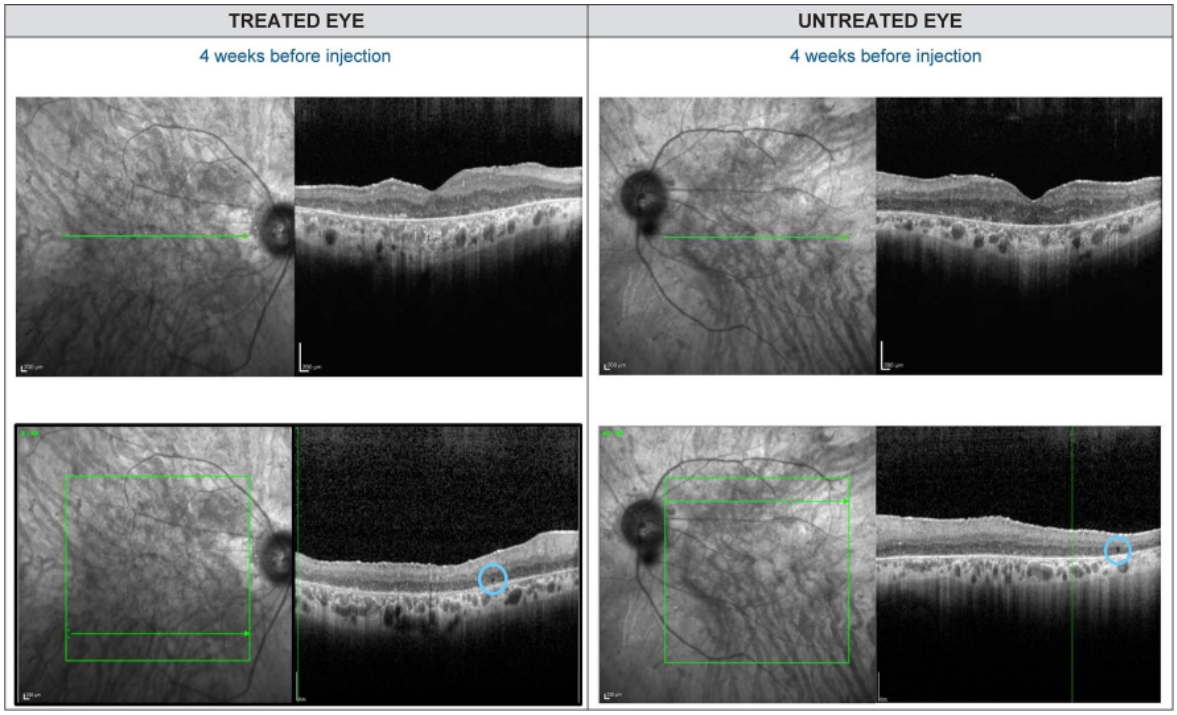

Figure F.3: OCT imaging of the retina 4 weeks before injection. OCT scans of the retina (location indicated by green arrow) taken 4 weeks before intravitreal injection of GS030-DP. Bilateral hyporeflective cyst-like spaces (shown in light-blue circles) are commonly found in late-stage RP and represent outer retinal degeneration.

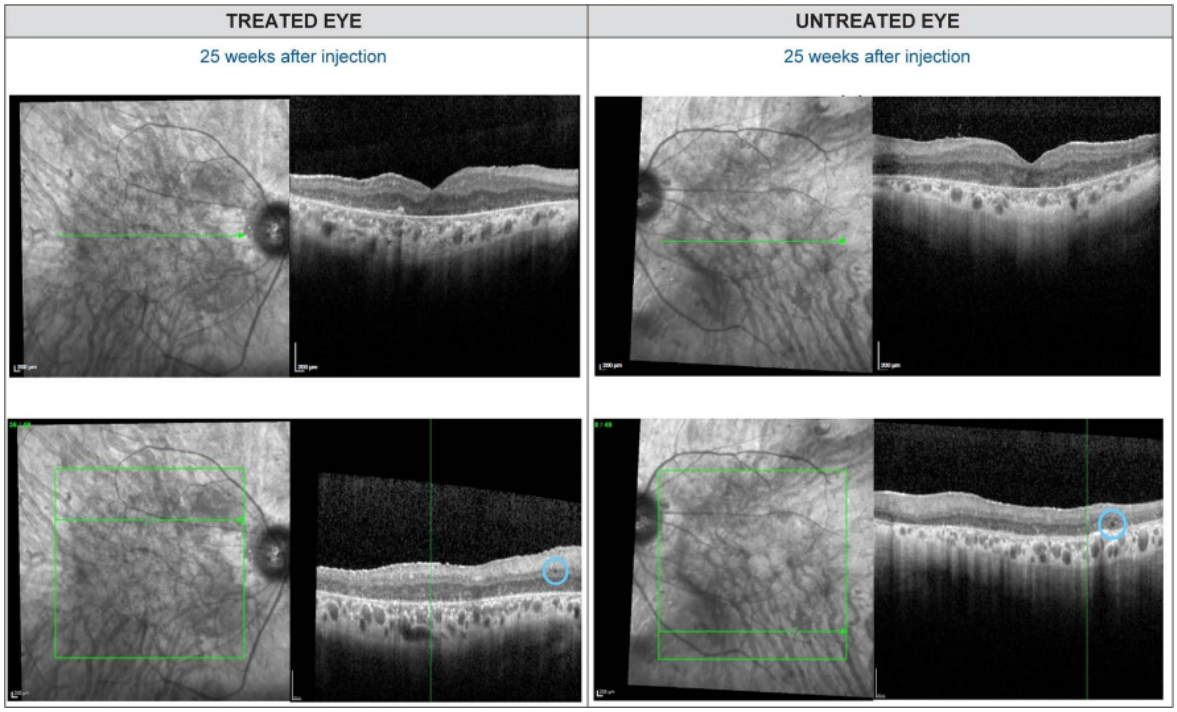

Figure F.4: OCT imaging of the retina 25 weeks after injection. OCT scans of the retina (location indicated by green arrow) taken 25 weeks after intravitreal injection of GS030-DP. Bilateral hyporeflective cyst-like spaces (shown in light-blue circles) are commonly found in late-stage RP and represent outer retinal degeneration.

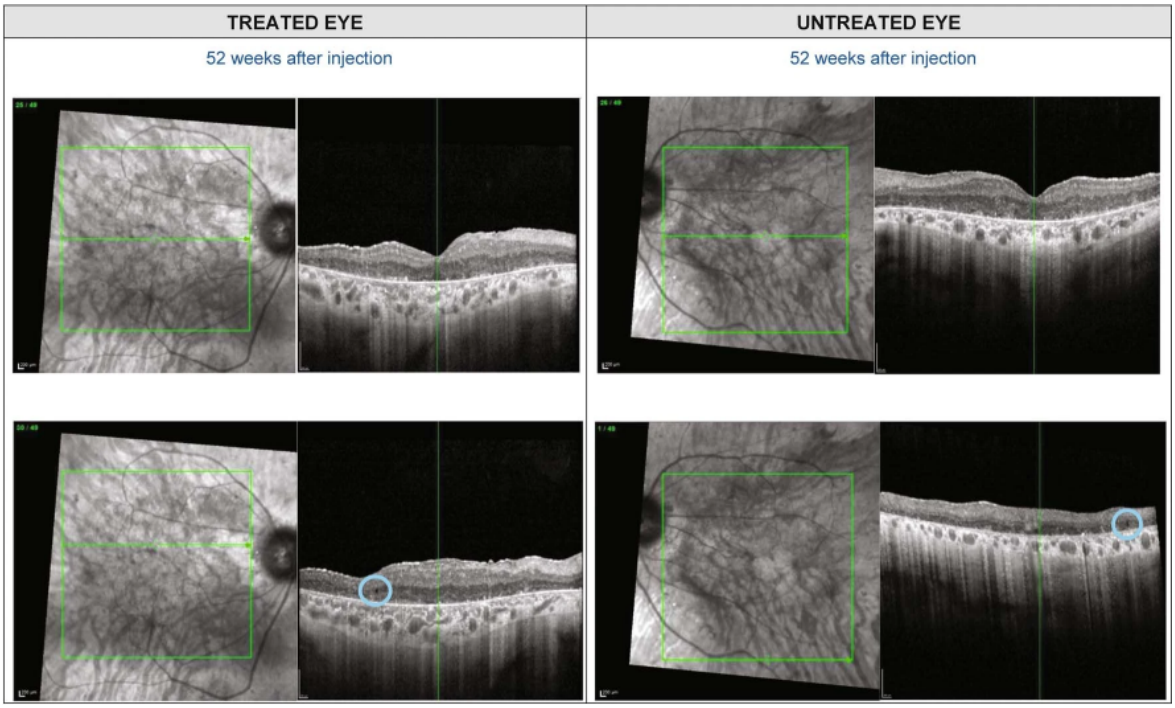

Figure F.5: OCT imaging of the retina 52 weeks after injection. OCT scans of the retina (location indicated by green arrow) taken 52 weeks after intravitreal injection of GS030-DP. Bilateral hyporeflective cyst-like spaces (shown in light-blue circles) are commonly found in late-stage RP and represent outer retinal degeneration.

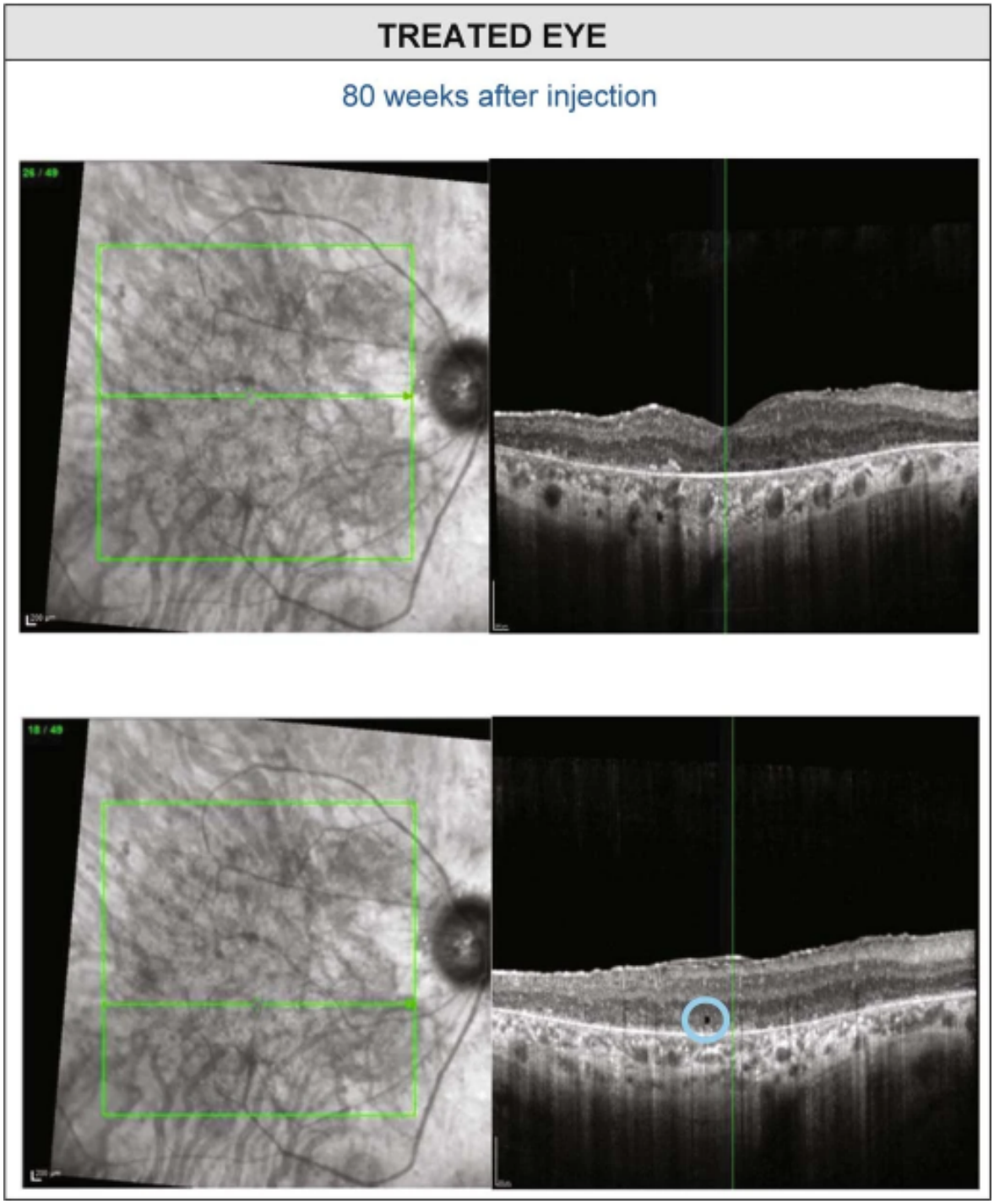

Figure F.6: OCT imaging of the retina 80 weeks after injection. OCT scans of the retina (location indicated by green arrow) taken 80 weeks after intravitreal injection of GS030-DP. Only the treated eye was assessed on that visit. Hyporeflective cyst-like spaces (example shown in light-blue circle) are commonly found in late-stage RP and represent outer retinal degeneration.

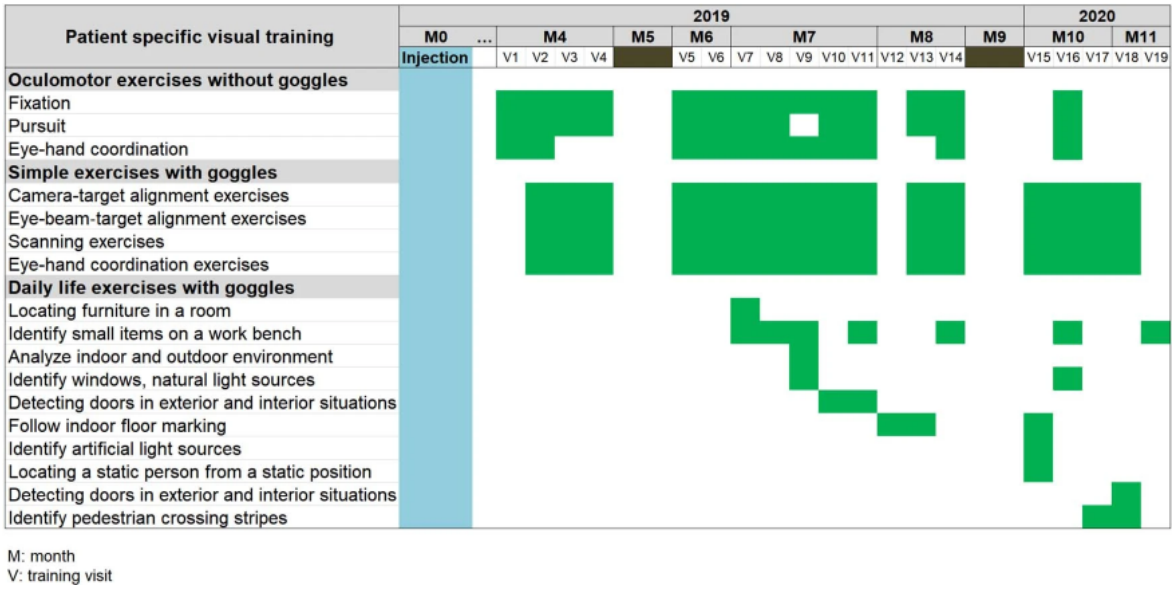

Figure F.7: Visual training program.

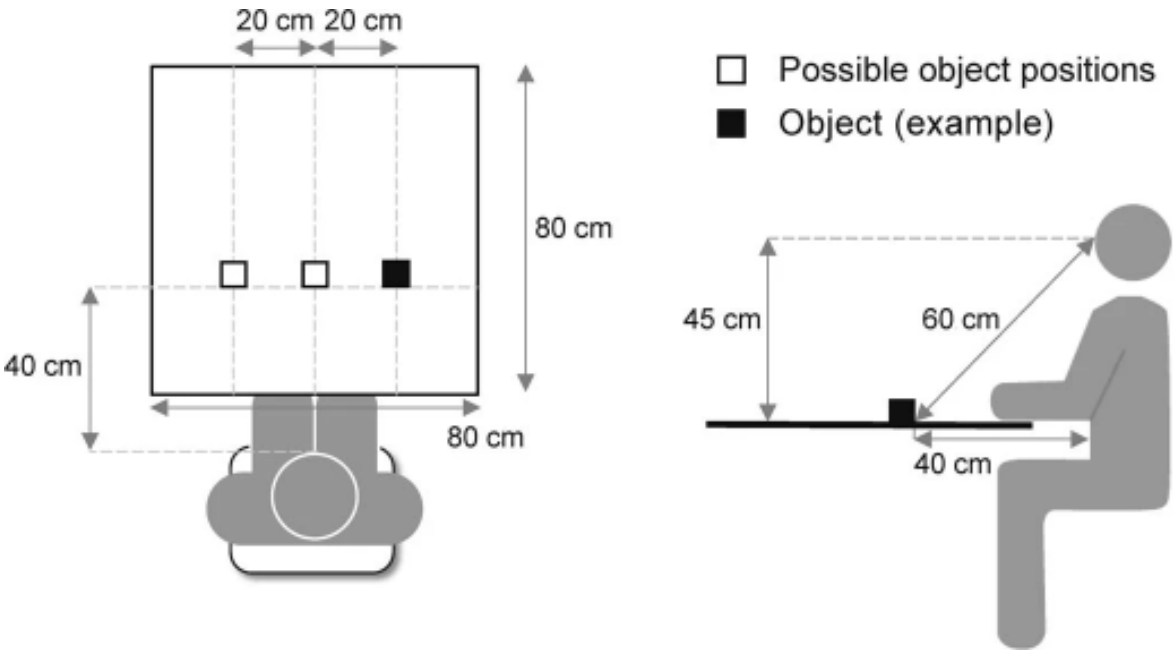

Figure F.8: Schematic of vision test 1: perceiving, locating, and touching a single object. The subject had to perceive, locate, and touch a single object placed on a white table (80×80 cm^2; $67.2° \times 50.9°$ visual angle) along an imaginary line at 40 cm from the subject (60 cm from the eyes of the subject), and 20 cm to the right or to the left (18.4°) or in front of the subject. The object was either a notebook (12.5×17.5 cm^2; $10.8° \times 10.3°$) or a staple box (3×5.5 cm^2; $2.8° \times 3.7°$), displayed individually in three different contrasts (Michelson contrasts 40%, 55%, and 100%; notebook: RMS contrasts 0.41, 0.53, 0.80; staple box: RMS contrasts 0.13, 0.16, 0.21) in a random order.

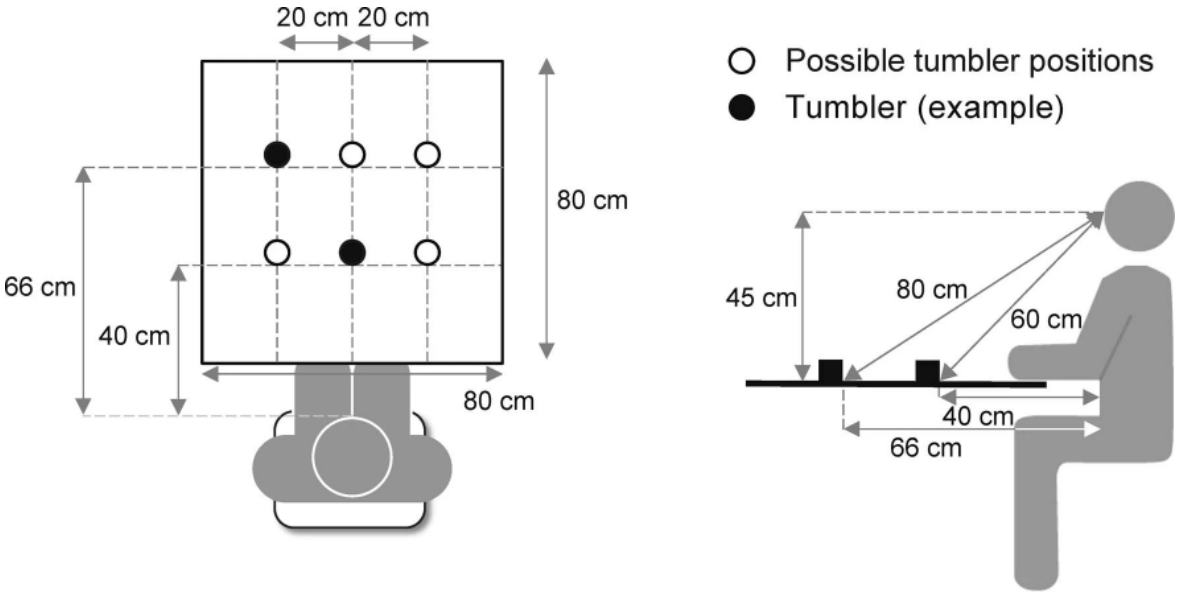

Figure F.9: Schematic of vision test 2: perceiving, counting, and locating more than one object. The subject had to count and locate two or three tumblers placed on a white table (80×80 cm^2; $67.2^\circ \times 50.9^\circ$ visual angle) and to point at them without touching. Tumblers (6 cm diameter and 6 cm height, 5.5° and 8.1° at 40 cm, 4.2° and 5.8° at 66 cm) were positioned at two or three of six possible positions along two imaginary lines: at 40 cm from the subject (60 cm from the eyes of the subject), and 20 cm to the right or to the left (18.4°) or in front of the subject; or at 66 cm from the subject (80 cm from the eyes of the subject), and 20 cm to the right or to the left (14°) or in front of the subject. The objects were displayed in three different contrasts (Michelson contrasts 40%, 55%, and 100%; RMS contrasts 0.29, 0.33, 0.41) in a random order.

BIBLIOGRAPHY

REFERENCES

Adamo, D. E., Briceño, E. M., Sindone, J. A., Alexander, N. B., & Moffat, S. D. (2012). Age differences in virtual environment and real world path integration. *Frontiers in Aging Neuroscience*, **4**:26. 10.3389/fnagi.2012.00026

Agathos, C. P., Bernardin, D., Huchet, D., Scherlen, A.-C., Assaiante, C., & Isableu, B. (2015). Sensorimotor and cognitive factors associated with the age-related increase of visual field dependence: a cross-sectional study. *AGE*, **37**(4), 67. 10.1007/s11357-015-9805-x

Agathos, C. P., Ramanoël, S., Bécu, M., Bernardin, D., Habas, C., & Arleo, A. (2020). Postural Control While Walking Interferes With Spatial Learning in Older Adults Navigating in a Real Environment. *Frontiers in Aging Neuroscience*, **12**:588653. 10.3389/fnagi.2020.588653

Aghajan, Z. M., Schuette, P., Fields, T. A., Tran, M. E., Siddiqui, S. M., Hasulak, N. R., … Suthana, N. (2017). Theta Oscillations in the Human Medial Temporal Lobe during Real-World Ambulatory Movement. *Current Biology*, **27**(24), pp. 3743–3751.e3. 10.1016/j.cub.2017.10.062

Akaike, H. (1974). A new look at the statistical model identification. *IEEE Transactions on Automatic Control*, **19**(6), pp. 716–723. 10.1109/TAC.1974.1100705

Akalin Acar, Z., & Makeig, S. (2013). Effects of Forward Model Errors on EEG Source Localization. *Brain Topography*, **26**(3), pp. 378–396. 10.1007/s10548-012-0274-6

Alexander, K. R., Rajagopalan, A. S., Seiple, W. H., Zemon, V. M., & Fishman, G. A. (2005). Contrast Response Properties of Magnocellular and Parvocellular Pathways in Retinitis Pigmentosa Assessed by the Visual Evoked Potential. *Investigative Opthalmology & Visual Science*, **46**(8), 2967. 10.1167/iovs.05-0231

Allen, G. L., Kirasic, K. C., Rashotte, M. A., & Haun, D. B. M. (2004). Aging and path integration skill: Kinesthetic and vestibular contributions to wayfinding. *Perception & Psychophysics*, **66**(1), pp. 170–179. 10.3758/BF03194870

Allison, S. L., Fagan, A. M., Morris, J. C., & Head, D. (2016). Spatial Navigation in Preclinical Alzheimer's Disease. *Journal of Alzheimer's Disease*, **52**(1), pp. 77–90. 10.3233/JAD-150855

Allison, S. L., & Head, D. (2017). Route repetition and route reversal: Effects of age and encoding method. *Psychology and Aging*, **32**(3), pp. 220–231. 10.1037/pag0000170

Alsuradi, H., Park, W., & Eid, M. (2020). EEG-Based Neurohaptics Research: A Literature Review. *IEEE Access*, **8**, pp. 49313–49328. 10.1109/ACCESS.2020.2979855

Aminoff, E. M., & Durham, T. (2023). Scene-selective brain regions respond to embedded objects of a scene. *Cerebral Cortex*, **33**(9), pp. 5066–5074. 10.1093/cercor/bhac399

Aminoff, E. M., & Tarr, M. J. (2021). Functional Context Affects Scene Processing. *Journal of Cognitive Neuroscience*, **33**(5), pp. 933–945. 10.1162/jocn_a_01694

Antonenko, P., Paas, F., Grabner, R., & van Gog, T. (2010). Using Electroencephalography to Measure Cognitive Load. *Educational Psychology Review*, **22**(4), pp. 425–438. 10.1007/s10648-010-9130-y

Antonova, E., Parslow, D., Brammer, M., Dawson, G. R., Jackson, S. H. D., & Morris, R. G. (2009). Age-related neural activity during allocentric spatial memory. *Memory*, **17**(2), pp. 125–143. 10.1080/09658210802077348

Ariel, R., & Moffat, S. D. (2018). Age-related similarities and differences in monitoring spatial cognition. *Aging, Neuropsychology, and Cognition*, **25**(3), pp. 351–377. 10.1080/13825585.2017.1305086

Arleo, A., & Rondi-Reig, L. (2007). Multimodal sensory integration and concurrent navigation strategies for spatial cognition in real and artificial organisms. *Journal of Integrative Neuroscience*, **06**(03), pp. 327–366. 10.1142/S0219635207001593

Artoni, F., Fanciullacci, C., Bertolucci, F., Panarese, A., Makeig, S., Micera, S., & Chisari, C. (2017). Unidirectional brain to muscle connectivity reveals motor cortex control of leg muscles during stereotyped walking. *NeuroImage*, **159**, pp. 403–416. 10.1016/j.neuroimage.2017.07.013

Atsumori, H., Kiguchi, M., Katura, T., Funane, T., Obata, A., Sato, H., … Kubota, K. (2010). Noninvasive imaging of prefrontal activation during attention-demanding tasks performed while walking using a wearable optical topography system. *Journal of Biomedical Optics*, **15**(4), 046002. 10.1117/1.3462996

Audelan, B., & Delingette, H. (2021). Unsupervised quality control of segmentations based on a smoothness and intensity probabilistic model. *Medical Image Analysis*, **68**:101895. 10.1016/j.media.2020.101895

Audo, I., Bujakowska, K. M., Léveillard, T., Mohand-Saïd, S., Lancelot, M.-E., Germain, A., … Zeitz, C. (2012). Development and application of a next-generation-sequencing (NGS) approach to detect known and novel gene defects underlying retinal diseases. *Orphanet Journal of Rare Diseases*, **7**:8. 10.1186/1750-1172-7-8

Auger, S. D., & Maguire, E. A. (2018). Dissociating Landmark Stability from Orienting Value Using Functional Magnetic Resonance Imaging. *Journal of Cognitive Neuroscience*, **30**(5), pp. 698–713. 10.1162/jocn_a_01231

Auger, S. D., Mullally, S. L., & Maguire, E. A. (2012). Retrosplenial Cortex Codes for Permanent Landmarks. *PLOS ONE*, **7**(8), e43620. 10.1371/journal.pone.0043620

Auger, S. D., Zeidman, P., & Maguire, E. A. (2015). A central role for the retrosplenial cortex in de novo environmental learning. *eLife*, **4**:e09031. 10.7554/eLife.09031

Awh, E., & Jonides, J. (2001). Overlapping mechanisms of attention and spatial working memory. *Trends in Cognitive Sciences*, **5**(3), pp. 119–126. 10.1016/S1364-6613(00)01593-X

Ayton, L. N., Barnes, N., Dagnelie, G., Fujikado, T., Goetz, G., Hornig, R., … Petoe, M. A. (2020). An update on retinal prostheses. *Clinical Neurophysiology*, **131**(6), pp. 1383–1398. 10.1016/j.clinph.2019.11.029

Bainbridge, W. A., & Oliva, A. (2015). Interaction envelope: Local spatial representations of objects at all scales in scene-selective regions. *NeuroImage*, **122**, pp. 408–416. 10.1016/j.neuroimage.2015.07.066

Baker, T. E., & Holroyd, C. B. (2009). Which Way Do I Go? Neural Activation in Response to Feedback and Spatial Processing in a Virtual T-Maze. *Cerebral Cortex*, **19**(8), pp. 1708–1722. 10.1093/cercor/bhn223

Baker, T. E., & Holroyd, C. B. (2013). The topographical N170: Electrophysiological evidence of a neural mechanism for human spatial navigation. *Biological Psychology*, **94**(1), pp. 90–105. 10.1016/j.biopsycho.2013.05.004

Baker, T. E., Umemoto, A., Krawitz, A., & Holroyd, C. B. (2015). Rightward-biased hemodynamic response of the parahippocampal system during virtual navigation. *Scientific Reports*, **5**:9063. 10.1038/srep09063

Baldassano, C., Esteva, A., Fei-Fei, L., & Beck, D. M. (2016). Two Distinct Scene-Processing Networks Connecting Vision and Memory. *eneuro*, **3**(5), pp. ENEURO.0178–16.2016. 10.1523/ENEURO.0178-16.2016

Barnes, C. A., Nadel, L., & Honig, W. K. (1980). Spatial memory deficit in senescent rats. *Canadian Journal of Psychology*, **34**(1), pp. 29–39. 10.1037/h0081022

Barnes, N., Scott, A. F., Lieby, P., Petoe, M. A., McCarthy, C., Stacey, A., … Walker, J. G. (2016). Vision function testing for a suprachoroidal retinal prosthesis: effects of image filtering. *Journal of Neural Engineering*, **13**(3), 036013. 10.1088/1741-2560/13/3/036013

Barrash, J. (1994). Age-related decline in route learning ability. *Developmental Neuropsychology*, **10**(3), pp. 189–201. 10.1080/87565649409540578

Barton, R. A. (2004). Binocularity and brain evolution in primates. *Proceedings of the National Academy of Sciences*, **101**(27), pp. 10113–10115. 10.1073/pnas.0401955101

Bates, D., Mächler, M., Bolker, B., & Walker, S. (2014). Fitting Linear Mixed-Effects Models using lme4. *arXiv*:1406.5823. 10.48550/arXiv.1406.5823

Bates, S. L., & Wolbers, T. (2014). How cognitive aging affects multisensory integration of navigational cues. *Neurobiology of Aging*, **35**(12), pp. 2761–2769. 10.1016/j.neurobiolaging.2014.04.003

Baumann, O., & Mattingley, J. B. (2010). Medial Parietal Cortex Encodes Perceived Heading Direction in Humans. *Journal of Neuroscience*, **30**(39), pp. 12897–12901. 10.1523/JNEUROSCI.3077-10.2010

Baysal, U., & Şengül, G. (2010). Single Camera Photogrammetry System for EEG Electrode Identification and Localization. *Annals of Biomedical Engineering*, **38**(4), pp. 1539–1547. 10.1007/s10439-010-9950-4

Bécu, M., Sheynikhovich, D., Ramanoël, S., Tatur, G., Ozier-Lafontaine, A., Authié, C. N., … Arleo, A. (2023). Landmark-based spatial navigation across the human lifespan. *eLife*, **12**:e81318. 10.7554/eLife.81318

Bécu, M., Sheynikhovich, D., Ramanoël, S., Tatur, G., Ozier-Lafontaine, A., Sahel, J.-A., & Arleo, A. (2020b). Modulation of spatial cue processing across the lifespan: a geometric polarization of space restores allocentric navigation strategies in children and older adults. *bioRxiv*:945808. 10.1101/2020.02.12.945808

Bécu, M., Sheynikhovich, D., Tatur, G., Agathos, C. P., Bologna, L. L., Sahel, J.-A., & Arleo, A. (2020a). Age-related preference for geometric spatial cues during real-world navigation. *Nature Human Behaviour*, **4**, pp. 88–99. 10.1038/s41562-019-0718-z

Bell, A. J., & Sejnowski, T. J. (1995). An Information-Maximization Approach to Blind Separation and Blind Deconvolution. *Neural Computation*, **7**(6), pp. 1129–1159. 10.1162/neco.1995.7.6.1129

Berger, H. (1929). Uber das Elektroenkephalogramm des Menschen. *Archiv für psychiatrie und nervenkrankheiten*, **87**(1), pp. 527–570.

Berryhill, M. E., & Olson, I. R. (2008). The right parietal lobe is critical for visual working memory. *Neuropsychologia*, **46**(7), pp. 1767–1774. 10.1016/j.neuropsychologia.2008.01.009

Beyeler, M., Rokem, A., Boynton, G. M., & Fine, I. (2017). Learning to see again: biological constraints on cortical plasticity and the implications for sight restoration technologies. *Journal of Neural Engineering*, **14**(5), 051003. 10.1088/1741-2552/aa795e

Bi, A., Cui, J., Ma, Y.-P., Olshevskaya, E., Pu, M., Dizhoor, A. M., & Pan, Z.-H. (2006). Ectopic Expression of a Microbial-Type Rhodopsin Restores Visual Responses in Mice with Photoreceptor Degeneration. *Neuron*, **50**(1), pp. 23–33. 10.1016/j.neuron.2006.02.026

Bian, Z., & Andersen, G. J. (2013). Aging and the perception of egocentric distance. *Psychology and Aging*, **28**(3), pp. 813–825. 10.1037/a0030991

Bigdely-Shamlo, N., Mullen, T. R., Kothe, C. A., Su, K.-M., & Robbins, K. A. (2015). The PREP pipeline: standardized preprocessing for large-scale EEG analysis. *Frontiers in Neuroinformatics*, **9**:16. 10.3389/fninf.2015.00016

Bilalić, M., Lindig, T., & Turella, L. (2019). Parsing rooms: the role of the PPA and RSC in perceiving object relations and spatial layout. *Brain Structure and Function*, **224**(7), pp. 2505–2524. 10.1007/s00429-019-01901-0

Bischof, W. F., & Boulanger, P. (2003). Spatial Navigation in Virtual Reality Environments: An EEG Analysis. *Cyberpsychology and Behavior*, **6**(5), pp. 487–495. 10.1089/109493103769710514

Bohbot, V. D., Copara, M. S., Gotman, J., & Ekstrom, A. D. (2017). Low-frequency theta oscillations in the human hippocampus during real-world and virtual navigation. *Nature Communications*, **8**:14415. 10.1038/ncomms14415

Bohbot, V. D., McKenzie, S., Konishi, K., Fouquet, C., Kurdi, V., Schachar, R., … Robaey, P. (2012). Virtual navigation strategies from childhood to senescence: evidence for changes across the life span. *Frontiers in Aging Neuroscience*, **4**:28. 10.3389/fnagi.2012.00028

Bohil, C. J., Alicea, B., & Biocca, F. A. (2011). Virtual reality in neuroscience research and therapy. *Nature Reviews Neuroscience*, **12**(12), pp. 752–762. 10.1038/nrn3122

Bohle, H., Rimpel, J., Schauenburg, G., Gebel, A., Stelzel, C., Heinzel, S., … Granacher, U. (2019). Behavioral and Neural Correlates of Cognitive-Motor Interference during Multitasking in Young and Old Adults. *Neural Plasticity*, **2019**:9478656. 10.1155/2019/9478656

Bonner, M. F., & Epstein, R. A. (2017). Coding of navigational affordances in the human visual system. *Proceedings of the National Academy of Sciences*, **114**(18), pp. 4793–4798. 10.1073/pnas.1618228114

Bonner, M. F., & Epstein, R. A. (2018). Computational mechanisms underlying cortical responses to the affordance properties of visual scenes. *PLOS Computational Biology*, **14**(4), e1006111. 10.1371/journal.pcbi.1006111

Bonner, M. F., & Epstein, R. A. (2021). Object representations in the human brain reflect the co-occurrence statistics of vision and language. *Nature Communications*, **12**:4081. 10.1038/s41467-021-24368-2

Borda, E., & Ghezzi, D. (2022). Advances in visual prostheses: engineering and biological challenges. *Progress in Biomedical Engineering*, **4**(3), 032003. 10.1088/2516-1091/ac812c

Boto, E., Holmes, N., Leggett, J., Roberts, G., Shah, V., Meyer, S. S., … Brookes, M. J. (2018). Moving magnetoencephalography towards real-world applications with a wearable system. *Nature*, **555**(7698), pp. 657–661. 10.1038/nature26147

Bottari, D., Troje, N. F., Ley, P., Hense, M., Kekunnaya, R., & Röder, B. (2016). Sight restoration after congenital blindness does not reinstate alpha oscillatory activity in humans. *Scientific Reports*, **6**:24683. 10.1038/srep24683

Botvinick, M., & Cohen, J. (1998). Rubber hands feel' touch that eyes see. *Nature*, **391**(6669), pp. 756–756. 10.1038/35784

Bourne, R. R. A., Steinmetz, J. D., Flaxman, S., Briant, P. S., Taylor, H. R., Resnikoff, S., … Vos, T. (2021). Trends in prevalence of blindness and distance and near vision impairment over 30 years: an analysis for the Global Burden of Disease Study. *The Lancet Global Health*, **9**(2), pp. e130–e143. 10.1016/S2214-109X(20)30425-3

Brennan, A. A., Bruderer, A. J., Liu-Ambrose, T., Handy, T. C., & Enns, J. T. (2017). Lifespan changes in attention revisited: Everyday visual search. *Canadian Journal of Experimental Psychology / Revue canadienne de psychologie expérimentale*, **71**(2), pp. 160–171. 10.1037/cep0000130

Brusini, I., Padilla, D. F., Barroso, J., Skoog, I., Smedby, Ö., Westman, E., & Wang, C. (2020). A deep learning-based pipeline for error detection and quality control of brain MRI segmentation results. *arXiv*:2005.13987. 10.48550/arXiv.2005.13987

Bulea, T. C., Kim, J., Damiano, D. L., Stanley, C. J., & Park, H. S. (2015). Prefrontal, posterior parietal and sensorimotor network activity underlying speed control during walking. *Frontiers in Human Neuroscience*, **9**:247. 10.3389/fnhum.2015.00247

Burgess, N. (2008). Spatial Cognition and the Brain. *Annals of the New York Academy of Sciences*, **1124**(1), pp. 77–97. 10.1196/annals.1440.002

Burles, F., Umiltá, A., McFarlane, L. H., Potocki, K., & Iaria, G. (2018). Ventral-Dorsal Functional Contribution of the Posterior Cingulate Cortex in Human Spatial Orientation: A Meta-Analysis. *Frontiers in Human Neuroscience*, **12**:190. 10.3389/fnhum.2018.00190

Burns, P. C. (1999). Navigation and the Mobility of Older Drivers. *The Journals of Gerontology Series B: Psychological Sciences and Social Sciences*, **54B**(1), pp. S49–S55. 10.1093/geronb/54B.1.S49

Burton, M. J., Ramke, J., Marques, A. P., Bourne, R. R. A., Congdon, N., Jones, I., … Faal, H. B. (2021). The Lancet Global Health Commission on Global Eye Health: vision beyond 2020. *The Lancet Global Health*, **9**(4), pp. e489–e551. 10.1016/S2214-109X(20)30488-5

Buschman, T. J., & Miller, E. K. (2007). Top-Down Versus Bottom-Up Control of Attention in the Prefrontal and Posterior Parietal Cortices. *Science*, **315**(5820), pp. 1860–1862. 10.1126/science.1138071

Buschman, T. J., & Miller, E. K. (2009). Serial, Covert Shifts of Attention during Visual Search Are Reflected by the Frontal Eye Fields and Correlated with Population Oscillations. *Neuron*, **63**(3), pp. 386–396. 10.1016/j.neuron.2009.06.020

Bush, D., Bisby, J. A., Bird, C. M., Gollwitzer, S., Rodionov, R., Diehl, B., … Burgess, N. (2017). Human hippocampal theta power indicates movement onset and distance travelled. *Proceedings of the National Academy of Sciences*, **114**(46), pp. 12297–12302. 10.1073/pnas.1708716114

Busskamp, V., Duebel, J., Balya, D., Fradot, M., Viney, T. J., Siegert, S., ... Roska, B. (2010). Genetic Reactivation of Cone Photoreceptors Restores Visual Responses in Retinitis Pigmentosa. *Science*, **329**(5990), pp. 413–417. 10.1126/science.1190897

Buzsáki, G., Anastassiou, C. A., & Koch, C. (2012). The origin of extracellular fields and currents - EEG, ECoG, LFP and spikes. *Nature Reviews Neuroscience*, **13**(6), pp. 407–420. 10.1038/nrn3241

Buzsáki, G., & Draguhn, A. (2004). Neuronal Oscillations in Cortical Networks. *Science*, **304**(5679), pp. 1926–1929. 10.1126/science.1099745

Cabeza, R. (2002). Hemispheric asymmetry reduction in older adults: The HAROLD model. *Psychology and Aging*, **17**(1), pp. 85–100. 10.1037/0882-7974.17.1.85

Cabeza, R., Ciaramelli, E., Olson, I. R., & Moscovitch, M. (2008). The parietal cortex and episodic memory: an attentional account. *Nature Reviews Neuroscience*, **9**(8), pp. 613–625. 10.1038/nrn2459

Campbell, K. L., Hasher, L., & Thomas, R. C. (2010). Hyper-Binding. *Psychological Science*, **21**(3), pp. 399–405. 10.1177/0956797609359910

Cao, L., Chen, X., & Händel, B. F. (2020). Overground Walking Decreases Alpha Activity and Entrains Eye Movements in Humans. *Frontiers in Human Neuroscience*, **14**:561755. 10.3389/fnhum.2020.561755

Cao, L., & Händel, B. F. (2019). Walking enhances peripheral visual processing in humans. *PLOS Biology*, **17**(10), e3000511. 10.1371/journal.pbio.3000511

Caplan, J. B., Madsen, J. R., Schulze-Bonhage, A., Aschenbrenner-Scheibe, R., Newman, E. L., & Kahana, M. J. (2003). Human θ Oscillations Related to Sensorimotor Integration and Spatial Learning. *Journal of Neuroscience*, **23**(11), pp. 4726–4736. 10.1523/JNEUROSCI.23-11-04726.2003

Carrasco, M., Talgar, C. P., & Cameron, E. L. (2001). Characterizing visual performance fields: effects of transient covert attention, spatial frequency, eccentricity, task and set size. *Spatial Vision*, **15**(1), pp. 61–75. 10.1163/15685680152692015

Castaldi, E., Cicchini, G. M., Cinelli, L., Biagi, L., Rizzo, S., & Morrone, M. C. (2016). Visual BOLD Response in Late Blind Subjects with Argus II Retinal Prosthesis. *PLOS Biology*, **14**(10), e1002569. 10.1371/journal.pbio.1002569

Castaldi, E., Lunghi, C., & Morrone, M. C. (2020). Neuroplasticity in adult human visual cortex. *Neuroscience & Biobehavioral Reviews*, **112**, pp. 542–552. 10.1016/j.neubiorev.2020.02.028

Castelhano, M. S., & Witherspoon, R. L. (2016). How You Use It Matters. *Psychological Science*, **27**(5), pp. 606–621. 10.1177/0956797616629130

Castermans, T., Duvinage, M., Cheron, G., & Dutoit, T. (2014). About the cortical origin of the low-delta and high-gamma rhythms observed in EEG signals during treadmill walking. *Neuroscience Letters*, **561**, pp. 166–170. 10.1016/j.neulet.2013.12.059

Cavanagh, J. F., & Frank, M. J. (2014). Frontal theta as a mechanism for cognitive control. *Trends in Cognitive Sciences*, **18**(8), pp. 414–421. 10.1016/j.tics.2014.04.012

Cepeda-Freyre, H. A., Garcia-Aguilar, G., Eguibar, J. R., & Cortes, C. (2020). Brain Processing of Complex Geometric Forms in a Visual Memory Task Increases P2 Amplitude. *Brain Sciences*, **10**(2), 114. 10.3390/brainsci10020114

Cevallos, C., Zarka, D., Hoellinger, T., Leroy, A., Dan, B., & Cheron, G. (2015). Oscillations in the human brain during walking execution, imagination and observation. *Neuropsychologia*, **79 B**, pp. 223–232. 10.1016/j.neuropsychologia.2015.06.039

Chaffiol, A., Provansal, M., Joffrois, C., Blaize, K., Labernede, G., Goulet, R., … Gauvain, G. (2022). In vivo optogenetic stimulation of the primate retina activates the visual cortex after long-term transduction. *Molecular Therapy - Methods & Clinical Development*, **24**, pp. 1–10. 10.1016/j.omtm.2021.11.009

Chaisilprungraung, T., & Park, S. (2021). Scene from inside: The representation of Observer's space in high-level visual cortex. *Neuropsychologia*, **161**:108010. 10.1016/j.neuropsychologia.2021.108010

Chan, E., Baumann, O., Bellgrove, M. A., & Mattingley, J. B. (2012). From Objects to Landmarks: The Function of Visual Location Information in Spatial Navigation. *Frontiers in Psychology*, **3**:304. 10.3389/fpsyg.2012.00304

Chance, S. S., Gaunet, F., Beall, A. C., & Loomis, J. M. (1998). Locomotion Mode Affects the Updating of Objects Encountered During Travel: The Contribution of Vestibular and Proprioceptive Inputs to Path Integration. *Presence: Teleoperators and Virtual Environments*, **7**(2), pp. 168–178. 10.1162/105474698565659

Chang, C.-Y., Hsu, S.-H., Pion-Tonachini, L., & Jung, T.-P. (2020). Evaluation of Artifact Subspace Reconstruction for Automatic Artifact Components Removal in Multi-Channel EEG Recordings. *IEEE Transactions on Biomedical Engineering*, **67**(4), pp. 1114–1121. 10.1109/TBME.2019.2930186

Chen, K. H., Chuah, L. Y., Sim, S. K., & Chee, M. W. (2010). Hippocampal region-specific contributions to memory performance in normal elderly. *Brain and Cognition*, **72**(3), pp. 400–407. 10.1016/j.bandc.2009.11.007

Chen, S. C., Suaning, G. J., Morley, J. W., & Lovell, N. H. (2009). Simulating prosthetic vision: I. Visual models of phosphenes. *Vision Research*, **49**(12), pp. 1493–1506. 10.1016/j.visres.2009.02.003

Chen, X., Cao, L., & Händel, B. F. (2022a). Differential effects of walking across visual cortical processing stages. *Cortex*, **149**, pp. 16–28. 10.1016/j.cortex.2022.01.007

Chen, X., Cao, L., & Händel, B. F. (2022b). Human visual processing during walking: Dissociable pre- and post-stimulus influences. *NeuroImage*, **264**(April), 119757. 10.1016/j.neuroimage.2022.119757

Chen, X., Li, C., Liu, A., McKeown, M. J., Qian, R., & Wang, Z. J. (2022). Toward Open-World Electroencephalogram Decoding Via Deep Learning: A comprehensive survey. *IEEE Signal Processing Magazine*, **39**(2), pp. 117–134. 10.1109/MSP.2021.3134629

Chenais, N. A. L., Airaghi Leccardi, M. J. I., & Ghezzi, D. (2021). Photovoltaic retinal prosthesis restores high-resolution responses to single-pixel stimulation in blind retinas. *Communications Materials*, **2**(1), 28. 10.1038/s43246-021-00133-2

Chevrie, K. (2020). Navigating the regulatory pathway for an innovative bionic vision system. In *Advanced Biomedical and Clinical Diagnostic and Surgical Guidance Systems XVIII* (Vol. 11229, p. 112290X). San Francisco, CA. 10.1117/12.2560182

Chiu, T.-C. C., Gramann, K., Ko, L.-W., Duann, J.-R., Jung, T.-P., & Lin, C.-T. (2012). Alpha modulation in parietal and retrosplenial cortex correlates with navigation performance. *Psychophysiology*, **49**(1), pp. 43–55. 10.1111/j.1469-8986.2011.01270.x

Chrastil, E. R., Nicora, G. L., & Huang, A. (2019). Vision and proprioception make equal contributions to path integration in a novel homing task. *Cognition*, **192**:103998. 10.1016/j.cognition.2019.06.010

Chrastil, E. R., Rice, C., Goncalves, M., Moore, K. N., Wynn, S. C., Stern, C. E., & Nyhus, E. (2022). Theta oscillations support active exploration in human spatial navigation. *NeuroImage*, **262**:119581. 10.1016/j.neuroimage.2022.119581

Clark, A. (1999). An embodied cognitive science? *Trends in Cognitive Sciences*, **3**(9), pp. 345–351. 10.1016/S1364-6613(99)01361-3

Cohen, M. X. (2014). *Analyzing Neural Time Series Data : Theory and Practice.* MIT Press.

Colombo, D., Serino, S., Tuena, C., Pedroli, E., Dakanalis, A., Cipresso, P., & Riva, G. (2017). Egocentric and allocentric spatial reference frames in aging: A systematic review. *Neuroscience & Biobehavioral Reviews*, **80**, pp. 605–621. 10.1016/j.neubiorev.2017.07.012

Cona, G., & Scarpazza, C. (2019). Where is the where in the brain? A meta-analysis of neuroimaging studies on spatial cognition. *Human Brain Mapping*, **40**(6), pp. 1867–1886. 10.1002/hbm.24496

Cona, G., & Semenza, C. (2017). Supplementary motor area as key structure for domain-general sequence processing: A unified account. *Neuroscience & Biobehavioral Reviews*, **72**, pp. 28–42. 10.1016/j.neubiorev.2016.10.033

Cottereau, B. R., Ales, J. M., & Norcia, A. M. (2012). Increasing the accuracy of electromagnetic inverses using functional area source correlation constraints. *Human Brain Mapping*, **33**(11), pp. 2694–2713. 10.1002/hbm.21394

Cottereau, B. R., Ales, J. M., & Norcia, A. M. (2015). How to use fMRI functional localizers to improve EEG/MEG source estimation. *Journal of Neuroscience Methods*, **250**, pp. 64–73. 10.1016/j.jneumeth.2014.07.015

Coughlan, G., Laczó, J., Hort, J., Minihane, A.-M., & Hornberger, M. (2018). Spatial navigation deficits - overlooked cognitive marker for preclinical Alzheimer disease? *Nature Reviews Neurology*, **14**(8), pp. 496–506. 10.1038/s41582-018-0031-x

Court, H., McLean, G., Guthrie, B., Mercer, S. W., & Smith, D. J. (2014). Visual impairment is associated with physical and mental comorbidities in older adults: a cross-sectional study. *BMC Medicine*, **12**(1), 181. 10.1186/s12916-014-0181-7

Courtney, S. M., Ungerleider, L. G., Keil, K., & Haxby, J. V. (1996). Object and Spatial Visual Working Memory Activate Separate Neural Systems in Human Cortex. *Cerebral Cortex*, **6**(1), pp. 39–49. 10.1093/cercor/6.1.39

Creel, D. J. (2019). Visually evoked potentials. In K. H. Levin & P. Chauvel (Eds.), *Handbook of Clinical Neurology* (Vol. 160, pp. 501–522). Elsevier. 10.1016/B978-0-444-64032-1.00034-5

Curcio, C. A., Sloan, K. R., Kalina, R. E., & Hendrickson, A. E. (1990). Human photoreceptor topography. *Journal of Comparative Neurology*, **292**(4), pp. 497–523. 10.1002/cne.902920402

Curcio, C. A., Sloan, K. R., Packer, O., Hendrickson, A. E., & Kalina, R. E. (1987). Distribution of Cones in Human and Monkey Retina: Individual Variability and Radial Asymmetry. *Science*, **236**(4801), pp. 579–582. 10.1126/science.3576186

da Cruz, J. R., Chicherov, V., Herzog, M. H., & Figueiredo, P. (2018). An automatic pre-processing pipeline for EEG analysis (APP) based on robust statistics. *Clinical Neurophysiology*, **129**(7), pp. 1427–1437. 10.1016/j.clinph.2018.04.600

da Cruz, L., Coley, B. F., Dorn, J. D., Merlini, F., Filley, E., Christopher, P., ... Dagnelie, G. (2013). The Argus II epiretinal prosthesis system allows letter and word reading and long-term function in patients with profound vision loss. *British Journal of Ophthalmology*, **97**(5), pp. 632–636. 10.1136/bjophthalmol-2012-301525

da Cruz, L., Dorn, J. D., Humayun, M. S., Dagnelie, G., Handa, J., Barale, P.-O., ... Greenberg, R. J. (2016). Five-Year Safety and Performance Results from the Argus II Retinal Prosthesis System Clinical Trial. *Ophthalmology*, **123**(10), pp. 2248–2254. 10.1016/j.ophtha.2016.06.049

Dagnelie, G., Christopher, P., Arditi, A., da Cruz, L., Duncan, J. L., Ho, A. C., ... Greenberg, R. J. (2017). Performance of real-world functional vision tasks by blind subjects improves after implantation with the Argus® II retinal prosthesis system. *Clinical & Experimental Ophthalmology*, **45**(2), pp. 152–159. 10.1111/ceo.12812

Dalkara, D., Byrne, L. C., Klimczak, R. R., Visel, M., Yin, L., Merigan, W. H., ... Schaffer, D. V. (2013). In VivoDirected Evolution of a New Adeno-Associated Virus for Therapeutic Outer Retinal Gene Delivery from the Vitreous. *Science Translational Medicine*, **5**(189), 189ra76. 10.1126/scitranslmed.3005708

De Beni, R., Meneghetti, C., Fiore, F., Gava, L., & Borella, E. (2014). *Visuo-spatial Battery: Instrument for assessing visuospatial abilities across the adult life span.* Florence: Hogrefe.

De Sanctis, P., Katz, R., Wylie, G. R., Sehatpour, P., Alexopoulos, G. S., & Foxe, J. J. (2008). Enhanced and bilateralized visual sensory processing in the ventral stream may be a feature of normal aging. *Neurobiology of Aging*, **29**(10), pp. 1576–1586. 10.1016/j.neurobiolaging.2007.03.021

Debener, S., Minow, F., Emkes, R., Gandras, K., & de Vos, M. (2012). How about taking a low-cost, small, and wireless EEG for a walk? *Psychophysiology*, **49**(11), pp. 1617–1621. 10.1111/j.1469-8986.2012.01471.x

de Condappa, O., & Wiener, J. M. (2016). Human place and response learning: navigation strategy selection, pupil size and gaze behavior. *Psychological Research*, **80**(1), pp. 82–93. 10.1007/s00426-014-0642-9

Deiber, M.-P., Missonnier, P., Bertrand, O., Gold, G., Fazio-Costa, L., Ibañez, V., & Giannakopoulos, P. (2007). Distinction between Perceptual and Attentional Processing in Working Memory Tasks: A Study of Phase-locked and Induced Oscillatory Brain Dynamics. *Journal of Cognitive Neuroscience*, **19**(1), pp. 158–172. 10.1162/jocn.2007.19.1.158

Delaux, A., de Saint Aubert, J.-B., Ramanoël, S., Bécu, M., Gehrke, L., Klug, M., ... Arleo, A. (2021). Mobile brain/body imaging of landmark-based navigation with high-density EEG. *European Journal of Neuroscience*, **54**(12), pp. 8256–8282. 10.1111/ejn.15190

Delorme, A., & Makeig, S. (2004). EEGLAB: an open source toolbox for analysis of single-trial EEG dynamics including independent component analysis. *Journal of Neuroscience Methods*, **134**(1), pp. 9–21. 10.1016/j.jneumeth.2003.10.009

Delorme, A., Palmer, J. A., Onton, J., Oostenveld, R., & Makeig, S. (2012). Independent EEG sources are dipolar. *PLOS ONE*, **7**(2), e30135. 10.1371/journal.pone.0030135

Delorme, A., Sejnowski, T. J., & Makeig, S. (2007). Enhanced detection of artifacts in EEG data using higher-order statistics and independent component analysis. *NeuroImage*, **34**(4), pp. 1443–1449. 10.1016/j.neuroimage.2006.11.004

Delval, A., Bayot, M., Defebvre, L., & Dujardin, K. (2020). Cortical Oscillations during Gait: Wouldn't Walking Be So Automatic? *Brain Sciences*, **10**(2), 90. 10.3390/brainsci10020090

Dempster, F. N. (1992). The rise and fall of the inhibitory mechanism: Toward a unified theory of cognitive development and aging. *Developmental Review*, **12**(1), pp. 45–75. 10.1016/0273-2297(92)90003-K

Di Marco, S., Tosoni, A., Altomare, E. C., Ferretti, G., Perrucci, M. G., & Committeri, G. (2019). Walking-related locomotion is facilitated by the perception of distant targets in the extrapersonal space. *Scientific Reports*, **9**:9884. 10.1038/s41598-019-46384-5

DiCarlo, J. J., Zoccolan, D., & Rust, N. C. (2012). How Does the Brain Solve Visual Object Recognition? *Neuron*, **73**(3), pp. 415–434. 10.1016/j.neuron.2012.01.010

Diersch, N., Valdés-Herrera, J. P., Tempelmann, C., & Wolbers, T. (2021). Increased Hippocampal Excitability and Altered Learning Dynamics Mediate Cognitive Mapping Deficits in Human Aging. *Journal of Neuroscience*, **41**(14), pp. 3204–3221. 10.1523/JNEUROSCI.0528-20.2021

Diersch, N., & Wolbers, T. (2019). The potential of virtual reality for spatial navigation research across the adult lifespan. *Journal of Experimental Biology*, **222**(Suppl 1), jeb187252. 10.1242/jeb.187252

di Fronso, S., Fiedler, P., Tamburro, G., Haueisen, J., Bertollo, M., & Comani, S. (2019). Dry EEG in Sports Sciences: A Fast and Reliable Tool to Assess Individual Alpha Peak Frequency Changes Induced by Physical Effort. *Frontiers in Neuroscience*, **13**:982. 10.3389/fnins.2019.00982

Dilks, D. D., Julian, J. B., Kubilius, J., Spelke, E. S., & Kanwisher, N. G. (2011). Mirror-Image Sensitivity and Invariance in Object and Scene Processing Pathways. *Journal of Neuroscience*, **31**(31), pp. 11305–11312. 10.1523/JNEUROSCI.1935-11.2011

Dilks, D. D., Julian, J. B., Paunov, A. M., & Kanwisher, N. G. (2013). The Occipital Place Area Is Causally and Selectively Involved in Scene Perception. *Journal of Neuroscience*, **33**(4), pp. 1331–1336. 10.1523/JNEUROSCI.4081-12.2013

Dilks, D. D., Kamps, F. S., & Persichetti, A. S. (2022). Three cortical scene systems and their development. *Trends in Cognitive Sciences*, **26**(2), pp. 117–127. 10.1016/j.tics.2021.11.002

Djebbara, Z., Fich, L. B., & Gramann, K. (2021). The brain dynamics of architectural affordances during transition. *Scientific Reports*, **11**:2796. 10.1038/s41598-021-82504-w

Djebbara, Z., Fich, L. B., Petrini, L., & Gramann, K. (2019). Sensorimotor brain dynamics reflect architectural affordances. *Proceedings of the National Academy of Sciences*, **116**(29), pp. 14769–14778. 10.1073/pnas.1900648116

Do, T.-t. N., Lin, C.-t., & Gramann, K. (2021). Human brain dynamics in active spatial navigation. *Scientific Reports*, **11**:13036. 10.1038/s41598-021-92246-4

Dolcos, F., Rice, H. J., & Cabeza, R. (2002). Hemispheric asymmetry and aging: right hemisphere decline or asymmetry reduction. *Neuroscience & Biobehavioral Reviews*, **26**(7), pp. 819–825. 10.1016/S0149-7634(02)00068-4

Donner, T. H., Siegel, M., Oostenveld, R., Fries, P., Bauer, M., & Engel, A. K. (2007). Population Activity in the Human Dorsal Pathway Predicts the Accuracy of Visual Motion Detection. *Journal of Neurophysiology*, **98**(1), pp. 345–359. 10.1152/jn.01141.2006

Dorn, J. D., Ahuja, A. K., Caspi, A., da Cruz, L., Dagnelie, G., Sahel, J.-A., … Argus II Study Group (2013). The Detection of Motion by Blind Subjects With the Epiretinal 60-Electrode (Argus II) Retinal Prosthesis. *JAMA Ophthalmology*, **131**(2), 183. 10.1001/2013.jamaophthalmol.221

Dowiasch, S., Marx, S., Einhäuser, W., & Bremmer, F. (2015). Effects of aging on eye movements in the real world. *Frontiers in Human Neuroscience*, **9**:46. 10.3389/fnhum.2015.00046

Draschkow, D., & Võ, M. L. (2017). Scene grammar shapes the way we interact with objects, strengthens memories, and speeds search. *Scientific Reports*, **7**:16471. 10.1038/s41598-017-16739-x

Driscoll, I., Hamilton, D. A., Petropoulos, H., Yeo, R. A., Brooks, W. M., Baumgartner, R. N., & Sutherland, R. J. (2003). The Aging Hippocampus: Cognitive, Biochemical and Structural Findings. *Cerebral Cortex*, **13**(12), pp. 1344–1351. 10.1093/cercor/bhg081

Durteste, M., Van Poucke, L., Combariza, S., Benziane, B. A., Sahel, J.-A., Ramanoël, S., & Arleo, A. (2023). The vertical position of visual information conditions spatial memory performance in healthy aging. *Communications Psychology*, **1**(1), 2. 10.1038/s44271-023-00002-3

Dwivedi, K., Cichy, R. M., & Roig, G. (2021). Unraveling Representations in Scene-selective Brain Regions Using Scene-Parsing Deep Neural Networks. *Journal of Cognitive Neuroscience*, **33**(10), pp. 2032–2043. 10.1162/jocn_a_01624

Ebe, M., Mikami, T., & Ito, H. (1964). Clinical Evaluation of Electrical Responses of Retina and Visual Cortex to Photic Stimulation in Ophthalmic Diseases. *The Tohoku Journal of Experimental Medicine*, **84**(1), pp. 92–103. 10.1620/tjem.84.92

Ehinger, B. V., Fischer, P., Gert, A. L., Kaufhold, L., Weber, F., Pipa, G., & König, P. (2014). Kinesthetic and vestibular information modulate alpha activity during spatial navigation: a mobile EEG study. *Frontiers in Human Neuroscience*, **8**:71. 10.3389/fnhum.2014.00071

Ekstrom, A. D. (2015). Why vision is important to how we navigate. *Hippocampus*, **25**(6), pp. 731–735. 10.1002/hipo.22449

Ekstrom, A. D., Arnold, A. E. G. F., & Iaria, G. (2014). A critical review of the allocentric spatial representation and its neural underpinnings: toward a network-based perspective. *Frontiers in Human Neuroscience*, **8**:803. 10.3389/fnhum.2014.00803

Ekstrom, A. D., Caplan, J. B., Ho, E., Shattuck, K., Fried, I., & Kahana, M. J. (2005). Human hippocampal theta activity during virtual navigation. *Hippocampus*, **15**(7), pp. 881–889. 10.1002/hipo.20109

Ekstrom, A. D., Huffman, D. J., & Starrett, M. J. (2017). Interacting networks of brain regions underlie human spatial navigation: a review and novel synthesis of the literature. *Journal of Neurophysiology*, **118**(6), pp. 3328–3344. 10.1152/jn.00531.2017

Ekstrom, A. D., Kahana, M. J., Caplan, J. B., Fields, T. A., Isham, E. A., Newman, E. L., & Fried, I. (2003). Cellular networks underlying human spatial navigation. *Nature*, **425**(6954), pp. 184–188. 10.1038/nature01964

Ekstrom, A. D., Spiers, H. J., Bohbot, V. D., & Rosenbaum, R. S. (2018). *Human Spatial Navigation*. Princeton University Press.

Ekstrom, A. D., Suthana, N., Millett, D., Fried, I., & Bookheimer, S. (2009). Correlation Between BOLD fMRI and Theta-Band Local Field Potentials in the Human Hippocampal Area. *Journal of Neurophysiology*, **101**(5), pp. 2668–2678. 10.1152/jn.91252.2008

Engel, A. K., & Fries, P. (2010). Beta-band oscillations - signalling the status quo? *Current Opinion in Neurobiology*, **20**(2), pp. 156–165. 10.1016/j.conb.2010.02.015

Enriquez-Geppert, S., Huster, R. J., & Herrmann, C. S. (2017). EEG-Neurofeedback as a Tool to Modulate Cognition and Behavior: A Review Tutorial. *Frontiers in Human Neuroscience*, **11**:51. 10.3389/fnhum.2017.00051

Epstein, R. A. (2005). The cortical basis of visual scene processing. *Visual Cognition*, **12**(6), pp. 954–978. 10.1080/13506280444000607

Epstein, R. A. (2008). Parahippocampal and retrosplenial contributions to human spatial navigation. *Trends in Cognitive Sciences*, **12**(10), pp. 388–396. 10.1016/j.tics.2008.07.004

Epstein, R. A., & Baker, C. I. (2019). Scene Perception in the Human Brain. *Annual Review of Vision Science*, **5**, pp. 373–397. 10.1146/annurev-vision-091718-014809

Epstein, R. A., Higgins, J. S., Jablonski, K., & Feiler, A. M. (2007). Visual Scene Processing in Familiar and Unfamiliar Environments. *Journal of Neurophysiology*, **97**(5), pp. 3670–3683. 10.1152/jn.00003.2007

Epstein, R. A., & Kanwisher, N. G. (1998). A cortical representation of the local visual environment. *Nature*, **392**(6676), pp. 598–601. 10.1038/33402

Epstein, R. A., Patai, E. Z., Julian, J. B., & Spiers, H. J. (2017). The cognitive map in humans: spatial navigation and beyond. *Nature Neuroscience*, **20**(11), pp. 1504–1513. 10.1038/nn.4656

Epstein, R. A., & Vass, L. K. (2014). Neural systems for landmark-based wayfinding in humans. *Philosophical Transactions of the Royal Society B: Biological Sciences*, **369**(1635), 20120533. 10.1098/rstb.2012.0533

Ergenoglu, T., Demiralp, T., Bayraktaroglu, Z., Ergen, M., Beydagi, H., & Uresin, Y. (2004). Alpha rhythm of the EEG modulates visual detection performance in humans. *Cognitive Brain Research*, **20**(3), pp. 376–383. 10.1016/j.cogbrainres.2004.03.009

Erickson-Davis, C., & Korzybska, H. (2021). What do blind people see with retinal prostheses? Observations and qualitative reports of epiretinal implant users. *PLOS ONE*, **16**(2), e0229189. 10.1371/journal.pone.0229189

Eudy, J. D., Weston, M. D., Yao, S., Hoover, D. M., Rehm, H. L., Ma-Edmonds, M., ... Sumegi, J. (1998). Mutation of a Gene Encoding a Protein with Extracellular Matrix Motifs in Usher Syndrome Type IIa. *Science*, **280**(5370), pp. 1753–1757. 10.1126/science.280.5370.1753

Farnum, A., & Pelled, G. (2020). New Vision for Visual Prostheses. *Frontiers in Neuroscience*, **14**:36. 10.3389/fnins.2020.00036

Faubert, J. (2002). Visual perception and aging. *Canadian Journal of Experimental Psychology/Revue canadienne de psychologie expérimentale*, **56**(3), pp. 164–176. 10.1037/h0087394

Fellner, M.-C., Volberg, G., Wimber, M., Goldhacker, M., Greenlee, M. W., & Hanslmayr, S. (2016). Spatial Mnemonic Encoding: Theta Power Decreases and Medial Temporal Lobe BOLD Increases Co-Occur during the Usage of the Method of Loci. *eneuro*, **3**(6), pp. ENEURO.0184–16.2016. 10.1523/ENEURO.0184-16.2016

Feng, J., Craik, F. I. M., Levine, B., Moreno, S., Naglie, G., & Choi, H. (2017). Differential age-related changes in localizing a target among distractors across an extended visual field. *European Journal of Ageing*, **14**(2), pp. 167–177. 10.1007/s10433-016-0399-7

Feng, W., Störmer, V. S., Martinez, A., McDonald, J. J., & Hillyard, S. A. (2017). Involuntary orienting of attention to a sound desynchronizes the occipital alpha rhythm and improves visual perception. *NeuroImage*, **150**, pp. 318–328. 10.1016/j.neuroimage.2017.02.033

Ferguson, T. D., Williams, C. C., Skelton, R. W., & Krigolson, O. E. (2019). Passively learned spatial navigation cues evoke reinforcement learning reward signals. *Cognition*, **189**, pp. 65–75. 10.1016/j.cognition.2019.03.015

Ferlauto, L., Airaghi Leccardi, M. J. I., Chenais, N. A. L., Gilliéron, S. C. A., Vagni, P., Bevilacqua, M., … Ghezzi, D. (2018). Design and validation of a foldable and photovoltaic wide-field epiretinal prosthesis. *Nature Communications*, **9**:992. 10.1038/s41467-018-03386-7

Ferrara, K., & Park, S. (2016). Neural representation of scene boundaries. *Neuropsychologia*, **89**, pp. 180–190. 10.1016/j.neuropsychologia.2016.05.012

Fiedler, P., Haueisen, J., Alvarez, A. M. C., Cheron, G., Cuesta, P., Maestú, F., & Funke, M. (2023). Noise characteristics in spaceflight multichannel EEG. *PLOS ONE*, **18**(2), e0280822. 10.1371/journal.pone.0280822

Finnigan, S., O'Connell, R. G., Cummins, T. D. R., Broughton, M., & Robertson, I. H. (2011). ERP measures indicate both attention and working memory encoding decrements in aging. *Psychophysiology*, **48**(5), pp. 601–611. 10.1111/j.1469-8986.2010.01128.x

Fischl, B., van der Kouwe, A., Destrieux, C., Halgren, E., Ségonne, F., Salat, D. H., … Dale, A. M. (2004). Automatically Parcellating the Human Cerebral Cortex. *Cerebral Cortex*, **14**(1), pp. 11–22. 10.1093/cercor/bhg087

Fleming, S. M., & Dolan, R. J. (2012). The neural basis of metacognitive ability. *Philosophical Transactions of the Royal Society B: Biological Sciences*, **367**(1594), pp. 1338–1349. 10.1098/rstb.2011.0417

Flückiger, M., & Baumberger, B. (1988). The Perception of an Optical Flow Projected on the Ground Surface. *Perception*, **17**(5), pp. 633–645. 10.1068/p170633

Foisy, A., & Kapoula, Z. (2018). Plantar cutaneous afferents influence the perception of Subjective Visual Vertical in quiet stance. *Scientific Reports*, **8**:14939. 10.1038/s41598-018-33268-3

Folstein, M. F., Folstein, S. E., & McHugh, P. R. (1975). Mini-mental state: A practical method for grading the cognitive state of patients for the clinician. *Journal of Psychiatric Research*, **12**(3), pp. 189–198. 10.1016/0022-3956(75)90026-6

Foo, P., Warren, W. H., Duchon, A. P., & Tarr, M. J. (2005). Do Humans Integrate Routes Into a Cognitive Map? Map- Versus Landmark-Based Navigation of Novel Shortcuts. *Journal of Experimental Psychology: Learning, Memory, and Cognition*, **31**(2), pp. 195–215. 10.1037/0278-7393.31.2.195

Fortun, D., Bouthemy, P., & Kervrann, C. (2015). Optical flow modeling and computation: A survey. *Computer Vision and Image Understanding*, **134**, pp. 1–21. 10.1016/j.cviu.2015.02.008

Francois, J., Stefens, R., & Derouck, A. (1954). [Electro-retino-encephalography in pigmented retinopathy]. *Annales d'oculistique*, **187**(10), pp. 908–937.

Freunberger, R., Klimesch, W., Doppelmayr, M., & Höller, Y. (2007). Visual P2 component is related to theta phase-locking. *Neuroscience Letters*, **426**(3), pp. 181–186. 10.1016/j.neulet.2007.08.062

Freunberger, R., Klimesch, W., Griesmayr, B., Sauseng, P., & Gruber, W. (2008). Alpha phase coupling reflects object recognition. *NeuroImage*, **42**(2), pp. 928–935. 10.1016/j.neuroimage.2008.05.020

Friedman, A., Kohler, B., Gunalp, P., Boone, A. P., & Hegarty, M. (2020). A computerized spatial orientation test. *Behavior Research Methods*, **52**(2), pp. 799–812. 10.3758/s13428-019-01277-3

Fries, P. (2005). A mechanism for cognitive dynamics: neuronal communication through neuronal coherence. *Trends in Cognitive Sciences*, **9**(10), pp. 474–480. 10.1016/j.tics.2005.08.011

Fries, P. (2015). Rhythms for Cognition: Communication through Coherence. *Neuron*, **88**(1), pp. 220–235. 10.1016/j.neuron.2015.09.034

Gable, P. A., Miller, M. W., & Bernat, E. M. (2022). *The Oxford Handbook of EEG Frequency* (P. A. Gable, M. W. Miller, & E. M. Bernat, Eds.). Oxford: Oxford University Press. 10.1093/oxfordhb/9780192898340.001.0001

Gauvain, G., Akolkar, H., Chaffiol, A., Arcizet, F., Khoei, M. A., Desrosiers, M., … Picaud, S. (2021). Optogenetic therapy: high spatiotemporal resolution and pattern discrimination compatible with vision restoration in non-human primates. *Communications Biology*, **4**(1), 125. 10.1038/s42003-020-01594-w

Gazzaley, A., Clapp, W., Kelley, J., McEvoy, K., Knight, R. T., & D'Esposito, M. (2008). Age-related top-down suppression deficit in the early stages of cortical visual memory processing. *Proceedings of the National Academy of Sciences*, **105**(35), pp. 13122–13126. 10.1073/pnas.0806074105

Gazzaley, A., & D'Esposito, M. (2007). Top-Down Modulation and Normal Aging. *Annals of the New York Academy of Sciences*, **1097**(1), pp. 67–83. 10.1196/annals.1379.010

Gehrke, L., & Gramann, K. (2021). Single-trial regression of spatial exploration behavior indicates posterior EEG alpha modulation to reflect egocentric coding. *European Journal of Neuroscience*, **54**(12), pp. 8318–8335. 10.1111/ejn.15152

Gelfo, F., Mandolesi, L., Serra, L., Sorrentino, G., & Caltagirone, C. (2018). The Neuroprotective Effects of Experience on Cognitive Functions: Evidence from Animal Studies on the Neurobiological Bases of Brain Reserve. *Neuroscience*, **370**, pp. 218–235. 10.1016/j.neuroscience.2017.07.065

Gevins, A., & Smith, M. E. (2003). Neurophysiological measures of cognitive workload during human-computer interaction. *Theoretical Issues in Ergonomics Science*, **4**(1-2), pp. 113–131. 10.1080/14639220210159717

Ghezzi, D. (2023). The role of the visual field size in artificial vision. *Journal of Neural Engineering*, **20**(2), 023001. 10.1088/1741-2552/acc7cd

Gibson, J. J. (1986). *The Ecological Approach to Visual Perception*. Taylor & Francis Group.

Gillespie, F. D., & Dohogne, V. Z. (1964). Electro-Encephalograms in Retinitis Pigmentosa. *American Journal of Ophthalmology*, **57**(6), pp. 1045–1050. 10.1016/0002-9394(64)91053-0

Glover, G. H. (2011). Overview of Functional Magnetic Resonance Imaging. *Neurosurgery Clinics of North America*, **22**(2), pp. 133–139. 10.1016/j.nec.2010.11.001

Gola, M., Magnuski, M., Szumska, I., & Wróbel, A. (2013). EEG beta band activity is related to attention and attentional deficits in the visual performance of elderly subjects. *International Journal of Psychophysiology*, **89**(3), pp. 334–341. 10.1016/j.ijpsycho.2013.05.007

Gomez, A., Cerles, M., Rousset, S., Rémy, C., & Baciu, M. (2014). Differential hippocampal and retrosplenial involvement in egocentric-updating, rotation, and allocentric processing during online spatial encoding: an fMRI study. *Frontiers in Human Neuroscience*, **8**:150. 10.3389/fnhum.2014.00150

Goodale, M. A., & Milner, A. (1992). Separate visual pathways for perception and action. *Trends in Neurosciences*, **15**(1), pp. 20–25. 10.1016/0166-2236(92)90344-8

Gramann, K. (2013). Embodiment of Spatial Reference Frames and Individual Differences in Reference Frame Proclivity. *Spatial Cognition & Computation*, **13**(1), pp. 1–25. 10.1080/13875868.2011.589038

Gramann, K., Ferris, D. P., Gwin, J. T., & Makeig, S. (2014). Imaging natural cognition in action. *International Journal of Psychophysiology*, **91**(1), pp. 22–29. 10.1016/j.ijpsycho.2013.09.003

Gramann, K., Gwin, J. T., Bigdely-Shamlo, N., Ferris, D. P., & Makeig, S. (2010a). Visual Evoked Responses During Standing and Walking. *Frontiers in Human Neuroscience*, **4**:202. 10.3389/fnhum.2010.00202

Gramann, K., Gwin, J. T., Ferris, D. P., Oie, K., Jung, T.-P., Lin, C.-T., … Makeig, S. (2011). Cognition in action: imaging brain/body dynamics in mobile humans. *Reviews in the Neurosciences*, **22**(6), pp. 593–608. 10.1515/RNS.2011.047

Gramann, K., Hohlefeld, F. U., Gehrke, L., & Klug, M. (2018). Heading computation in the human retrosplenial complex during full-body rotation. *bioRxiv*:417972. 10.1101/417972

Gramann, K., Hohlefeld, F. U., Gehrke, L., & Klug, M. (2021). Human cortical dynamics during full-body heading changes. *Scientific Reports*, **11**:18186. 10.1038/s41598-021-97749-8

Gramann, K., Onton, J., Riccobon, D., Mueller, H. J., Bardins, S., & Makeig, S. (2010b). Human Brain Dynamics Accompanying Use of Egocentric and Allocentric Reference Frames during Navigation. *Journal of Cognitive Neuroscience*, **22**(12), pp. 2836–2849. 10.1162/jocn.2009.21369

Gramfort, A., Luessi, M., Larson, E., Engemann, D. A., Strohmeier, D., Brodbeck, C., … Hämäläinen, M. S. (2013). MEG and EEG data analysis with MNE-Python. *Frontiers in Neuroscience*, **7**:267. 10.3389/fnins.2013.00267

Grandchamp, R., & Delorme, A. (2011). Single-Trial Normalization for Event-Related Spectral Decomposition Reduces Sensitivity to Noisy Trials. *Frontiers in Psychology*, **2**:236. 10.3389/fpsyg.2011.00236

Greene, M. R. (2013). Statistics of high-level scene context. *Frontiers in Psychology*, **4**:777. 10.3389/fpsyg.2013.00777

Greene, M. R., Baldassano, C., Esteva, A., Beck, D. M., & Fei-Fei, L. (2016). Visual scenes are categorized by function. *Journal of Experimental Psychology: General*, **145**(1), pp. 82–94. 10.1037/xge0000129

Greene, M. R., Botros, A. P., Beck, D. M., & Fei-Fei, L. (2015). What you see is what you expect: rapid scene understanding benefits from prior experience. *Attention, Perception, & Psychophysics*, **77**(4), pp. 1239–1251. 10.3758/s13414-015-0859-8

Greene, M. R., & Oliva, A. (2009a). The Briefest of Glances. *Psychological Science*, **20**(4), pp. 464–472. 10.1111/j.1467-9280.2009.02316.x

Greene, M. R., & Oliva, A. (2009b). Recognition of natural scenes from global properties: Seeing the forest without representing the trees. *Cognitive Psychology*, **58**(2), pp. 137–176. 10.1016/j.cogpsych.2008.06.001

Groen, I. I. A., Ghebreab, S., Prins, H., Lamme, V. A., & Scholte, H. S. (2013). From Image Statistics to Scene Gist: Evoked Neural Activity Reveals Transition from Low-Level Natural Image Structure to Scene Category. *Journal of Neuroscience*, **33**(48), pp. 18814–18824. 10.1523/JNEUROSCI.3128-13.2013

Groen, I. I. A., Silson, E. H., & Baker, C. I. (2017). Contributions of low- and high-level properties to neural processing of visual scenes in the human brain. *Philosophical Transactions of the Royal Society B: Biological Sciences*, **372**(1714), 20160102. 10.1098/rstb.2016.0102

Gruber, T., Müller, M. M., Keil, A., & Elbert, T. (1999). Selective visual-spatial attention alters induced gamma band responses in the human EEG. *Clinical Neurophysiology*, **110**(12), pp. 2074–2085. 10.1016/S1388-2457(99)00176-5

Grzeschik, R., Conroy-Dalton, R., Innes, A., Shanker, S., & Wiener, J. M. (2019). The contribution of visual attention and declining verbal memory abilities to age-related route learning deficits. *Cognition*, **187**, pp. 50–61. 10.1016/j.cognition.2019.02.012

Güntekin, B., & Başar, E. (2016). Review of evoked and event-related delta responses in the human brain. *International Journal of Psychophysiology*, **103**, pp. 43–52. 10.1016/j.ijpsycho.2015.02.001

Gwin, J. T., Gramann, K., Makeig, S., & Ferris, D. P. (2010). Removal of Movement Artifact From High-Density EEG Recorded During Walking and Running. *Journal of Neurophysiology*, **103**(6), pp. 3526–3534. 10.1152/jn.00105.2010

Gwin, J. T., Gramann, K., Makeig, S., & Ferris, D. P. (2011). Electrocortical activity is coupled to gait cycle phase during treadmill walking. *NeuroImage*, **54**(2), pp. 1289–1296. 10.1016/j.neuroimage.2010.08.066

Hafed, Z. M., & Chen, C.-Y. (2016). Sharper, Stronger, Faster Upper Visual Field Representation in Primate Superior Colliculus. *Current Biology*, **26**(13), pp. 1647–1658. 10.1016/j.cub.2016.04.059

Hallum, L. E., & Dakin, S. C. (2021). Retinal Implantation of Electronic Vision Prostheses to Treat Retinitis Pigmentosa: A Systematic Review. *Translational Vision Science & Technology*, **10**(10), 8. 10.1167/tvst.10.10.8

Hämäläinen, M. S., Hari, R., Ilmoniemi, R. J., Knuutila, J., & Lounasmaa, O. V. (1993). Magnetoencephalography-theory, instrumentation, and applications to noninvasive studies of the working human brain. *Reviews of Modern Physics*, **65**(2), pp. 413–497. 10.1103/RevModPhys.65.413

Hamel, C. (2006). Retinitis pigmentosa. *Orphanet Journal of Rare Diseases*, **1**:40. 10.1186/1750-1172-1-40

Hamid, S. N., Stankiewicz, B. J., & Hayhoe, M. (2010). Gaze patterns in navigation: Encoding information in large-scale environments. *Journal of Vision*, **10**(12), 28. 10.1167/10.12.28

Hamilton, R., Bach, M., Heinrich, S. P., Hoffmann, M. B., Odom, J. V., McCulloch, D. L., & Thompson, D. A. (2021). VEP estimation of visual acuity: a systematic review. *Documenta Ophthalmologica*, **142**(1), pp. 25–74. 10.1007/s10633-020-09770-3

Hanks, T. D., & Summerfield, C. (2017). Perceptual Decision Making in Rodents, Monkeys, and Humans. *Neuron*, **93**(1), pp. 15–31. 10.1016/j.neuron.2016.12.003

Hansen, N. E., Noesen, B. T., Nador, J. D., & Harel, A. (2018). The influence of behavioral relevance on the processing of global scene properties: An ERP study. *Neuropsychologia*, **114**, pp. 168–180. 10.1016/j.neuropsychologia.2018.04.040

Hansen, P. C. (2007). Regularization Tools version 4.0 for Matlab 7.3. *Numerical Algorithms*, **46**(2), pp. 189–194. 10.1007/s11075-007-9136-9

Hardcastle, K., Ganguli, S., & Giocomo, L. M. (2017). Cell types for our sense of location: where we are and where we are going. *Nature Neuroscience*, **20**(11), pp. 1474–1482. 10.1038/nn.4654

Harel, A., Groen, I. I. A., Kravitz, D. J., Deouell, L. Y., & Baker, C. I. (2016). The Temporal Dynamics of Scene Processing: A Multifaceted EEG Investigation. *eneuro*, **3**(5), pp. ENEURO.0139–16.2016. 10.1523/ENEURO.0139-16.2016

Harel, A., Mzozoyana, M. W., Al Zoubi, H., Nador, J. D., Noesen, B. T., Lowe, M. X., & Cant, J. S. (2020). Artificially-generated scenes demonstrate the importance of global scene properties for scene perception. *Neuropsychologia*, **141**:107434. 10.1016/j.neuropsychologia.2020.107434

Harel, A., Nador, J. D., Bonner, M. F., & Epstein, R. A. (2022). Early Electrophysiological Markers of Navigational Affordances in Scenes. *Journal of Cognitive Neuroscience*, **34**(3), pp. 397–410. 10.1162/jocn_a_01810

Harmony, T. (2013). The functional significance of delta oscillations in cognitive processing. *Frontiers in Integrative Neuroscience*, **7**:83. 10.3389/fnint.2013.00083

Harmony, T., Fernández, T., Silva, J. C., Bernal, J., Díaz-Comas, L., Reyes, A., … Rodríguez, M. (1996). EEG delta activity: an indicator of attention to internal processing during performance of mental tasks. *International Journal of Psychophysiology*, **24**(1-2), pp. 161–171. 10.1016/S0167-8760(96)00053-0

Harootonian, S. K., Wilson, R. C., Hejtmánek, L., Ziskin, E. M., & Ekstrom, A. D. (2020). Path integration in large-scale space and with novel geometries: Comparing vector addition and encoding-error models. *PLOS Computational Biology*, **16**(5), e1007489. 10.1371/journal.pcbi.1007489

Harris, M. A., Wiener, J. M., & Wolbers, T. (2012). Aging specifically impairs switching to an allocentric navigational strategy. *Frontiers in Aging Neuroscience*, **4**:29. 10.3389/fnagi.2012.00029

Harris, M. A., & Wolbers, T. (2012). Ageing effects on path integration and landmark navigation. *Hippocampus*, **22**(8), pp. 1770–1780. 10.1002/hipo.22011

Hartley, T., Maguire, E. A., Spiers, H. J., & Burgess, N. (2003). The Well-Worn Route and the Path Less Traveled: Distinct Neural Bases of Route Following and Wayfinding in Humans. *Neuron*, **37**(5), pp. 877–888. 10.1016/S0896-6273(03)00095-3

Hartmeyer, S., Grzeschik, R., Wolbers, T., & Wiener, J. M. (2017). The Effects of Attentional Engagement on Route Learning Performance in a Virtual Environment: An Aging Study. *Frontiers in Aging Neuroscience*, **9**:235. 10.3389/fnagi.2017.00235

Hartong, D. T., Berson, E. L., & Dryja, T. P. (2006). Retinitis pigmentosa. *The Lancet*, **368**(9549), pp. 1795–1809. 10.1016/S0140-6736(06)69740-7

Hassler, U., Trujillo Barreto, N., & Gruber, T. (2011). Induced gamma band responses in human EEG after the control of miniature saccadic artifacts. *NeuroImage*, **57**(4), pp. 1411–1421. 10.1016/j.neuroimage.2011.05.062

Hasson, U., Harel, M., Levy, I., & Malach, R. (2003). Large-Scale Mirror-Symmetry Organization of Human Occipito-Temporal Object Areas. *Neuron*, **37**(6), pp. 1027–1041. 10.1016/S0896-6273(03)00144-2

Hayasaka, S., & Nichols, T. E. (2004). Combining voxel intensity and cluster extent with permutation test framework. *NeuroImage*, **23**(1), pp. 54–63. 10.1016/j.neuroimage.2004.04.035

He, Y., Huang, N., Caspi, A., Roy, A., Engel, S., Legge, G. E., ... Montezuma, S. R. (2018). Development of an electroencephalogram (EEG) protocol to map electrically-elicited visual responses in blind patients implanted with the Argus II retinal prosthesis. *Investigative Ophthalmology & Visual Science*, **59**(9), 4572. Retrieved from https://iovs.arvojournals.org/article.aspx?articleid=2692174

Head, D., & Isom, M. (2010). Age effects on wayfinding and route learning skills. *Behavioural Brain Research*, **209**(1), pp. 49–58. 10.1016/j.bbr.2010.01.012

Hebb, D. O. (1949). *The Organization of Behavior: A Neurophychological Theory*. John Wiley & Sons, Inc.

Heekeren, H. R., Marrett, S., & Ungerleider, L. G. (2008). The neural systems that mediate human perceptual decision making. *Nature Reviews Neuroscience*, **9**(6), pp. 467–479. 10.1038/nrn2374

Heft, H. (1996). The Ecological Approach to Navigation: A Gibsonian Perspective. In J. Portugali (Ed.), *The Construction of Cognitive Maps* (pp. 105–132). Dordrecht: Springer Netherlands. 10.1007/978-0-585-33485-1_6

Henderson, J. M., & Hollingworth, A. (1999). High-level scene perception. *Annual Review of Psychology*, **50**, pp. 243–271. 10.1146/annurev.psych.50.1.243

Herrmann, C. S., Rach, S., Vosskuhl, J., & Strüber, D. (2014). TimeFrequency Analysis of Event-Related Potentials: A Brief Tutorial. *Brain Topography*, **27**(4), pp. 438–450. 10.1007/s10548-013-0327-5

Herweg, N. A., & Kahana, M. J. (2018). Spatial Representations in the Human Brain. *Frontiers in Human Neuroscience*, **12**:297. 10.3389/fnhum.2018.00297

Hillyard, S. A., Vogel, E. K., & Luck, S. J. (1998). Sensory gain control (amplification) as a mechanism of selective attention: electrophysiological and neuroimaging evidence. *Philosophical Transactions of the Royal Society B: Biological Sciences*, **353**(1373), pp. 1257–1270. 10.1098/rstb.1998.0281

Hilton, C., Miellet, S., Slattery, T. J., & Wiener, J. M. (2020). Are age-related deficits in route learning related to control of visual attention? *Psychological Research*, **84**(6), pp. 1473–1484. 10.1007/s00426-019-01159-5

Holm, A., Lukander, K., Korpela, J., Sallinen, M., & Müller, K. M. I. (2009). Estimating Brain Load from the EEG. *The Scientific World Journal*, **9**(973791), pp. 639–651. 10.1100/tsw.2009.83

Holmes, C. A., Newcombe, N. S., & Shipley, T. F. (2018). Move to learn: Integrating spatial information from multiple viewpoints. *Cognition*, **178**, pp. 7–25. 10.1016/j.cognition.2018.05.003

Holtzer, R., Epstein, N., Mahoney, J. R., Izzetoglu, M., & Blumen, H. M. (2014). Neuroimaging of Mobility in Aging: A Targeted Review. *The Journals of Gerontology: Series A*, **69**(11), pp. 1375–1388. 10.1093/gerona/glu052

Holtzer, R., Verghese, J., Xue, X., & Lipton, R. B. (2006). Cognitive processes related to gait velocity: Results from the Einstein aging study. *Neuropsychology*, **20**(2), pp. 215–223. 10.1037/0894-4105.20.2.215

Homölle, S., & Oostenveld, R. (2019). Using a structured-light 3D scanner to improve EEG source modeling with more accurate electrode positions. *Journal of Neuroscience Methods*, **326**:108378. 10.1016/j.jneumeth.2019.108378

Horak, F. B., & Macpherson, J. M. (2011). Postural Orientation and Equilibrium. In R. Terjung (Ed.), *Comprehensive Physiology* (pp. 255 – 292). Hoboken, NJ, USA: John Wiley & Sons, Inc. 10.1002/cphy.cp120107

Hossain, G., & Yeasin, M. (2014). Understanding Effects of Cognitive Load from Pupillary Responses Using Hilbert Analytic Phase. In *2014 IEEE Conference on Computer Vision and Pattern Recognition Workshops* (pp. 381–386). Columbus, OH: IEEE. 10.1109/CVPRW.2014.62

Hsu, S.-H., Pion-Tonachini, L., Palmer, J. A., Miyakoshi, M., Makeig, S., & Jung, T.-P. (2018). Modeling brain dynamic state changes with adaptive mixture independent component analysis. *NeuroImage*, **183**, pp. 47–61. 10.1016/j.neuroimage.2018.08.001

Humayun, M. S., de Juan Jr, E., & Dagnelie, G. (2016). The Bionic Eye: A Quarter Century of Retinal Prosthesis Research and Development. *Ophthalmology*, **123**(10), pp. S89–S97. 10.1016/j.ophtha.2016.06.044

Hurlebaus, R., Basten, K., Mallot, H. A., & Wiener, J. M. (2008). Route Learning Strategies in a Virtual Cluttered Environment. In C. Freksa, N. Newcombe, P. Gärdenfors, & S. Wölfl (Eds.), *Spatial Cognition VI. Learning, Reasoning, and Talking about Space* (Vol. 5248, pp. 104–120). Springer, Berlin, Heidelberg. 10.1007/978-3-540-87601-4_10

Iaria, G., Petrides, M., Dagher, A., Pike, B., & Bohbot, V. D. (2003). Cognitive Strategies Dependent on the Hippocampus and Caudate Nucleus in Human Navigation: Variability and Change with Practice. *Journal of Neuroscience*, **23**(13), pp. 5945–5952. 10.1523/JNEUROSCI.23-13-05945.2003

International Commission on Non-Ionizing Radiation Protection (ICNIRP). (1997). Guidelines on limits of exposure to broad-band incoherent optical radiation (0.38 to 3μM). *Health Physics*, **73**(3), pp. 539–554. Retrieved from `https://www.icnirp.org/cms/upload/publications/ICNIRPbroadband.pdf`

International Electrotechnical Commission (IEC). (2014). *IEC 60825-1-2014: Safety of Laser Products - Part 1: Equipment Classification and Requirements.* Retrieved from `https://standards.globalspec.com/std/1682187/iec-60825-1`

International Standards Organization (ISO). (2007). *ISO 15004-2:2007: Ophthalmic instruments - Fundamental requirements and test methods - Part 2: light hazard protection.* Retrieved from `https://www.iso.org/standard/38952.html`

Jabbari, Y., Kenney, D. M., von Mohrenschildt, M., & Shedden, J. M. (2021). Vestibular cues improve landmark-based route navigation: A simulated driving study. *Memory & Cognition*, **49**(8), pp. 1633–1644. 10.3758/s13421-021-01181-2

Jabès, A., Klencklen, G., Ruggeri, P., Antonietti, J.-P., Banta Lavenex, P., & Lavenex, P. (2021). Age-Related Differences in Resting-State EEG and Allocentric Spatial Working Memory Performance. *Frontiers in Aging Neuroscience*, **13**:704362. 10.3389/fnagi.2021.704362

Jacobs, J. (2014). Hippocampal theta oscillations are slower in humans than in rodents: implications for models of spatial navigation and memory. *Philosophical Transactions of the Royal Society B: Biological Sciences*, **369**(1635), 20130304. 10.1098/rstb.2013.0304

Jacobs, J., Weidemann, C. T., Miller, J. F., Solway, A., Burke, J. F., Wei, X.-X., ... Kahana, M. J. (2013). Direct recordings of grid-like neuronal activity in human spatial navigation. *Nature Neuroscience*, **16**(9), pp. 1188–1190. 10.1038/nn.3466

Jansen, P., Schmelter, A., & Heil, M. (2010). Spatial Knowledge Acquisition in Younger and Elderly Adults. *Experimental Psychology*, **57**(1), pp. 54–60. 10.1027/1618-3169/a000007

Janzen, G. (2006). Memory for object location and route direction in virtual large-scale space. *Quarterly Journal of Experimental Psychology*, **59**(3), pp. 493–508. 10.1080/02724980443000746

Janzen, G., & van Turennout, M. (2004). Selective neural representation of objects relevant for navigation. *Nature Neuroscience*, **7**(6), pp. 673–677. 10.1038/nn1257

Javadi, A.-H., Emo, B., Howard, L. R., Zisch, F. E., Yu, Y., Knight, R., … Spiers, H. J. (2017). Hippocampal and prefrontal processing of network topology to simulate the future. *Nature Communications*, **8**:14652. 10.1038/ncomms14652

Javadi, A.-H., Patai, E. Z., Marin-Garcia, E., Margois, A., Tan, H.-R. M., Kumaran, D., … Spiers, H. J. (2019). Backtracking during navigation is correlated with enhanced anterior cingulate activity and suppression of alpha oscillations and the default-mode' network. *Proceedings of the Royal Society B: Biological Sciences*, **286**(1908), 20191016. 10.1098/rspb.2019.1016

Jenkinson, M., Pechaud, M., & Smith, S. M. (2005). BET2: MR-based estimation of brain, skull and scalp surfaces. In K. Zilles, J.-B. Poline, & C. Grady (Eds.), *Eleventh Annual Meeting of the Organization for Human Brain Mapping (OHBM 2005)* (p. e1). Toronto: NeuroImage. Retrieved from `http://mickaelpechaud.free.fr/these/HBM05.pdfhttps://www.sciencedirect.com/journal/neuroimage/vol/26/suppl/S1`

Jensen, O., Gips, B., Bergmann, T. O., & Bonnefond, M. (2014). Temporal coding organized by coupled alpha and gamma oscillations prioritize visual processing. *Trends in Neurosciences*, **37**(7), pp. 357–369. 10.1016/j.tins.2014.04.001

Jensen, O., Kaiser, J., & Lachaux, J.-P. (2007). Human gamma-frequency oscillations associated with attention and memory. *Trends in Neurosciences*, **30**(7), pp. 317–324. 10.1016/j.tins.2007.05.001

Jóhannesson, Ó. I., Tagu, J., & Kristjánsson, Á. (2018). Asymmetries of the visual system and their influence on visual performance and oculomotor dynamics. *European Journal of Neuroscience*, **48**(11), pp. 3426–3445. 10.1111/ejn.14225

Jovancevic-Misic, J., & Hayhoe, M. (2009). Adaptive Gaze Control in Natural Environments. *Journal of Neuroscience*, **29**(19), pp. 6234–6238. 10.1523/JNEUROSCI.5570-08.2009

Julian, J. B., Keinath, A. T., Marchette, S. A., & Epstein, R. A. (2018). The Neurocognitive Basis of Spatial Reorientation. *Current Biology*, **28**(17), pp. R1059–R1073. 10.1016/j.cub.2018.04.057

Julian, J. B., Ryan, J., Hamilton, R. H., & Epstein, R. A. (2016). The Occipital Place Area Is Causally Involved in Representing Environmental Boundaries during Navigation. *Current Biology*, **26**(8), pp. 1104–1109. 10.1016/j.cub.2016.02.066

Jung, T.-P., Makeig, S., Humphries, C., Lee, T.-W., McKeown, M. J., Iragui, V., & Sejnowski, T. J. (2000). Removing electroencephalographic artifacts by blind source separation. *Psychophysiology*, **37**(2), pp. 163–178. 10.1111/1469-8986.3720163

Kahana, M. J., Sekuler, R., Caplan, J. B., Kirschen, M., & Madsen, J. R. (1999). Human theta oscillations exhibit task dependence during virtual maze navigation. *Nature*, **399**(6738), pp. 781–784. 10.1038/21645

Kaiser, D., & Cichy, R. M. (2018a). Typical visual-field locations enhance processing in object-selective channels of human occipital cortex. *Journal of Neurophysiology*, **120**(2), pp. 848–853. 10.1152/jn.00229.2018

Kaiser, D., & Cichy, R. M. (2018b). Typical visual-field locations facilitate access to awareness for everyday objects. *Cognition*, **180**, pp. 118–122. 10.1016/j.cognition.2018.07.009

Kaiser, D., Häberle, G., & Cichy, R. M. (2020). Cortical sensitivity to natural scene structure. *Human Brain Mapping*, **41**(5), pp. 1286–1295. 10.1002/hbm.24875

Kaiser, D., Moeskops, M. M., & Cichy, R. M. (2018). Typical retinotopic locations impact the time course of object coding. *NeuroImage*, **176**, pp. 372–379. 10.1016/j.neuroimage.2018.05.006

Kaiser, D., Turini, J., & Cichy, R. M. (2019). A neural mechanism for contextualizing fragmented inputs during naturalistic vision. *eLife*, **8**:e48182. 10.7554/eLife.48182

Kajiwara, K., Berson, E. L., & Dryja, T. P. (1994). Digenic Retinitis Pigmentosa Due to Mutations at the Unlinked Peripherin/ RDS and ROM1 Loci. *Science*, **264**(5165), pp. 1604–1608. 10.1126/science.8202715

Kalafat, M., Hugonot-Diener, L., & Poitrenaud, J. (2003). Standardisation et étalonnage français du Mini Mental State (MMS) version GRECO. *Revue de neuropsychologie*, **13**(2), pp. 209–236.

Kamps, F. S., Julian, J. B., Kubilius, J., Kanwisher, N. G., & Dilks, D. D. (2016b). The occipital place area represents the local elements of scenes. *NeuroImage*, **132**, pp. 417–424. 10.1016/j.neuroimage.2016.02.062

Kamps, F. S., Lall, V., & Dilks, D. D. (2016a). The occipital place area represents first-person perspective motion information through scenes. *Cortex*, **83**, pp. 17–26. 10.1016/j.cortex.2016.06.022

Kang, J., & Park, S. (2023). Combined representation of visual features in the scene-selective cortex. *bioRxiv*:550280. 10.1101/2023.07.24.550280

Kaplan, S. (1992). Environmental preference in a knowledge-seeking, knowledge-using organism. In J. H. Barkow, L. Cosmides, & J. Tooby (Eds.), *The adapted mind: Evolutionary psychology and the generation of culture* (pp. 581–598). Oxford University Press. Retrieved from `https://psycnet.apa.org/record/1992-98504-016`

Karlsson, A. E., & Sander, M. C. (2023). Altered alpha/beta desynchronization during itemcontext binding contributes to the associative deficit in older age. *Cerebral Cortex*, **33**(6), pp. 2455–2469. 10.1093/cercor/bhac219

Kavcic, V., Fernandez, R., Logan, D., & Duffy, C. J. (2006). Neurophysiological and perceptual correlates of navigational impairment in Alzheimer's disease. *Brain*, **129**(3), pp. 736–746. 10.1093/brain/awh727

Kennedy, R. S., Lane, N. E., Berbaum, K. S., & Lilienthal, M. G. (1993). Simulator Sickness Questionnaire: An Enhanced Method for Quantifying Simulator Sickness. *The International Journal of Aviation Psychology*, **3**(3), pp. 203–220. 10.1207/s15327108ijap0303_3

Kim, M., Jeffery, K. J., & Maguire, E. A. (2017). Multivoxel Pattern Analysis Reveals 3D Place Information in the Human Hippocampus. *Journal of Neuroscience*, **37**(16), pp. 4270–4279. 10.1523/JNEUROSCI.2703-16.2017

Kim, S., Hasher, L., & Zacks, R. T. (2007). Aging and a benefit of distractibility. *Psychonomic Bulletin & Review*, **14**(2), pp. 301–305. 10.3758/BF03194068

Kim, S. Y., Sadda, S., Pearlman, J., Humayun, M. S., de Juan Jr, E., Melia, B. M., & Green, W. R. (2002). Morphometric analysis of the macula in eyes with disciform age-related macular degeneration. *Retina*, **22**(4), pp. 471–477. 10.1097/00006982-200208000-00012

Kimura, K., Reichert, J. F., Kelly, D. M., & Moussavi, Z. (2019). Older Adults Show Less Flexible Spatial Cue Use When Navigating in a Virtual Reality Environment Compared With Younger Adults. *Neuroscience Insights*, **14**:263310551989680. 10.1177/2633105519896803

Kimura, K., Reichert, J. F., Olson, A., Pouya, O. R., Wang, X., Moussavi, Z., & Kelly, D. M. (2017). Orientation in Virtual Reality Does Not Fully Measure Up to the Real-World. *Scientific Reports*, **7**:18109. 10.1038/s41598-017-18289-8

Kirasic, K. C. (1991). Spatial cognition and behavior in young and elderly adults: Implications for learning new environments. *Psychology and Aging*, **6**(1), pp. 10–18. 10.1037/0882-7974.6.1.10

Klapoetke, N. C., Murata, Y., Kim, S. S., Pulver, S. R., Birdsey-Benson, A., Cho, Y. K., … Boyden, E. S. (2014). Independent optical excitation of distinct neural populations. *Nature Methods*, **11**(3), pp. 338–346. 10.1038/nmeth.2836

Klencklen, G., Després, O., & Dufour, A. (2012). What do we know about aging and spatial cognition? Reviews and perspectives. *Ageing Research Reviews*, **11**(1), pp. 123–135. 10.1016/j.arr.2011.10.001

Klier, E., & Angelaki, D. E. (2008). Spatial updating and the maintenance of visual constancy. *Neuroscience*, **156**(4), pp. 801–818. 10.1016/j.neuroscience.2008.07.079

Klimesch, W. (1999). EEG alpha and theta oscillations reflect cognitive and memory performance: a review and analysis. *Brain Research Reviews*, **29**(2-3), pp. 169–195. 10.1016/S0165-0173(98)00056-3

Klimesch, W. (2012). Alpha-band oscillations, attention, and controlled access to stored information. *Trends in Cognitive Sciences*, **16**(12), pp. 606–617. 10.1016/j.tics.2012.10.007

Klimesch, W., Fellinger, R., & Freunberger, R. (2011). Alpha Oscillations and Early Stages of Visual Encoding. *Frontiers in Psychology*, **2**:118. 10.3389/fpsyg.2011.00118

Kline, J. E., Poggensee, K., & Ferris, D. P. (2014). Your brain on speed: cognitive performance of a spatial working memory task is not affected by walking speed. *Frontiers in Human Neuroscience*, **8**:288. 10.3389/fnhum.2014.00288

Klistorner, A. I., Graham, S. L., Grigg, J. R., & Billson, F. A. (1998). Multifocal topographic visual evoked potential: improving objective detection of local visual field defects. *Investigative Ophthalmology & Visual Science*, **39**(6), pp. 937–50. Retrieved from `http://www.ncbi.nlm.nih.gov/pubmed/9579473`

Kluft, N., Bruijn, S. M., Weijer, R. H. A., van Dieën, J. H., & Pijnappels, M. (2017). On the validity and consistency of misjudgment of stepping ability in young and older adults. *PLOS ONE*, **12**(12), e0190088. 10.1371/journal.pone.0190088

Klug, M., Gehrke, L., Hohlefeld, F. U., & Gramann, K. (2018). *The BeMoBIL Pipeline*. Retrieved from [2019-08-30]`https://github.com/MariusKlug/bemobil-pipeline`

Klug, M., & Gramann, K. (2021). Identifying key factors for improving ICA-based decomposition of EEG data in mobile and stationary experiments. *European Journal of Neuroscience*, **54**(12), pp. 8406–8420. 10.1111/ejn.14992

Klug, M., Jeung, S., Wunderlich, A., Gehrke, L., Protzak, J., Djebbara, Z., … Gramann, K. (2022). The BeMoBIL Pipeline for automated analyses of multimodal mobile brain and body imaging data. *bioRxiv*:510051. 10.1101/2022.09.29.510051

Klug, M., & Kloosterman, N. A. (2022). Zapline-plus: A Zapline extension for automatic and adaptive removal of frequency-specific noise artifacts in M/ <scp>EEG</scp>. *Human Brain Mapping*, **43**(9), pp. 2743–2758. 10.1002/hbm.25832

Kober, S. E., Kurzmann, J., & Neuper, C. (2012). Cortical correlate of spatial presence in 2D and 3D interactive virtual reality: An EEG study. *International Journal of Psychophysiology*, **83**(3), pp. 365–374. 10.1016/j.ijpsycho.2011.12.003

Kober, S. E., & Neuper, C. (2011). Sex differences in human EEG theta oscillations during spatial navigation in virtual reality. *International Journal of Psychophysiology*, **79**(3), pp. 347–355. 10.1016/j.ijpsycho.2010.12.002

Koch, C., Li, S.-C., Polk, T. A., & Schuck, N. W. (2020). Effects of aging on encoding of walking direction in the human brain. *Neuropsychologia*, **141**:107379. 10.1016/j.neuropsychologia.2020.107379

Koessler, L., Cecchin, T., Ternisien, E., & Maillard, L. (2010). 3D handheld laser scanner based approach for automatic identification and localization of EEG sensors. In *2010 Annual International Conference of the IEEE Engineering in Medicine and Biology* (pp. 3707–3710). Buenos Aires: IEEE. 10.1109/IEMBS.2010.5627659

Koessler, L., Maillard, L., Benhadid, A., Vignal, J.-P., Braun, M., & Vespignani, H. (2007). Spatial localization of EEG electrodes. *Neurophysiologie Clinique/Clinical Neurophysiology*, **37**(2), pp. 97–102. 10.1016/j.neucli.2007.03.002

König, S. U., Keshava, A., Clay, V., Rittershofer, K., Kuske, N., & König, P. (2021). Embodied Spatial Knowledge Acquisition in Immersive Virtual Reality: Comparison to Map Exploration. *Frontiers in Virtual Reality*, **2**:625548. 10.3389/frvir.2021.625548

Konishi, K., Etchamendy, N., Roy, S., Marighetto, A., Rajah, M. N., & Bohbot, V. D. (2013). Decreased functional magnetic resonance imaging activity in the hippocampus in favor of the caudate nucleus in older adults tested in a virtual navigation task. *Hippocampus*, **23**(11), pp. 1005–1014. 10.1002/hipo.22181

Kononowicz, T. W., & van Rijn, H. (2015). Single trial beta oscillations index time estimation. *Neuropsychologia*, **75**, pp. 381–389. 10.1016/j.neuropsychologia.2015.06.014

Kothe, C. A. (2014). *Lab Streaming Layer (LSL).* Retrieved from `https://labstreaminglayer.readthedocs.io/info/getting{_}started.html`

Kothe, C. A., & Jung, T.-P. (2015). *Artifact removal techniques with signal reconstruction.* Retrieved from `https://patents.google.com/patent/WO2015047462A9/en`

Kozhevnikov, M., & Hegarty, M. (2001). A dissociation between object manipulation spatial ability and spatial orientation ability. *Memory & Cognition*, **29**(5), pp. 745–756. 10.3758/BF03200477

Kramer, A. F., Hahn, S., Irwin, D. E., & Theeuwes, J. (2000). Age Differences in the Control of Looking Behavior: Do You Know Where Your Eyes Have Been? *Psychological Science*, **11**(3), pp. 210–217. 10.1111/1467-9280.00243

Kravitz, D. J., Saleem, K. S., Baker, C. I., Ungerleider, L. G., & Mishkin, M. (2013). The ventral visual pathway: an expanded neural framework for the processing of object quality. *Trends in Cognitive Sciences*, **17**(1), pp. 26–49. 10.1016/j.tics.2012.10.011

Krill, A. E., & Stamps, F. W. (1960). The Electroencephalogram in Retinitis Pigmentosa. *American Journal of Ophthalmology*, **49**(4), pp. 762–773. 10.1016/0002-9394(60)92051-1

Kropotov, J., Ponomarev, V., Tereshchenko, E. P., Müller, A., & Jäncke, L. (2016). Effect of Aging on ERP Components of Cognitive Control. *Frontiers in Aging Neuroscience*, **8**:69. 10.3389/fnagi.2016.00069

Krugliak, A., & Clarke, A. (2022). Towards real-world neuroscience using mobile EEG and augmented reality. *Scientific Reports*, **12**:2291. 10.1038/s41598-022-06296-3

Kuehn, E., Perez-Lopez, M. B., Diersch, N., Döhler, J., Wolbers, T., & Riemer, M. (2018). Embodiment in the aging mind. *Neuroscience & Biobehavioral Reviews*, **86**, pp. 207–225. 10.1016/j.neubiorev.2017.11.016

Kumar, N., & Kumar, J. (2016). Measurement of Cognitive Load in HCI Systems Using EEG Power Spectrum: An Experimental Study. *Procedia Computer Science*, **84**, pp. 70–78. 10.1016/j.procs.2016.04.068

Kunz, L., Maidenbaum, S., Chen, D., Wang, L., Jacobs, J., & Axmacher, N. (2019). Mesoscopic Neural Representations in Spatial Navigation. *Trends in Cognitive Sciences*, **23**(7), pp. 615–630. 10.1016/j.tics.2019.04.011

Lachaux, J.-P., George, N., Tallon-Baudry, C., Martinerie, J., Hugueville, L., Minotti, L., … Renault, B. (2005). The many faces of the gamma band response to complex visual stimuli. *NeuroImage*, **25**(2), pp. 491–501. 10.1016/j.neuroimage.2004.11.052

Ladouce, S., Donaldson, D. I., Dudchenko, P. A., & Ietswaart, M. (2017). Understanding Minds in Real-World Environments: Toward a Mobile Cognition Approach. *Frontiers in Human Neuroscience*, **10**:694. 10.3389/fnhum.2016.00694

Ladouce, S., Donaldson, D. I., Dudchenko, P. A., & Ietswaart, M. (2019). Mobile EEG identifies the re-allocation of attention during real-world activity. *Scientific Reports*, **9**:15851. 10.1038/s41598-019-51996-y

Ladouce, S., Mustile, M., Ietswaart, M., & Dehais, F. (2022). Capturing Cognitive Events Embedded in the Real World Using Mobile Electroencephalography and Eye-Tracking. *Journal of Cognitive Neuroscience*, **34**(12), pp. 2237–2255. 10.1162/jocn_a_01903

Lagali, P. S., Balya, D., Awatramani, G. B., Münch, T. A., Kim, D. S., Busskamp, V., … Roska, B. (2008). Light-activated channels targeted to ON bipolar cells restore visual function in retinal degeneration. *Nature Neuroscience*, **11**(6), pp. 667–675. 10.1038/nn.2117

Lagrené, K., Bécu, M., Seiple, W. H., Raphanel Bataille, M., Combariza, S., Paques, M., … Arleo, A. (2019). Healthy and pathological visual aging in a French follow-up cohort study. *Investigative Ophthalmology & Visual Science*, **60**(9), 5915. Retrieved from `https://iovs.arvojournals.org/article.aspx?articleid=2747032`

Lakha, L., & Humphreys, G. (2005). Lower visual field advantage for motion segmentation during high competition for selection. *Spatial Vision*, **18**(4), pp. 447–460. 10.1163/1568568054389570

Lancaster, J. L., Woldorff, M. G., Parsons, L. M., Liotti, M., Freitas, C. S., Rainey, L., … Fox, P. T. (2000). Automated Talairach Atlas labels for functional brain mapping. *Human Brain Mapping*, **10**(3), pp. 120–131. 10.1002/1097-0193(200007)10:3<120::AID-HBM30>3.0.CO;2-8

Laser Institute of America (LIA). (2014). *ANSI Z136.1-2014: American National Standard for Safe Use of Lasers*. Retrieved from `https://webstore.ansi.org/Standards/LIA/ANSIZ1362014`

Laszlo, S., Ruiz-Blondet, M., Khalifian, N., Chu, F., & Jin, Z. (2014). A direct comparison of active and passive amplification electrodes in the same amplifier system. *Journal of Neuroscience Methods*, **235**, pp. 298–307. 10.1016/j.jneumeth.2014.05.012

Learmonth, G., Benwell, C. S., Thut, G., & Harvey, M. (2017). Age-related reduction of hemispheric lateralisation for spatial attention: An EEG study. *NeuroImage*, **153**, pp. 139–151. 10.1016/j.neuroimage.2017.03.050

Lefebvre, C. D., Marchand, Y., Eskes, G. A., & Connolly, J. F. (2005). Assessment of working memory abilities using an event-related brain potential (ERP)-compatible digit span backward task. *Clinical Neurophysiology*, **116**(7), pp. 1665–1680. 10.1016/j.clinph.2005.03.015

Lehmann, D., & Skrandies, W. (1980). Reference-free identification of components of checkerboard-evoked multichannel potential fields. *Electroencephalography and Clinical Neurophysiology*, **48**(6), pp. 609–621. 10.1016/0013-4694(80)90419-8

Lenggenhager, B., Tadi, T., Metzinger, T., & Blanke, O. (2007). Video Ergo Sum: Manipulating Bodily Self-Consciousness. *Science*, **317**(5841), pp. 1096–1099. 10.1126/science.1143439

Leroy, A., & Cheron, G. (2020). EEG dynamics and neural generators of psychological flow during one tightrope performance. *Scientific Reports*, **10**:12449. 10.1038/s41598-020-69448-3

Lester, A. W., Moffat, S. D., Wiener, J. M., Barnes, C. A., & Wolbers, T. (2017). The Aging Navigational System. *Neuron*, **95**(5), pp. 1019–1035. 10.1016/j.neuron.2017.06.037

Levine, M. W., & McAnany, J. J. (2005). The relative capabilities of the upper and lower visual hemifields. *Vision Research*, **45**(21), pp. 2820–2830. 10.1016/j.visres.2005.04.001

Li, A. W., & King, J. A. (2019). Spatial memory and navigation in ageing: A systematic review of MRI and fMRI studies in healthy participants. *Neuroscience & Biobehavioral Reviews*, **103**, pp. 33–49. 10.1016/j.neubiorev.2019.05.005

Liang, M., Starrett, M. J., & Ekstrom, A. D. (2018). Dissociation of frontal-midline delta-theta and posterior alpha oscillations: A mobile EEG study. *Psychophysiology*, **55**:e13090. 10.1111/psyp.13090

Liang, M., Zheng, J., Isham, E. A., & Ekstrom, A. D. (2021). Common and Distinct Roles of Frontal Midline Theta and Occipital Alpha Oscillations in Coding Temporal Intervals and Spatial Distances. *Journal of Cognitive Neuroscience*, **33**(11), pp. 2311–2327. 10.1162/jocn_a_01765

Lin, C.-T., Chiu, T.-C. C., & Gramann, K. (2015). EEG correlates of spatial orientation in the human retrosplenial complex. *NeuroImage*, **120**, pp. 123–132. 10.1016/j.neuroimage.2015.07.009

Lin, C.-T., Chiu, T.-C. C., Wang, Y.-K., Chuang, C.-H., & Gramann, K. (2018). Granger causal connectivity dissociates navigation networks that subserve allocentric and egocentric path integration. *Brain Research*, **1679**, pp. 91–100. 10.1016/j.brainres.2017.11.016

Lin, C.-T., Yang, F.-S., Chiou, T.-C., Ko, L.-W., Duann, J.-R., & Gramann, K. (2009). EEG-Based Spatial Navigation Estimation in a Virtual Reality Driving Environment. In *2009 Ninth IEEE International Conference on Bioinformatics and BioEngineering* (pp. 435–438). Taichung: IEEE. 10.1109/BIBE.2009.65

Lin, F.-H., Witzel, T., Hämäläinen, M. S., Dale, A. M., Belliveau, J. W., & Stufflebeam, S. M. (2004). Spectral spatiotemporal imaging of cortical oscillations and interactions in the human brain. *NeuroImage*, **23**(2), pp. 582–595. 10.1016/j.neuroimage.2004.04.027

Lin, M.-H., Liran, O., Bauer, N., & Baker, T. E. (2022). Scalp recorded theta activity is modulated by reward, direction, and speed during virtual navigation in freely moving humans. *Scientific Reports*, **12**:2041. 10.1038/s41598-022-05955-9

Lipman, P. D. (1991). Age and exposure differences in acquisition of route information. *Psychology and Aging*, **6**(1), pp. 128–133. 10.1037/0882-7974.6.1.128

Lithfous, S., Dufour, A., Blanc, F., & Després, O. (2014). Allocentric but not egocentric orientation is impaired during normal aging: An ERP study. *Neuropsychology*, **28**(5), pp. 761–771. 10.1037/neu0000084

Lithfous, S., Dufour, A., Bouix, C., Pebayle, T., & Després, O. (2018). Reduced parahippocampal theta activity during spatial navigation in low, but not in high elderly performers. *Neuropsychology*, **32**(1), pp. 40–53. 10.1037/neu0000392

Lithfous, S., Dufour, A., & Després, O. (2013). Spatial navigation in normal aging and the prodromal stage of Alzheimer's disease: Insights from imaging and behavioral studies. *Ageing Research Reviews*, **12**(1), pp. 201–213. 10.1016/j.arr.2012.04.007

Lithfous, S., Tromp, D., Dufour, A., Pebayle, T., Goutagny, R., & Després, O. (2015). Decreased theta power at encoding and cognitive mapping deficits in elderly individuals during a spatial memory task. *Neurobiology of Aging*, **36**(10), pp. 2821–2829. 10.1016/j.neurobiolaging.2015.07.007

Lozano, A., Suárez, J. S., Soto-Sánchez, C., Garrigós, J., Martínez-Alvarez, J. J., Ferrández, J. M., & Fernández, E. (2020). Neurolight: A Deep Learning Neural Interface for Cortical Visual Prostheses. *International Journal of Neural Systems*, **30**(09), 2050045. 10.1142/S0129065720500458

Luck, S. J. (2014). *An introduction to the event-related potential technique*. MIT press.

Luck, S. J., & Handy, T. C. (2005). Ten simple rules for designing ERP Experiments. In *Event-Related Potentials: A Methods Handbook* (pp. 17–32). New York: MIT Press.

Luck, S. J., Woodman, G. F., & Vogel, E. K. (2000). Event-related potential studies of attention. *Trends in Cognitive Sciences*, **4**(11), pp. 432–440. 10.1016/S1364-6613(00)01545-X

Lustig, C., Hasher, L., & Zacks, R. T. (2007). Inhibitory deficit theory: Recent developments in a "new view". In D. S. Gorfein & C. M. MacLeod (Eds.), *Inhibition in cognition* (pp. 145–162). Washington: American Psychological Association. 10.1037/11587-008

Luu, T. P., Brantley, J. A., Nakagome, S., Zhu, F., & Contreras-Vidal, J. L. (2017a). Electrocortical correlates of human level-ground, slope, and stair walking. *PLOS ONE*, **12**(11), e0188500. 10.1371/journal.pone.0188500

Luu, T. P., Nakagome, S., He, Y., & Contreras-Vidal, J. L. (2017b). Real-time EEG-based brain-computer interface to a virtual avatar enhances cortical involvement in human treadmill walking. *Scientific Reports*, **7**:8895. 10.1038/s41598-017-09187-0

Macé, M. J.-M., Guivarch, V., Denis, G., & Jouffrais, C. (2015). Simulated Prosthetic Vision: The Benefits of Computer-Based Object Recognition and Localization. *Artificial Organs*, **39**(7), pp. E102–E113. 10.1111/aor.12476

Mahmood, O., Adamo, D. E., Briceño, E. M., & Moffat, S. D. (2009). Age differences in visual path integration. *Behavioural Brain Research*, **205**(1), pp. 88–95. 10.1016/j.bbr.2009.08.001

Maidenbaum, S., Patel, A., Garlin, I. C., & Jacobs, J. (2019). Studying Spatial Memory in Augmented and Virtual reality. *bioRxiv*:777946. 10.1101/777946

Maiello, G., Chessa, M., Bex, P. J., & Solari, F. (2020). Near-optimal combination of disparity across a log-polar scaled visual field. *PLOS Computational Biology*, **16**(4), e1007699. 10.1371/journal.pcbi.1007699

Makeig, S., Bell, A. J., Jung, T.-P., & Sejnowski, T. J. (1995). Independent Component Analysis of Electroencephalographic Data. In *Proceedings of the 8th International Conference on Neural Information Processing Systems (NIPS'95)* (pp. 145–151). Denver, Colorado: MIT Press. 10.5555/2998828.2998849

Makeig, S., Gramann, K., Jung, T.-P., Sejnowski, T. J., & Poizner, H. (2009). Linking brain, mind and behavior. *International Journal of Psychophysiology*, **73**(2), pp. 95–100. 10.1016/j.ijpsycho.2008.11.008

Makeig, S., Jung, T.-P., Bell, A. J., Ghahremani, D., & Sejnowski, T. J. (1997). Blind separation of auditory event-related brain responses into independent components. *Proceedings of the National Academy of Sciences*, **94**(20), pp. 10979–10984. 10.1073/pnas.94.20.10979

Malcolm, B. R., Foxe, J. J., Butler, J. S., & De Sanctis, P. (2015). The aging brain shows less flexible reallocation of cognitive resources during dual-task walking: A mobile brain/body imaging (MoBI) study. *NeuroImage*, **117**, pp. 230–242. 10.1016/j.neuroimage.2015.05.028

Malcolm, B. R., Foxe, J. J., Joshi, S., Verghese, J., Mahoney, J. R., Molholm, S., & De Sanctis, P. (2021). Aging-related changes in cortical mechanisms supporting postural control during base of support and optic flow manipulations. *European Journal of Neuroscience*, **54**(12), pp. 8139–8157. 10.1111/ejn.15004

Malcolm, G. L., Groen, I. I. A., & Baker, C. I. (2016). Making Sense of Real-World Scenes. *Trends in Cognitive Sciences*, **20**(11), pp. 843–856. 10.1016/j.tics.2016.09.003

Malcolm, G. L., Nuthmann, A., & Schyns, P. G. (2014). Beyond Gist: Strategic and Incremental Information Accumulation for Scene Categorization. *Psychological Science*, **25**(5), pp. 1087–1097. 10.1177/0956797614522816

Malcolm, G. L., Silson, E. H., Henry, J. R., & Baker, C. I. (2018). Transcranial Magnetic Stimulation to the Occipital Place Area Biases Gaze During Scene Viewing. *Frontiers in Human Neuroscience*, **12**:189. 10.3389/fnhum.2018.00189

Mamassian, P. (2020). Confidence Forced-Choice and Other Metaperceptual Tasks*. *Perception*, **49**(6), pp. 616–635. 10.1177/0301006620928010

Maniscalco, B., & Lau, H. (2016). The signal processing architecture underlying subjective reports of sensory awareness. *Neuroscience of Consciousness*, **2016**(1), niw002. 10.1093/nc/niw002

Mao, D., Avila, E., Caziot, B., Laurens, J., Dickman, J. D., & Angelaki, D. E. (2021). Spatial modulation of hippocampal activity in freely moving macaques. *Neuron*, **109**(21), pp. 3521–3534.e6. 10.1016/j.neuron.2021.09.032

Marcar, V. L., Bridenbaugh, S. A., Kool, J., Niedermann, K., & Kressig, R. W. (2014). A simple procedure to synchronize concurrent measurements of gait and brain electrical activity and preliminary results from a pilot measurement involving motor-cognitive dual-tasking in healthy older and young volunteers. *Journal of Neuroscience Methods*, **228**, pp. 46–49. 10.1016/j.jneumeth.2014.03.003

Marchette, S. A., Vass, L. K., Ryan, J., & Epstein, R. A. (2014). Anchoring the neural compass: coding of local spatial reference frames in human medial parietal lobe. *Nature Neuroscience*, **17**(11), pp. 1598–1606. 10.1038/nn.3834

Marchette, S. A., Vass, L. K., Ryan, J., & Epstein, R. A. (2015). Outside Looking In: Landmark Generalization in the Human Navigational System. *Journal of Neuroscience*, **35**(44), pp. 14896–14908. 10.1523/JNEUROSCI.2270-15.2015

Maris, E., & Oostenveld, R. (2007). Nonparametric statistical testing of EEG- and MEG-data. *Journal of Neuroscience Methods*, **164**(1), pp. 177–190. 10.1016/j.jneumeth.2007.03.024

McAvan, A. S., Du, Y. K., Oyao, A., Doner, S., Grilli, M. D., & Ekstrom, A. D. (2021). Older Adults Show Reduced Spatial Precision but Preserved Strategy-Use During Spatial Navigation Involving Body-Based Cues. *Frontiers in Aging Neuroscience*, **13**:640188. 10.3389/fnagi.2021.640188

McCourt, M. (1999). Visuospatial attention in line bisection: stimulusmodulation of pseudoneglect. *Neuropsychologia*, **37**(7), pp. 843–855. 10.1016/S0028-3932(98)00140-7

McGregor, J. E., Williams, D. R., & Merigan, W. H. (2019). Functional Assessment of Vision Restoration. In C. Bowes Rickman, C. Grimm, R. Anderson, J. Ash, M. LaVail, & J. Hollyfield (Eds.), *Retinal Degenerative Diseases* (Vol. 1185, pp. 145–149). Springer, Cham. 10.1007/978-3-030-27378-1_24

Merriman, N. A., Ondej, J., Rybicki, A., Roudaia, E., O'Sullivan, C., & Newell, F. N. (2018). Crowded environments reduce spatial memory in older but not younger adults. *Psychological Research*, **82**(2), pp. 407–428. 10.1007/s00426-016-0819-5

Mertes, C., Wascher, E., & Schneider, D. (2017). Compliance instead of flexibility? On age-related differences in cognitive control during visual search. *Neurobiology of Aging*, **53**, pp. 169–180. 10.1016/j.neurobiolaging.2017.02.003

Meulenbroek, O., Petersson, K. M., Voermans, N., Weber, B., & Fernández, G. (2004). Age differences in neural correlates of route encoding and route recognition. *NeuroImage*, **22**(4), pp. 1503–1514. 10.1016/j.neuroimage.2004.04.007

Michel, C. M., & Brunet, D. (2019). EEG Source Imaging: A Practical Review of the Analysis Steps. *Frontiers in Neurology*, **10**:325. 10.3389/fneur.2019.00325

Miller, J., & Carlson, L. (2011). Selecting landmarks in novel environments. *Psychonomic Bulletin & Review*, **18**(1), pp. 184–191. 10.3758/s13423-010-0038-9

Minguillon, J., Lopez-Gordo, M. A., & Pelayo, F. (2017). Trends in EEG-BCI for daily-life: Requirements for artifact removal. *Biomedical Signal Processing and Control*, **31**, pp. 407–418. 10.1016/j.bspc.2016.09.005

Minguillon, J., Perez, E., Lopez-Gordo, M. A., Pelayo, F., & Sanchez-Carrion, M. (2018). Portable System for Real-Time Detection of Stress Level. *Sensors*, **18**(8), 2504. 10.3390/s18082504

Mirochnik, R. M., & Pezaris, J. S. (2019). Contemporary approaches to visual prostheses. *Military Medical Research*, **6**(1), 19. 10.1186/s40779-019-0206-9

Mishkin, M., Ungerleider, L. G., & Macko, K. A. (1983). Object vision and spatial vision: two cortical pathways. *Trends in Neurosciences*, **6**, pp. 414–417. 10.1016/0166-2236(83)90190-X

Missonnier, P., Herrmann, F. R., Rodriguez, C., Deiber, M.-P., Millet, P., Fazio-costa, L., … Giannakopoulos, P. (2011). Age-related differences on event-related potentials and brain rhythm oscillations during working memory activation. *Journal of Neural Transmission*, **118**(6), pp. 945–955. 10.1007/s00702-011-0600-2

Mitchell, A. S., Czajkowski, R., Zhang, N., Jeffery, K. J., & Nelson, A. J. D. (2018). Retrosplenial cortex and its role in spatial cognition. *Brain and Neuroscience Advances*, **2**:239821281875709. 10.1177/2398212818757098

Mittelstaedt, M.-L., & Mittelstaedt, H. (1980). Homing by path integration in a mammal. *Naturwissenschaften*, **67**(11), pp. 566–567. 10.1007/BF00450672

Miyakoshi, M., Gehrke, L., Gramann, K., Makeig, S., & Iversen, J. (2021). The AudioMaze : An EEG and motion capture study of human spatial navigation in sparse augmented reality. *European Journal of Neuroscience*, **54**(12), pp. 8283–8307. 10.1111/ejn.15131

Moca, V. V., Bârzan, H., Nagy-Dăbâcan, A., & Mureşan, R. C. (2021). Time-frequency super-resolution with superlets. *Nature Communications*, **12**:337. 10.1038/s41467-020-20539-9

Moffat, S. D. (2009). Aging and Spatial Navigation: What Do We Know and Where Do We Go? *Neuropsychology Review*, **19**(4), pp. 478–489. 10.1007/s11065-009-9120-3

Moffat, S. D., Elkins, W., & Resnick, S. M. (2006). Age differences in the neural systems supporting human allocentric spatial navigation. *Neurobiology of Aging*, **27**(7), pp. 965–972. 10.1016/j.neurobiolaging.2005.05.011

Moffat, S. D., Kennedy, K. M., Rodrigue, K. M., & Raz, N. (2007). Extrahippocampal Contributions to Age Differences in Human Spatial Navigation. *Cerebral Cortex*, **17**(6), pp. 1274–1282. 10.1093/cercor/bhl036

Moffat, S. D., & Resnick, S. M. (2002). Effects of age on virtual environment place navigation and allocentric cognitive mapping. *Behavioral Neuroscience*, **116**(5), pp. 851–859. 10.1037/0735-7044.116.5.851

Mueller, V., Brehmer, Y., von Oertzen, T., Li, S.-C., & Lindenberger, U. (2008). Electrophysiological correlates of selective attention: A lifespan comparison. *BMC Neuroscience*, **9**(1), 18. 10.1186/1471-2202-9-18

Müller, M. M., Gruber, T., & Keil, A. (2000). Modulation of induced gamma band activity in the human EEG by attention and visual information processing. *International Journal of Psychophysiology*, **38**(3), pp. 283–299. 10.1016/S0167-8760(00)00171-9

Murias, K., Kwok, K., Castillejo, A. G., Liu, I., & Iaria, G. (2016). The effects of video game use on performance in a virtual navigation task. *Computers in Human Behavior*, **58**, pp. 398–406. 10.1016/j.chb.2016.01.020

Mustile, M., Kourtis, D., Ladouce, S., Learmonth, G., Edwards, M. G., Donaldson, D. I., & Ietswaart, M. (2021). Mobile EEG reveals functionally dissociable dynamic processes supporting real-world ambulatory obstacle avoidance: Evidence for early proactive control. *European Journal of Neuroscience*, **54**(12), pp. 8106–8119. 10.1111/ejn.15120

Myers, M. H., Iannaccone, A., & Bidelman, G. M. (2017). A pilot investigation of audiovisual processing and multisensory integration in patients with inherited retinal dystrophies. *BMC Ophthalmology*, **17**(1), 240. 10.1186/s12886-017-0640-y

Nakamura, K., Kawashima, R., Sato, N., Nakamura, A., Sugiura, M., Kato, T., … Zilles, K. (2000). Functional delineation of the human occipito-temporal areas related to face and scene processing: A PET study. *Brain*, **123**(9), pp. 1903–1912. 10.1093/brain/123.9.1903

Nathan, K., & Contreras-Vidal, J. L. (2016). Negligible Motion Artifacts in Scalp Electroencephalography (EEG) During Treadmill Walking. *Frontiers in Human Neuroscience*, **9**:708. 10.3389/fnhum.2015.00708

Navarro, J., Reynaud, E., & Osiurak, F. (2018). Neuroergonomics of car driving: A critical meta-analysis of neuroimaging data on the human brain behind the wheel. *Neuroscience & Biobehavioral Reviews*, **95**, pp. 464–479. 10.1016/j.neubiorev.2018.10.016

Naveh-Benjamin, M. (2000). Adult age differences in memory performance: Tests of an associative deficit hypothesis. *Journal of Experimental Psychology: Learning, Memory, and Cognition*, **26**(5), pp. 1170–1187. 10.1037/0278-7393.26.5.1170

Niebauer, C. L., & Christman, S. D. (1998). Upper and lower visual field differences in categorical and coordinate judgments. *Psychonomic Bulletin & Review*, **5**(1), pp. 147–151. 10.3758/BF03209471

Nishiguchi, K. M., Tearle, R. G., Liu, Y. P., Oh, E. C., Miyake, N., Benaglio, P., … Rivolta, C. (2013). Whole genome sequencing in patients with retinitis pigmentosa reveals pathogenic DNA structural changes and NEK2 as a new disease gene. *Proceedings of the National Academy of Sciences*, **110**(40), pp. 16139–16144. 10.1073/pnas.1308243110

Norcia, A. M., Appelbaum, L. G., Ales, J. M., Cottereau, B. R., & Rossion, B. (2015). The steady-state visual evoked potential in vision research: A review. *Journal of Vision*, **15**(6), 4. 10.1167/15.6.4

Nordin, A. D., Hairston, W. D., & Ferris, D. P. (2018). Dual-electrode motion artifact cancellation for mobile electroencephalography. *Journal of Neural Engineering*, **15**(5), 056024. 10.1088/1741-2552/aad7d7

Nordin, A. D., Hairston, W. D., & Ferris, D. P. (2019). Human electrocortical dynamics while stepping over obstacles. *Scientific Reports*, **9**:4693. 10.1038/s41598-019-41131-2

Nordin, A. D., Hairston, W. D., & Ferris, D. P. (2020). Faster Gait Speeds Reduce Alpha and Beta EEG Spectral Power From Human Sensorimotor Cortex. *IEEE Transactions on Biomedical Engineering*, **67**(3), pp. 842–853. 10.1109/TBME.2019.2921766

Norman, J. F., Adkins, O. C., Pedersen, L. E., Reyes, C. M., Wulff, R. A., & Tungate, A. (2015). The visual perception of exocentric distance in outdoor settings. *Vision Research*, **117**, pp. 100–104. 10.1016/j.visres.2015.10.003

Norman, J. F., Crabtree, C. E., Bartholomew, A. N., & Ferrell, E. L. (2009). Aging and the perception of slant from optical texture, motion parallax, and binocular disparity. *Perception & Psychophysics*, **71**(1), pp. 116–130. 10.3758/APP.71.1.116

Nunez, P. L., & Srinivasan, R. (2006). *Electric Fields of the Brain: The Neurophysics of EEG*. Oxford University Press. 10.1093/acprof:oso/9780195050387.001.0001

Nussenblatt, R. B., Palestine, A. G., Chan, C.-C., & Roberge, F. (1985). Standardizatlon of Vitreal inflammatory Activity in Intermediate and Posterior Uveitis. *Ophthalmology*, **92**(4), pp. 467–471. 10.1016/S0161-6420(85)34001-0

O'Craven, K. M., & Kanwisher, N. G. (2000). Mental Imagery of Faces and Places Activates Corresponding Stimulus-Specific Brain Regions. *Journal of Cognitive Neuroscience*, **12**(6), pp. 1013–1023. 10.1162/08989290051137549

Ojeda, A., Bigdely-Shamlo, N., & Makeig, S. (2014). MoBILAB: an open source toolbox for analysis and visualization of mobile brain/body imaging data. *Frontiers in Human Neuroscience*, **8**:121. 10.3389/fnhum.2014.00121

O'Keefe, J., & Nadel, L. (1978). *The Hippocampus as a Cognitive Map*. Oxford University Press.

Oliva, A., & Torralba, A. (2001). Modeling the shape of the scene: A holistic representation of the spatial envelope. *International Journal of Computer Vision*, **42**(3), pp. 145–175. 10.1023/A:1011139631724

Oliveira, A. S., Schlink, B. R., Hairston, W. D., König, P., & Ferris, D. P. (2016). Proposing Metrics for Benchmarking Novel EEG Technologies Towards Real-World Measurements. *Frontiers in Human Neuroscience*, **10**:188. 10.3389/fnhum.2016.00188

O'Malley, M., Innes, A., & Wiener, J. M. (2022). (Dis)orientation and Design Preferences Within an Unfamiliar Care Environment: A Content Analysis of Older Adults' Qualitative Reports After Route Learning. *Environment and Behavior*, **54**(1), pp. 116–142. 10.1177/0013916520953148

Oostenveld, R., Fries, P., Maris, E., & Schoffelen, J.-M. (2011). FieldTrip: Open Source Software for Advanced Analysis of MEG, EEG, and Invasive Electrophysiological Data. *Computational Intelligence and Neuroscience*, **2011**:156869. 10.1155/2011/156869

Oostenveld, R., & Oostendorp, T. F. (2002). Validating the boundary element method for forward and inverse EEG computations in the presence of a hole in the skull. *Human Brain Mapping*, **17**(3), pp. 179–192. 10.1002/hbm.10061

Osaka, N. (1976). Reaction Time as a Function of Peripheral Retinal Locus around Fovea: Effect of Stimulus Size. *Perceptual and Motor Skills*, **43**(2), pp. 603–606. 10.2466/pms.1976.43.2.603

Osipova, D., Takashima, A., Oostenveld, R., Fernández, G., Maris, E., & Jensen, O. (2006). Theta and Gamma Oscillations Predict Encoding and Retrieval of Declarative Memory. *Journal of Neuroscience*, **26**(28), pp. 7523–7531. 10.1523/JNEUROSCI.1948-06.2006

Palmer, J. A., Makeig, S., Kreutz-Delgado, K., & Rao, B. D. (2008). Newton method for the ICA mixture model. In *2008 IEEE International Conference on Acoustics, Speech and Signal Processing* (pp. 1805–1808). Las Vegas, NV: IEEE. 10.1109/ICASSP.2008.4517982

Papathanasopoulos, P., & Papakostopoulos, D. (1994). Pattern reversal visual evoked potentials in retinitis pigmentosa. *International Journal of Psychophysiology*, **16**(2-3), pp. 245–250. 10.1016/0167-8760(89)90051-2

Paranhos, F. R. L., Katsumi, O., Arai, M., Nehemy, M. B., & Hirose, T. (1998). Pattern reversal visual evoked response in retinitis pigmentosa. *Documenta Ophthalmologica*, **96**(4), pp. 321–331. 10.1023/A:1001853420082

Parisi, V., Ziccardi, L., Stifano, G., Montrone, L., Gallinaro, G., & Falsini, B. (2010). Impact of regional retinal responses on cortical visually evoked responses: Multifocal ERGs and VEPs in the retinitis pigmentosa model. *Clinical Neurophysiology*, **121**(3), pp. 380–385. 10.1016/j.clinph.2009.09.032

Park, J., & Park, S. (2020). Coding of Navigational Distance and Functional Constraint of Boundaries in the Human Scene-Selective Cortex. *Journal of Neuroscience*, **40**(18), pp. 3621–3630. 10.1523/JNEUROSCI.1991-19.2020

Park, J. L., & Donaldson, D. I. (2019). Detecting the neural correlates of episodic memory with mobile EEG: Recollecting objects in the real world. *NeuroImage*, **193**, pp. 1–9. 10.1016/j.neuroimage.2019.03.013

Park, J. L., Dudchenko, P. A., & Donaldson, D. I. (2018). Navigation in Real-World Environments: New Opportunities Afforded by Advances in Mobile Brain Imaging. *Frontiers in Human Neuroscience*, **12**:361. 10.3389/fnhum.2018.00361

Parker, P. R., Brown, M. A., Smear, M. C., & Niell, C. M. (2020). Movement-Related Signals in Sensory Areas: Roles in Natural Behavior. *Trends in Neurosciences*, **43**(8), pp. 581–595. 10.1016/j.tins.2020.05.005

Parsons, T. D. (2015). Virtual Reality for Enhanced Ecological Validity and Experimental Control in the Clinical, Affective and Social Neurosciences. *Frontiers in Human Neuroscience*, **9**:660. 10.3389/fnhum.2015.00660

Pascual-Leone, A., Amedi, A., Fregni, F., & Merabet, L. B. (2005). The Plastic Human Brain Cortex. *Annual Review of Neuroscience*, **28**, pp. 377–401. 10.1146/annurev.neuro.27.070203.144216

Pascual-Marqui, R. D., Michel, C. M., & Lehmann, D. (1994). Low resolution electromagnetic tomography: a new method for localizing electrical activity in the brain. *International Journal of Psychophysiology*, **18**(1), pp. 49–65. 10.1016/0167-8760(84)90014-X

Pastel, S., Bürger, D., Chen, C. H., Petri, K., & Witte, K. (2022). Comparison of spatial orientation skill between real and virtual environment. *Virtual Reality*, **26**(1), pp. 91–104. 10.1007/s10055-021-00539-w

Patai, E. Z., & Spiers, H. J. (2017). Human Navigation: Occipital Place Area Detects Potential Paths in a Scene. *Current Biology*, **27**(12), pp. R599–R600. 10.1016/j.cub.2017.05.012

Patel, S. H., & Azzam, P. N. (2005). Characterization of N200 and P300: selected studies of the Event-Related Potential. *International journal of medical sciences*, **2**(4), pp. 147–54. 10.7150/ijms.2.147

Pedroni, A., Bahreini, A., & Langer, N. (2019). Automagic: Standardized preprocessing of big EEG data. *NeuroImage*, **200**, pp. 460–473. 10.1016/j.neuroimage.2019.06.046

Peer, M., & Epstein, R. A. (2021). The human brain uses spatial schemas to represent segmented environments. *Current Biology*, **31**(21), pp. 4677–4688.e8. 10.1016/j.cub.2021.08.012

Persichetti, A. S., & Dilks, D. D. (2016). Perceived egocentric distance sensitivity and invariance across scene-selective cortex. *Cortex*, **77**, pp. 155–163. 10.1016/j.cortex.2016.02.006

Persichetti, A. S., & Dilks, D. D. (2018). Dissociable Neural Systems for Recognizing Places and Navigating through Them. *Journal of Neuroscience*, **38**(48), pp. 10295–10304. 10.1523/JNEUROSCI.1200-18.2018

Persichetti, A. S., & Dilks, D. D. (2019). Distinct representations of spatial and categorical relationships across human scene-selective cortex. *Proceedings of the National Academy of Sciences*, **116**(42), pp. 21312–21317. 10.1073/pnas.1903057116

Peterson, S. M., & Ferris, D. P. (2019). Group-level cortical and muscular connectivity during perturbations to walking and standing balance. *NeuroImage*, **198**, pp. 93–103. 10.1016/j.neuroimage.2019.05.038

Peterson, S. M., Rios, E., & Ferris, D. P. (2018). Transient visual perturbations boost short-term balance learning in virtual reality by modulating electrocortical activity. *Journal of Neurophysiology*, **120**(4), pp. 1998–2010. 10.1152/jn.00292.2018

Petzschner, F. H., & Glasauer, S. (2011). Iterative Bayesian Estimation as an Explanation for Range and Regression Effects: A Study on Human Path Integration. *Journal of Neuroscience*, **31**(47), pp. 17220–17229. 10.1523/JNEUROSCI.2028-11.2011

Pflugshaupt, T., von Wartburg, R., Wurtz, P., Chaves, S., Déruaz, A., Nyffeler, T., … Mueri, R. M. (2009). Linking physiology with behaviour: Functional specialisation of the visual field is reflected in gaze patterns during visual search. *Vision Research*, **49**(2), pp. 237–248. 10.1016/j.visres.2008.10.021

Pfurtscheller, G., & Klimesch, W. (1991). Event-related desynchronization during motor behavior and visual information processing. *Electroencephalography and clinical neurophysiology. Supplement*, **42**, pp. 58–65. Retrieved from `http://www.ncbi.nlm.nih.gov/pubmed/1915032`

Pfurtscheller, G., Neuper, C., & Mohl, W. (1994). Event-related desynchronization (ERD) during visual processing. *International Journal of Psychophysiology*, **16**(2-3), pp. 147–153. 10.1016/0167-8760(89)90041-X

Phillips, J., Walford, N., Hockey, A., Foreman, N., & Lewis, M. (2013). Older people and outdoor environments: Pedestrian anxieties and barriers in the use of familiar and unfamiliar spaces. *Geoforum*, **47**, pp. 113–124. 10.1016/j.geoforum.2013.04.002

Picaud, S., Dalkara, D., Marazova, K., Goureau, O., Roska, B., & Sahel, J.-A. (2019). The primate model for understanding and restoring vision. *Proceedings of the National Academy of Sciences*, **116**(52), pp. 26280–26287. 10.1073/pnas.1902292116

Pion-Tonachini, L., Kreutz-Delgado, K., & Makeig, S. (2019). ICLabel: An automated electroencephalographic independent component classifier, dataset, and website. *NeuroImage*, **198**, pp. 181–197. 10.1016/j.neuroimage.2019.05.026

Plank, M., Müller, H. J., Onton, J., Makeig, S., & Gramann, K. (2010). Human EEG Correlates of Spatial Navigation within Egocentric and Allocentric Reference Frames. In C. Hölscher, T. Shipley, M. Olivetti Belardinelli, J. Bateman, & N. Newcombe (Eds.), *Spatial Cognition VII* (Vol. 6222, pp. 191–206). Springer, Berlin, Heidelberg. 10.1007/978-3-642-14749-4_18

Plank, M., Snider, J., Kaestner, E., Halgren, E., & Poizner, H. (2015). Neurocognitive stages of spatial cognitive mapping measured during free exploration of a large-scale virtual environment. *Journal of Neurophysiology*, **113**(3), pp. 740–753. 10.1152/jn.00114.2014

Plewan, T., & Rinkenauer, G. (2017). Simple reaction time and sizedistance integration in virtual 3D space. *Psychological Research*, **81**(3), pp. 653–663. 10.1007/s00426-016-0769-y

Posch, C., & Matolin, D. (2011). Sensitivity and uniformity of a 0.18ţm CMOS temporal contrast pixel array. In *2011 IEEE International Symposium of Circuits and Systems (ISCAS)* (pp. 1572–1575). Rio de Janeiro: IEEE. 10.1109/ISCAS.2011.5937877

Posch, C., Matolin, D., & Wohlgenannt, R. (2011). A QVGA 143 dB Dynamic Range Frame-Free PWM Image Sensor With Lossless Pixel-Level Video Compression and Time-Domain CDS. *IEEE Journal of Solid-State Circuits*, **46**(1), pp. 259–275. 10.1109/JSSC.2010.2085952

Possti, D., Fahoum, F., Sosnik, R., Giladi, N., Hausdorff, J. M., Mirelman, A., & Maidan, I. (2021). Changes in the EEG spectral power during dual-task walking with aging and Parkinson's disease: initial findings using Event-Related Spectral Perturbation analysis. *Journal of Neurology*, **268**(1), pp. 161–168. 10.1007/s00415-020-10104-1

Poulter, S., Hartley, T., & Lever, C. (2018). The Neurobiology of Mammalian Navigation. *Current Biology*, **28**(17), pp. R1023–R1042. 10.1016/j.cub.2018.05.050

Presacco, A., Goodman, R., Forrester, L., & Contreras-Vidal, J. L. (2011). Neural decoding of treadmill walking from noninvasive electroencephalographic signals. *Journal of Neurophysiology*, **106**(4), pp. 1875–1887. 10.1152/jn.00104.2011

Presson, C. C., & Montello, D. R. (1988). Points of reference in spatial cognition: Stalking the elusive landmark. *British Journal of Developmental Psychology*, **6**(4), pp. 378–381. 10.1111/j.2044-835X.1988.tb01113.x

Previc, F. H. (1990). Functional specialization in the lower and upper visual fields in humans: Its ecological origins and neurophysiological implications. *Behavioral and Brain Sciences*, **13**(3), pp. 519–542. 10.1017/S0140525X00080018

Previc, F. H., & Naegele, P. D. (2001). Target-tilt and vertical-hemifield asymmetries in free-scan search for 3-D targets. *Perception & Psychophysics*, **63**(3), pp. 445–457. 10.3758/BF03194411

Prince, M., Bryce, R., Albanese, E., Wimo, A., Ribeiro, W., & Ferri, C. P. (2013). The global prevalence of dementia: A systematic review and metaanalysis. *Alzheimer's & Dementia*, **9**(1), pp. 63–75.e2. 10.1016/j.jalz.2012.11.007

Protzak, J., & Gramann, K. (2021). EEG beta-modulations reflect age-specific motor resource allocation during dual-task walking. *Scientific Reports*, **11**:16110. 10.1038/s41598-021-94874-2

Protzak, J., Wiczorek, R., & Gramann, K. (2021). Peripheral visual perception during natural overground dual-task walking in older and younger adults. *Neurobiology of Aging*, **98**, pp. 146–159. 10.1016/j.neurobiolaging.2020.10.009

Qi, Q., Weng, Y., Zheng, S., Wang, S., Liu, S., Huang, Q., & Huang, R. (2022). Task-related connectivity of decision points during spatial navigation in a schematic map. *Brain Structure and Function*, **227**(5), pp. 1697–1710. 10.1007/s00429-022-02466-1

Ramanoël, S., Durteste, M., Bécu, M., Habas, C., & Arleo, A. (2020). Differential Brain Activity in Regions Linked to Visuospatial Processing During Landmark-Based Navigation in Young and Healthy Older Adults. *Frontiers in Human Neuroscience*, **14**:552111. 10.3389/fnhum.2020.552111

Ramanoël, S., Durteste, M., Delaux, A., de Saint Aubert, J.-B., & Arleo, A. (2022). Future trends in brain aging research: Visuo-cognitive functions at stake during mobility and spatial navigation. *Aging Brain*, **2**:100034. 10.1016/j.nbas.2022.100034

Ramanoël, S., Kauffmann, L., Cousin, E., Dojat, M., & Peyrin, C. (2015). Age-Related Differences in Spatial Frequency Processing during Scene Categorization. *PLOS ONE*, **10**(8), e0134554. 10.1371/journal.pone.0134554

Ramanoël, S., York, E., Le Petit, M., Lagrené, K., Habas, C., & Arleo, A. (2019). Age-Related Differences in Functional and Structural Connectivity in the Spatial Navigation Brain Network. *Frontiers in Neural Circuits*, **13**:69. 10.3389/fncir.2019.00069

Rausch, M., Spengler, F., & Eysel, U. T. (1998). Proprioception acts as the main source of input in human S-I activation experiments: A functional MRI study. *NeuroReport*, **9**(12), pp. 2865–2868. 10.1097/00001756-199808240-00034

Raz, N., Rodrigue, K. M., Head, D., Kennedy, K. M., & Acker, J. D. (2004). Differential aging of the medial temporal lobe: A study of a five-year change. *Neurology*, **62**(3), pp. 433–438. 10.1212/01.WNL.0000106466.09835.46

Reeves, S. (1994). Optimal space-varying regularization in iterative image restoration. *IEEE Transactions on Image Processing*, **3**(3), pp. 319–324. 10.1109/83.287028

Regan, D., Erkelens, C. J., & Collewijn, H. (1986). Visual field defects for vergence eye movements and for stereomotion perception. *Investigative Ophthalmology & Visual Science*, **27**(5), pp. 806–19. Retrieved from `http://www.ncbi.nlm.nih.gov/pubmed/3700030`

Reiser, J. E., Wascher, E., & Arnau, S. (2019). Recording mobile EEG in an outdoor environment reveals cognitive-motor interference dependent on movement complexity. *Scientific Reports*, **9**:13086. 10.1038/s41598-019-49503-4

Rémy, F., Vayssière, N., Saint-Aubert, L., Bacon-Macé, N., Pariente, J., Barbeau, E., & Fabre-Thorpe, M. (2020). Age effects on the neural processing of object-context associations in briefly flashed natural scenes. *Neuropsychologia*, **136**:107264. 10.1016/j.neuropsychologia.2019.107264

Rezec, A., & Dobkins, K. (2004). Attentional weighting: A possible account of visual field asymmetries in visual search? *Spatial Vision*, **17**(4), pp. 269–293. 10.1163/1568568041920203

Richardson, A. E., Powers, M. E., & Bousquet, L. G. (2011). Video game experience predicts virtual, but not real navigation performance. *Computers in Human Behavior*, **27**(1), pp. 552–560. 10.1016/j.chb.2010.10.003

Richer, N., Downey, R. J., Hairston, W. D., Ferris, D. P., & Nordin, A. D. (2020). Motion and Muscle Artifact Removal Validation Using an Electrical Head Phantom, Robotic Motion Platform, and Dual Layer Mobile EEG. *IEEE Transactions on Neural Systems and Rehabilitation Engineering*, **28**(8), pp. 1825–1835. 10.1109/TNSRE.2020.3000971

Richer, N., Downey, R. J., Nordin, A. D., Hairston, W. D., & Ferris, D. P. (2019). Adding neck muscle activity to a head phantom device to validate mobile EEG muscle and motion artifact removal. In *2019 9th International IEEE/EMBS Conference on Neural Engineering (NER)* (pp. 275–278). San Francisco, CA: IEEE. 10.1109/NER.2019.8716959

Robbins, K. A., Touryan, J., Mullen, T. R., Kothe, C. A., & Bigdely-Shamlo, N. (2020). How Sensitive Are EEG Results to Preprocessing Methods: A Benchmarking Study. *IEEE Transactions on Neural Systems and Rehabilitation Engineering*, **28**(5), pp. 1081–1090. 10.1109/TNSRE.2020.2980223

Robinson, E. M., & Wiener, M. (2021). Dissociable neural indices for time and space estimates during virtual distance reproduction. *NeuroImage*, **226**:117607. 10.1016/j.neuroimage.2020.117607

Rodgers, M. K., Sindone, J. A., & Moffat, S. D. (2012). Effects of age on navigation strategy. *Neurobiology of Aging*, **33**(1), pp. 202.e15–202.e22. 10.1016/j.neurobiolaging.2010.07.021

Roeder, L., Boonstra, T. W., & Kerr, G. K. (2020). Corticomuscular control of walking in older people and people with Parkinson's disease. *Scientific Reports*, **10**:2980. 10.1038/s41598-020-59810-w

Roeder, L., Boonstra, T. W., Smith, S. S., & Kerr, G. K. (2018). Dynamics of corticospinal motor control during overground and treadmill walking in humans. *Journal of Neurophysiology*, **120**(3), pp. 1017–1031. 10.1152/jn.00613.2017

Roll, R., Kavounoudias, A., & Roll, J.-P. (2002). Cutaneous afferents from human plantar sole contribute to body posture awareness. *NeuroReport*, **13**(15), pp. 1957–1961. Retrieved from `https://journals.lww.com/neuroreport/Fulltext/2002/10280/Cutaneous{_}afferents{_}from{_}human{_}plantar{_}sole.25.aspx`

Rolls, E. T., & Wirth, S. (2018). Spatial representations in the primate hippocampus, and their functions in memory and navigation. *Progress in Neurobiology*, **171**, pp. 90–113. 10.1016/j.pneurobio.2018.09.004

Romei, V., Brodbeck, V., Michel, C. M., Amedi, A., Pascual-Leone, A., & Thut, G. (2008). Spontaneous Fluctuations in Posterior -Band EEG Activity Reflect Variability in Excitability of Human Visual Areas. *Cerebral Cortex*, **18**(9), pp. 2010–2018. 10.1093/cercor/bhm229

Romei, V., Gross, J., & Thut, G. (2010). On the Role of Prestimulus Alpha Rhythms over Occipito-Parietal Areas in Visual Input Regulation: Correlation or Causation? *Journal of Neuroscience*, **30**(25), pp. 8692–8697. 10.1523/JNEUROSCI.0160-10.2010

Rondina II, R., Olsen, R. K., Li, L., Meltzer, J. A., & Ryan, J. D. (2019). Age-related changes to oscillatory dynamics during maintenance and retrieval in a relational memory task. *PLOS ONE*, **14**(2), e0211851. 10.1371/journal.pone.0211851

Roska, B., & Sahel, J.-A. (2018). Restoring vision. *Nature*, **557**(7705), pp. 359–367. 10.1038/s41586-018-0076-4

Roy, V., Shukla, S., Shukla, P. K., & Rawat, P. (2017). Gaussian Elimination-Based Novel Canonical Correlation Analysis Method for EEG Motion Artifact Removal. *Journal of Healthcare Engineering*, **2017**:9674712. 10.1155/2017/9674712

Rubega, M., Formaggio, E., Di Marco, R., Bertuccelli, M., Tortora, S., Menegatti, E., … Del Felice, A. (2021). Cortical correlates in upright dynamic and static balance in the elderly. *Scientific Reports*, **11**:14132. 10.1038/s41598-021-93556-3

Ruddle, R. A., Volkova, E., & Bülthoff, H. H. (2011b). Walking improves your cognitive map in environments that are large-scale and large in extent. *ACM Transactions on Computer-Human Interaction*, **18**(2), 10. 10.1145/1970378.1970384

Ruddle, R. A., Volkova, E., Mohler, B., & Bülthoff, H. H. (2011a). The effect of landmark and body-based sensory information on route knowledge. *Memory & Cognition*, **39**(4), pp. 686–699. 10.3758/s13421-010-0054-z

Ruggiero, G., D'Errico, O., & Iachini, T. (2016). Development of egocentric and allocentric spatial representations from childhood to elderly age. *Psychological Research*, **80**(2), pp. 259–272. 10.1007/s00426-015-0658-9

Rushworth, M. F., Noonan, M. P., Boorman, E. D., Walton, M. E., & Behrens, T. E. (2011). Frontal Cortex and Reward-Guided Learning and Decision-Making. *Neuron*, **70**(6), pp. 1054–1069. 10.1016/j.neuron.2011.05.014

Russell, S., Bennett, J., Wellman, J. A., Chung, D. C., Yu, Z.-F., Tillman, A., … Maguire, A. M. (2017). Efficacy and safety of voretigene neparvovec (AAV2-hRPE65v2) in patients with RPE65 -mediated inherited retinal dystrophy: a randomised, controlled, open-label, phase 3 trial. *The Lancet*, **390**(10097), pp. 849–860. 10.1016/S0140-6736(17)31868-8

Rutkowski, J. S., Crewther, D. P., & Crewther, S. G. (2002). Normal readers have an upper visual field advantage in change detection. *Clinical & Experimental Ophthalmology*, **30**(3), pp. 227–330. 10.1046/j.1442-9071.2002.00509.x

Sahel, J.-A., Bennett, J., & Roska, B. (2019). Depicting brighter possibilities for treating blindness. *Science Translational Medicine*, **11**(494), eaax2324. 10.1126/scitranslmed.aax2324

Sahel, J.-A., Boulanger-Scemama, E., Pagot, C., Arleo, A., Galluppi, F., Martel, J. N., … Roska, B. (2021). Partial recovery of visual function in a blind patient after optogenetic therapy. *Nature Medicine*, **27**(7), pp. 1223–1229. 10.1038/s41591-021-01351-4

Sahel, J.-A., & Roska, B. (2013). Gene Therapy for Blindness. *Annual Review of Neuroscience*, **36**, pp. 467–488. 10.1146/annurev-neuro-062012-170304

Saleem, A. B. (2020). Two stream hypothesis of visual processing for navigation in mouse. *Current Opinion in Neurobiology*, **64**, pp. 70–78. 10.1016/j.conb.2020.03.009

Salthouse, T. A. (2019). Trajectories of normal cognitive aging. *Psychology and Aging*, **34**(1), pp. 17–24. 10.1037/pag0000288

Sanchez-Garcia, M., Martinez-Cantin, R., & Guerrero, J. (2019). Indoor Scenes Understanding for Visual Prosthesis with Fully Convolutional Networks. In *Proceedings of the 14th International Joint Conference on Computer Vision, Imaging and Computer Graphics Theory and Applications (VISIGRAPP 2019)* (Vol. 5, pp. 218–225). Prague: SciTePress. 10.5220/0007257602180225

Saucier, D. M., Green, S. M., Leason, J., MacFadden, A., Bell, S., & Elias, L. J. (2002). Are sex differences in navigation caused by sexually dimorphic strategies or by differences in the ability to use the strategies? *Behavioral Neuroscience*, **116**(3), pp. 403–410. 10.1037/0735-7044.116.3.403

Schaefer, S. (2014). The ecological approach to cognitive-motor dual-tasking: findings on the effects of expertise and age. *Frontiers in Psychology*, **5**:1167. 10.3389/fpsyg.2014.01167

Schmitz, T. W., Cheng, F. H. T., & De Rosa, E. (2010). Failing to Ignore: Paradoxical Neural Effects of Perceptual Load on Early Attentional Selection in Normal Aging. *Journal of Neuroscience*, **30**(44), pp. 14750–14758. 10.1523/JNEUROSCI.2687-10.2010

Schmitz, T. W., Dixon, M. L., Anderson, A. K., & De Rosa, E. (2014). Distinguishing attentional gain and tuning in young and older adults. *Neurobiology of Aging*, **35**(11), pp. 2514–2525. 10.1016/j.neurobiolaging.2014.04.028

Scholl, H. P. N., Strauss, R. W., Singh, M. S., Dalkara, D., Roska, B., Picaud, S., & Sahel, J.-A. (2016). Emerging therapies for inherited retinal degeneration. *Science Translational Medicine*, **8**(368), 368rv6. 10.1126/scitranslmed.aaf2838

Scrivener, C. L. (2021). When Is Simultaneous Recording Necessary? A Guide for Researchers Considering Combined EEG-fMRI. *Frontiers in Neuroscience*, **15**:636424. 10.3389/fnins.2021.636424

Seeber, M., Scherer, R., Wagner, J., Solis-Escalante, T., & Müller-Putz, G. R. (2014). EEG beta suppression and low gamma modulation are different elements of human upright walking. *Frontiers in Human Neuroscience*, **8**:485. 10.3389/fnhum.2014.00485

Seeber, M., Scherer, R., Wagner, J., Solis-Escalante, T., & Müller-Putz, G. R. (2015). High and low gamma EEG oscillations in central sensorimotor areas are conversely modulated during the human gait cycle. *NeuroImage*, **112**, pp. 318–326. 10.1016/j.neuroimage.2015.03.045

Seiple, W. H., Holopigian, K., Clemens, C., Greenstein, V. C., & Hood, D. C. (2005). The multifocal visual evoked potential: An objective measure of visual fields? *Vision Research*, **45**(9), pp. 1155–1163. 10.1016/j.visres.2004.11.010

Sengupta, A., Chaffiol, A., Macé, E., Caplette, R., Desrosiers, M., Lampič, M., … Duebel, J. (2016). Red-shifted channelrhodopsin stimulation restores light responses in blind mice, macaque retina, and human retina. *EMBO Molecular Medicine*, **8**(11), pp. 1248–1264. 10.15252/emmm.201505699

Sergent, J., Ohta, S., & MacDonald, B. (1992). Functional neuroanatomy of face and object processing. A positron emission tomography study. *Brain*, **115**(1), pp. 15–36. 10.1093/brain/115.1.15

Sharma, K., Jain, N., & Pal, P. K. (2020). Detection of eye closing/opening from EOG and its application in robotic arm control. *Biocybernetics and Biomedical Engineering*, **40**(1), pp. 173–186. 10.1016/j.bbe.2019.10.004

Shine, J. P., Valdés-Herrera, J. P., Hegarty, M., & Wolbers, T. (2016). The Human Retrosplenial Cortex and Thalamus Code Head Direction in a Global Reference Frame. *Journal of Neuroscience*, **36**(24), pp. 6371–6381. 10.1523/JNEUROSCI.1268-15.2016

Shine, J. P., Valdés-Herrera, J. P., Tempelmann, C., & Wolbers, T. (2019). Evidence for allocentric boundary and goal direction information in the human entorhinal cortex and subiculum. *Nature Communications*, **10**:4004. 10.1038/s41467-019-11802-9

Shirazi, S. Y., & Huang, H. J. (2019). More Reliable EEG Electrode Digitizing Methods Can Reduce Source Estimation Uncertainty, but Current Methods Already Accurately Identify Brodmann Areas. *Frontiers in Neuroscience*, **13**:1159. 10.3389/fnins.2019.01159

Shire, D. B., Ellersick, W., Kelly, S. K., Doyle, P., Priplata, A., Drohan, W., … Rizzo, J. F. (2012). ASIC design and data communications for the Boston retinal prosthesis. In *2012 Annual International Conference of the IEEE Engineering in Medicine and Biology Society* (pp. 292–295). San Diego, CA: IEEE. 10.1109/EMBC.2012.6345927

Silson, E. H., Chan, A. W.-Y., Reynolds, R. C., Kravitz, D. J., & Baker, C. I. (2015). A Retinotopic Basis for the Division of High-Level Scene Processing between Lateral and Ventral Human Occipitotemporal Cortex. *Journal of Neuroscience*, **35**(34), pp. 11921–11935. 10.1523/JNEUROSCI.0137-15.2015

Silson, E. H., Steel, A. D., & Baker, C. I. (2016). Scene-Selectivity and Retinotopy in Medial Parietal Cortex. *Frontiers in Human Neuroscience*, **10**:412. 10.3389/fnhum.2016.00412

Silson, E. H., Zeidman, P., Knapen, T., & Baker, C. I. (2021). Representation of Contralateral Visual Space in the Human Hippocampus. *Journal of Neuroscience*, **41**(11), pp. 2382–2392. 10.1523/JNEUROSCI.1990-20.2020

Simon, S. R., Meunier, M., Piettre, L., Berardi, A. M., Segebarth, C. M., & Boussaoud, D. (2002). Spatial attention and memory versus motor preparation: Premotor cortex involvement as revealed by fMRI. *Journal of Neurophysiology*, **88**(4), pp. 2047–2057. 10.1152/jn.2002.88.4.2047

Sipp, A. R., Gwin, J. T., Makeig, S., & Ferris, D. P. (2013). Loss of balance during balance beam walking elicits a multifocal theta band electrocortical response. *Journal of Neurophysiology*, **110**(9), pp. 2050–2060. 10.1152/jn.00744.2012

Skrandies, W. (1987). The Upper and Lower Visual Field of Man: Electrophysiological and Functional Differences. In H. Autrum, D. Ottoson, E. Perl, R. Schmidt, H. Shimazu, & W. Willis (Eds.), *Progress in Sensory Physiology* (Vol. 8, pp. 1–93). Springer, Berlin, Heidelberg. 10.1007/978-3-642-71060-5_1

Smith, E. E., Jonides, J., Koeppe, R. A., Awh, E., Schumacher, E. H., & Minoshima, S. (1995). Spatial versus Object Working Memory: PET Investigations. *Journal of Cognitive Neuroscience*, **7**(3), pp. 337–356. 10.1162/jocn.1995.7.3.337

Smith, S. M. (2002). Fast robust automated brain extraction. *Human Brain Mapping*, **17**(3), pp. 143–155. 10.1002/hbm.10062

Sneider, J. T., Cohen-Gilbert, J. E., Hamilton, D. A., Stein, E. R., Golan, N., Oot, E. N., … Silveri, M. M. (2018). Adolescent Hippocampal and Prefrontal Brain Activation During Performance of the Virtual Morris Water Task. *Frontiers in Human Neuroscience*, **12**:238. 10.3389/fnhum.2018.00238

Snider, J., Plank, M., Lynch, G., Halgren, E., & Poizner, H. (2013). Human Cortical during Free Exploration Encodes Space and Predicts Subsequent Memory. *Journal of Neuroscience*, **33**(38), pp. 15056–15068. 10.1523/JNEUROSCI.0268-13.2013

Snyder, K. L., Kline, J. E., Huang, H. J., & Ferris, D. P. (2015). Independent Component Analysis of Gait-Related Movement Artifact Recorded using EEG Electrodes during Treadmill Walking. *Frontiers in Human Neuroscience*, **9**:639. 10.3389/fnhum.2015.00639

Snytte, J., Fenerci, C., Rajagopal, S., Beaudoin, C., Hooper, K., Sheldon, S., … Rajah, M. N. (2022). Volume of the posterior hippocampus mediates age-related differences in spatial context memory and is correlated with increased activity in lateral frontal, parietal and occipital regions in healthy aging. *NeuroImage*, **254**:119164. 10.1016/j.neuroimage.2022.119164

Song, J., Smaoui, N., Ayyagari, R., Stiles, D., Benhamed, S., MacDonald, I. M., … Wang, X. (2011). High-Throughput Retina-Array for Screening 93 Genes Involved in Inherited Retinal Dystrophy. *Investigative Opthalmology & Visual Science*, **52**(12), 9053. 10.1167/iovs.11-7978

Sowell, E. R., Peterson, B. S., Thompson, P. M., Welcome, S. E., Henkenius, A. L., & Toga, A. W. (2003). Mapping cortical change across the human life span. *Nature Neuroscience*, **6**(3), pp. 309–315. 10.1038/nn1008

Sperandio, I., Savazzi, S., Gregory, R. L., & Marzi, C. A. (2009). Visual Reaction Time and Size Constancy. *Perception*, **38**(11), pp. 1601–1609. 10.1068/p6421

Sperry, R. (1974). Lateral specialization in the surgically separated hemispheres. *The Neurosciences Third study program*, pp. 5–19. Retrieved from `https://cir.nii.ac.jp/crid/1573950399122363264`

Spiers, H. J., & Barry, C. (2015). Neural systems supporting navigation. *Current Opinion in Behavioral Sciences*, **1**, pp. 47–55. 10.1016/j.cobeha.2014.08.005

Spiers, H. J., & Gilbert, S. J. (2015). Solving the detour problem in navigation: a model of prefrontal and hippocampal interactions. *Frontiers in Human Neuroscience*, **9**:125. 10.3389/fnhum.2015.00125

Spiers, H. J., & Maguire, E. A. (2006). Thoughts, behaviour, and brain dynamics during navigation in the real world. *NeuroImage*, **31**(4), pp. 1826–1840. 10.1016/j.neuroimage.2006.01.037

Srokova, S., Hill, P. F., Koen, J. D., King, D. R., & Rugg, M. D. (2020). Neural Differentiation is Moderated by Age in Scene-Selective, But Not Face-Selective, Cortical Regions. *eneuro*, **7**(3), pp. ENEURO.0142–20.2020. 10.1523/ENEURO.0142-20.2020

Standardization of Uveitis Nomenclature (SUN) working group. (2005). Standardization of Uveitis Nomenclature for Reporting Clinical Data. Results of the First International Workshop. *American Journal of Ophthalmology*, **140**(3), pp. 509–516. 10.1016/j.ajo.2005.03.057

Stangl, M., Achtzehn, J., Huber, K., Dietrich, C., Tempelmann, C., & Wolbers, T. (2018). Compromised Grid-Cell-like Representations in Old Age as a Key Mechanism to Explain Age-Related Navigational Deficits. *Current Biology*, **28**(7), pp. 1108–1115.e6. 10.1016/j.cub.2018.02.038

Stangl, M., Maoz, S. L., & Suthana, N. (2023). Mobile cognition: imaging the human brain in the real world'. *Nature Reviews Neuroscience*, **24**(6), pp. 347–362. 10.1038/s41583-023-00692-y

Stangl, M., Topalovic, U., Inman, C. S., Hiller, S., Villaroman, D., Aghajan, Z. M., … Suthana, N. (2021). Boundary-anchored neural mechanisms of location-encoding for self and others. *Nature*, **589**(7842), pp. 420–425. 10.1038/s41586-020-03073-y

Stankiewicz, B. J., & Kalia, A. A. (2007). Acquistion of structural versus object landmark knowledge. *Journal of Experimental Psychology: Human Perception and Performance*, **33**(2), pp. 378–390. 10.1037/0096-1523.33.2.378

Starrett, M. J., & Ekstrom, A. D. (2018). Perspective: Assessing the Flexible Acquisition, Integration, and Deployment of Human Spatial Representations and Information. *Frontiers in Human Neuroscience*, **12**:281. 10.3389/fnhum.2018.00281

Steel, A. D., Silson, E. H., Garcia, B. D., & Robertson, C. E. (2023). A retinotopic code structures the interaction between perception and memory systems. *bioRxiv*:540807. 10.1101/2023.05.15.540807

Stefanucci, J. K., Brickler, D., Finney, H. C., Wilson, E., Drew, T., & Creem-Regehr, S. H. (2022). Effects of simulated augmented reality cueing in a virtual navigation task. *Frontiers in Virtual Reality*, **3**:971310. 10.3389/frvir.2022.971310

Stewart, E. E. M., Valsecchi, M., & Schütz, A. C. (2020). A review of interactions between peripheral and foveal vision. *Journal of Vision*, **20**(12), 2. 10.1167/jov.20.12.2

Stone, J. L., Barlow, W. E., Humayun, M. S., de Juan Jr, E., & Milam, A. H. (1992). Morphometric Analysis of Macular Photoreceptors and Ganglion Cells in Retinas With Retinitis Pigmentosa. *Archives of Ophthalmology*, **110**(11), 1634. 10.1001/archopht.1992.01080230134038

Streifler, M., & Landau, J. (1955). Electrical Brain Potentials in Retinitis Pigmentosa and Familial Hemeralopia. *Ophthalmologica*, **130**(2), pp. 116–127. 10.1159/000302655

Strube, A., Rose, M., Fazeli, S., & Büchel, C. (2021). Alpha-to-beta- and gamma-band activity reflect predictive coding in affective visual processing. *Scientific Reports*, **11**:23492. 10.1038/s41598-021-02939-z

Strunk, J., James, T., Arndt, J., & Duarte, A. (2017). Age-related changes in neural oscillations supporting context memory retrieval. *Cortex*, **91**, pp. 40–55. 10.1016/j.cortex.2017.01.020

Sturz, B. R., Kilday, Z. A., & Bodily, K. D. (2013). Does constraining field of view prevent extraction of geometric cues for humans during virtual-environment reorientation? *Journal of Experimental Psychology: Animal Behavior Processes*, **39**(4), pp. 390–396. 10.1037/a0032543

Sugovic, M., & Witt, J. K. (2013). An older view on distance perception: older adults perceive walkable extents as farther. *Experimental Brain Research*, **226**(3), pp. 383–391. 10.1007/s00221-013-3447-y

Sulpizio, V., Committeri, G., Lambrey, S., Berthoz, A., & Galati, G. (2013). Selective role of lingual/parahippocampal gyrus and retrosplenial complex in spatial memory across viewpoint changes relative to the environmental reference frame. *Behavioural Brain Research*, **242**, pp. 62–75. 10.1016/j.bbr.2012.12.031

Sulpizio, V., Galati, G., Fattori, P., Galletti, C., & Pitzalis, S. (2020). A common neural substrate for processing scenes and egomotion-compatible visual motion. *Brain Structure and Function*, **225**(7), pp. 2091–2110. 10.1007/s00429-020-02112-8

Sun, L., Frank, S. M., Epstein, R. A., & Tse, P. U. (2021). The parahippocampal place area and hippocampus encode the spatial significance of landmark objects. *NeuroImage*, **236**:118081. 10.1016/j.neuroimage.2021.118081

Sur, S., & Sinha, V. (2009). Event-related potential: An overview. *Industrial Psychiatry Journal*, **18**(1), 70. 10.4103/0972-6748.57865

Sutton, S., Braren, M., Zubin, J., & John, E. R. (1965). Evoked-Potential Correlates of Stimulus Uncertainty. *Science*, **150**(3700), pp. 1187–1188. 10.1126/science.150.3700.1187

Suzuki, S., Kamps, F. S., Dilks, D. D., & Treadway, M. T. (2021). Two scene navigation systems dissociated by deliberate versus automatic processing. *Cortex*, **140**, pp. 199–209. 10.1016/j.cortex.2021.03.027

Symeonidou, E.-R., Nordin, A. D., Hairston, W. D., & Ferris, D. P. (2018). Effects of Cable Sway, Electrode Surface Area, and Electrode Mass on Electroencephalography Signal Quality during Motion. *Sensors*, **18**(4), 1073. 10.3390/s18041073

Taberna, G. A., Marino, M., Ganzetti, M., & Mantini, D. (2019). Spatial localization of EEG electrodes using 3D scanning. *Journal of Neural Engineering*, **16**(2), 026020. 10.1088/1741-2552/aafdd1

Taillade, M., N'Kaoua, B., & Sauzéon, H. (2016). Age-Related Differences and Cognitive Correlates of Self-Reported and Direct Navigation Performance: The Effect of Real and Virtual Test Conditions Manipulation. *Frontiers in Psychology*, **6**:2034. 10.3389/fpsyg.2015.02034

Taube, J. S., Valerio, S., & Yoder, R. M. (2013). Is Navigation in Virtual Reality with fMRI Really Navigation? *Journal of Cognitive Neuroscience*, **25**(7), pp. 1008–1019. 10.1162/jocn_a_00386

Thorn, J. T., Migliorini, E., & Ghezzi, D. (2020). Virtual reality simulation of epiretinal stimulation highlights the relevance of the visual angle in prosthetic vision. *Journal of Neural Engineering*, **17**(5), 056019. 10.1088/1741-2552/abb5bc

Thut, G., Nietzel, A., Brandt, S. A., & Pascual-Leone, A. (2006). α-Band electroencephalographic activity over occipital cortex indexes visuospatial attention bias and predicts visual target detection. *Journal of Neuroscience*, **26**(37), pp. 9494–9502. 10.1523/JNEUROSCI.0875-06.2006

Tommasi, L., Chiandetti, C., Pecchia, T., Sovrano, V. A., & Vallortigara, G. (2012). From natural geometry to spatial cognition. *Neuroscience & Biobehavioral Reviews*, **36**(2), pp. 799–824. 10.1016/j.neubiorev.2011.12.007

Torralba, A., & Oliva, A. (2003). Statistics of natural image categories. *Network: Computation in Neural Systems*, **14**(3), pp. 391–412. 10.1088/0954-898X_14_3_302

Tosoni, A., Altomare, E. C., Brunetti, M., Croce, P., Zappasodi, F., & Committeri, G. (2021). Sensory-Motor Modulations of EEG Event-Related Potentials Reflect Walking-Related Macro-Affordances. *Brain Sciences*, **11**(11), 1506. 10.3390/brainsci11111506

Tripathi, S., Verghese, J., & Blumen, H. M. (2019). Gray matter volume covariance networks associated with dual-task cost during walking-while-talking. *Human Brain Mapping*, **40**(7), pp. 2229–2240. 10.1002/hbm.24520

Trusko, B., Thorne, J., Jabs, D., Belfort, R., Dick, A., Gangaputra, S., … Rosenbaum, J. (2013). The Standardization of Uveitis Nomenclature (SUN) Project. *Methods of Information in Medicine*, **52**(03), pp. 259–265. 10.3414/ME12-01-0063

Tsang, P. S. (2013). Ageing and attentional control. *Quarterly Journal of Experimental Psychology*, **66**(8), pp. 1517–1547. 10.1080/17470218.2012.752019

Tuckute, G., Hansen, S. T., Kjaer, T. W., & Hansen, L. K. (2021). Real-Time Decoding of Attentional States Using Closed-Loop EEG Neurofeedback. *Neural Computation*, **33**(4), pp. 967–1004. 10.1162/neco_a_01363

Uhlhaas, P. J., Roux, F., Rodriguez, E., Rotarska-Jagiela, A., & Singer, W. (2010). Neural synchrony and the development of cortical networks. *Trends in Cognitive Sciences*, **14**(2), pp. 72–80. 10.1016/j.tics.2009.12.002

Uiga, L., Cheng, K. C., Wilson, M. R., Masters, R. S., & Capio, C. M. (2015). Acquiring visual information for locomotion by older adults: A systematic review. *Ageing Research Reviews*, **20**, pp. 24–34. 10.1016/j.arr.2014.12.005

Uyar, F., Shomstein, S., Greenberg, A. S., & Behrmann, M. (2016). Retinotopic information interacts with category selectivity in human ventral cortex. *Neuropsychologia*, **92**, pp. 90–106. 10.1016/j.neuropsychologia.2016.05.022

Vagni, P., Airaghi Leccardi, M. J. I., Vila, C.-H., Zollinger, E. G., Sherafatipour, G., Wolfensberger, T. J., & Ghezzi, D. (2022). POLYRETINA restores light responses in vivo in blind Göttingen minipigs. *Nature Communications*, **13**:3678. 10.1038/s41467-022-31180-z

Vandenberg, S. G., & Kuse, A. R. (1978). Mental Rotations, a Group Test of Three-Dimensional Spatial Visualization. *Perceptual and Motor Skills*, **47**(2), pp. 599–604. 10.2466/pms.1978.47.2.599

van der Ham, I. J. M., & Claessen, M. H. G. (2020). How age relates to spatial navigation performance: Functional and methodological considerations. *Ageing Research Reviews*, **58**:101020. 10.1016/j.arr.2020.101020

van der Linden, M., Berkers, R. M., Morris, R. G., & Fernández, G. (2017). Angular Gyrus Involvement at Encoding and Retrieval Is Associated with Durable But Less Specific Memories. *Journal of Neuroscience*, **37**(39), pp. 9474–9485. 10.1523/JNEUROSCI.3603-16.2017

Vandewalle, G., van Ackeren, M. J., Daneault, V., Hull, J. T., Albouy, G., Lepore, F., … Collignon, O. (2018). Light modulates oscillatory alpha activity in the occipital cortex of totally visually blind individuals with intact non-image-forming photoreception. *Scientific Reports*, **8**:16968. 10.1038/s41598-018-35400-9

van Dijk, H., Schoffelen, J.-M., Oostenveld, R., & Jensen, O. (2008). Prestimulus Oscillatory Activity in the Alpha Band Predicts Visual Discrimination Ability. *Journal of Neuroscience*, **28**(8), pp. 1816–1823. 10.1523/JNEUROSCI.1853-07.2008

Vann, S. D., Aggleton, J. P., & Maguire, E. A. (2009). What does the retrosplenial cortex do? *Nature Reviews Neuroscience*, **10**(11), pp. 792–802. 10.1038/nrn2733

Vanni, S., Revonsuo, A., & Hari, R. (1997). Modulation of the Parieto-Occipital Alpha Rhythm during Object Detection. *Journal of Neuroscience*, **17**(18), pp. 7141–7147. 10.1523/JNEUROSCI.17-18-07141.1997

Varela, F., Lachaux, J.-P., Rodriguez, E., & Martinerie, J. (2001). The brainweb: Phase synchronization and large-scale integration. *Nature Reviews Neuroscience*, **2**(4), pp. 229–239. 10.1038/35067550

Vass, L. K., Copara, M. S., Seyal, M., Shahlaie, K., Farias, S. T., Shen, P. Y., & Ekstrom, A. D. (2016). Oscillations Go the Distance: Low-Frequency Human Hippocampal Oscillations Code Spatial Distance in the Absence of Sensory Cues during Teleportation. *Neuron*, **89**(6), pp. 1180–1186. 10.1016/j.neuron.2016.01.045

Vass, L. K., & Epstein, R. A. (2013). Abstract Representations of Location and Facing Direction in the Human Brain. *Journal of Neuroscience*, **33**(14), pp. 6133–6142. 10.1523/JNEUROSCI.3873-12.2013

Võ, M. L., & Wolfe, J. M. (2013). Differential Electrophysiological Signatures of Semantic and Syntactic Scene Processing. *Psychological Science*, **24**(9), pp. 1816–1823. 10.1177/0956797613476955

Vogel, E. K., & Luck, S. J. (2000). The visual N1 component as an index of a discrimination process. *Psychophysiology*, **37**(2), pp. 190–203. 10.1111/1469-8986.3720190

Vortmann, L.-M., Kroll, F., & Putze, F. (2019). EEG-Based Classification of Internally- and Externally-Directed Attention in an Augmented Reality Paradigm. *Frontiers in Human Neuroscience*, **13**:348. 10.3389/fnhum.2019.00348

Voyer, D., Voyer, S. D., & Bryden, M. P. (1995). Magnitude of sex differences in spatial abilities: A meta-analysis and consideration of critical variables. *Psychological Bulletin*, **117**(2), pp. 250–270. 10.1037/0033-2909.117.2.250

Vu, T. A., Fenwick, E. K., Gan, A. T., Man, R. E., Tan, B. K., Gupta, P., ... Lamoureux, E. L. (2021). The Bidirectional Relationship between Vision and Cognition. *Ophthalmology*, **128**(7), pp. 981–992. 10.1016/j.ophtha.2020.12.010

Wagner, J., Makeig, S., Gola, M., Neuper, C., & Müller-Putz, G. R. (2016). Distinct β Band Oscillatory Networks Subserving Motor and Cognitive Control during Gait Adaptation. *Journal of Neuroscience*, **36**(7), pp. 2212–2226. 10.1523/JNEUROSCI.3543-15.2016

Wagner, J., Solis-Escalante, T., Grieshofer, P., Neuper, C., Müller-Putz, G. R., & Scherer, R. (2012). Level of participation in robotic-assisted treadmill walking modulates midline sensorimotor EEG rhythms in able-bodied subjects. *NeuroImage*, **63**(3), pp. 1203–1211. 10.1016/j.neuroimage.2012.08.019

Wagner, J., Solis-Escalante, T., Scherer, R., Neuper, C., & Müller-Putz, G. R. (2014). It's how you get there: walking down a virtual alley activates premotor and parietal areas. *Frontiers in Human Neuroscience*, **8**:93. 10.3389/fnhum.2014.00093

Wagshul, M. E., Lucas, M., Ye, K., Izzetoglu, M., & Holtzer, R. (2019). Multi-modal neuroimaging of dual-task walking: Structural MRI and fNIRS analysis reveals prefrontal grey matter volume moderation of brain activation in older adults. *NeuroImage*, **189**, pp. 745–754. 10.1016/j.neuroimage.2019.01.045

Walker, M. E., Vibell, J. F., Dewald, A. D., & Sinnett, S. (2022). Ageing and selective inhibition of irrelevant information in an attention-demanding rapid serial visual presentation task. *Brain and Neuroscience Advances*, **6**:239821282110734. 10.1177/23982128211073427

Waller, D., & Lippa, Y. (2007). Landmarks as beacons and associative cues: Their role in route learning. *Memory & Cognition*, **35**(5), pp. 910–924. 10.3758/BF03193465

Wandell, B. A., Brewer, A. A., & Dougherty, R. F. (2005). Visual field map clusters in human cortex. *Philosophical Transactions of the Royal Society B: Biological Sciences*, **360**(1456), pp. 693–707. 10.1098/rstb.2005.1628

Wandell, B. A., Dumoulin, S. O., & Brewer, A. A. (2007). Visual Field Maps in Human Cortex. *Neuron*, **56**(2), pp. 366–383. 10.1016/j.neuron.2007.10.012

Wang, J., Zhu, H., Liu, J., Li, H., Han, Y., Zhou, R., & Zhang, Y. (2021). The application of computer vision to visual prosthesis. *Artificial Organs*, **45**(10), pp. 1141–1154. 10.1111/aor.14022

Warren, W. H., Blackwell, A. W., & Morris, M. W. (1989). Age Differences in Perceiving the Direction of Self-Motion From Optical Flow. *Journal of Gerontology*, **44**(5), pp. P147–P153. 10.1093/geronj/44.5.P147

Warren, W. H., Rothman, D. B., Schnapp, B. H., & Ericson, J. D. (2017). Wormholes in virtual space: From cognitive maps to cognitive graphs. *Cognition*, **166**, pp. 152–163. 10.1016/j.cognition.2017.05.020

Watrous, A. J., Fried, I., & Ekstrom, A. D. (2011). Behavioral correlates of human hippocampal delta and theta oscillations during navigation. *Journal of Neurophysiology*, **105**(4), pp. 1747–1755. 10.1152/jn.00921.2010

Wei, E. X., Anson, E. R., Resnick, S. M., & Agrawal, Y. (2020). Psychometric Tests and Spatial Navigation: Data From the Baltimore Longitudinal Study of Aging. *Frontiers in Neurology*, **11**:484. 10.3389/fneur.2020.00484

Weiland, J. D., Cho, A. K., & Humayun, M. S. (2011). Retinal Prostheses: Current Clinical Results and Future Needs. *Ophthalmology*, **118**(11), pp. 2227–2237. 10.1016/j.ophtha.2011.08.042

Weiland, J. D., Walston, S. T., & Humayun, M. S. (2016). Electrical Stimulation of the Retina to Produce Artificial Vision. *Annual Review of Vision Science*, **2**, pp. 273–294. 10.1146/annurev-vision-111815-114425

Weintraub, S., & Marsel Mesulam, M. (1987). Right Cerebral Dominance in Spatial Attention. *Archives of Neurology*, **44**(6), pp. 621–625. 10.1001/archneur.1987.00520180043014

Weitz, A. C., Nanduri, D., Behrend, M. R., Gonzalez-Calle, A., Greenberg, R. J., Humayun, M. S., … Weiland, J. D. (2015). Improving the spatial resolution of epiretinal implants by increasing stimulus pulse duration. *Science Translational Medicine*, **7**(318), 318ra203. 10.1126/scitranslmed.aac4877

Wenczel, F., Hepperle, L., & von Stülpnagel, R. (2017). Gaze behavior during incidental and intentional navigation in an outdoor environment. *Spatial Cognition & Computation*, **17**(1-2), pp. 121–142. 10.1080/13875868.2016.1226838

White, D. J., Congedo, M., Ciorciari, J., & Silberstein, R. B. (2012). Brain Oscillatory Activity during Spatial Navigation: Theta and Gamma Activity Link Medial Temporal and Parietal Regions. *Journal of Cognitive Neuroscience*, **24**(3), pp. 686–697. 10.1162/jocn_a_00098

Wiener, J. M., Berthoz, A., & Wolbers, T. (2011). Dissociable cognitive mechanisms underlying human path integration. *Experimental Brain Research*, **208**(1), pp. 61–71. 10.1007/s00221-010-2460-7

Wiener, J. M., Carroll, D., Moeller, S., Bibi, I., Ivanova, D., Allen, P., & Wolbers, T. (2020). A novel virtual-reality-based route-learning test suite: Assessing the effects of cognitive aging on navigation. *Behavior Research Methods*, **52**(2), pp. 630–640. 10.3758/s13428-019-01264-8

Wiener, J. M., de Condappa, O., Harris, M. A., & Wolbers, T. (2013). Maladaptive Bias for Extrahippocampal Navigation Strategies in Aging Humans. *Journal of Neuroscience*, **33**(14), pp. 6012–6017. 10.1523/JNEUROSCI.0717-12.2013

Wiener, J. M., Kmecova, H., & de Condappa, O. (2012). Route repetition and route retracing: effects of cognitive aging. *Frontiers in Aging Neuroscience*, **4**:7. 10.3389/fnagi.2012.00007

Wilkniss, S. M., Jones, M. G., Korol, D. L., Gold, P. E., & Manning, C. A. (1997). Age-related differences in an ecologically based study of route learning. *Psychology and Aging*, **12**(2), pp. 372–375. 10.1037/0882-7974.12.2.372

Wolbers, T., & Büchel, C. (2005). Dissociable Retrosplenial and Hippocampal Contributions to Successful Formation of Survey Representations. *Journal of Neuroscience*, **25**(13), pp. 3333–3340. 10.1523/JNEUROSCI.4705-04.2005

Wolbers, T., & Hegarty, M. (2010). What determines our navigational abilities? *Trends in Cognitive Sciences*, **14**(3), pp. 138–146. 10.1016/j.tics.2010.01.001

Wolbers, T., Weiller, C., & Büchel, C. (2004). Neural foundations of emerging route knowledge in complex spatial environments. *Cognitive Brain Research*, **21**(3), pp. 401–411. 10.1016/j.cogbrainres.2004.06.013

Womelsdorf, T., Vinck, M., Leung, L. S., & Everling, S. (2010). Selective Theta-Synchronization of Choice-Relevant Information Subserves Goal-Directed Behavior. *Frontiers in Human Neuroscience*, **4**:210. 10.3389/fnhum.2010.00210

World Health Organization (WHO) team. (2019). *World report on vision* (Tech. Rep.). Geneva. Retrieved from `https://www.who.int/publications-detail/world-report-on-vision`

Wurtz, R. H., & Kandel, E. R. (2000). Central Visual Pathways. In E. R. Kandel, J. H. Schwartz, & T. M. Jessel (Eds.), *Principles of Neural Science, Fourth Edition* (pp. 523–547). McGraw-Hill.

Wyart, V., & Tallon-Baudry, C. (2008). Neural Dissociation between Visual Awareness and Spatial Attention. *Journal of Neuroscience*, **28**(10), pp. 2667–2679. 10.1523/JNEUROSCI.4748-07.2008

Yeung, N., & Summerfield, C. (2012). Metacognition in human decision-making: confidence and error monitoring. *Philosophical Transactions of the Royal Society B: Biological Sciences*, **367**(1594), pp. 1310–1321. 10.1098/rstb.2011.0416

Yogev-Seligmann, G., Hausdorff, J. M., & Giladi, N. (2008). The role of executive function and attention in gait. *Movement Disorders*, **23**(3), pp. 329–342. 10.1002/mds.21720

Yue, L., Weiland, J. D., Roska, B., & Humayun, M. S. (2016). Retinal stimulation strategies to restore vision: Fundamentals and systems. *Progress in Retinal and Eye Research*, **53**, pp. 21–47. 10.1016/j.preteyeres.2016.05.002

Yuval-Greenberg, S., Tomer, O., Keren, A. S., Nelken, I., & Deouell, L. Y. (2008). Transient Induced Gamma-Band Response in EEG as a Manifestation of Miniature Saccades. *Neuron*, **58**(3), pp. 429–441. 10.1016/j.neuron.2008.03.027

Zabcikova, M., Koudelkova, Z., Jasek, R., & Lorenzo Navarro, J. J. (2022). Recent advances and current trends in brain-computer interface research and their applications. *International Journal of Developmental Neuroscience*, **82**(2), pp. 107–123. 10.1002/jdn.10166

Zaitsev, M., Maclaren, J., & Herbst, M. (2015). Motion artifacts in MRI: A complex problem with many partial solutions. *Journal of Magnetic Resonance Imaging*, **42**(4), pp. 887–901. 10.1002/jmri.24850

Zhao, M., Bonassi, G., Guarnieri, R., Pelosin, E., Nieuwboer, A., Avanzino, L., & Mantini, D. (2021). A multi-step blind source separation approach for the attenuation of artifacts in mobile high-density electroencephalography data. *Journal of Neural Engineering*, **18**(6), 066041. 10.1088/1741-2552/ac4084

Zhao, Y., Stefanucci, J. K., Creem-Regehr, S. H., & Bodenheimer, B. (2023). Evaluating Augmented Reality Landmark Cues and Frame of Reference Displays with Virtual Reality. *IEEE Transactions on Visualization and Computer Graphics*, **29**(5), pp. 2710–2720. 10.1109/TVCG.2023.3247078

Zhong, J. Y., & Moffat, S. D. (2016). Age-Related Differences in Associative Learning of Landmarks and Heading Directions in a Virtual Navigation Task. *Frontiers in Aging Neuroscience*, **8**:122. 10.3389/fnagi.2016.00122

Zhong, J. Y., & Moffat, S. D. (2018). Extrahippocampal Contributions to Age-Related Changes in Spatial Navigation Ability. *Frontiers in Human Neuroscience*, **12**:272. 10.3389/fnhum.2018.00272

Zhou, R., Belge, T., & Wolbers, T. (2023). Reaching the Goal: Superior Navigators in Late Adulthood Provide a Novel Perspective into Successful Cognitive Aging. *Topics in Cognitive Science*, **15**(1), pp. 15–45. 10.1111/tops.12608

Zink, R., Hunyadi, B., Van Huffel, S., & De Vos, M. (2016). Mobile EEG on the bike: Disentangling attentional and physical contributions to auditory attention tasks. *Journal of Neural Engineering*, **13**(4), 046017. 10.1088/1741-2560/13/4/046017

Zrenner, E. (2002). Will Retinal Implants Restore Vision? *Science*, **295**(5557), pp. 1022–1025. 10.1126/science.1067996

Zumer, J. M., Scheeringa, R., Schoffelen, J.-M., Norris, D. G., & Jensen, O. (2014). Occipital Alpha Activity during Stimulus Processing Gates the Information Flow to Object-Selective Cortex. *PLOS Biology*, **12**(10), e1001965. 10.1371/journal.pbio.1001965

SUMMARY

In everyday life, the brain relies on all sensory information to interpret and interact with its environment. However, current tools for studying brain activity require the immobility of the participant, calling into question their conclusions outside the laboratory. This thesis therefore proposes a brain imaging approach that allows moving during the experiment, to study the influence of mobility on visual functions. The first area of application is the perception of visual cues used for spatial orientation during healthy aging. Indeed, the age-related decline of the ability to locate oneself and find one's way around greatly reduces the autonomy of older adults. This new approach is also being used in a clinical setting to quantify the effects of vision restoration therapy on the brain in everyday activities. This is a key step in guaranteeing the long-term success of such therapies.

Au quotidien, le cerveau s'appuie sur l'ensemble des informations sensorielles pour interpréter et interagir avec son environnement. Pourtant, les outils d'étude de l'activité cérébrale actuels requièrent l'immobilité du participant, remettant en cause leurs conclusions en dehors du laboratoire. Cette thèse propose donc une approche d'imagerie cérébrale qui autorise la mobilité pendant l'expérience, pour étudier son influence sur les fonctions visuelles. Le premier domaine d'application est la perception des repères visuels servant à l'orientation dans l'espace au cours du vieillissement sain. En effet, le déclin avec l'âge de la capacité à se situer et à trouver son chemin réduit fortement l'autonomie des seniors. Cette nouvelle approche est aussi utilisée dans un cadre clinique pour quantifier, dans des activités quotidiennes, les effets, sur le cerveau, d'une thérapie de restauration de la vision. C'est une étape clé pour garantir le succès à long terme de ces thérapies.